NASA CONTRACTOR REPORT

NASA CR-2485

NASA CR-2485

EFFECTS OF SELECTED DESIGN VARIABLES ON THREE RAMP, EXTERNAL COMPRESSION INLET PERFORMANCE

by James H. Kamman and Charles L. Hall

Prepared by
MCDONNELL AIRCRAFT COMPANY
St. Louis, Mo.
for Ames Research Center

NATIONAL AERONAUTICS AND SPACE ADMINISTRATION • WASHINGTON, D. C. • JANUARY 1975

1. Report No.	2. Government Accession No.	3. Recipient's Catalog No.
NASA CR - 2485		

4. Title and Subtitle	5. Report Date
EFFECTS OF SELECTED DESIGN VARIABLES ON THREE RAMP, EXTERNAL COMPRESSION INLET PERFORMANCE	January 1975
	6. Performing Organization Code
7. Author(s)	8. Performing Organization Report No.
James H. Kamman and Charles L. Hall	
	10. Work Unit No.
9. Performing Organization Name and Address	
McDonnell Aircraft Company St. Louis, Missouri	11. Contract or Grant No. NAS 2-7012
	13. Type of Report and Period Covered Contractor Report
12. Sponsoring Agency Name and Address	
National Aeronautics and Space Administration Washington, D. C.	14. Sponsoring Agency Code

15. Supplementary Notes

16. Abstract

Two inlet performance tests and one inlet/airframe drag test were conducted in 1969 at the NASA-Ames Research Center by McDonnell Aircraft Company. The basic inlet system was two-dimensional, three ramp (overhead), external compression, with variable capture area. The data from these tests have been analyzed to show the effects of selected design variables on the performance of this type of inlet system. The inlet design variables investigated include inlet bleed, bypass, operating mass flow ratio, inlet geometry, and variable capture area.

17. Key Words (Suggested by Author(s))

Inlet Design
Boundary-Layer Bleed Systems
Bypass Systems
Total Pressure Recovery
Inlet/Airframe Drag, Lift
Engine/Face Distortion

18. Distribution Statement

Unclassified-Unlimited

CAT. 28

19. Security Classif. (of this report)	20. Security Classif. (of this page)	21. No. of Pages	22. Price*
Unclassified	Unclassified	276	$6.50

*For sale by the National Technical Information Service, Springfield, Virginia 22151

SUMMARY

The importance of designing inlets to achieve the maximum possible performance has increased as the performance requirements of supersonic air superiority fighter aircraft have increased. While the basic inlet design can be established using primarily analytical techniques, experimental investigations of the major inlet design variables are required to ensure a high level of performance. The objective of this program was to evaluate performance data for selected design variables on a two-dimensional, overhead, three ramp, external compression inlet system with variable capture area. These data were obtained from inlet tests that were primarily directed toward the development of a high performance inlet for a specific aircraft and mission application. The development test program consisted of two inlet performance tests and one inlet/airframe drag test which were conducted at the NASA Ames Research Center by McDonnell Aircraft Company (MCAIR) in 1969.

Two types of variable capture area inlets were tested. On one type, the capture area was varied by rotating only the first ramp, and the associated portion of the outboard sideplate, about the first ramp hinge line. On the other type, the capture area was varied by rotating the entire three ramp system and sideplates about a hinge point near the cowl lip.

The inlet performance data were analyzed to determine the effects of selected inlet design variables on the engine face pressure recovery, turbulence, and steady state distortion over a Mach number range of 0.9 to 2.5 and over an angle of attack range of -4° to 26°. The performance tests were conducted at Reynolds numbers of 7.38×10^6 per meter (2.25×10^6 per foot) for transonic conditions and 6.56×10^6 per meter (2.0×10^6 per foot) for supersonic conditions using a 16.7 percent scale model. In addition, the effects of varying the ramp angles, angle of attack, and operating mass flow ratio on net propulsive force were evaluated. The net propulsive force changes include changes in engine net thrust resulting from measured variations in pressure recovery and analytically determined changes in spillage drag, bleed drag, and bypass drag.

The inlet/airframe drag data were analyzed to determine the effects of variation in inlet capture area on inlet and aircraft drag over a Mach number range of 0.6 to 1.2 and over an angle of attack range of -3° to 20°. The drag test was conducted at Reynolds numbers values of 5.84, 7.22, and 7.58×10^6 per meter (1.78, 2.20, and 2.31×10^6 per foot) at Mach numbers of 0.6, 0.9 and 1.2, respectively, using a 7.5 percent scale model.

The most significant results of the analyses are:

(a) Throat slot bleed increases inlet performance at supersonic flight conditions even when the boundary layer upstream of the throat is completely removed by ramp bleed.

(b) The inlet operating point for maximum net propulsive force above Mach 1.6 occurs between 95 and 100 percent of the critical mass flow ratio.

(c) The second and third ramp angles required for maximum net propulsive force at Mach 2.2 are lower than the ramp angles providing maximum recovery because of reduced spillage drag associated with the lower angles.

(d) Reducing the second and third ramp angles as a function of angle of attack to prevent shock detachment from the third ramp increases the net propulsive force.

(e) An inlet utilizing a rotating three ramp system maintains a high level of performance over a wide angle of attack range at Mach 2.2, whereas a fixed geometry inlet provides high performance only over a small angle of attack range.

(f) A variable capture area inlet utilizing a rotating ramp system which varies with angle of attack causes lower spillage drag at transonic conditions than an inlet which has a capture area fixed with angle of attack.

TABLE OF CONTENTS

INTRODUCTION

Advanced air superiority fighter aircraft require inlets that provide high performance in terms of pressure recovery, pressure distortion, drag, and operating stability, over a wide range of speed and maneuvering conditions. In the initial development stages of such an inlet, McDonnell Aircraft Company built and tested models of two different two-dimensional overhead, three ramp, external compression configurations. Both configurations included variable capture area provisions. One provided for variation of the first ramp only, while the other provided for varying the entire external ramp system. Each was designed to permit evaluation of the effects on inlet performance of such variables as bleed and bypass mass flow, in addition to inlet geometry. These models were tested at NASA-Ames Research Center in 1969.

Three inlet development tests were conducted. These included two inlet performance tests and one inlet/airframe drag test. The first two tests were directed toward inlet performance development, and covered Mach number ranges as follows:

- o First ramp system variable - Mach 0.9 to 2.5
- o Entire ramp system variable - Mach 1.6 to 2.5

The tests were conducted at Reynolds numbers of 7.38×10^6 per meter (2.25×10^6 per foot) for transonic conditions and 6.56×10^6 per meter (2.0×10^6 per foot) for supersonic conditions using a 16.7 percent scale model. The inlet/airframe drag tests included evaluation of both inlet configurations at transonic speeds with Mach number of 0.6, 0.9, and 1.2 for Reynolds numbers of 5.84, 7.22, and 7.58×10^6 per meter (1.78, 2.20, and 2.31×10^6 per foot), respectively, using a 7.5 percent scale model.

Although these tests were directed toward the development of a unique inlet type for a specific aircraft and mission, much of the resulting data have general application. The significant results have been summarized and are presented in this report.

The first section provides descriptions of the models tested. Next, the instrumentation of each model is described, the test conditions and data reduction are defined, and the data accuracy is presented. Subsequently, a discussion of the data analyses is presented. The basic performance data used in the analyses are included in Appendix A. The procedure used to calculate bleed and bypass drags is given in Appendix B, and the analytical technique used to determine inlet spillage drag is explained in Appendix C.

SYMBOLS

A_c	Inlet capture area
A_{c_o}	Inlet reference capture area (constant for a given configuration)
A_D	Main duct area
C_D	Aircraft drag coefficient, aircraft drag/$q_0 S$
C_L	Aircraft lift coefficient, aircraft lift/$q_0 S$
$C_{L_{INLET}}$	Inlet lift coefficient, inlet lift/$q_0 A_c$
C_M	Aircraft pitching moment coefficient, moment/$q_0 S\bar{c}$
$\bar{c}$	Mean aerodynamic chord of wing
D	Drag force
D_{Bleed}	Bleed drag
D_{BP}	Bypass drag
$D_{Spillage}$	Spillage drag
D_2	Engine face diameter; or steady state distortion parameter, defined as the difference between the maximum and minimum total pressure divided by the average total pressure at the engine face
F_{BAL}	Balance measured force
F_{Base}	Base correction force
$F_{BL_{exit}}$	Ramp and throat bleed exit force
F_{CAV}	Cavity correction force
F_{Cl}	Lower cowl force
F_{Cu}	Upper cowl force
F_{Exit}	Exit stream thrust
F_I	Stream thrust at the inlet cowl lip plane
F_{IN}	Forces acting on the inlet
F_L	Inlet lift force

SYMBOLS (Cont'd.)

F_N	Net thrust
F_{NP}	Net propulsive force
F_R	Forces acting on the compression ramps
F_{SP}	Forces acting on the sideplates
F_x	Forces acting on the model in the axial (body axis) direction
F_y	Forces acting on the model in the normal (body axis) direction
F_o	Inlet entrance stream thrust
h	Inlet capture height
h_c	Distance from the third ramp to the cowl lip (perpendicular to third ramp)
L	Distance from leading edge of first ramp to cowl lip parallel to an aircraft waterline
M	Mach number
m_i/m_o	Inlet mass flow ratio (sum of the main duct, throat slot bleed, and engine face bypass mass flow ratios) based on A_c
m_{BP}/m_o	Bypass mass flow ratio
m_{RB}/m_o	Third ramp bleed mass flow ratio
m_{TS}/m_o	Throat slot bleed mass flow ratio
m_o	Reference mass flow
P	Static pressure
P_T	Total pressure
$\frac{P_{T_2}}{P_{T_0}}$	Average steady state engine face total pressure recovery
q_0	Dynamic pressure, $\frac{\gamma}{2} P_0 M_0^2$
R_{LIP}	Cowl lip radius
R_{L1}	First ramp length
R_{L2}	Second ramp length

SYMBOLS (Cont'd.)

R_{L3}	Third ramp length
R_{L4}	Diffuser ramp length
RN	Reynolds number
R_{SP}	Sideplate leading edge radius
S	Wing area of aircraft (used as reference area in drag coefficient)
T	Turbulence - dynamic distortion parameter, defined as the average of the rms values of the fluctuating total pressure components divided by the average steady state total pressure ($\Delta P_{rms}/P_{T2}$)
W	Inlet width
WL	Model waterline
$X_{F.S.}$	Fuselage station
x	Axial direction (aircraft body axis)
Y	Perpendicular distance between third oblique shock and the cowl lip
y	Normal direction (aircraft body axis)
α	Angle of attack - degrees (relative to model waterline)
β	Angle of sideslip - degrees (relative to model buttline)
γ	Ratio of specific heats
δ_H	Horizontal tail deflection angle
δ_1, δ_2, δ_3	Boundary layer thickness at end of first ramp, second ramp, and third ramp, respectively
Δ_1, Δ_2, Δ_3	First, second, and third ramp angles, respectively, relative to an inlet reference line - degrees
Δ'_1, Δ'_2, Δ'_3	First, second, and third ramp angles, respectively, relative to model waterline - degrees
ρ	Ramp system rotation angle relative to a waterline (positive when leading edge of first ramp rotates downward) - degrees

Subscripts

avg	Average
max	Maximum
min	Minimum
0	Freestream conditions
2	Engine face conditions

TEST FACILITY AND MODELS

Test Facility

The test facility employed was the NASA Ames Research Center Unitary Plan Wind Tunnel. This facility is a closed circuit, variable density, continuous flow wind tunnel having three test sections which permit testing over a Mach number range from 0.6 to 3.5. The transonic tests were conducted in the 11 x 11-foot section, which has a Mach number range of 0.6 to 1.4. The supersonic tests were conducted in the 9 x 7-foot section, which has a Mach number range of 1.55 to 2.55.

Inlet Performance Models

Two different 16.7 percent scale inlet models, side-mounted on partial fuselages, were used in the two inlet performance tests. These models, designated as Configurations 1 and 2, were both two-dimensional, overhead, three ramp, external compression inlets with variable capture area.

Configuration 1 - The Configuration 1 inlet performance model is shown in Figure 1. The capture area was varied by rotating the first ramp and the forward portion of the outboard sideplate about the first ramp hinge line. The inboard sideplate and boundary layer diverter could not be rotated. The second and third ramp angles were varied independent of first ramp rotation. The ramp angle nomenclature is defined in Figure 2. The first ramp rotation was scheduled as a function of Mach number.

The inlet dimensions and duct area distribution are provided in Figure 3. The inlet lower cowl lip coordinates are presented in Figure 4. The design Mach number, that is, the Mach number at which the ramp oblique shocks intersect at the cowl lip, was 2.5.

The inlet model used second and third ramp bleed, sideplate bleed, and throat slot bleed, as shown in Figure 5. The ramp bleed rates, throat slot bleed rates, and main duct flow rate were measured using the calibrated mass flow plug assemblies shown in Figure 1.

A bypass system consisting of a slotted duct section upstream of the engine face was employed as shown in Figure 6. The bypass flow rate was also measured using a calibrated mass flow plug assembly.

Configuration 2 - The Configuration 2 inlet performance model is shown in Figure 7. The capture area was varied by rotating the entire ramp system and sideplates about a hinge point near the lower cowl lip. The boundary layer diverter could not be rotated. The second and third ramp angles were varied independent of ramp system rotation. The ramp angles and ramp systems rotation angle are defined in Figure 8. The ramp system rotation was scheduled as a function of both Mach number and angle of attack.

The inlet dimensions and duct area distribution are given in Figure 9. The inlet lower cowl lip coordinates are provided in Figure 10. The inlet design Mach number was 2.5.

Second and third ramp bleed, sideplate bleed, and throat slot bleed were used as shown in Figure 11. The calibrated mass flow plug assemblies illustrated in Figure 7 were used to measure the flow rates through the ramp bleed systems, throat slot bleed system, and the main duct. The bypass was incorporated in the throat slot bleed system.

Inlet/Airframe Drag Model

The 7.5 percent scale model for measuring the inlet/airframe drag is illustrated in Figure 12. This complete aircraft model incorporated two side-mounted, two-dimensional, overhead, three ramp, external compression inlets, which were based on the same full scale dimensions as the Configuration 2 inlet performance model. However, the inlets on the drag model were designed with the flexibility to simulate either of the variable capture area systems employed by the inlet performance models (Configuration 1 or 2). The model configuration which simulated the rotating first ramp system was designated Configuration 3, as shown in Figure 13. The configuration which simulated the rotating ramp system was designated Configuration 4, as shown in Figure 14.

The inlets employed second and third ramp bleed and throat slot bleed. Each bleed rate was measured using a calibrated exit. The ramp and throat slot bleed systems for the drag model are shown in Figure 15. The main duct flow rate was controlled by calibrated exit chokes.

INSTRUMENTATION

Inlet Performance Model Instrumentation

The Configuration 1 inlet performance model was instrumented with a 36-probe steady state/dynamic total pressure rake to measure the engine face pressure recovery and turbulence. The pressure rake is illustrated in Figure 16.

The Configuration 2 inlet performance model was instrumented with a 36-probe steady state/dynamic total pressure rake as shown in Figure 17 to measure the engine face pressure recovery and turbulence. Note that this rake location differs from that of Configuration 1. Possible differences in total pressure measurements between the rake locations do not affect the analyses reported in the Discussion section since no direct comparisons are made between Configurations 1 and 2. A high frequency transducer was mounted in the duct wall of Configuration 2 (see Figure 17) to detect duct flow instability (inlet "buzz"). Static pressure taps were provided on the surface of the first ramp as shown in Figure 17 to determine local flow angularity.

Inlet/Airframe Drag Model Instrumentation

The inlet/airframe force data were measured with a Task Corporation Mark XXI six-component internal strain gage balance located in the fuselage as illustrated in Figure 18.

The base and the balance cavity were instrumented with pressure taps to provide the data required to correct the balance measurements for the base and cavity forces.

The main duct and bleed exits were provided with total and static pressure instrumentation to allow the computation of the respective flow rates and to provide the data necessary for the correction of the balance measurements for the entrance and exit stream forces.

The left-hand inlet ramps, sideplates, and cowl surfaces were instrumented with static pressure taps, and a total pressure rake was provided at the cowl lip plane (see Figure 18) to allow the computation of inlet lift and drag forces.

PROCEDURE

Test Conditions

The ranges of test conditions over which the inlet performance tests and the inlet/airframe drag test were run are given in Table 1.

TABLE 1 - TEST CONDITIONS

Test	Configuration	Ranges of Test Conditions: Mach No.	Angle of Attack	Sideslip
Inlet Performance	1	0.9 to 2.5	-2.5° to 26°	-8° to 8°
Inlet Performance	2	1.6 to 2.5	-4° to 24°	0° to 6°
Inlet/Airframe Drag	3,4	0.6 to 1.2	-3° to 20°	0°

Data Reduction

The internal performance parameters computed were total pressure recovery, turbulence, steady state distortion, inlet stable range, net propulsive force, and inlet mass flow ratio. The inlet/airframe drag parameters used in the analyses were aircraft drag coefficient and inlet lift coefficient. These parameters are defined as follows:

Total Pressure Recovery, $\frac{P_{T_2}}{P_{T_0}}$ - The ratio of the average steady state total pressures measured at the engine face to the freestream total pressure.

Turbulence, $T = \frac{\Delta P_{rms}}{P_{T_2}}$ - The average of the root mean square (rms) values of the fluctuating total pressure components divided by the average steady state total pressure.

Steady State Distortion, $D_2 = \left[\left(\frac{P_{T_2}}{P_{T_0}}\right)_{max} - \left(\frac{P_{T_2}}{P_{T_0}}\right)_{min}\right] \Big/ \left(\frac{P_{T_2}}{P_{T_0}}\right)_{avg}$ - The difference between the maximum and the minimum total pressure divided by the average total pressure at the engine face.

Inlet Stable Range $= \left[\left(\frac{m_i}{m_o}\right)_{crit} - \left(\frac{m_i}{m_o}\right)_{buzz}\right] \Big/ \left(\frac{m_i}{m_o}\right)_{crit}$ - The mass flow range between the critical (maximum) inlet mass flow ratio and the mass flow ratio at which the inlet flow became unstable (onset of inlet "buzz") divided by the critical mass flow ratio.

Net Propulsive Force Change,

$$\frac{\Delta F_{NP}}{F_N} = \frac{\Delta\left(\frac{P_{T_2}}{P_{T_0}}\right) \cdot \frac{\partial F_N}{\partial(P_{T_2}/P_{T_0})} - \Delta D_{Spillage} - \Delta D_{Bleed} - \Delta D_{Bypass}}{F_N}$$

where changes from a selected reference condition are denoted by Δ. The first term in the equation above represents the effect of a recovery change on the net thrust, and was computed for the analyses at Mach 1.6 and 2.2 using the relationships shown in Figure 19. These relationships are typical of fighter-type turbofan engines.

For the second term above, inlet spillage drag, defined as inlet additive drag plus the change in cowl drag due to subcritical spillage, was analytically determined. The additive drag at the critical (maximum) capture condition was computed by pressure integration along the captured streamline. A drag slope was then calculated for reduced mass capture ratios, extending a technique developed in References 1 and 2 for pitot intakes to two-dimensional inlets with pre-compression. A more detailed explanation of the inlet additive drag calculation is given in Appendix C.

The bleed and bypass drag terms above were evaluated by computing the loss in momentum between the inlet and the exit of each system, using the flush exit thrust coefficients from References 3 and 4. The calculation procedures used to determine the bleed and bypass drags are presented in Appendix B along with curves which can be used to simplify these calculations.

Inlet Mass Flow Ratio, $m_i/m_o = m_2/m_o + m_{TS}/m_o + m_{BP}/m_o$ - The total mass flow entering the inlet at the cowl lip plane determined by summing the main duct, throat slot bleed, and (where applicable) engine face bypass mass flow ratios. As stated previously, the individual mass flow ratios were measured using the calibrated mass flow plug assemblies shown in Figures 1 and 7.

The inlet mass flow ratio as defined above is based on an inlet capture area, A_c, which changes as a function of both angle of attack and first ramp angle. The manner in which the inlet height (and thus capture area) varies with changes in angles of attack and alternate first ramp angles for Configurations 1 and 2 is illustrated in Figure 20. An alternate definition of inlet mass flow ratio based on a fixed value of capture area, A_{c_o}, is used to provide comparative inlet capture characteristics for airflow matching. This reference capture area remains constant for a given configuration and was selected at zero degrees angle of attack and a specific first ramp angle. The relationship between A_c and A_{c_o} is presented in Figure 21 over the range of first ramp angles and angles of attack tested. The mass flow ratio values presented in the text and the appendices are based on A_c unless otherwise noted.

Aircraft Drag Coefficient, $C_D = D/q_0S$ - The aircraft drag force divided by the dynamic pressure and wing planform area. The aircraft drag coefficient obtained from force balance and pressure measurements was used to establish the aircraft drag coefficient increment between alternate inlet configurations.

The aircraft drag was determined by summation of the forces shown in Figure 22.

Inlet Lift Coefficient, $C_{L_{INLET}} = F_L/q_0S$ - The inlet lift force divided by the dynamic pressure and the wing planform area. The inlet lift coefficient was obtained from static and total pressure measurements on the ramps, cowl, sideplates, and inlet lip plane. The inlet lift force was determined by summation of the force components shown in Figure 23.

DATA ACCURACY

The inlet data analyses performed in these investigations are discussed primarily in terms of changes in selected inlet performance parameters. Therefore, the data accuracy was evaluated in terms of data repeatability. The absolute levels of data accuracy were not specifically determined but are consistent with typical pressure and force and moment wind tunnel tests. The ranges of repeatability determined from the test data are given in Table 2.

TABLE 2 - DATA ACCURACY

	Repeatability Ranges		
	Configuration 1	Configuration 2	Configurations 3&4
Mass flow (m/m_o)	$\pm$1%	$\pm$1%	N/A
Pressure recovery (P_{T_2}/P_{T_0})	$\pm$0.5%	$\pm$0.5%	N/A
Turbulence (T)	$\pm$.005 (ΔT)	$\pm$.002 (ΔT)	N/A
Steady state distortion (D_2)	$\pm$.015 (ΔD_2)	$\pm$.007 (ΔD_2)	N/A
Aircraft drag (C_D)	N/A	N/A	$\pm$.0006

DISCUSSION

The results of the analyses are divided into two parts: (1) discussions of inlet performance parameters and (2) discussions of inlet/airframe force data.

Inlet Performance Data Analyses

The data from the inlet performance models, Configurations 1 and 2, were analyzed to determine the effects of the following variables on the performance of a two-dimensional, overhead, three-ramp, external compression inlet:

Variables Investigated	Performance Parameters
o Inlet bleed	o Total pressure recovery
o Bypass flow	o Turbulence
o Operating mass flow ratio	o Steady state distortion
o Inlet ramp angles	o Net propulsive force
o Angle of attack	o Inlet stable range
o Sideslip	
o Ramp system rotation	
o Terminal shock strength	

The analyses were performed using the test data presented in Appendix A. Typical inlet/engine airflow characteristics were used to select the inlet operating points. In general, the operating point is 95 percent of critical (maximum) inlet flow at supersonic conditions, and varies between 86 and 88 percent of maximum inlet flow at subsonic conditions. In practice, maintenance of a 95 percent critical operating point at all supersonic conditions presupposes the use of a bypass system.

In the test program, emphasis was placed on the Mach 2.2 condition. This condition was the maximum Mach number for which high inlet performance and aircraft maneuverability were critical requirements for the specific aircraft and mission application to which the tests were directed. Thus, the majority of the investigations of the effects of design variables discussed in this report were performed at Mach 2.2.

The results of the inlet performance data analyses have general application to three ramp, external compression inlets. The results indicate inlet bleed requirements, operating conditions in terms of mass flow ratio and inlet geometry, and a variable capture area system to maintain a high level of inlet performance with angle of attack.

Effects of Inlet Bleed Variations

The inlet models employed second and third ramp, throat slot, and sideplate bleed systems to remove the boundary layer formed on the inlet compression surfaces and sideplates. The effects of varying the bleed rate through the third ramp on the pressure recovery, turbulence, and distortion were investigated at Mach 2.2 on Configuration 2. The effects of

varying the throat slot bleed rate were investigated at Mach 2.2 on both Configurations 1 and 2. Since no variations of second ramp and sideplate bleed were made, an evaluation of the effect of these bleeds on inlet performance could not be made.

Third Ramp Bleed Variation - The effect of third ramp bleed on inlet performance was investigated on Configuration 2, only under conditions where the second ramp, sideplates, and throat slot bleed mass flow ratios were 0.008, 0.020, and 0.062, respectively. Under these conditions, the total pressure recovery decreases as the third ramp bleed was increased above a mass flow ratio of 0.003, as shown in Figure 24. This is believed to be caused by the bleed flow modifying the third ramp supersonic flow field, thereby accelerating the flow ahead of the terminal normal shock.

To investigate the effect of the third ramp bleed on the ramp boundary layer, computations were made using the boundary layer computer program described in Reference 5 and 6. The results indicated that, with a third ramp bleed mass flow ratio of 0.003, 32 percent of the third ramp boundary layer is removed and, with a bleed mass flow ratio of 0.012, the boundary layer is completely removed. Therefore, it is apparent that maximum pressure recovery is obtained with ramp bleed rates less than those required for complete boundary layer removal, when throat slot bleed is also employed. In fact, the data suggest that third ramp bleed may not improve the performance of Configuration 2, although no data were obtained at zero third ramp bleed rate to verify this point.

Throat Slot Bleed Variation - The effects of throat bleed were investigated on Configurations 1 and 2 under the following conditions:

Configuration	Second Ramp Bleed Rate*	Third Ramp Bleed Rate*	Sideplate Bleed Rate*
1	.012	.021	.020
2	.008	.020	.020

*Mass flow ratios

Under these conditions, performance improved with increasing throat slot bleed for both configurations up to a bleed mass flow ratio of approximately 0.04, as shown in Figure 25.

The lower pressure recovery of Configuration 2 shown in Figure 25 is a result of the ramp rotation schedule used during the test. Note that the total compression angle for Configuration 2 is almost two degrees less than that for Configuration 1. As will be discussed in the paragraph on Effects of Ramp System Rotation, increasing the external compression can result in significant increases in pressure recovery.

To investigate the effect of throat slot bleed illustrated in Figure 25 computations using the boundary layer analysis technique described in References 5 and 6 were made. These computations indicated that the entire ramp boundary layer was removed upstream of the throat by the ramp bleed systems

on both configurations. Therefore, it is apparent that the performance improvement obtained with throat slot bleed resulted from some mechanism other than boundary layer removal. To determine the mechanism involved, the flow conditions at the engine face were examined. The inlet performance parameters at 0.95 critical mass flow and the engine face total pressure recovery maps are shown in Figure 26. These indicate that the flow conditions at the engine face are more uniform with throat slot bleed than without throat slot bleed. It appears, therefore, that bleeding air through the slot helps to turn the flow and together with the effect of mass flow removal, changes the subsonic diffusion characteristics in a favorable manner. The improvement in performance with throat slot bleed may be caused by either the elimination of a separated region at the diffuser ramp leading edge or by the removal of distorted flow induced by the terminal normal shock.

Effects of Bypass Flow Variation

The effects on inlet performance of bypassing flow from either an engine face (aft) bypass or a throat (forward) bypass were obtained at Mach 1.6 and 2.2 on Configuration 1.

The effects of variations in aft bypass flow on inlet performance are presented in Figure 27. No significant effect is seen at Mach 1.6 (Figure 27a). However, at Mach 2.2, bypass mass flow ratios above approximately 0.06 cause the inlet recovery to decrease and the engine face distortion and turbulence to increase (Figure 27b).

At bypass mass flow ratios below 0.06, the inlet performance is not significantly affected by the bypass location at Mach 2.2, as shown in Figure 28.

Effects of Operating Mass Flow Ratio Variation

The effects on inlet performance and net propulsive force produced by changing the operating mass flow ratio were investigated at Mach 1.6 and 2.2. The results presented are for Configuration 2 only, but similar trends were indicated for Configuration 1.

The distortion and turbulence increase and the pressure recovery decreases as the operating point approaches the critical mass flow ratio, as shown in Figure 29.

For this inlet configuration, the maximum net propulsive force occurs at 95 percent critical mass flow ratio for Mach 1.6 and at the critical point for Mach 2.2, as shown in Figure 30. This maximum net propulsive force is achieved when the increase in spillage drag with decreasing operating mass flow ratio exceeds the net thrust improvement which results from the increase in pressure recovery. In this evaluation, the inlet size was assumed to vary with the operating mass flow ratio so that no bypass was required.

In summary, the inlet operating point providing maximum net propulsive force for a two-dimensional, overhead, three ramp, external compression inlet has been shown to be between 95 and 100 percent of the critical mass flow ratio above Mach 1.6. However, the final selection of an operating mass flow ratio must only be made after also considering inlet stability, distortion, and inlet/engine control system transients.

Effects of Inlet Ramp Angle Variations

The effects of varying the second and third ramp angles on the performance of three ramp, external compression inlets at Mach 2.2 were investigated. Analyses are presented showing the effect of varying the ramp angles both at a fixed angle of attack and as a function of angle of attack.

Reduced Second and Third Ramp Angles at a Given Angle of Attack - Two inlet ramp geometry variations on Configuration 2 were investigated at $\alpha = 3°$. The critical (maximum) mass capture ratio was higher and the pressure recovery and inlet stable operating range were lower at reduced second and third ramp angles, as shown in Figures 31 and 32. However, no significant changes in turbulence or steady state distortion occurred with the ramp angle variations.

To evaluate the effect of the second and third ramp angle variation on the net propulsive force for an inlet with a fixed first ramp, two propulsion system design approaches were considered as defined below:

Case 1: Without Bypass - For each ramp geometry, the inlet was sized to capture the required airflow. Therefore, no bypass was required.

Case 2: With Bypass - The inlet size was the same for each ramp geometry and the design case was considered to be the inlet geometry having a third ramp angle of 24.6°. Additional flow captured with the lower ramp angles was bypassed through the throat slot.

For Case 1, where the inlet was properly sized for each ramp geometry, the net propulsive force increases as the ramp angles decrease, as shown in Figure 33. The lower ramp angles and the reduced capture area cause a reduction in inlet drag which more than compensates for the reduction in net thrust resulting from the decrease in pressure recovery.

For Case 2, where the excess flow captured with the lower ramp angles was bypassed overboard, the net propulsive force decreases as the ramp angles decrease, as shown in Figure 33. The reduction in spillage drag associated with the lower ramp angles does not compensate for the bypass drag and the decrease in net thrust due to the pressure recovery reduction.

Reduced Second and Third Ramp Angles with Angles of Attack - The effect on inlet performance of reducing the second and third ramp angles of Configuration 1 with increasing angle of attack was compared to the effect of maintaining fixed ramp angles. This comparison was made to determine if there is a performance advantage associated with either delaying oblique shock detachment from the third ramp or preventing vortex sheet ingestion as the angle of attack increases.

To make this comparison, inlet performance data for constant third ramp angles of 17.4° and 22.3° were used. The pressure recovery for a third ramp angle of 22.3° is higher than for 17.4° up to an angle of attack of approximately 8.5° but is lower above 8.5°, as shown in Figure 34. This result correlates with the predicted angle of attack for third ramp shock detachment of 8° for a third ramp angle of 22.3°. Vortex sheet ingestion is not predicted for this configuration at a third ramp angle of 22.3° over the angle of attack range tested. Thus, no conclusion can be made from this data concerning the effect of vortex sheet ingestion.

To determine the effects of reduced ramp angles on the net propulsive force at angle of attack, a second/third ramp schedule which provides a linear decrease in ramp angles with increasing angle of attack was assumed. No bypass is required for the case where the third ramp angle remains constant as angle of attack increases, but with reduced ramp angles a significant bypass requirement occurs above $\alpha = 3°$. However, even with the bypass requirement, the net propulsive force is improved above $\alpha = 7°$ with the reduced ramp angles as shown in Figure 35. As with the pressure recovery and distortion data, these results correlate with the predicted detachment angle for the higher third ramp angles. Thus, it is apparent that reduced second and third ramp angles are advantageous when third ramp shock detachment is prevented.

Effects of Angle of Attack

The effects of angle of attack on the performance of three ramp, external compression inlets were investigated at both transonic and supersonic conditions. Data were obtained at transonic test conditions for Configuration 1 and at supersonic conditions for both Configurations 1 and 2. The test conditions and inlet geometry definitions are presented in Figure 36.

Transonic Angle of Attack Performance - At transonic conditions, the pressure recovery, turbulence, steady state distortion, and maximum mass flow ratio are generally insensitive to angle of attack, as shown in Figures 37 and 38. The maximum mass flow ratio values presented reflect the relatively constant absolute capture characteristics of the inlet at transonic conditions.

Supersonic Angle of Attack Performance - In terms of pressure recovery, turbulence, steady state distortion, and maximum mass flow ratio, Configuration 1 performance is much more sensitive to angle of attack at supersonic conditions than that of Configuration 2, as shown in Figures 39 and 40. In these figures, the performance effects are shown for the inlet ramp schedule tested for each particular configuration and Mach number. Configuration 1 performance is more sensitive to angle of attack because the ramp geometry is fixed with angle of attack. The maximum pressure recovery for Configuration 2 is less than that for Configuration 1 (Figures 39b and c) as a result of the ramp rotation schedule employed during the test. In the section on the Effects of Ramp System Rotation, it is shown that adjusting the ramp rotation schedule of Configuration 2 to increase the external compression would significantly increase the pressure recovery.

The effects of angle of attack on the inlet stable range are shown in Figure 41 for Configuration 2. The large increase in stable range observed between $\alpha = 12°$ and $\alpha = 16°$ at Mach 2.2 is attributed to the detachment of the oblique shock from the third ramp.

The maximum net propulsive force at Mach 2.2 occurs at $\alpha = 3°$ for Configuration 1 and at $\alpha = 0°$ for Configuration 2 as shown in Figure 42. For Configuration 1 (Figure 42a), the decrease in net propulsive force below $\alpha = 3°$ is mainly caused by a reduction in recovery and a large bypass drag. Above $\alpha = 3°$, the decrease in net propulsive force is primarily caused by an increase in spillage drag. In this case, the 95 percent critical operating point can be maintained even without assuming a bypass at angles of attack greater than 3°. The variation in net propulsive force is less affected by angle of attack for Configuration 2 (Figure 42b) than for Configuration 1 because the ramp system rotation tends to maintain spillage drag at a constant level as angle of attack increases. With an optimum ramp system rotation schedule, the effect of angle of attack on the Configuration 2 net propulsive force can be further reduced by improving the pressure recovery at angle of attack. This improvement in recovery is discussed in the section on Effects of Ramp System Rotation.

In summary, a variable capture area inlet with ramp system rotation (Configuration 2) will provide a high level of inlet performance at Mach 2.2 over a wider angle of attack than an inlet which has a fixed geometry with angle of attack (Configuration 1).

Effects of Sideslip

The effects of sideslip on the performance of three ramp, external compression inlets were investigated at transonic conditions for Configuration 1 and at supersonic conditions for both Configurations 1 and 2. A summary of the test conditions and inlet geometry variations at sideslip are presented in Figure 43.

Transonic Sideslip Performance - No significant sideslip effect can be seen at Mach 0.9, as shown in Figure 44a, but at Mach 1.2 (Figure 44b), the pressure recovery decreases and the distortion increases at the high angles of attack for the inlet on the leeward side of the fuselage.

Supersonic Sideslip Performance - At supersonic conditions, the performance of the inlet on the leeward side of the fuselage is progressively degraded as sideslip increases, as shown in Figure 45. This effect becomes more pronounced with increasing Mach number. The inlet on the windward side of the fuselage, however, is much less sensitive to sideslip (see Figure 45b). For clarity, the sideslip effects for Configuration 1 are shown in Figures 45a through 45c, and for Configuration 2, in Figures 45d through 45f.

Sideslip also causes a significant reduction in stable range for the leeward inlet as shown in Figure 46 for the Mach 2.2 condition.

Effects of Ramp System Rotation

The performance advantages of a three ramp system which rotates with angle of attack have already been noted. In addition to maintaining high performance over a wide angle of attack range, a rotating ramp system also provides the capability to compensate for the forebody-induced angularity of the flow approaching the inlet. The local flow angularity at the inlet at Mach 2.2, shown in Figure 47, was determined using static pressure measurements on the first ramp. To provide the data necessary for the selection of an inlet rotation schedule, inlet performance at Mach 2.2 and 2.5, as a function of rotation, was investigated at several angles of attack. These data, presented in Figures 48 and 49, indicate that significant increases in pressure recovery and decreases in distortion can be achieved by upward (negative) inlet rotation, due to the increases in external compression.

Effects of Terminal Shock Strength

Terminal shock strength is defined here as the static pressure ratio across the terminal normal shock, as illustrated in Figure 50. Correlations of terminal shock strength and oblique shock system position relative to the cowl lip with inlet stable range, turbulence, and steady state distortion were investigated at Mach 2.2 and 2.5, using the Configuration 2 data. The terminal shock strength values are theoretical.

Inlet Stable Range - The inlet stable range is a function of the oblique shock system position as well as the terminal shock strength, as shown in Figure 51. The shock displacement ratio defined in Figure 51 was used to describe the oblique shock system position relative to the inlet cowl lip. The increase in inlet stable range with increasing shock displacement ratio is attributed to delaying the ingestion of the vortex sheet formed at the intersection between the normal shock and the third ramp oblique shock. In Reference 7, it was shown that near the inlet design Mach number, the vortex sheet ingestion triggers inlet "buzz".

The dependence of the stable range on the terminal shock strength is attributed to the shock translation required to provide a given change in mass flow rate. That is, for the same shock translation, a weak terminal shock produces a smaller change in mass flow rate than a strong terminal shock. Consequently, for a given shock displacement ratio, the ingestion of the vortex sheet occurs with a lower stable range when the terminal shock is weak.

Turbulence and Steady State Distortion - Steady state distortion is completely insensitive to terminal shock strength as shown in Figure 52. Turbulence is insensitive to terminal shock strength below a value of 2.2, but then increases significantly with terminal shock strength.

Inlet/Airframe Drag Data Analyses

The transonic drag test data obtained with the inlet/airframe drag model were analyzed to determine the effects of variations in inlet capture area on aircraft drag and inlet lift. The analyses are based on data obtained between Mach 0.6 and 1.2 with a fixed exit choke representing typical operating conditions of approximately 80% of maximum inlet flow.

The results of the inlet/airframe drag analysis illustrate the significance of considering inlet lift as well as inlet drag when determining integrated inlet/airframe performance.

Effects of Inlet Capture Area Variation on Aircraft Drag

The variable capture area inlet with ramp system rotation as a function of angle of attack has a drag advantage over an inlet that has fixed capture area with angle of attack at transonic conditions, as shown in Figure 53. These results were obtained by determining the difference in airframe drags incurred with inlet Configurations 3 and 4. The inlet ramp angle and rotation schedules for each configuration are presented in Figures 13 and 14. At transonic conditions, the ramp angles of Configuration 3 were fixed while the entire ramp system of Configuration 4 was rotated as a function of angle of attack up to approximately 4° angle of attack. Above 4° angle of attack where the first ramp angle of Configuration 4 is fixed at 4° less than that of Configuration 3, the drag of Configuration 4 increases at a lesser rate than Configuration 3. This is consistent with data from a recent investigation in which a comparison of similar inlet configurations was made. In this comparison, the increasing drag advantage at high angles of attack for an inlet having lower ramp angles can be shown to be a result of reduced spillage drag and upper cowl drag.

Effects of Inlet Capture Area Variation on Inlet Lift

Rotation of the inlet ramp system with angle of attack reduces the inlet lift force as shown by the comparison of inlet lift coefficients for Configurations 3 and 4 in Figure 54. Included in the inlet lift force are the lift forces on the cowl surfaces and on the sideplates, and the lift force resulting from air spillage.

Since the inlets were not located at the aircraft center of gravity, the inlet lift directly affects the aircraft pitching moment as shown in Figure 55 for Mach 0.9. Above 0° angle of attack, the aircraft model having variable capture area inlets (Configuration 4) has the lower inlet lift (Figure 54b) and the higher negative pitching moment (Figure 55). Since a change in pitching moment can affect the aircraft trim characteristics, careful consideration must be given to inlet/airframe integration to retain the full drag advantage of the variable capture area inlet.

CONCLUSIONS

The conclusions derived from analyses of two-dimensional, overhead, three ramp, external compression inlet performance and inlet/airframe drag data are as follows:

1. Maximum pressure recovery at Mach 2.2 is obtained with ramp bleed rates less than those required for complete boundary layer removal, when throat slot bleed is also employed.

2. Throat slot bleed increases inlet performance at supersonic flight conditions even when the boundary layer upstream of the throat is completely removed by ramp bleed.

3. Inlet performance is not affected by bypass location for bypass flow ratios less than 0.06 at Mach 2.2. Bypass mass flow ratios in excess of 0.06 from an aft location can degrade inlet performance.

4. The inlet operating point for maximum net propulsive force above Mach 1.6 occurs between 95 and 100 percent of the critical mass flow ratio.

5. The second and third ramp angles required for maximum net propulsive force at Mach 2.2 are lower than the ramp angles providing maximum inlet recovery.

6. Reducing the second and third ramp angles as a function of angle of attack to prevent shock detachment from the third ramp increases the net propulsive force.

7. Inlet performance is generally insensitive to angle of attack at transonic conditions.

8. A variable capture area inlet with a rotating ramp system maintains a high level of inlet performance at Mach 2.2 over a wider angle of attack range than an inlet which has a fixed geometry with angle of attack.

9. Inlet performance is insensitive to sideslip angles between -6° and +6° at Mach 0.9.

10. Inlet performance at supersonic conditions is degraded at sideslip for the inlet on the leeward side of the fuselage to a greater extent than for the inlet on the windward side.

11. Near the design Mach number the inlet stable range is related primarily to the terminal shock strength and the oblique shock system position relative to the cowl lip.

12. A terminal shock strength in excess of a static pressure ratio of 2.2 significantly increases the engine face turbulence levels.

13. A variable capture area inlet utilizing ramp system rotation with angle of attack causes less spillage drag at transonic conditions than an inlet which has a fixed capture area with angle of attack, thus producing more efficient operation at typical cruise conditions.

14. The change in inlet lift force accompanying inlet ramp rotation must be considered in the inlet/airframe integration in order to retain the full drag advantage of the variable capture area inlet.

McDonnell Aircraft Company
McDonnell Douglas Corporation
St. Louis, Missouri January 21, 1974

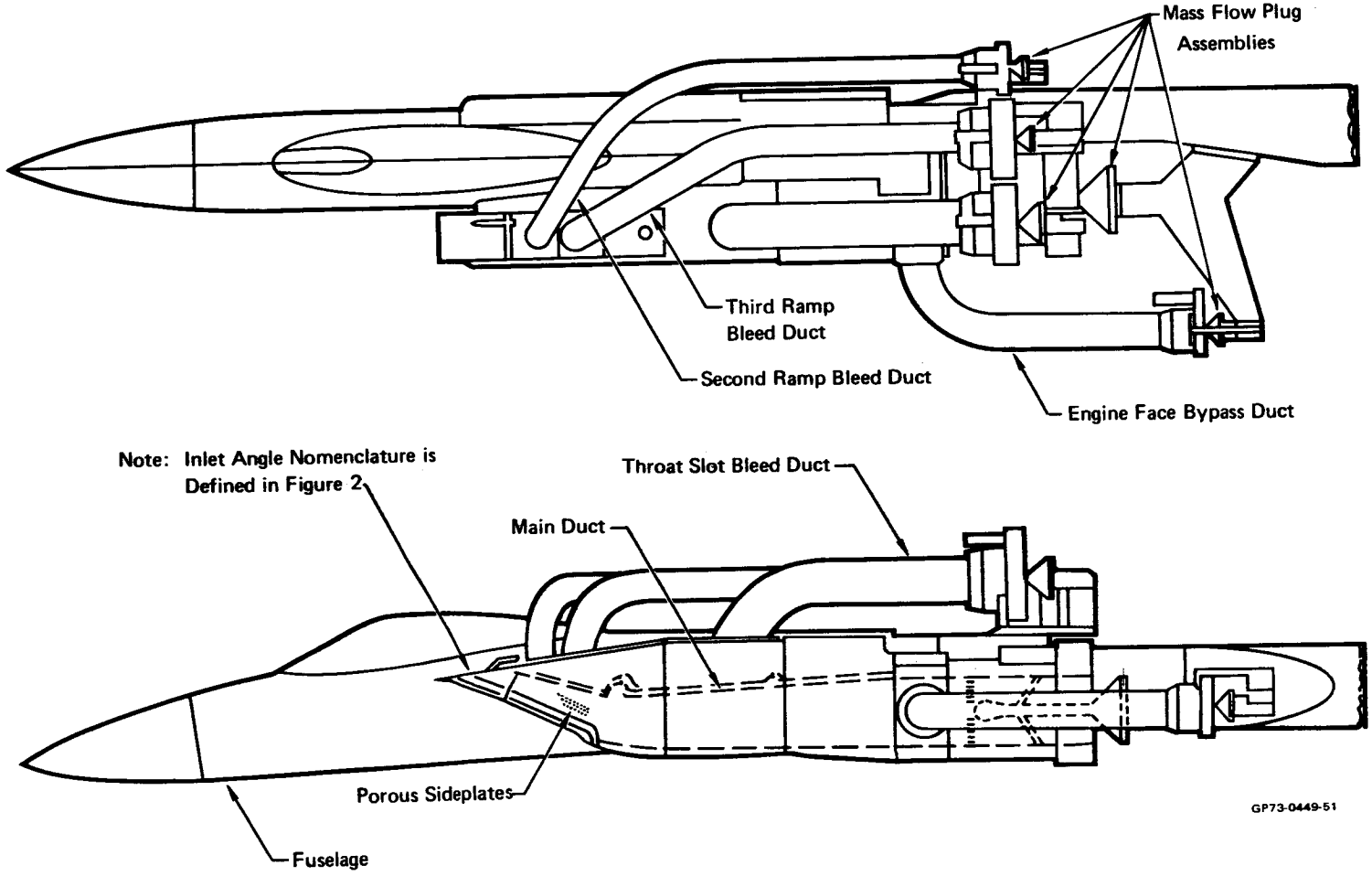

FIGURE 1 - CONFIGURATION 1 INLET MODEL

CONFIGURATION 1

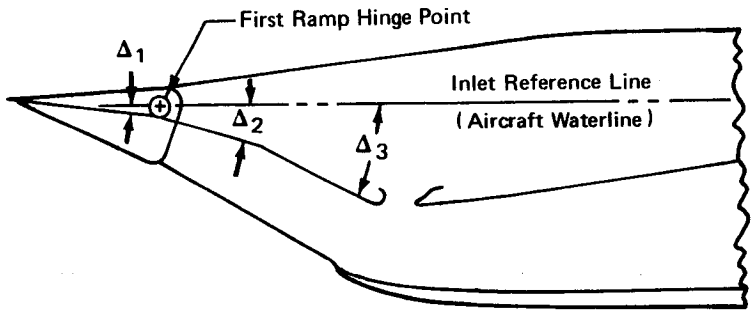

FIGURE 2 - CONFIGURATION 1 INLET ANGLE NOMENCLATURE

CONFIGURATION 1

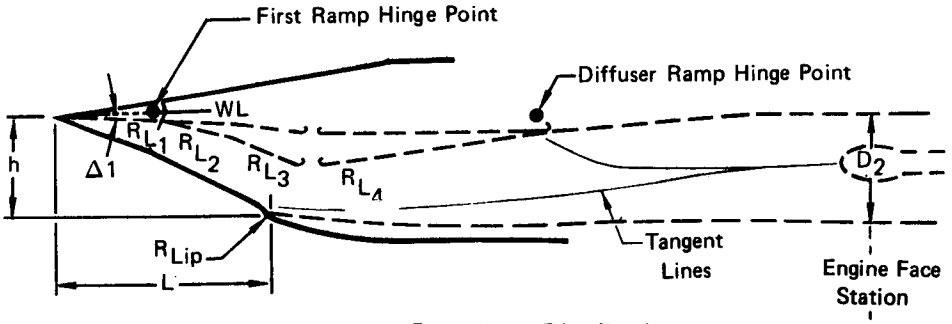

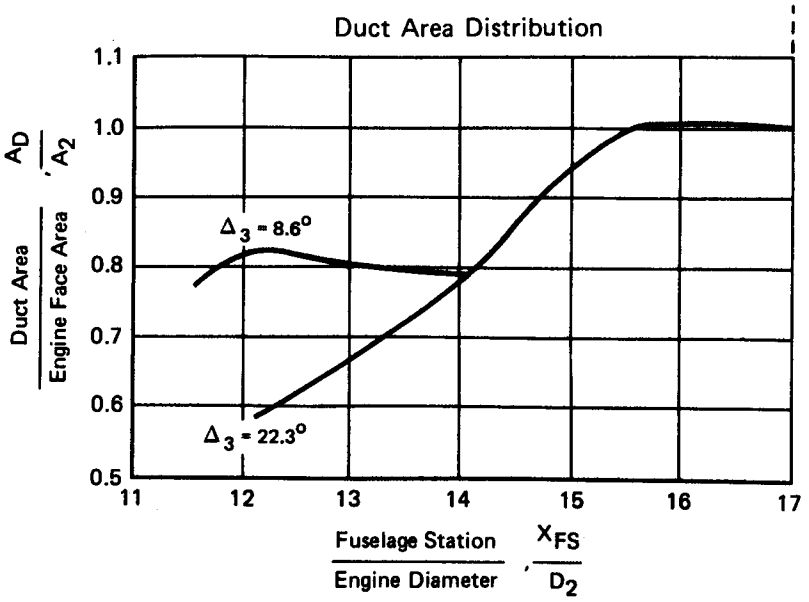

Summary of Dimensions

(Referenced to D_2) D_2 = 5.90 inches or 14.986 cm. (Model Scale)

Ramp Lengths		Inlet Width, W/D_2	0.736
R_{L_1}/D_2	0.996		
R_{L_2}/D_2	0.606	Ramp System Length, L/D_2	
R_{L_3}/D_2	0.801	@ $\Delta_1 = 0^o$	2.064
R_{L_4}/D_2	2.210	@ $\Delta_1 = 5.6^o$	2.066
Cowl Lip Radius			
R_{Lip}/D_2	0.005	Sideplate Leading Edge Radius, R_{SP}/D_2	0.002
Inlet Height, h/D_2			
@ $\Delta_1 = 0^o$	0.933		
$\Delta_1 = 5.6^o$	1.030		

First Ramp Angle Schedule Tested

M_o	$\Delta_1(^o)$
0.9	0.0
1.2	0.0
1.6	2.8
2.2	5.6
2.5	7.0

Note: 1 inch = 2.54 cm

FIGURE 3 - CONFIGURATION 1 INLET GEOMETRY DEFINITION

Configuration 1

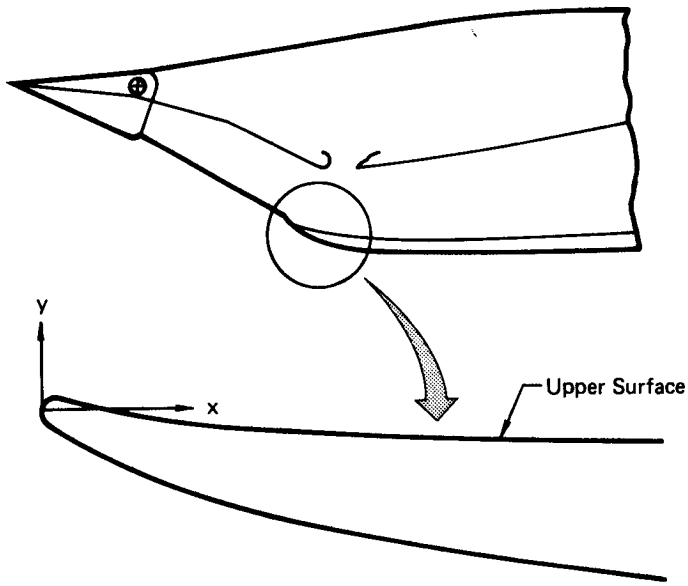

D_2 = 5.9 in. or 14.986 cm
(Model Scale)

Cowl Lip Coordinates

x/D_2	y/D_2	
	Upper Surface	Lower Surface
0	0	0
0.009	0.007	−0.008
0.028	0.001	−0.021
0.056	−0.008	−0.039
0.085	−0.018	−0.054
0.113	−0.025	−0.068
0.141	−0.033	−0.081
0.170	−0.040	−0.091
0.226	−0.055	−0.108
0.283	−0.065	−0.121
0.339	−0.077	−0.133
0.396	−0.087	−0.145
0.480	−0.099	−0.159
0.565	−0.109	−0.174
0.650	−0.118	−0.186
0.734	−0.125	−0.197

FIGURE 4 - CONFIGURATION 1 COWL LIP COORDINATES

GP74-0119-14

Configuration 1

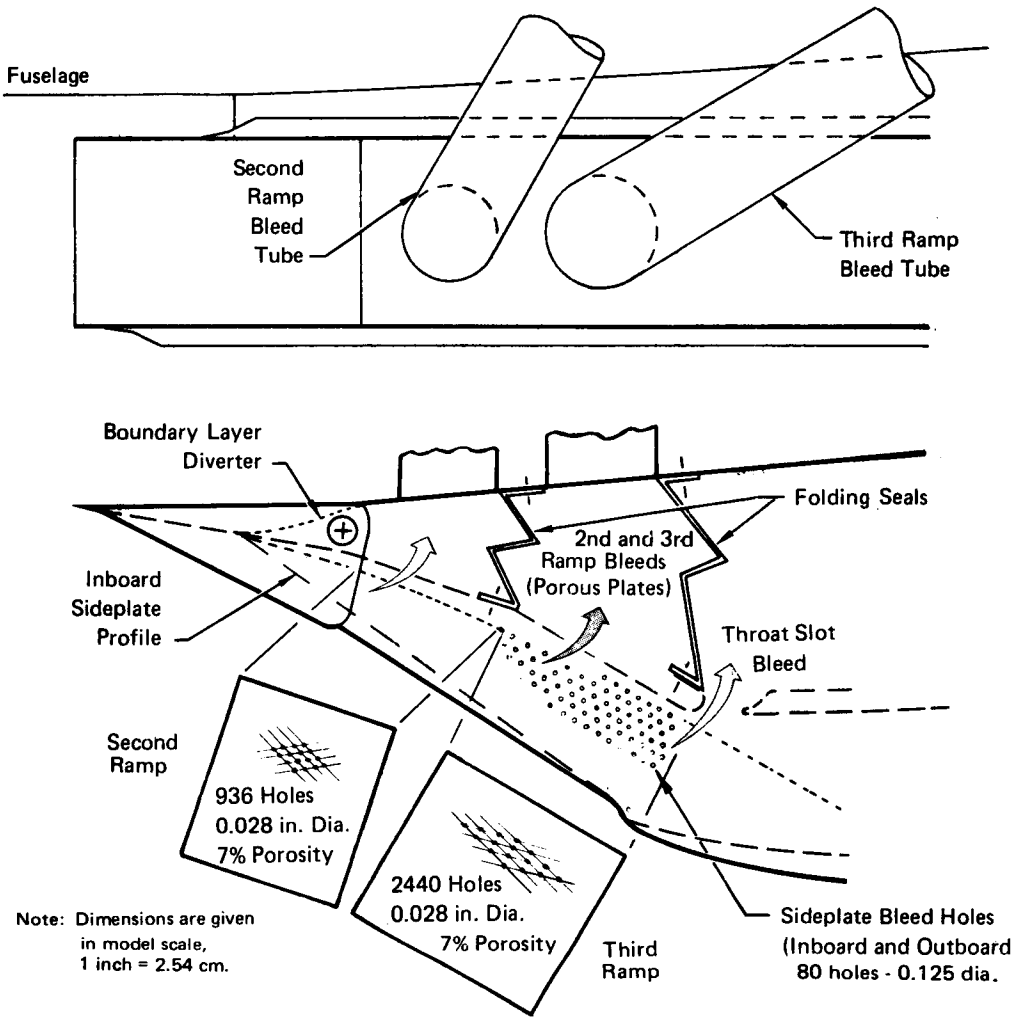

Nominal Bleeds at 0.95 Critical Operating Condition (in terms of m_{bleed}/m_o):

Bleed	$M_o = 0.9$	$M_o = 1.2$	$M_o = 1.6$	$M_o = 2.2$	$M_o = 2.5$
2nd Ramp	0.0	0.0	0.015	0.012	0.012
3rd Ramp	0.0	0.0	0.025	0.021	0.022
Throat Slot	0.0	0.0	0.034	0.070	0.089
Sideplate	–	–	–	0.020*	–

* (Estimated)

FIGURE 5 - CONFIGURATION 1 INLET BLEED SYSTEM AND SIDEPLATE GEOMETRY

Configuration 1

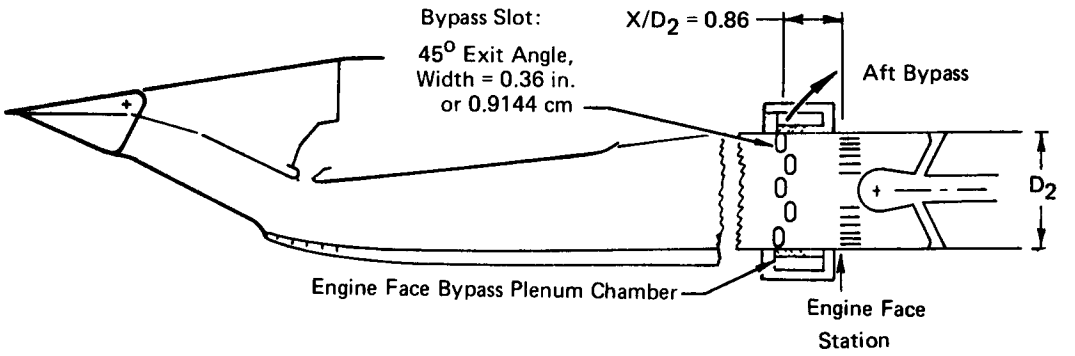

Nominal Bypass Mass Flow Ratios
at 0.95 Critical Operation Condition
(in Terms of m_{BP}/m_o):

M_o:	0.9	1.2	1.6	2.2	2.5
m_{BP}/m_o:	0.0	0.0	0.034	0.048	0.058

Aft Bypass Slot Arrangement

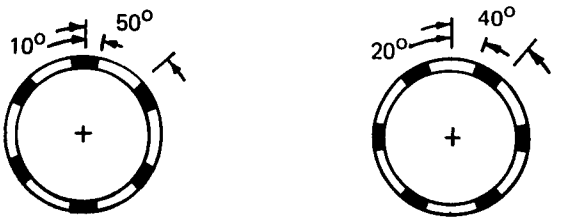

Note: Dimensions are given in model scale, 1 inch = 2.54 cm.

FIGURE 6 - AFT BYPASS SYSTEM OF CONFIGURATION 1

GP74-0119-11

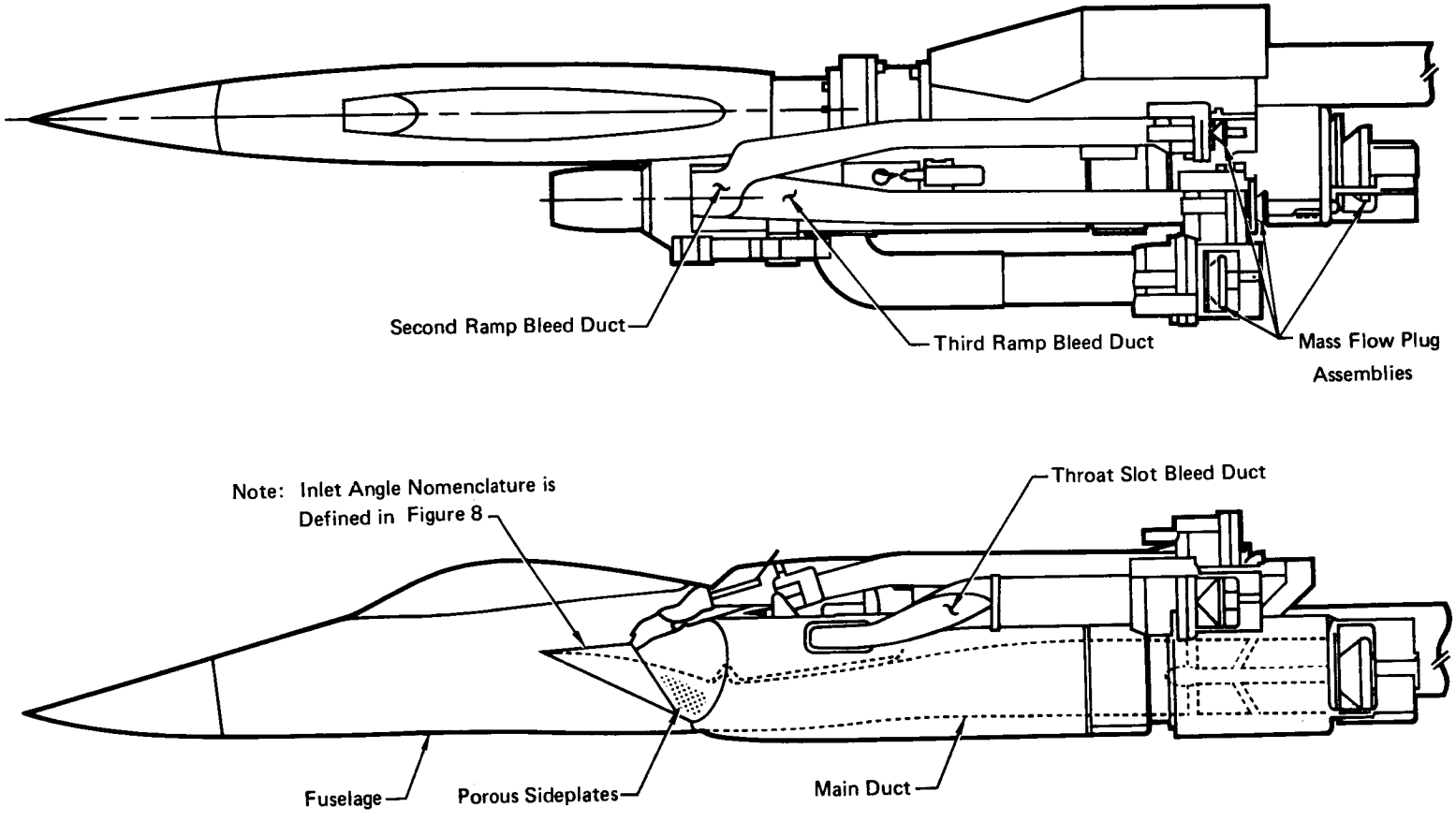

FIGURE 7 - CONFIGURATION 2 INLET MODEL

CONFIGURATION 2

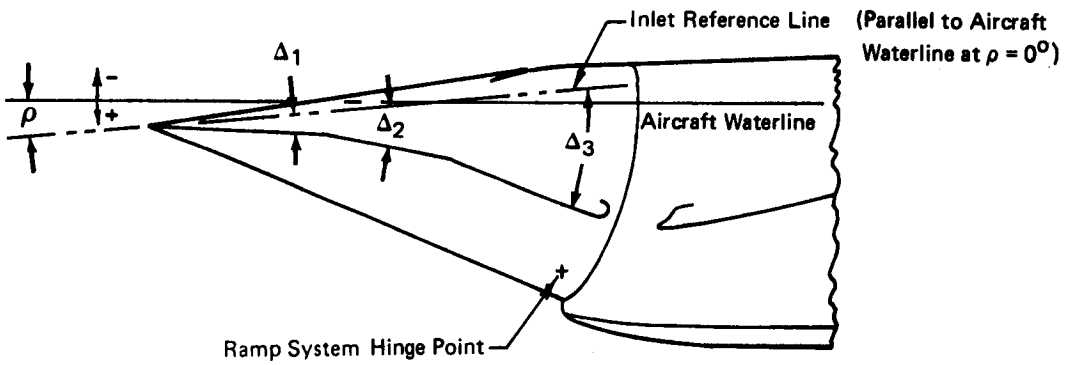

To determine ramp angles relative to waterline, apply this equation: $\Delta' = \Delta - \rho$

FIGURE 8 - CONFIGURATION 2 INLET ANGLE NOMENCLATURE

CONFIGURATION 2

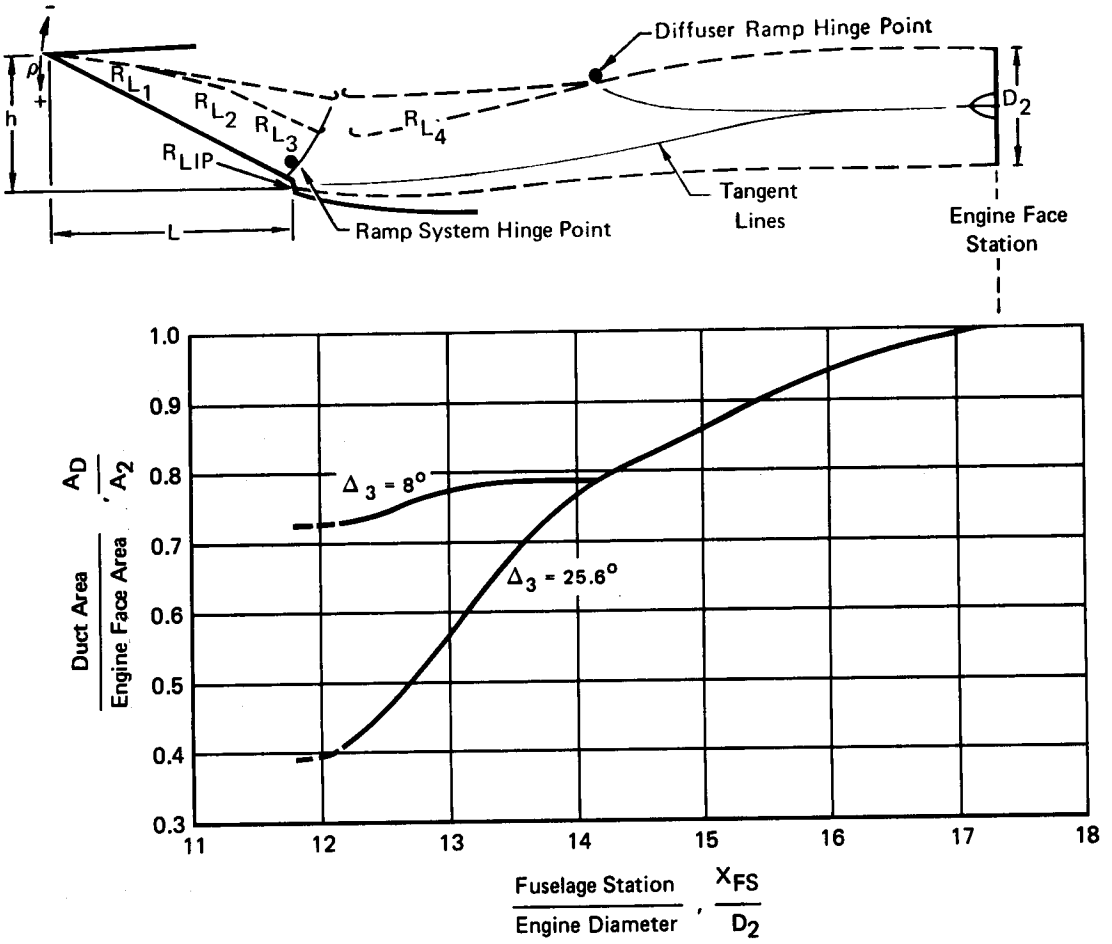

Summary of Dimensions

(Referenced to D_2) D_2 = 5.80 inches or 14.732 cm. (Model Scale)

Ramp Lengths		Inlet Width, W/D_2	0.747
R_{L_1}/D_2	0.834	Ramp System Length, L/D_2	
R_{L_2}/D_2	0.654	@ $\rho = 0^o$ ($\Delta_1 = 7^o$)	1.955
R_{L_3}/D_2	0.778		
R_{L_4}/D_2	2.160	Sideplate Leading Edge Radius, R_{SP}/D_2	0.002
Cowl Lip Radius R_{LIP}/D_2	0.005		
Inlet Height, h/D_2 @ $\rho = 0^o$ ($\Delta_1 = 7^o$)	1.070		

FIGURE 9 - CONFIGURATION 2 INLET GEOMETRY DEFINITION

Configuration 2

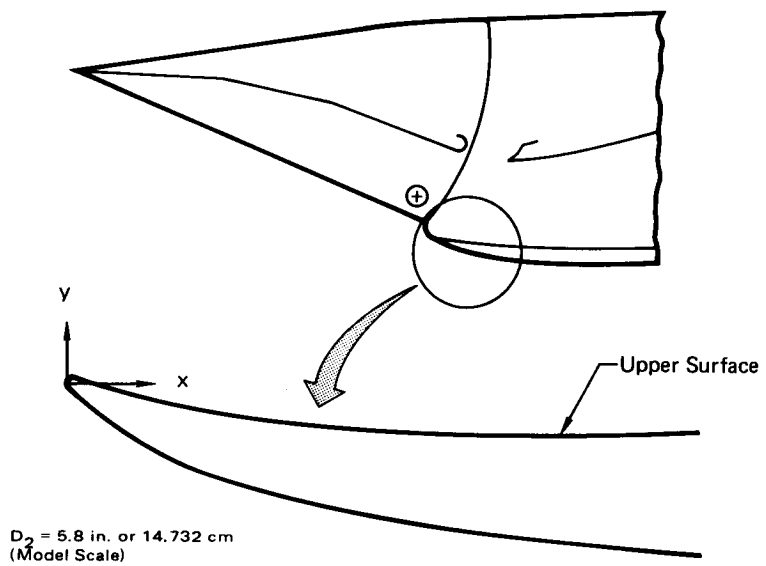

D_2 = 5.8 in. or 14.732 cm
(Model Scale)

Cowl Lip Coordinates

x/D_2	y/D_2	
	Upper Surface	Lower Surface
0	0	0
0.006	0.005	−0.009
0.017	0.002	−0.020
0.028	0	−0.029
0.051	−0.007	−0.045
0.084	−0.016	−0.066
0.124	−0.025	−0.085
0.169	−0.032	−0.102
0.225	−0.039	−0.118
0.281	−0.045	−0.133
0.337	−0.047	−0.143
0.393	−0.049	−0.151
0.449	−0.051	−0.157
0.506	−0.052	−0.163
0.562	−0.052	−0.167

FIGURE 10 - CONFIGURATION 2 COWL LIP COORDINATES

GP74-0119-13

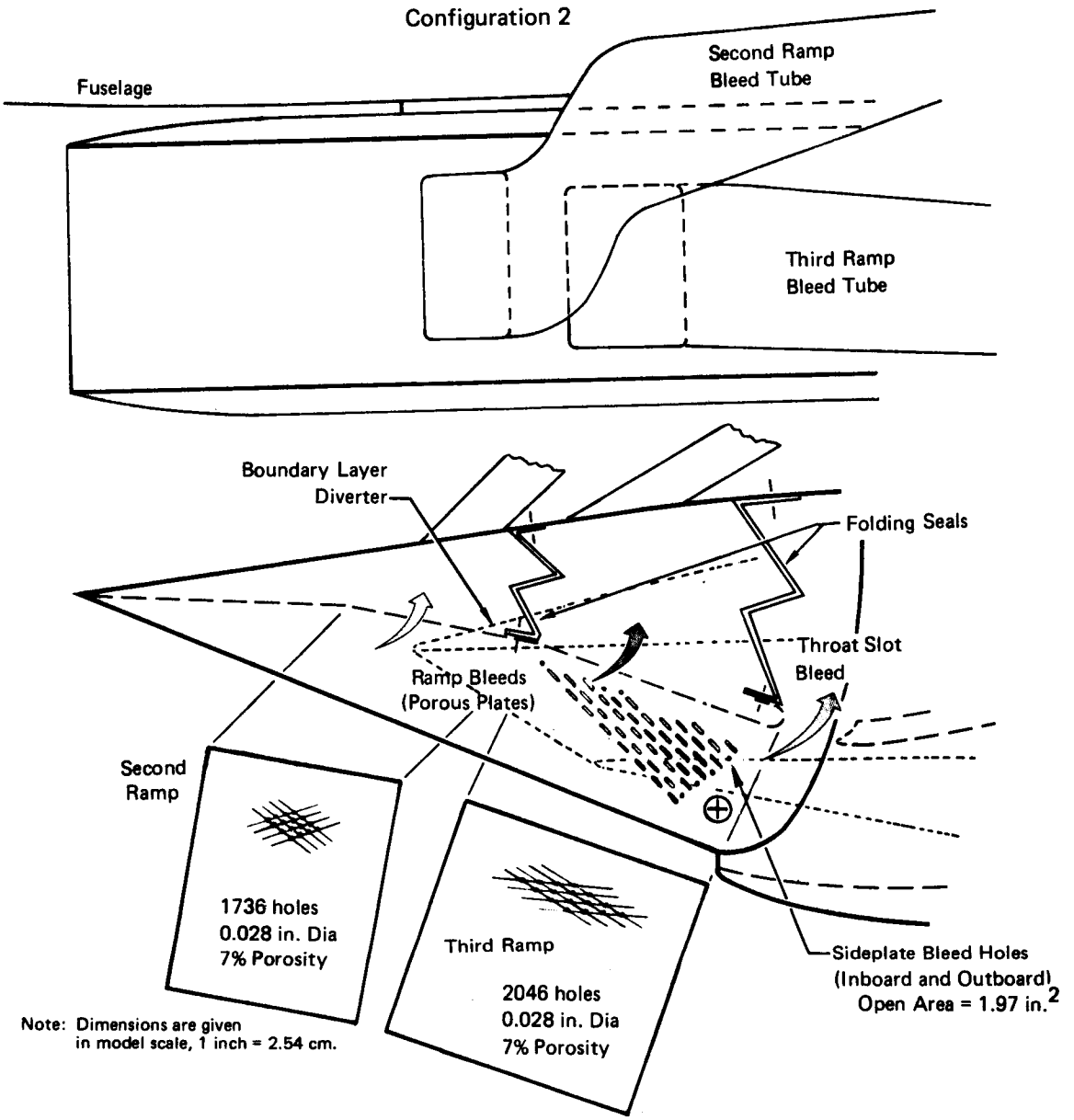

Nominal Bleeds at 0.95 Critical Operating Condition :

(in terms of m_{bleed}/m_o)

* (Estimated)

Bleed	$M_o = 1.6$	$M_o = 2.2$	$M_o = 2.5$
2nd Ramp	0.011	0.008	0.008
3rd Ramp	0.003	0.020	0.023
Throat Slot	0.054	0.062	0.065
Sideplate	–	0.020*	–

GP74-0119-12

FIGURE 11 - CONFIGURATION 2 INLET BLEED SYSTEM AND SIDEPLATE GEOMETRY

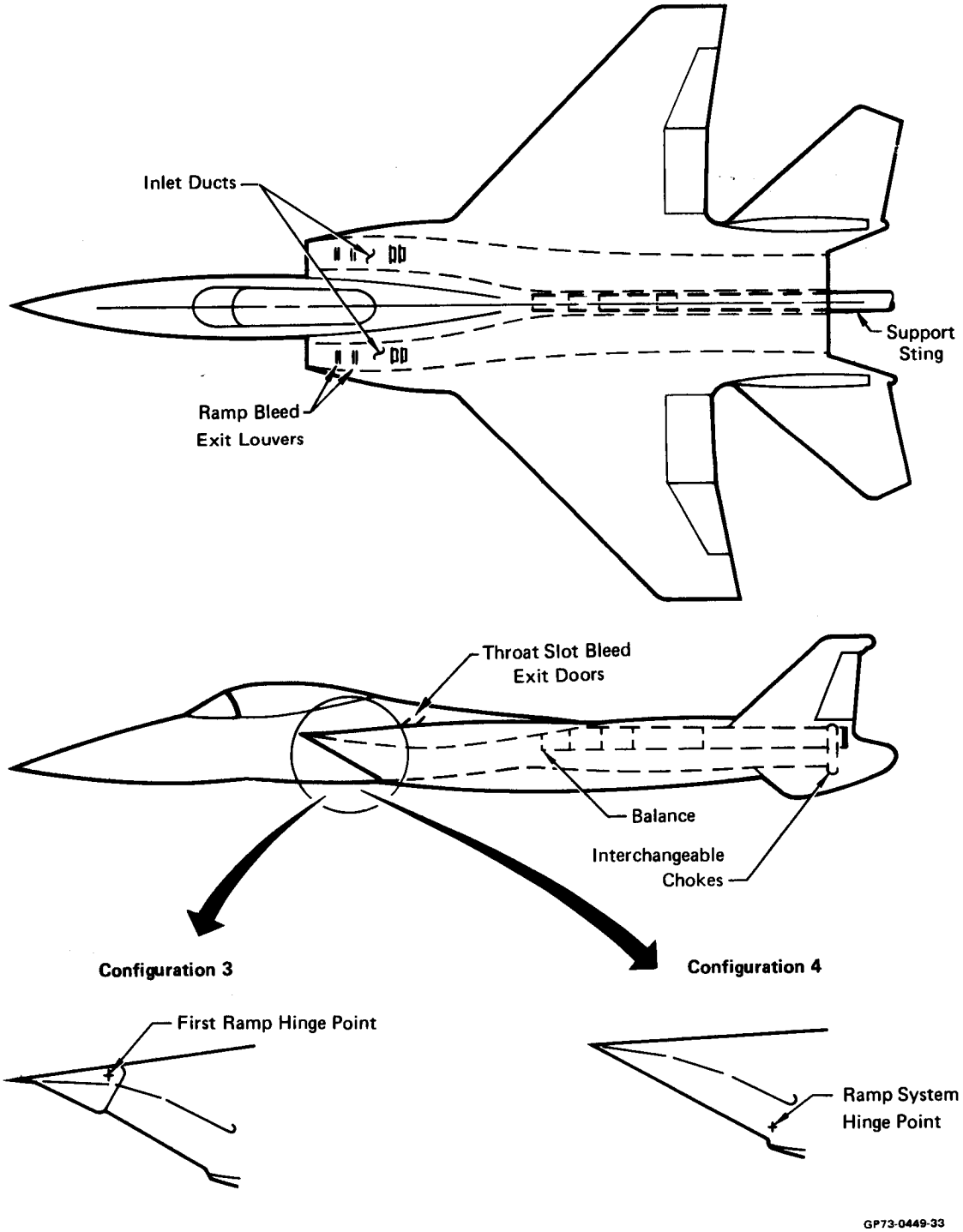

FIGURE 12 - INLET/AIRFRAME DRAG MODEL

Configuration 3

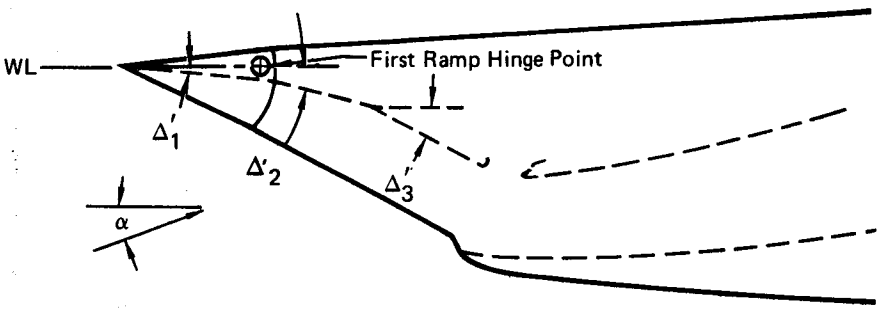

Note: Inlet dimensions are the same as those given for Configuration 2 in Figure 9.

Inlet Ramp Schedules
M_o = 0.6, 0.9, and 1.2

α (°)	Δ'_1 (°)	Δ'_2 (°)	Δ'_3 (°)
−3	0.0	7.8	9.6
0	↓	↓	↓
4	↓	↓	↓
8	↓	↓	↓
12	↓	↓	↓
16	↓	↓	↓
20	↓	↓	↓

FIGURE 13 - CONFIGURATION 3 INLET GEOMETRY DEFINITION

Configuration 4

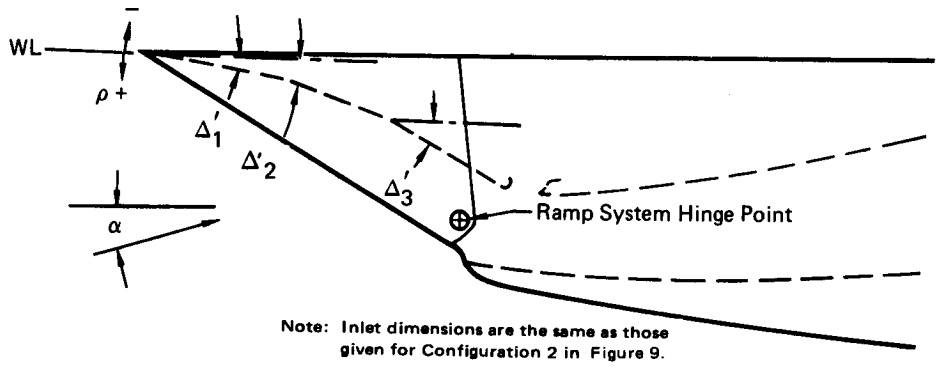

Note: Inlet dimensions are the same as those given for Configuration 2 in Figure 9.

Inlet Ramp Schedules
M_o = 0.6 and 0.9

α (°)	Rotation Angle, ρ (°)	Δ'_1 (°)	Δ'_2 (°)	Δ'_3 (°)
−3	4	3	4.8°	7.6
0	7	0	2.5	4.1
4	11	−4	−2.8	−0.5
8	↓	↓	↓	↓
12				
16				
20				

M_o = 1.2

α (°)	Rotation Angle, ρ (°)	Δ'_1 (°)	Δ'_2 (°)	Δ'_3 (°)
−3	3	4	5.9	8.8
0	6	1	2.8	6.7
4	10	−3	−1.6	1.0
8	11	−4	−2.6	−0.2
12	↓	↓	↓	↓
16				
20				

FIGURE 14 - CONFIGURATION 4 INLET GEOMETRY DEFINITION

Configurations 3 and 4

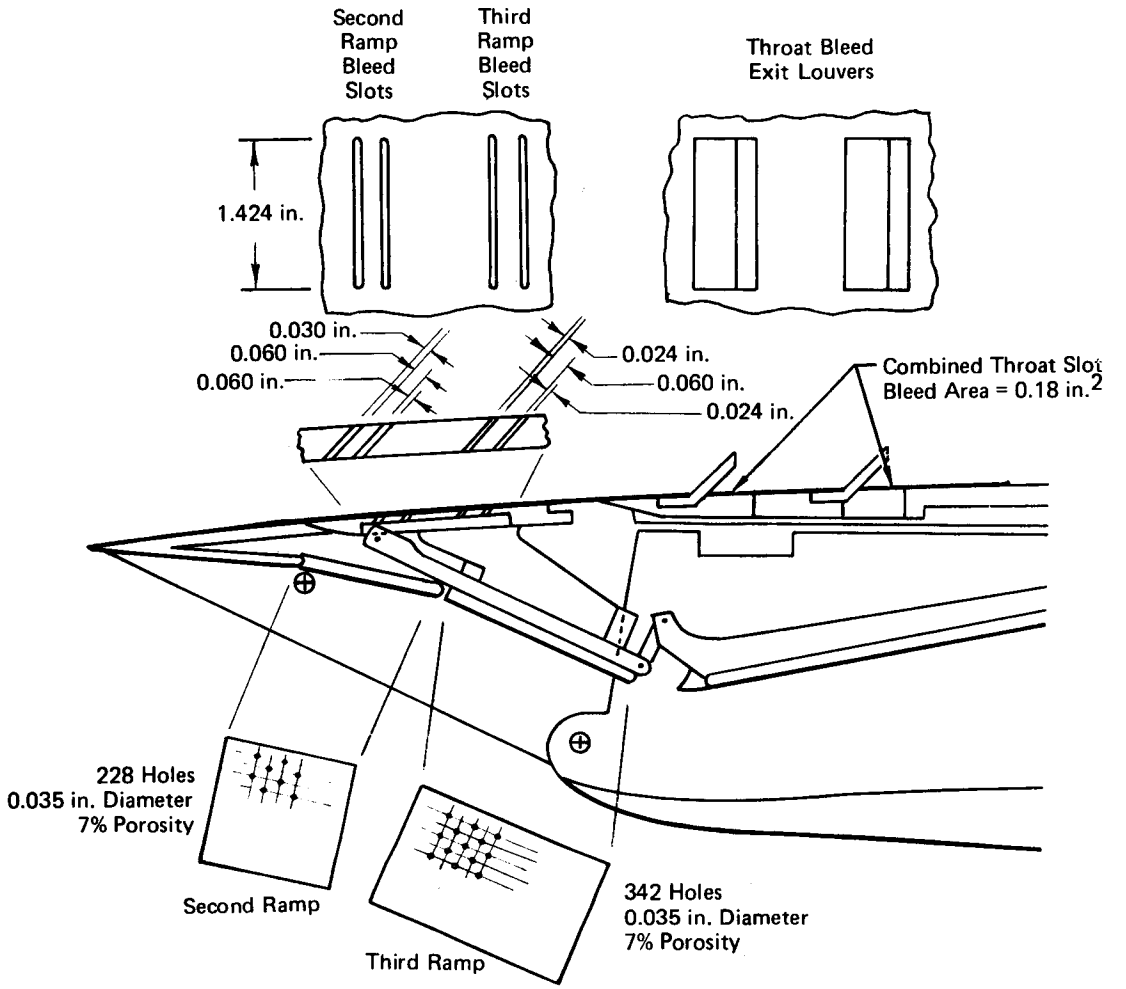

Notes: • At transonic conditions the bleed rates are negligible.

• Dimensions are given in model scale, 1 in. = 2.54 cm

FIGURE 15 - INLET/AIRFRAME DRAG MODEL BLEED SYSTEM

GP74-0119-7

Configuration 1

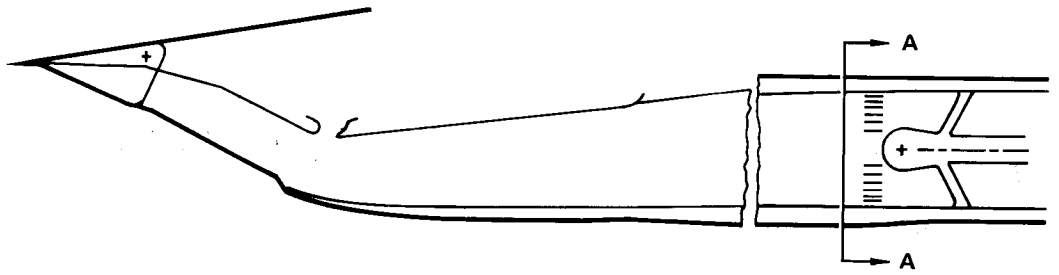

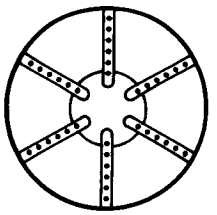

A-A

Engine Face Total Pressure Rake
(Steady State and Dynamic
Total Pressures Measured)

FIGURE 16 - CONFIGURATION 1 INLET PERFORMANCE MODEL INSTRUMENTATION

GP74-0119-10

Configuration 2

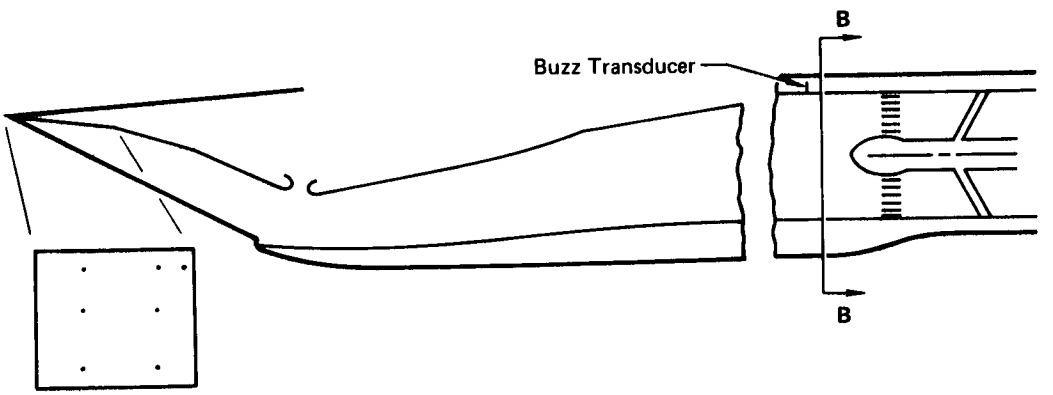

• First Ramp
Static Pressure Taps

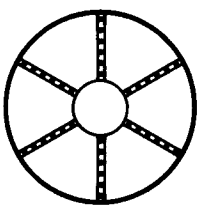

B-B

Engine Face Total Pressure Rake

(Steady State and Dynamic
Total Pressures Measured)

FIGURE 17 - CONFIGURATION 2 INLET PERFORMANCE MODEL INSTRUMENTATION

GP74-0119-8

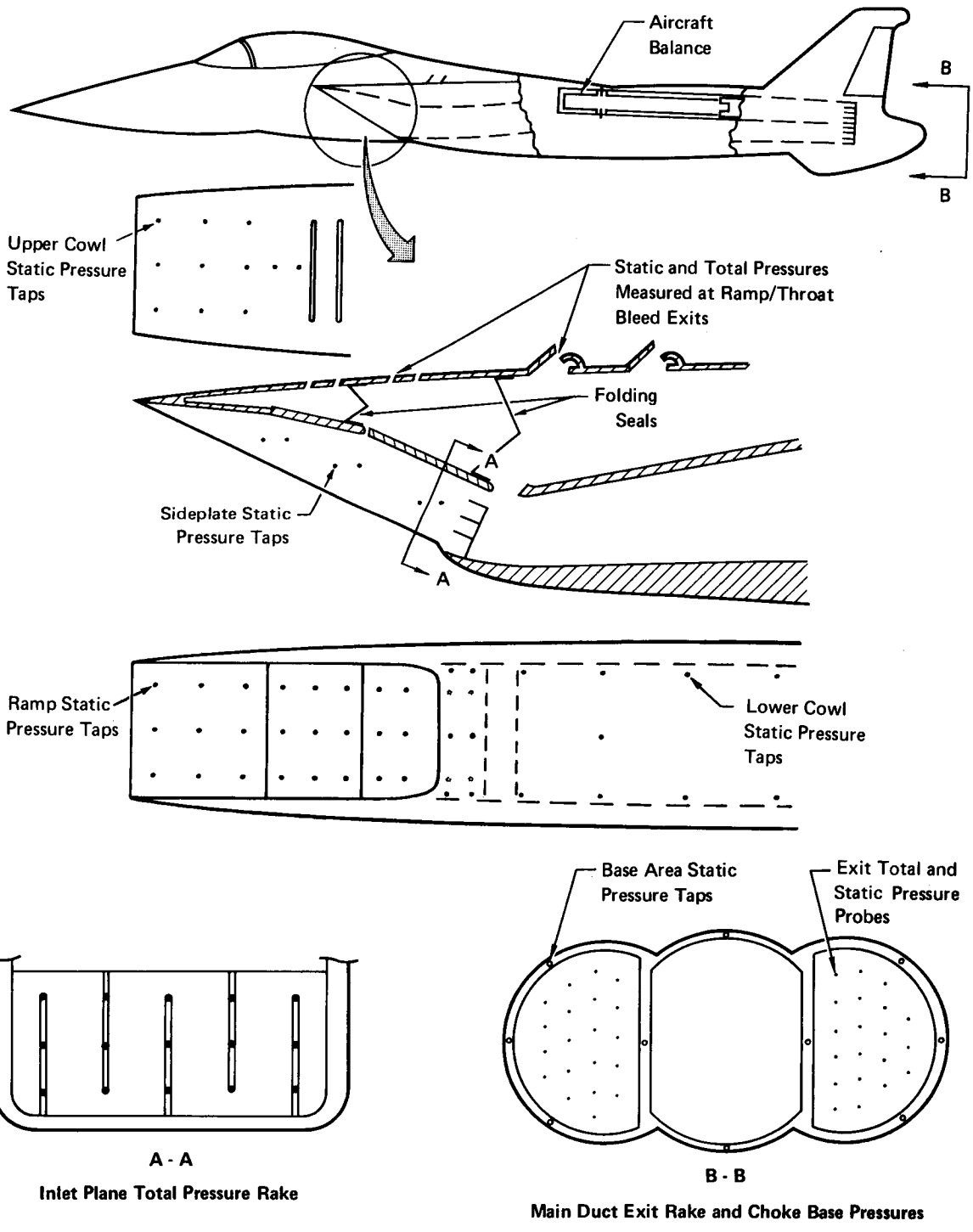

A - A

Inlet Plane Total Pressure Rake

B - B

Main Duct Exit Rake and Choke Base Pressures

FIGURE 18 - INLET/AIRFRAME DRAG MODEL INSTRUMENTATION

GP73-0449-81

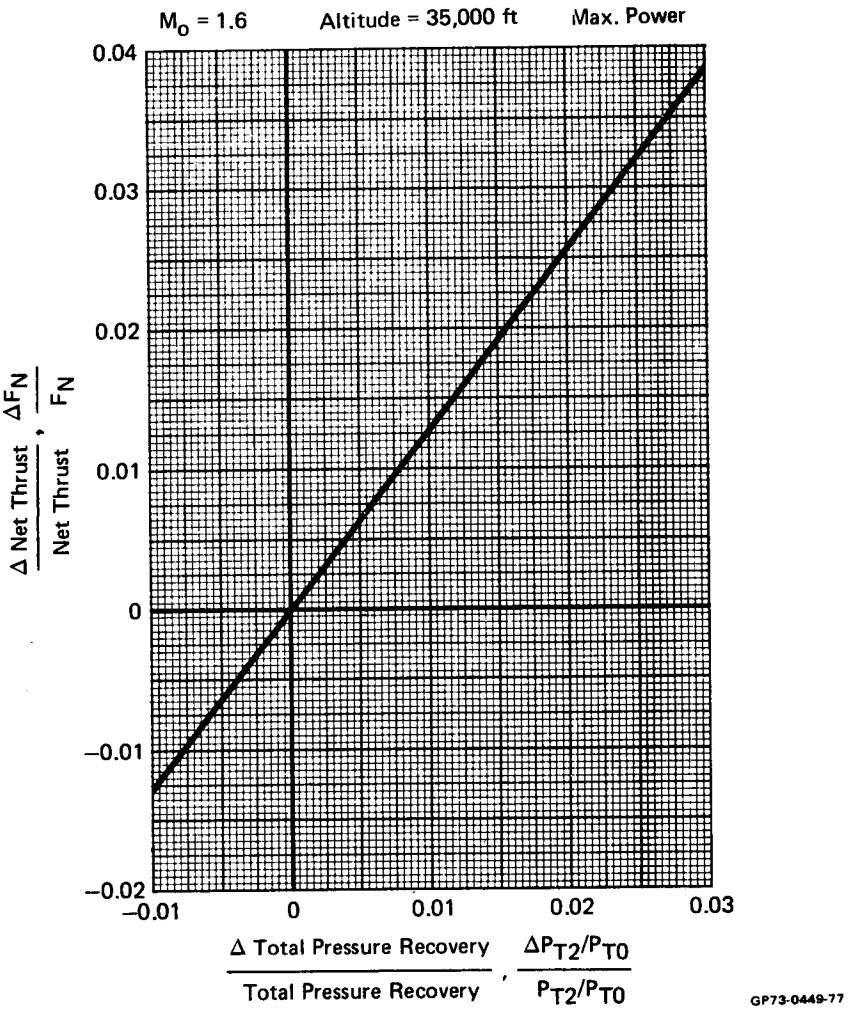

(a) M_o = 1.6

FIGURE 19 - NET THRUST CHANGE DUE TO PRESSURE RECOVERY CHANGE

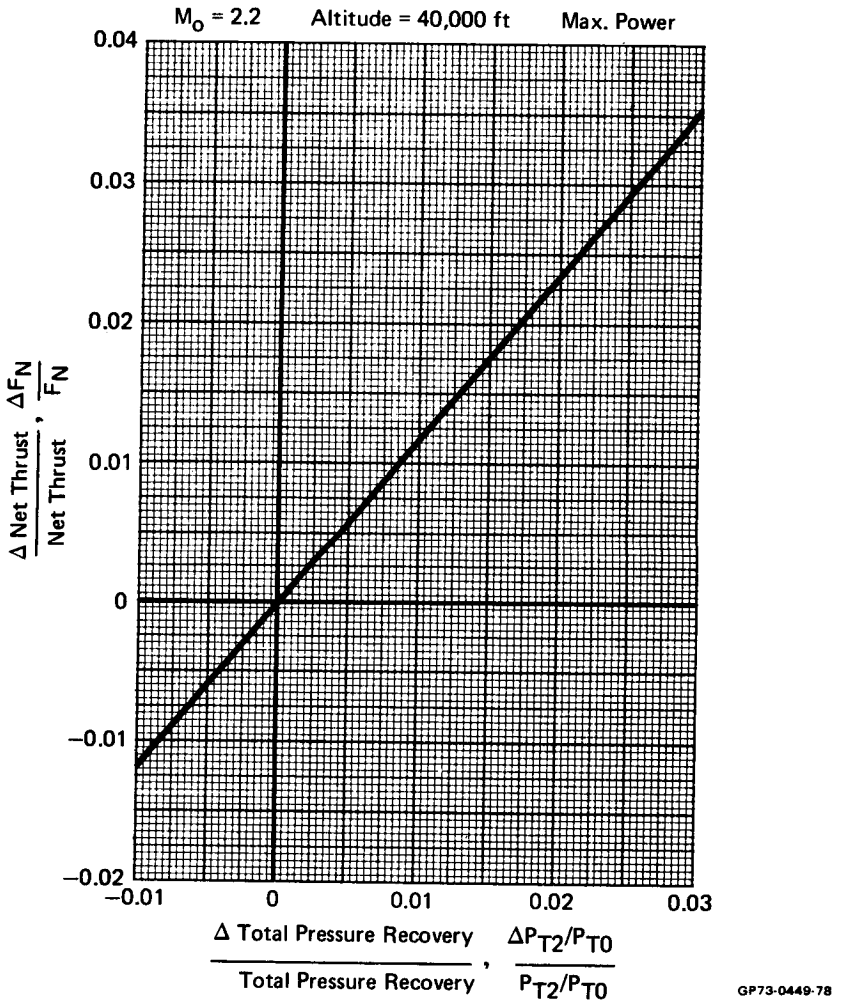

(b) M_o = 2.2

FIGURE 19 (Concl.) - NET THRUST CHANGE DUE TO PRESSURE RECOVERY CHANGE

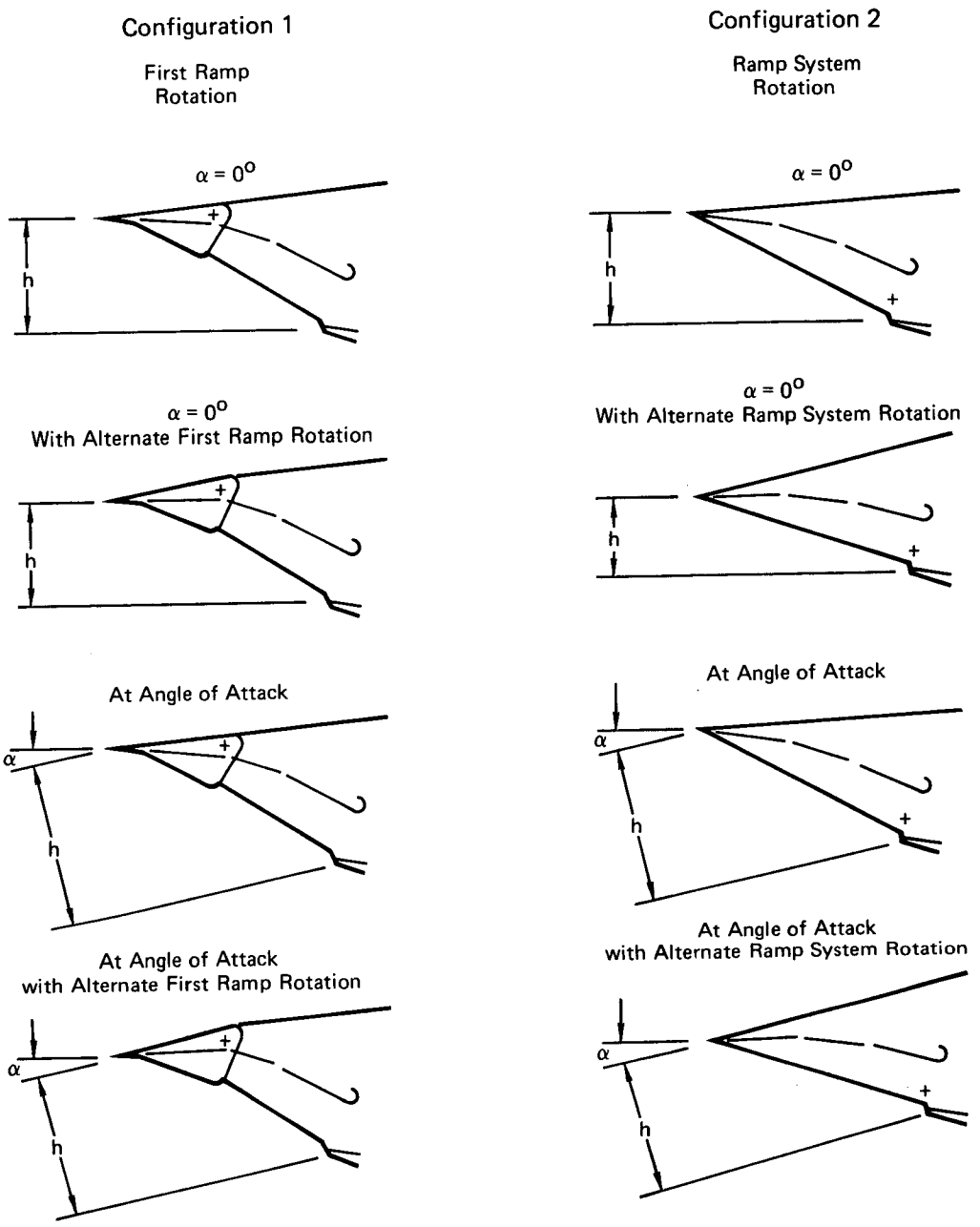

Note: Inlet capture area, A_c, is directly proportional to inlet height, h

FIGURE 20 - EFFECT OF ANGLE OF ATTACK AND FIRST RAMP ANGLE ON INLET CAPTURE AREA

Configuration 1

Transonic Conditions

Mach Number	0.9 and 1.2
Angle of Attack (^{o})	Capture Area, A_c/A_{c_o}
−2.5	0.822
0	0.909
4	1.046
8	1.176
12	1.304
16	1.421
20	1.537
24	1.637
26.25	1.698

Supersonic Conditions

Mach Number	1.6	2.2	2.5
Angle of Attack (^{o})	Capture Area, A_c/A_{c_o}	Capture Area, A_c/A_{c_o}	Capture Area, A_c/A_{c_o}
0		1.000	
3		1.103	1.126
4	1.088		
5		1.169	1.192
7	1.186	1.235	1.258
9		1.300	
10	1.283		
11		1.361	
13	1.375	1.422	1.445
16	1.462	1.510	
20	1.575	1.621	
22.5	1.641	1.684	

Note: Reference Capture Area, A_{c_o}, determined at $\alpha = 0^o$, $\Delta_1 = 5.6^o$ is 6.51 ft^2 (full scale) or 0.605 m^2 [1 ft = 0.3048 m]

Inlet Capture Area, $A_c = h \times W$ (Minus Corrections for Cowl Lip Radius)

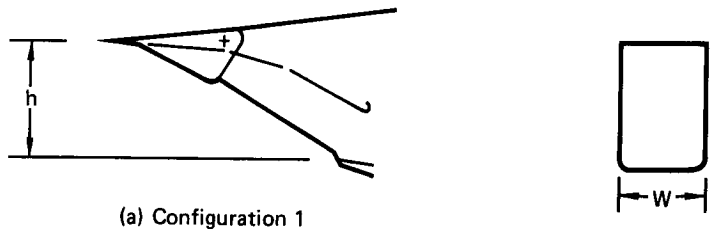

(a) Configuration 1

FIGURE 21 - INLET CAPTURE AREA VARIATIONS

GP74-0119-1

Configuration 2

M_o = 1.6		
α (^{o})	ρ (^{o})	A_c/A_{c_o}
−4	−2	0.936
0	2	0.936
4	6	0.932
8	10	0.932
12	11	1.019
16	11	1.142
20	11	1.259
24	11	1.370

M_o = 2.2		
α (^{o})	ρ (^{o})	A_c/A_{c_o}
−4	−4*	0.993
−4	0	0.873
−4	1.9	0.808
0	−2	1.065
0	0*	1.000
2	2	1.001
4	2	1.064
4	4*	0.994
8	4	1.120
8	6	1.059
	8*	0.994
12	11	1.020
16	11	1.143
20	11	1.259
24	11	1.370

M_o = 2.2		
α (^{o})	ρ (^{o})	A_c/A_{c_o}
0	−3	1.090
4	1	1.094
8	5	1.088
12	9	1.090
16	11	1.142

Note: Reference Capture Area, A_{c_o}, determined at $\alpha = 0^o$, $\Delta_1 = 7^o$ ($\rho = 0^o$) is 6.91 ft^2 or 0.642 m^2 [1 ft = 0.3048m]

*Denotes nominal ramp rotation when more than one value of ρ is given at a certain angle of attack

Inlet Capture Area, $A_c = h \times W$ (Minus Corrections for Cowl Lip Radius)

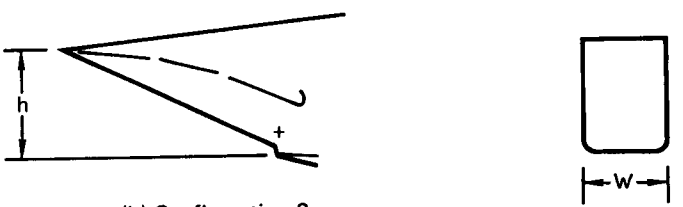

(b) Configuration 2

FIGURE 21 (Concl.) - INLET CAPTURE AREA VARIATIONS

GP74-0119-2

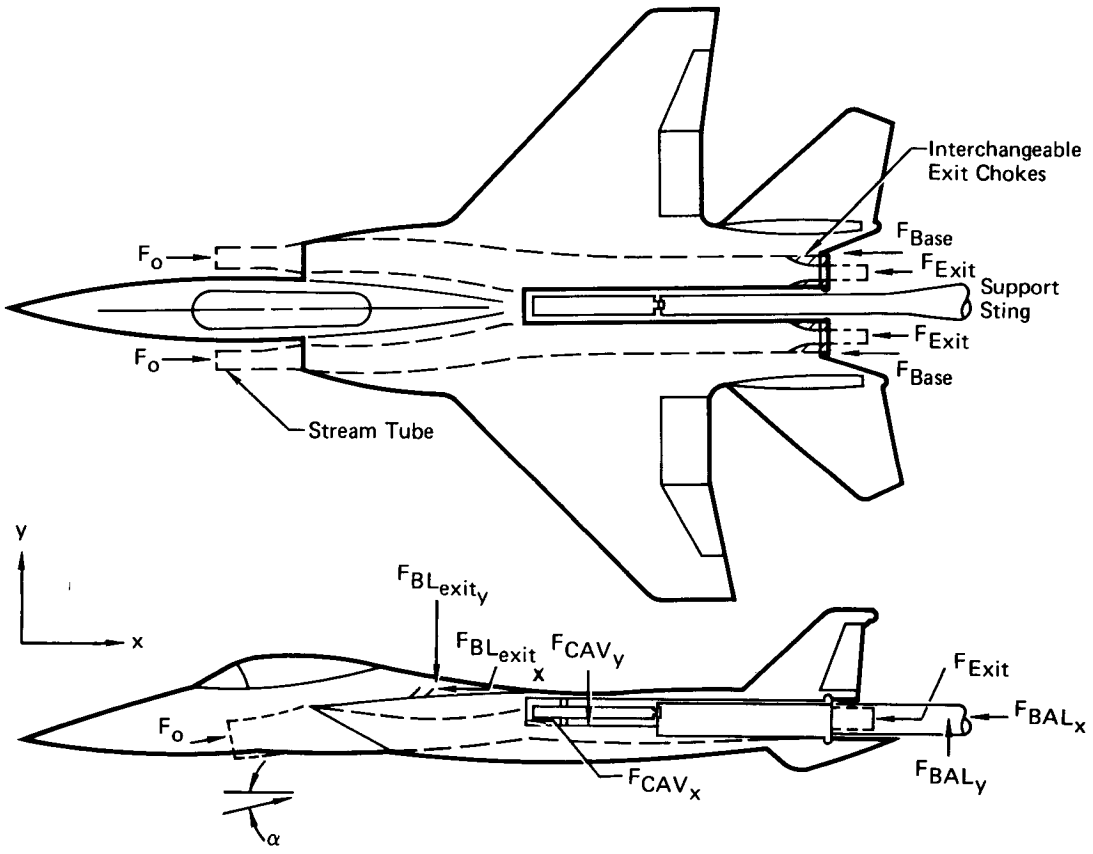

Aircraft Drag Force, $D = F_x \cos\alpha + F_y \sin\alpha - F_o$

Where $F_x = F_{BAL_x} + F_{Exit} + F_{BL_{exit_x}} + F_{Base} + F_{CAV_x}$

And $F_y = F_{BAL_y} + F_{CAV_y} + F_{BL_{exit_y}}$

FIGURE 22 - COMPONENT FORCES ACTING ON THE INLET/AIRFRAME DRAG MODEL

GP74-0119-3

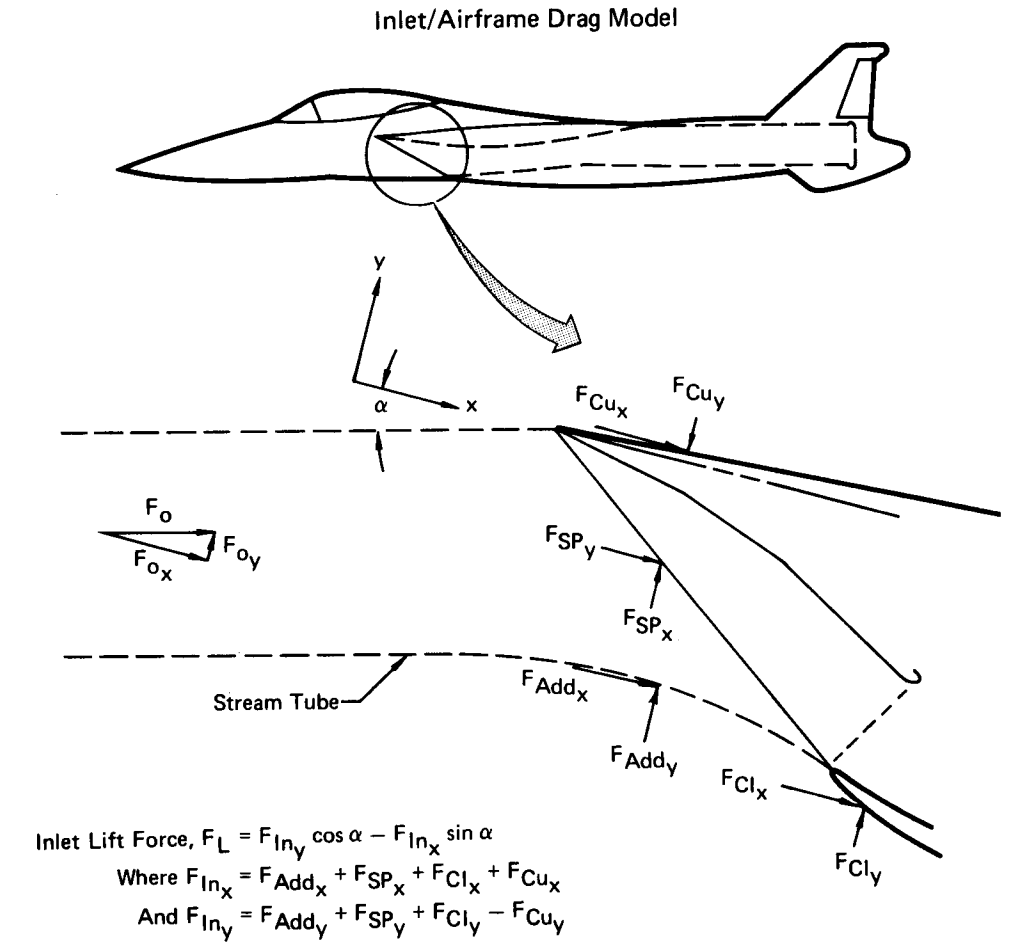

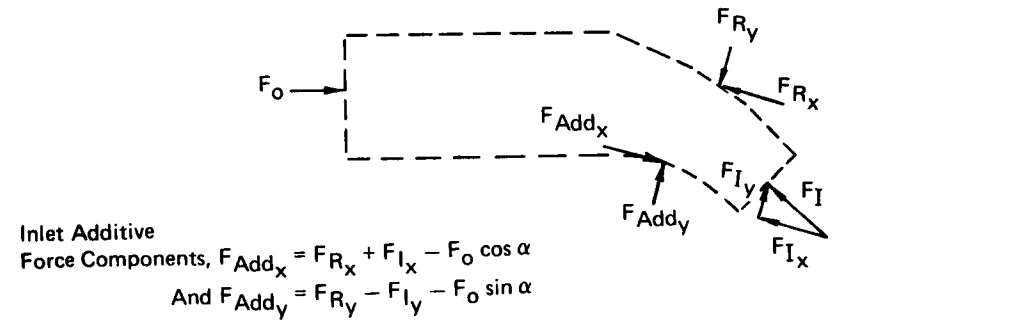

FIGURE 23 - COMPONENTS OF THE INLET LIFT FORCE ACTING ON THE INLET/AIRFRAME DRAG MODEL

GP74-0119-4

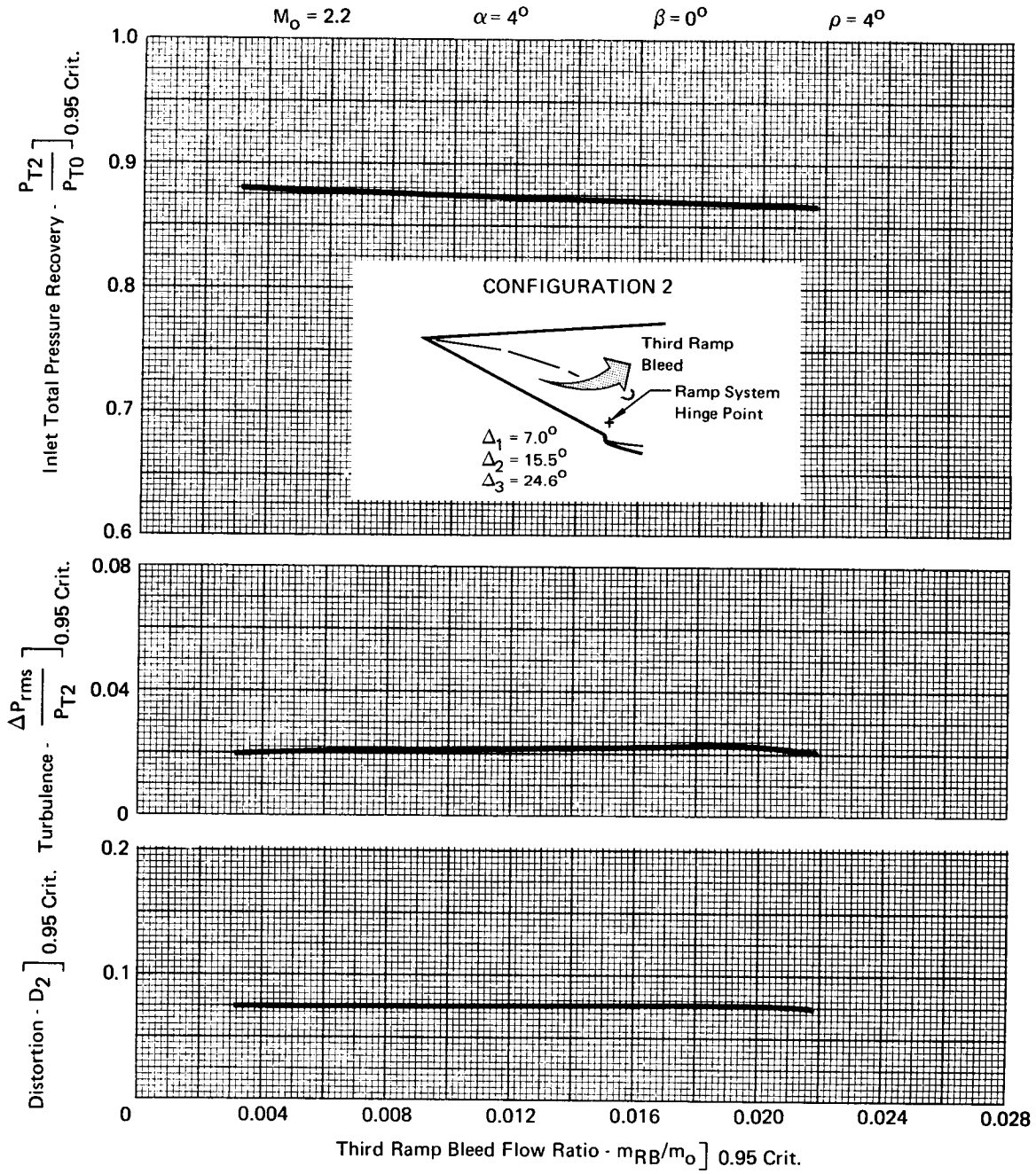

FIGURE 24 - EFFECTS OF THIRD RAMP BLEED ON PRESSURE RECOVERY, TURBULENCE, AND DISTORTION

GP73-0449-4

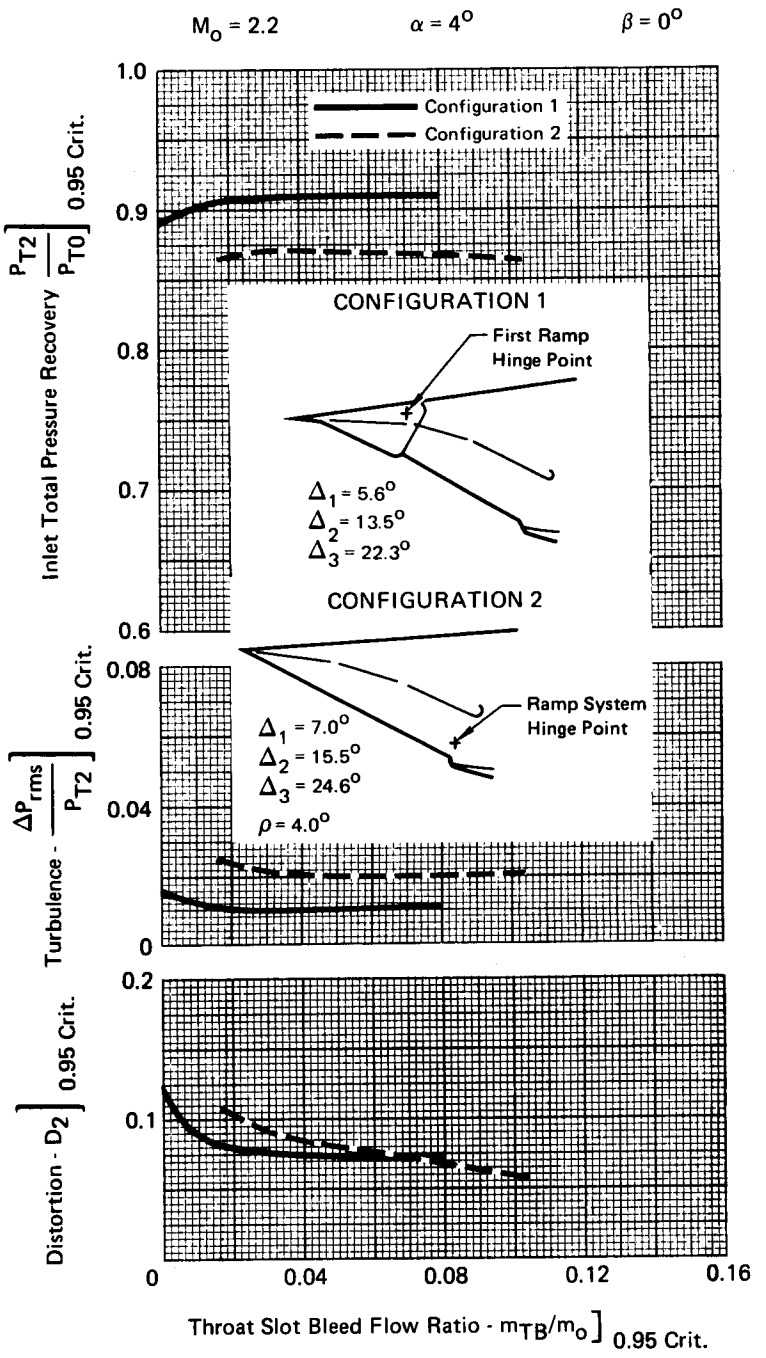

FIGURE 25 -EFFECTS OF THROAT SLOT BLEED ON PRESSURE RECOVERY, TURBULENCE, AND DISTORTION

GP73-0449-6

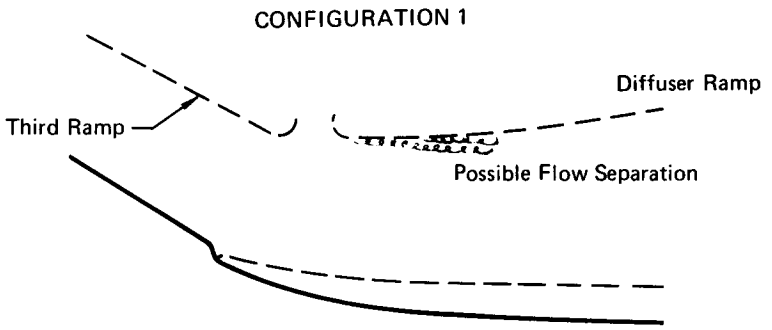

Total Pressure Recovery Maps at Engine Face
(View Looking Aft)

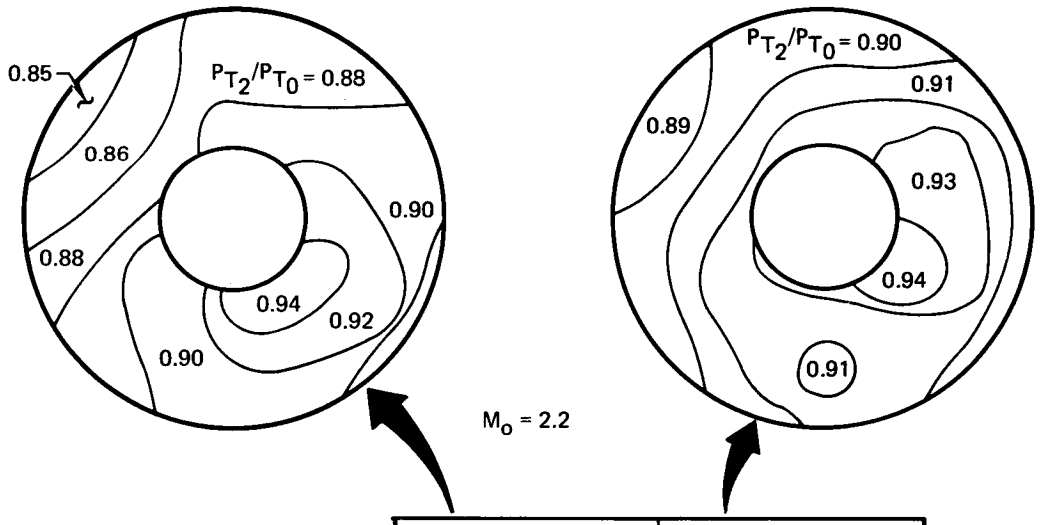

	Without Throat Bleed	With Throat Bleed
Throat Bleed, m_{TB}/m_o	0.0	0.08
Pressure Recovery P_{T_2}/P_{T_0}	0.900	0.915
Turbulence, T	0.014	0.011
Steady State Distortion, D_2	0.112	0.070

GP73-0449-18

FIGURE 26 - EFFECTS OF THROAT SLOT BLEED ON DIFFUSER FLOW PROPERTIES AT MACH 2.2

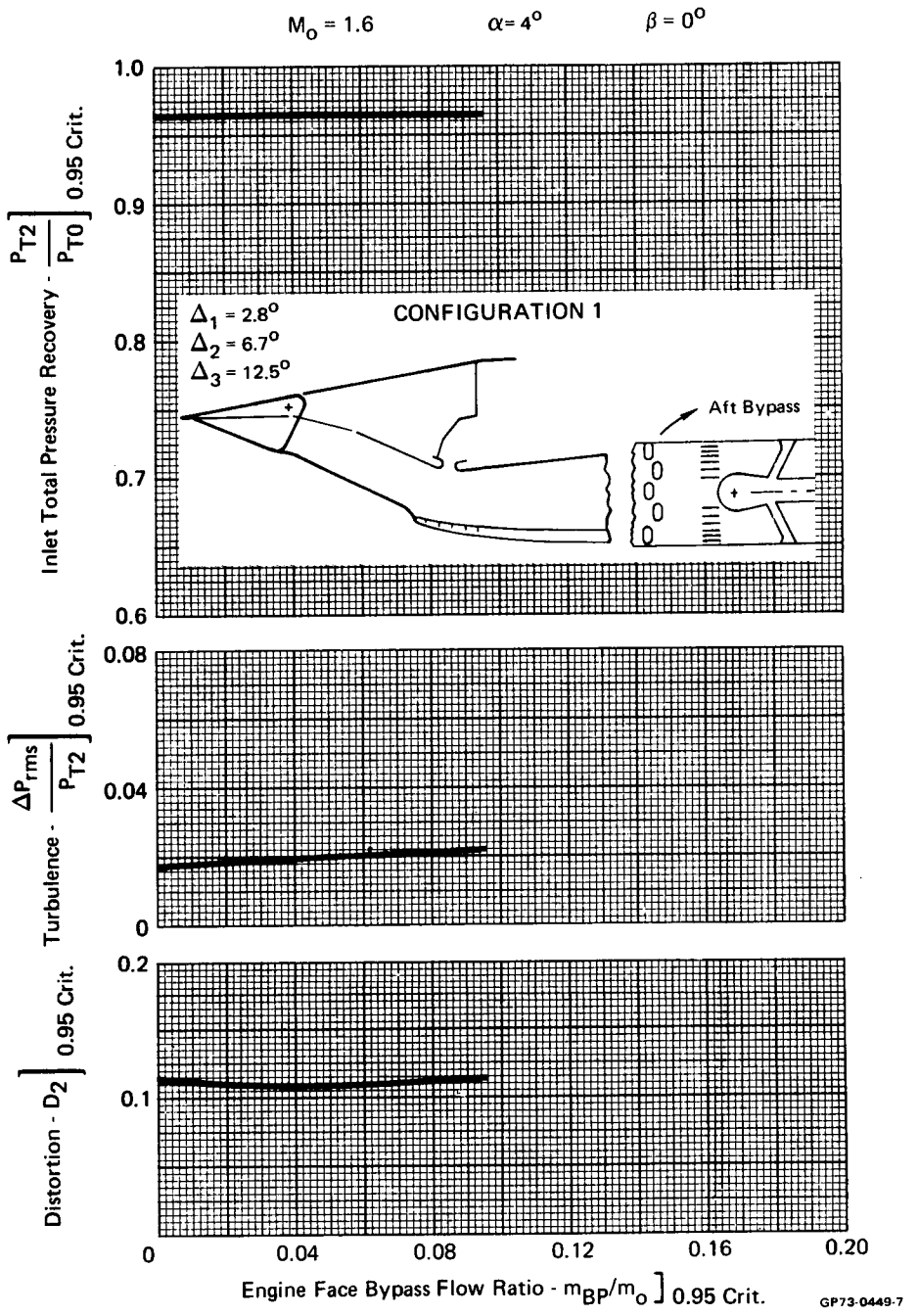

(a) M_o = 1.6

FIGURE 27 - EFFECTS OF BYPASS FLOW ON PRESSURE RECOVERY, TURBULENCE, AND DISTORTION

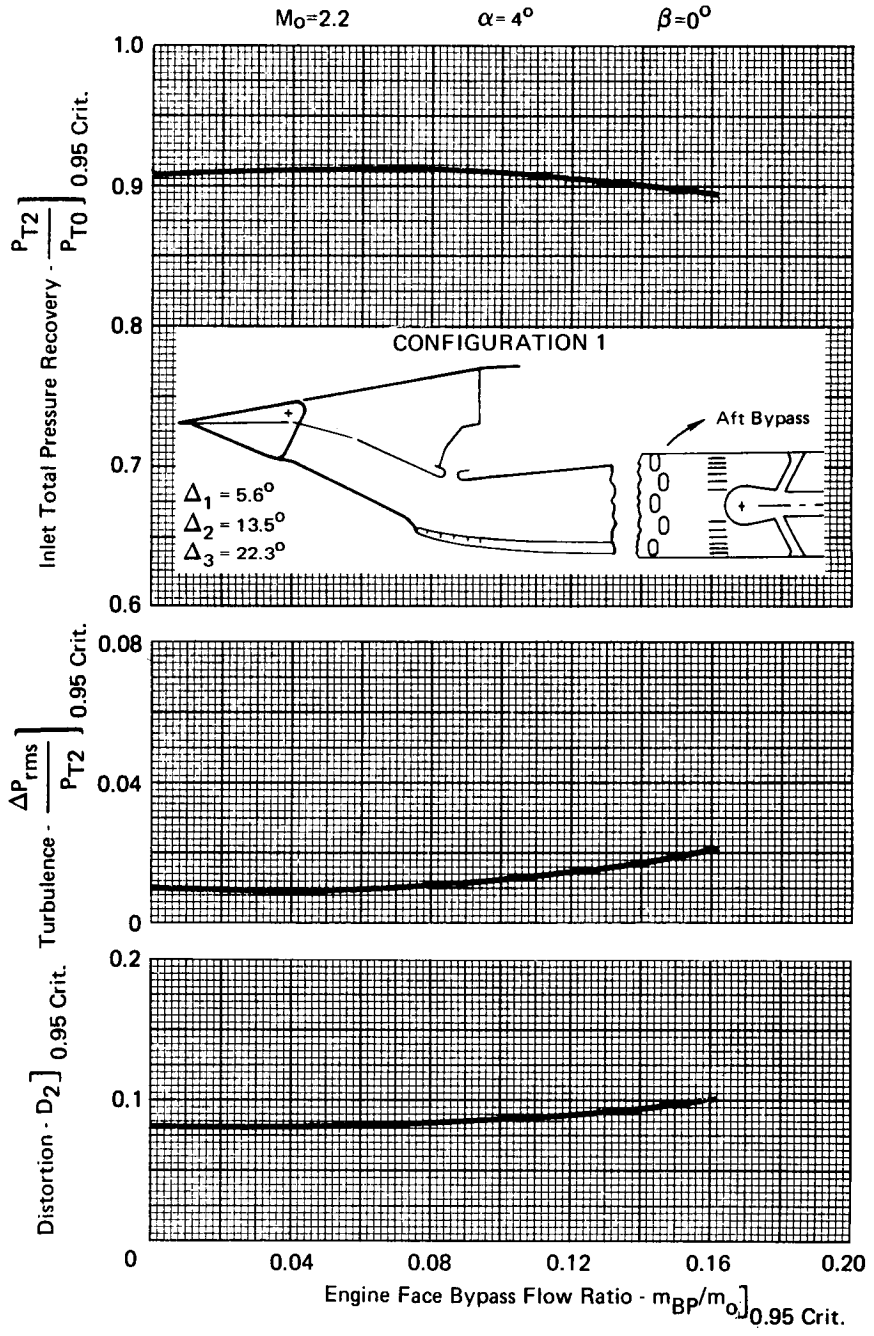

(b) M_o = 2.2

FIGURE 27 (Concl.) - EFFECTS OF BYPASS FLOW ON PRESSURE RECOVERY, TURBULENCE, AND DISTORTION

GP73-0449-8

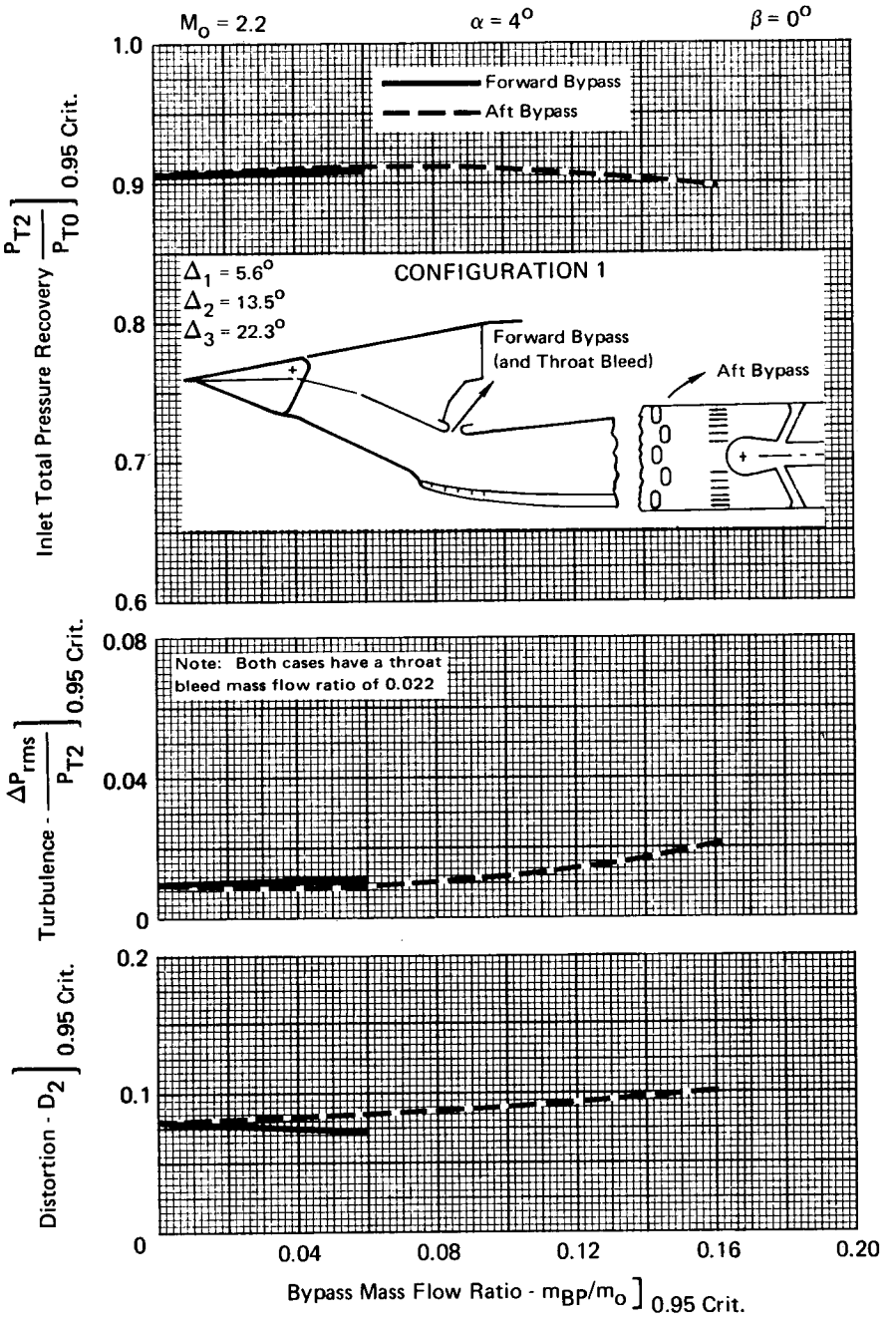

FIGURE 28 - COMPARISON OF THE EFFECTS OF FORWARD AND AFT BYPASS ON PRESSURE RECOVERY, TURBULENCE, AND DISTORTION

GP73-0449-9

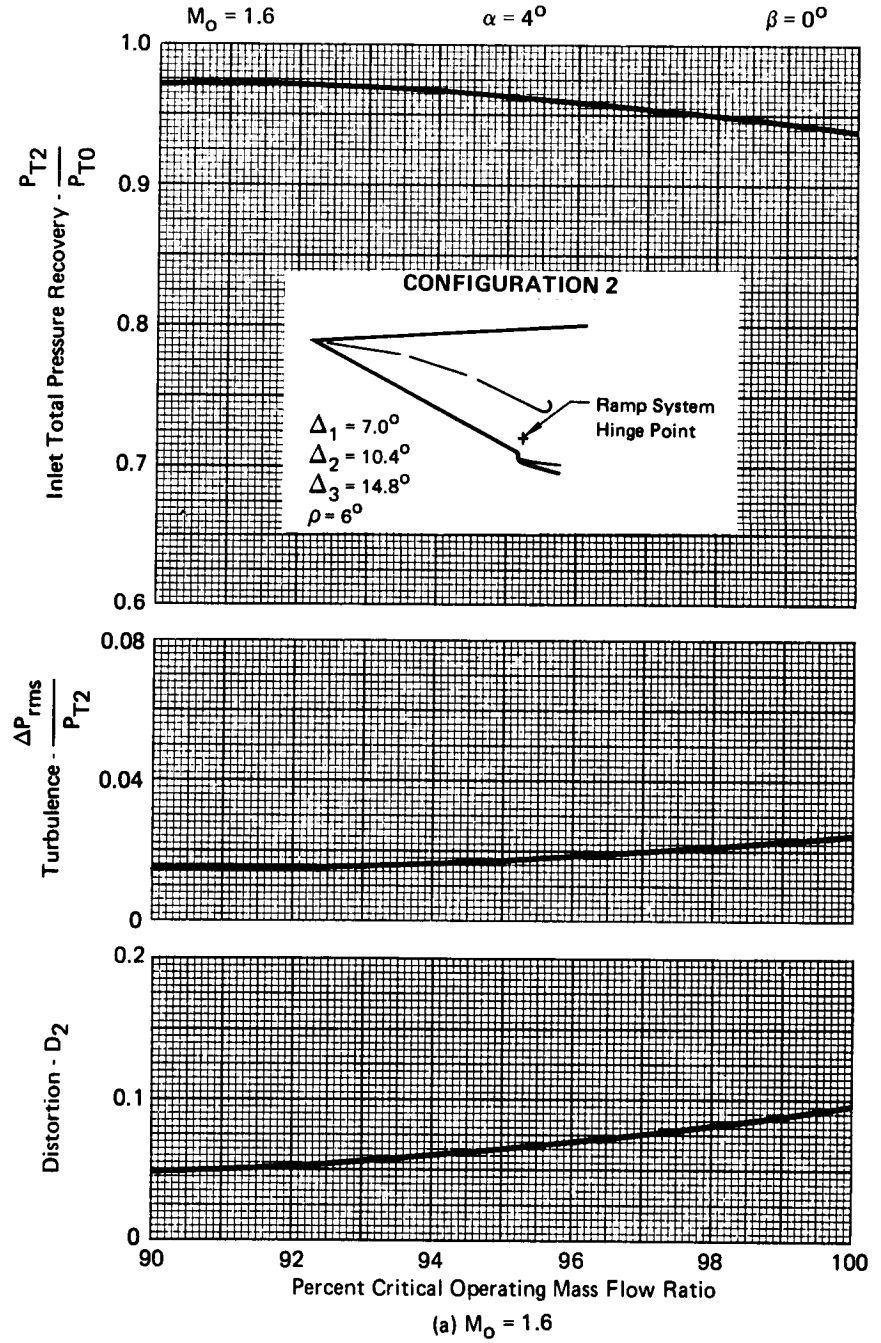

(a) M_o = 1.6

FIGURE 29 - EFFECTS OF OPERATING MASS FLOW RATIO ON PRESSURE RECOVERY, TURBULENCE, AND DISTORTION

GP73-0449-10

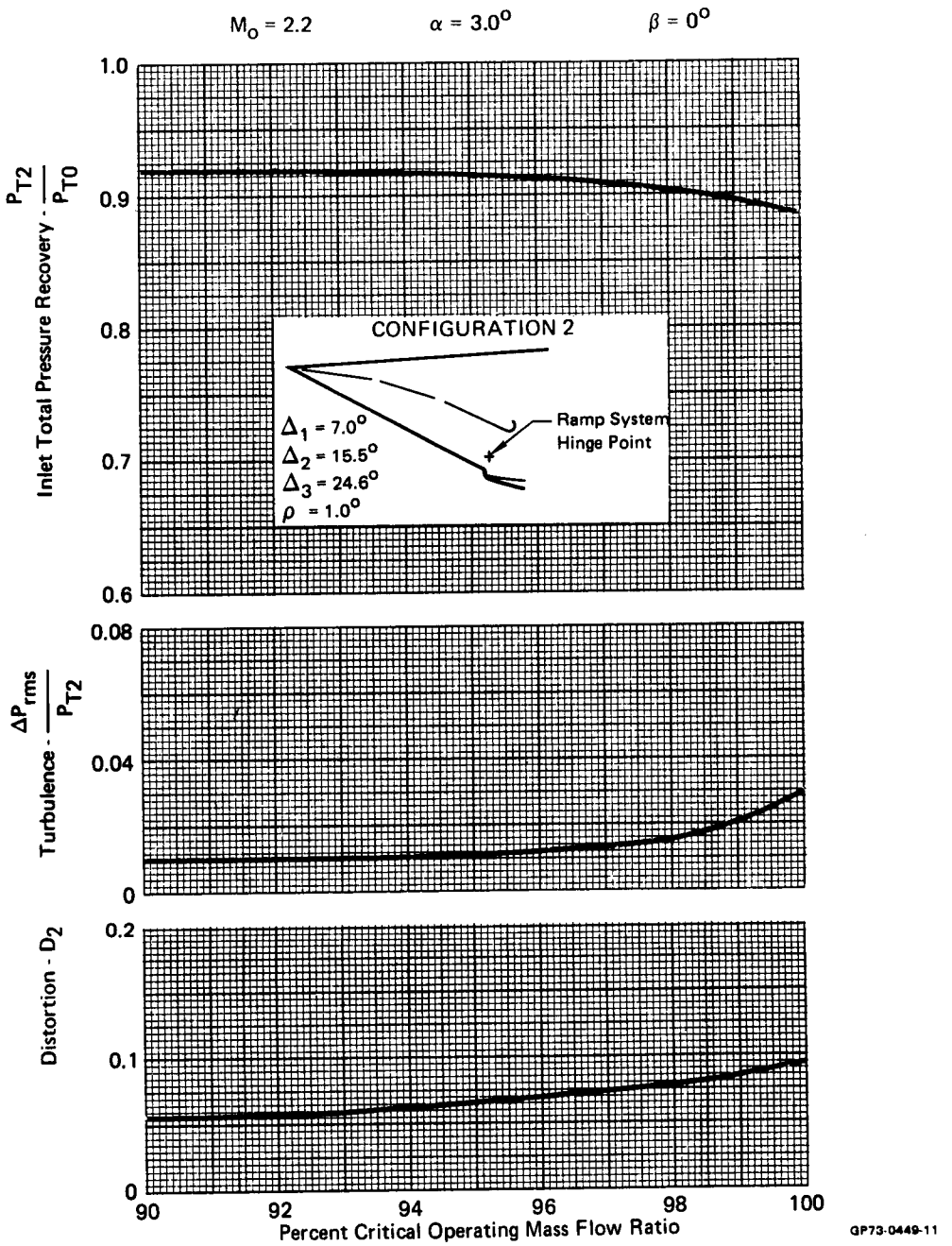

(b) M_o = 2.2

FIGURE 29 (Concl.) - EFFECTS OF OPERATING MASS FLOW RATIO ON PRESSURE RECOVERY, TURBULENCE, AND DISTORTION

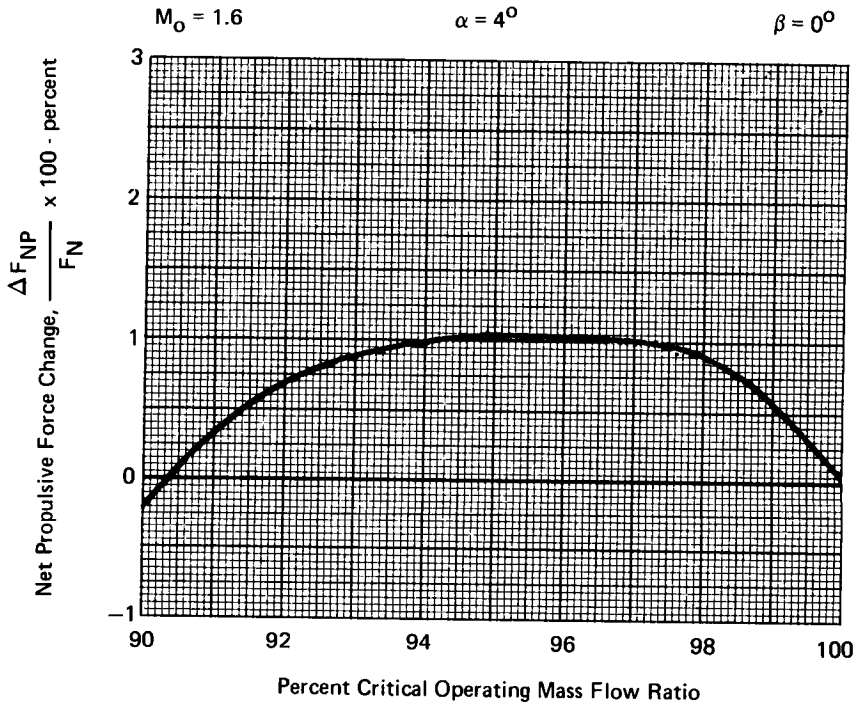

CONFIGURATION 2

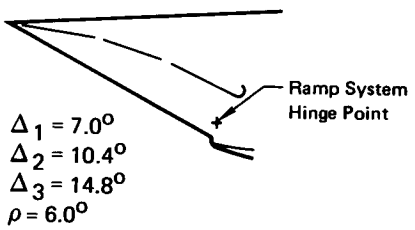

GP73-0449-12

(a) M_o = 1.6

FIGURE 30 - EFFECT OF OPERATING MASS FLOW RATIO ON NET PROPULSIVE FORCE

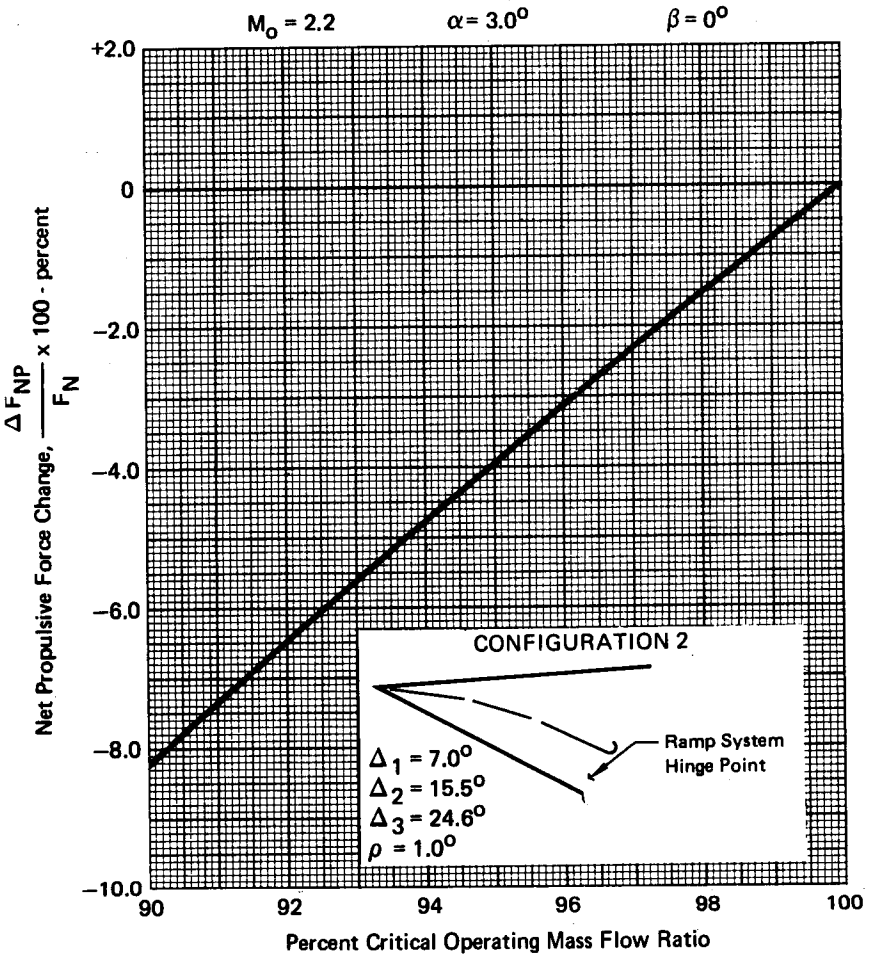

(b) M_o = 2.2

FIGURE 30 (Concl.)- EFFECT OF OPERATING MASS FLOW RATIO ON NET PROPULSIVE FORCE

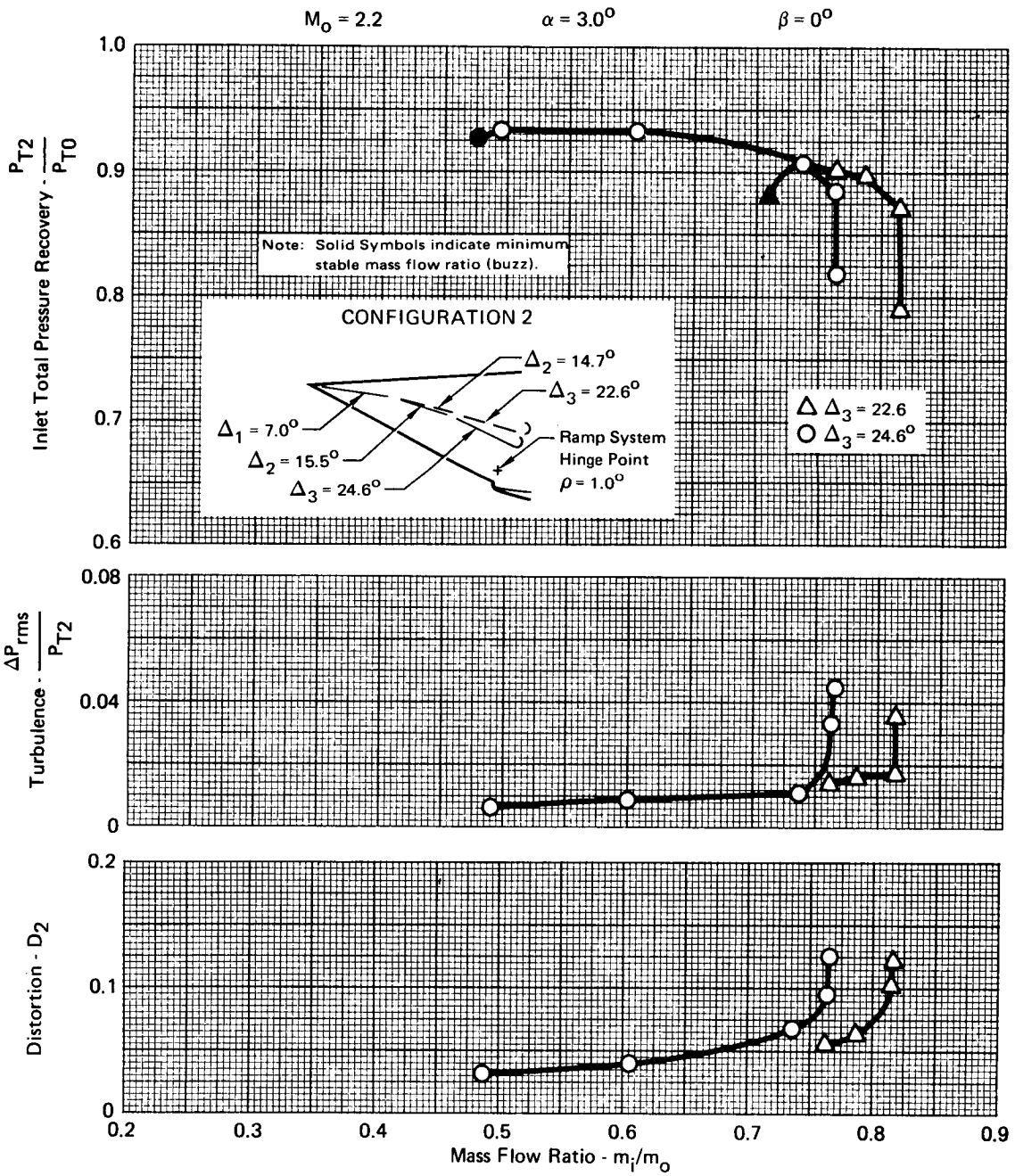

FIGURE 31 - EFFECTS OF INLET RAMP ANGLE VARIATIONS ON PRESSURE RECOVERY, TURBULENCE, AND DISTORTION

GP73-0449-14

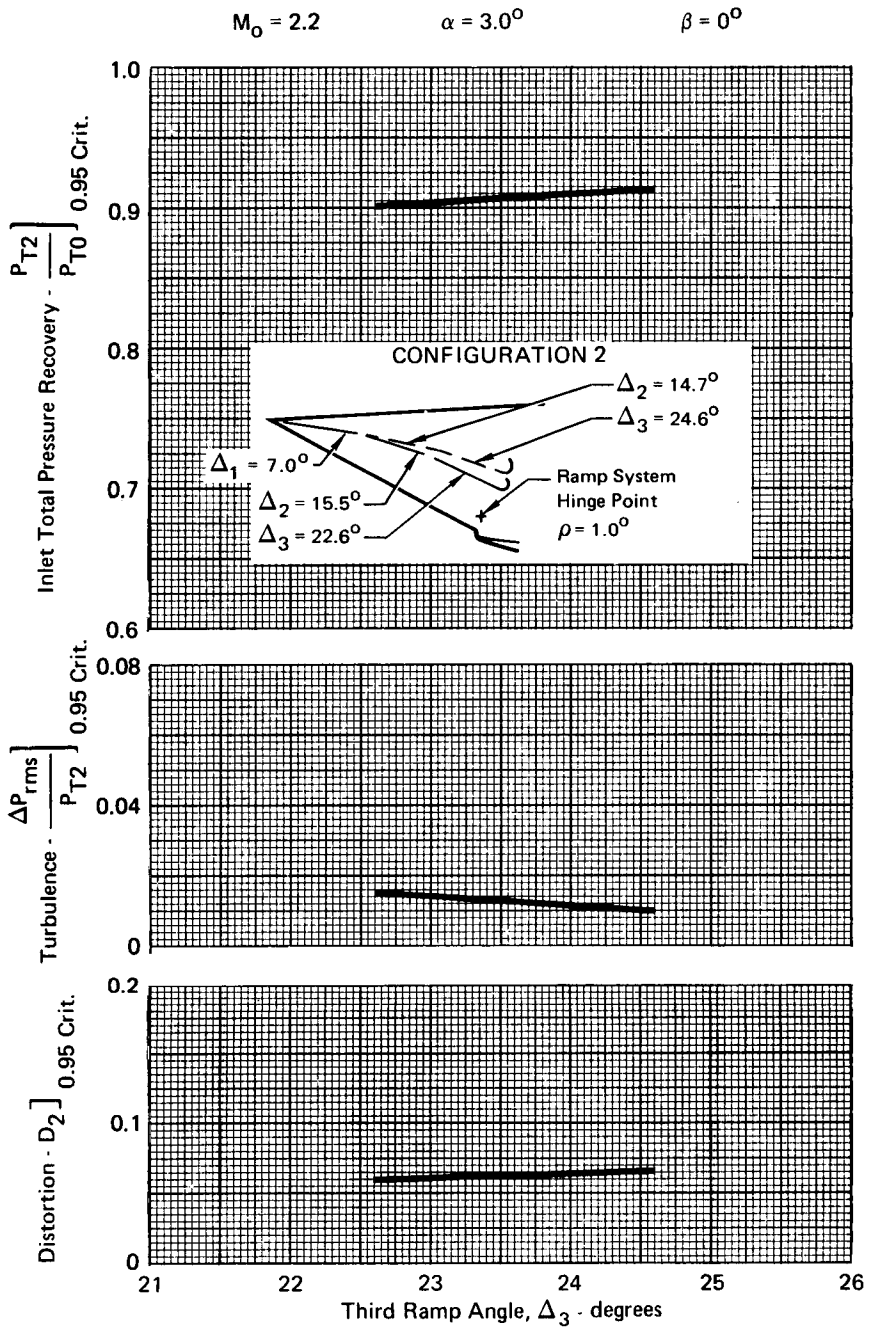

FIGURE 32 - EFFECTS OF INLET RAMP ANGLE VARIATIONS ON PRESSURE RECOVERY, TURBULENCE, AND DISTORTION AT 0.95 CRITICAL POINT

GP73-0449-15

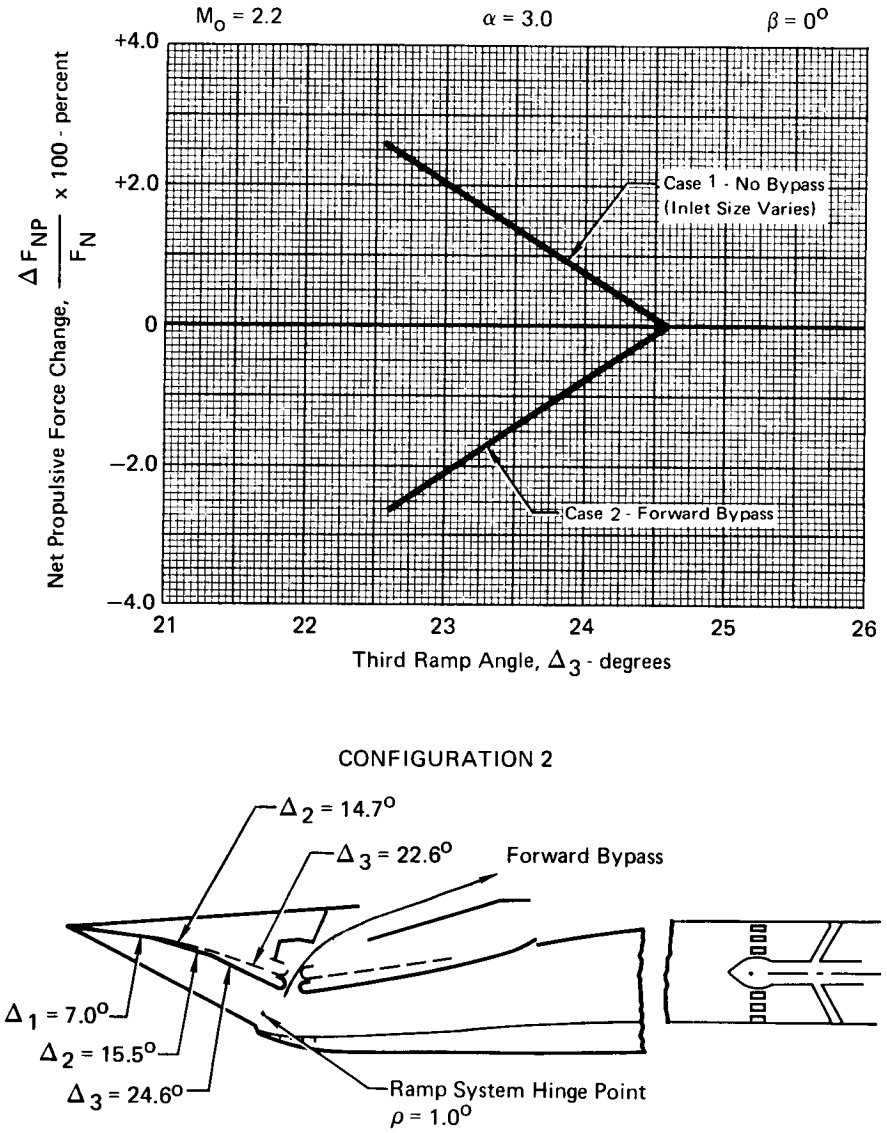

FIGURE 33 - EFFECT OF INLET RAMP ANGLE VARIATIONS ON NET PROPULSIVE FORCE

GP73-0449-16

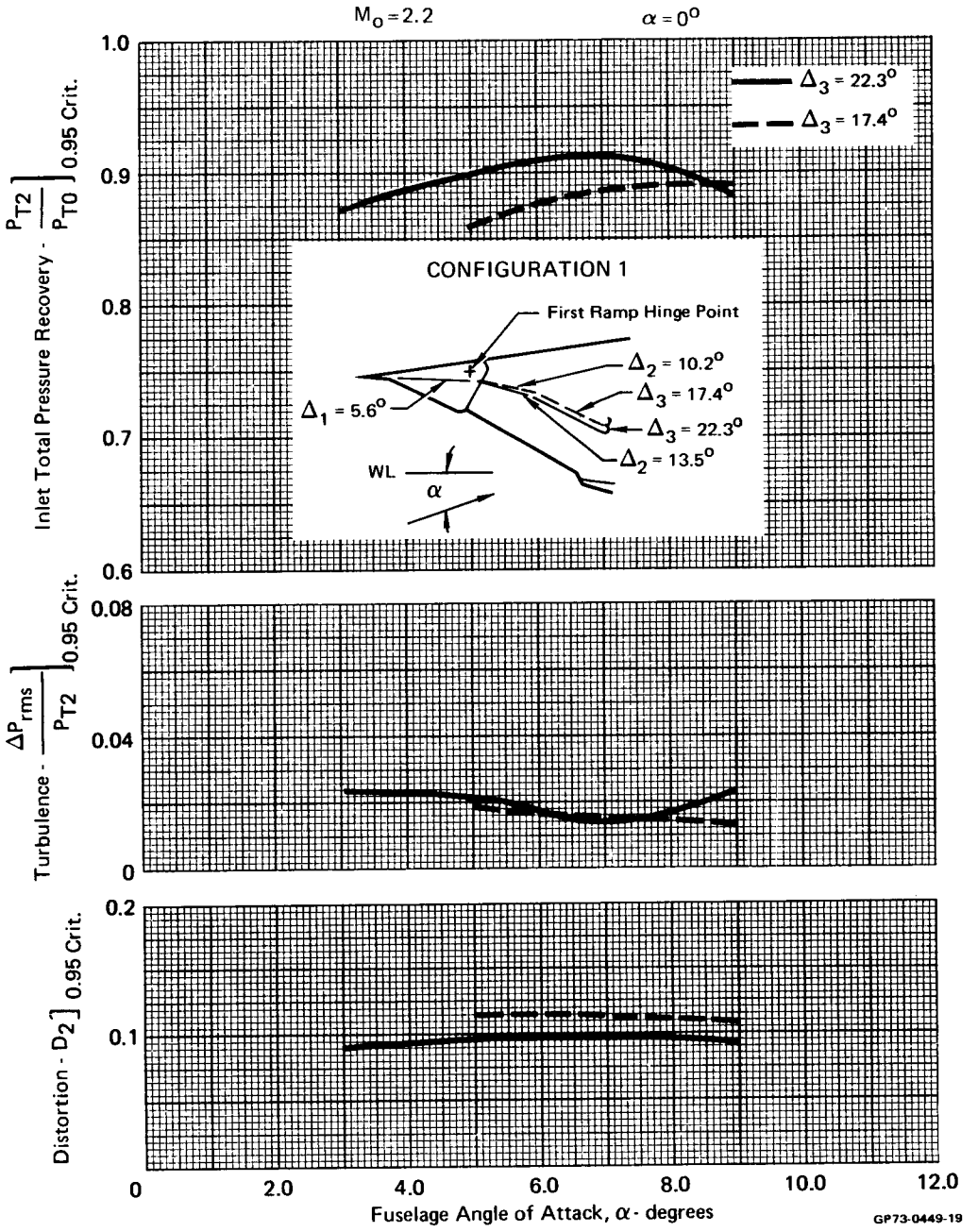

FIGURE 34 – EFFECTS OF REDUCED SECOND AND THIRD RAMP ANGLES AT ANGLE OF ATTACK ON PRESSURE RECOVERY, TURBULENCE, AND DISTORTION

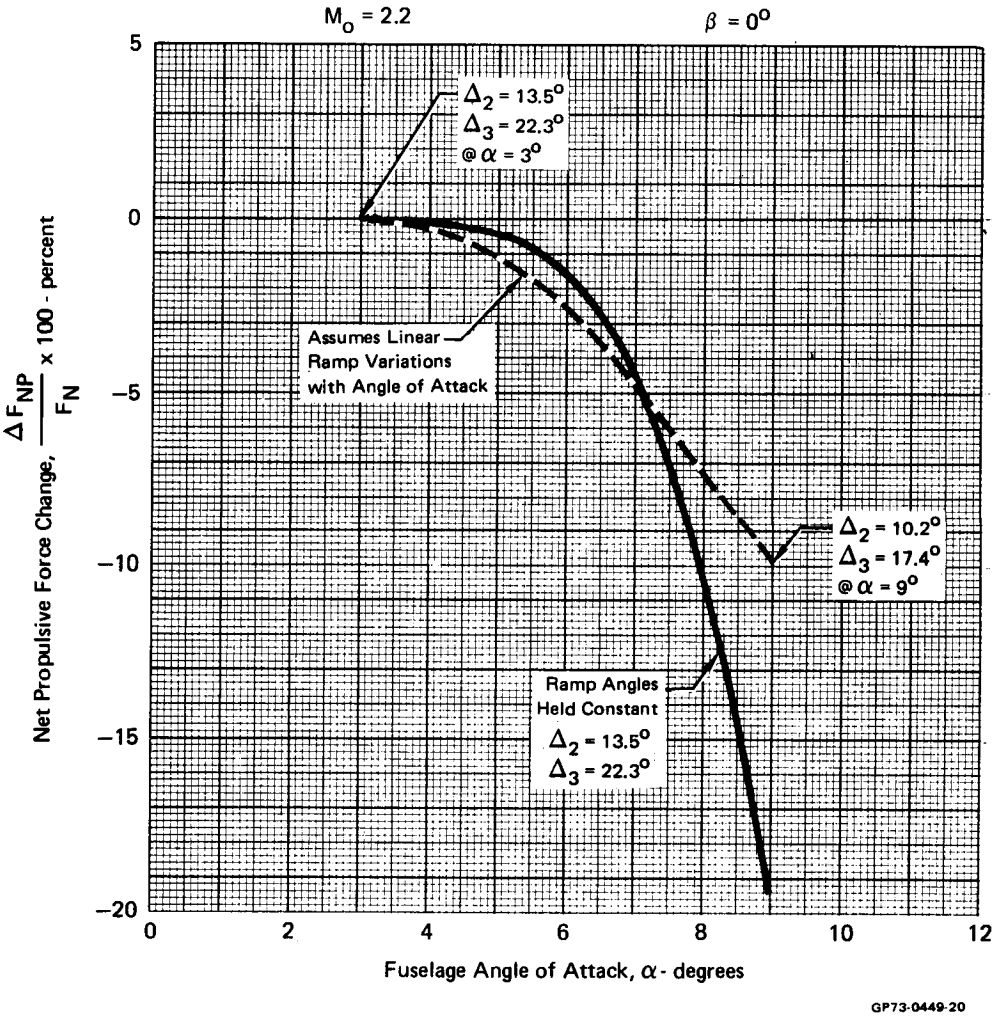

CONFIGURATION 1

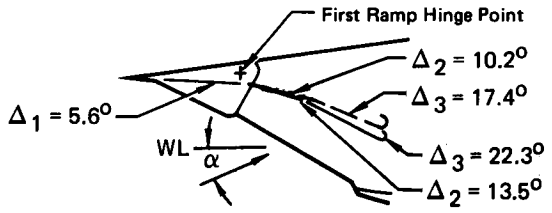

FIGURE 35 · EFFECT OF REDUCED RAMP ANGLES AT ANGLE OF ATTACK ON NET PROPULSIVE FORCE

CONFIGURATION 1

M_o	α (°)	Δ_1 (°)	Δ_2 (°)	Δ_3 (°)
0.9	−2.5 to 26.25	0	3.9	8.6
1.2	−2.5 to 26.25	0	3.9	8.6
1.6	4 to 22.5	2.8	6.7	12.5
2.2	0 to 22.5	5.6	13.5	22.3
2.5	3 to 13	7.0	15.7	25.5

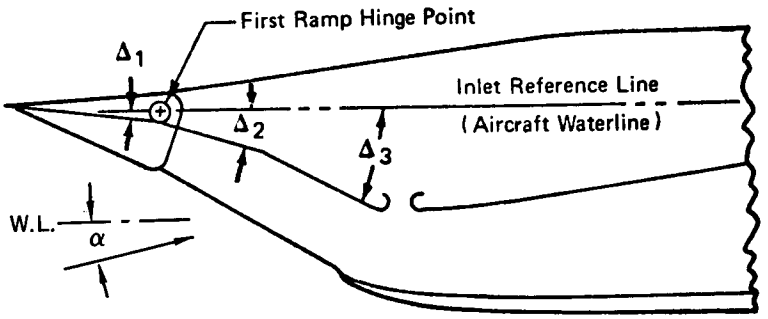

CONFIGURATION 2

M_o	α (°)	ρ (°)*	Δ_1 (°)	Δ_2 (°)	Δ_3 (°)
1.6	−4 to 24	−2 to 11	7.0	10.4	14.8
2.2	−4 to 24	−4 to 11	7.0	15.5	24.6
2.5	0 to 16	−3 to 11	7.0	16.1	25.6

*Ramp System Rotation Schedules are shown at each Mach Number in Figure 39.

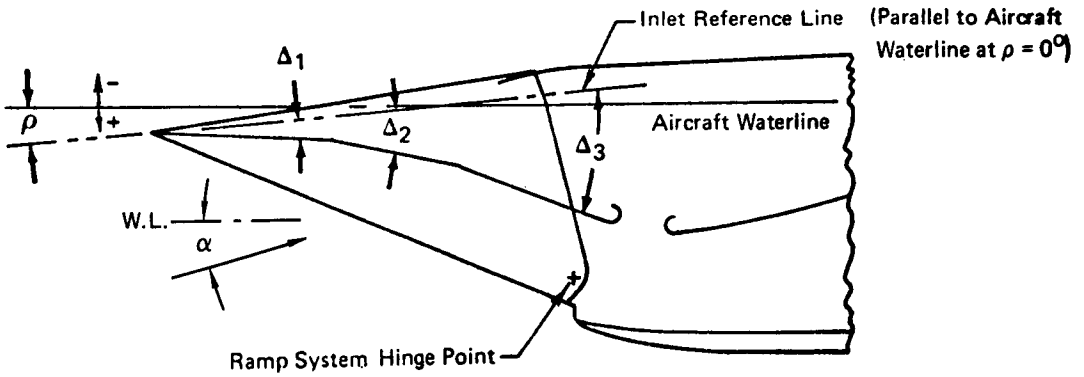

FIGURE 36 - ANGLE OF ATTACK RANGES AND INLET GEOMETRY VARIATIONS

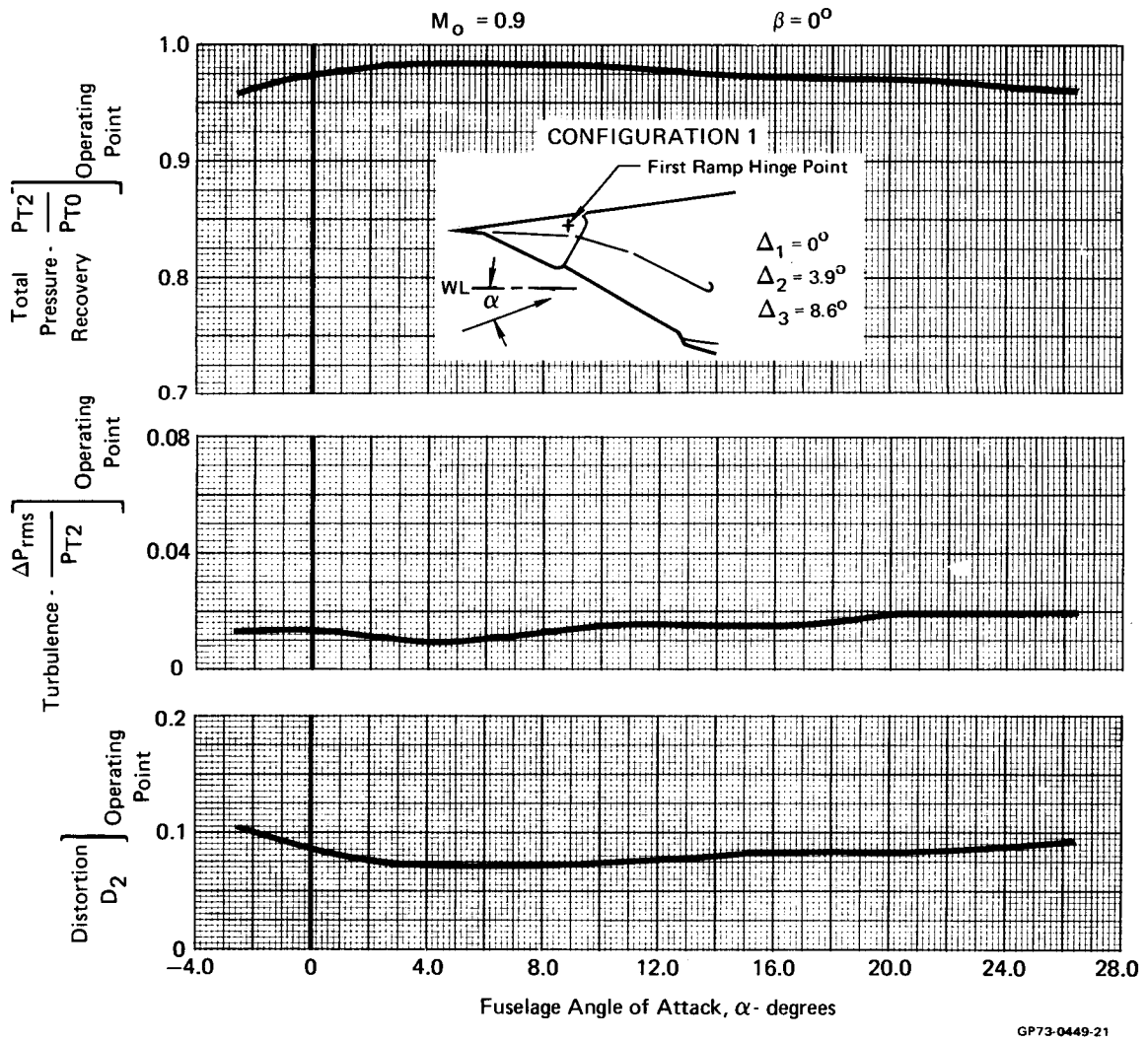

(a) M_o = 0.9

FIGURE 37 - EFFECTS OF ANGLE OF ATTACK ON PRESSURE RECOVERY, TURBULENCE, AND DISTORTION AT TRANSONIC CONDITIONS

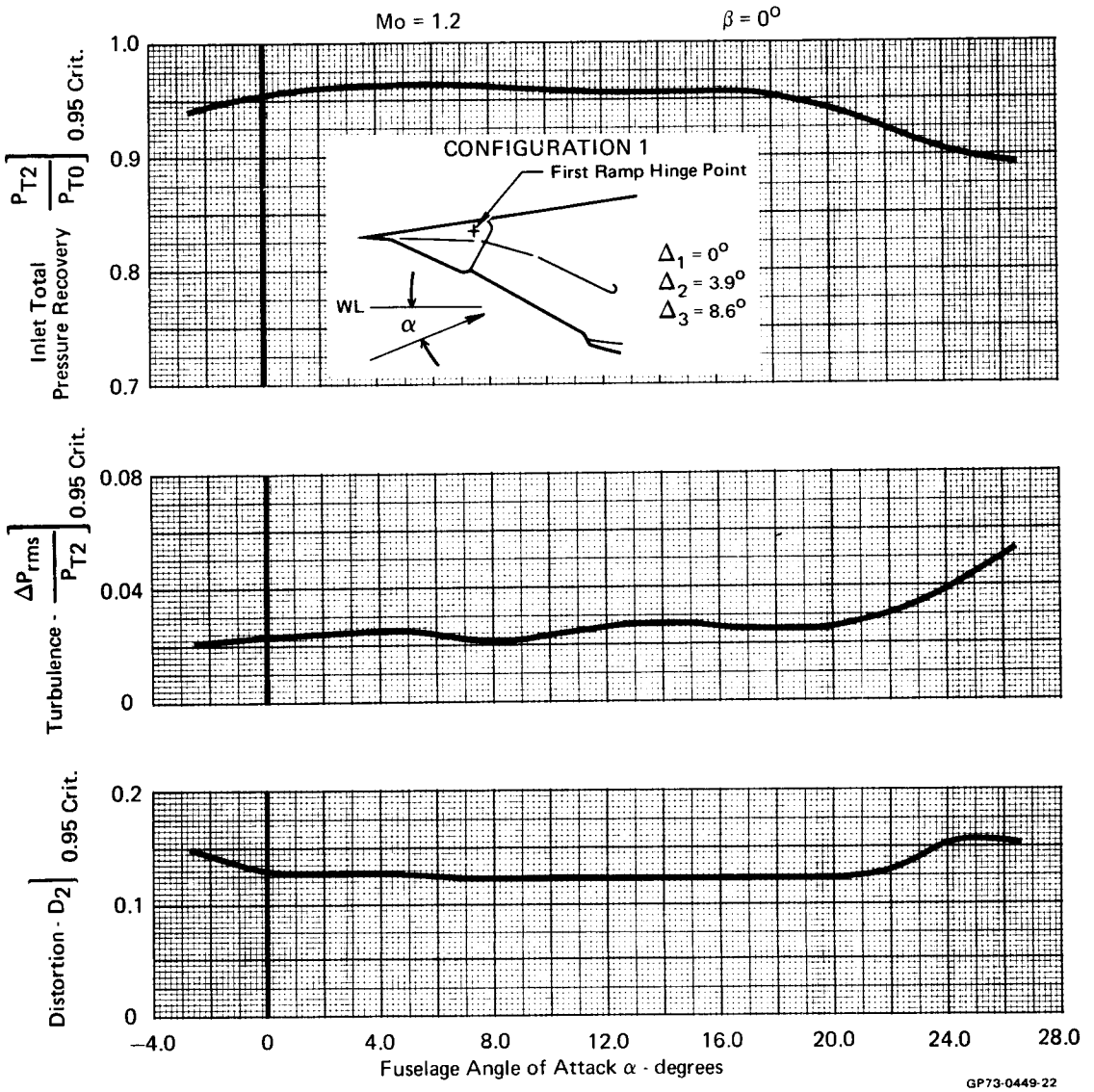

(b) M_o = 1.2

FIGURE 37 (Concl.) - EFFECTS OF ANGLE OF ATTACK ON PRESSURE RECOVERY, TURBULENCE, AND DISTORTION AT TRANSONIC CONDITIONS

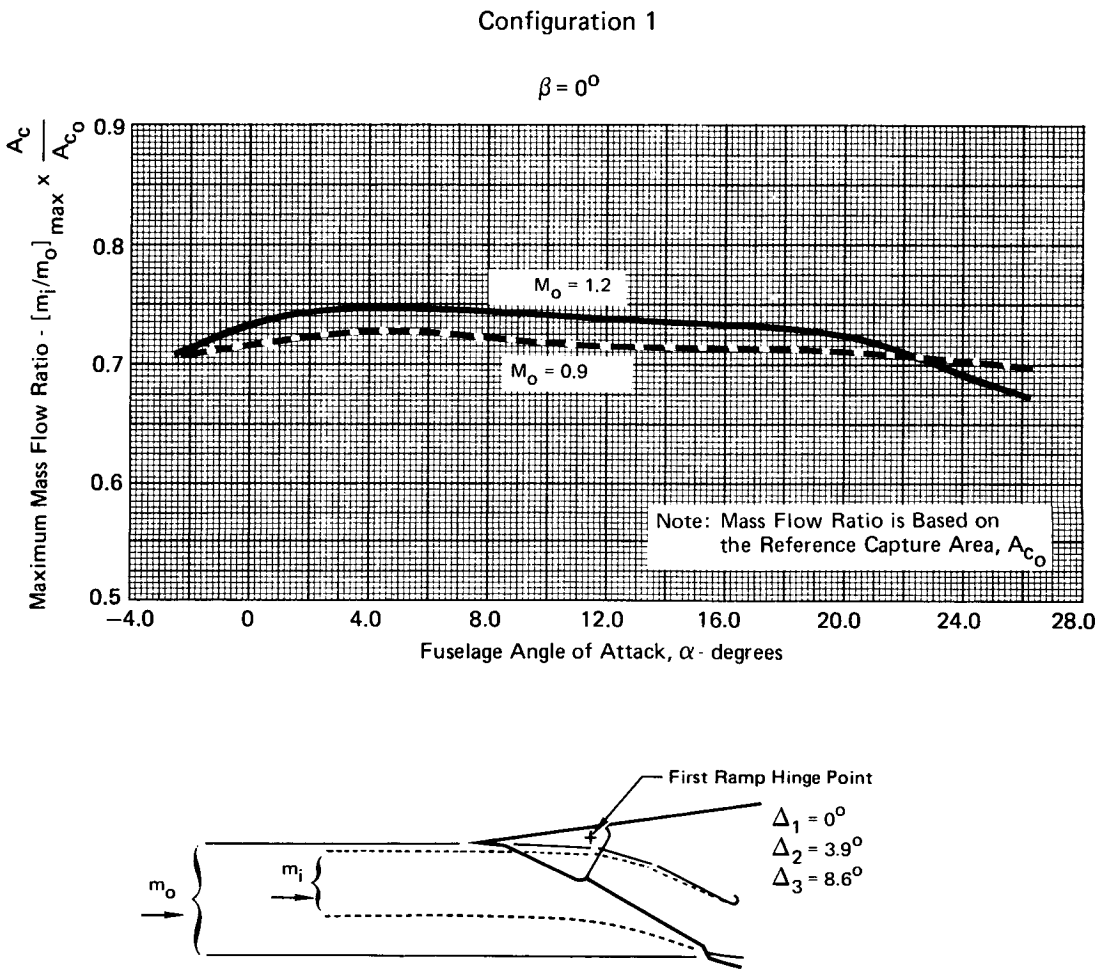

FIGURE 38 - EFFECT OF ANGLE OF ATTACK ON MAXIMUM MASS FLOW RATIO AT TRANSONIC CONDITIONS

GP74-0119-6

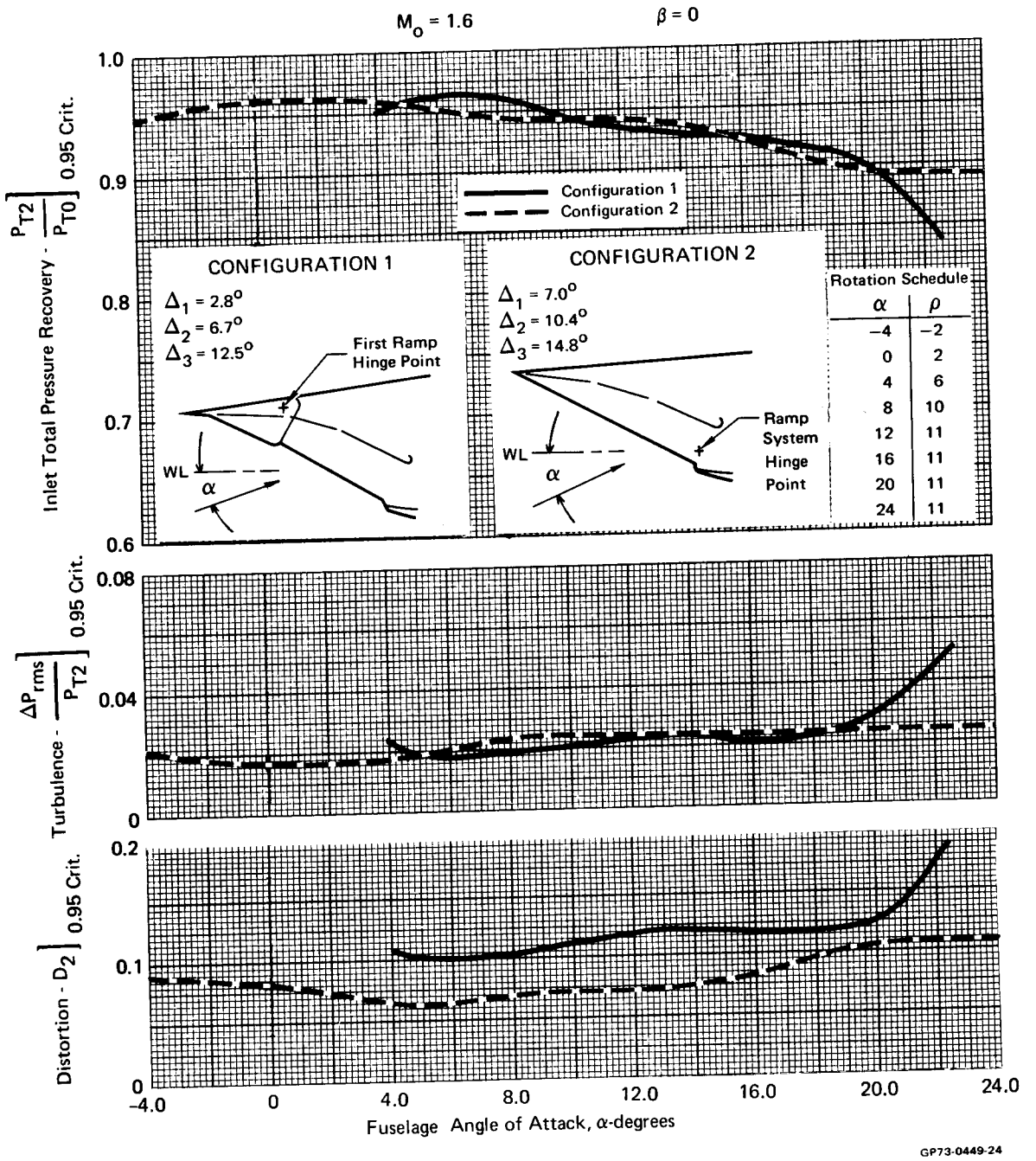

(a) M_o = 1.6

FIGURE 39 - EFFECTS OF ANGLE OF ATTACK ON PRESSURE RECOVERY, TURBULENCE, AND DISTORTION AT SUPERSONIC CONDITIONS

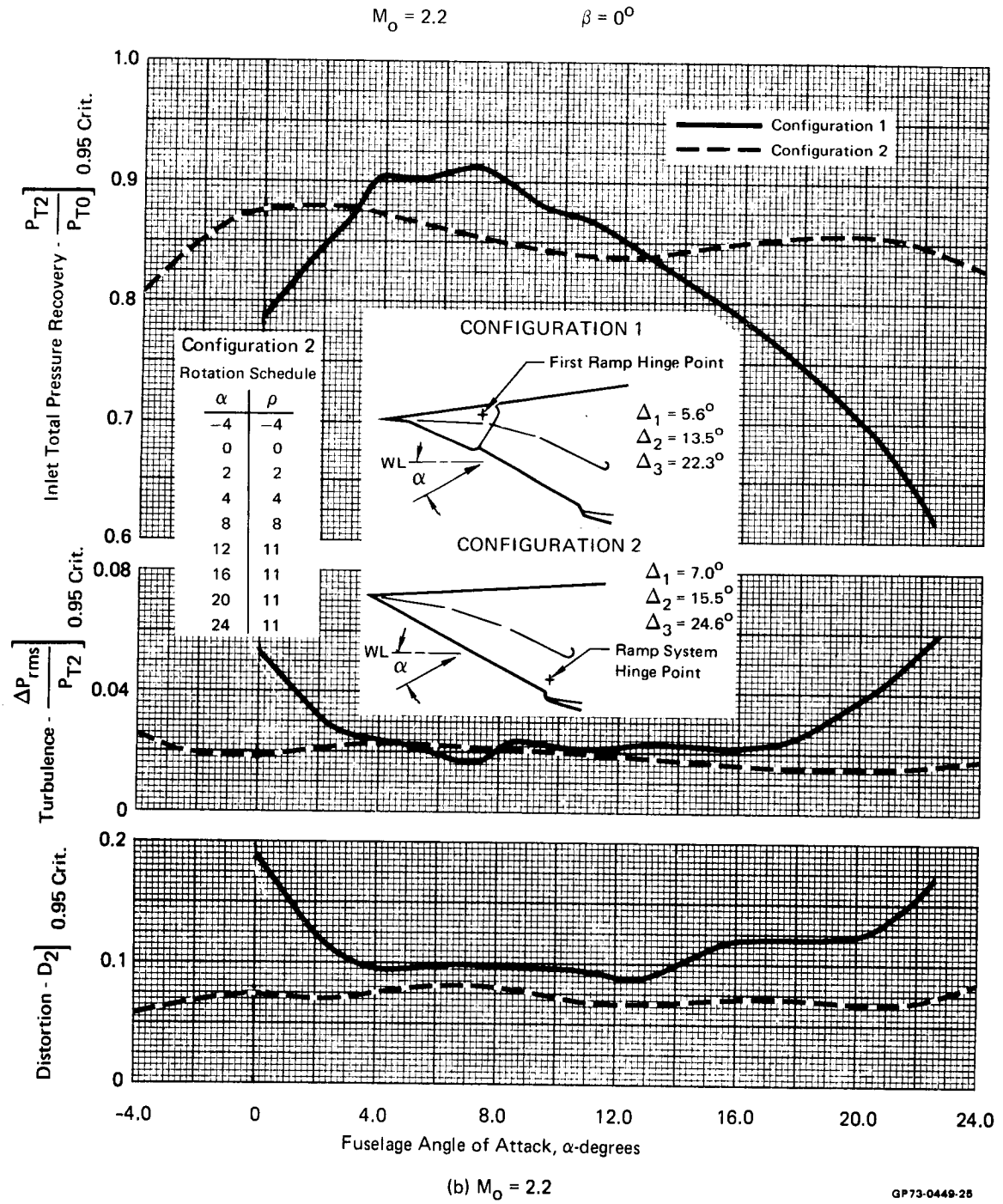

FIGURE 39 (Cont'd) - EFFECTS OF ANGLE OF ATTACK ON PRESSURE RECOVERY, TURBULENCE, AND DISTORTION AT SUPERSONIC CONDITIONS

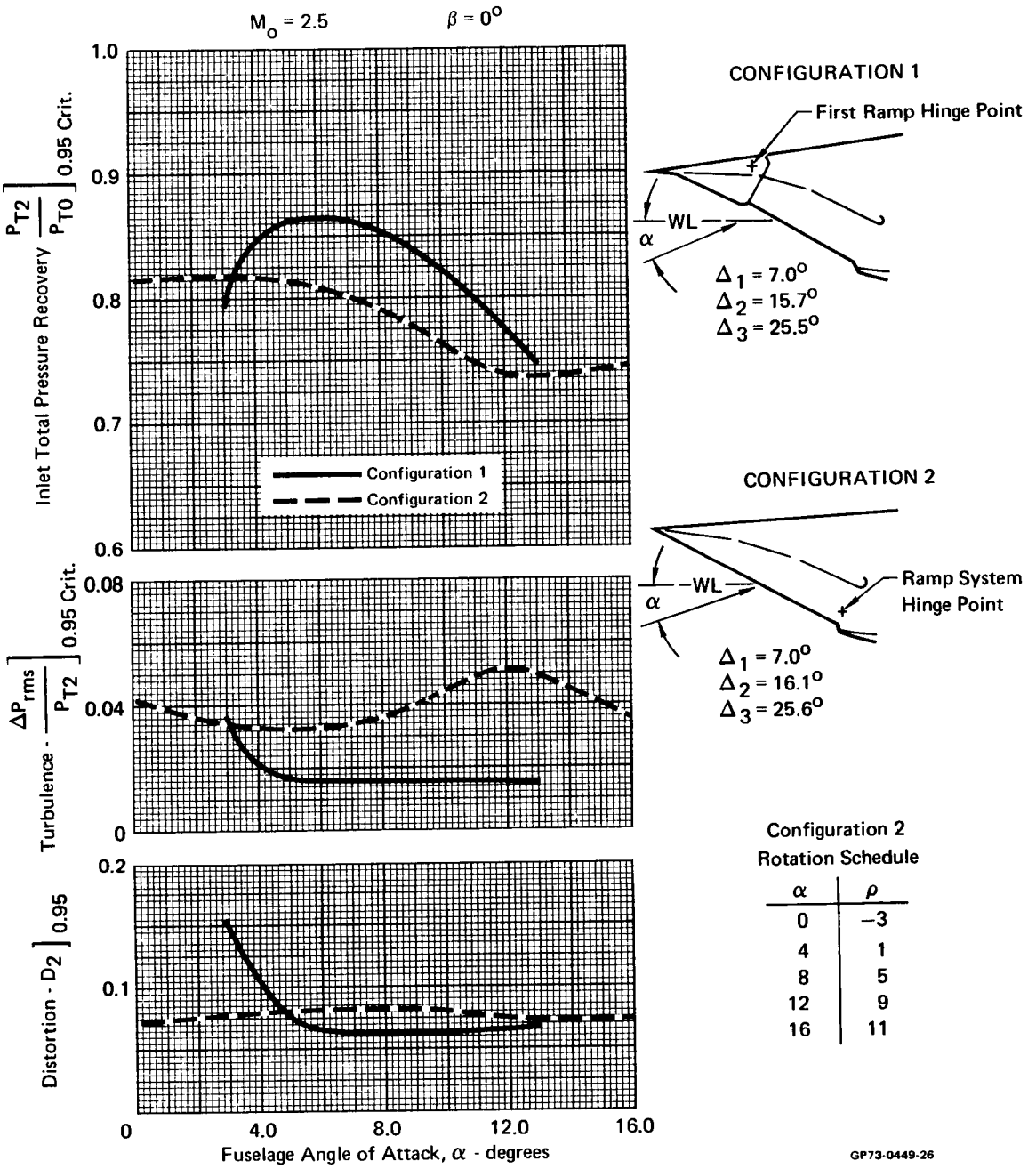

(c) M_o = 2.5

FIGURE 39 (Concl.) - EFFECTS OF ANGLE OF ATTACK ON PRESSURE RECOVERY, TURBULENCE, AND DISTORTION AT SUPERSONIC CONDITIONS

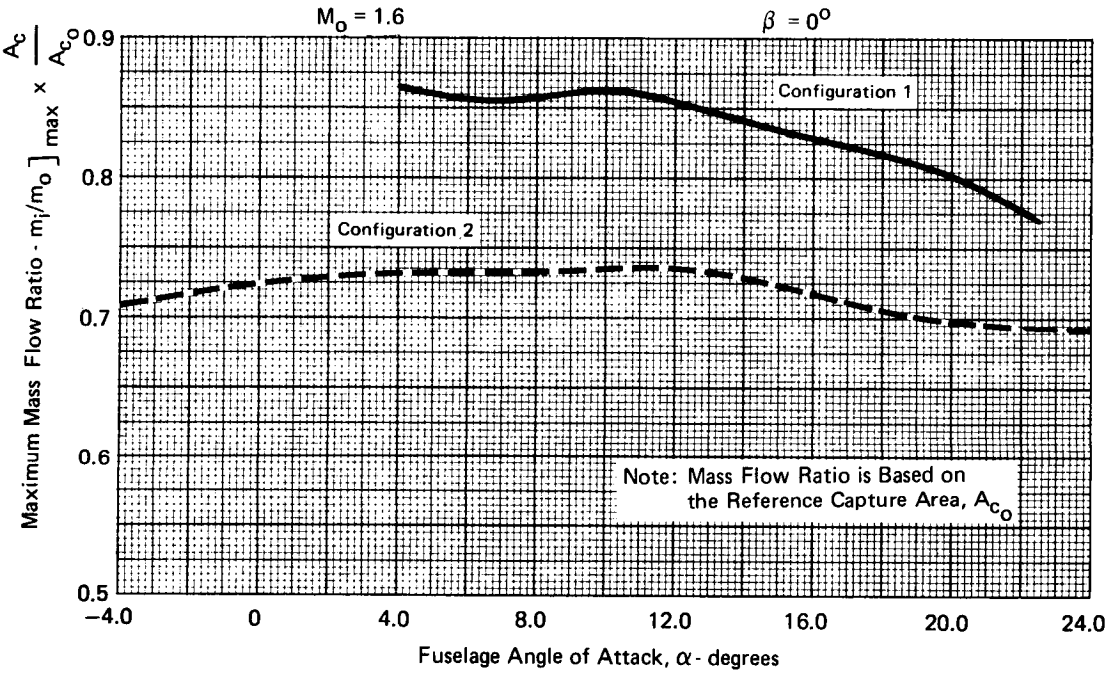

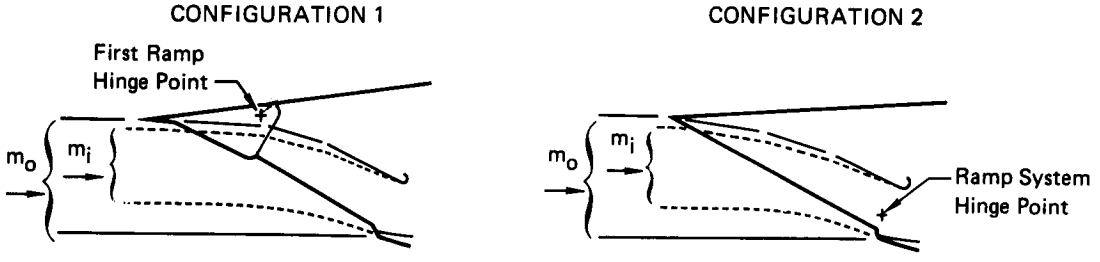

$\Delta_1 = 2.8^o$
$\Delta_2 = 6.7^o$
$\Delta_3 = 12.5^o$

$\Delta_1 = 7.0^o$
$\Delta_2 = 10.4^o$
$\Delta_3 = 14.8^o$

See Figure 39 (a) for Rotation Schedule

(a) $M_o = 1.6$

FIGURE 40 - EFFECT OF ANGLE OF ATTACK ON MAXIMUM MASS FLOW RATIO AT SUPERSONIC CONDITIONS

GP73-0449-28

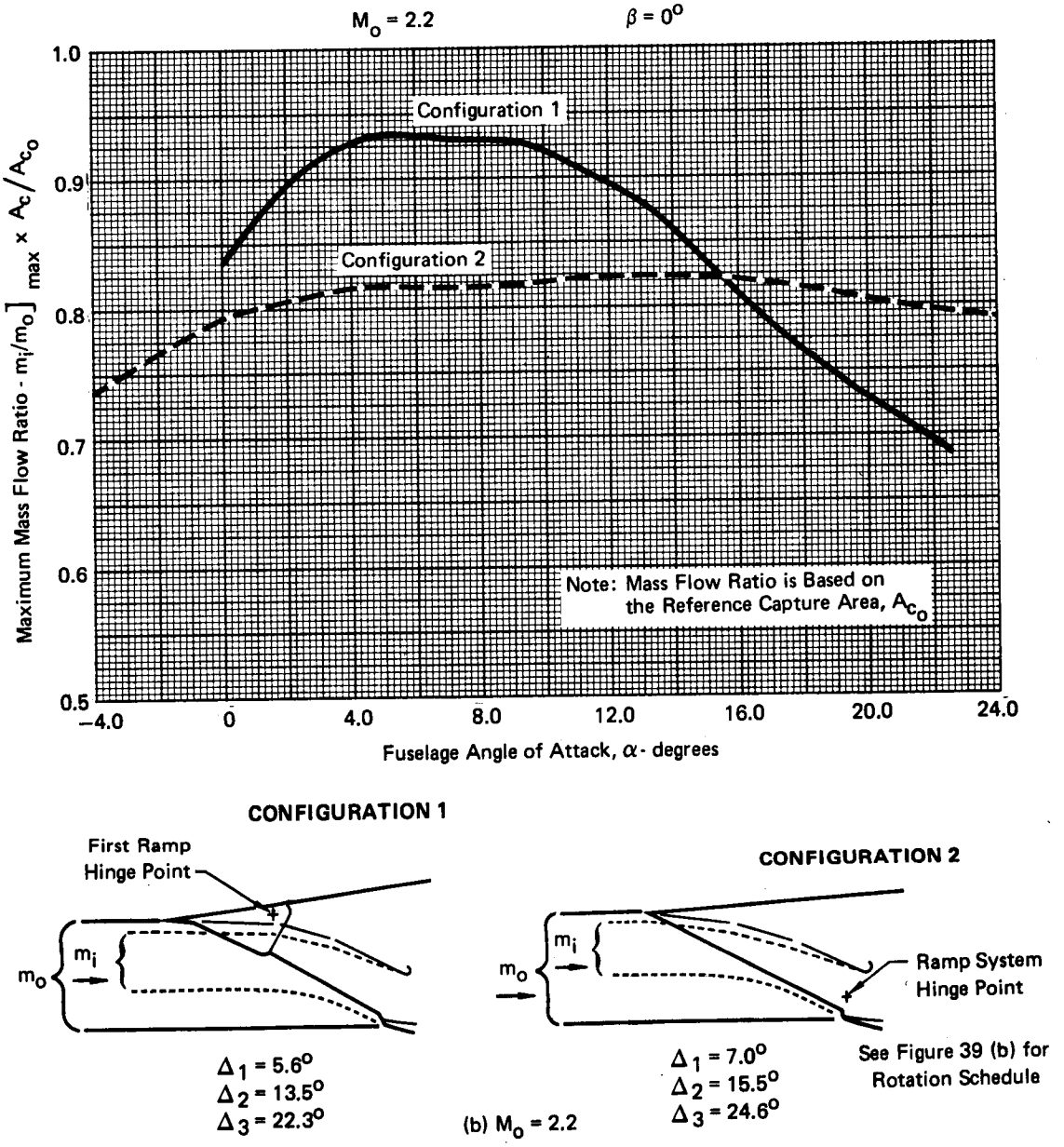

FIGURE 40 (Cont'd) - EFFECT OF ANGLE OF ATTACK ON MAXIMUM MASS FLOW RATIO AT SUPERSONIC CONDITIONS

GP73-0449-29

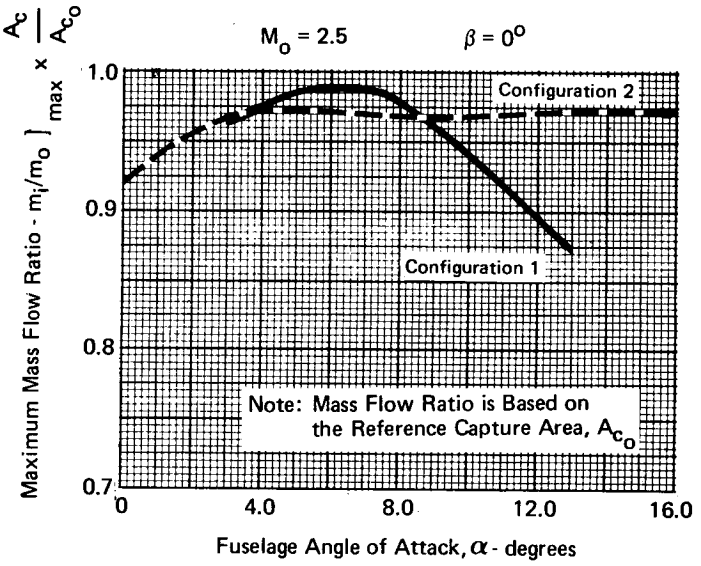

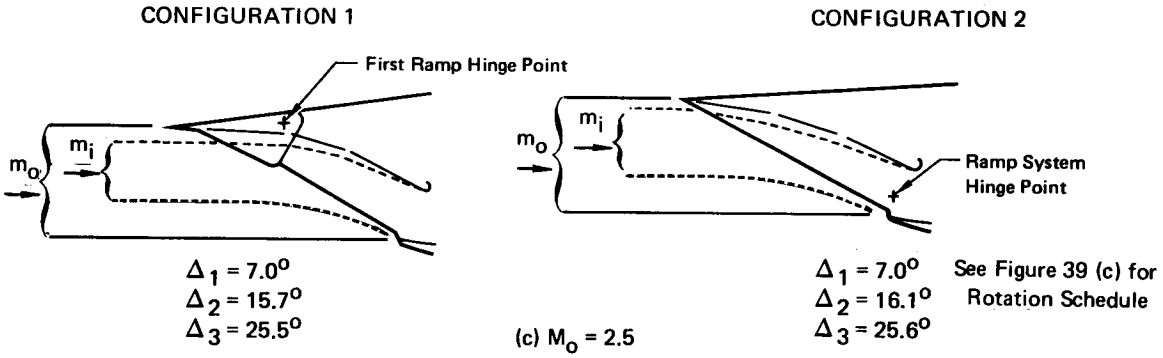

FIGURE 40 (Concl.) - EFFECT OF ANGLE OF ATTACK ON MAXIMUM MASS FLOW RATIO AT SUPERSONIC CONDITIONS

GP73-0449-27

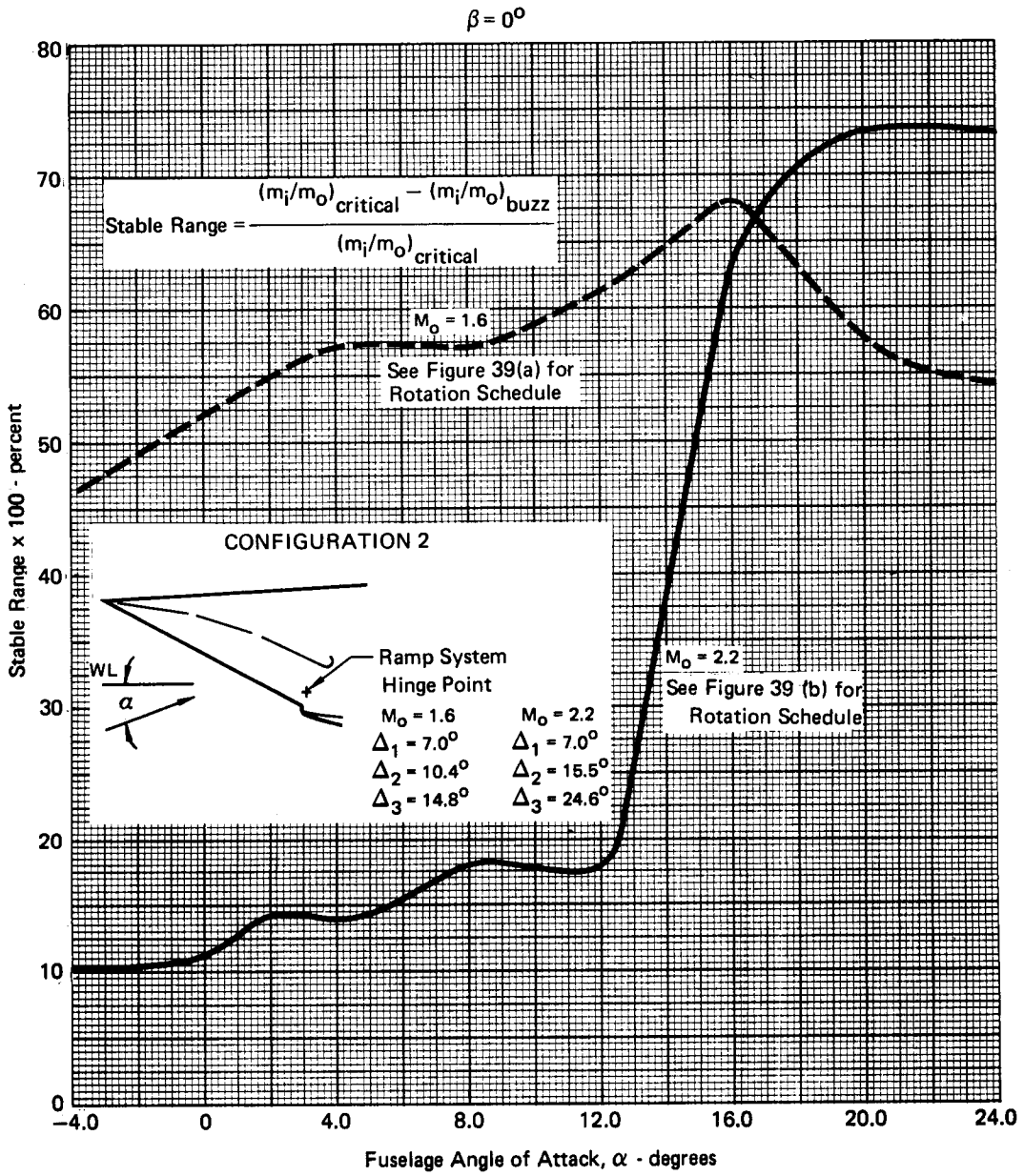

FIGURE 41 - EFFECTS OF ANGLE OF ATTACK ON STABLE RANGE GP73-0449-30

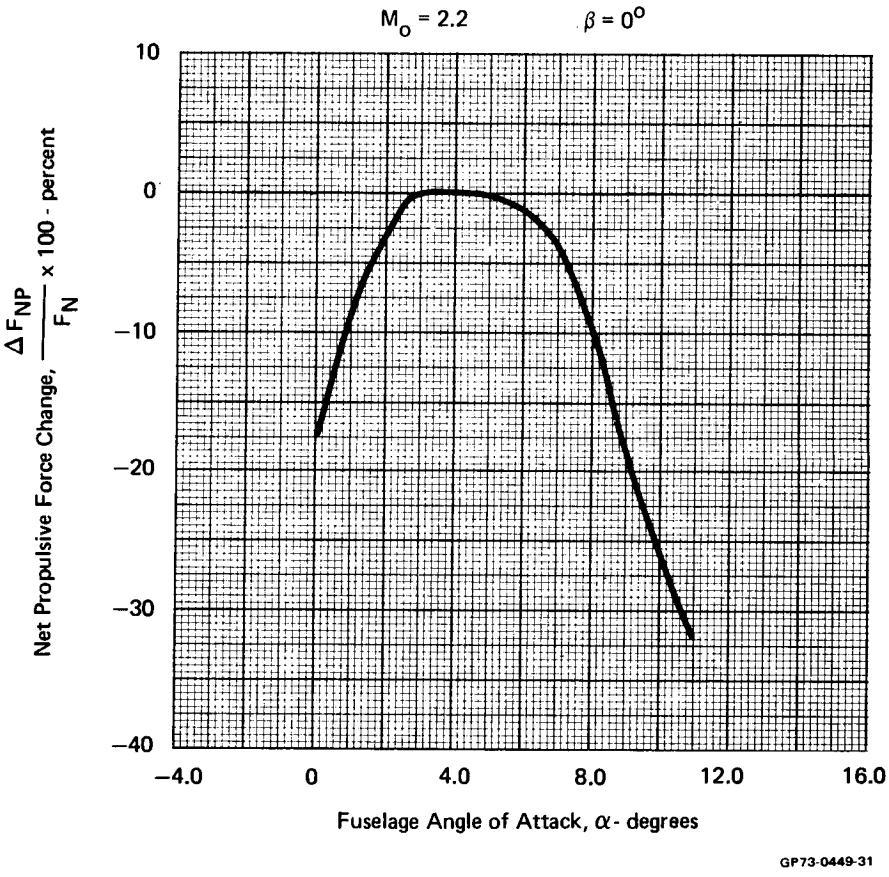

CONFIGURATION 1

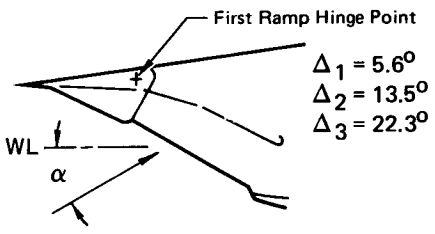

(a) Configuration 1

FIGURE 42 - EFFECT OF ANGLE OF ATTACK ON NET PROPULSIVE FORCE

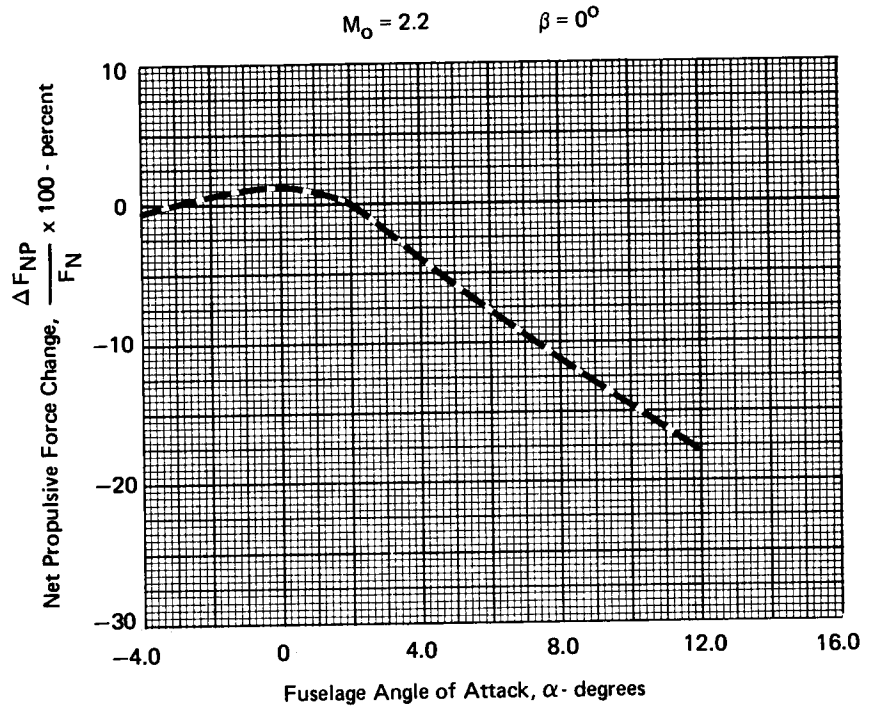

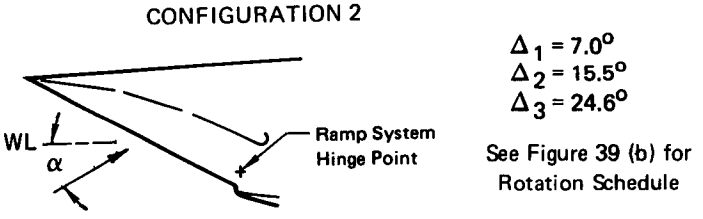

(b) Configuration 2

FIGURE 42 (Concl.) - EFFECT OF ANGLE OF ATTACK ON NET PROPULSIVE FORCE

CONFIGURATION 1

M_o	α (°)	β (°)	Δ_1 (°)	Δ_2 (°)	Δ_3 (°)
0.9	0 to 24	−6 to +6	0	3.9	8.6
1.2	0 to 24	6	0	3.9	8.6
1.6	4 to 16	4, 8	2.8	6.7	12.5
2.2	0 to 13	4	5.6	13.5	22.3
↓	4, 7	8	5.6	13.5	22.3
↓	4, 7, 9	−8	5.6	13.5	22.3
2.5	3, 7	0, 4, 8	7.0	15.7	25.5

Note: Inlet geometries for $\beta = 0^o$ are given in Figure 36.

CONFIGURATION 1

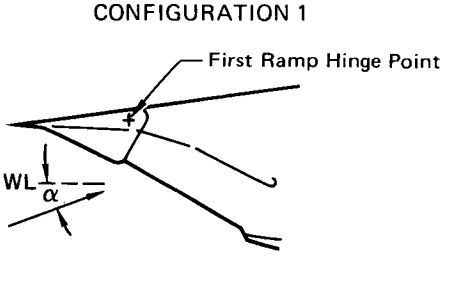

CONFIGURATION 2

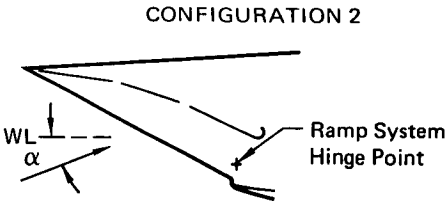

CONFIGURATION 2

M_o	α (°)	β (°)	ρ (°)	Δ_1 (°)	Δ_2 (°)	Δ_3 (°)
1.6	0	3, 6	2	7.0	10.4	14.8
↓	4	↓	6	↓	↓	↓
	8		10			
↓	16	↓	11	↓	↓	↓
2.2	−4	3	−4	7.0	15.5	24.6
↓	0	↓	0	↓	↓	↓
	2		2			
	4		4			
	8		8			
	2	6	2			
	4	↓	4			
↓	8	↓	6, 8	↓	↓	↓
2.5	4	3	1	7.0	16.1	25.6

GP73-0449-32

FIGURE 43 - SIDESLIP CONDITIONS AND INLET GEOMETRY VARIATIONS

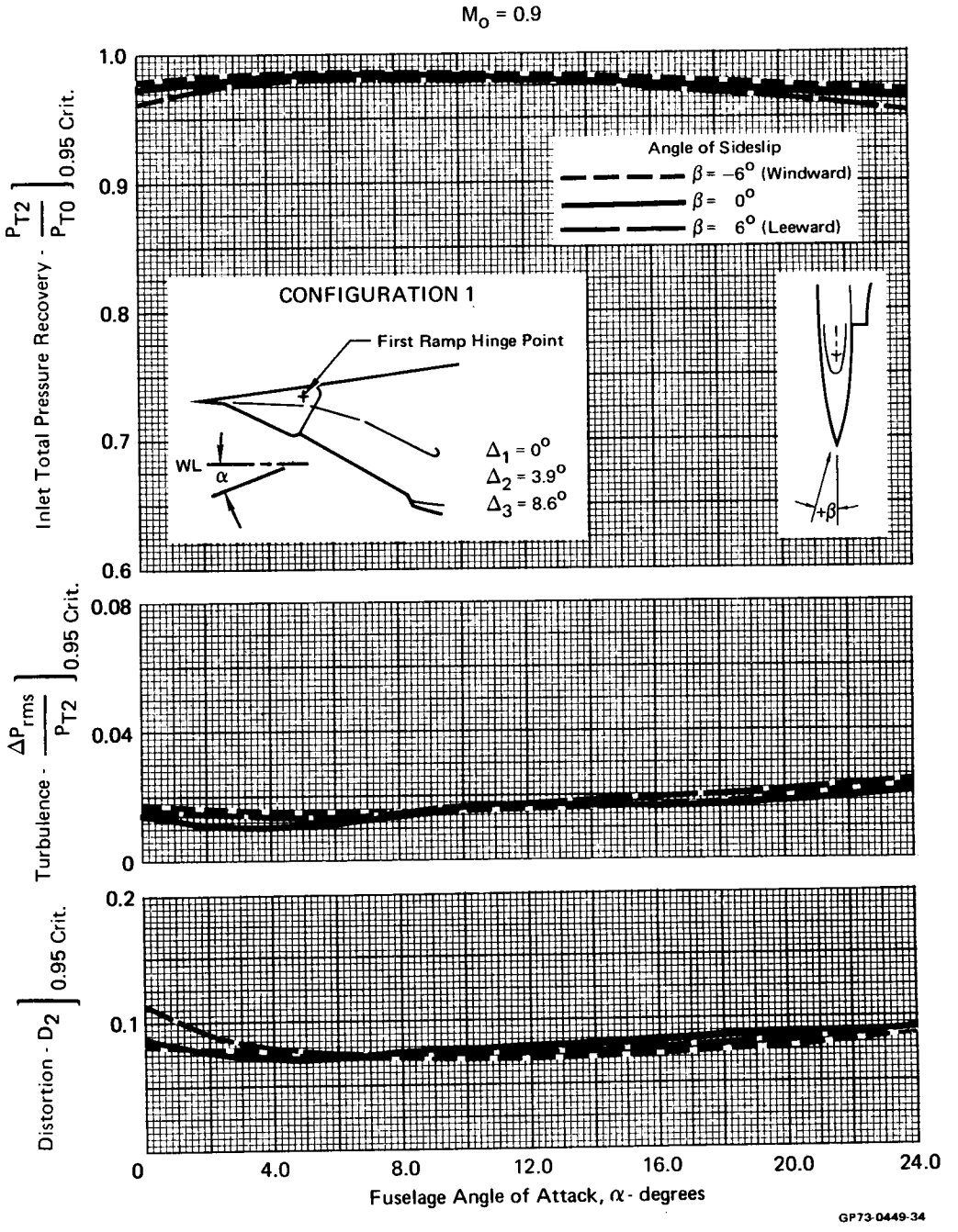

(a) M_o = 0.9

FIGURE 44 - EFFECTS OF ANGLE OF SIDESLIP ON PRESSURE RECOVERY, TURBULENCE, AND DISTORTION AT TRANSONIC CONDITIONS

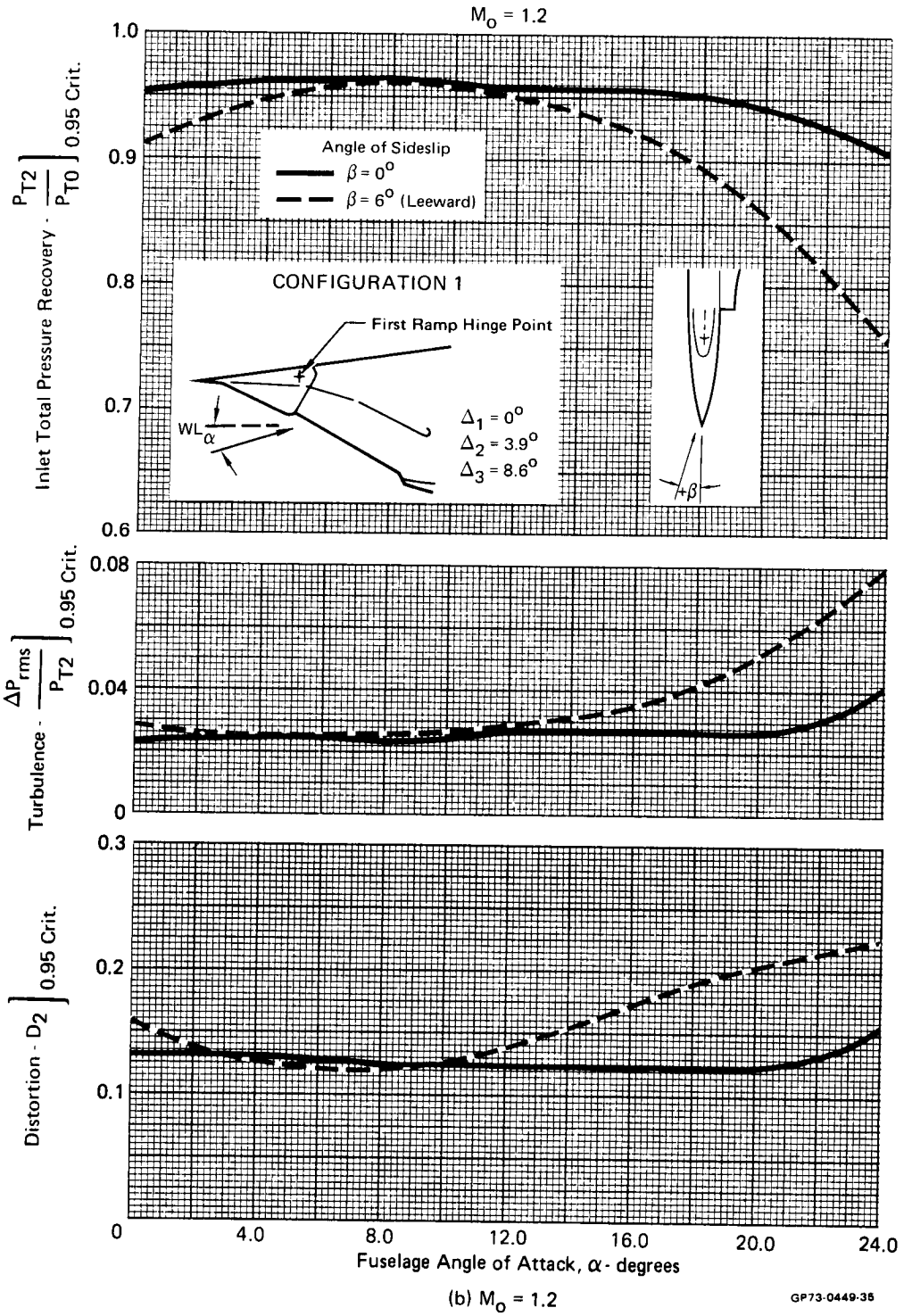

FIGURE 44 (Concl.) - EFFECTS OF ANGLE OF SIDESLIP ON PRESSURE RECOVERY, TURBULENCE, AND DISTORTION AT TRANSONIC CONDITIONS

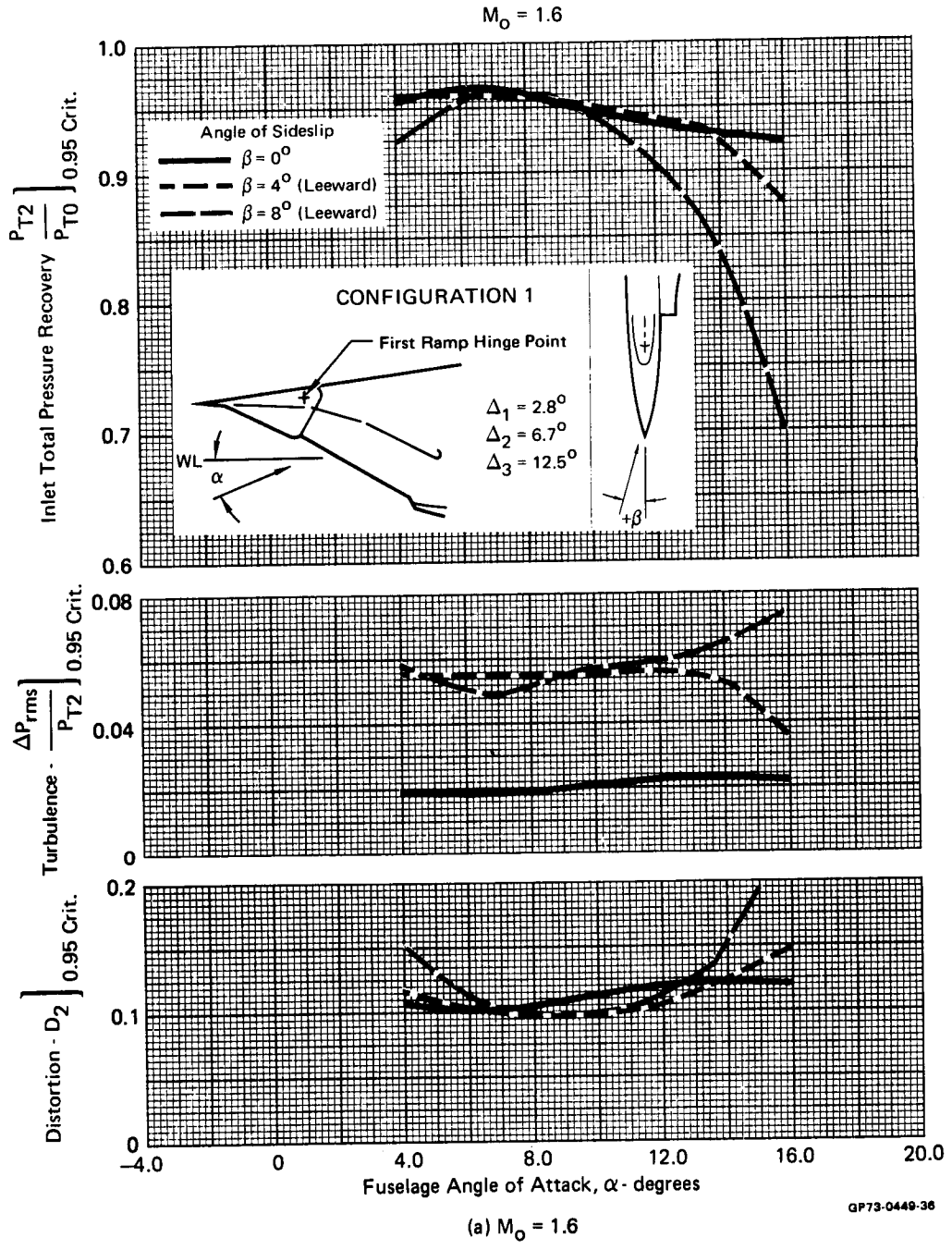

(a) M_o = 1.6

FIGURE 45 - EFFECTS OF ANGLE OF SIDESLIP ON PRESSURE RECOVERY, TURBULENCE, AND DISTORTION AT SUPERSONIC CONDITIONS

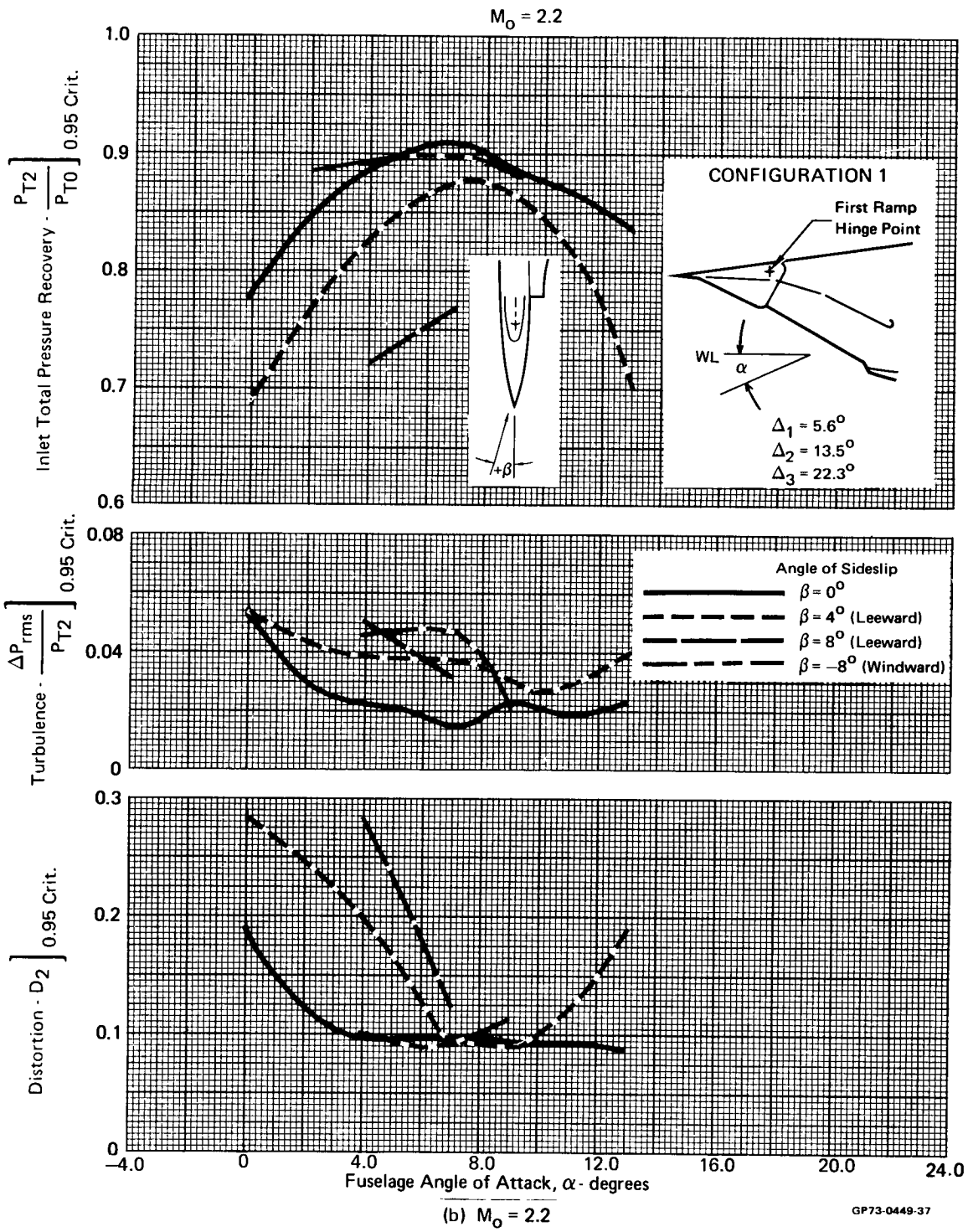

(b) M_o = 2.2

FIGURE 45(Cont'd) - EFFECTS OF ANGLE OF SIDESLIP ON PRESSURE RECOVERY, TURBULENCE, AND DISTORTION AT SUPERSONIC CONDITIONS

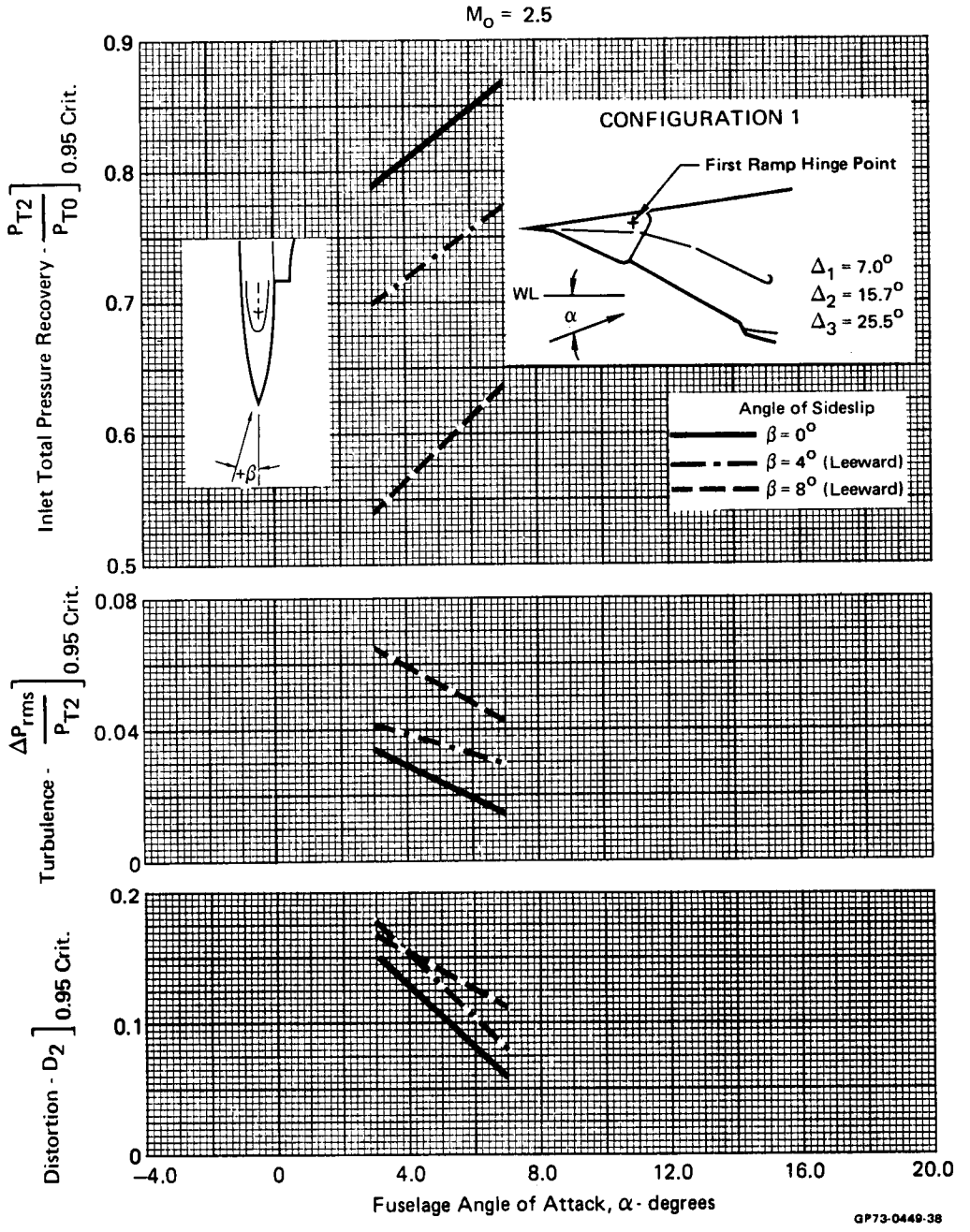

(c) M_o = 2.5

FIGURE 45 (Cont'd.) - EFFECTS OF ANGLE OF SIDESLIP ON PRESSURE RECOVERY, TURBULENCE, AND DISTORTION AT SUPERSONIC CONDITIONS

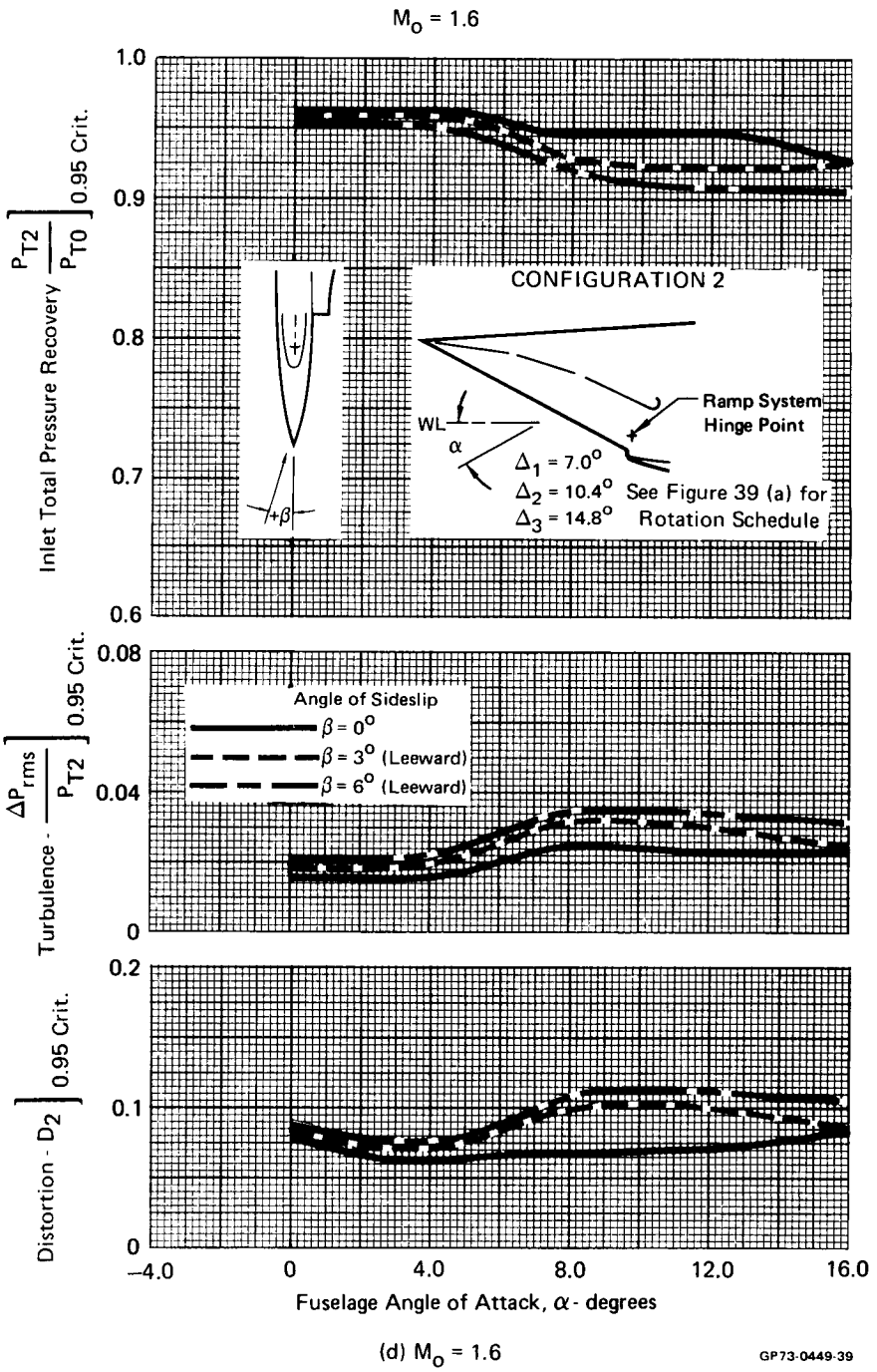

FIGURE 45 (Cont'd.) - EFFECTS OF ANGLE OF SIDESLIP ON PRESSURE RECOVERY, TURBULENCE, AND DISTORTION AT SUPERSONIC CONDITIONS

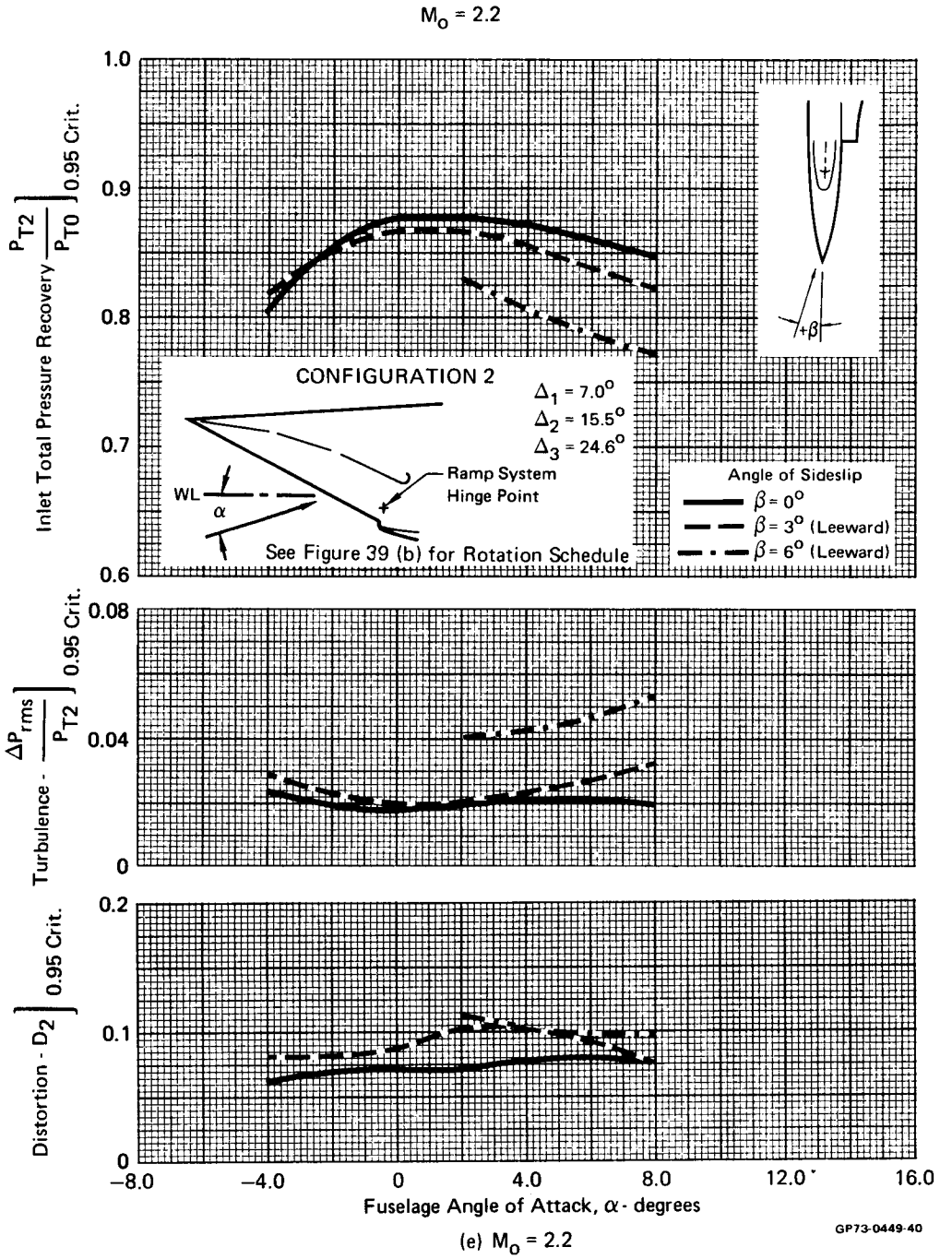

(e) M_o = 2.2

FIGURE 45 (Cont'd.) - EFFECTS OF ANGLE OF SIDESLIP ON PRESSURE RECOVERY, TURBULENCE, AND DISTORTION AT SUPERSONIC CONDITIONS

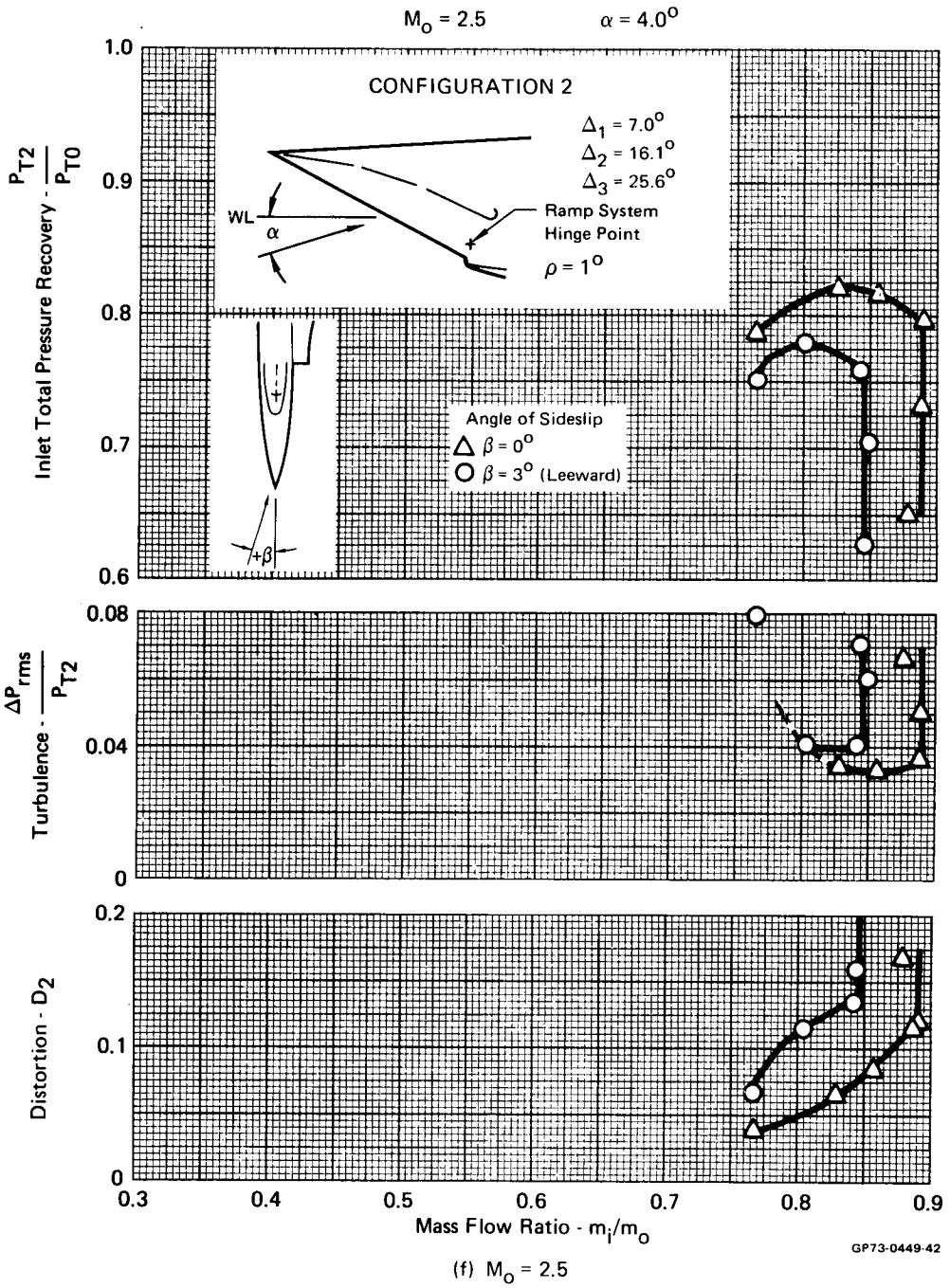

(f) M_o = 2.5

FIGURE 45 (Concl.) - EFFECTS OF ANGLE OF SIDESLIP ON PRESSURE RECOVERY, TURBULENCE, AND DISTORTION AT SUPERSONIC CONDITIONS

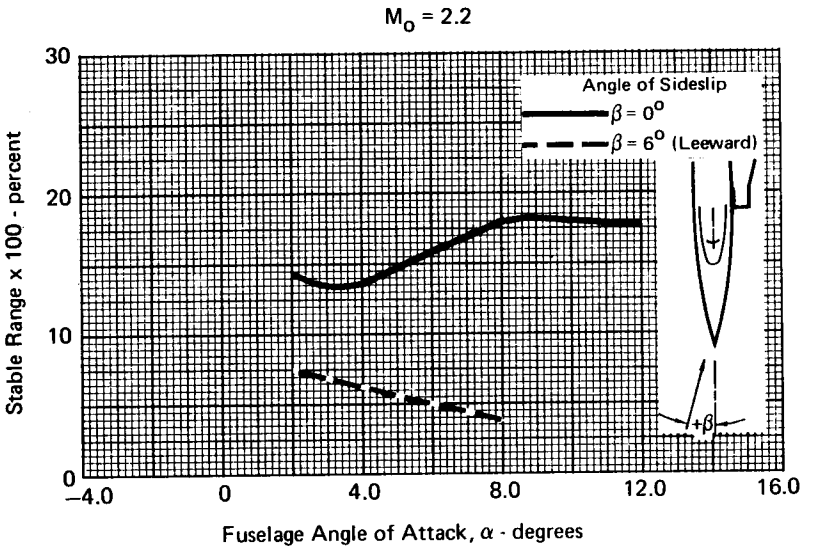

Ramp Rotation Schedule

α (^{o})	ρ (^{o})
2	2
4	4
8	8
12	11

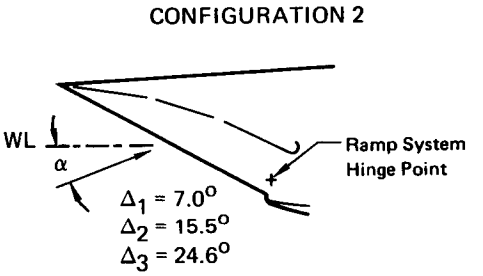

FIGURE 46 - EFFECT OF ANGLE OF SIDESLIP ON STABLE RANGE

GP73-0449-43

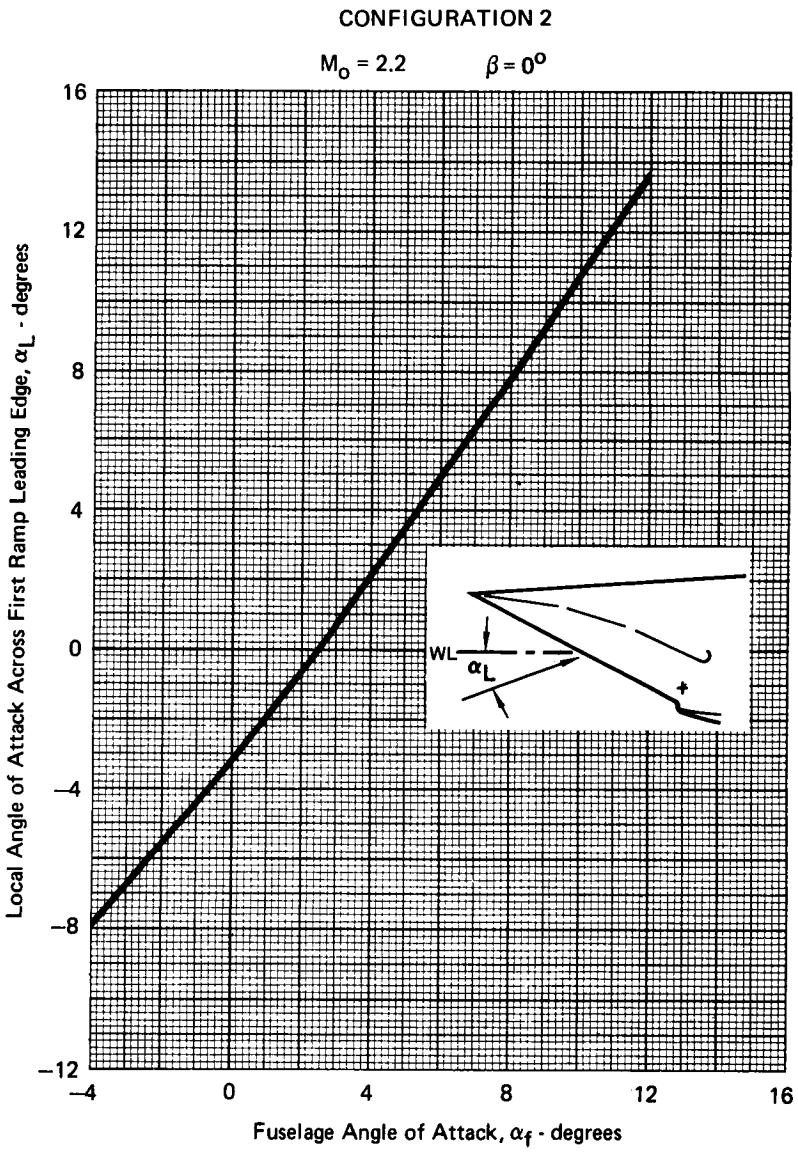

FIGURE 47 - EFFECTS OF FORWARD FUSELAGE ON FLOW ANGULARITY AT INLET

GP73-0449-44

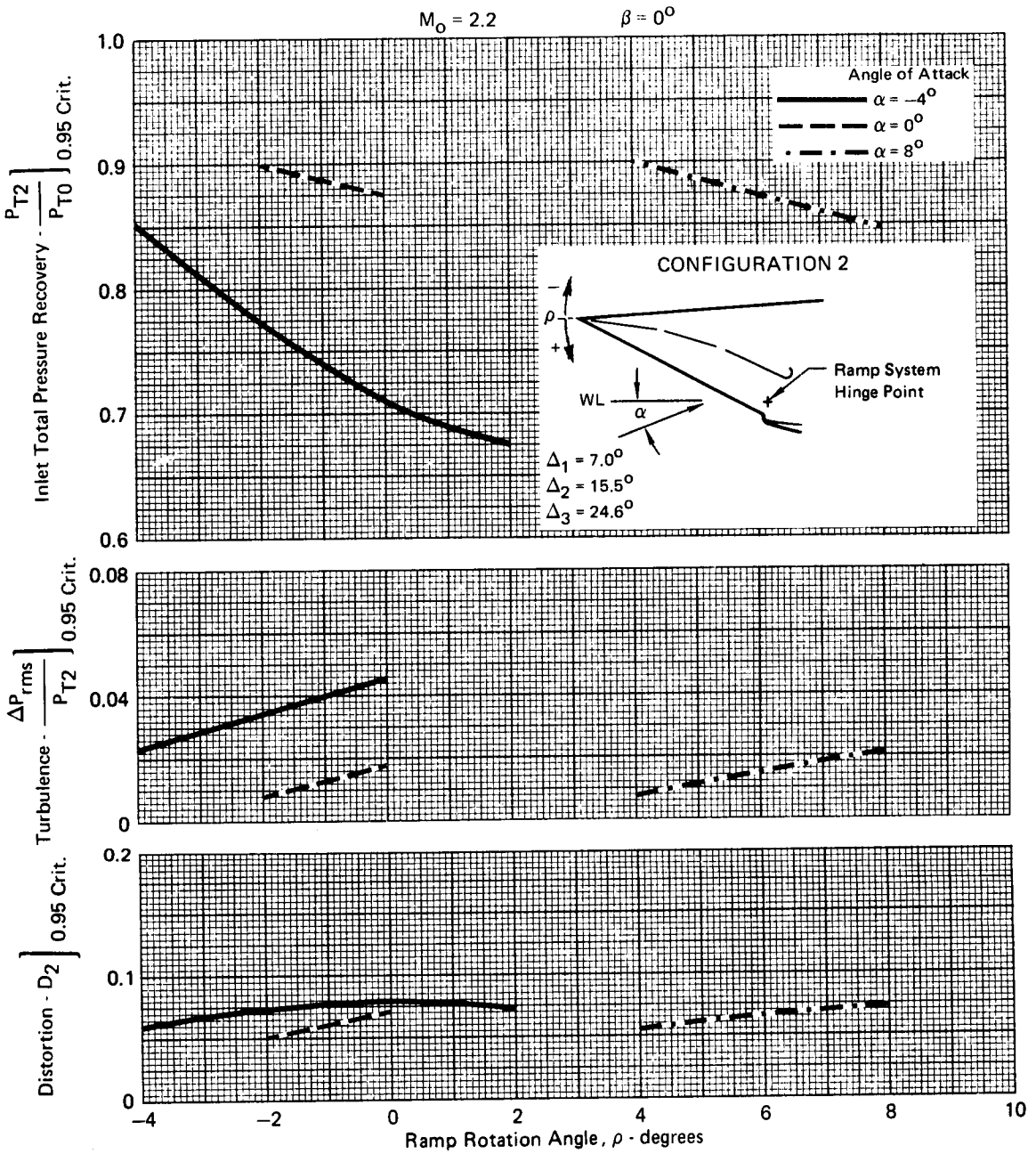

(a) M_o = 2.2

FIGURE 48 - EFFECTS OF RAMP SYSTEM ROTATION ON PRESSURE RECOVERY, TURBULENCE, AND DISTORTION

GP73-0449-45

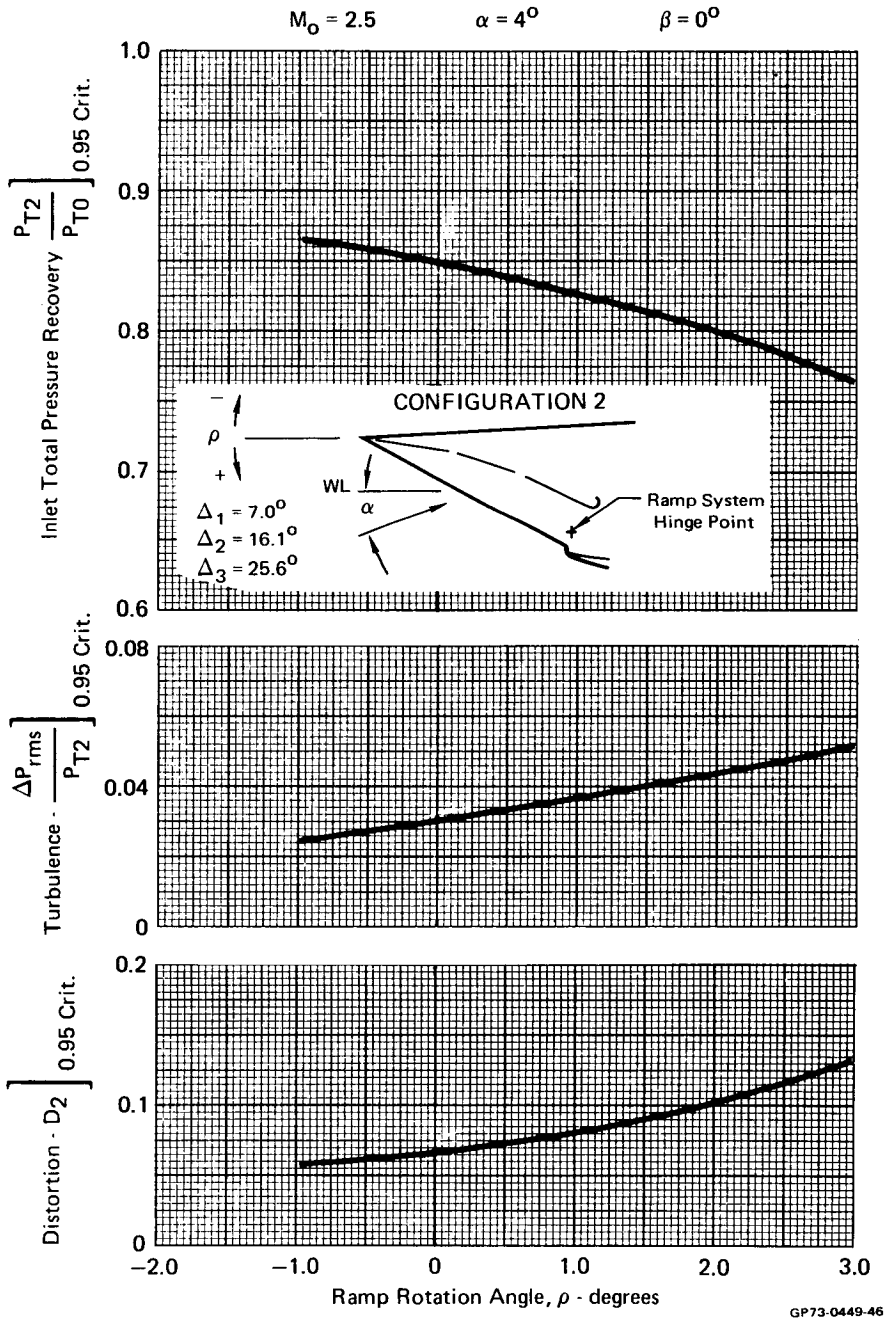

(b) M_o = 2.5

FIGURE 48 (Concl.) - EFFECTS OF RAMP SYSTEM ROTATION ON PRESSURE RECOVERY, TURBULENCE, AND DISTORTION

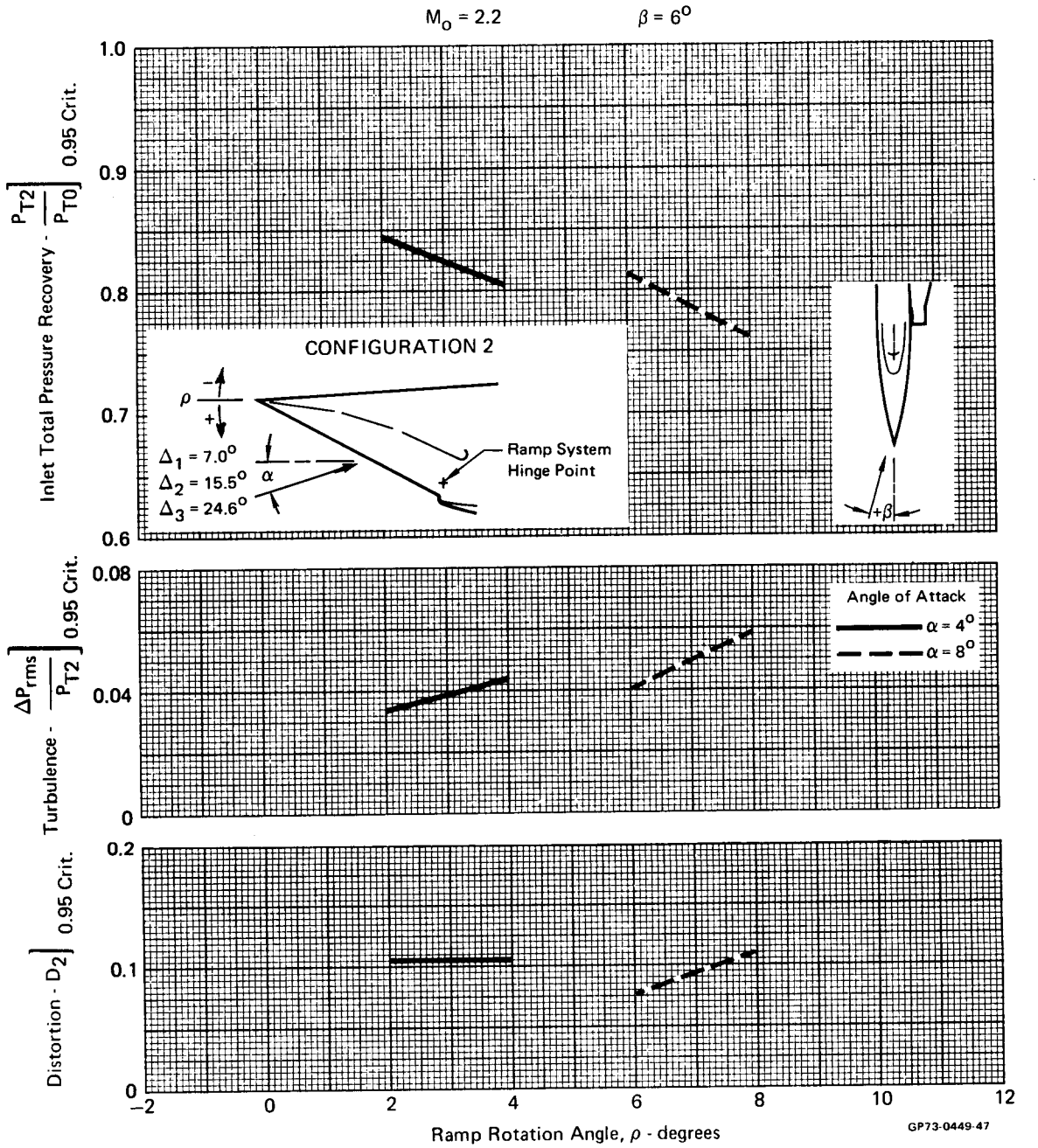

FIGURE 49 - EFFECTS OF RAMP SYSTEM ROTATION ON PRESSURE RECOVERY, TURBULENCE, AND DISTORTION AT SIDESLIP

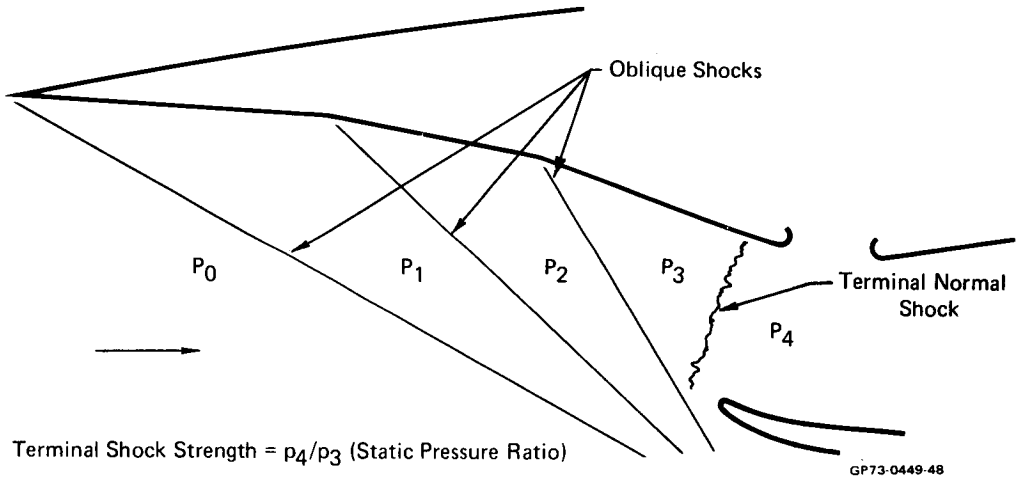

FIGURE 50 - TERMINAL SHOCK STRENGTH

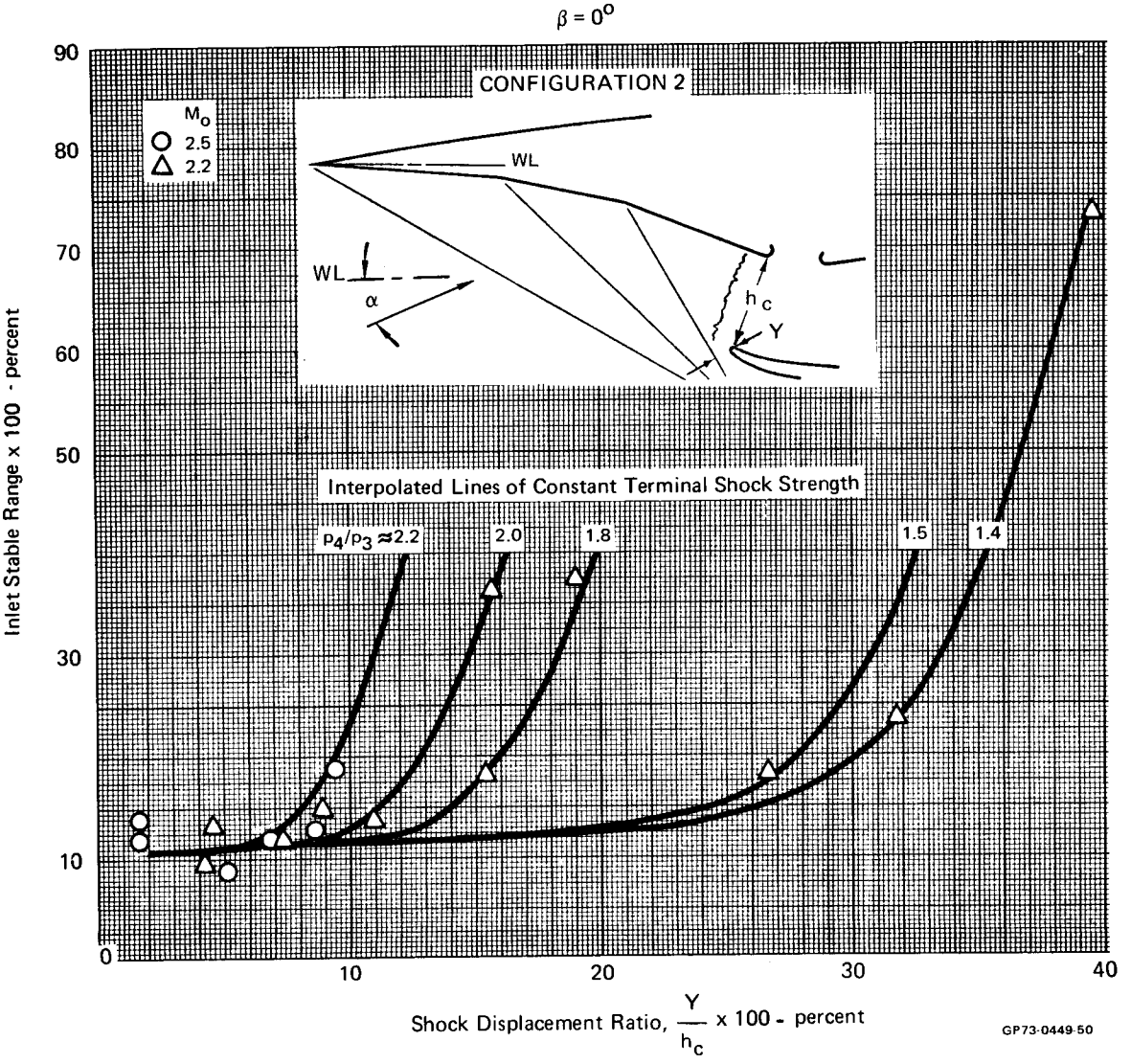

FIGURE 51 - EFFECTS OF TERMINAL SHOCK STRENGTH AND OBLIQUE SHOCK SYSTEM POSITION ON INLET STABLE RANGE

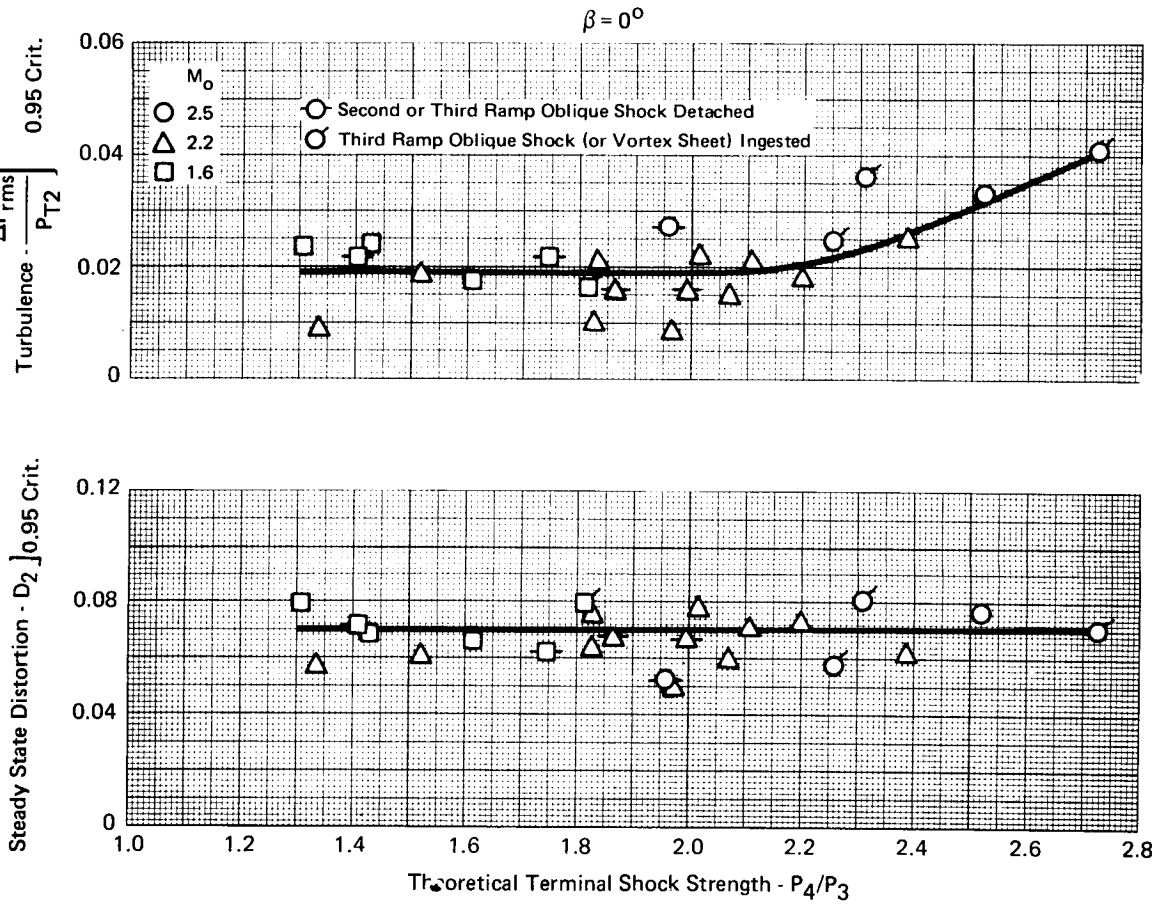

CONFIGURATION 2

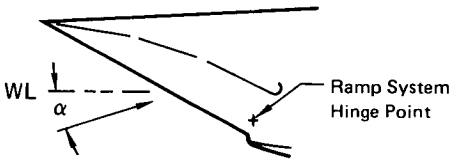

(a) $\beta = 0^{o}$

FIGURE 52 - EFFECTS OF TERMINAL SHOCK STRENGTH ON TURBULENCE AND STEADY STATE DISTORTION

GP73-0449-73

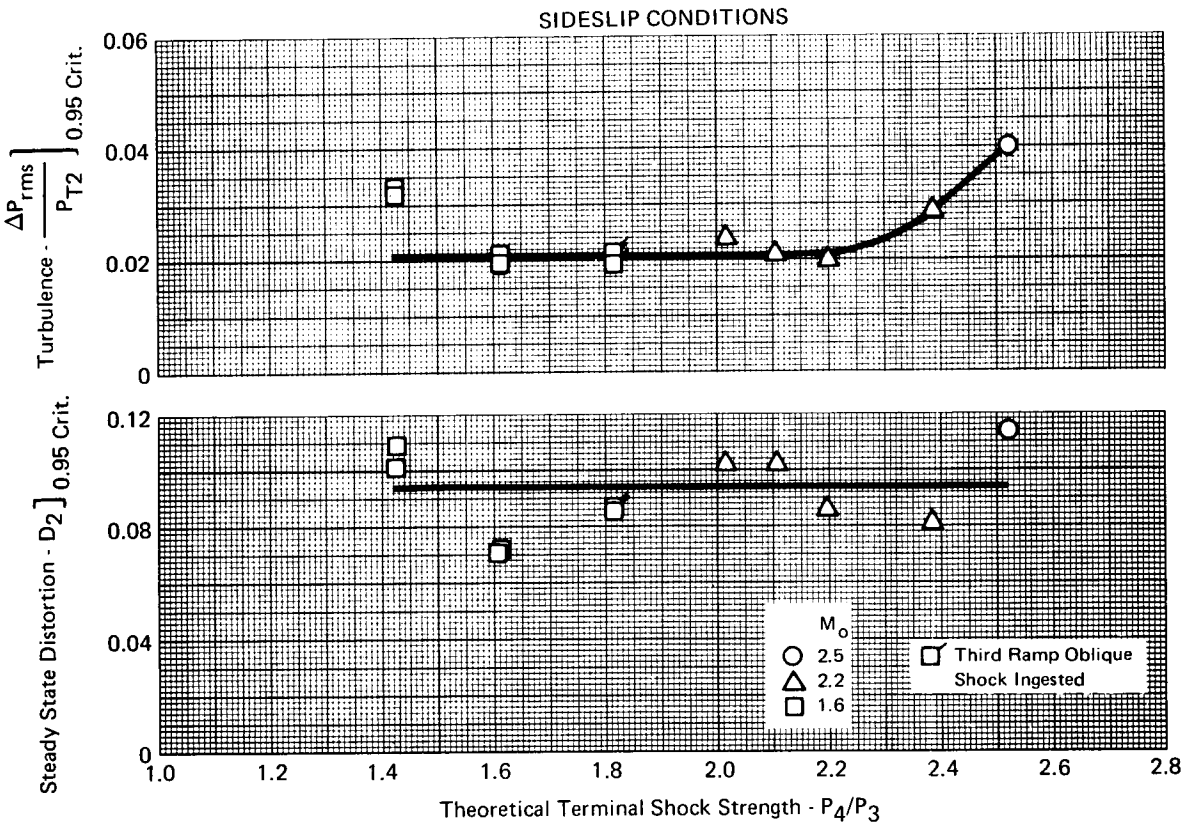

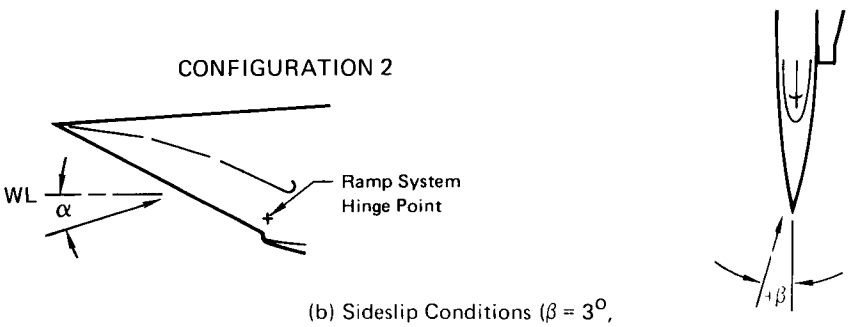

(b) Sideslip Conditions ($\beta = 3^o$, or 6^o Leeward Sideslip)

FIGURE 52 (Concl.) - EFFECTS OF TERMINAL SHOCK STRENGTH ON TURBULENCE AND STEADY STATE DISTORTION

GP73-0449-74

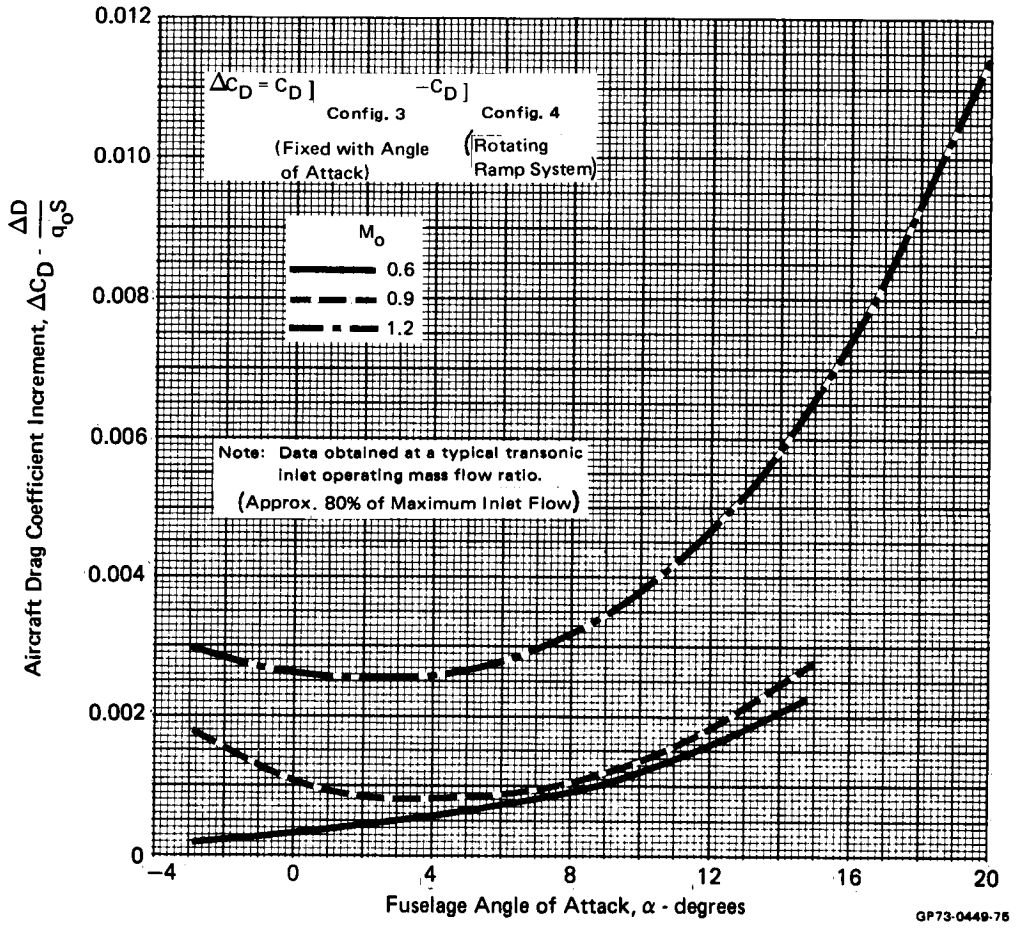

FIGURE 53 - EFFECT ON DRAG OF VARYING INLET CAPTURE AREA WITH ANGLE OF ATTACK

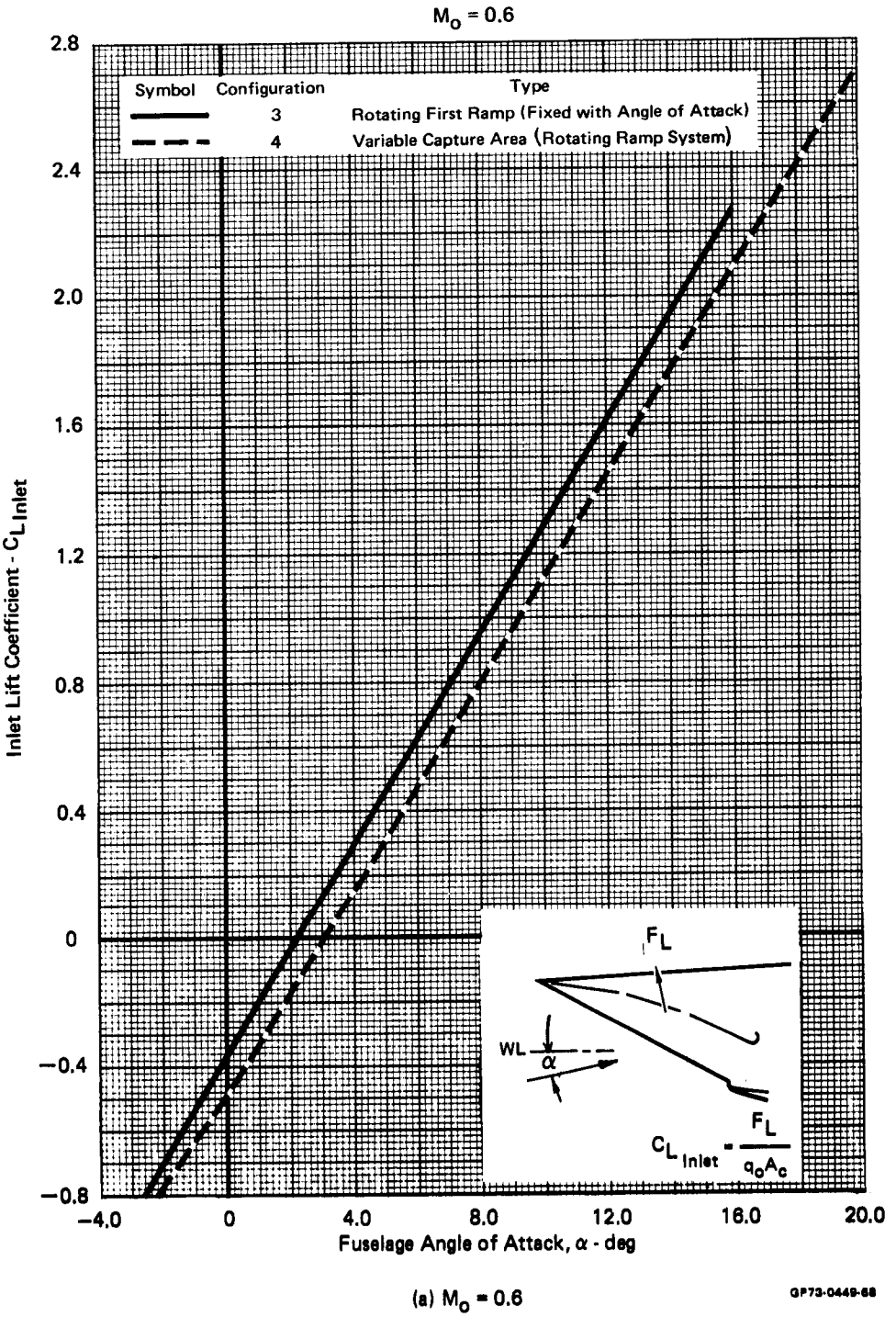

FIGURE 54 COMPARISON OF INLET LIFT COEFFICIENTS

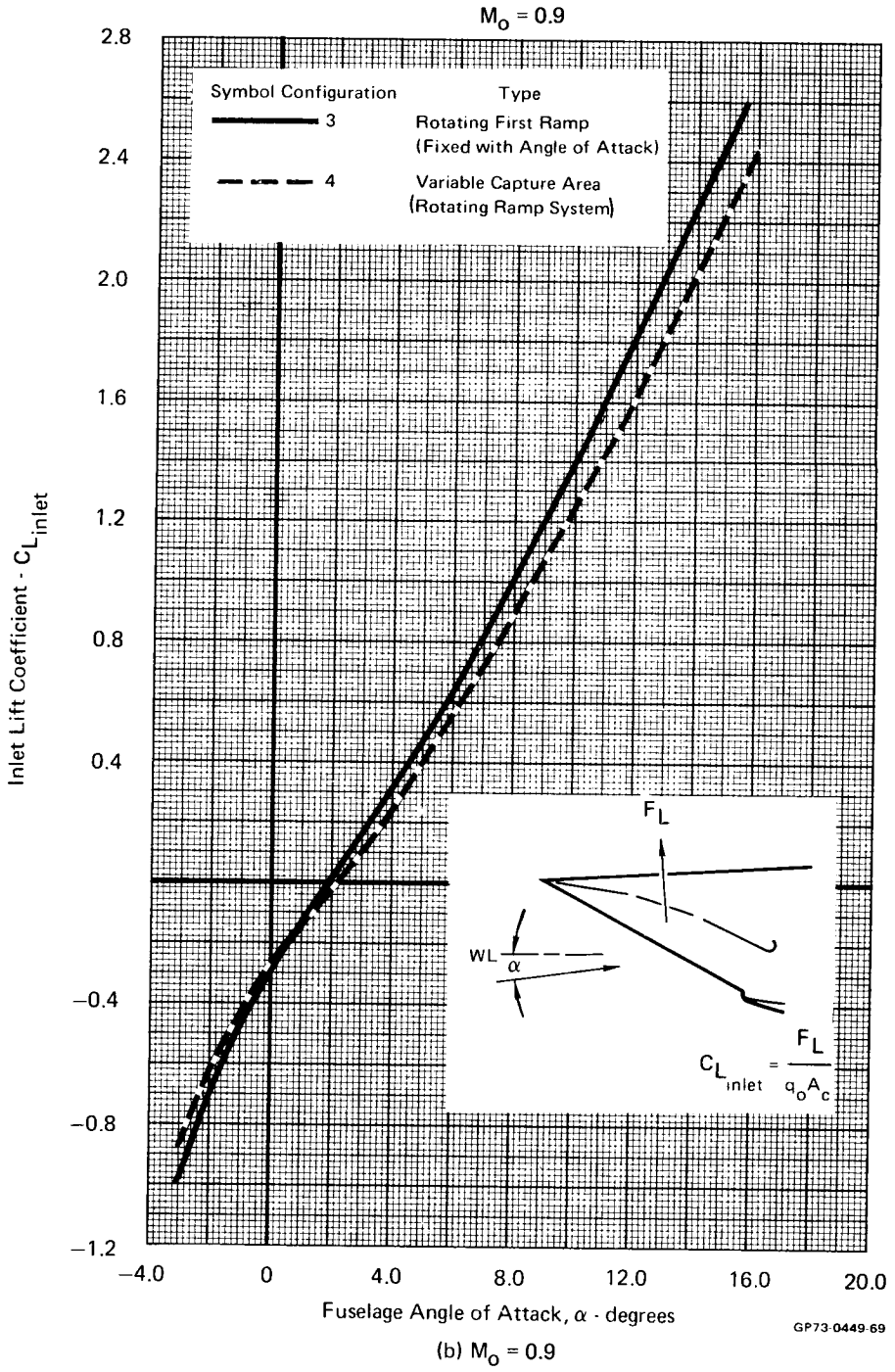

(b) M_o = 0.9

FIGURE 54 (Cont'd) - COMPARISON OF INLET LIFT COEFFICIENTS

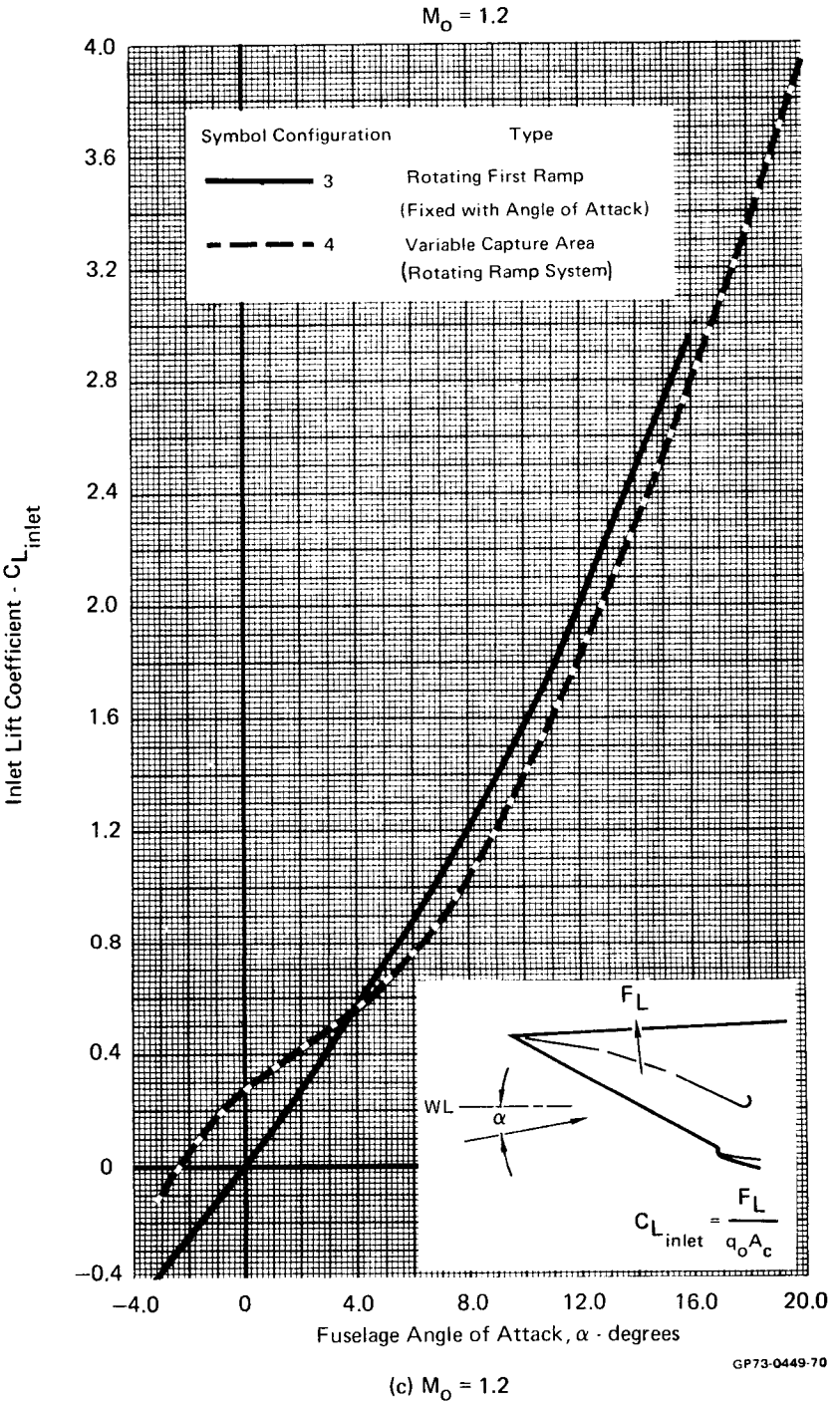

(c) M_o = 1.2

FIGURE 54(Concl.) - COMPARISON OF INLET LIFT COEFFICIENTS

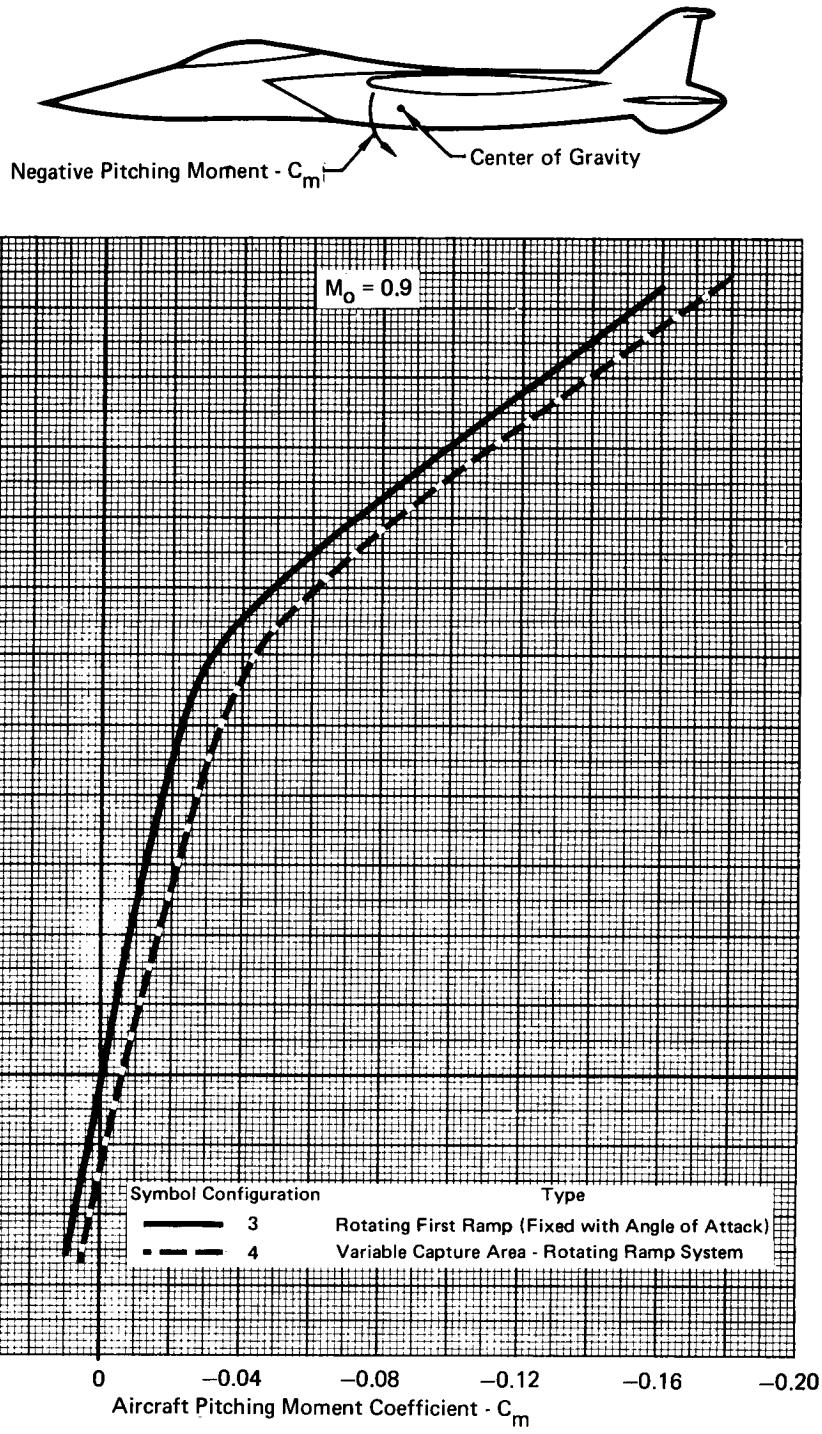

FIGURE 55 - COMPARISON OF AIRCRAFT PITCHING MOMENTS

GP73-0449-71

APPENDIX A

Performance Data

Presented herein are the pressure recovery, turbulence, and steady state distortion data used in the inlet performance analyses discussed in this report. The data plots are separated into sections corresponding to each analysis as listed below.

Analysis	Figures
Effects of Third Ramp Bleed Variation	A-1 through A-4
Effects of Throat Slot Bleed Variation	A-5 through A-11
Effects of Bypass Flow Variation	A-12 through A-17
Effects of Operating Mass Flow Ratio Variation	A-18 through A-19
Effects of Inlet Ramp Angle Variations	A-20 through A-23
Effects of Angle of Attack	A-24 through A-84
Effects of Sideslip	A-85 through A-144
Effects of Ramp System Rotation	A-145 through A-150

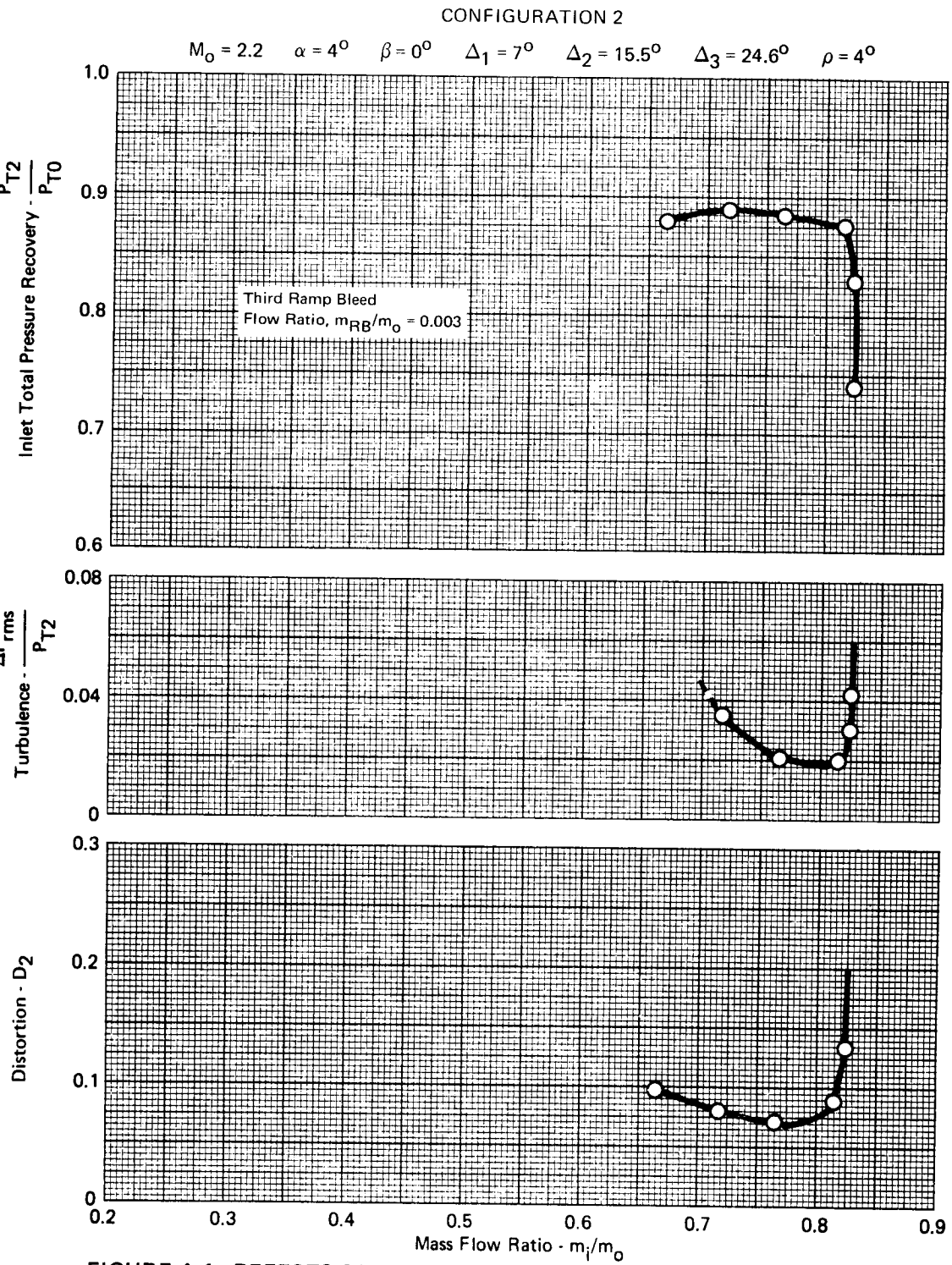

FIGURE A-1 - EFFECTS OF THIRD RAMP BLEED ON PRESSURE RECOVERY, TURBULENCE, AND DISTORTION

GP73-0449-58

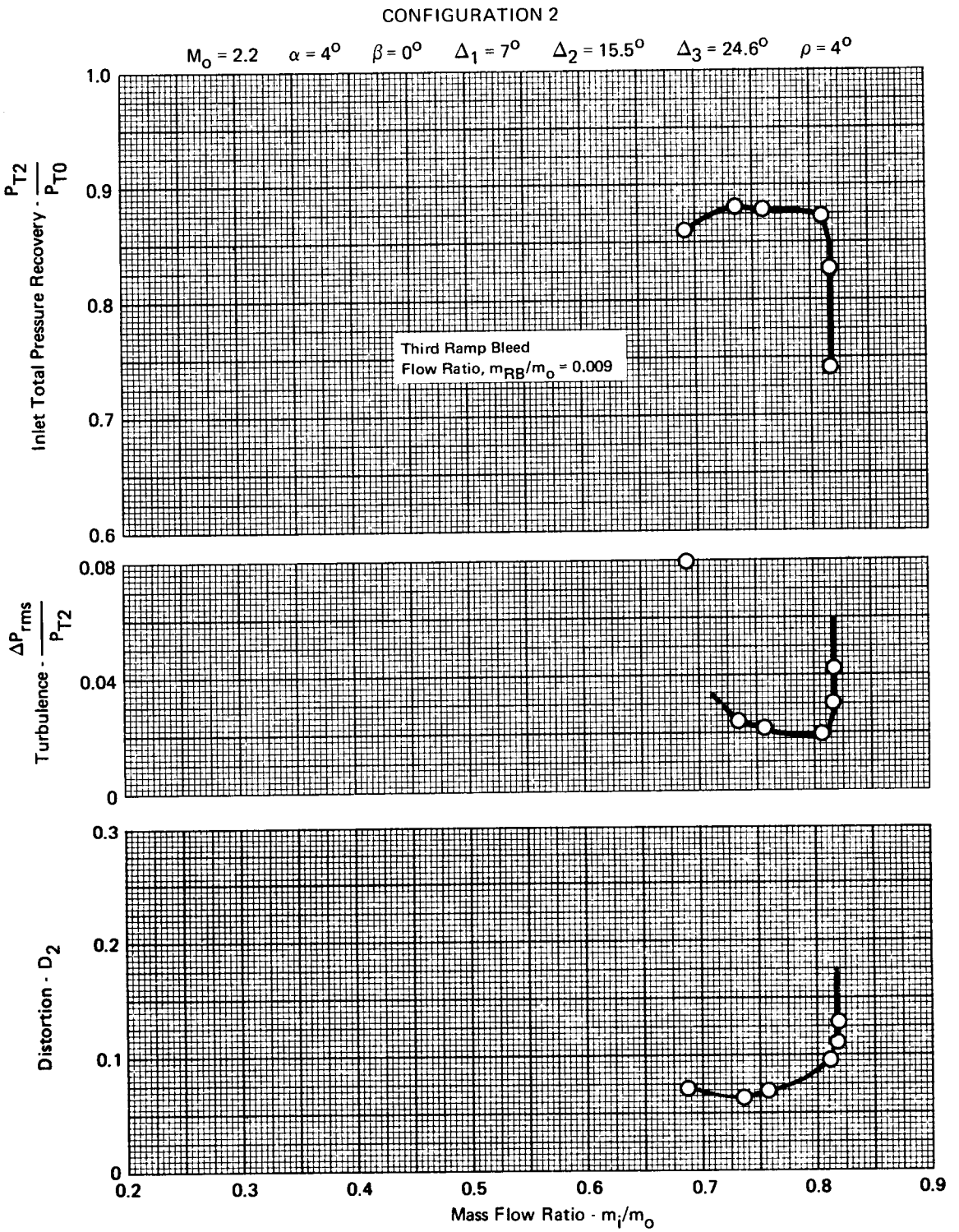

FIGURE A-2 - EFFECTS OF THIRD RAMP BLEED ON PRESSURE RECOVERY, TURBULENCE, AND DISTORTION

GP73-0449-59

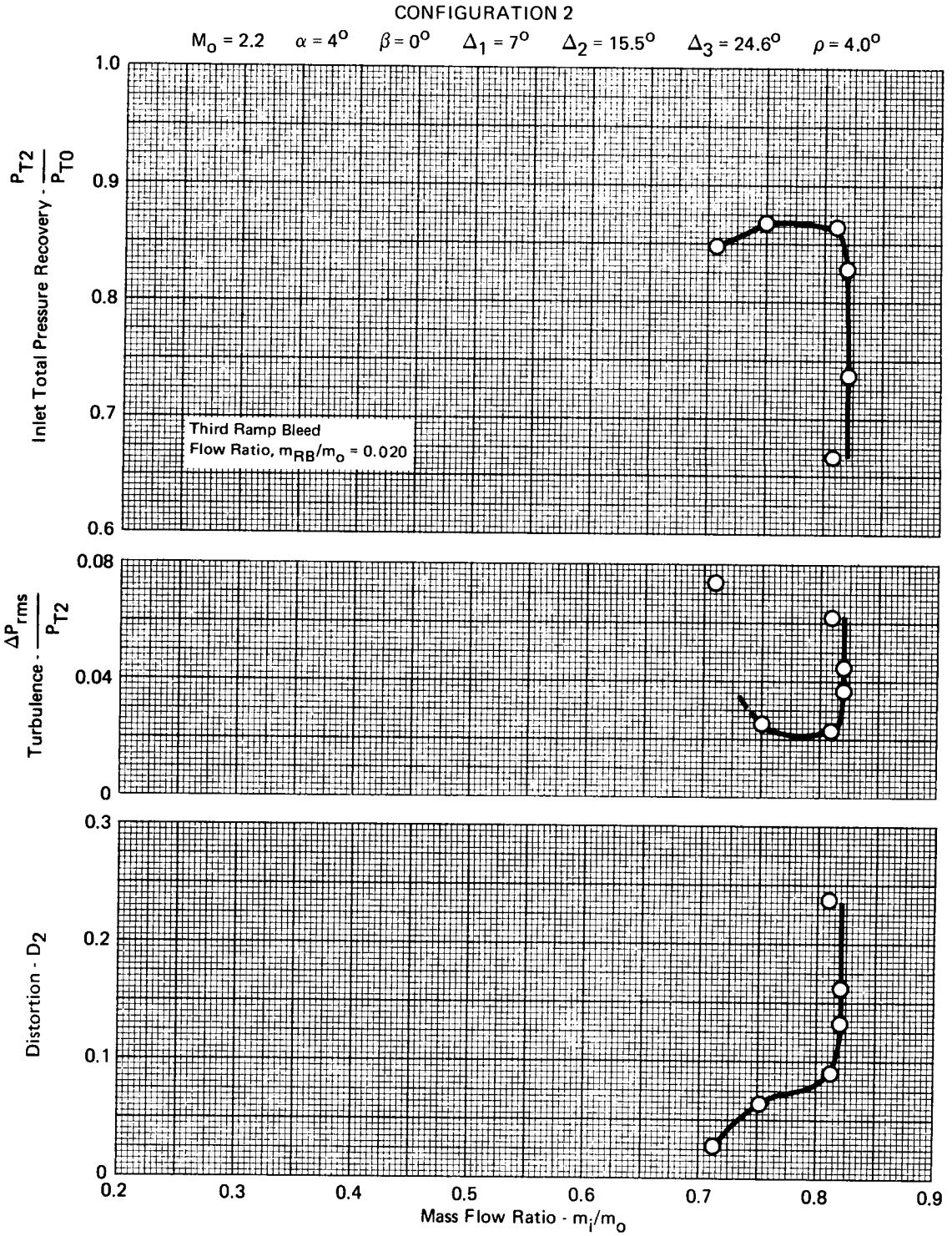

FIGURE A-3 - EFFECTS OF THIRD RAMP BLEED ON PRESSURE RECOVERY, TURBULENCE, AND DISTORTION

GP73-0449-60

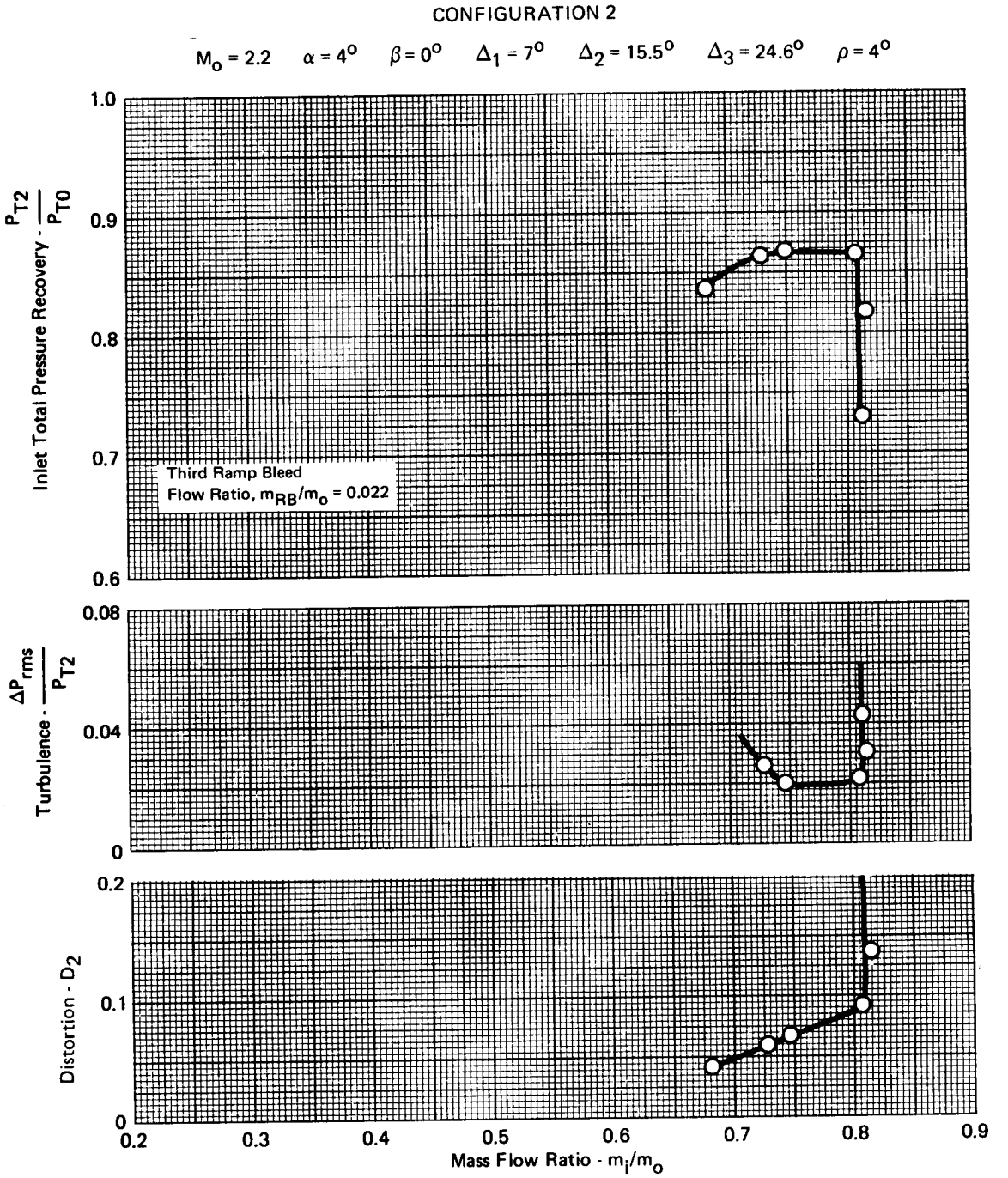

FIGURE A-4 - EFFECTS OF THIRD RAMP BLEED ON PRESSURE RECOVERY, TURBULENCE, AND DISTORTION

GP73-0449-61

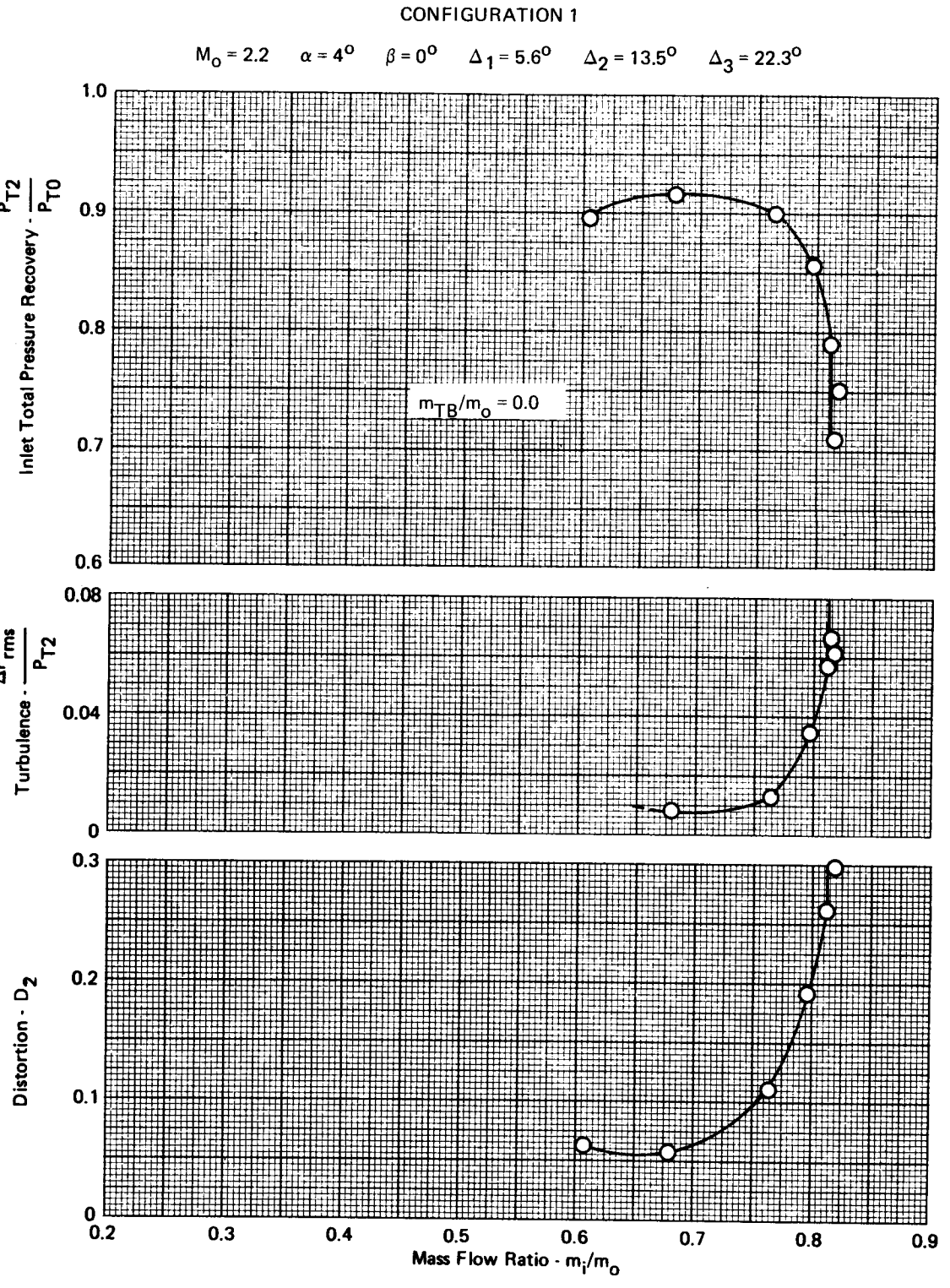

FIGURE A-5 - EFFECTS OF THROAT SLOT BLEED ON PRESSURE RECOVERY, TURBULENCE, AND DISTORTION

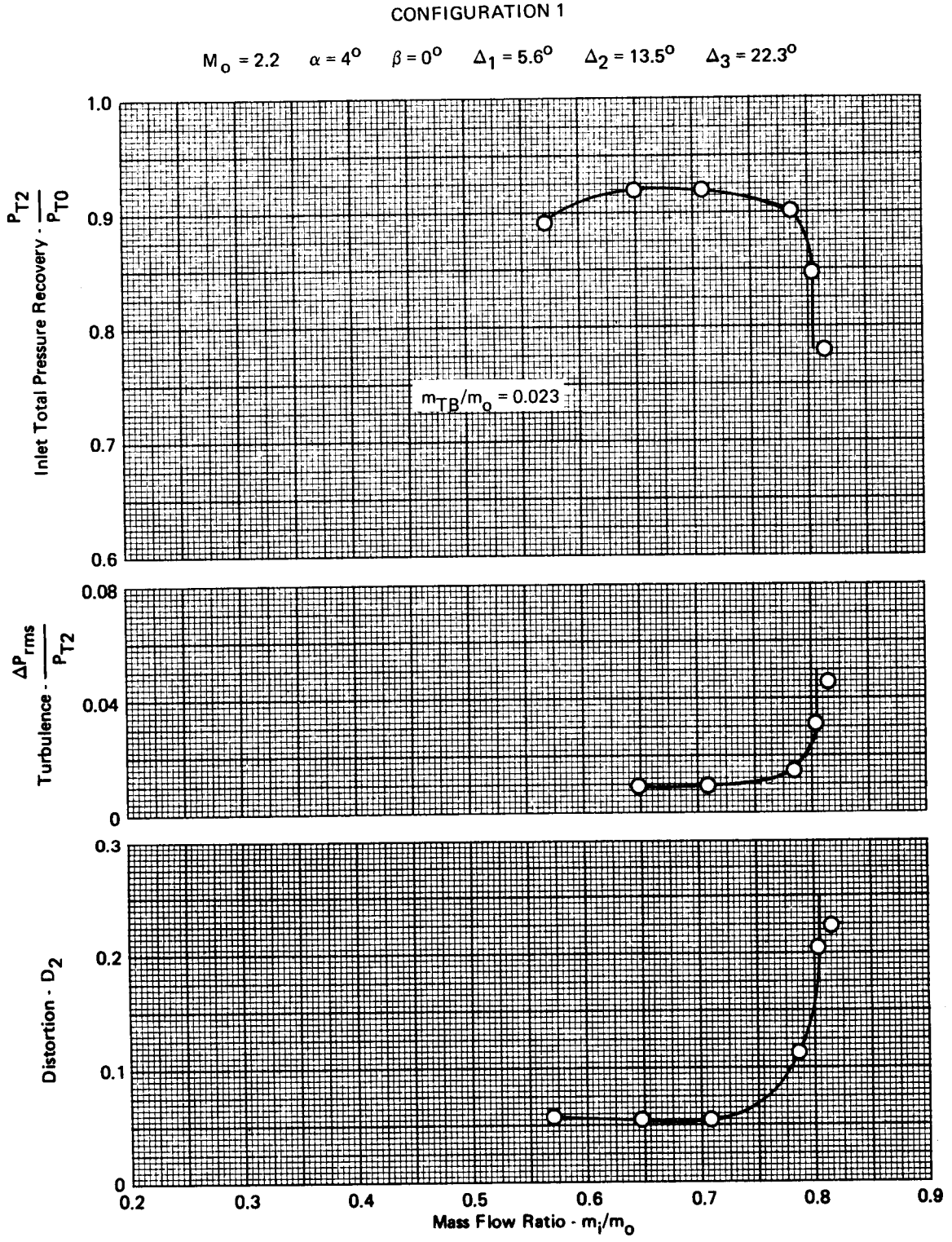

FIGURE A-6 - EFFECTS OF THROAT SLOT BLEED ON PRESSURE RECOVERY, TURBULENCE, AND DISTORTION

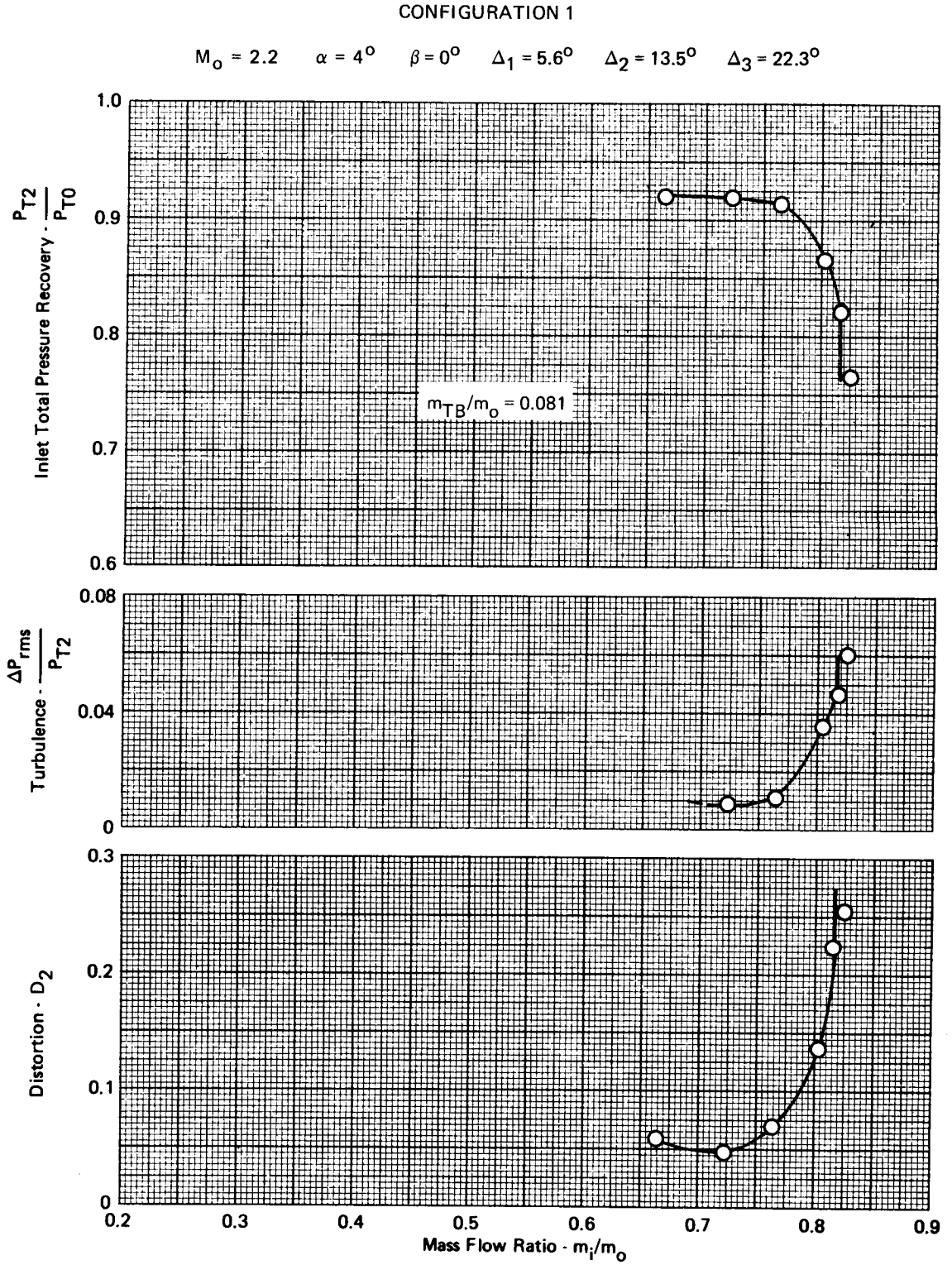

FIGURE A-7 - EFFECTS OF THROAT SLOT BLEED ON PRESSURE RECOVERY, TURBULENCE, AND DISTORTION

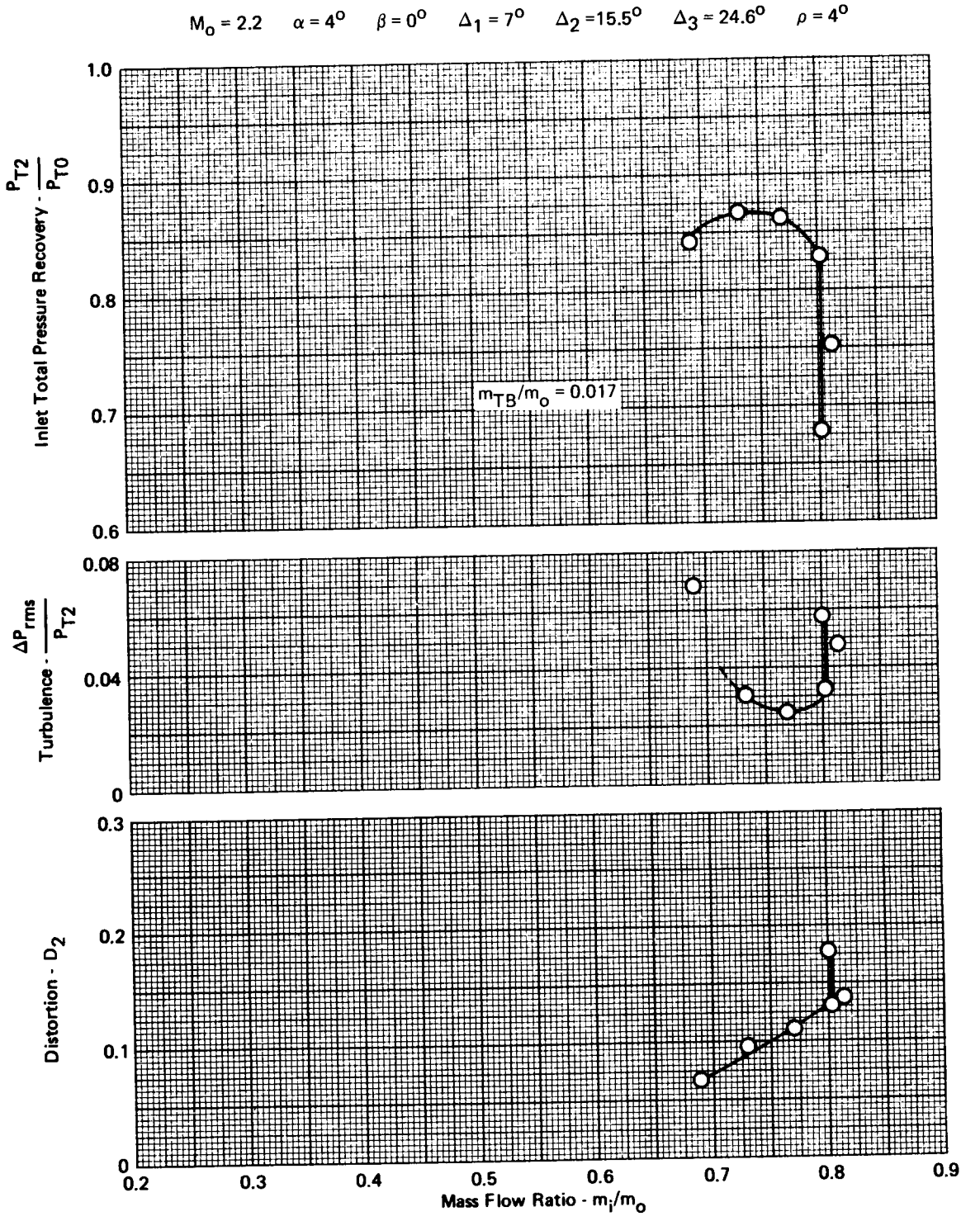

FIGURE A-8 - EFFECTS OF THROAT SLOT BLEED ON PRESSURE RECOVERY, TURBULENCE, AND DISTORTION

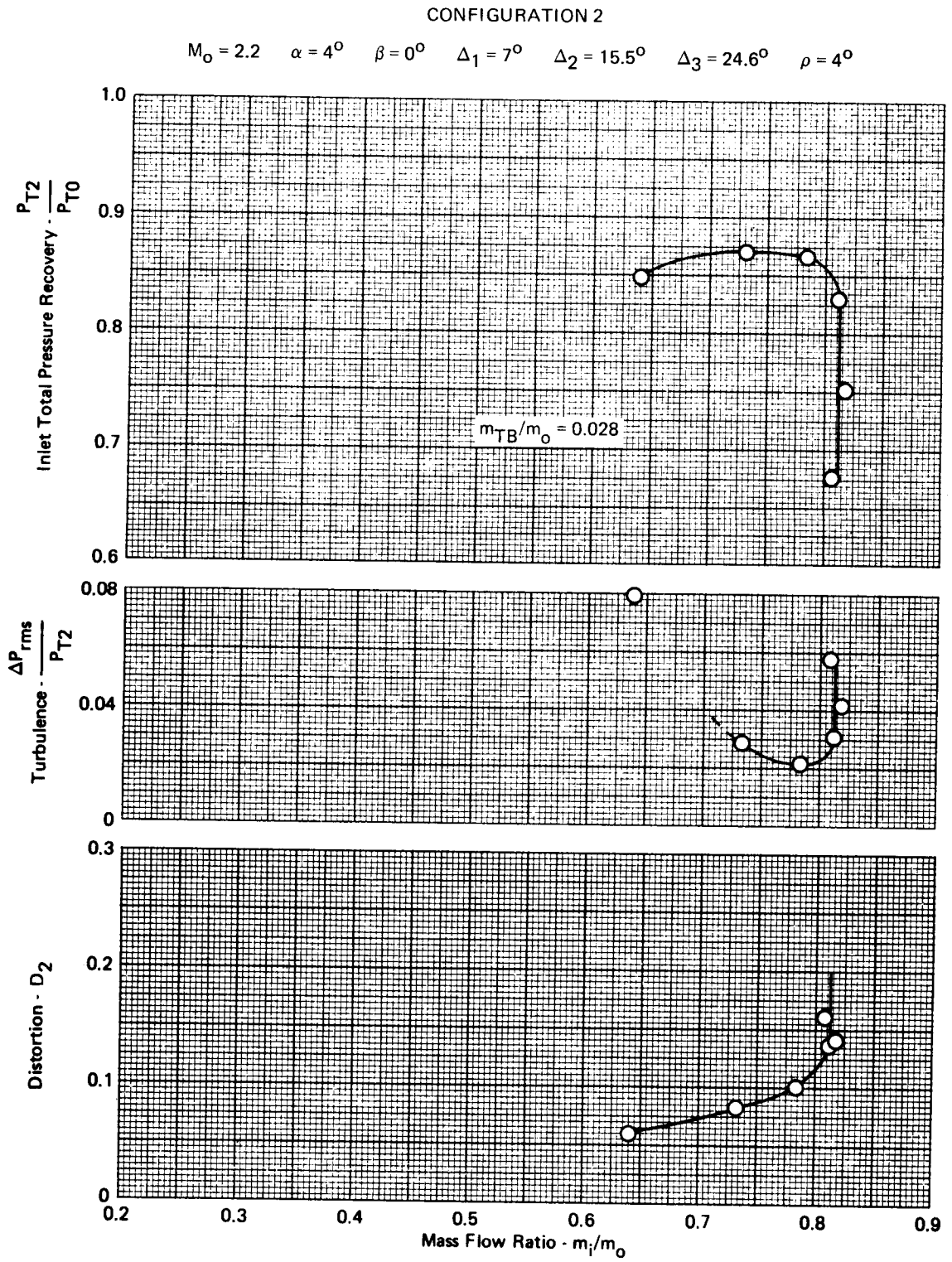

FIGURE A-9 - EFFECTS OF THROAT SLOT BLEED ON PRESSURE RECOVERY, TURBULENCE, AND DISTORTION

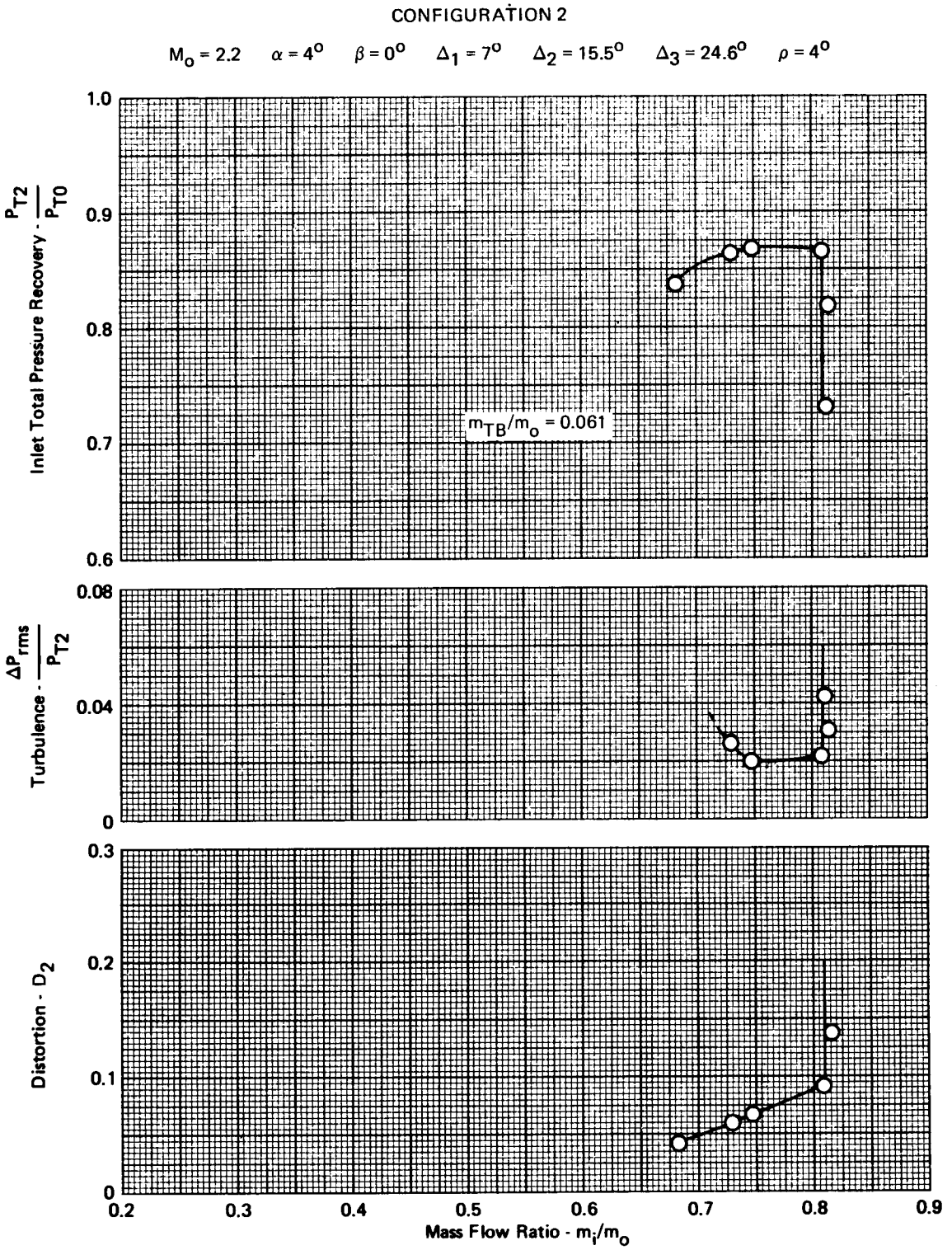

FIGURE A-10 - EFFECTS OF THROAT SLOT BLEED ON PRESSURE RECOVERY, TURBULENCE, AND DISTORTION

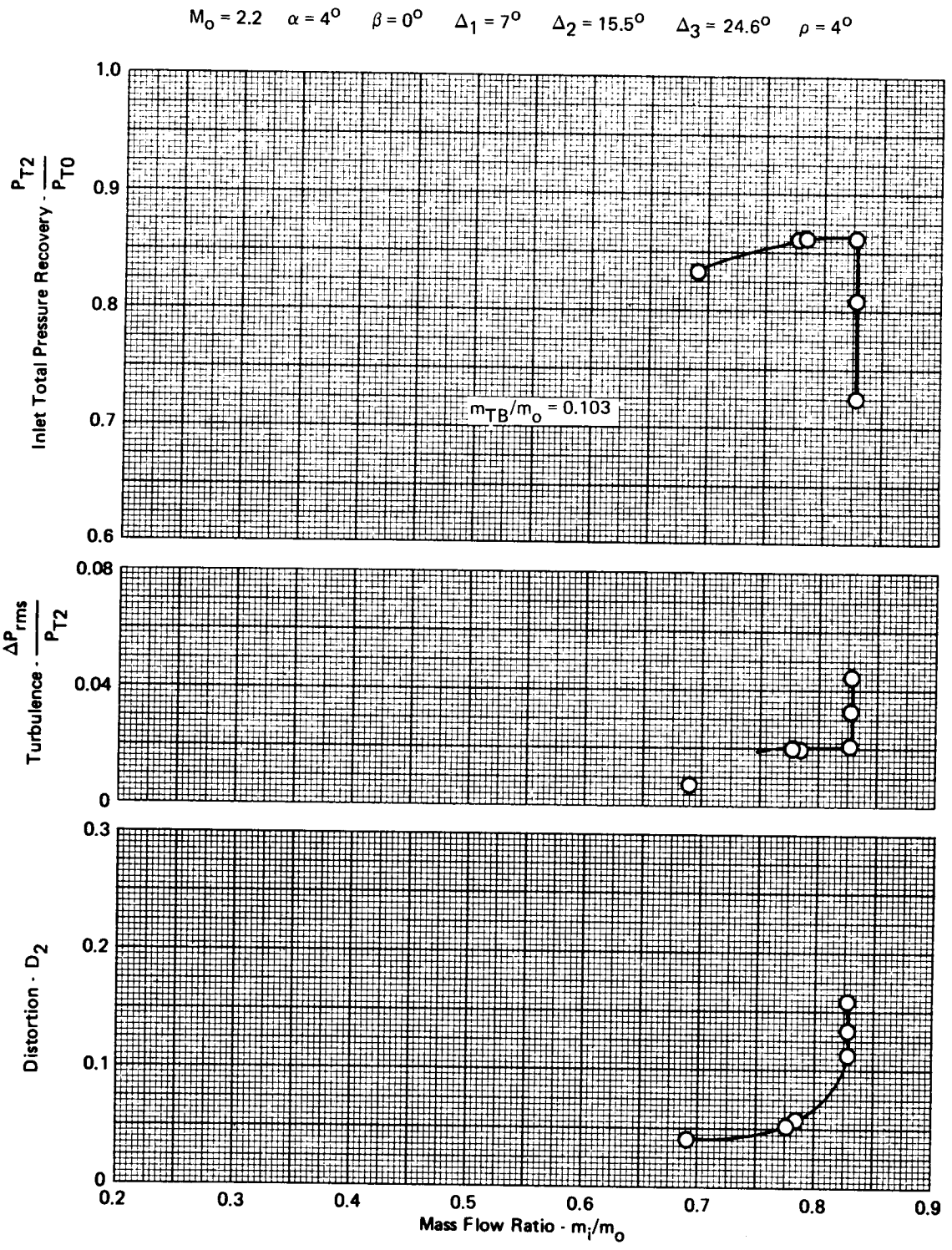

FIGURE A-11 - EFFECTS OF THROAT SLOT BLEED ON PRESSURE RECOVERY, TURBULENCE, AND DISTORTION

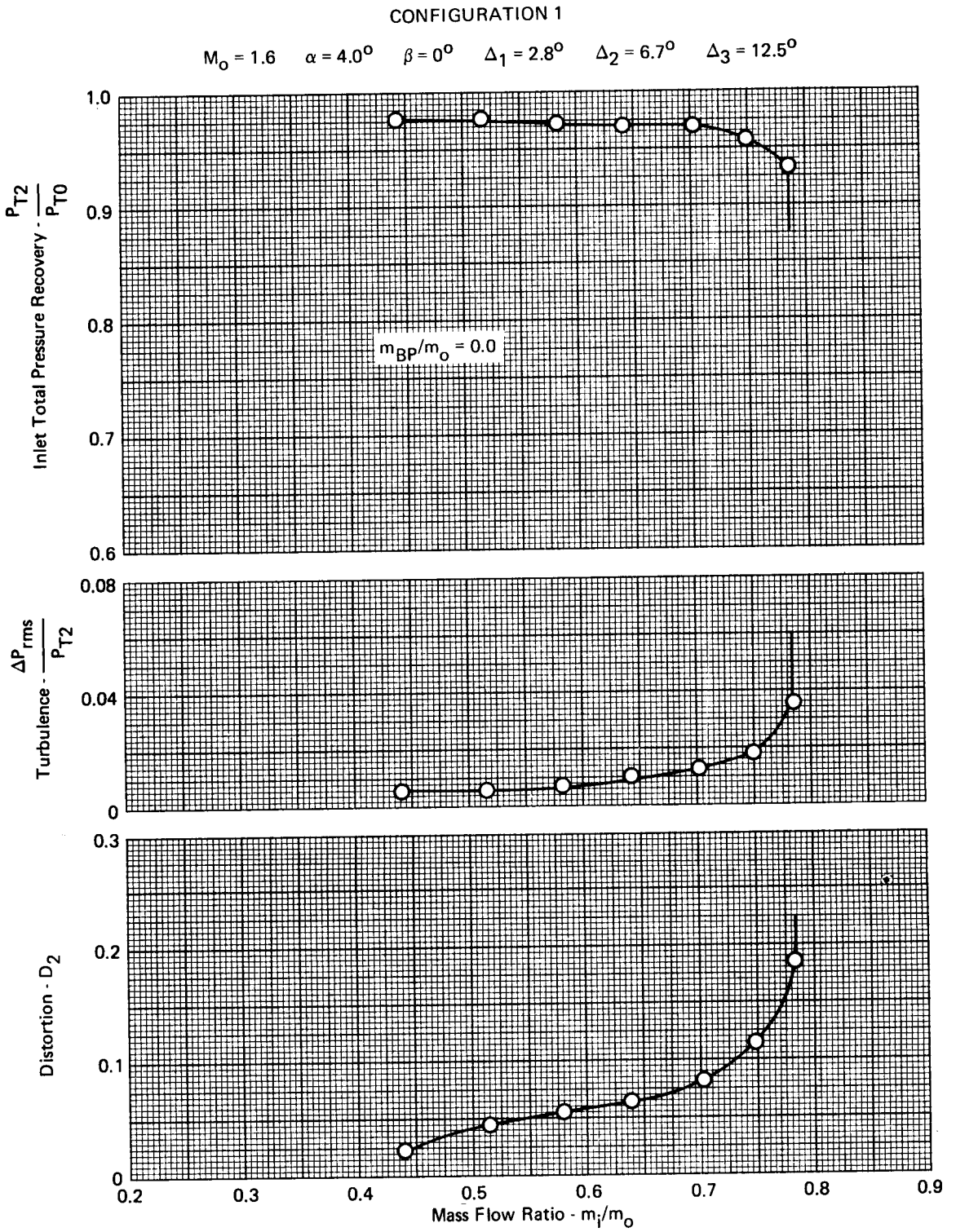

FIGURE A-12 - EFFECTS OF BYPASS FLOW ON PRESSURE RECOVERY, TURBULENCE, AND DISTORTION

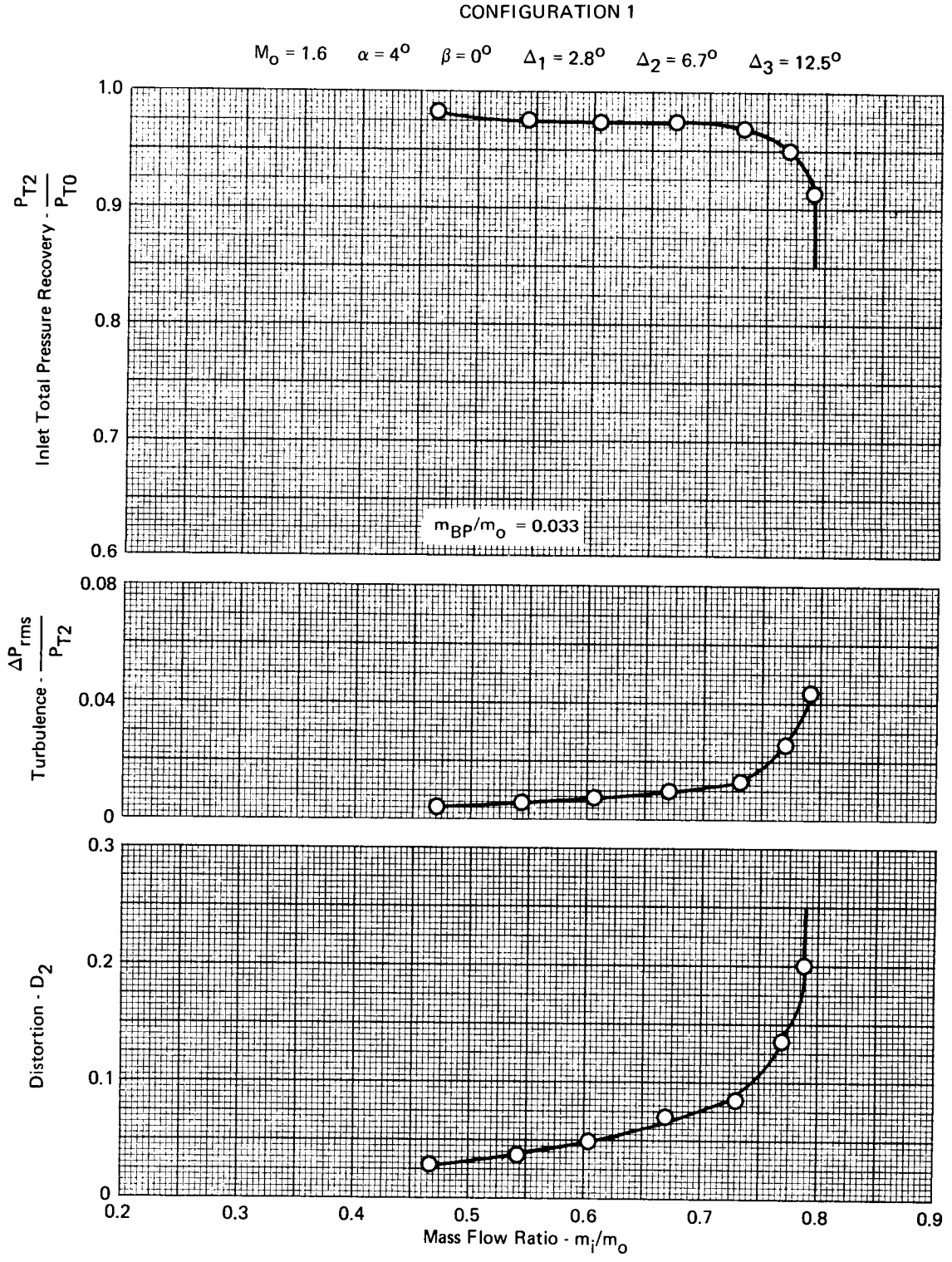

FIGURE A-13 - EFFECTS OF BYPASS FLOW ON PRESSURE RECOVERY, TURBULENCE, AND DISTORTION

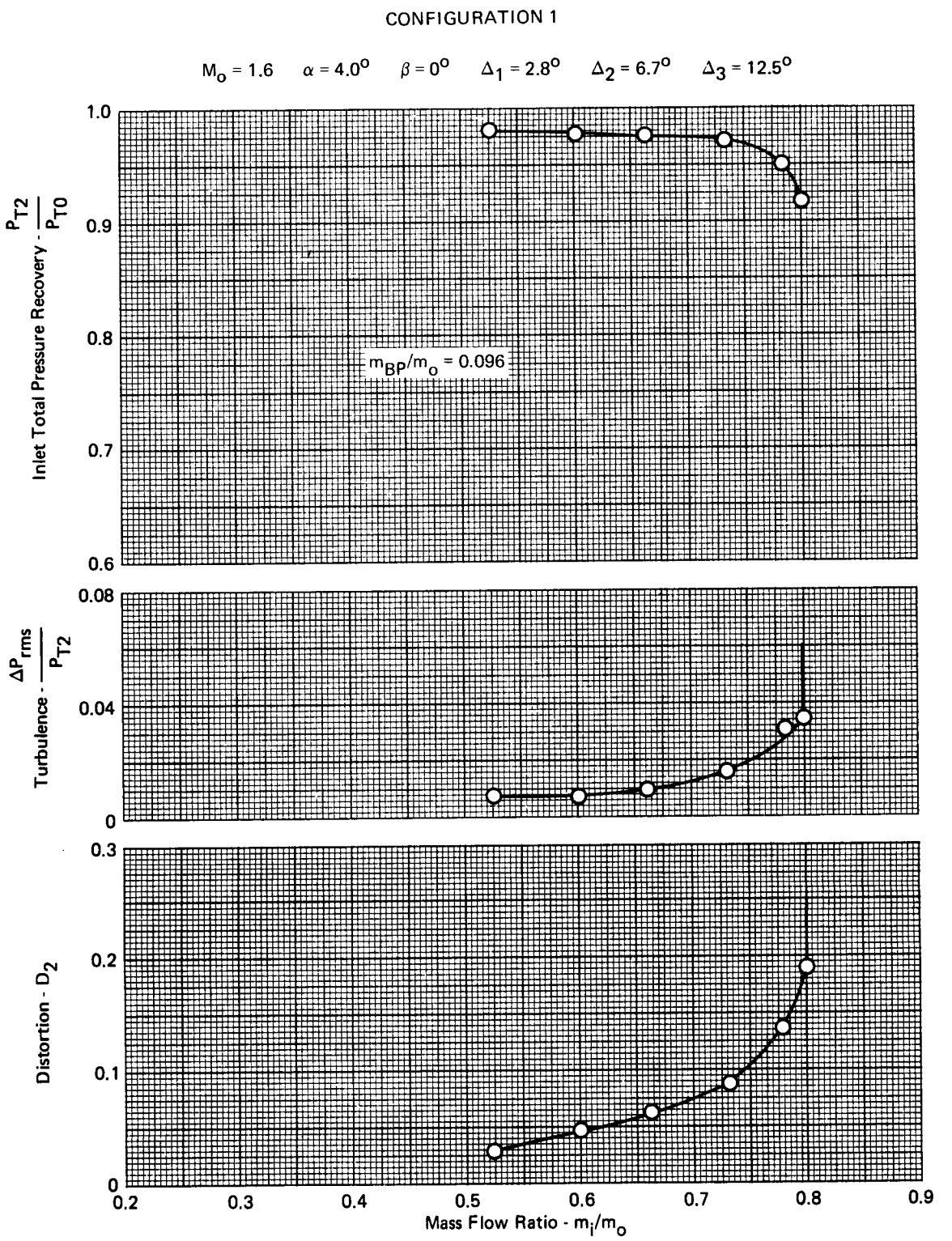

FIGURE A-14 - EFFECTS OF BYPASS FLOW ON PRESSURE RECOVERY, TURBULENCE, AND DISTORTION

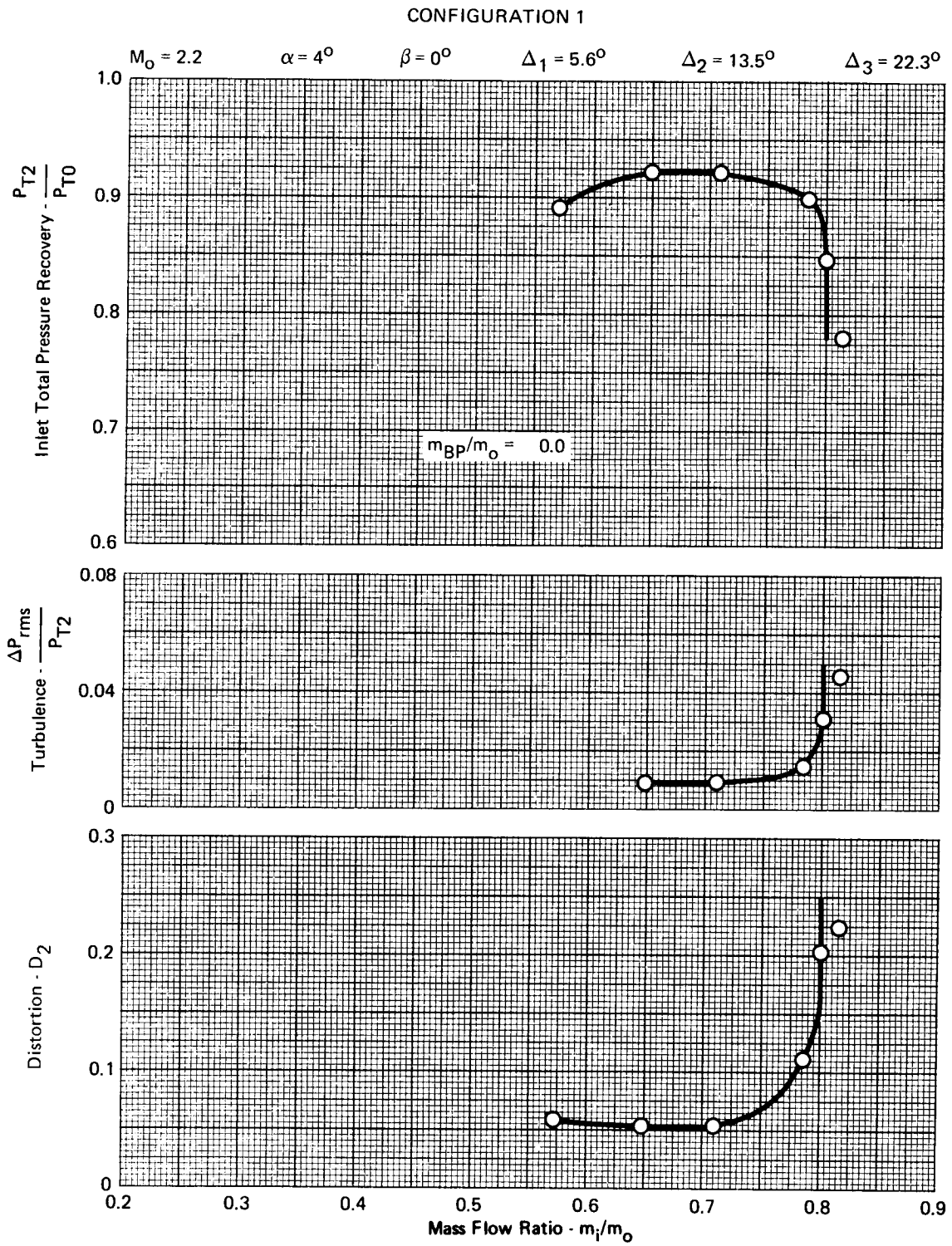

FIGURE A-15 - EFFECTS OF BYPASS FLOW ON PRESSURE RECOVERY, TURBULENCE, AND DISTORTION

GP73-0449-63

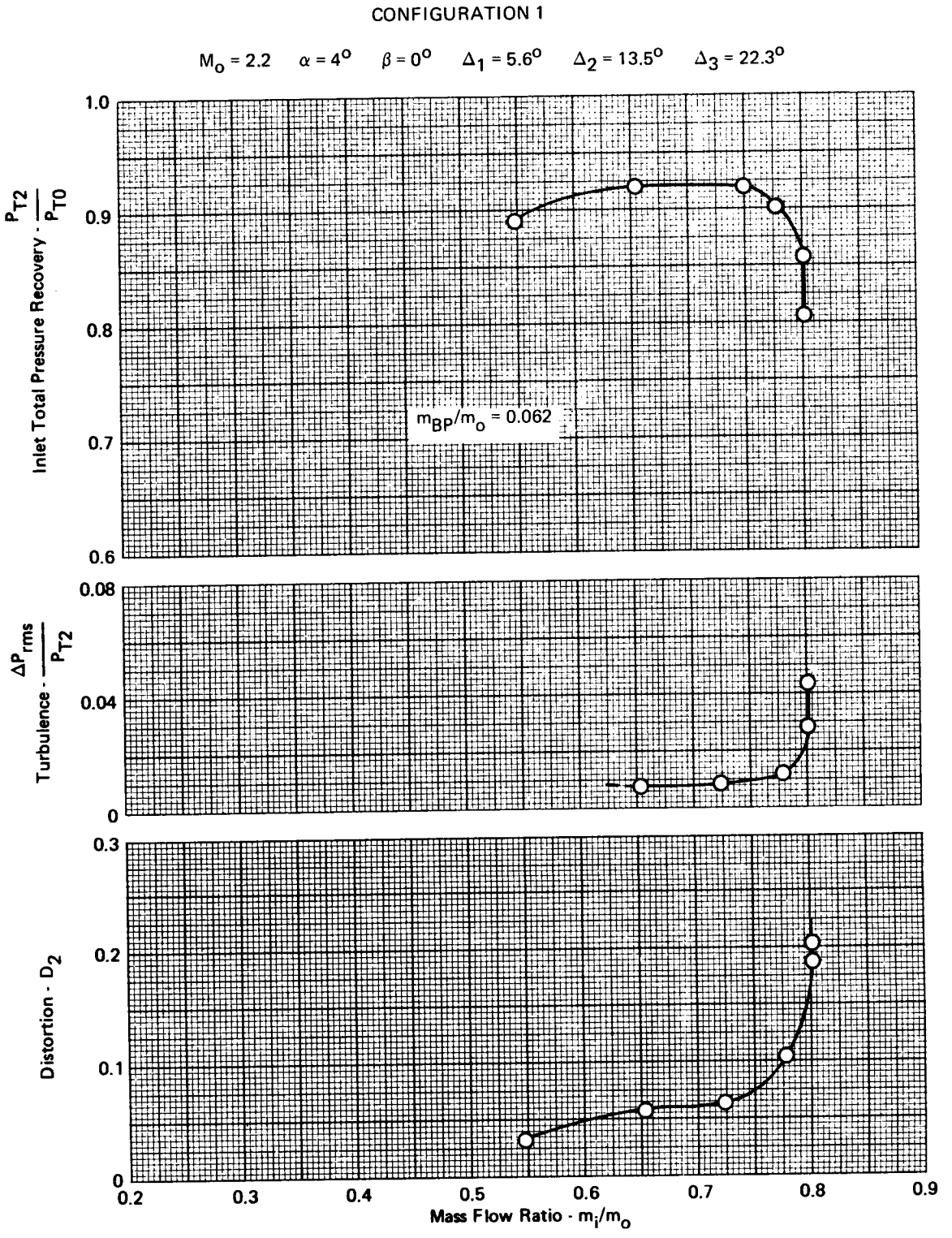

FIGURE A-16 - EFFECTS OF BYPASS FLOW ON PRESSURE RECOVERY, TURBULENCE, AND DISTORTION

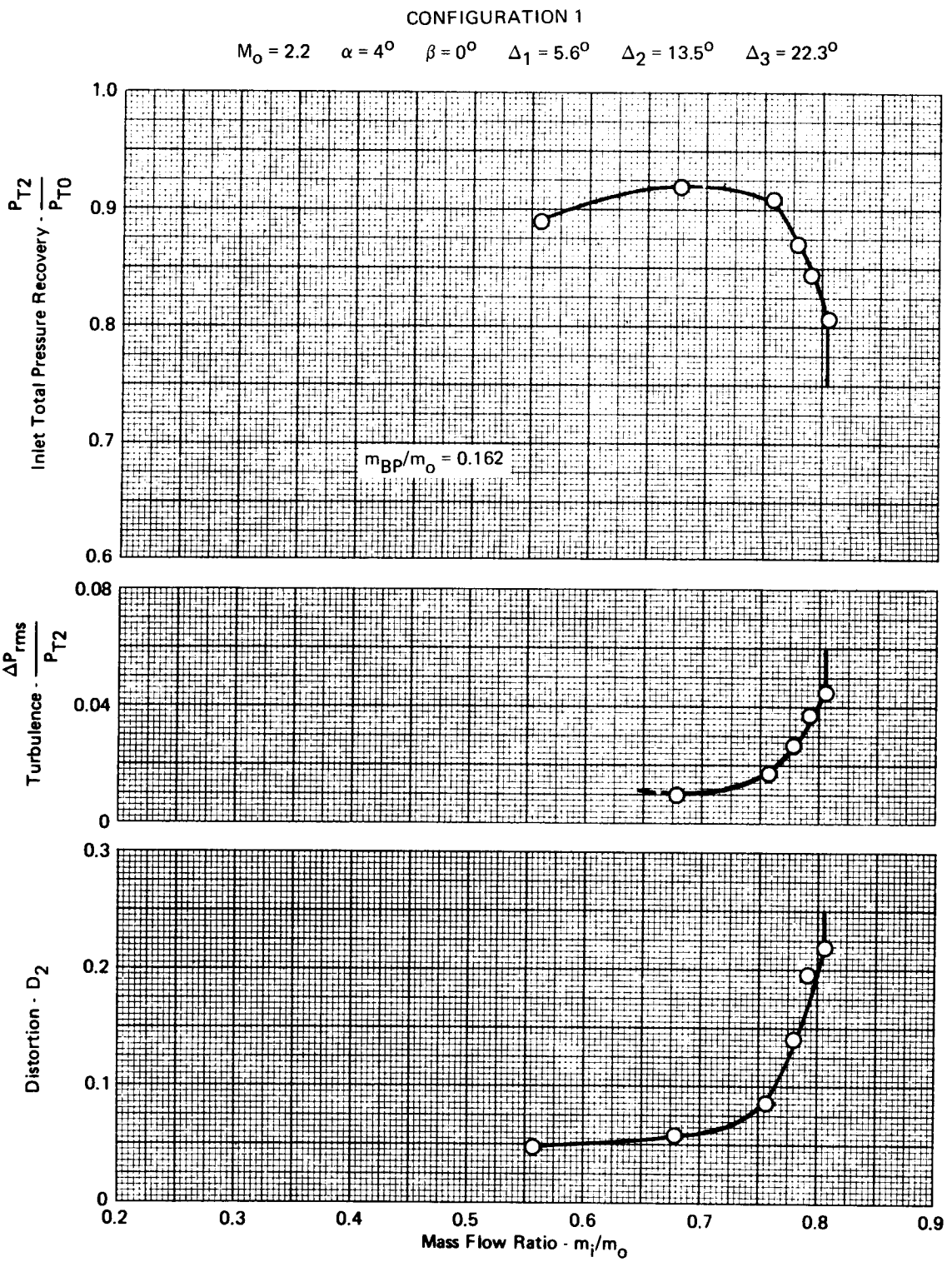

FIGURE A-17 - EFFECTS OF BYPASS FLOW ON PRESSURE RECOVERY, TURBULENCE, AND DISTORTION

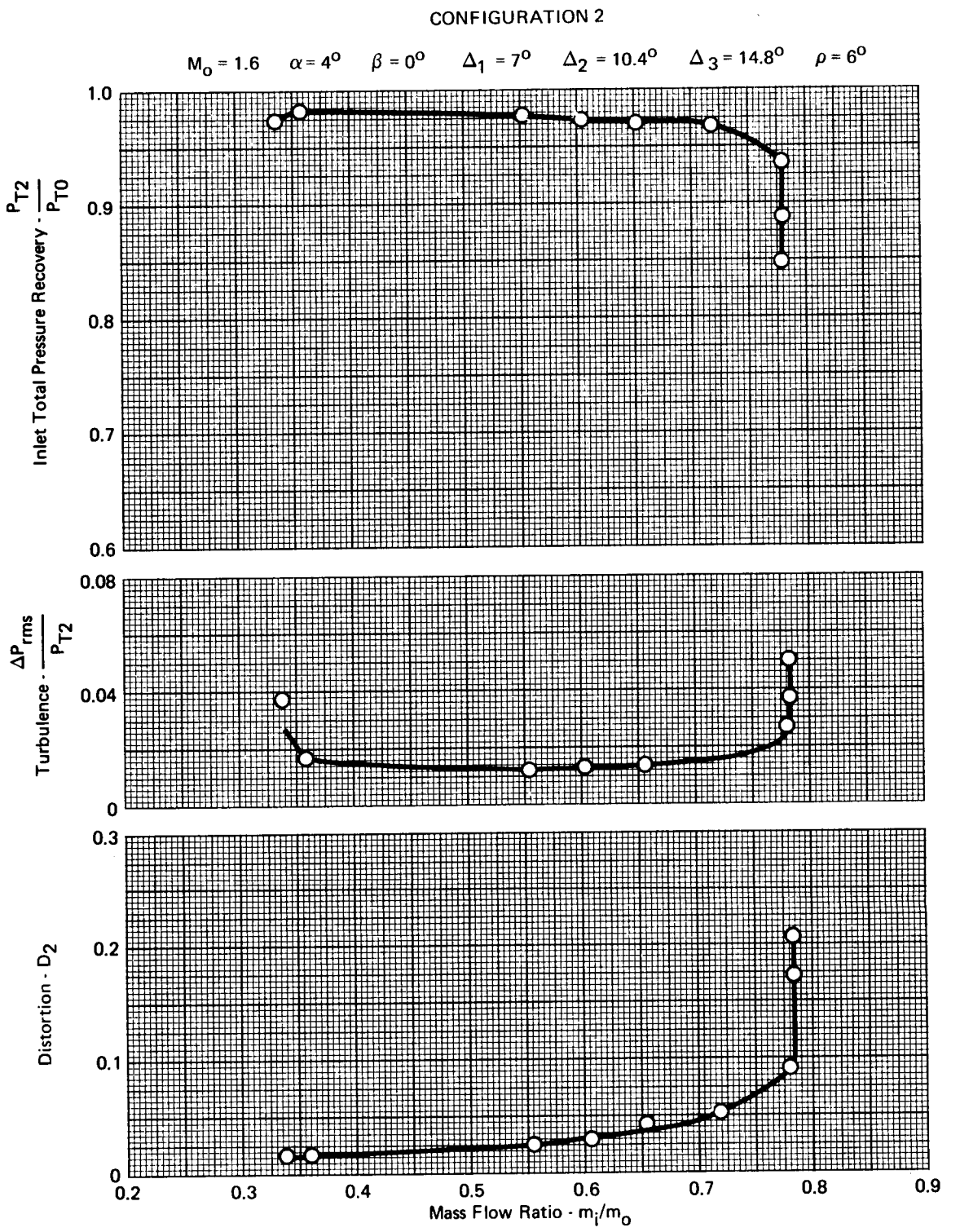

FIGURE A-18 - EFFECTS OF OPERATING MASS FLOW ON PRESSURE RECOVERY TURBULENCE, AND DISTORTION

GP73-0449-65

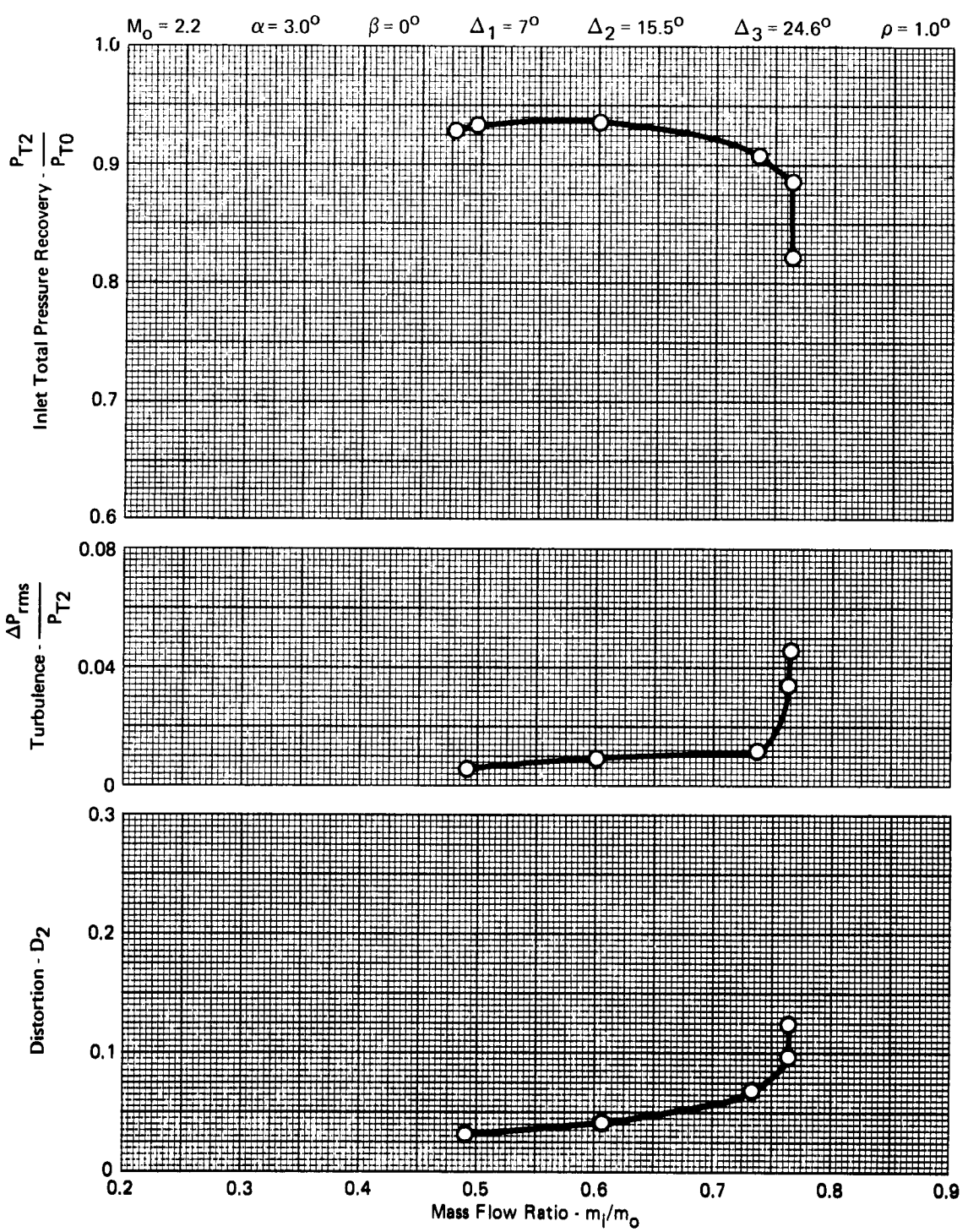

FIGURE A-19- EFFECTS OF OPERATING MASS FLOW ON PRESSURE RECOVERY, TURBULENCE, AND DISTORTION

GP73-0449-67

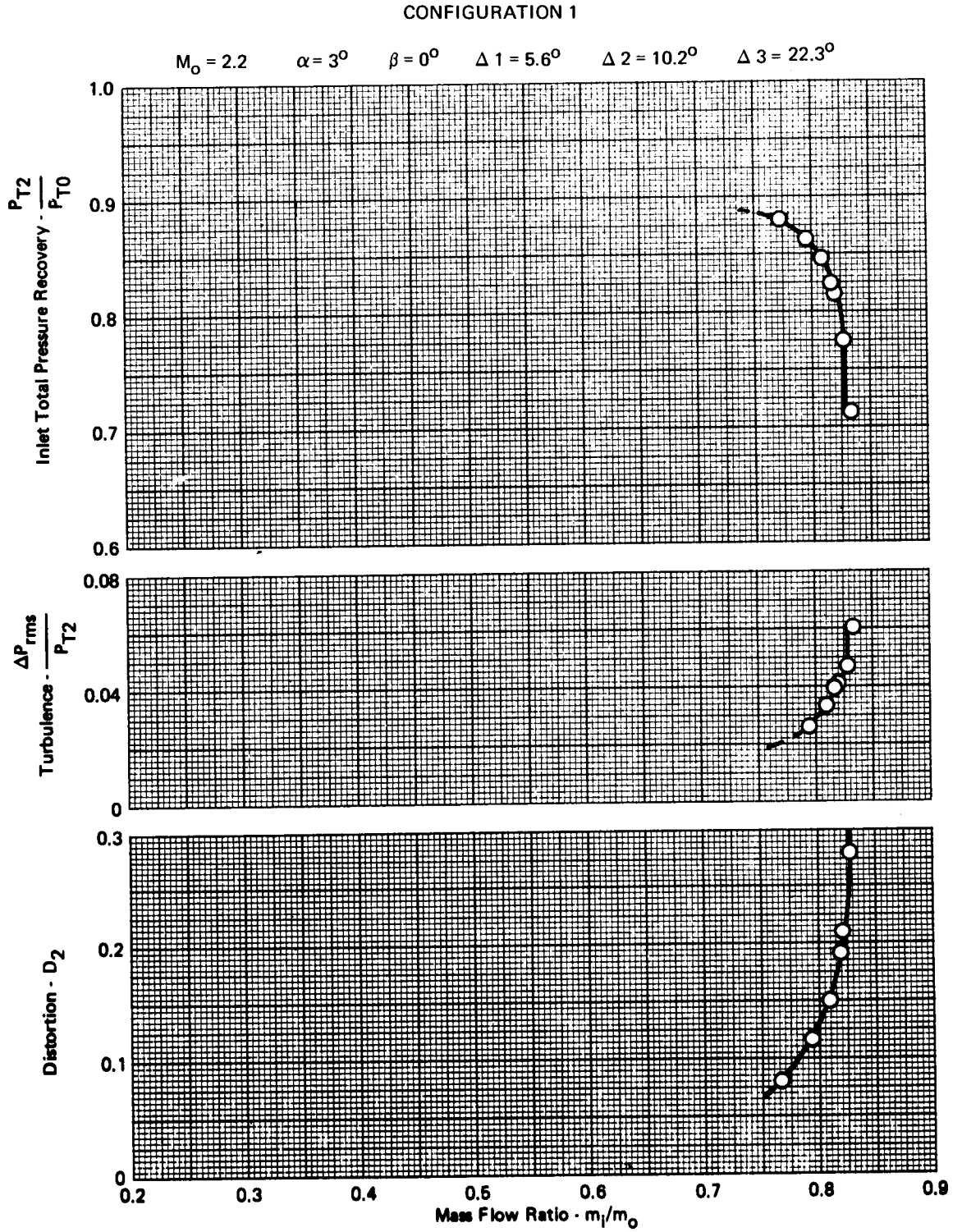

FIGURE A-20 - EFFECTS OF INLET RAMP ANGLE VARIATIONS ON PRESSURE RECOVERY, TURBULENCE, AND DISTORTION

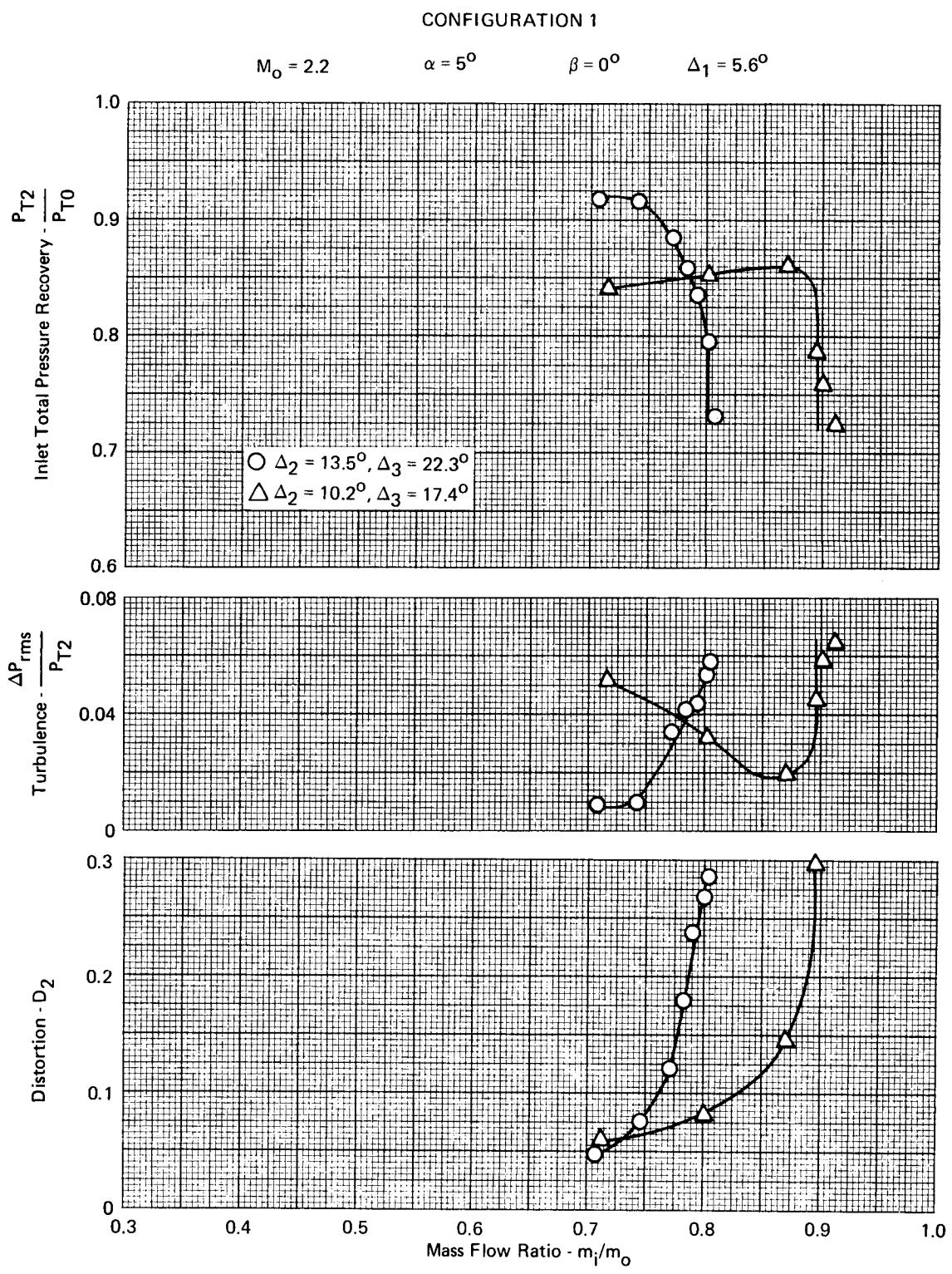

FIGURE A-21 - EFFECTS OF INLET RAMP ANGLE VARIATIONS ON PRESSURE RECOVERY, TURBULENCE, AND DISTORTION

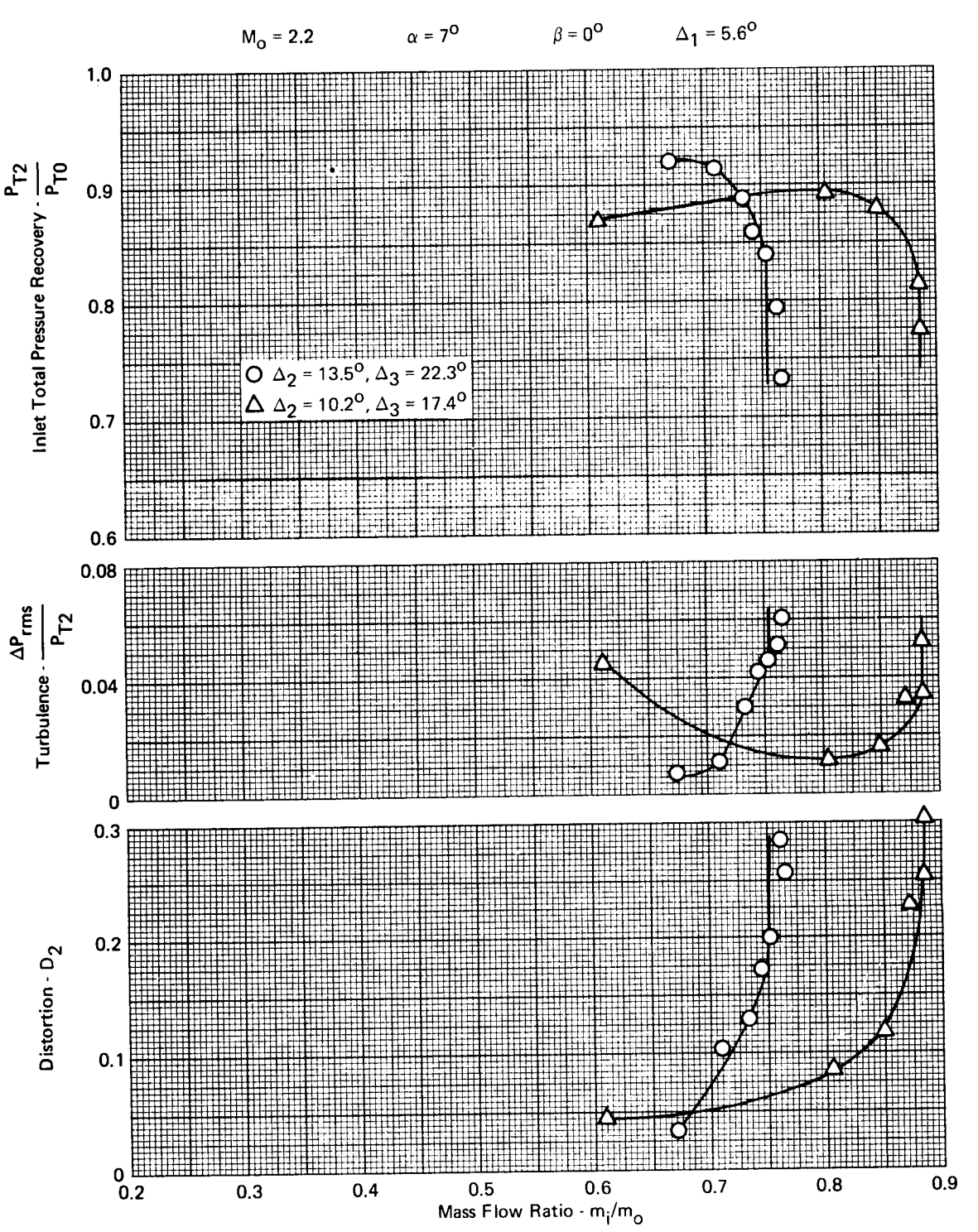

FIGURE A-22 - EFFECTS OF INLET RAMP ANGLE VARIATIONS ON PRESSURE RECOVERY TURBULENCE, AND DISTORTION

GP72-0979-64

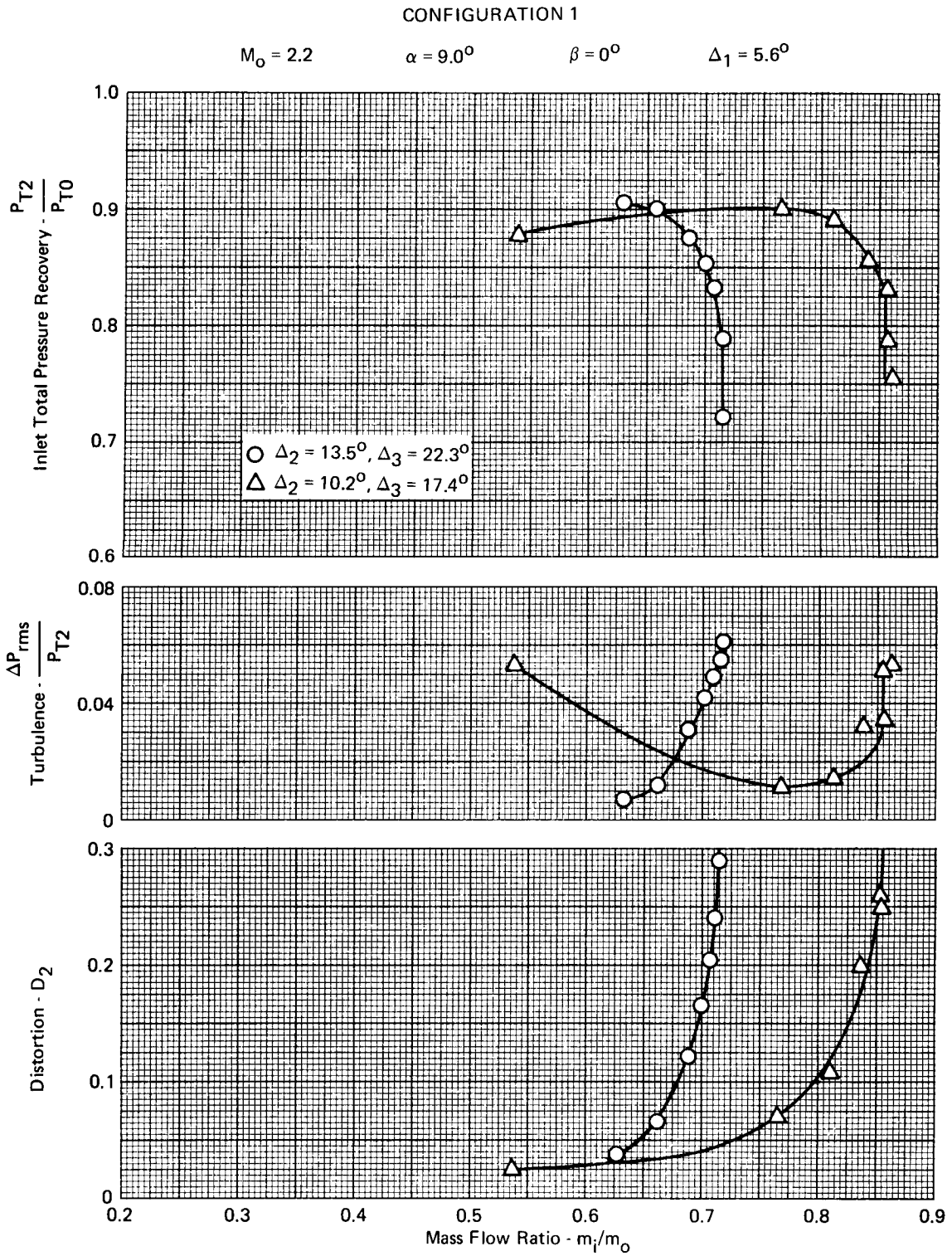

FIGURE A-23 - EFFECTS OF INLET RAMP ANGLE VARIATIONS ON PRESSURE RECOVERY, TURBULENCE, AND DISTORTION

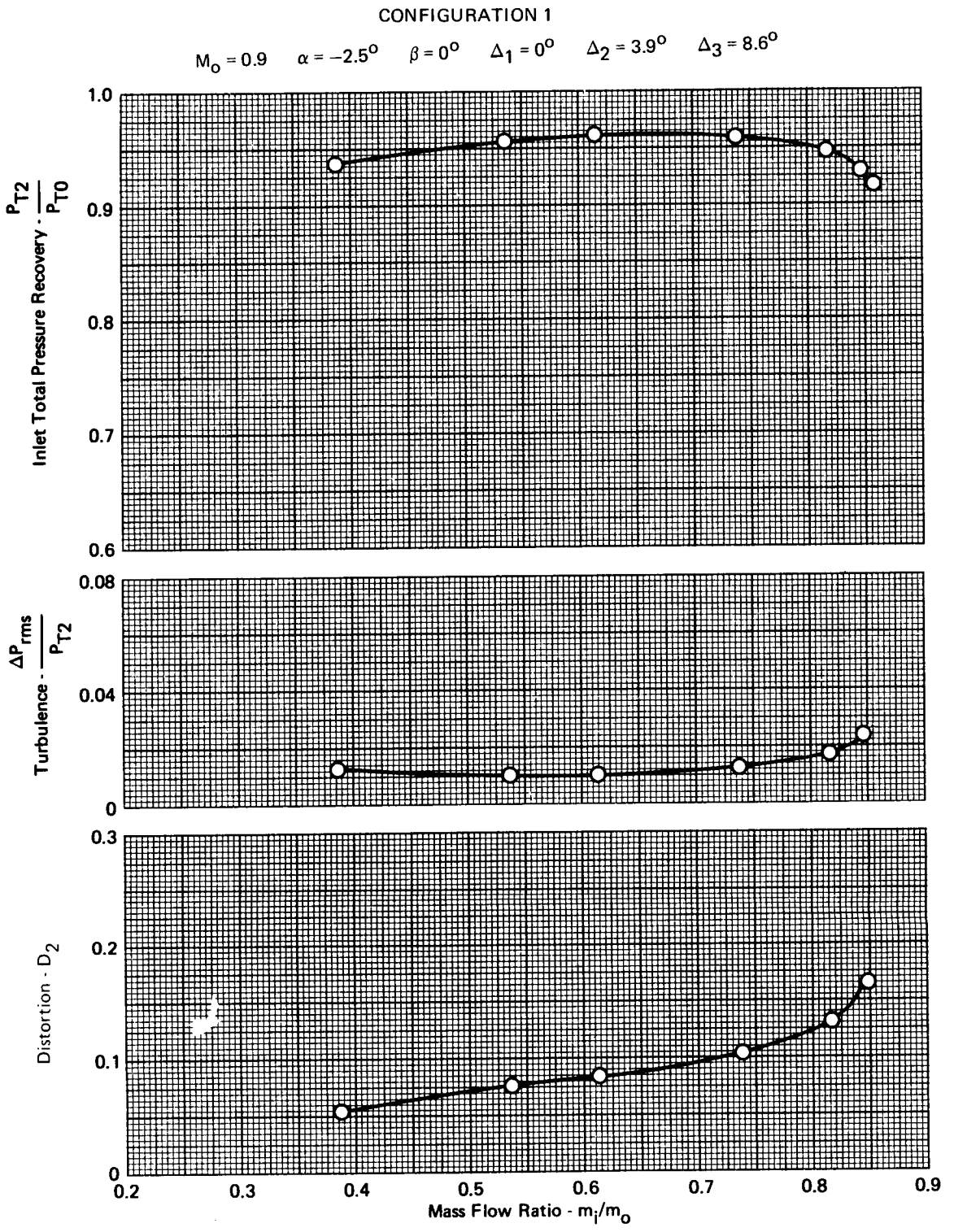

FIGURE A-24 - EFFECTS OF ANGLE OF ATTACK ON PRESSURE RECOVERY, TURBULENCE, AND DISTORTION

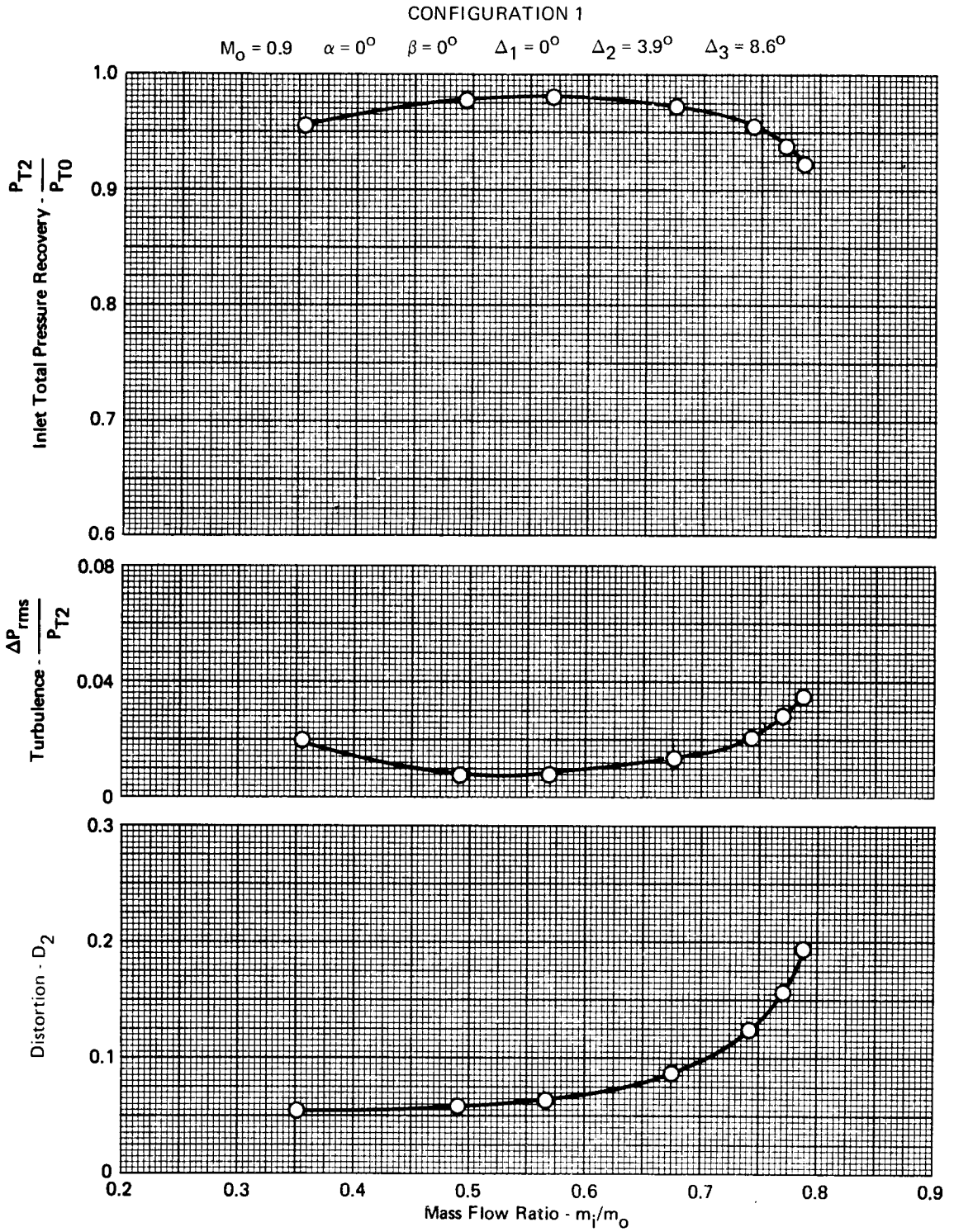

FIGURE A-25 - EFFECTS OF ANGLE OF ATTACK ON PRESSURE RECOVERY, TURBULENCE, AND DISTORTION

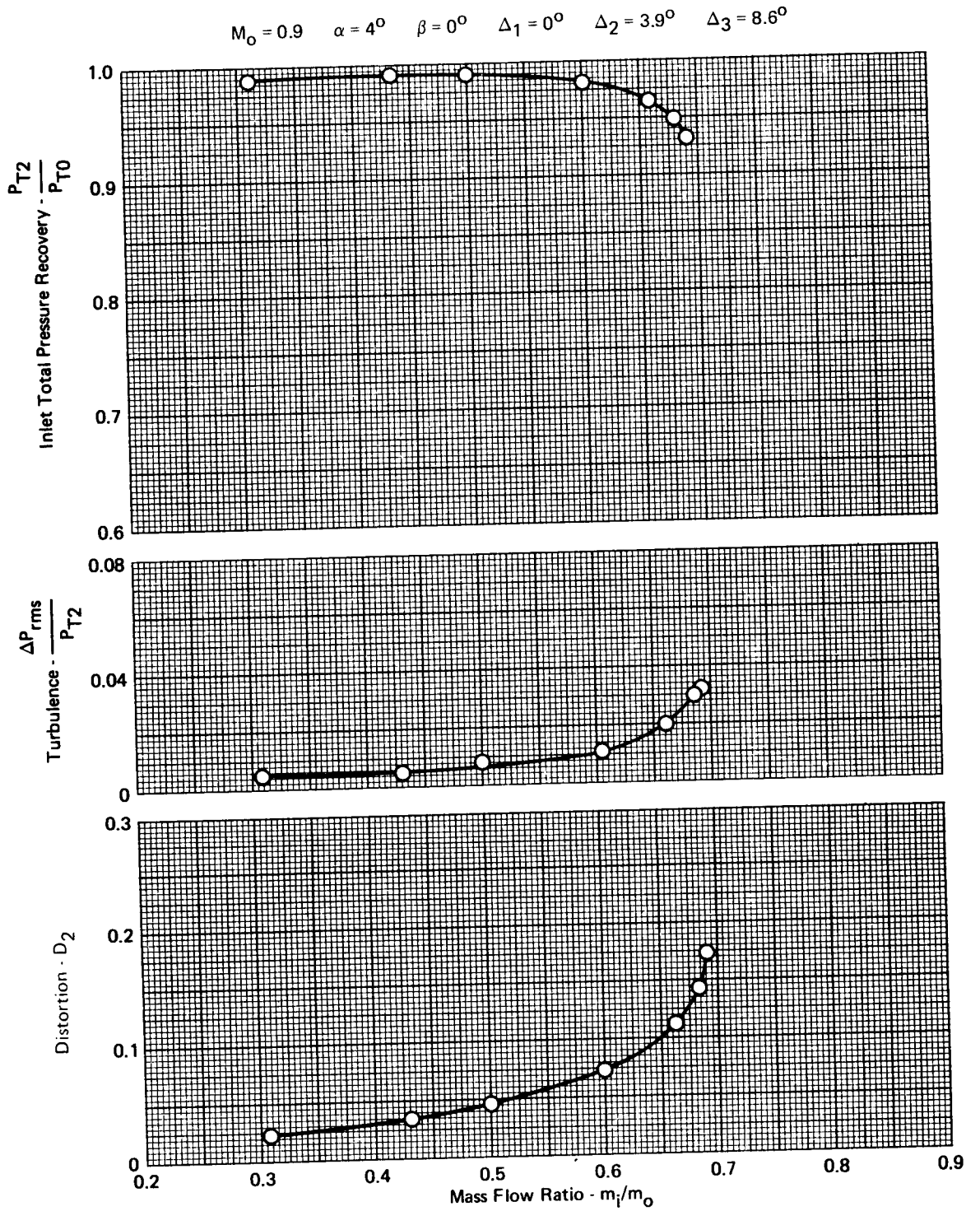

FIGURE A-26- EFFECTS OF ANGLE OF ATTACK ON PRESSURE RECOVERY, TURBULENCE, AND DISTORTION

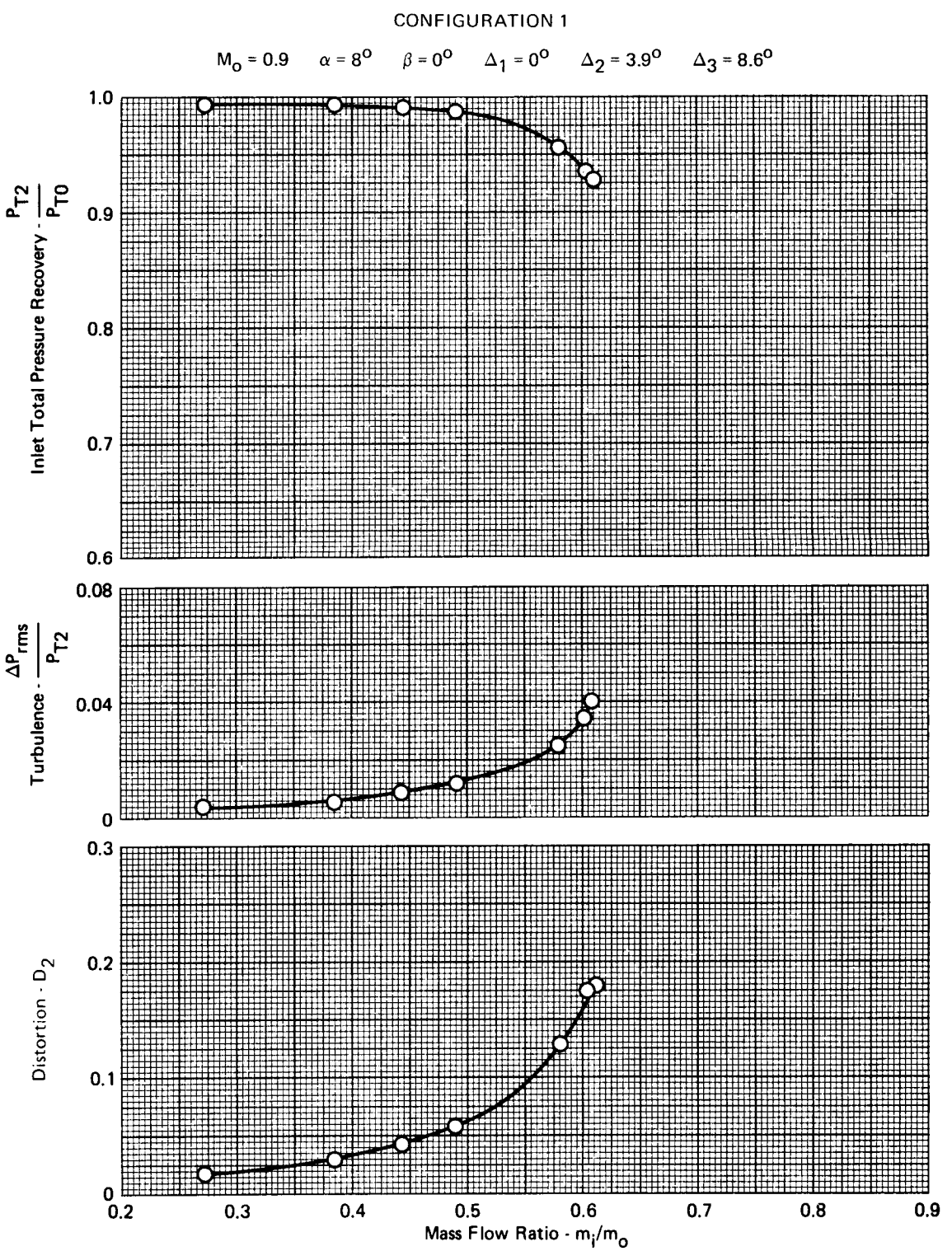

FIGURE A-27 - EFFECTS OF ANGLE OF ATTACK ON PRESSURE RECOVERY, TURBULENCE, AND DISTORTION

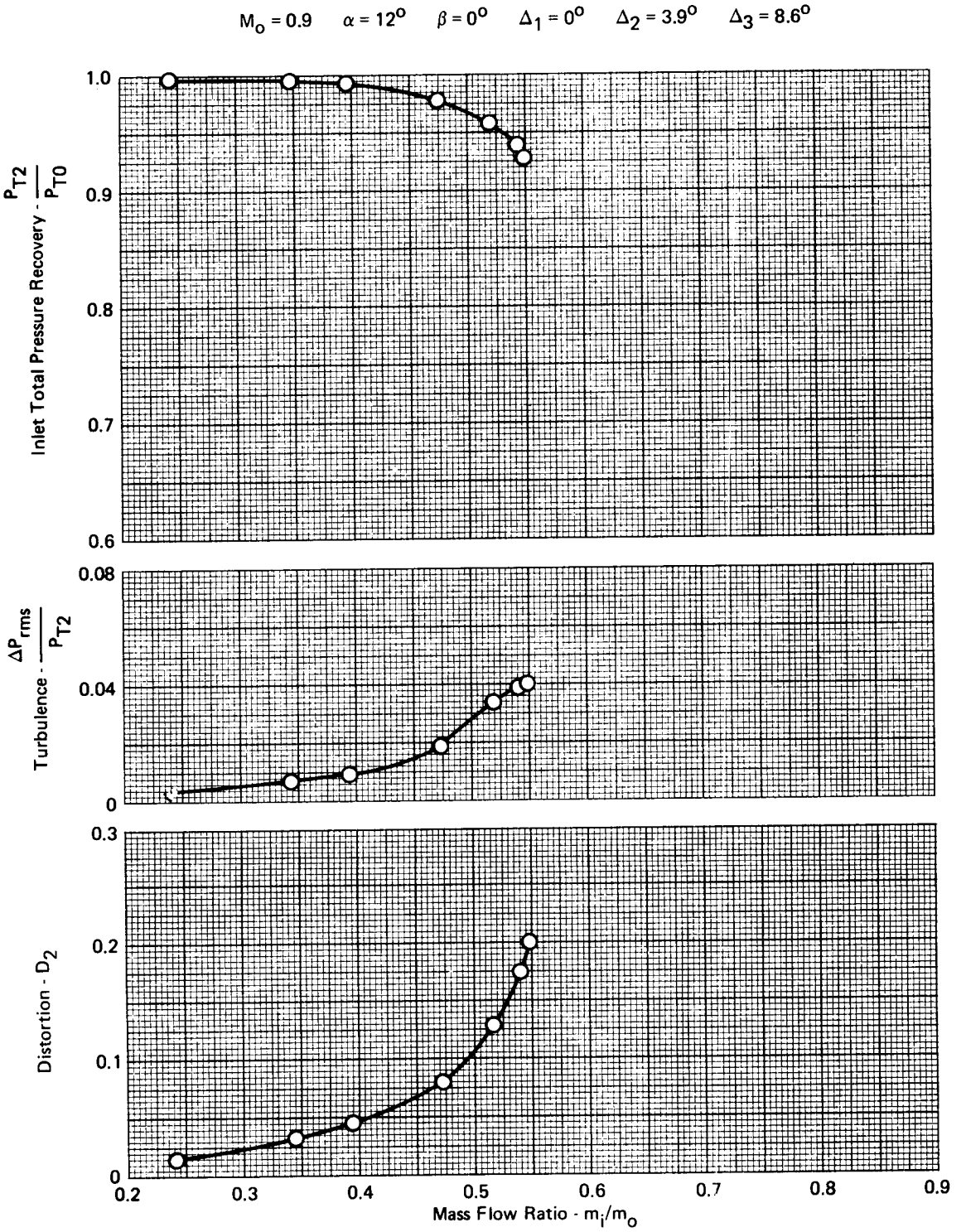

FIGURE A-28 - EFFECTS OF ANGLE OF ATTACK ON PRESSURE RECOVERY, TURBULENCE, AND DISTORTION

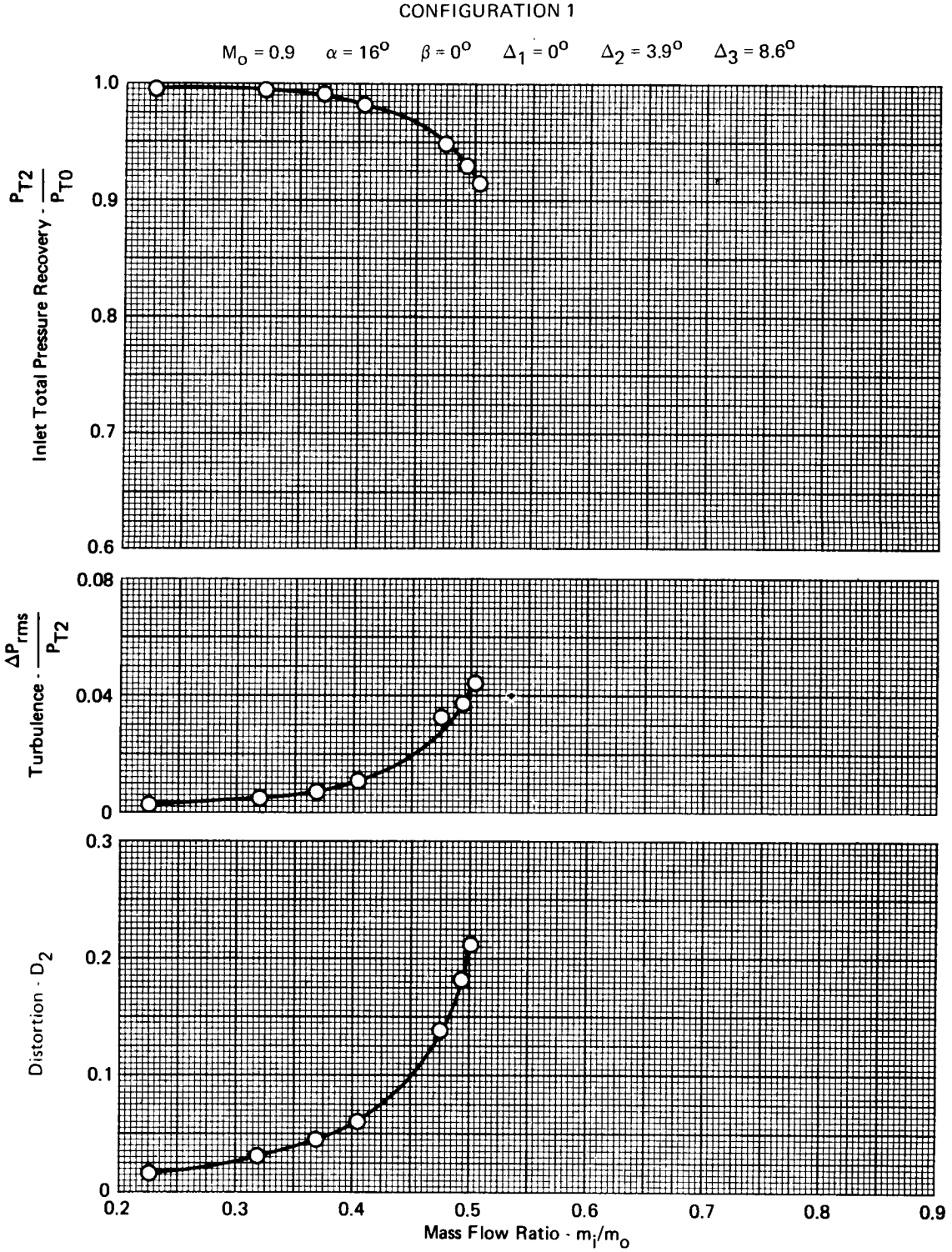

FIGURE A-29 - EFFECTS OF ANGLE OF ATTACK ON PRESSURE RECOVERY, TURBULENCE, AND DISTORTION

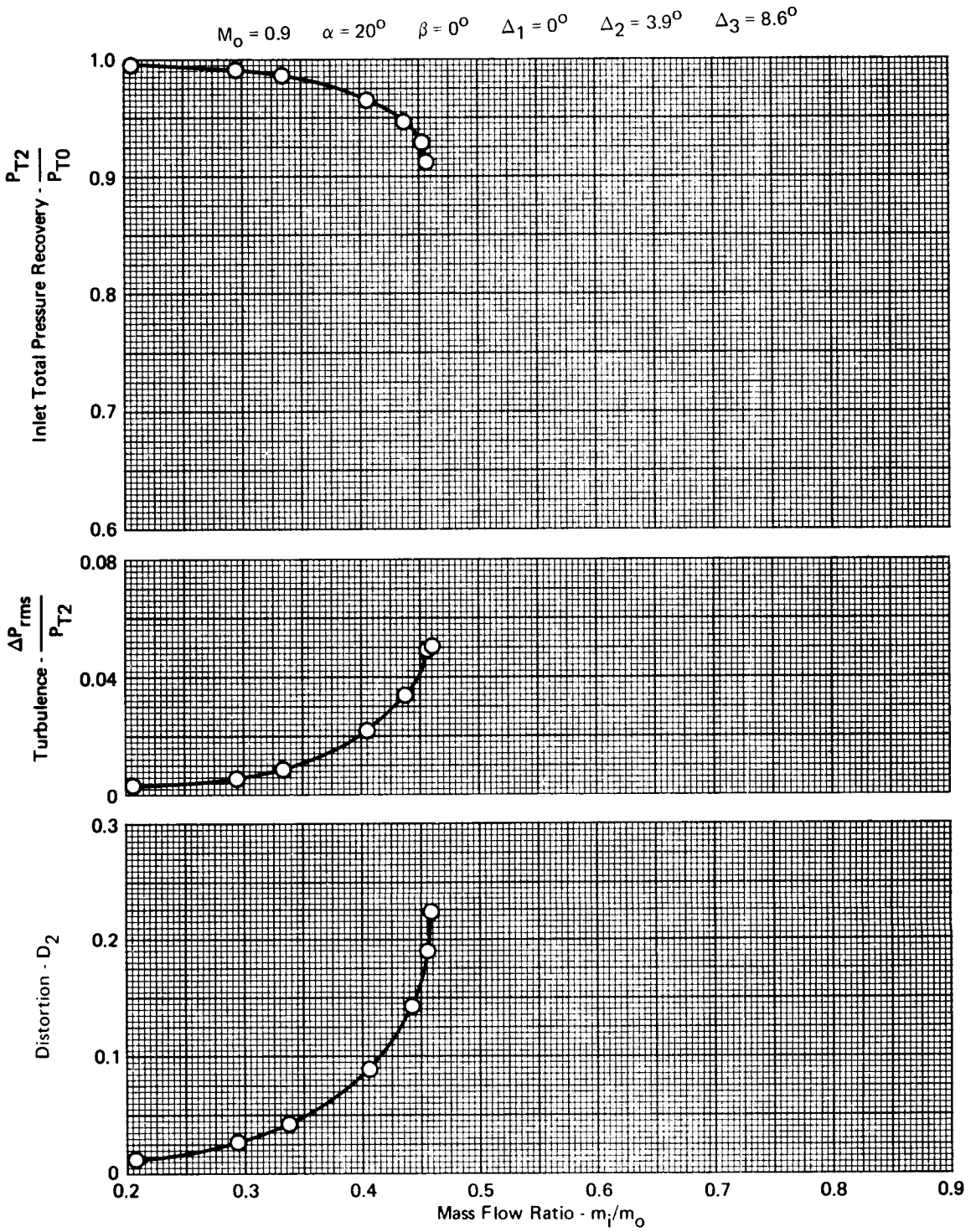

FIGURE A-30 - EFFECTS OF ANGLE OF ATTACK ON PRESSURE RECOVERY, TURBULENCE, AND DISTORTION

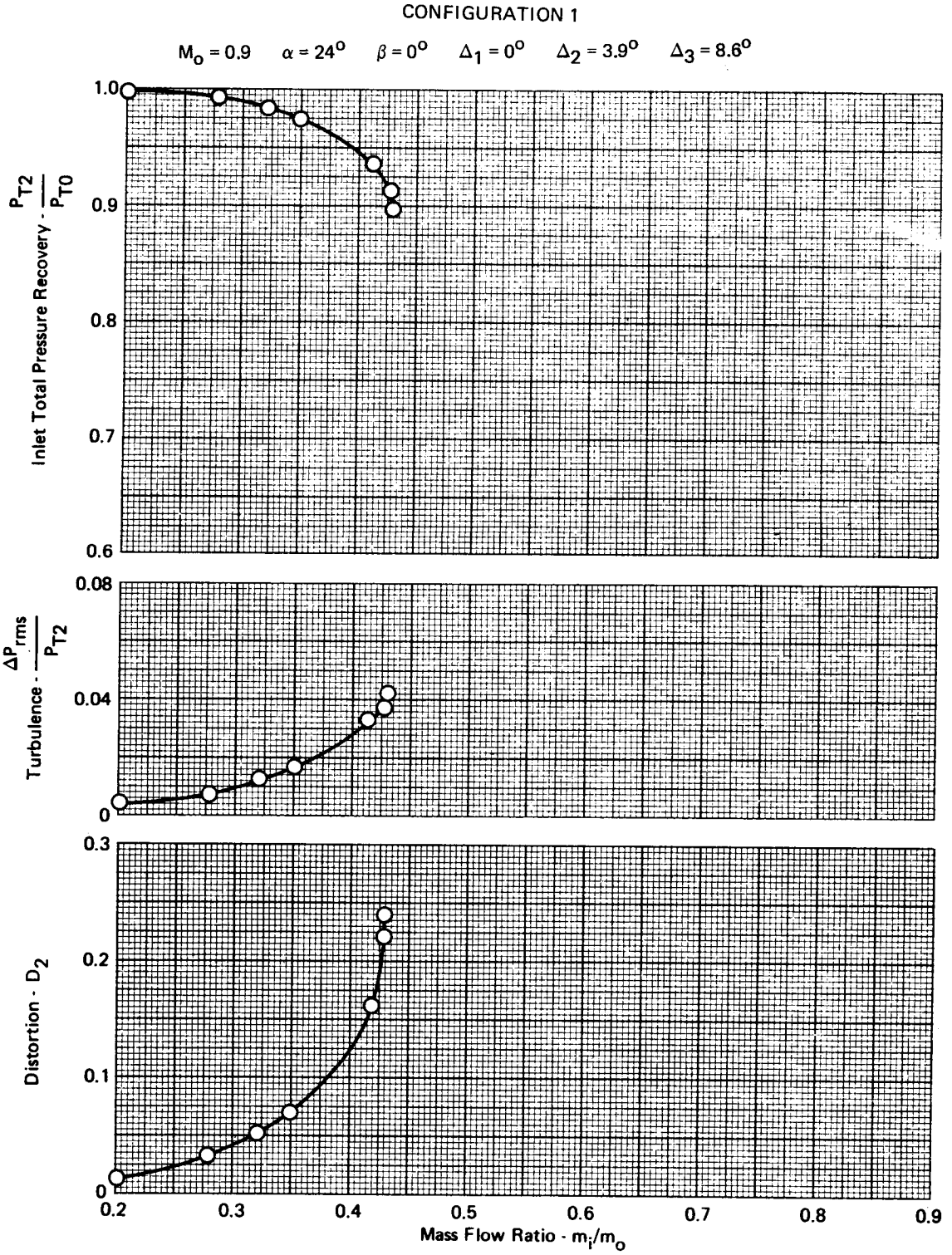

FIGURE A-31 - EFFECTS OF ANGLE OF ATTACK ON PRESSURE RECOVERY, TURBULENCE, AND DISTORTION

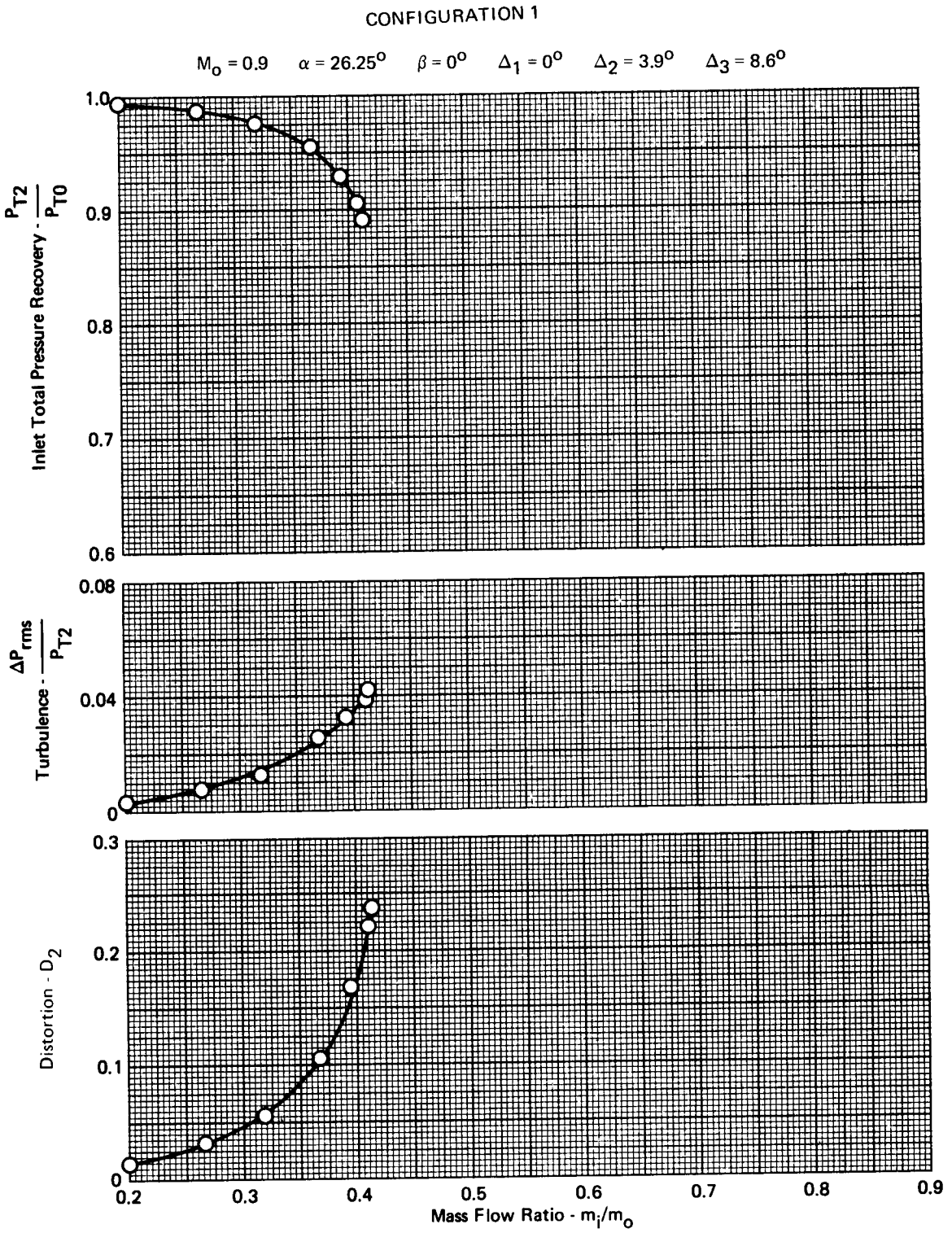

FIGURE A-32 - EFFECTS OF ANGLE OF ATTACK ON PRESSURE RECOVERY, TURBULENCE,AND DISTORTION

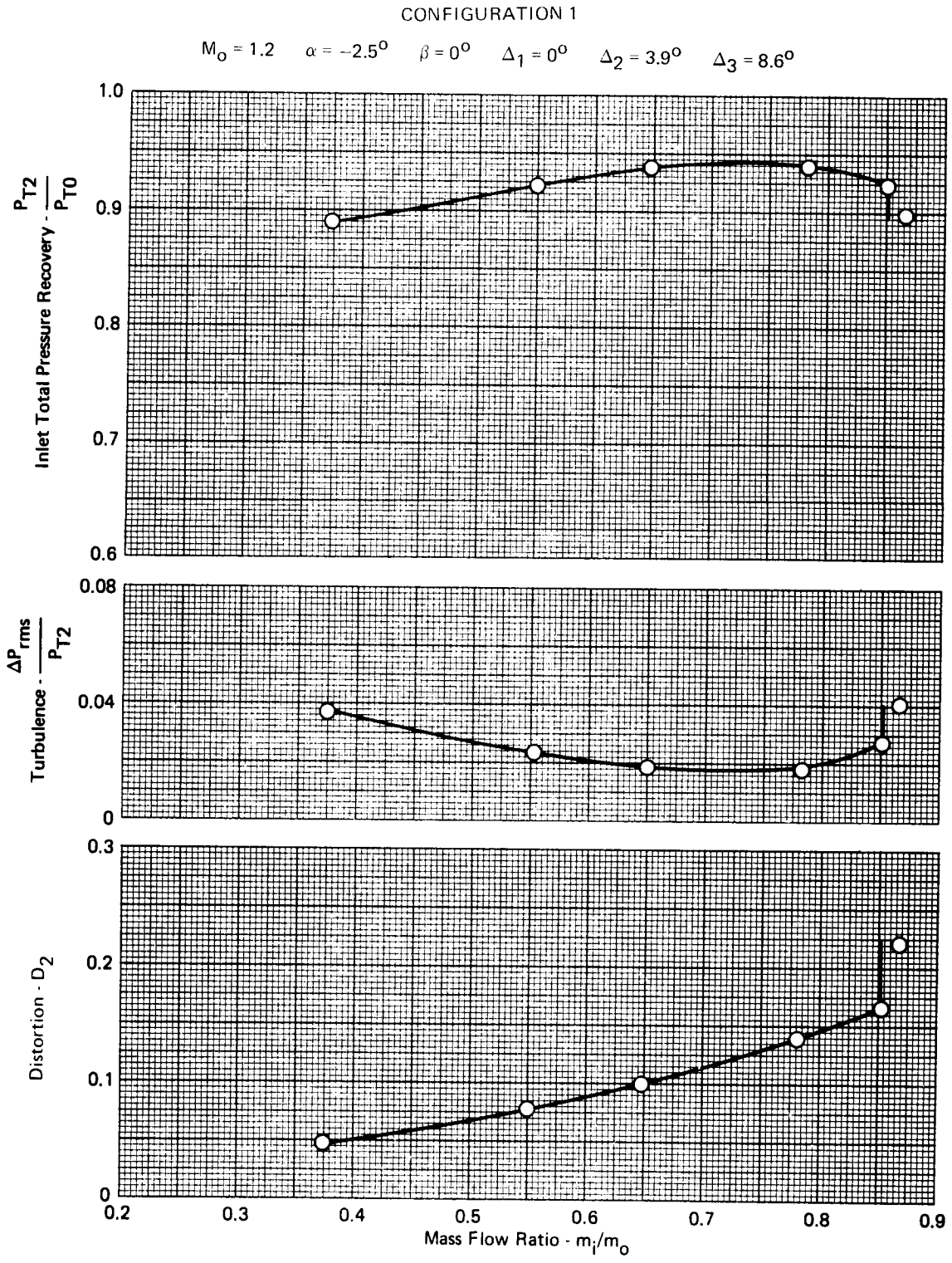

FIGURE A-33 - EFFECTS OF ANGLE OF ATTACK ON PRESSURE RECOVERY, TURBULENCE, AND DISTORTION

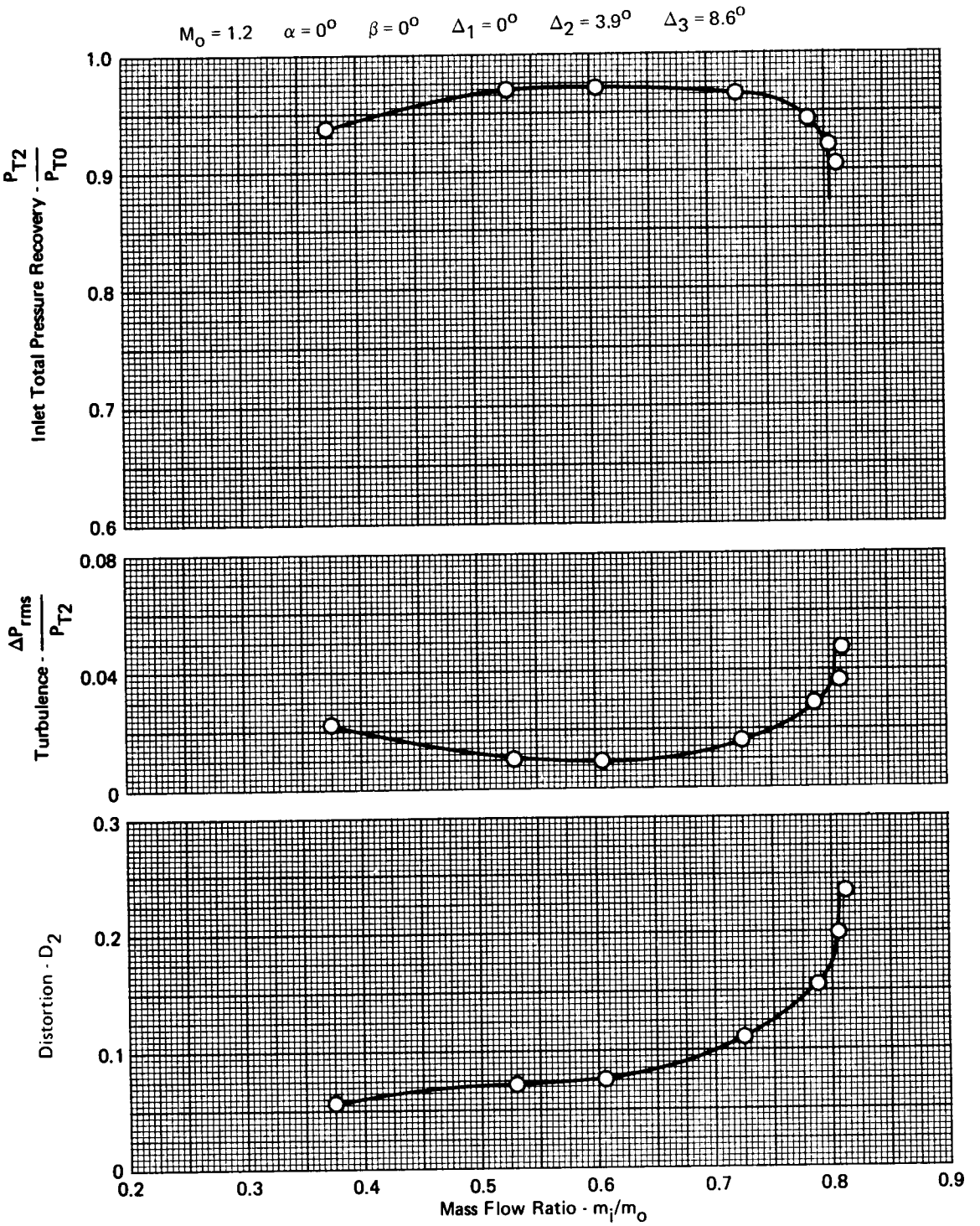

FIGURE A-34 - EFFECTS OF ANGLE OF ATTACK ON PRESSURE RECOVERY, TURBULENCE, AND DISTORTION

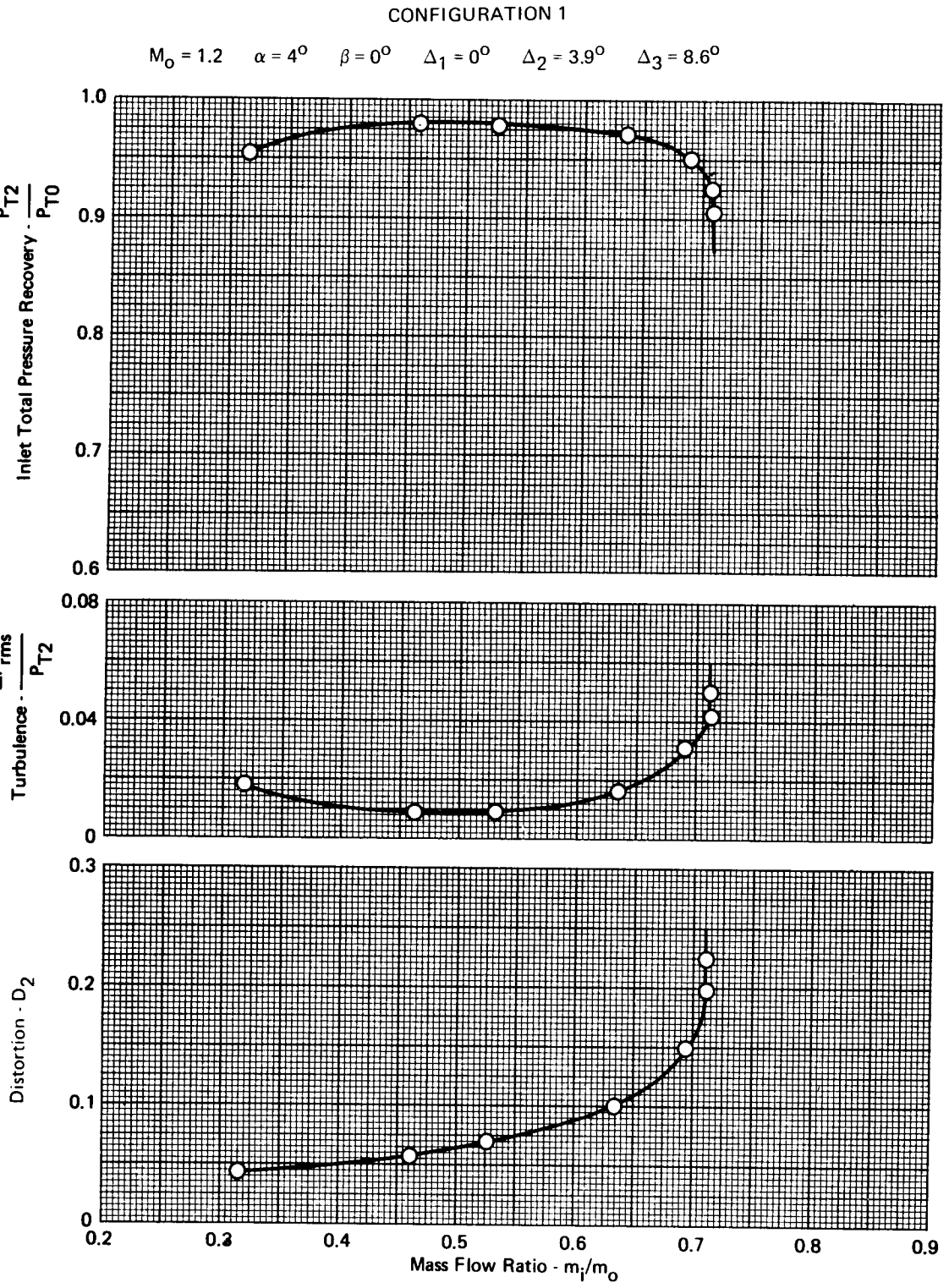

FIGURE A-35 - EFFECTS OF ANGLE OF ATTACK ON PRESSURE RECOVERY, TURBULENCE, AND DISTORTION

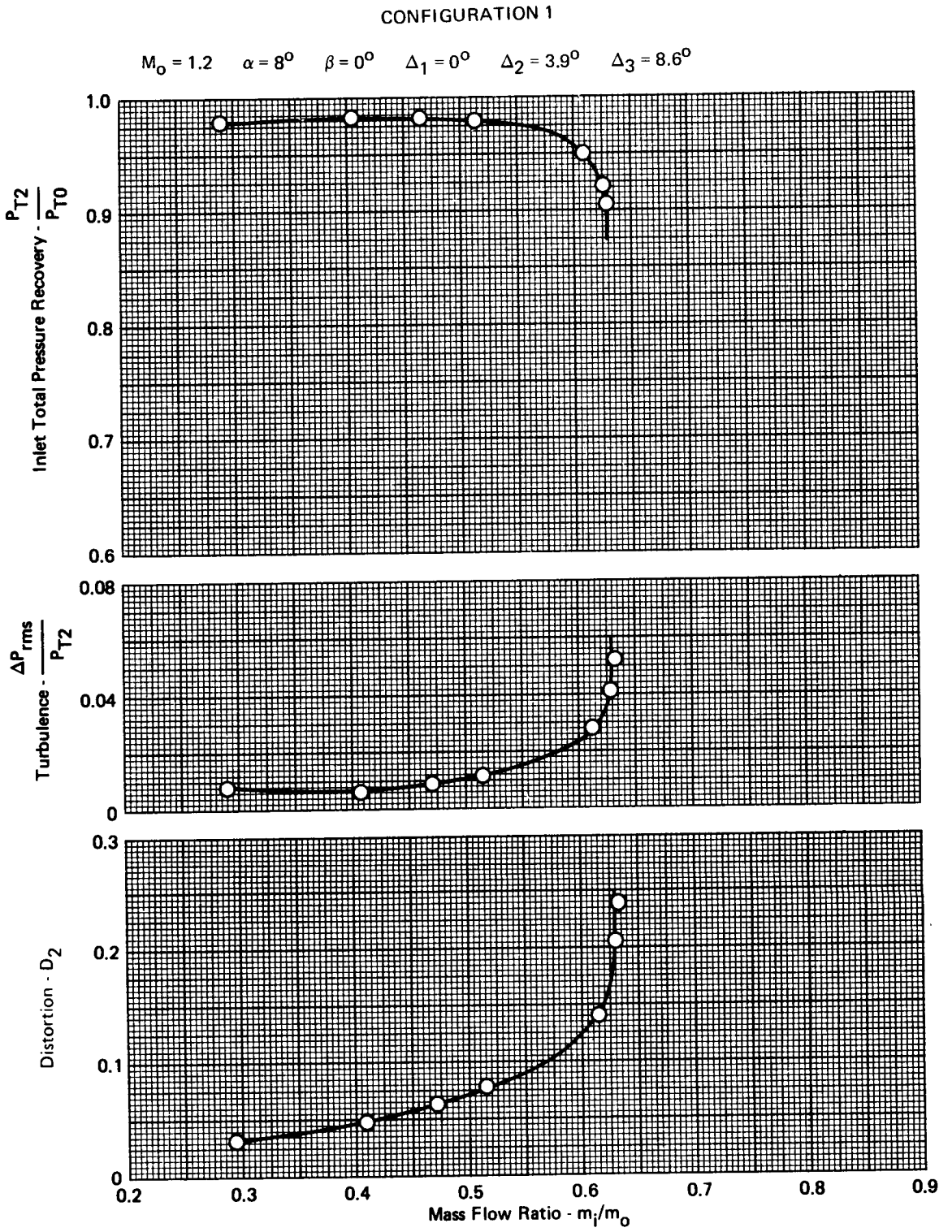

FIGURE A-36 - EFFECTS OF ANGLE OF ATTACK ON PRESSURE RECOVERY, TURBULENCE, AND DISTORTION

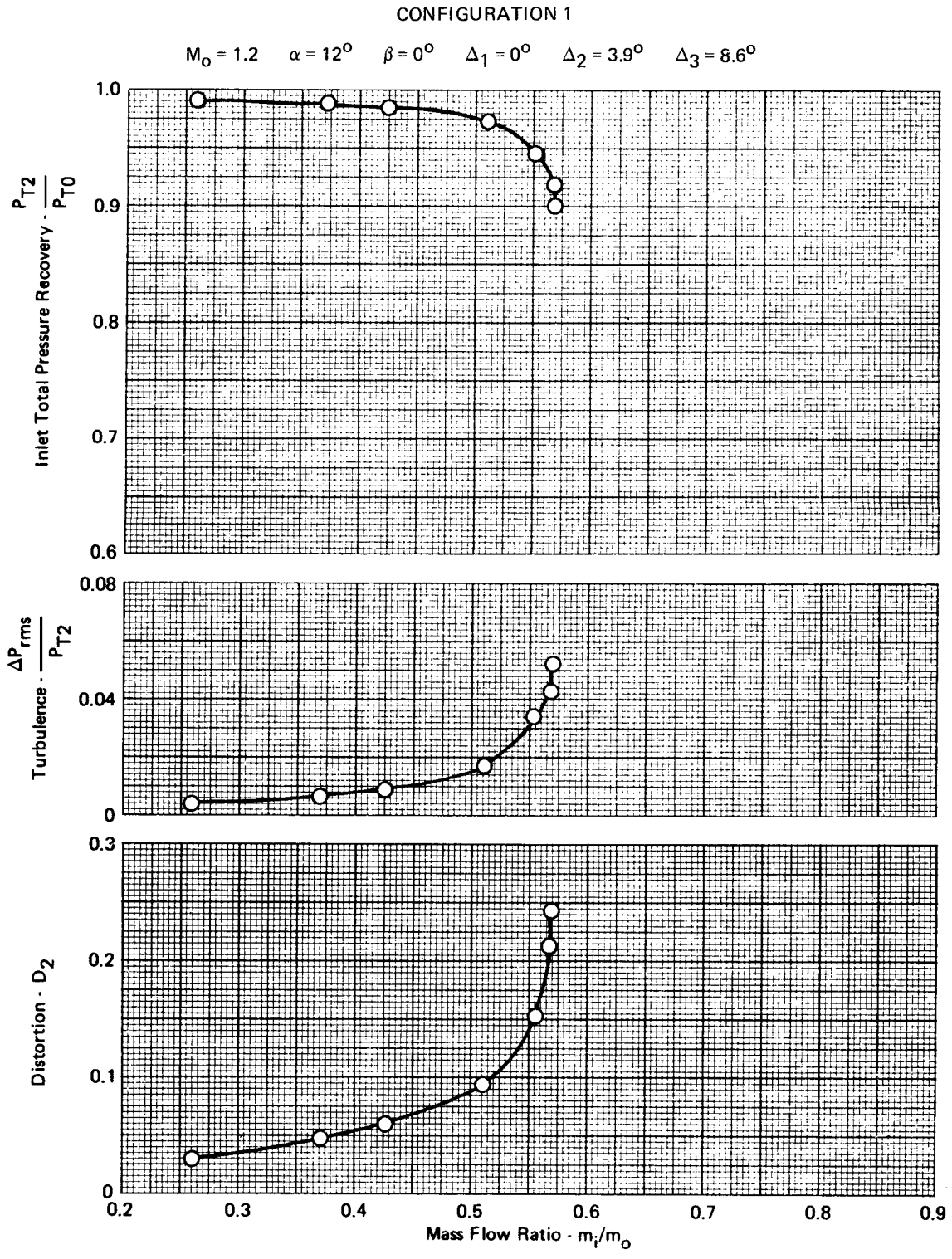

FIGURE A-37 - EFFECTS OF ANGLE OF ATTACK ON PRESSURE RECOVERY, TURBULENCE, AND DISTORTION

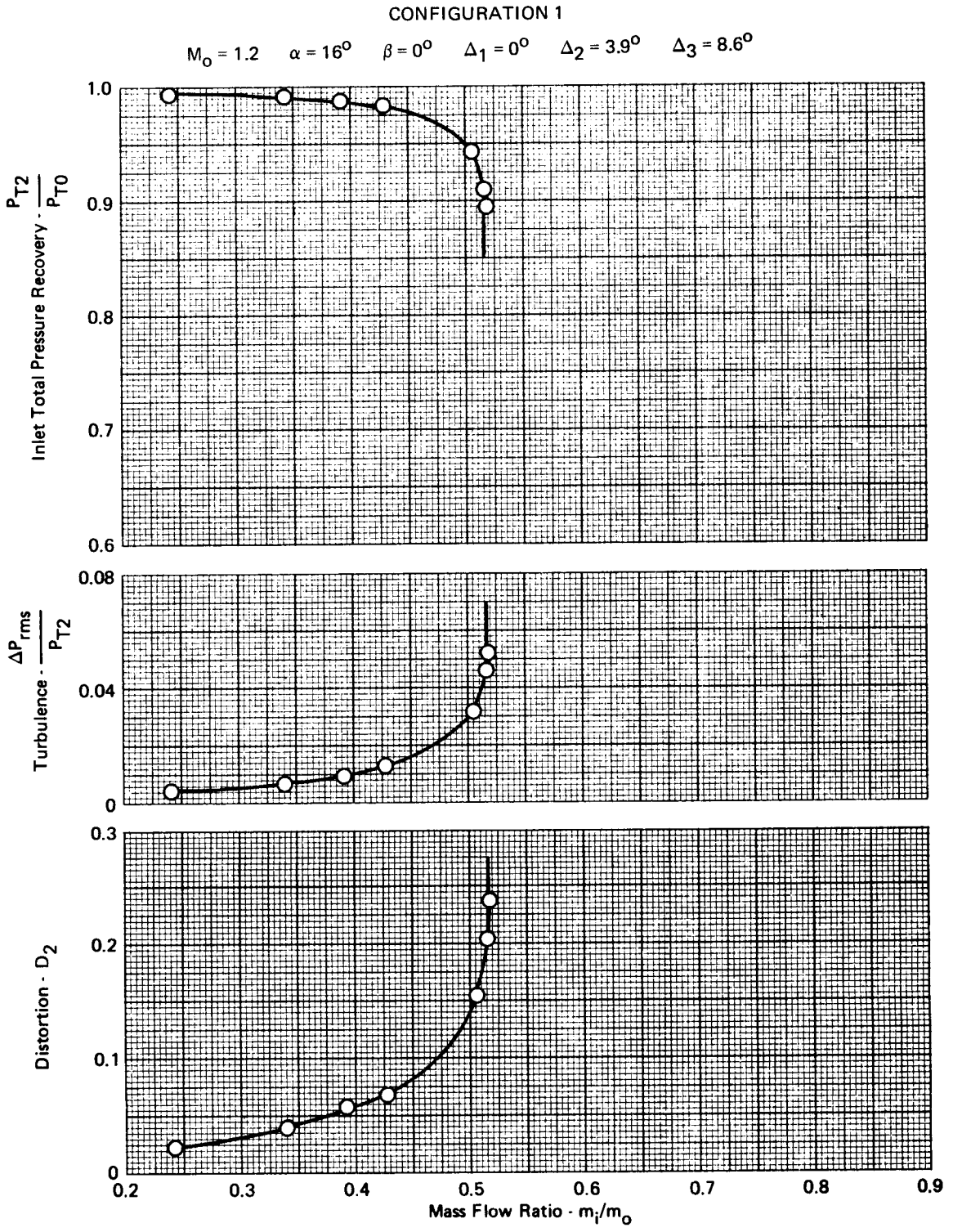

FIGURE A-38 - EFFECTS OF ANGLE OF ATTACK ON PRESSURE RECOVERY, TURBULENCE, AND DISTORTION

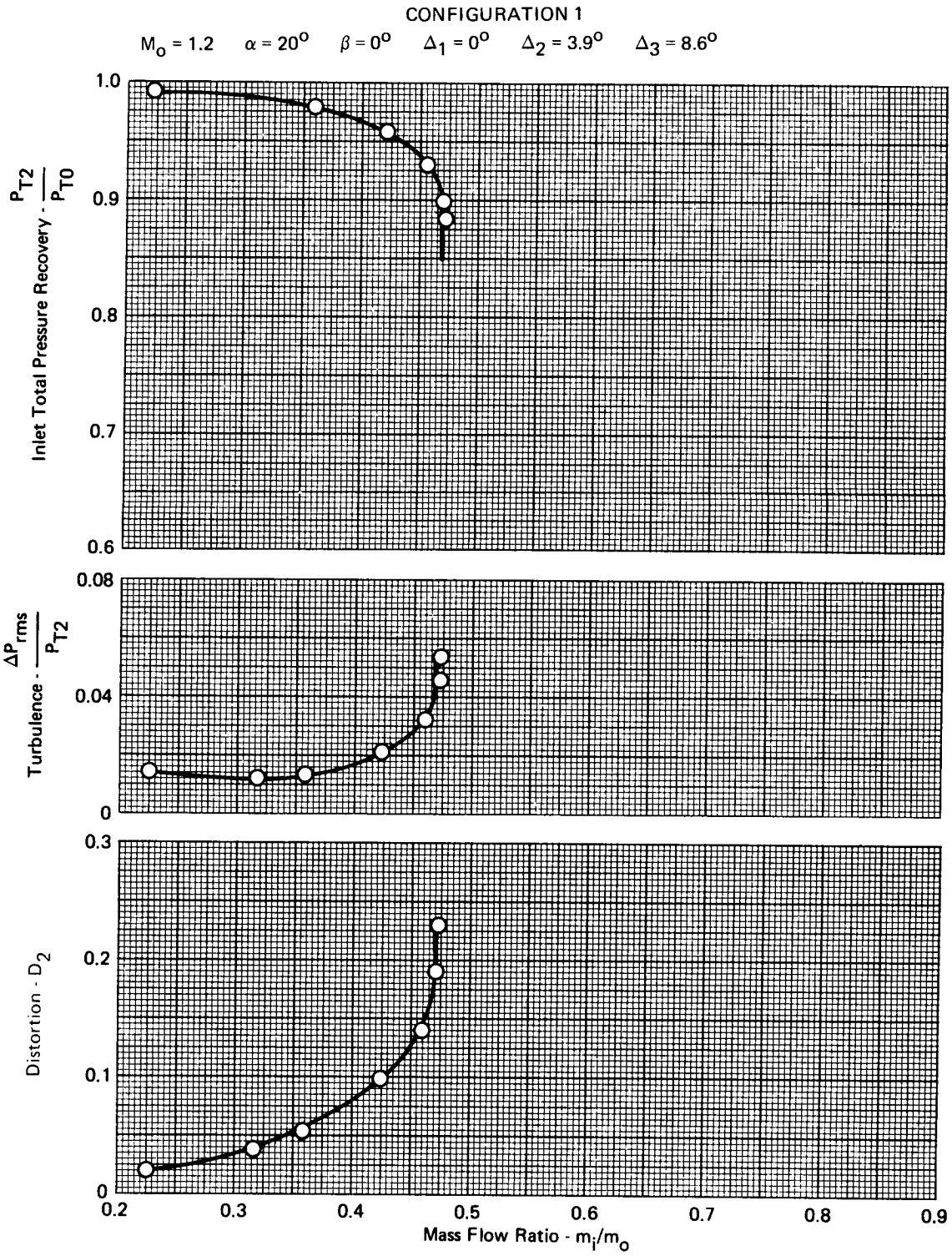

FIGURE A-39- EFFECTS OF ANGLE OF ATTACK ON PRESSURE RECOVERY, TURBULENCE, AND DISTORTION

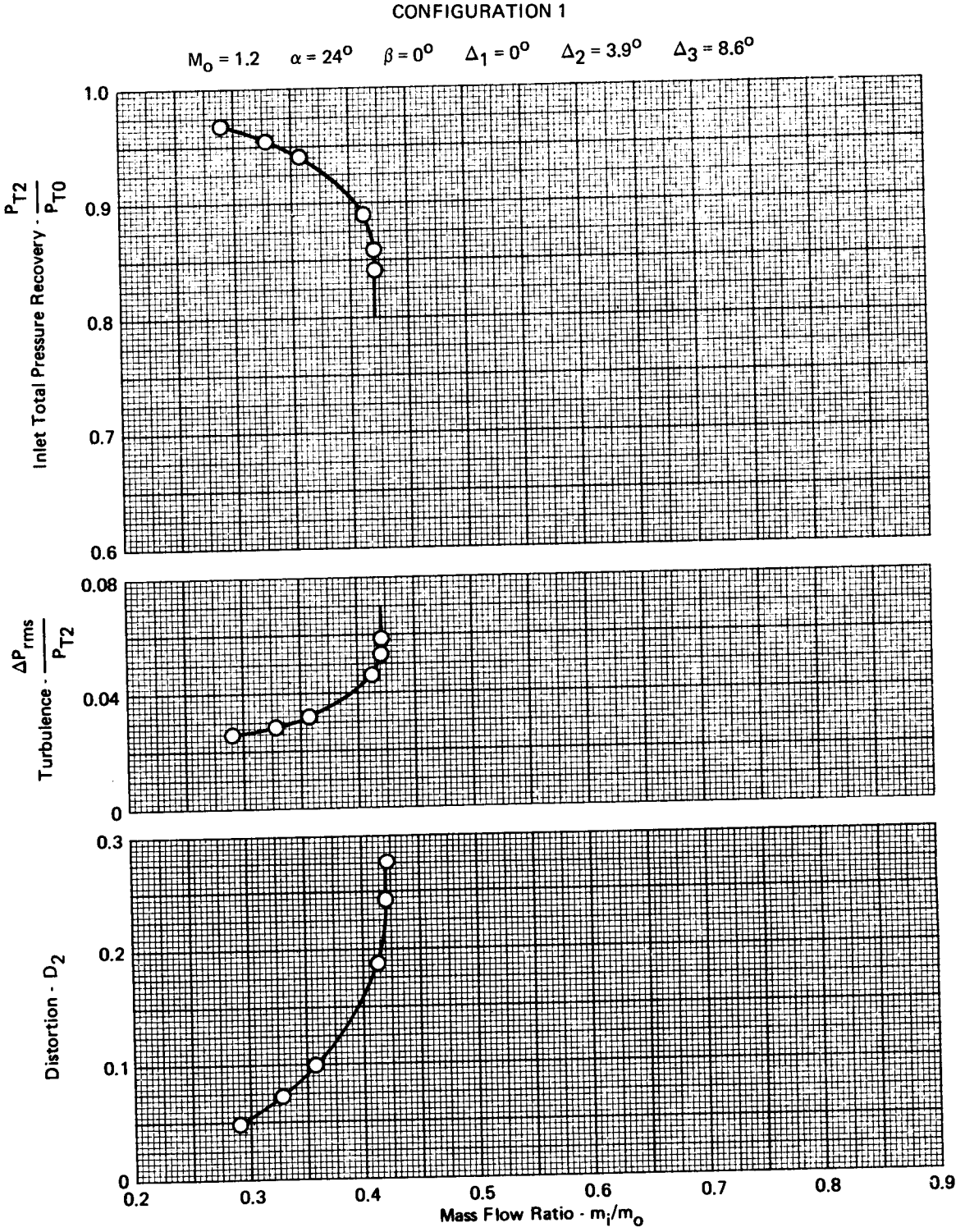

FIGURE A-40 - EFFECTS OF ANGLE OF ATTACK ON PRESSURE RECOVERY, TURBULENCE, AND DISTORTION

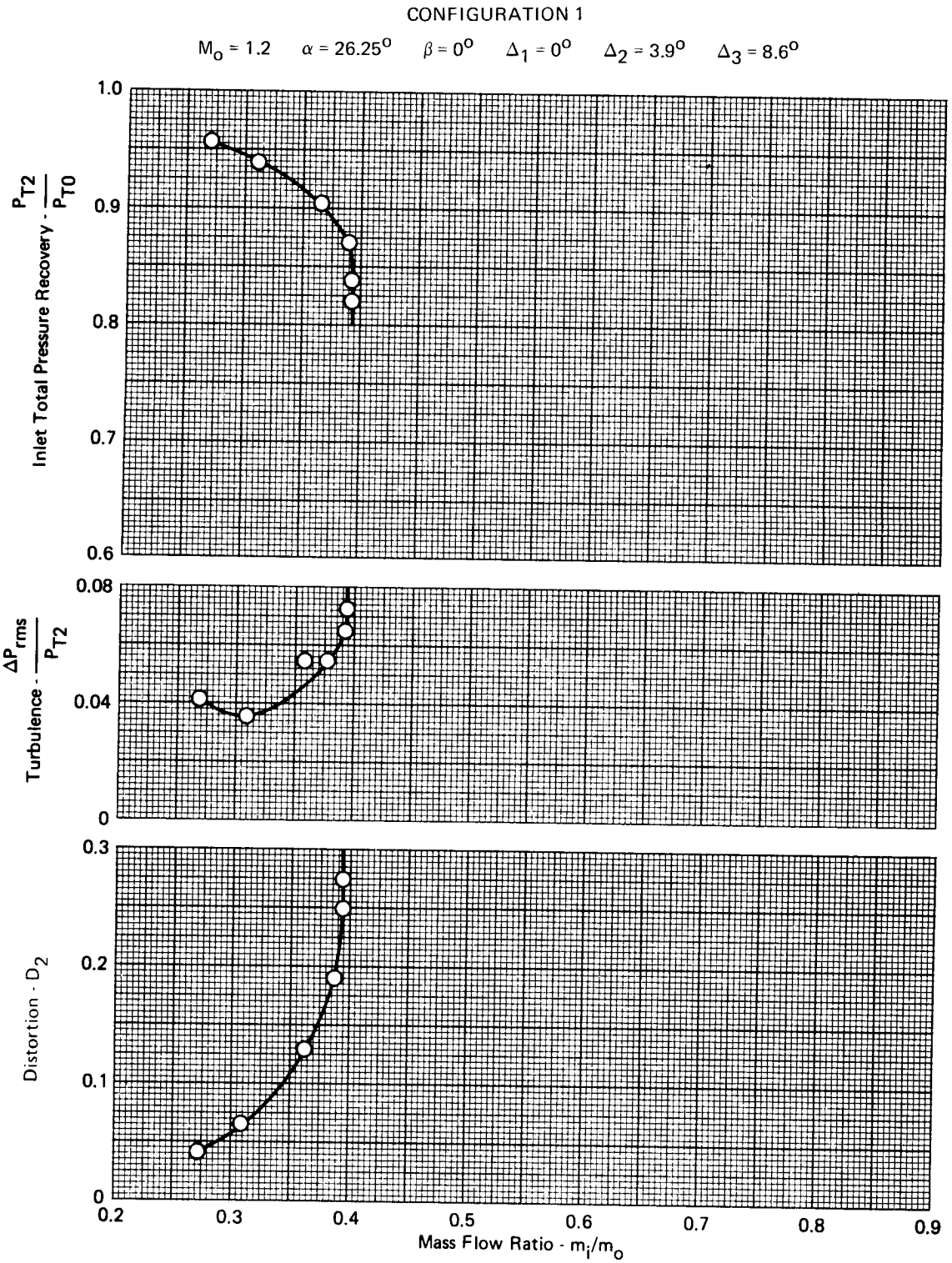

FIGURE A-41 - EFFECTS OF ANGLE OF ATTACK ON PRESSURE RECOVERY, TURBULENCE, AND DISTORTION

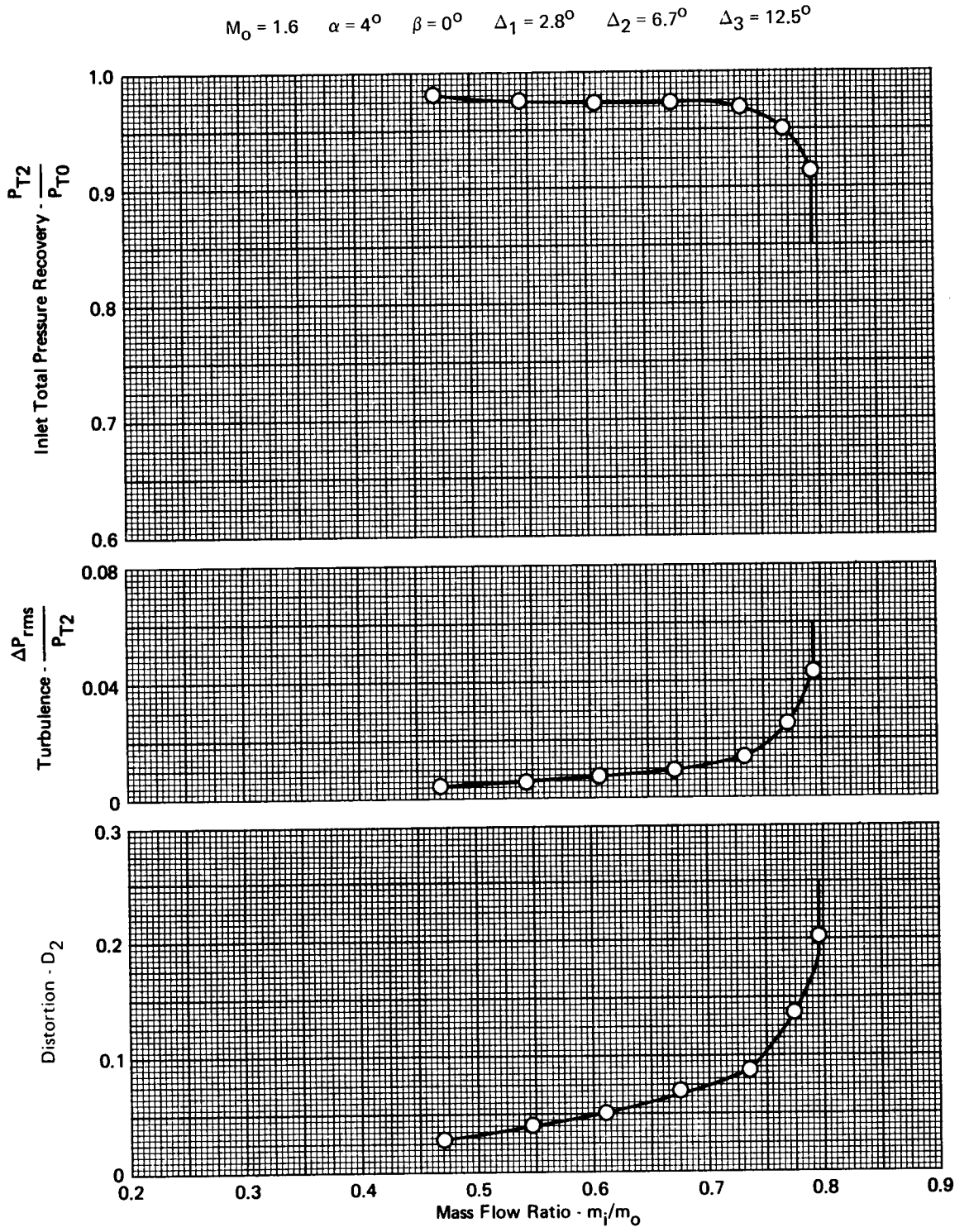

FIGURE A-42 - EFFECTS OF ANGLE OF ATTACK ON PRESSURE RECOVERY, TURBULENCE, AND DISTORTION

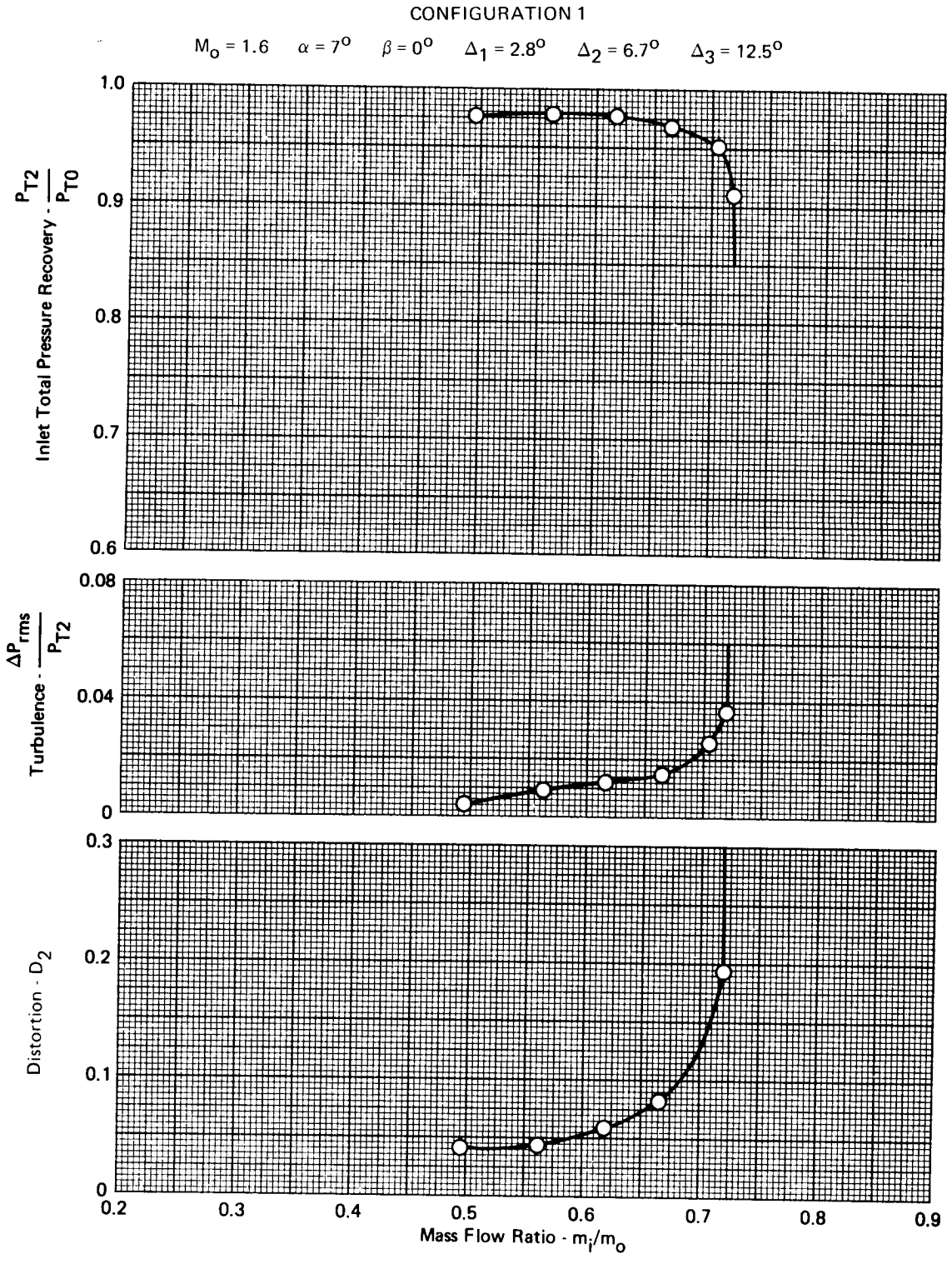

FIGURE A-43 - EFFECTS OF ANGLE OF ATTACK ON PRESSURE RECOVERY, TURBULENCE, AND DISTORTION

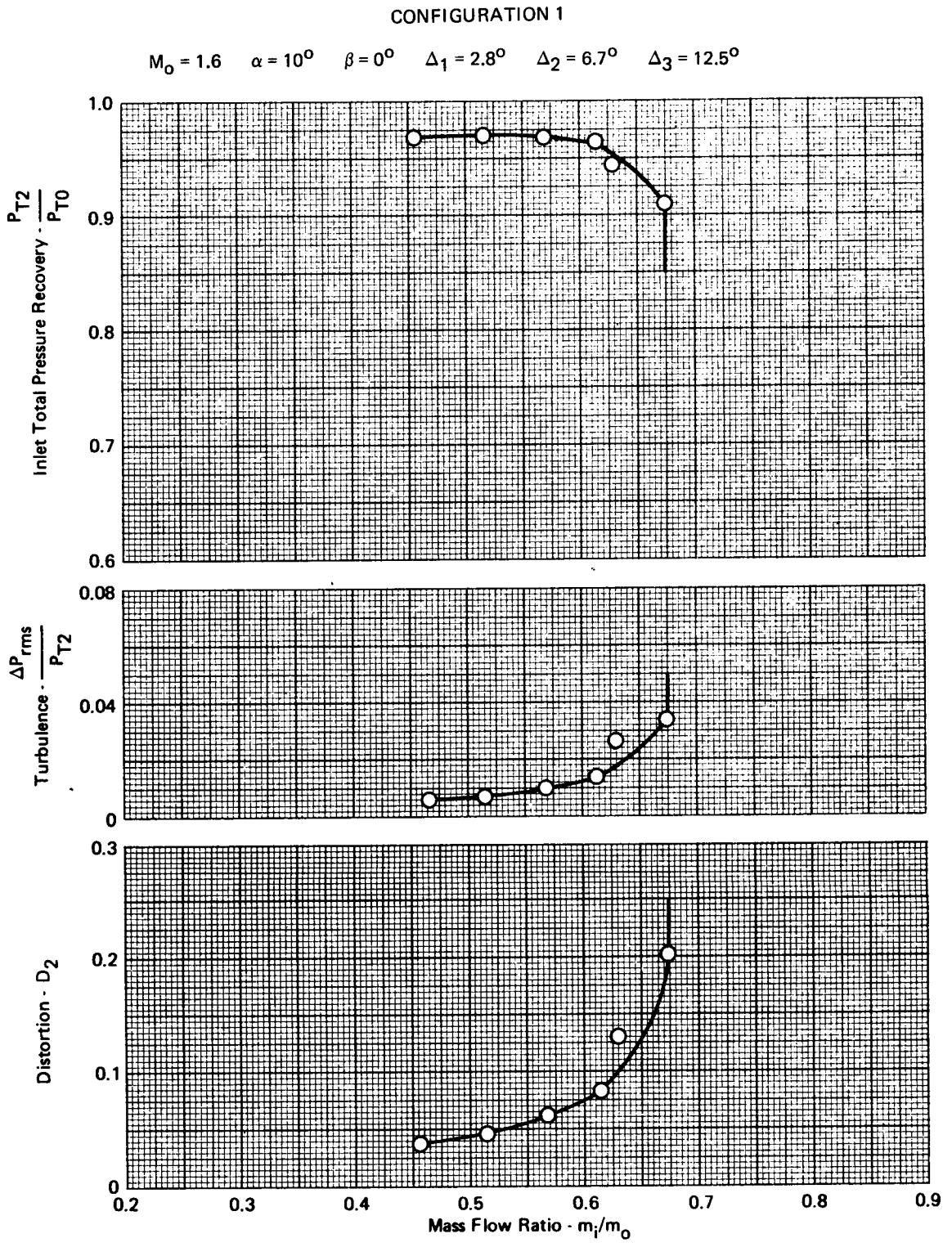

FIGURE A-44 - EFFECTS OF ANGLE OF ATTACK ON PRESSURE RECOVERY, TURBULENCE, AND DISTORTION

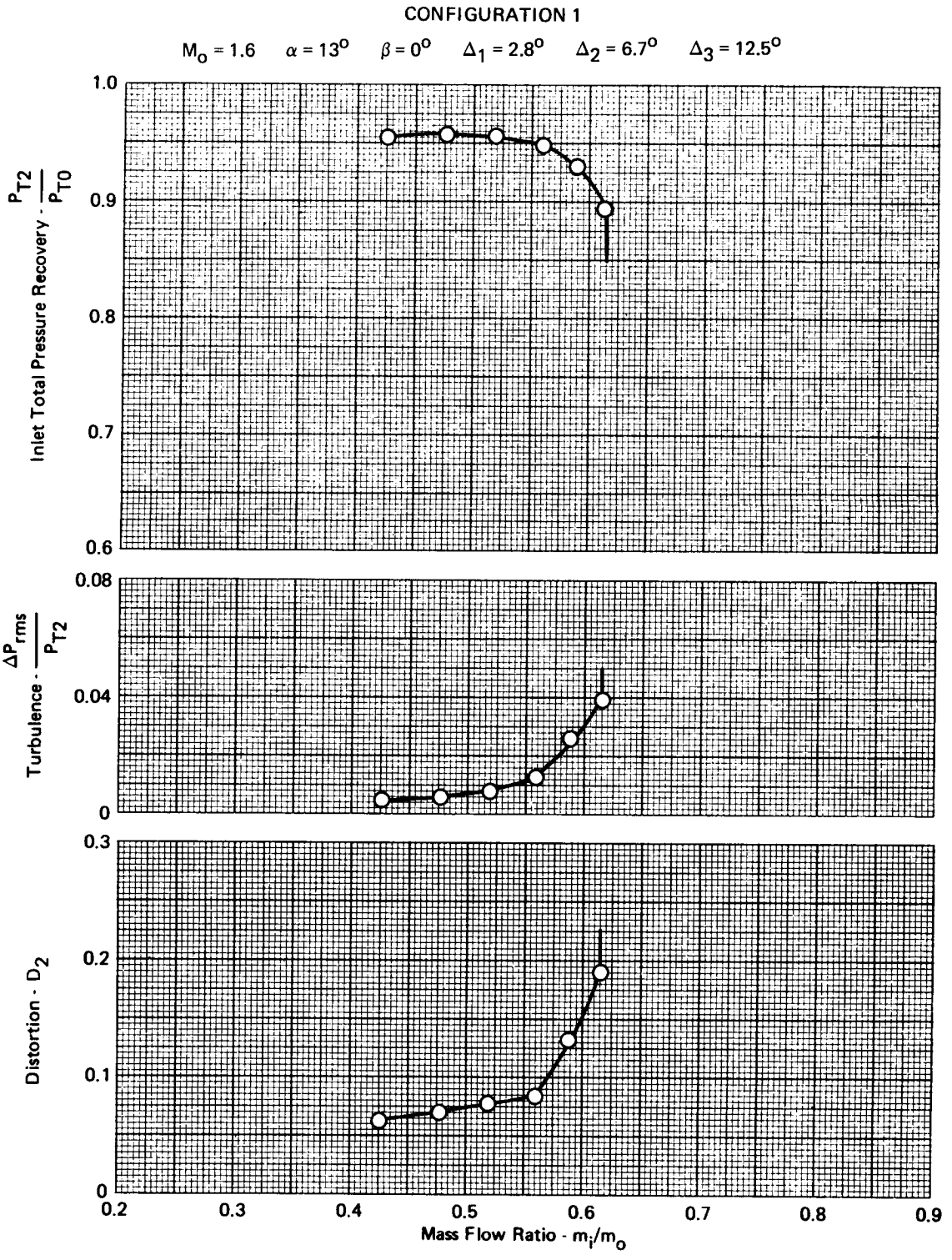

FIGURE A-45 - EFFECTS OF ANGLE OF ATTACK ON PRESSURE RECOVERY, TURBULENCE,AND DISTORTION

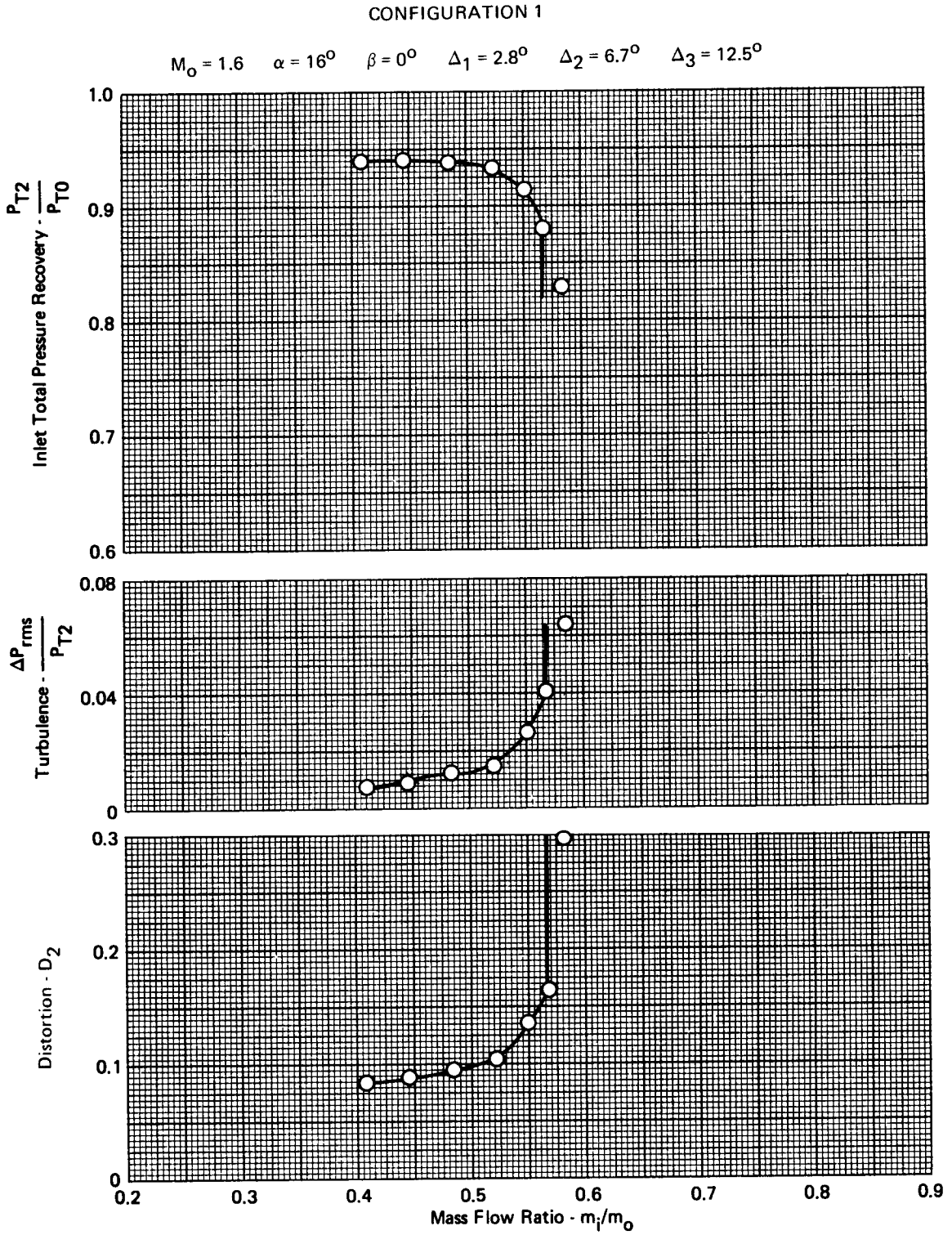

FIGURE A-46 - EFFECTS OF ANGLE OF ATTACK ON PRESSURE RECOVERY, TURBULENCE, AND DISTORTION

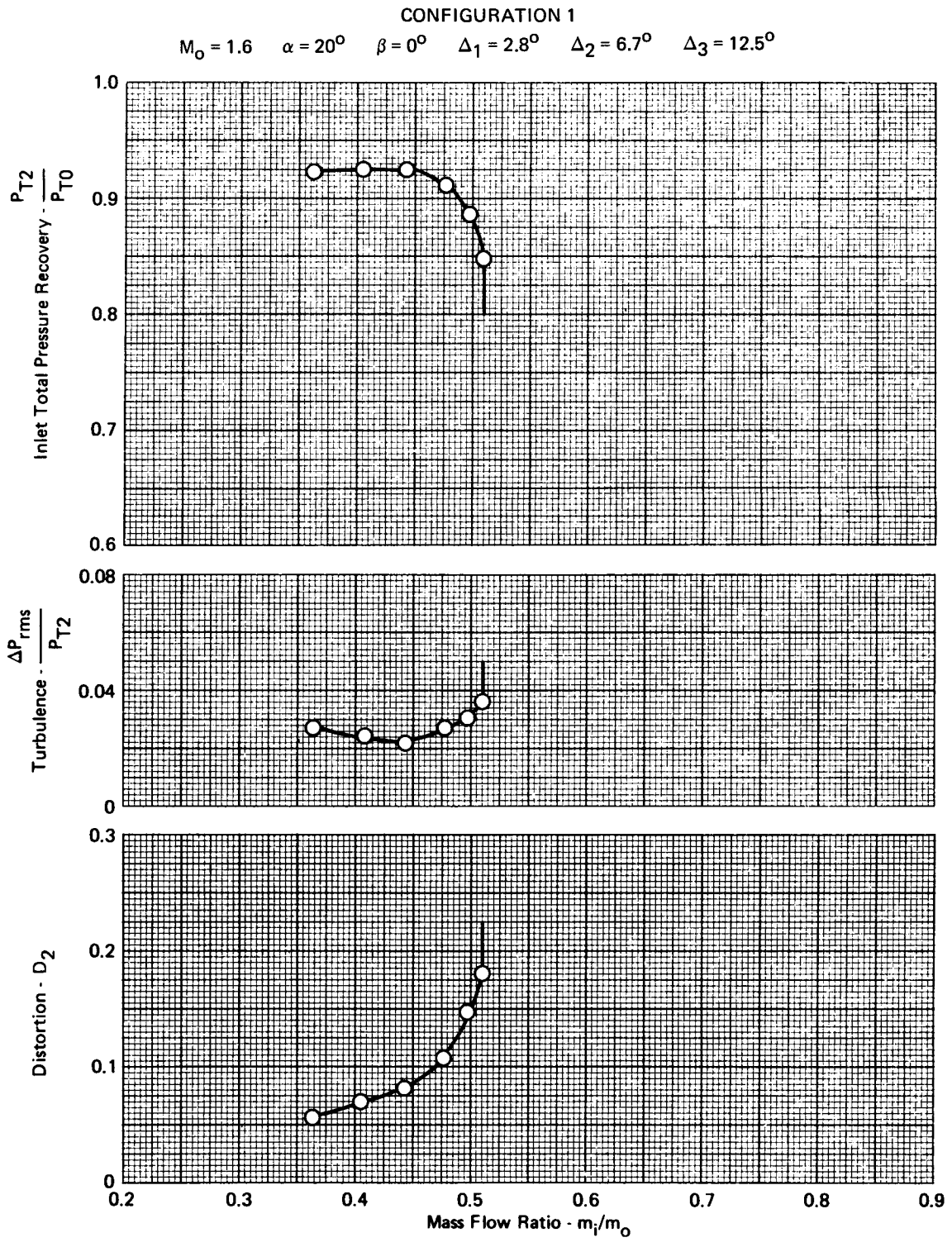

FIGURE A-47 - EFFECTS OF ANGLE OF ATTACK ON PRESSURE RECOVERY, TURBULENCE, AND DISTORTION

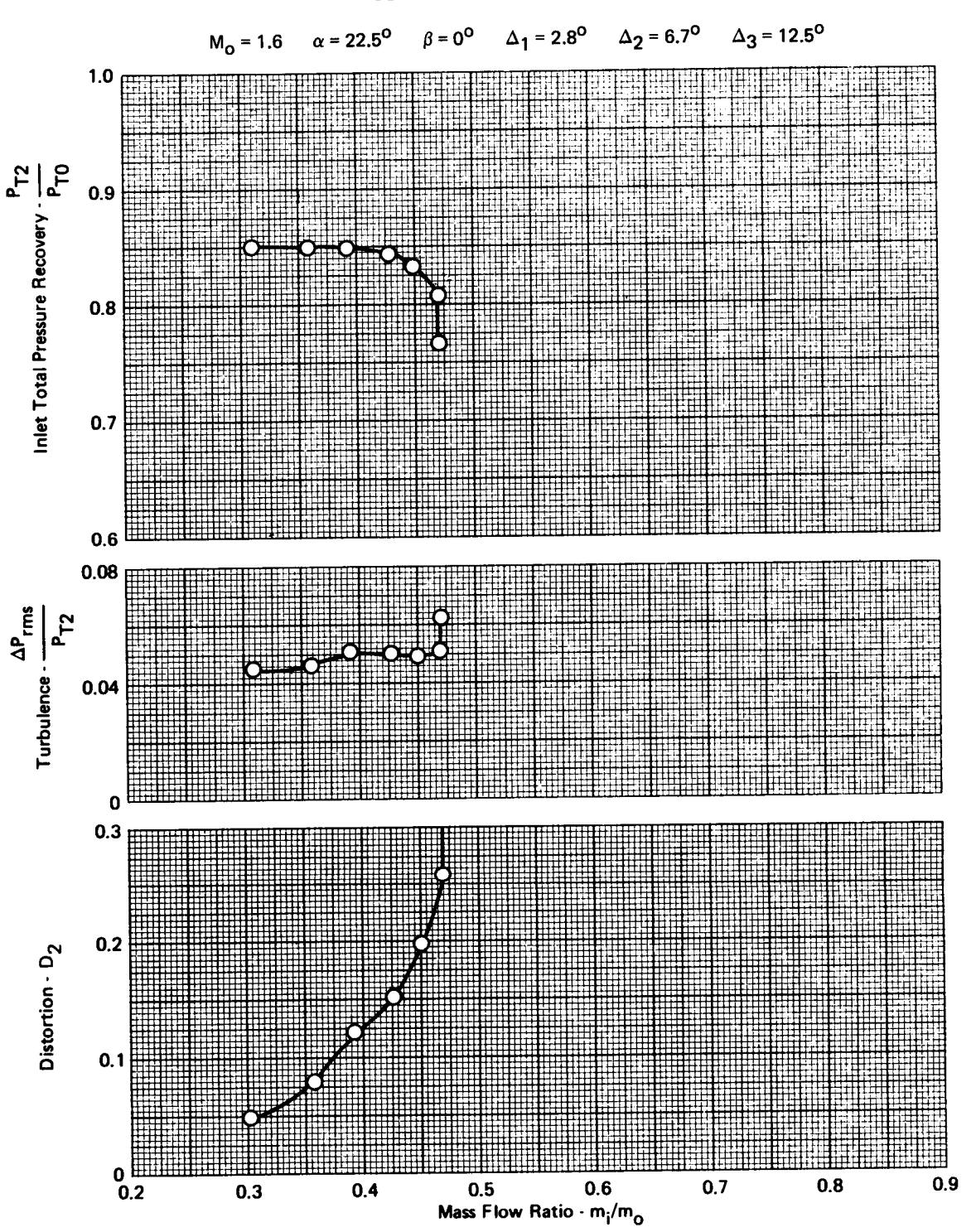

FIGURE A-48 - EFFECTS OF ANGLE OF ATTACK ON PRESSURE RECOVERY, TURBULENCE, AND DISTORTION

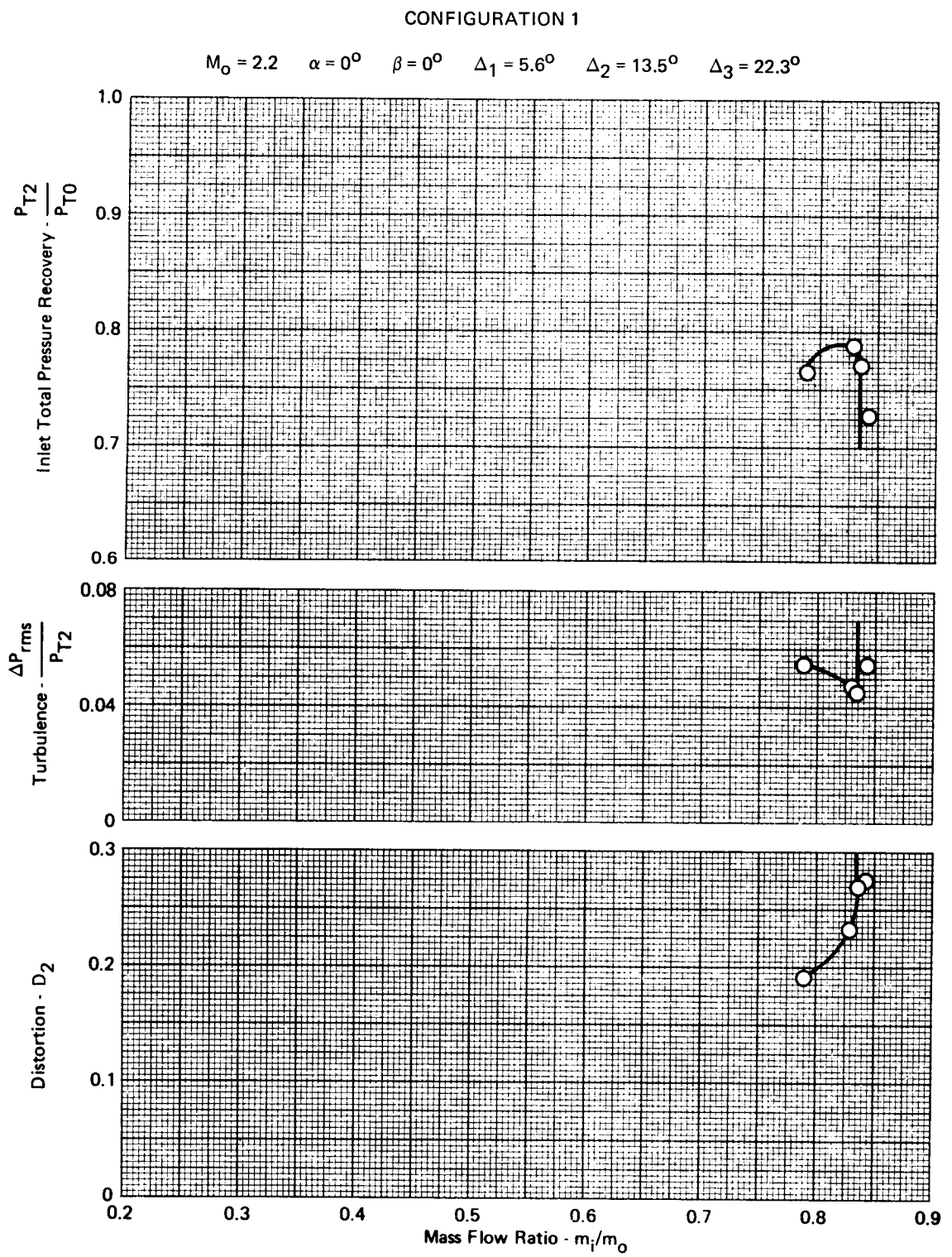

FIGURE A-49 - EFFECTS OF ANGLE OF ATTACK ON PRESSURE RECOVERY, TURBULENCE,AND DISTORTION

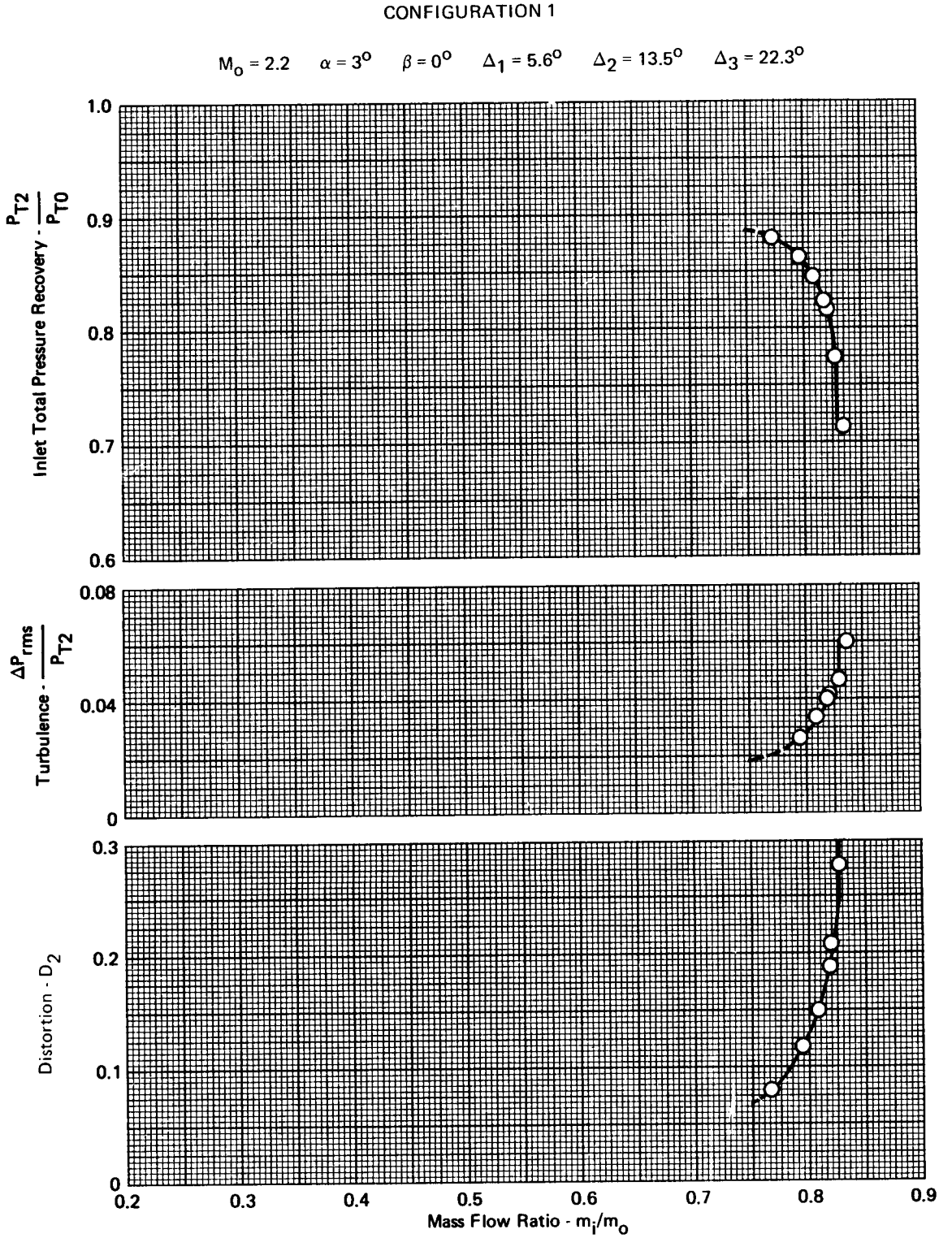

FIGURE A-50 - EFFECTS OF ANGLE OF ATTACK ON PRESSURE RECOVERY, TURBULENCE, AND DISTORTION

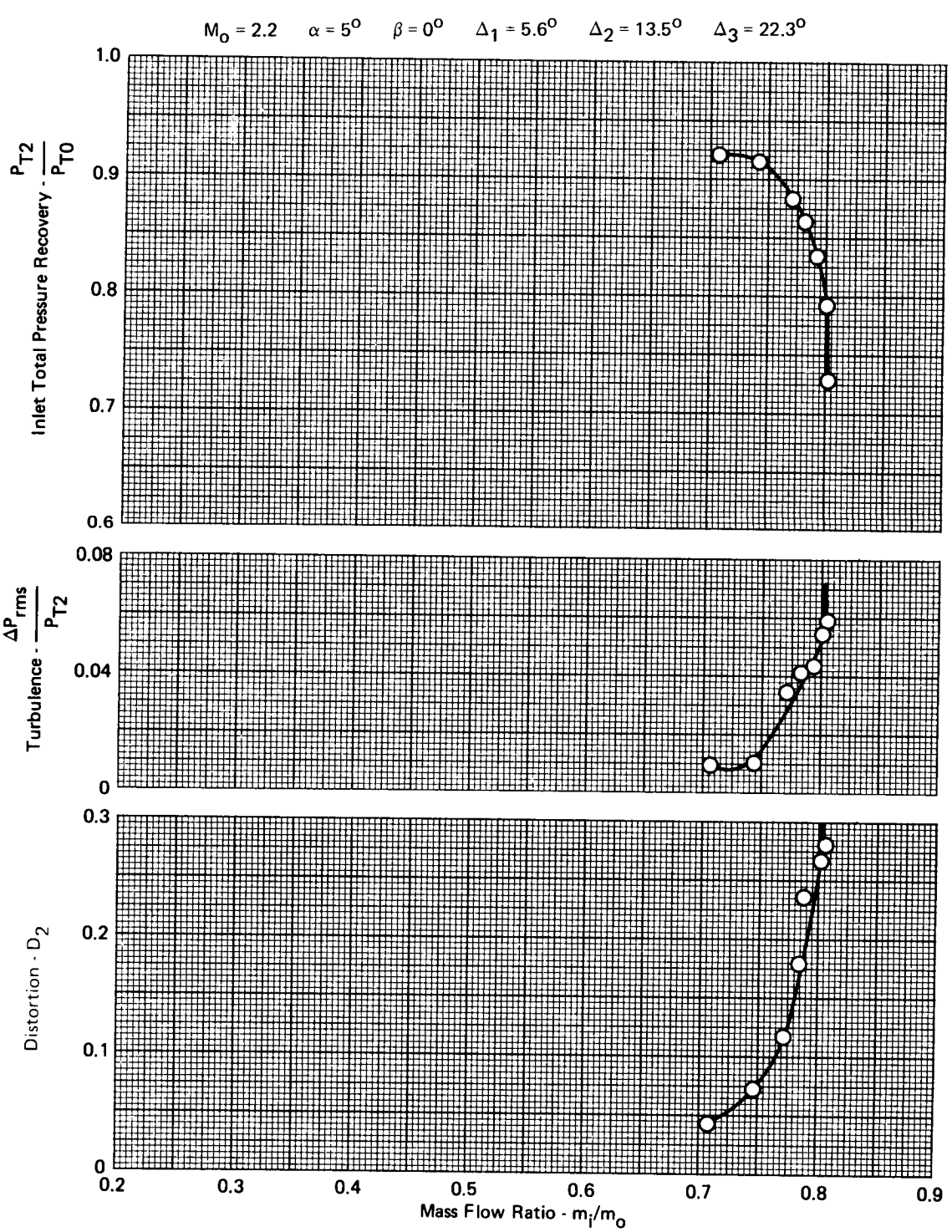

FIGURE A-51 - EFFECTS OF ANGLE OF ATTACK ON PRESSURE RECOVERY, TURBULENCE, AND DISTORTION

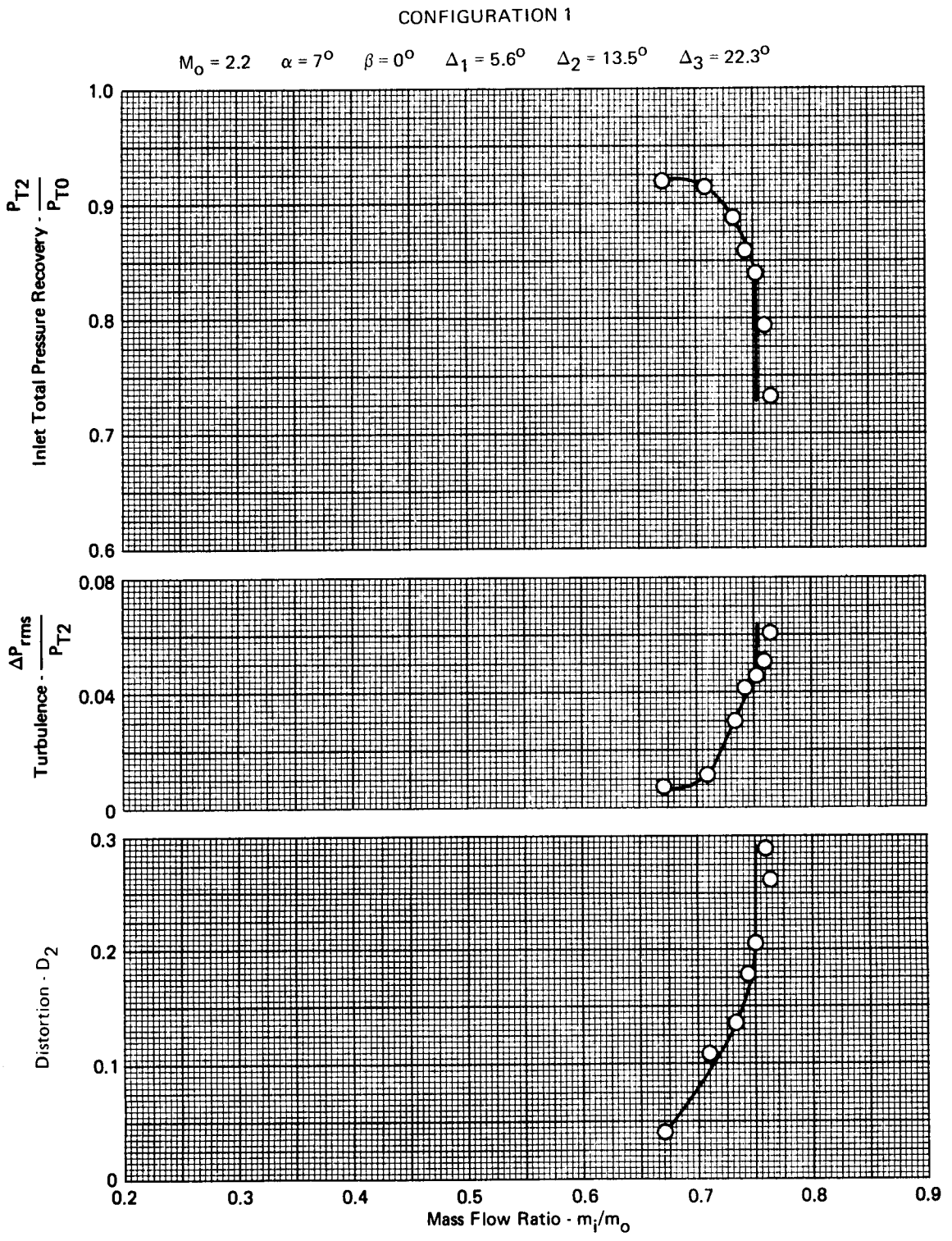

FIGURE A-52- EFFECTS OF ANGLE OF ATTACK ON PRESSURE RECOVERY, TURBULENCE, AND DISTORTION

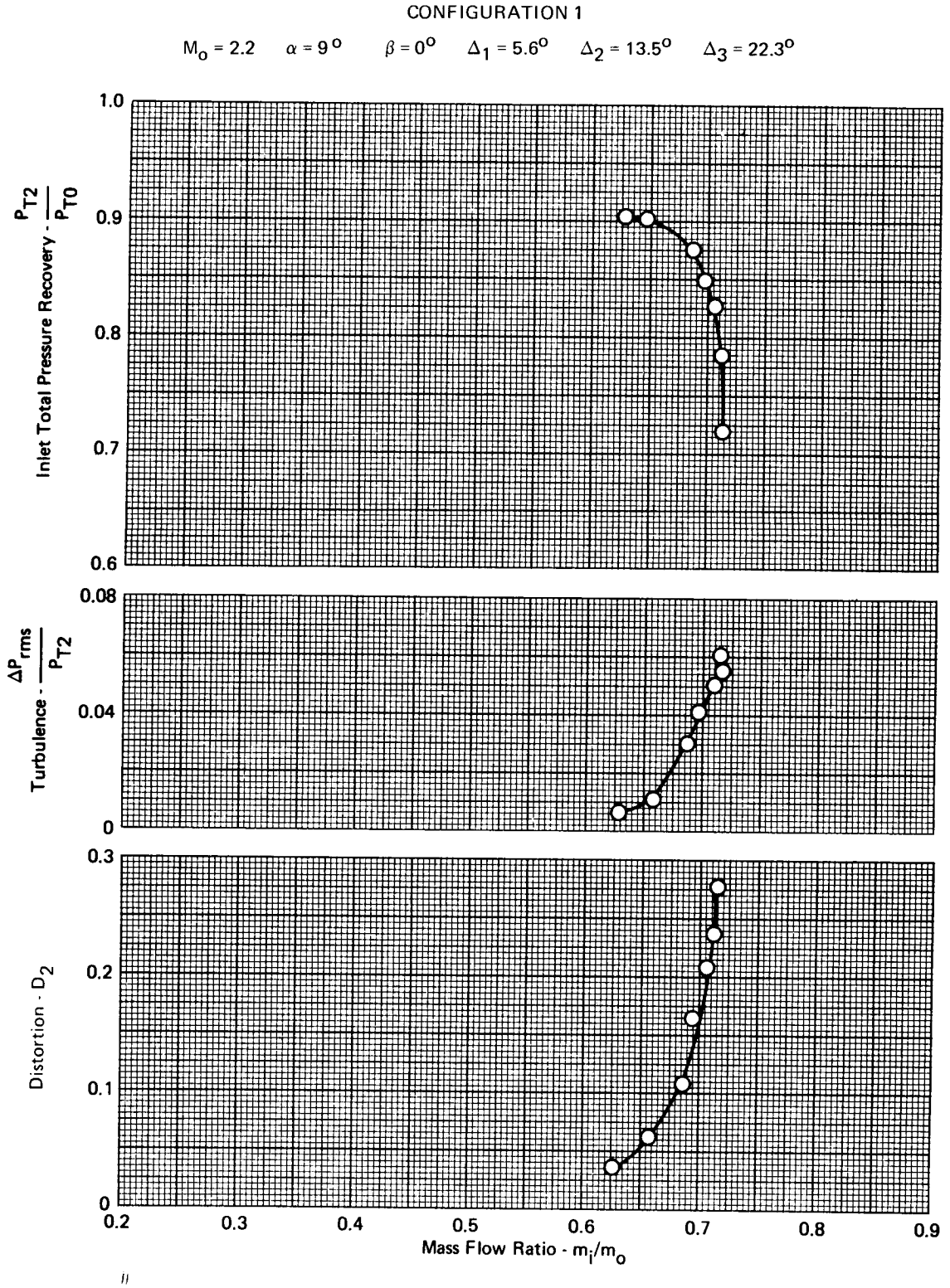

FIGURE A-53 - EFFECTS OF ANGLE OF ATTACK ON PRESSURE RECOVERY, TURBULENCE, AND DISTORTION

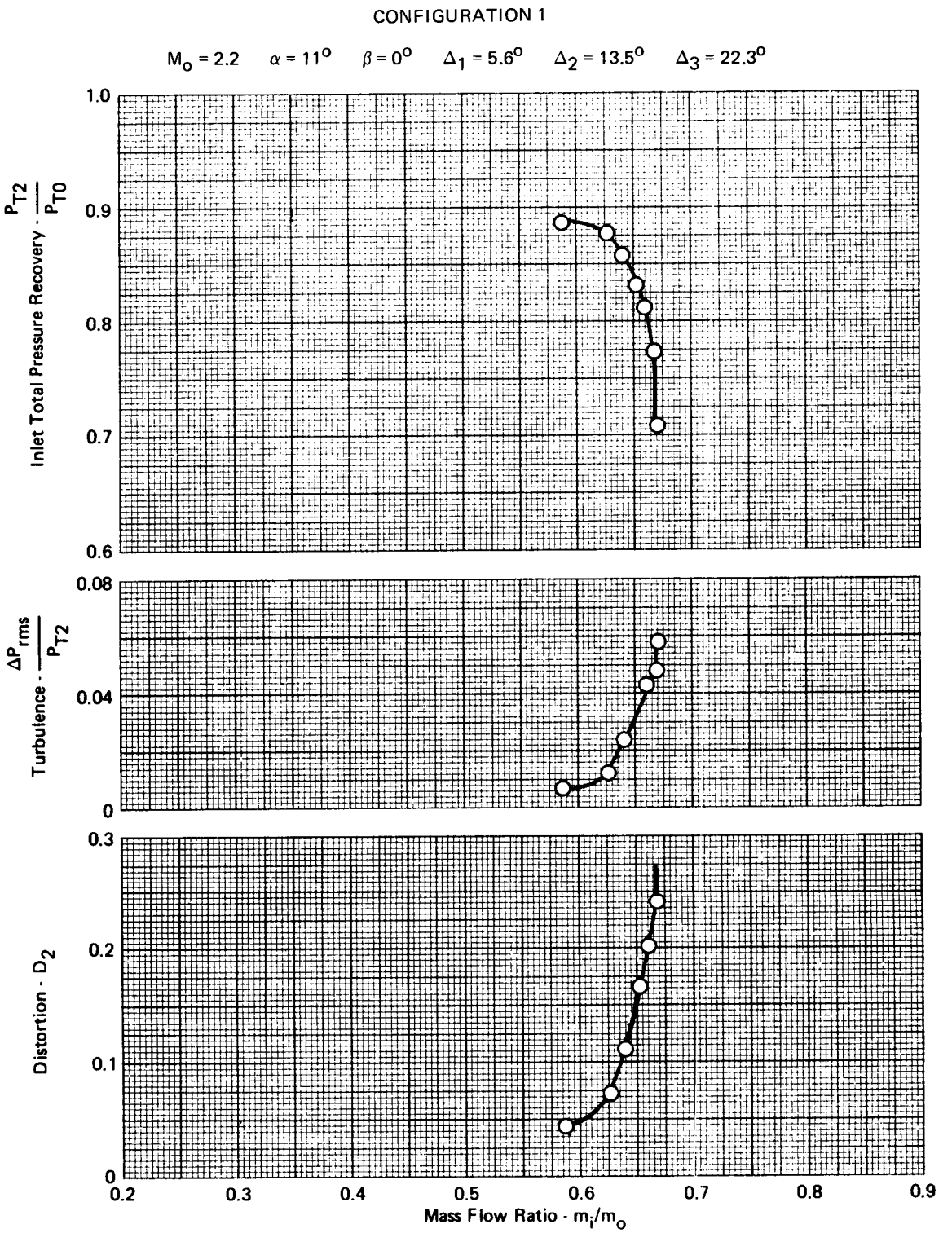

FIGURE A-54 - EFFECTS OF ANGLE OF ATTACK ON PRESSURE RECOVERY, TURBULENCE, AND DISTORTION

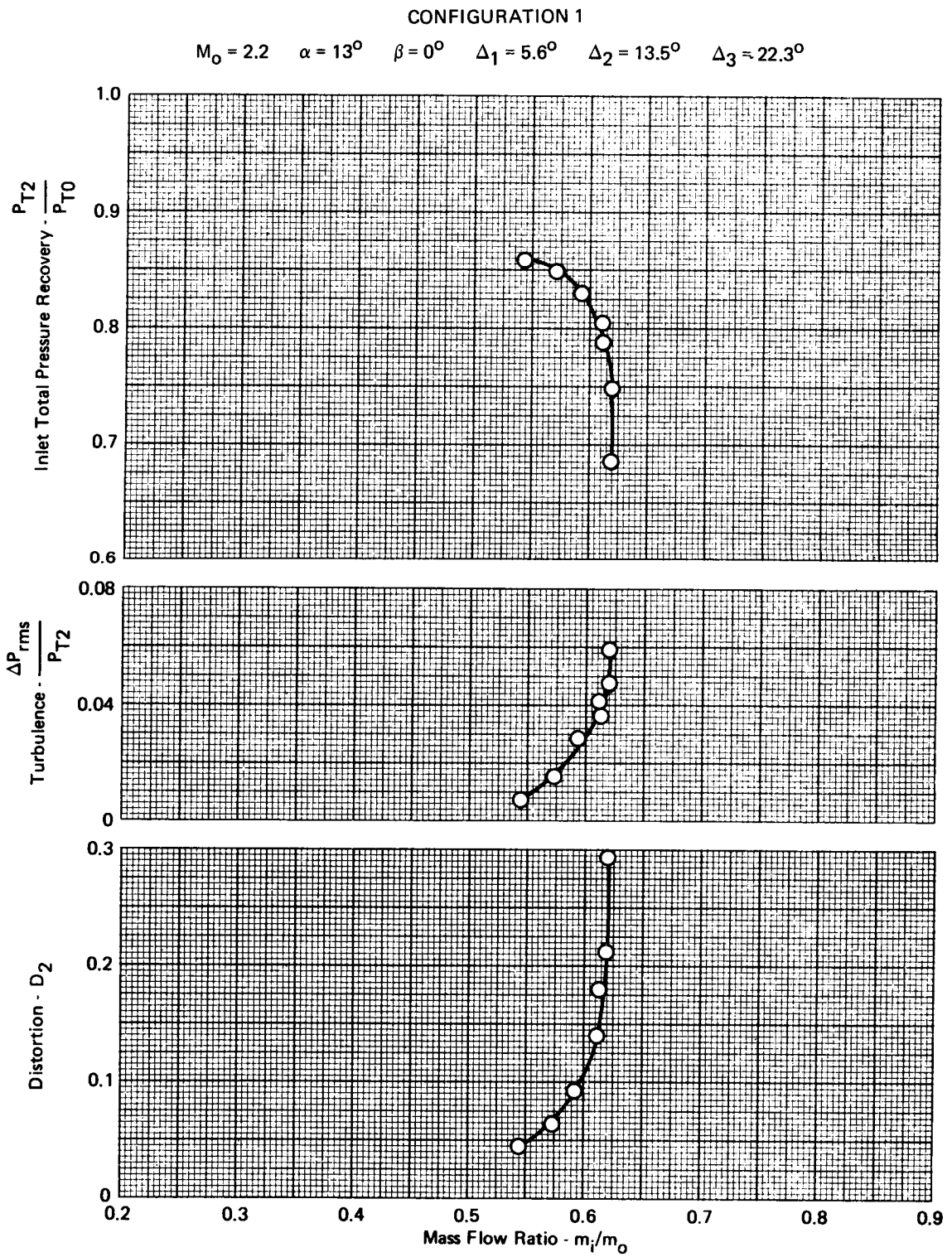

FIGURE A-55 - EFFECTS OF ANGLE OF ATTACK ON PRESSURE RECOVERY, TURBULENCE,AND DISTORTION

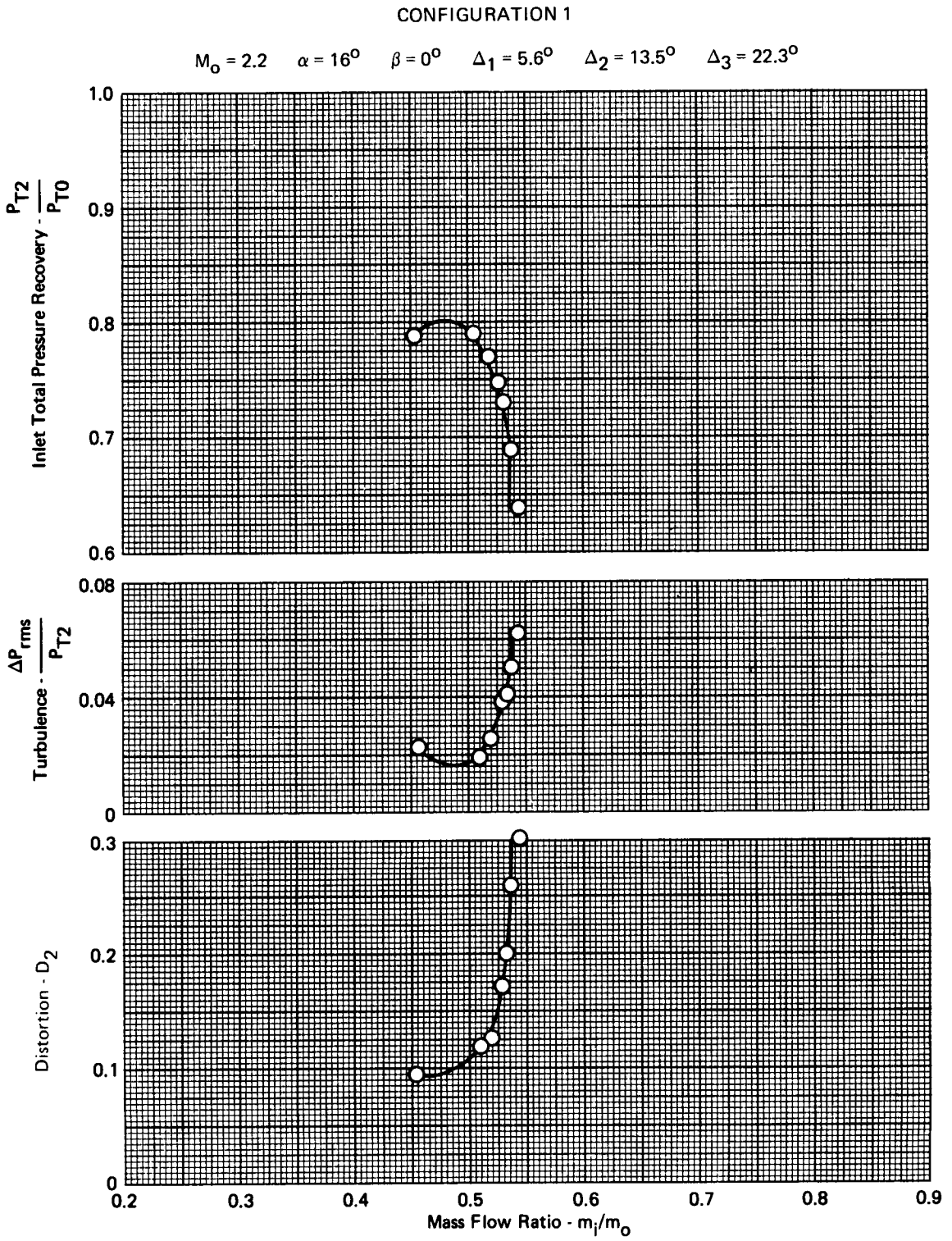

FIGURE A-56 - EFFECTS OF ANGLE OF ATTACK ON PRESSURE RECOVERY, TURBULENCE, AND DISTORTION

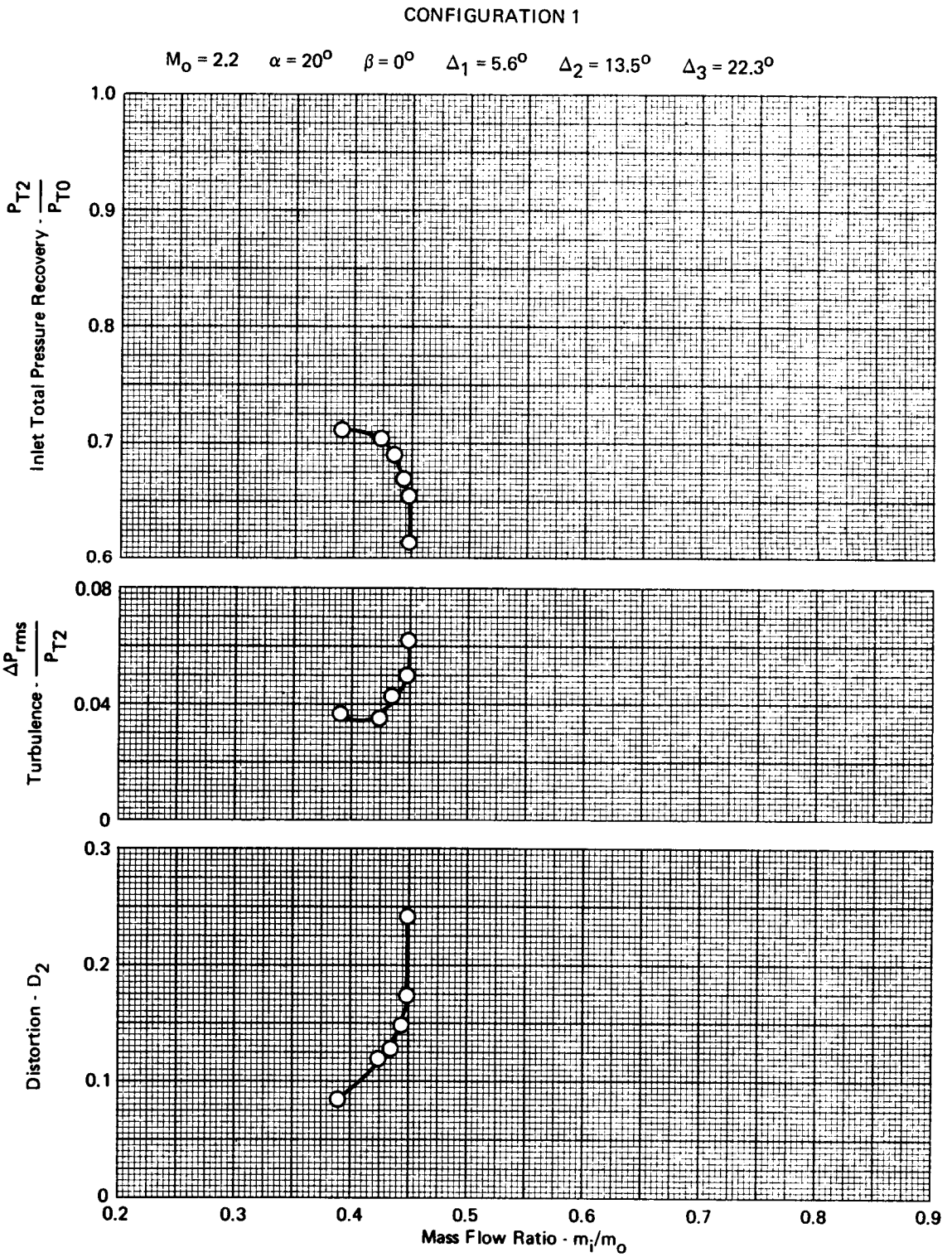

FIGURE A-57 - EFFECTS OF ANGLE OF ATTACK ON PRESSURE RECOVERY, TURBULENCE, AND DISTORTION

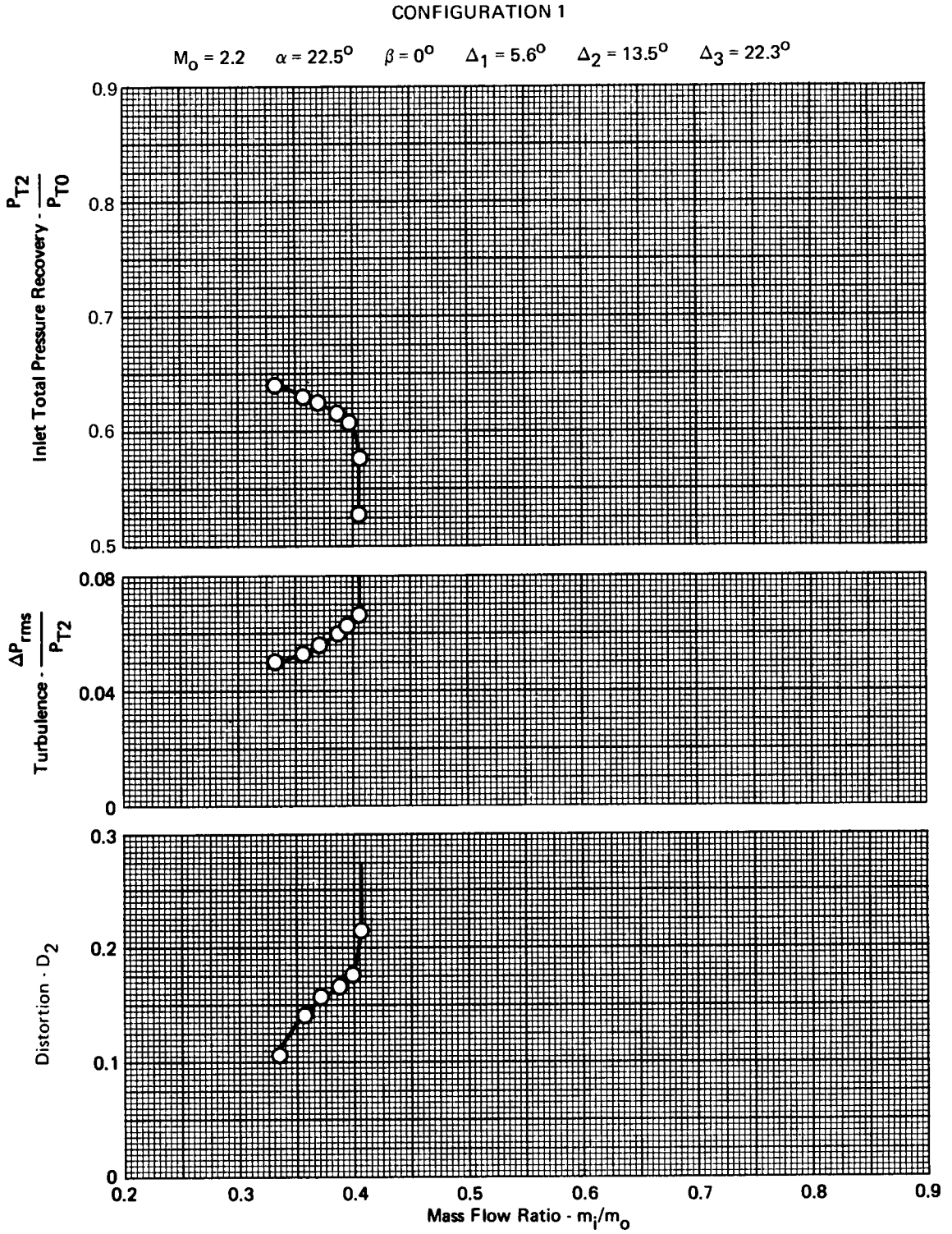

FIGURE A-58 - EFFECTS OF ANGLE OF ATTACK ON PRESSURE RECOVERY, TURBULENCE, AND DISTORTION

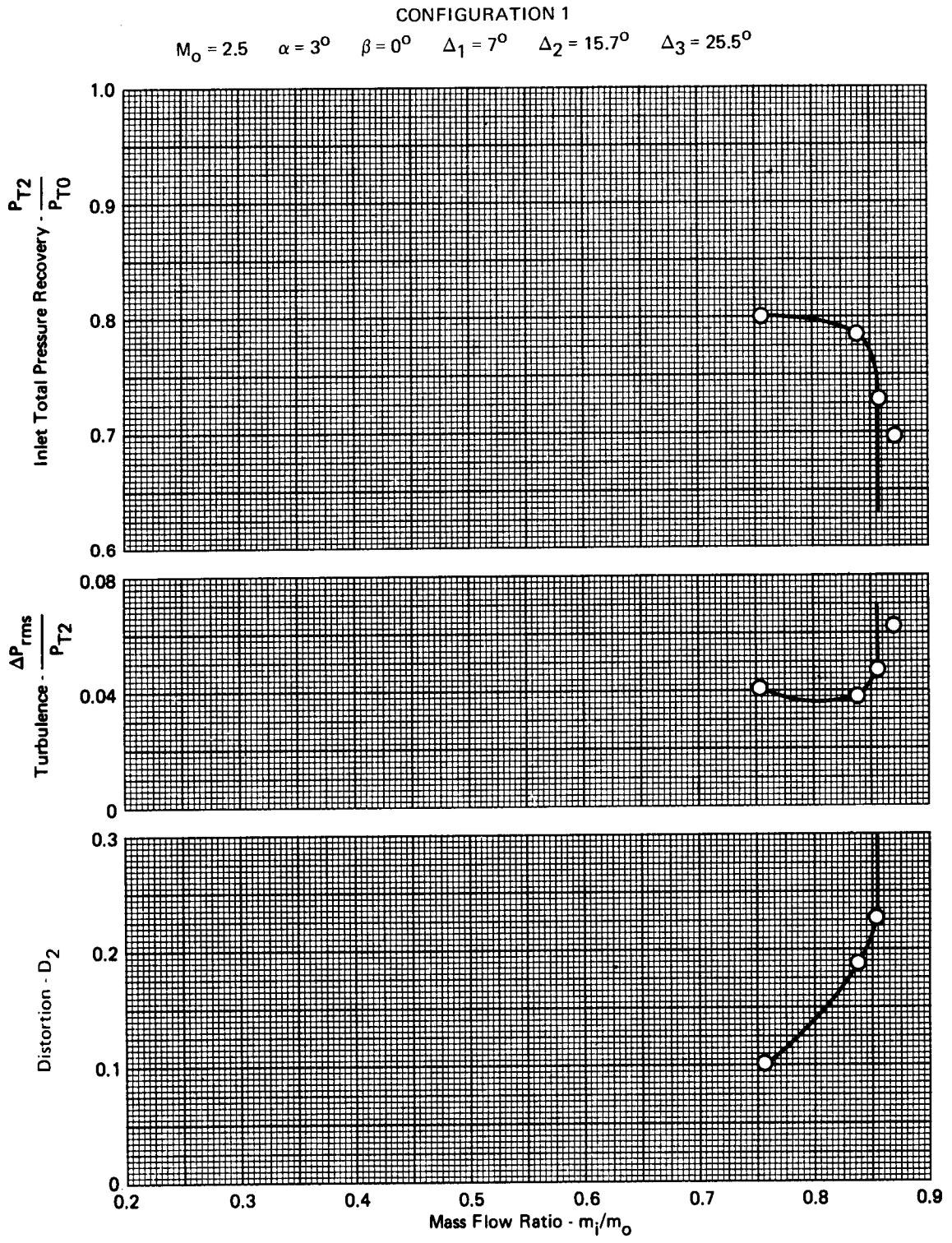

FIGURE A-59- EFFECTS OF ANGLE OF ATTACK ON PRESSURE RECOVERY, TURBULENCE, AND DISTORTION

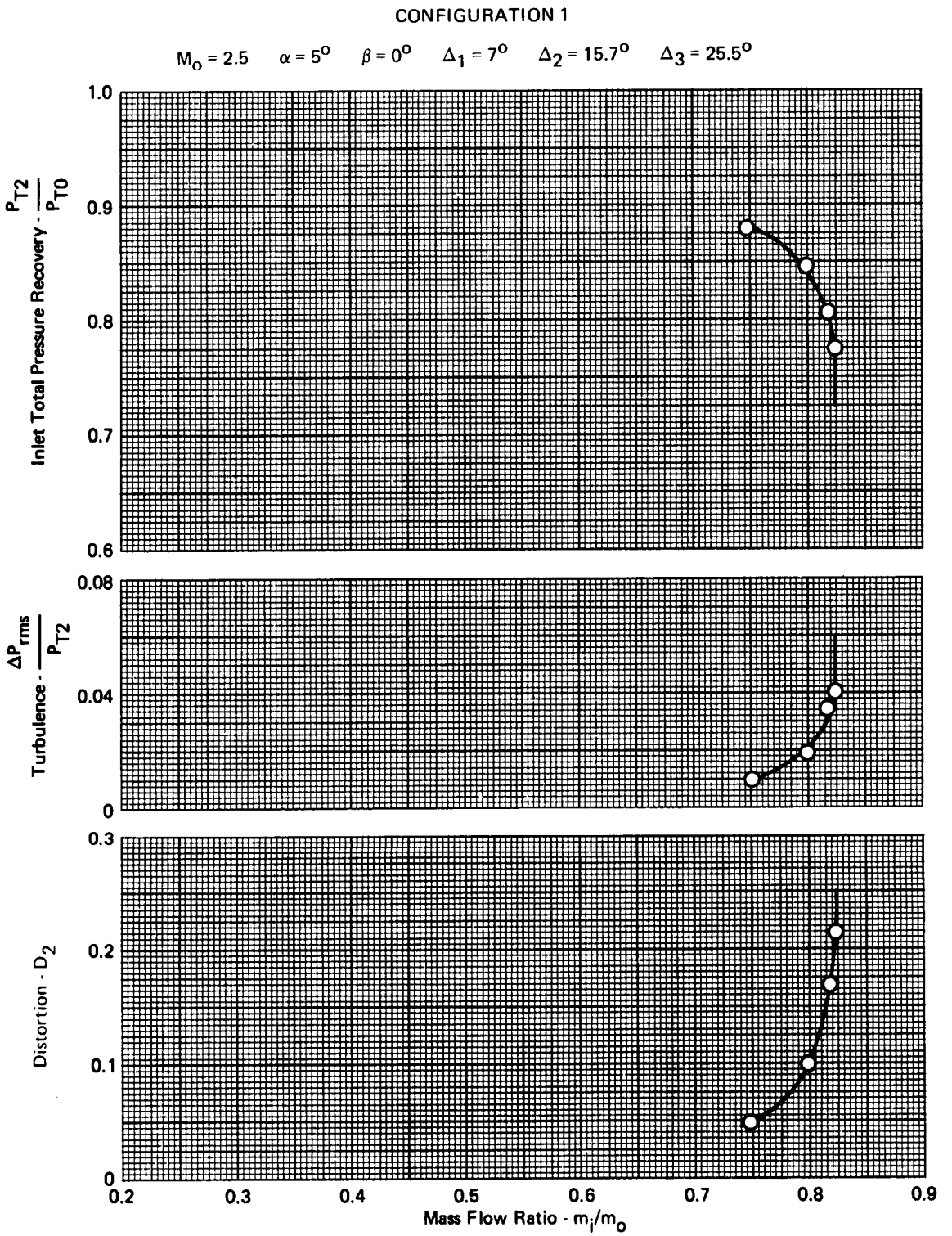

FIGURE A-60 - EFFECTS OF ANGLE OF ATTACK ON PRESSURE RECOVERY, TURBULENCE, AND DISTORTION

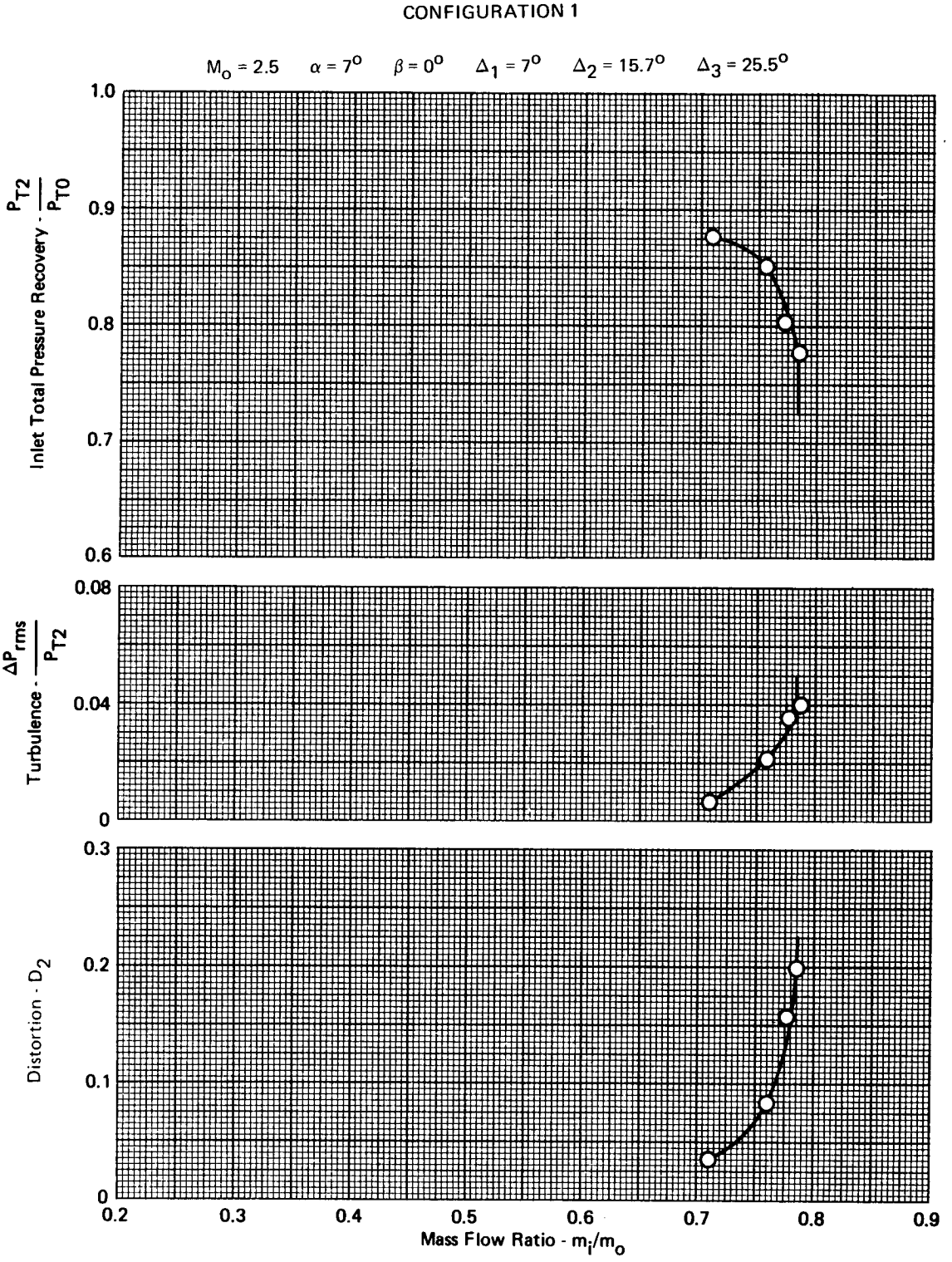

FIGURE A-61 - EFFECTS OF ANGLE OF ATTACK ON PRESSURE RECOVERY, TURBULENCE, AND DISTORTION

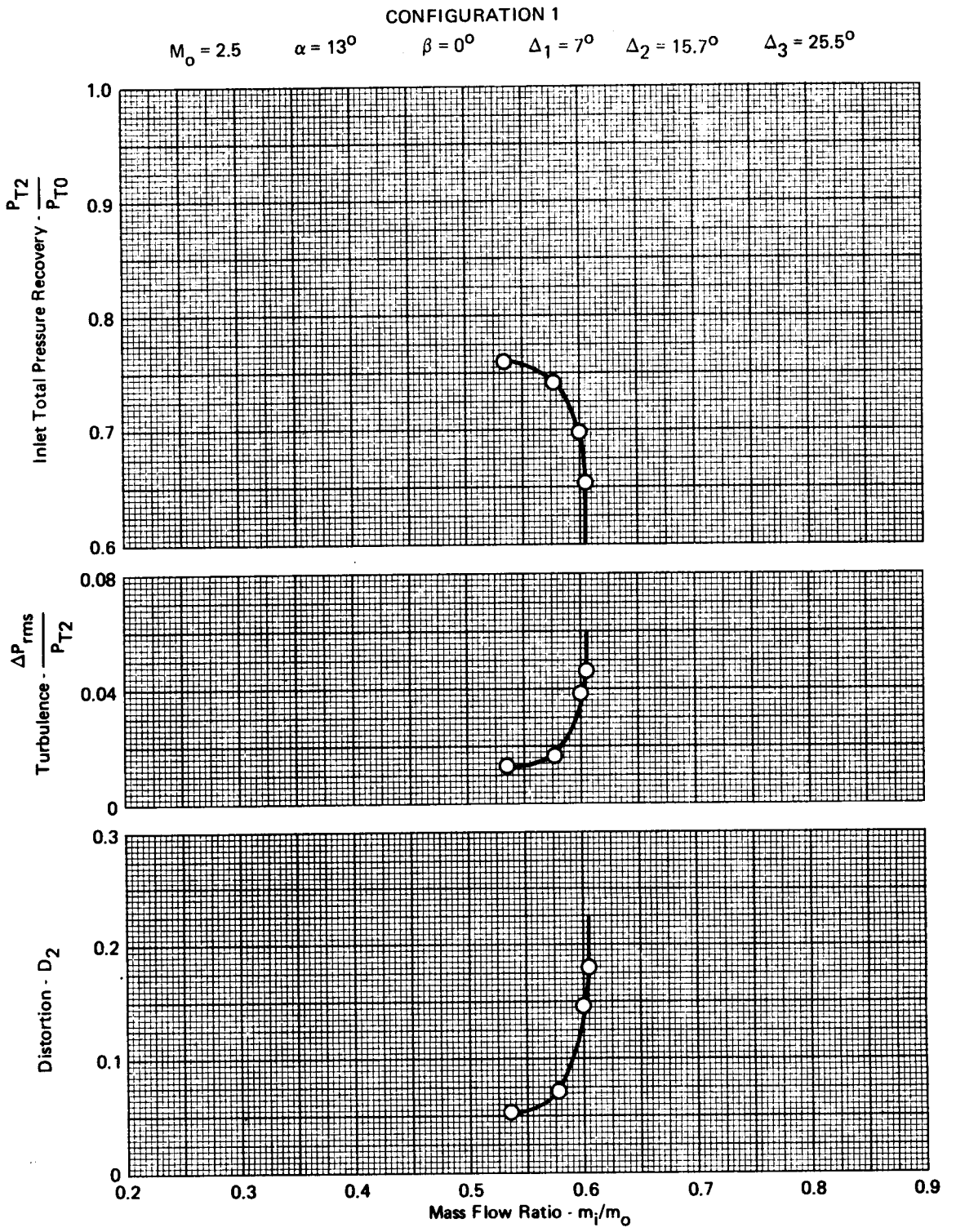

FIGURE A-62 - EFFECTS OF ANGLE OF ATTACK ON PRESSURE RECOVERY, TURBULENCE, AND DISTORTION

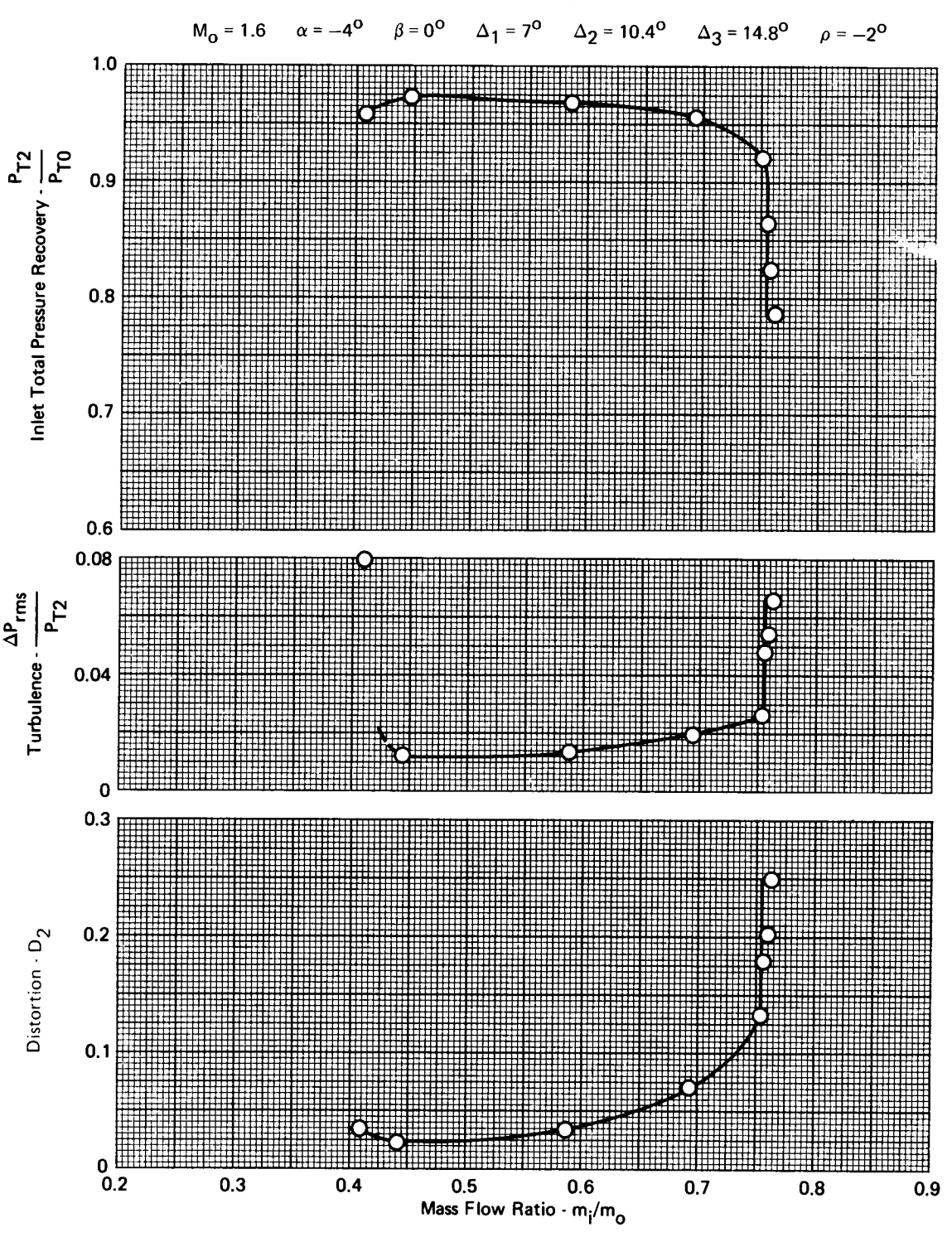

FIGURE A-63 - EFFECTS OF ANGLE OF ATTACK ON PRESSURE RECOVERY, TURBULENCE, AND DISTORTION

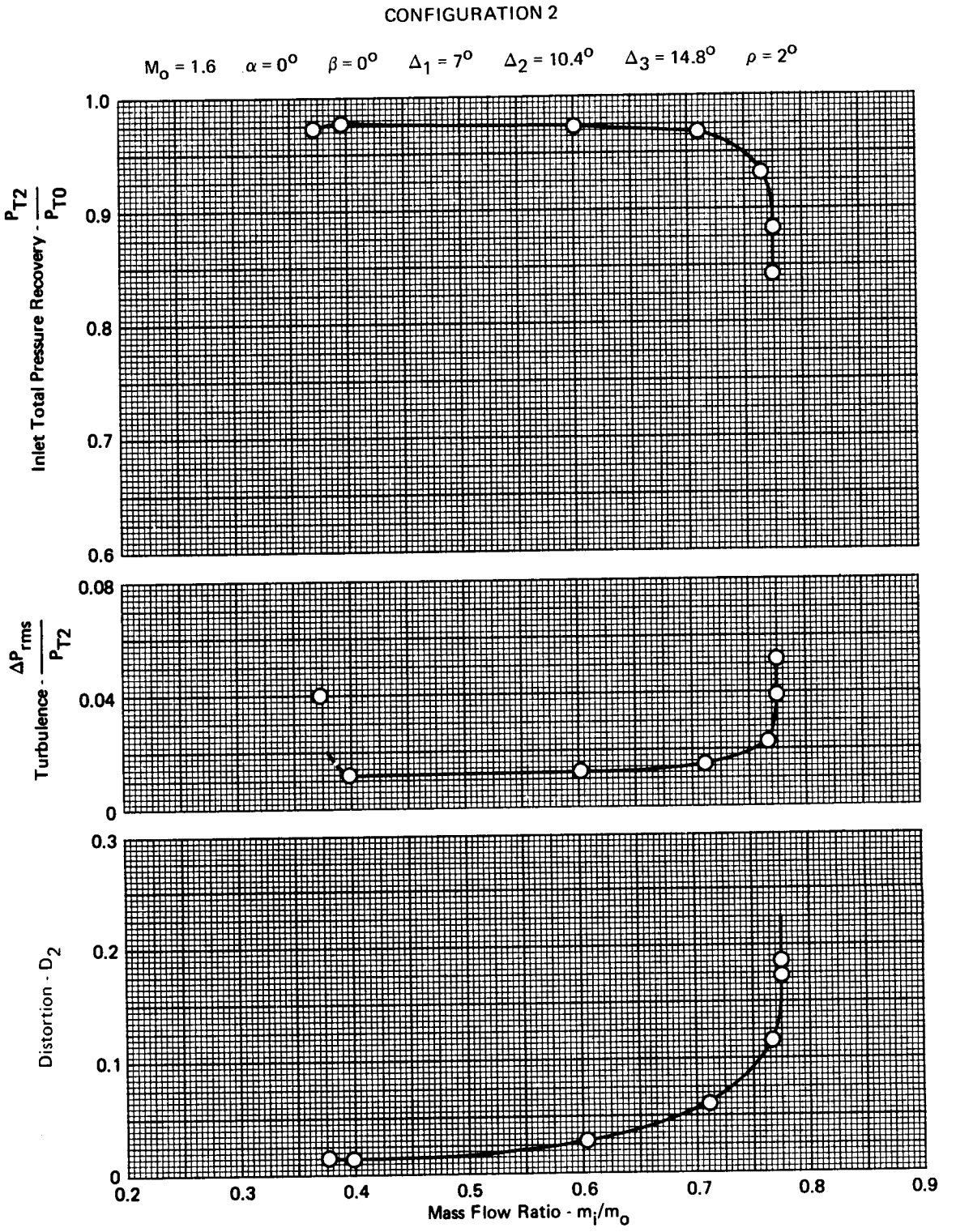

FIGURE A-64 - EFFECTS OF ANGLE OF ATTACK ON PRESSURE RECOVERY, TURBULENCE, AND DISTORTION

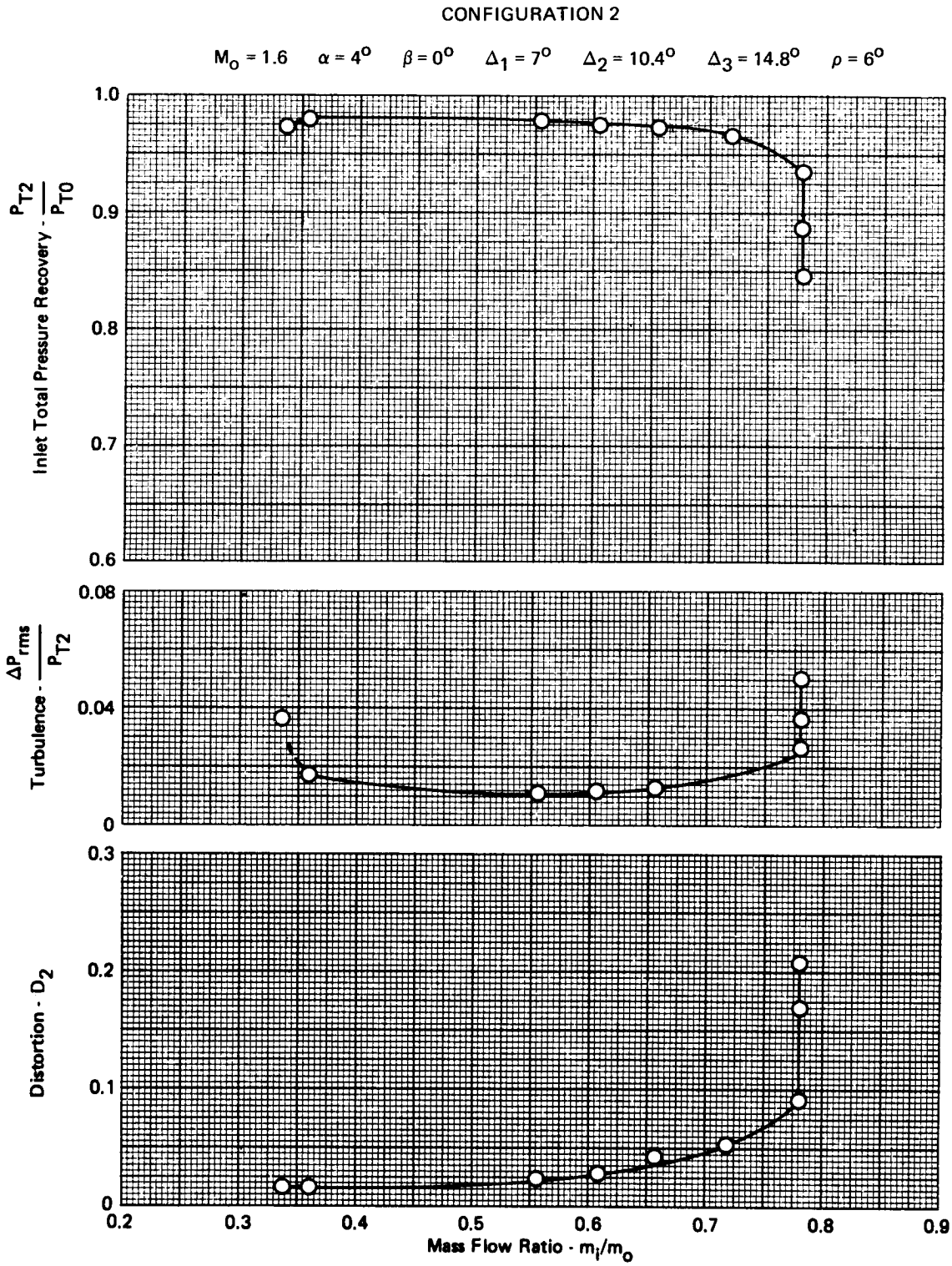

FIGURE A-65 - EFFECTS OF ANGLE OF ATTACK ON PRESSURE RECOVERY, TURBULENCE, AND DISTORTION

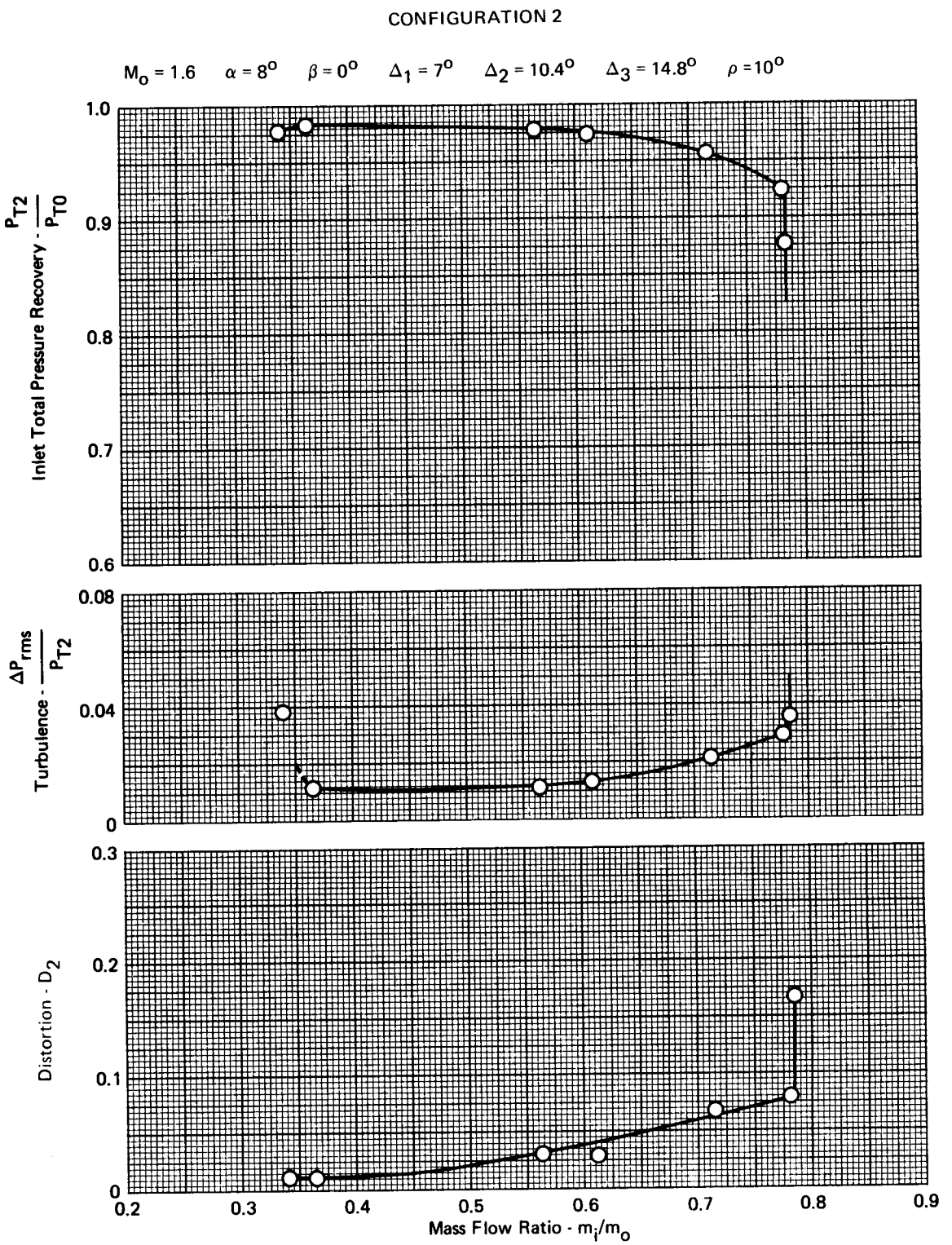

FIGURE A-66 - EFFECTS OF ANGLE OF ATTACK ON PRESSURE RECOVERY, TURBULENCE, AND DISTORTION

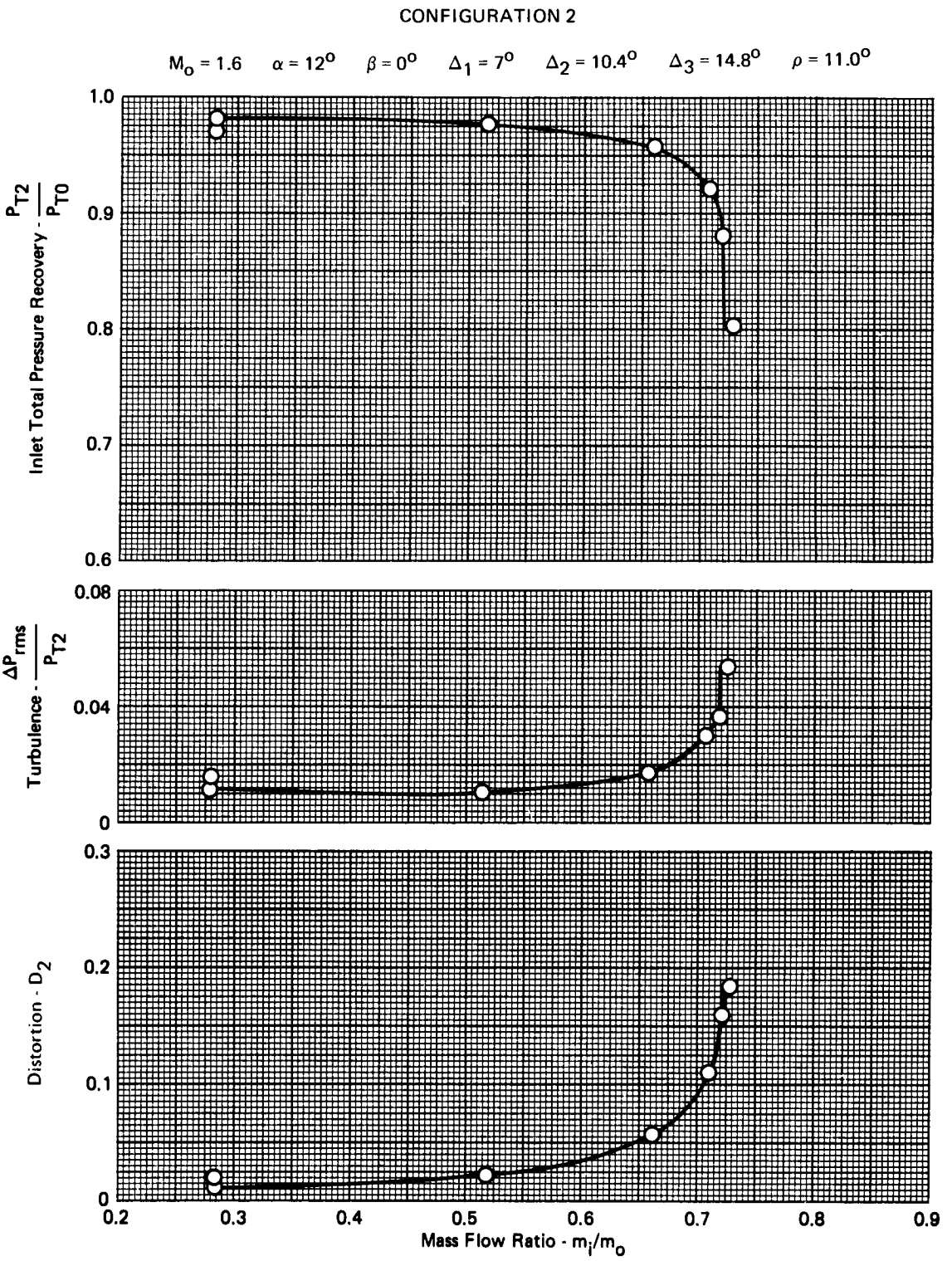

FIGURE A-67 - EFFECTS OF ANGLE OF ATTACK ON PRESSURE RECOVERY, TURBULENCE, AND DISTORTION

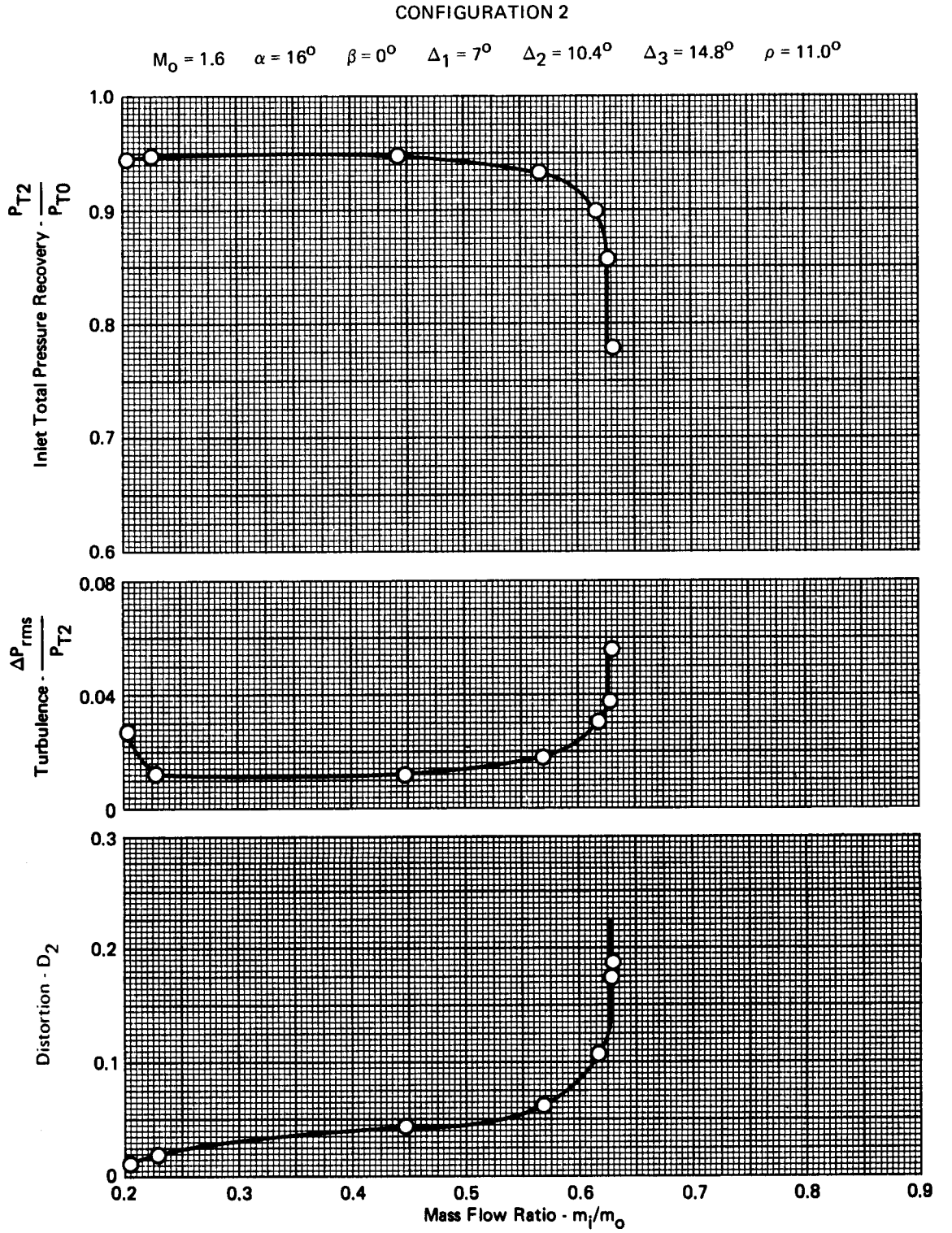

FIGURE A-68 - EFFECTS OF ANGLE OF ATTACK ON PRESSURE RECOVERY, TURBULENCE, AND DISTORTION

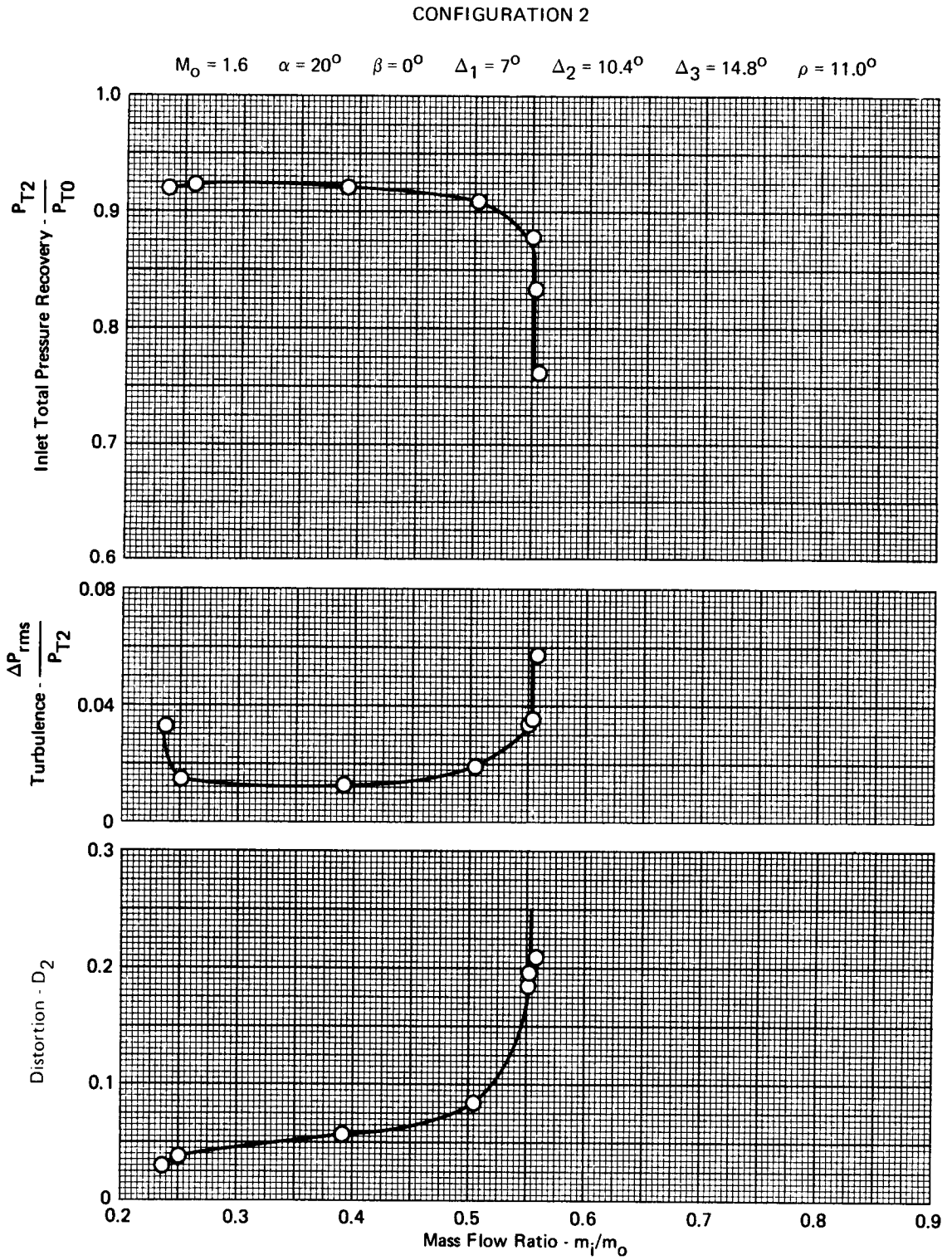

FIGURE A-69 - EFFECTS OF ANGLE OF ATTACK ON PRESSURE RECOVERY, TURBULENCE, AND DISTORTION

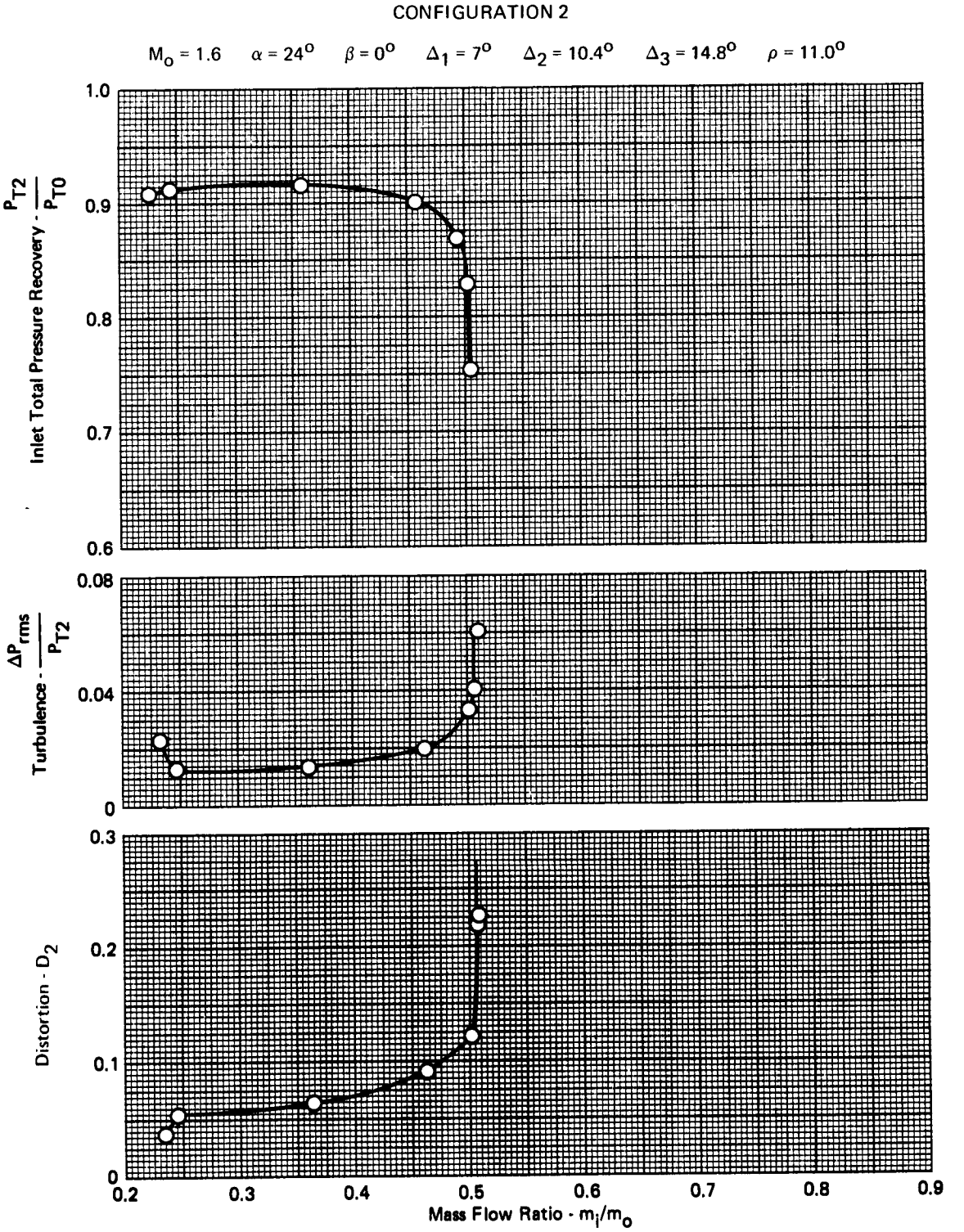

FIGURE A-70 - EFFECTS OF ANGLE OF ATTACK ON PRESSURE RECOVERY, TURBULENCE, AND DISTORTION

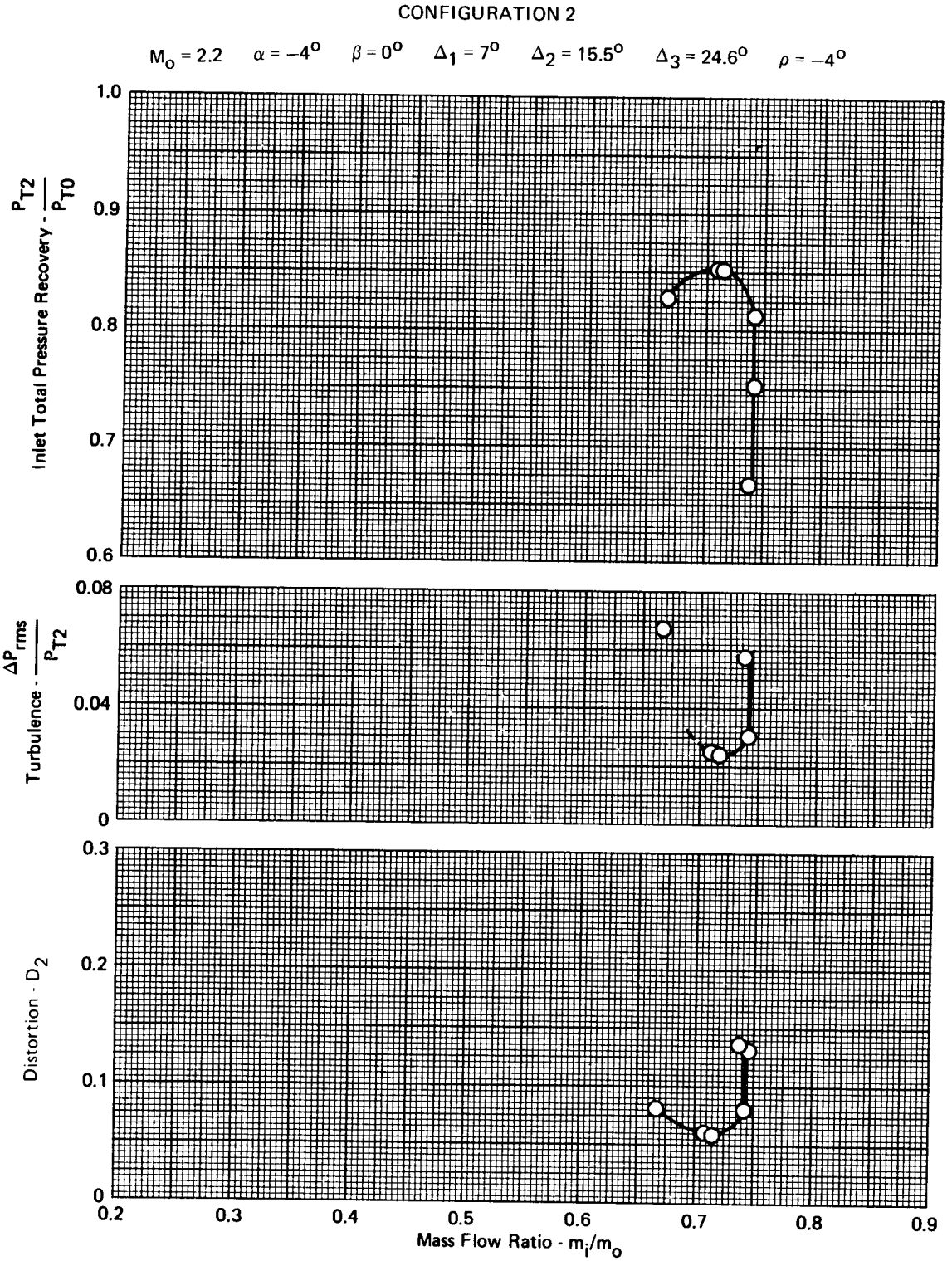

FIGURE A-71- EFFECTS OF ANGLE OF ATTACK ON PRESSURE RECOVERY, TURBULENCE, AND DISTORTION

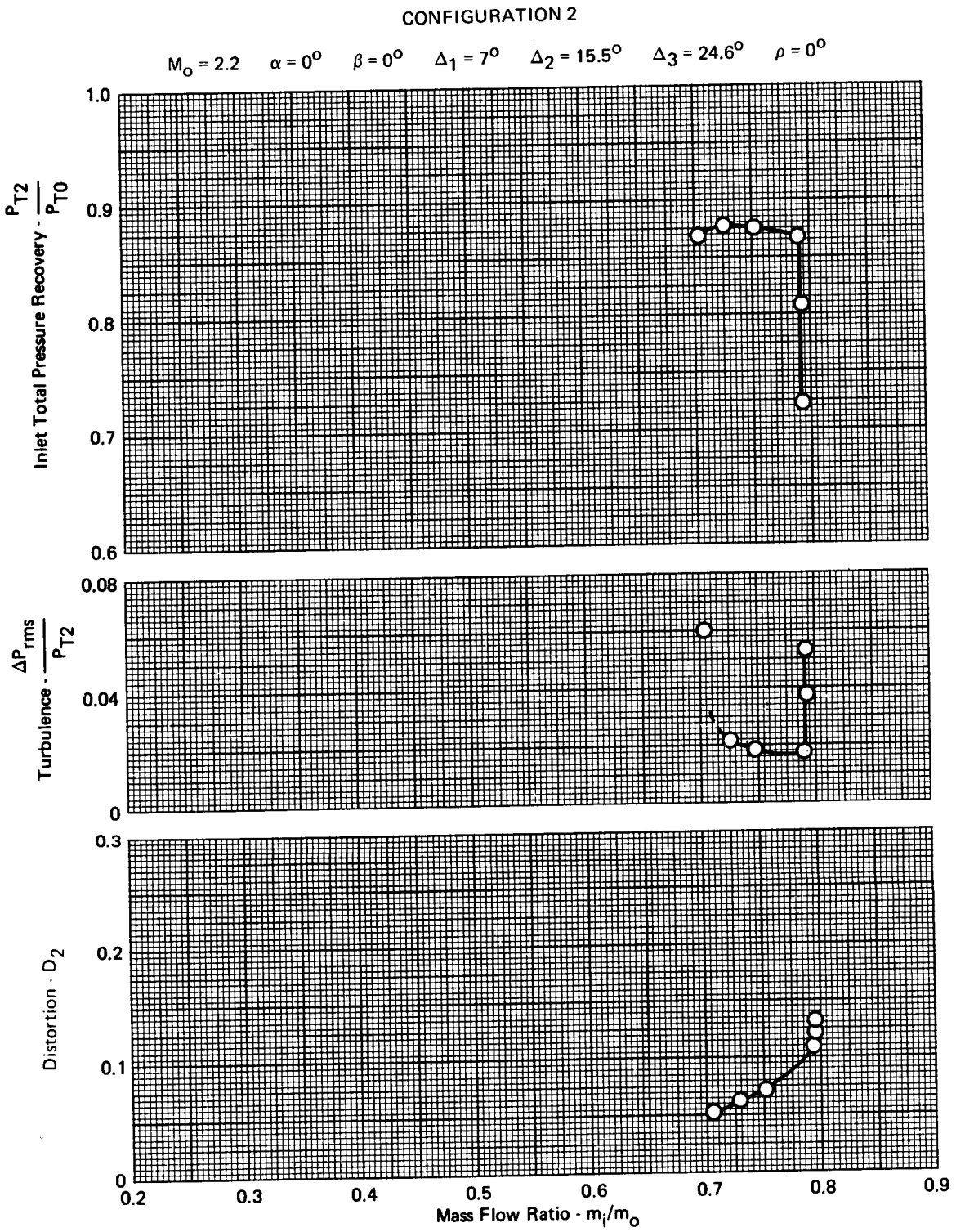

FIGURE A-72 - EFFECTS OF ANGLE OF ATTACK ON PRESSURE RECOVERY, TURBULENCE, AND DISTORTION

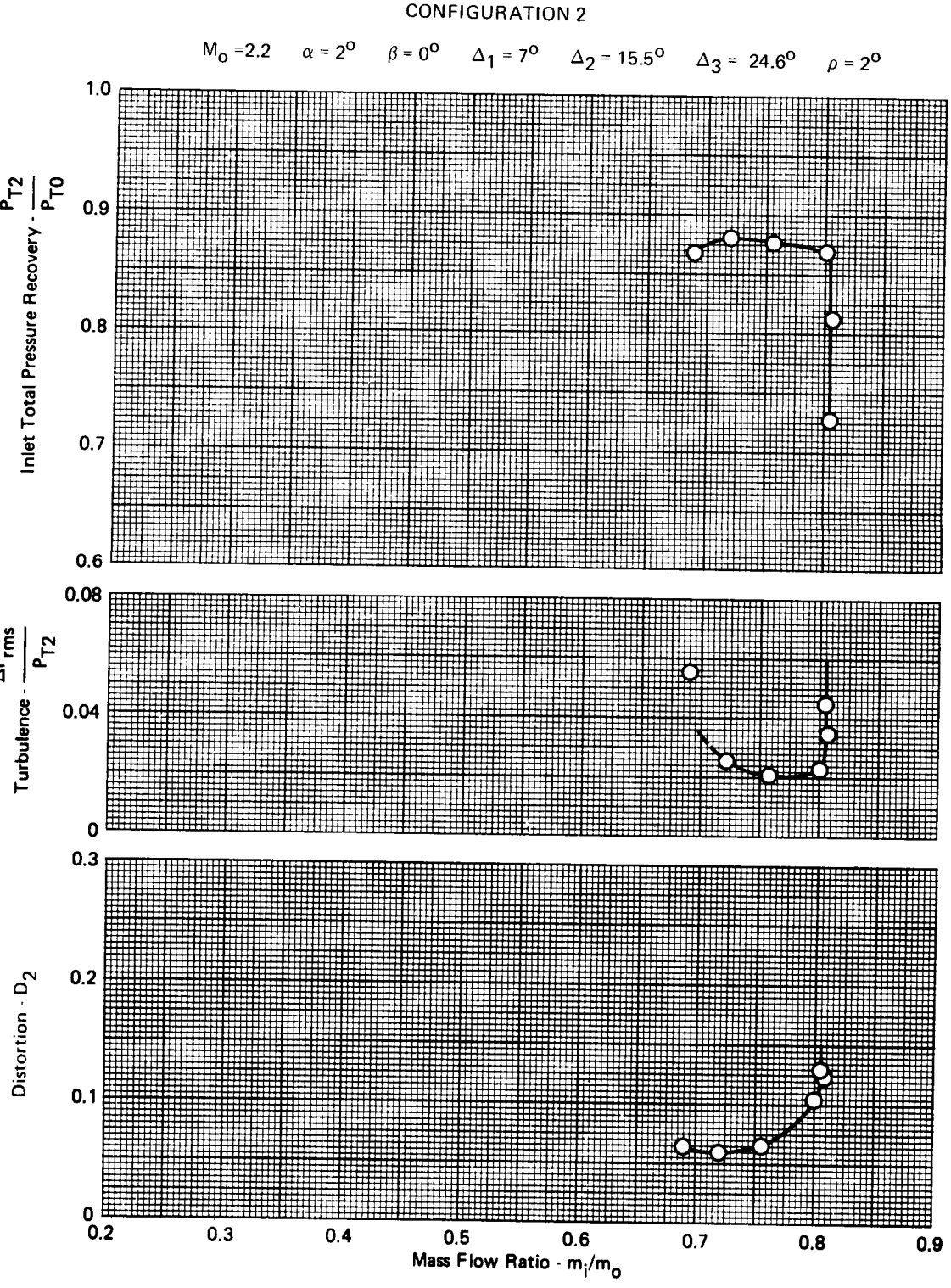

FIGURE A-73- EFFECTS OF ANGLE OF ATTACK ON PRESSURE RECOVERY, TURBULENCE, AND DISTORTION

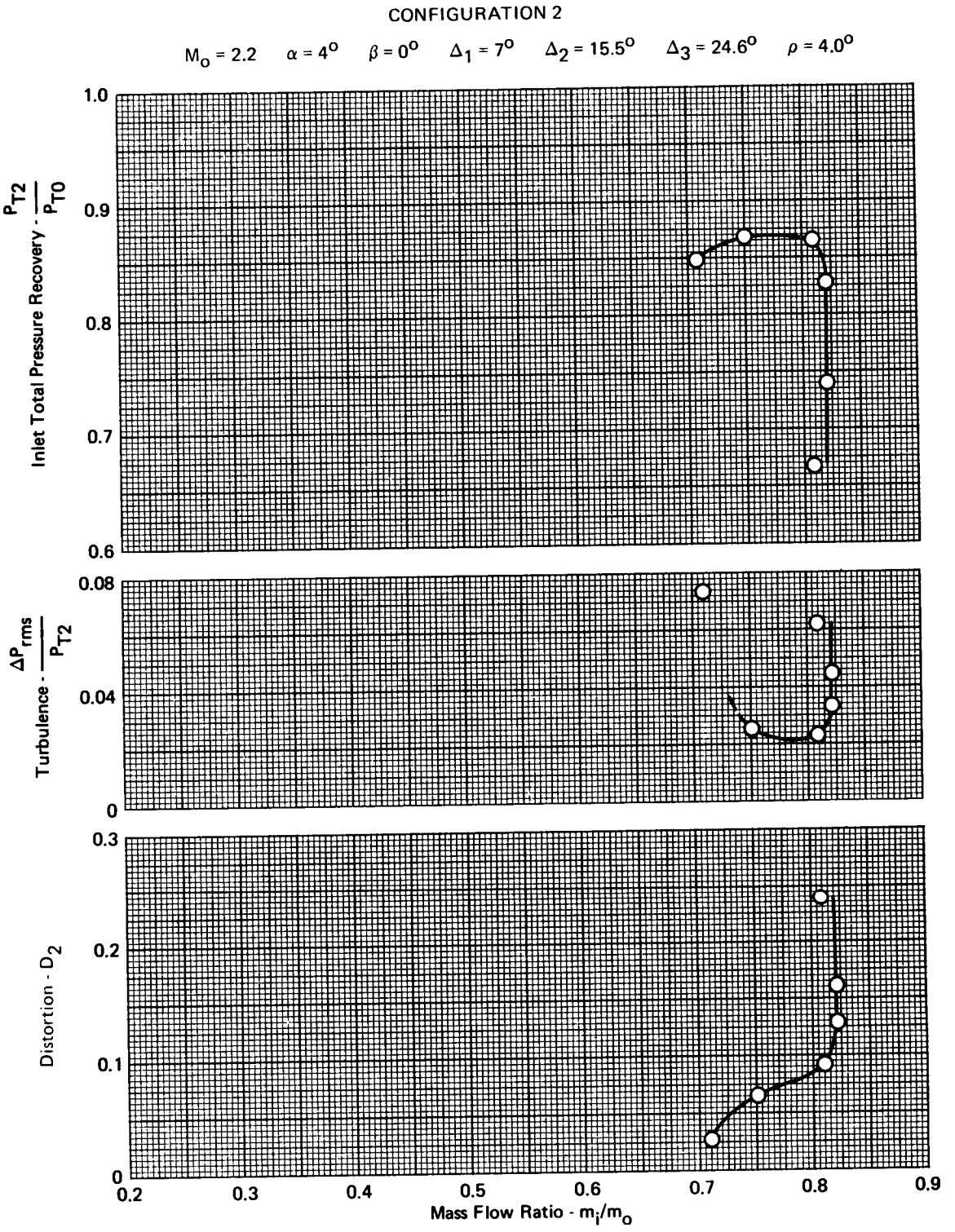

FIGURE A-74 - EFFECTS OF ANGLE OF ATTACK ON PRESSURE RECOVERY, TURBULENCE, AND DISTORTION

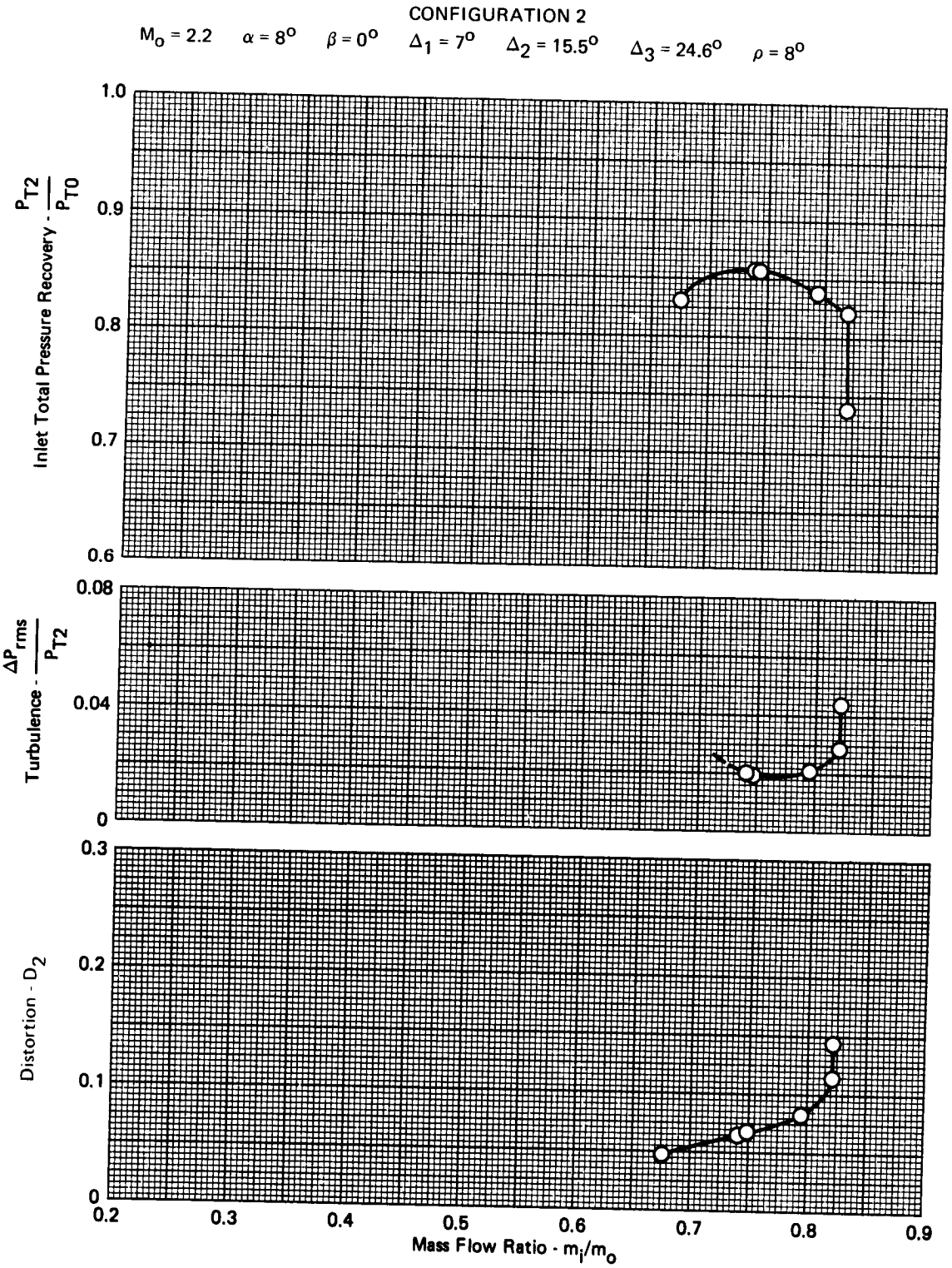

FIGURE A-75 - EFFECTS OF ANGLE OF ATTACK ON PRESSURE RECOVERY, TURBULENCE, AND DISTORTION

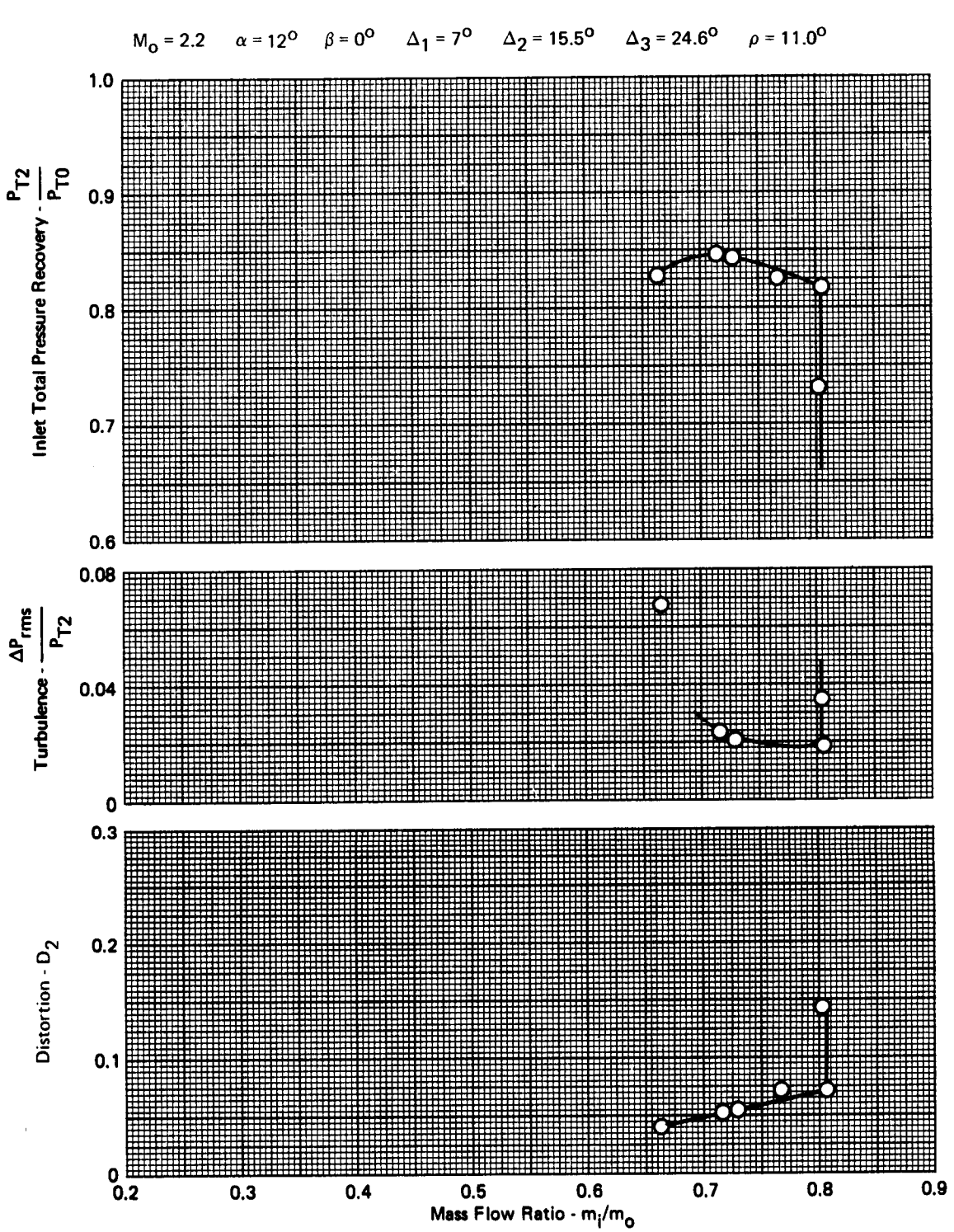

FIGURE A-76- EFFECTS OF ANGLE OF ATTACK ON PRESSURE RECOVERY, TURBULENCE, AND DISTORTION

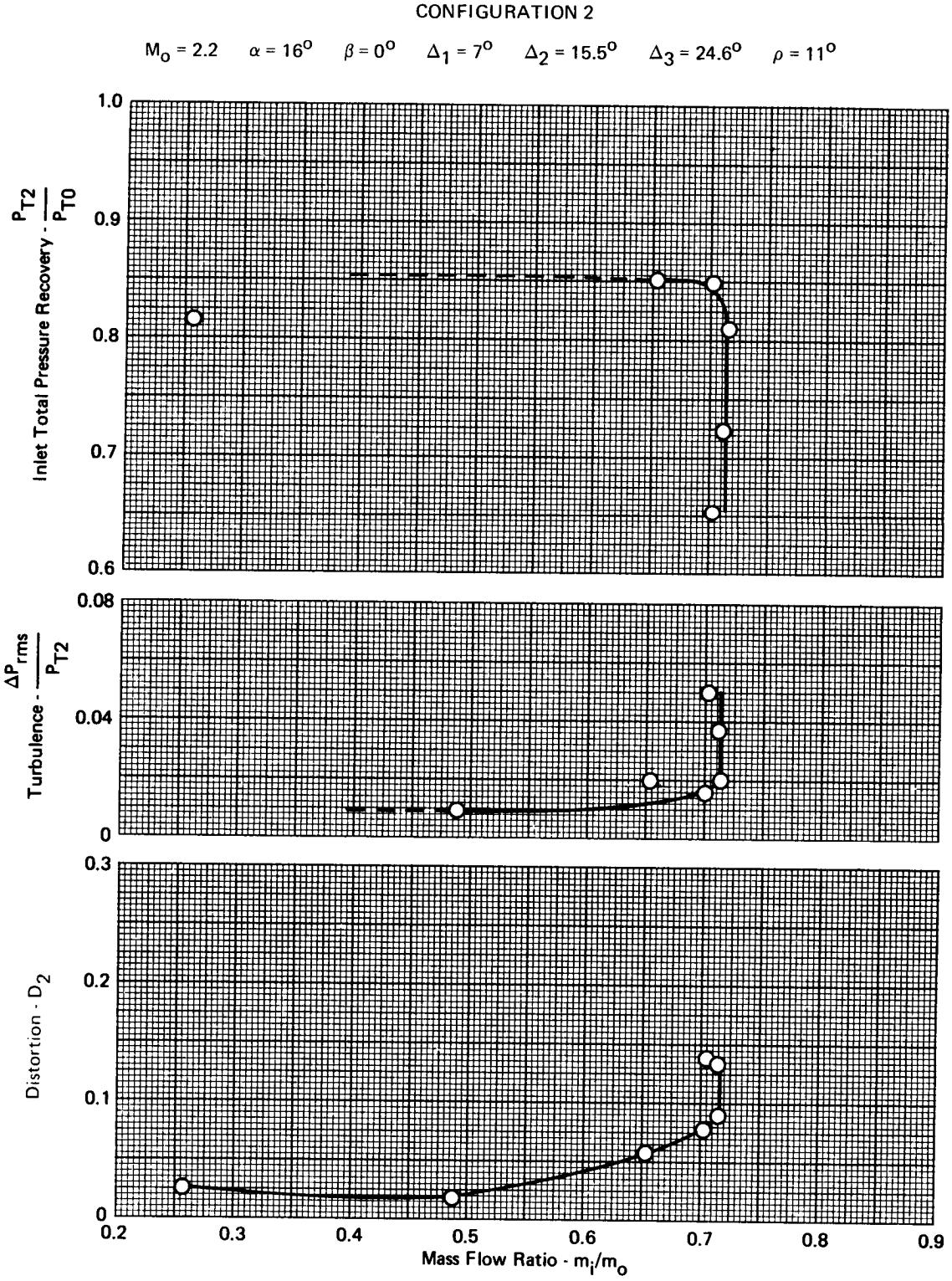

FIGURE A-77 - EFFECTS OF ANGLE OF ATTACK ON PRESSURE RECOVERY TURBULENCE, AND DISTORTION

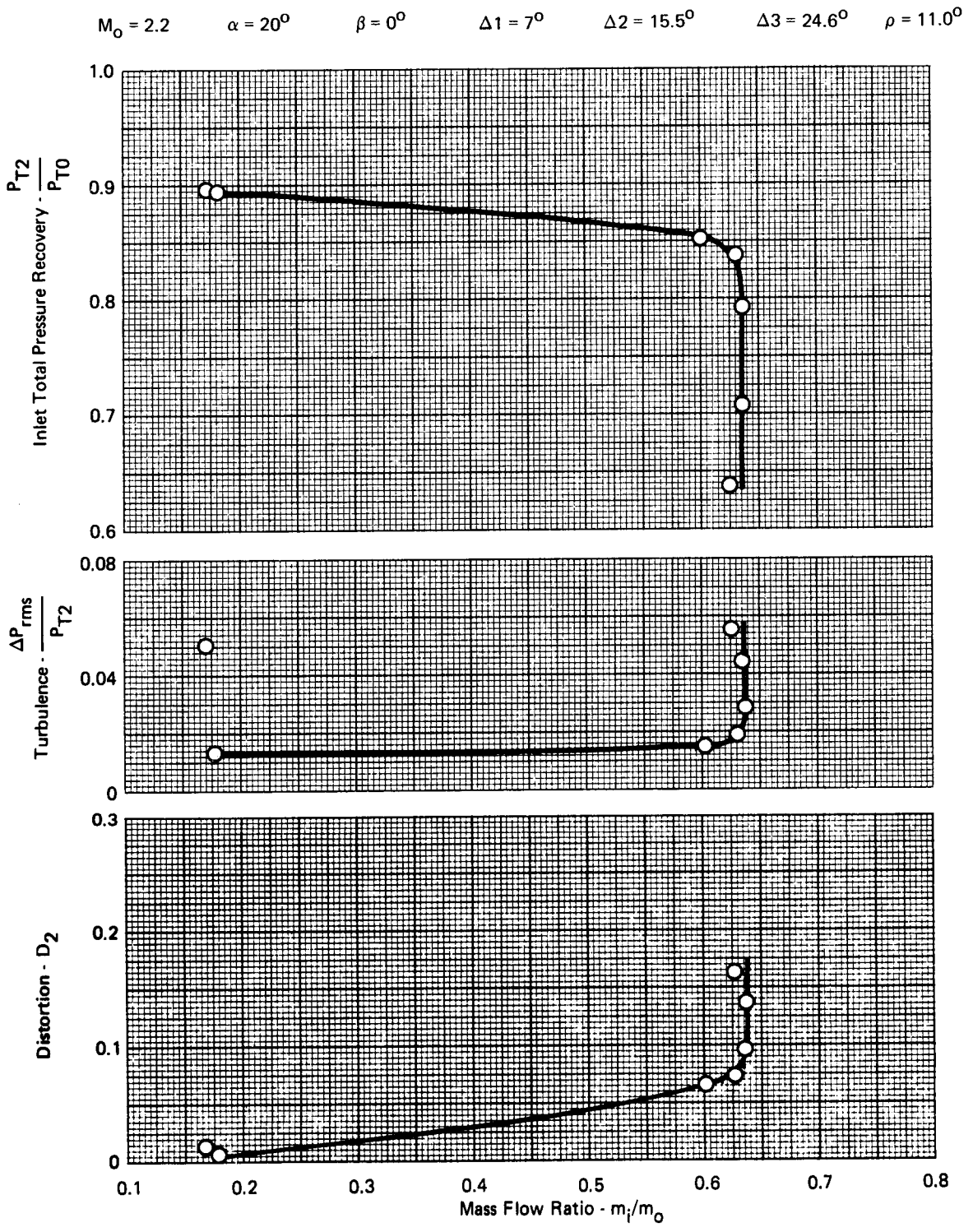

FIGURE A-78 - EFFECTS OF ANGLE OF ATTACK ON PRESSURE RECOVERY, TURBULENCE, AND DISTORTION

GP73-0449-54

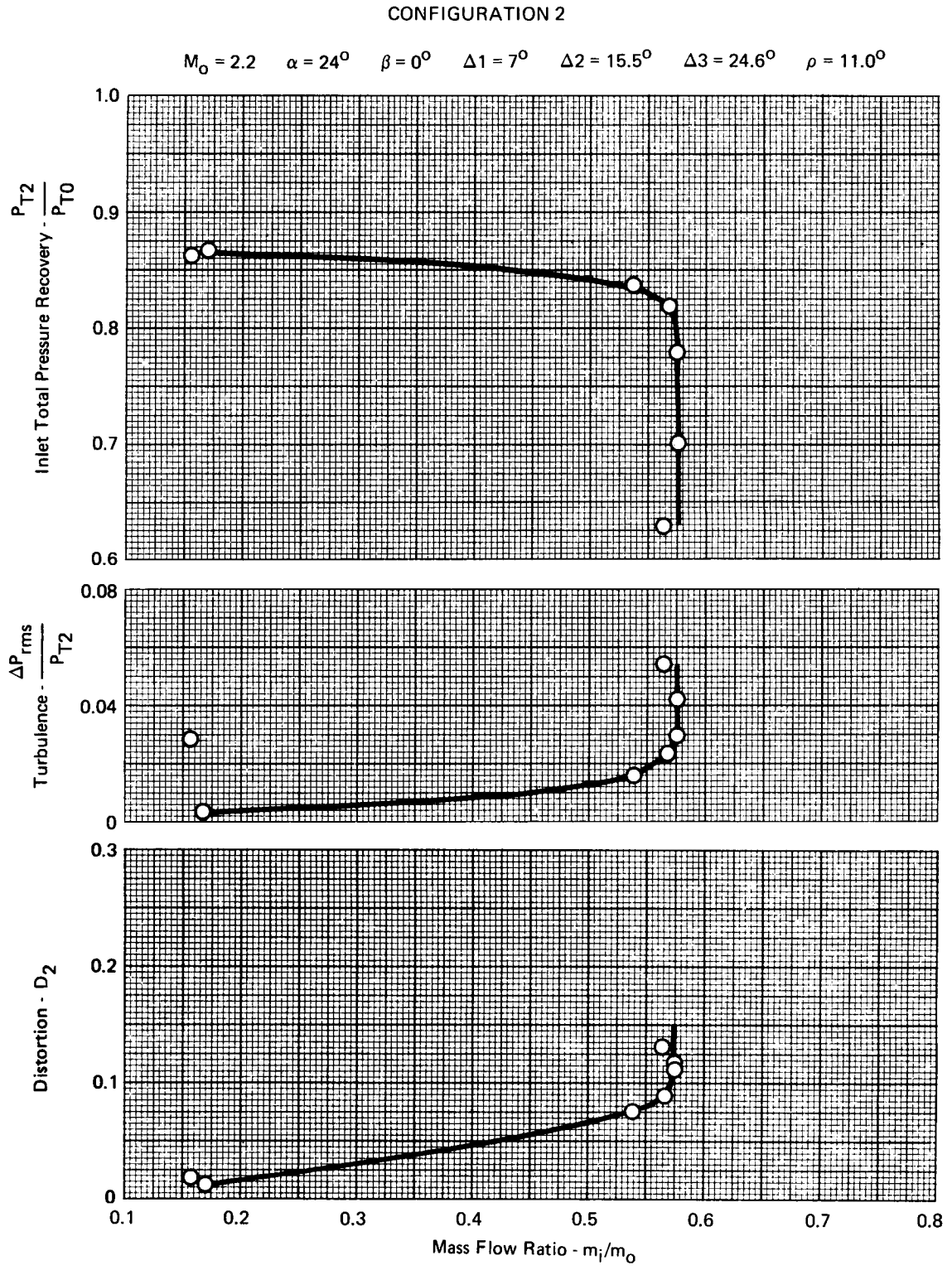

FIGURE A-79 - EFFECTS OF ANGLE OF ATTACK ON PRESSURE RECOVERY, TURBULENCE, AND DISTORTION

GP73-0449-55

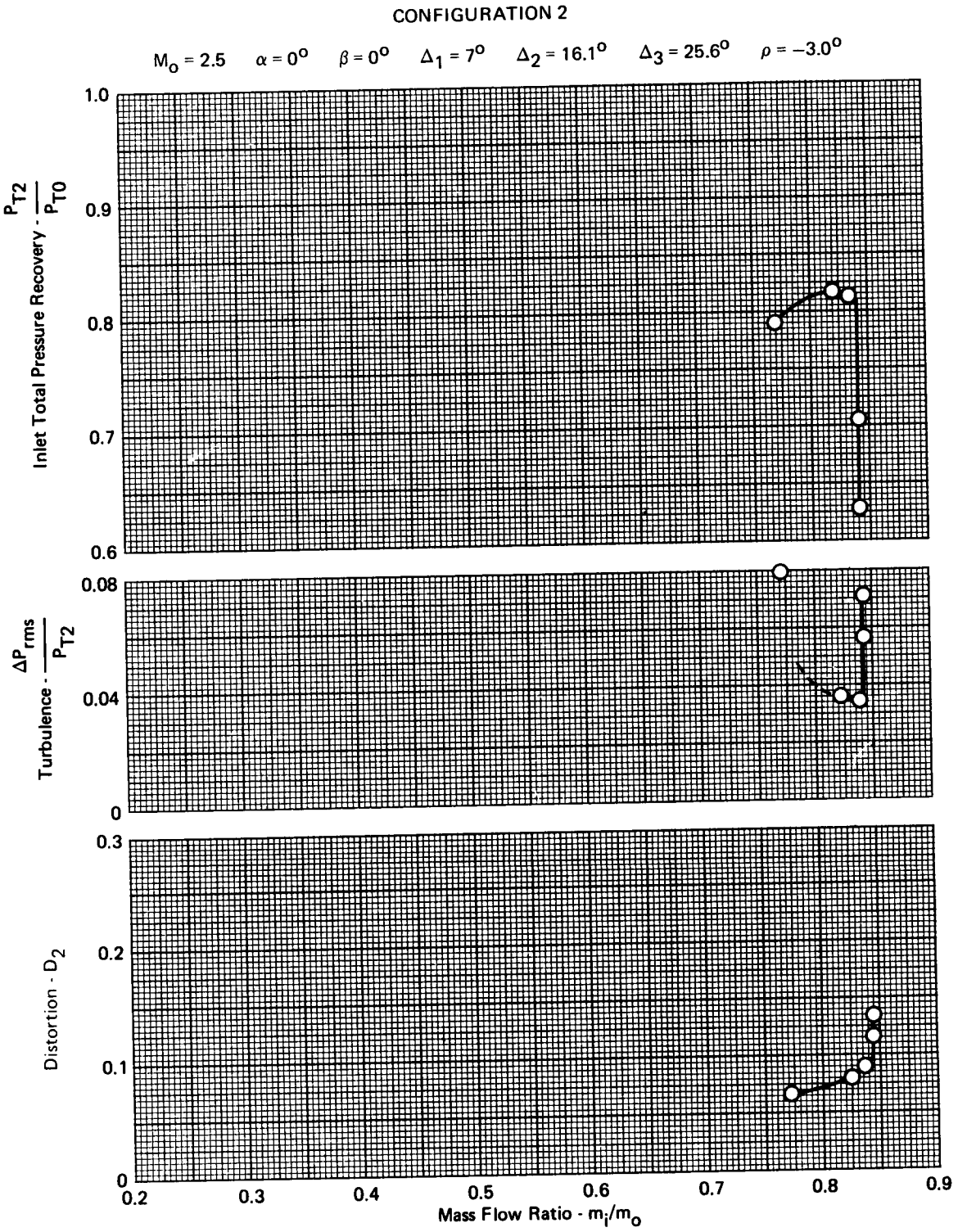

FIGURE A-80 - EFFECTS OF ANGLE OF ATTACK ON PRESSURE RECOVERY, TURBULENCE, AND DISTORTION

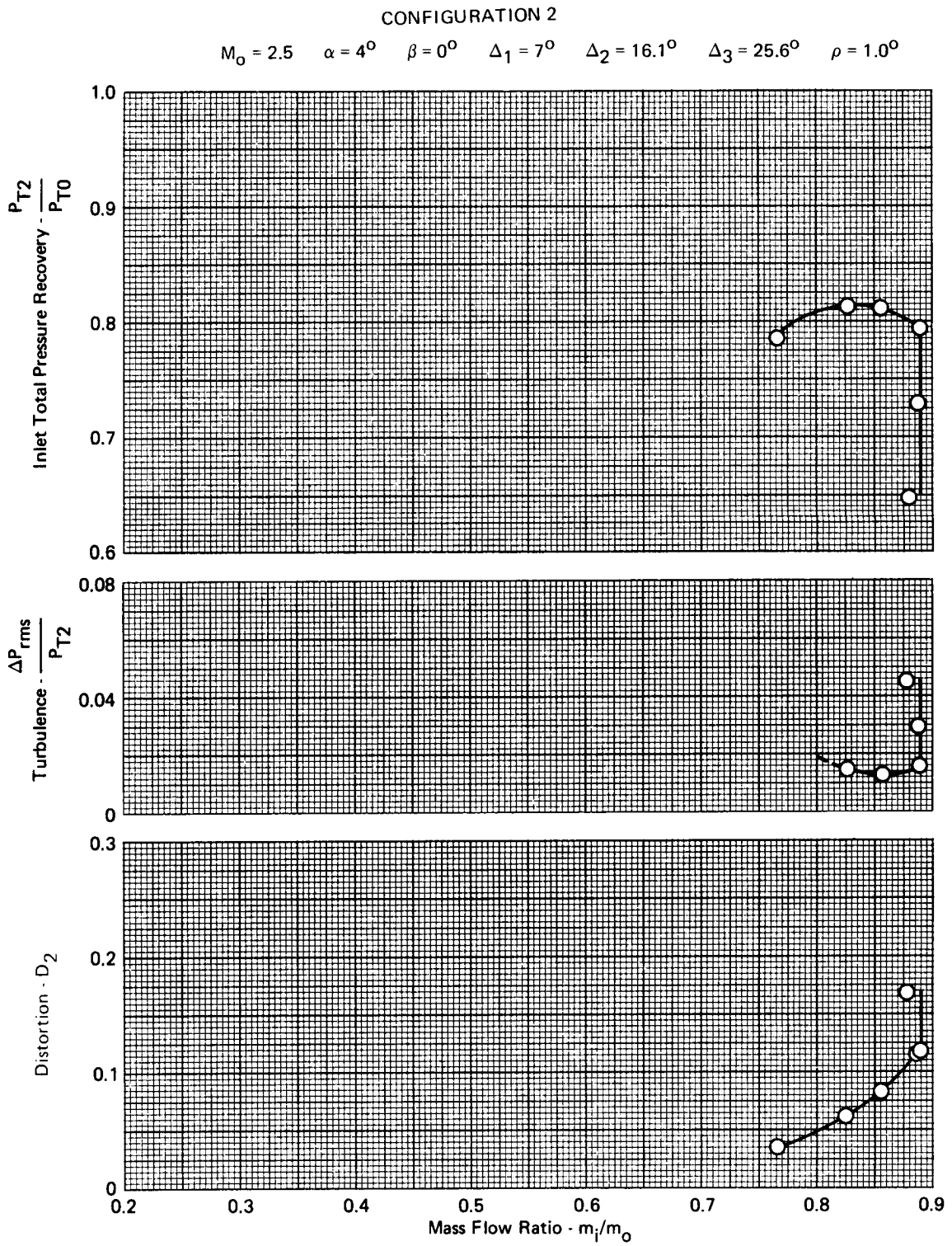

FIGURE A-81 - EFFECTS OF ANGLE OF ATTACK ON PRESSURE RECOVERY, TURBULENCE, AND DISTORTION

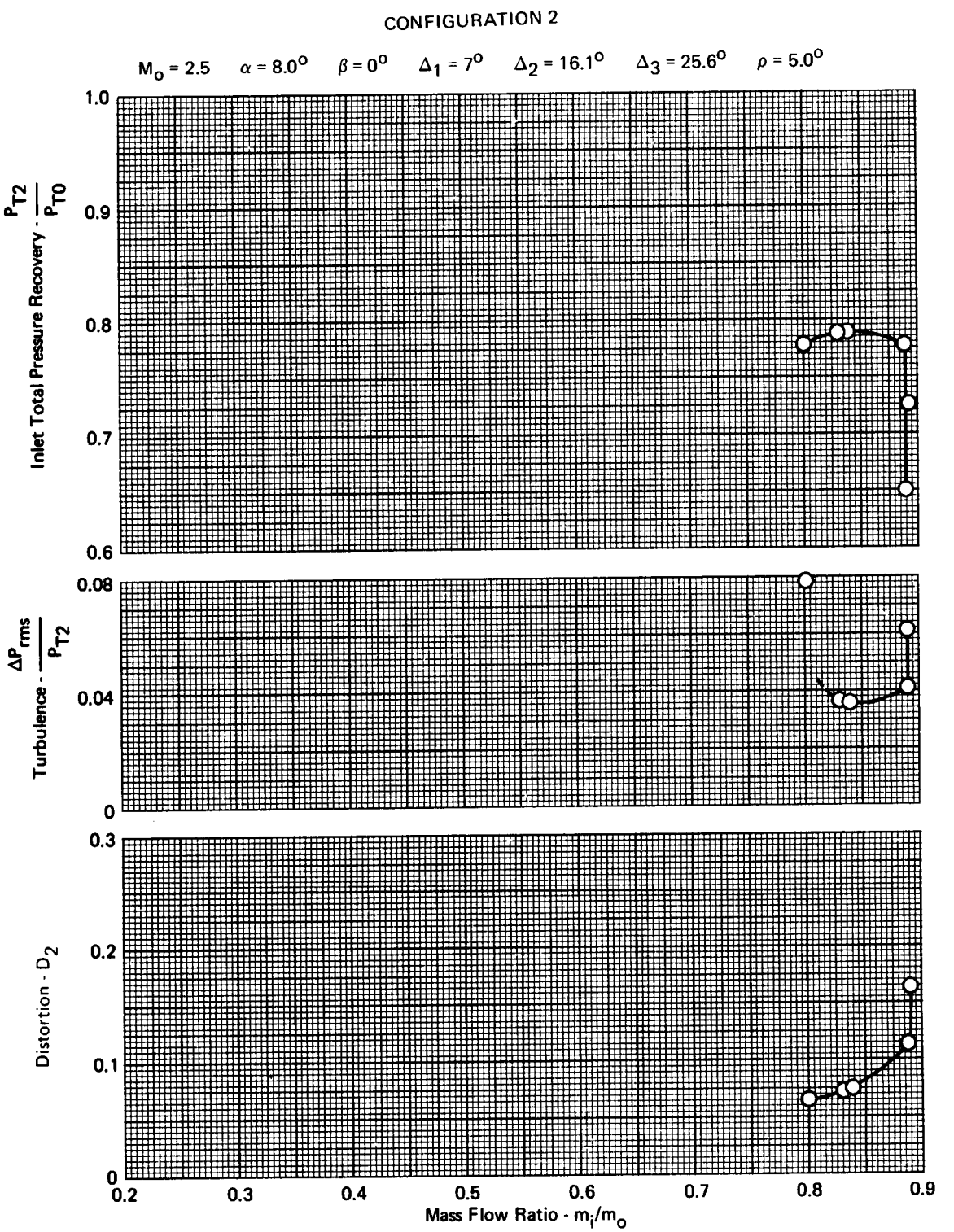

FIGURE A-82 - EFFECTS OF ANGLE OF ATTACK ON PRESSURE RECOVERY, TURBULENCE, AND DISTORTION

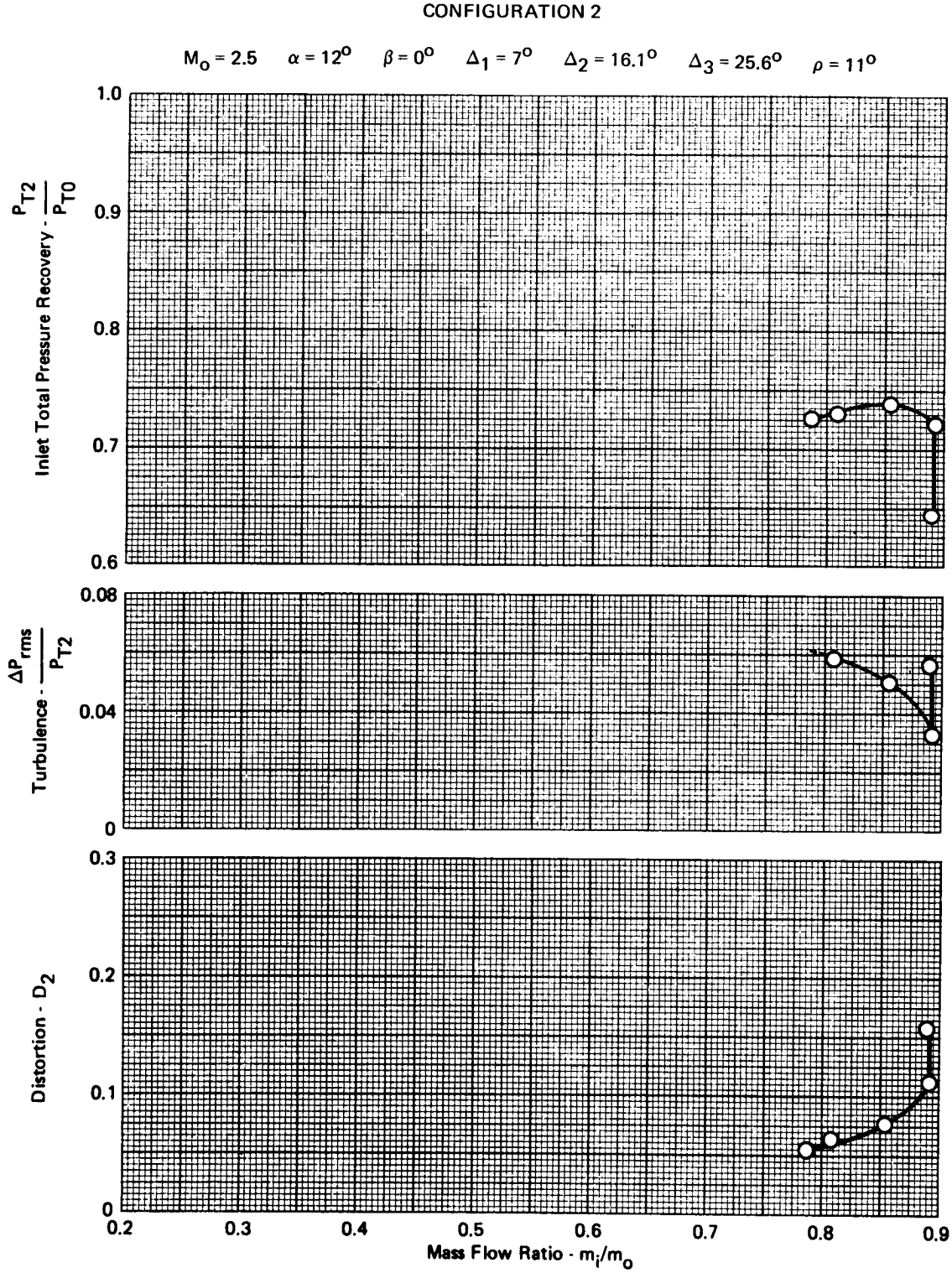

FIGURE A-83 - EFFECTS OF ANGLE OF ATTACK ON PRESSURE RECOVERY, TURBULENCE, AND DISTORTION

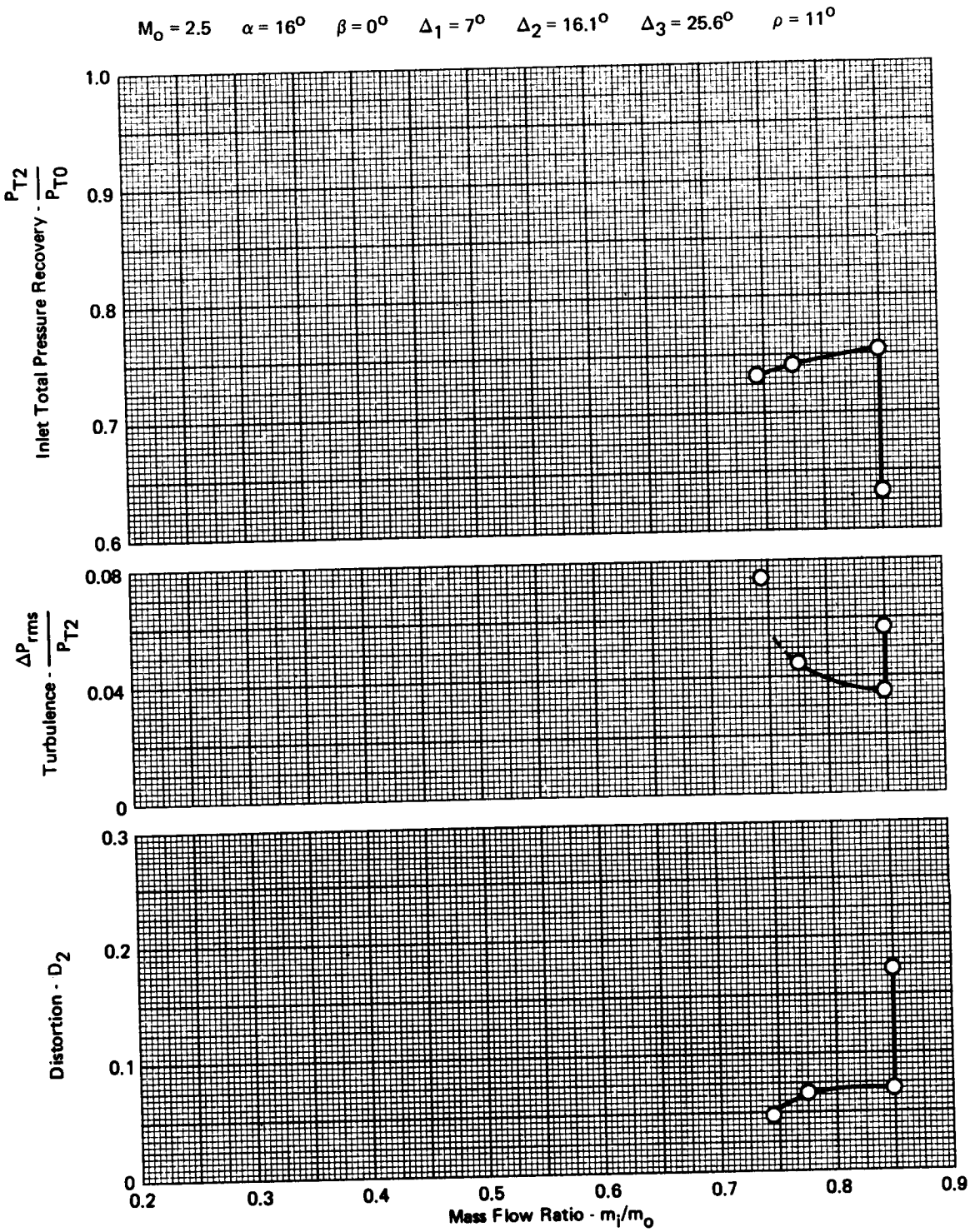

FIGURE A-84 - EFFECTS OF ANGLE OF ATTACK ON PRESSURE RECOVERY, TURBULENCE, AND DISTORTION

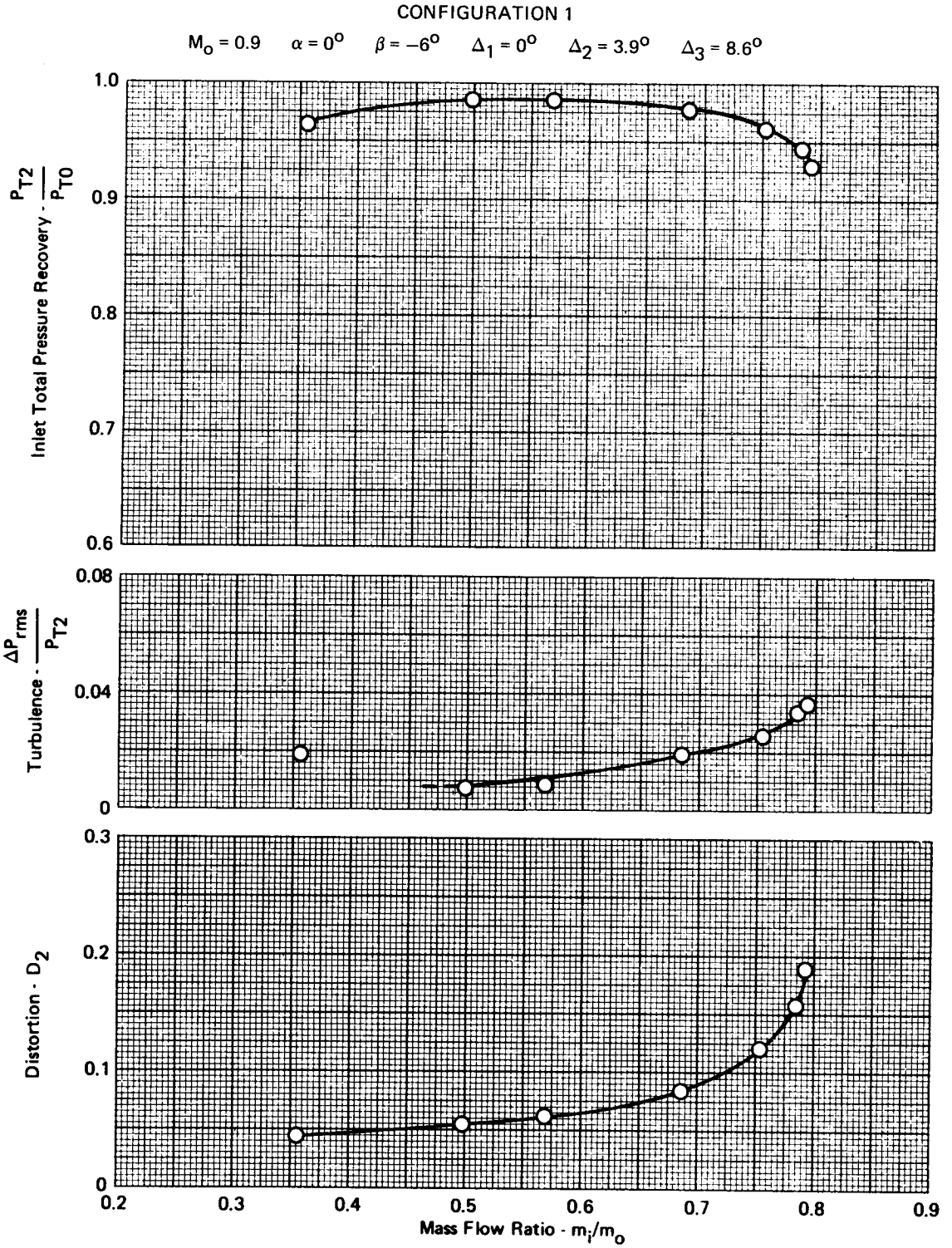

FIGURE A-85 - EFFECTS OF ANGLE OF SIDESLIP ON PRESSURE RECOVERY, TURBULENCE, AND DISTORTION

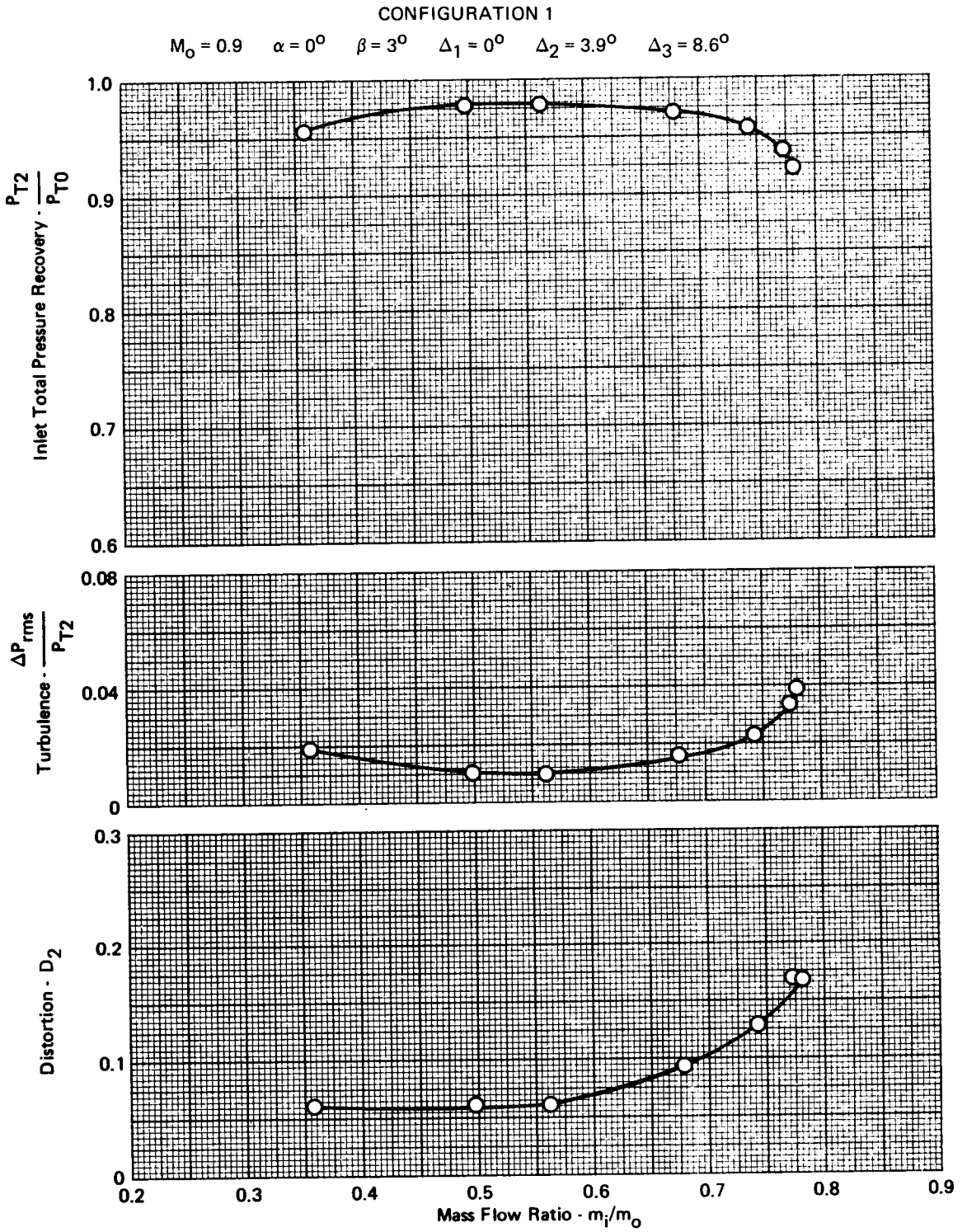

FIGURE A-86 - EFFECTS OF ANGLE OF SIDESLIP ON PRESSURE RECOVERY, TURBULENCE, AND DISTORTION

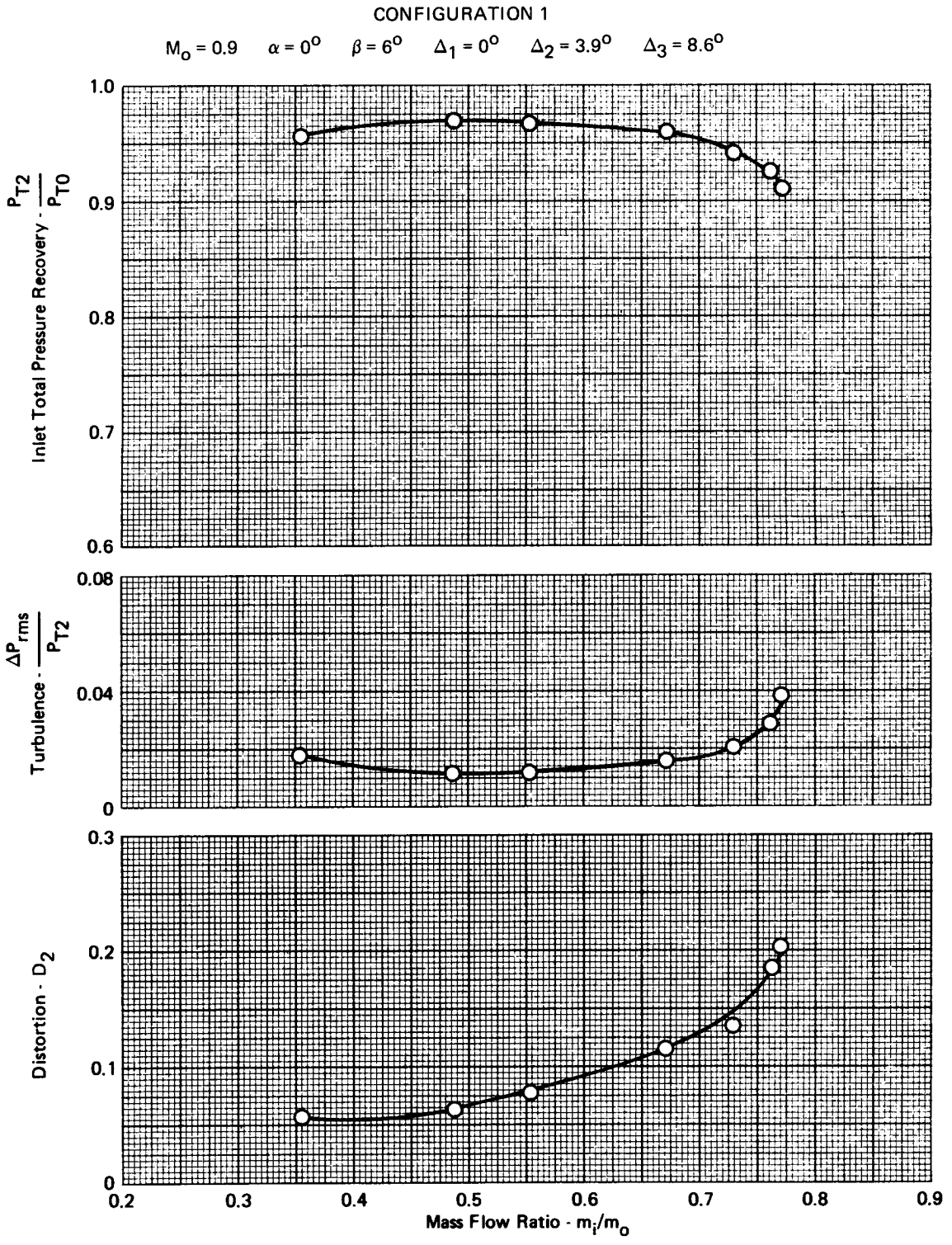

FIGURE A-87 - EFFECTS OF ANGLE OF SIDESLIP ON PRESSURE RECOVERY, TURBULENCE, AND DISTORTION

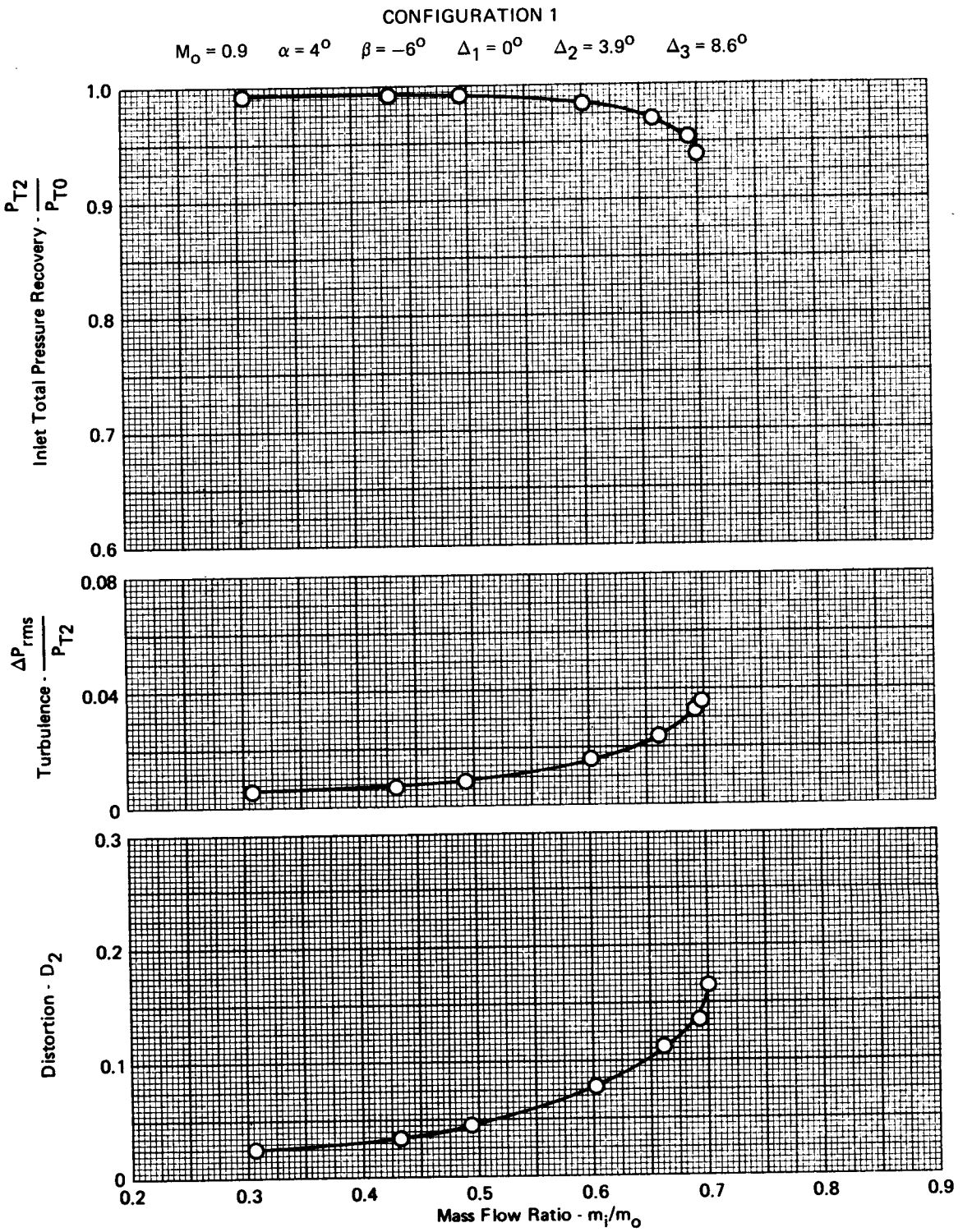

FIGURE A-88 - EFFECTS OF ANGLE OF SIDESLIP ON PRESSURE RECOVERY, TURBULENCE, AND DISTORTION

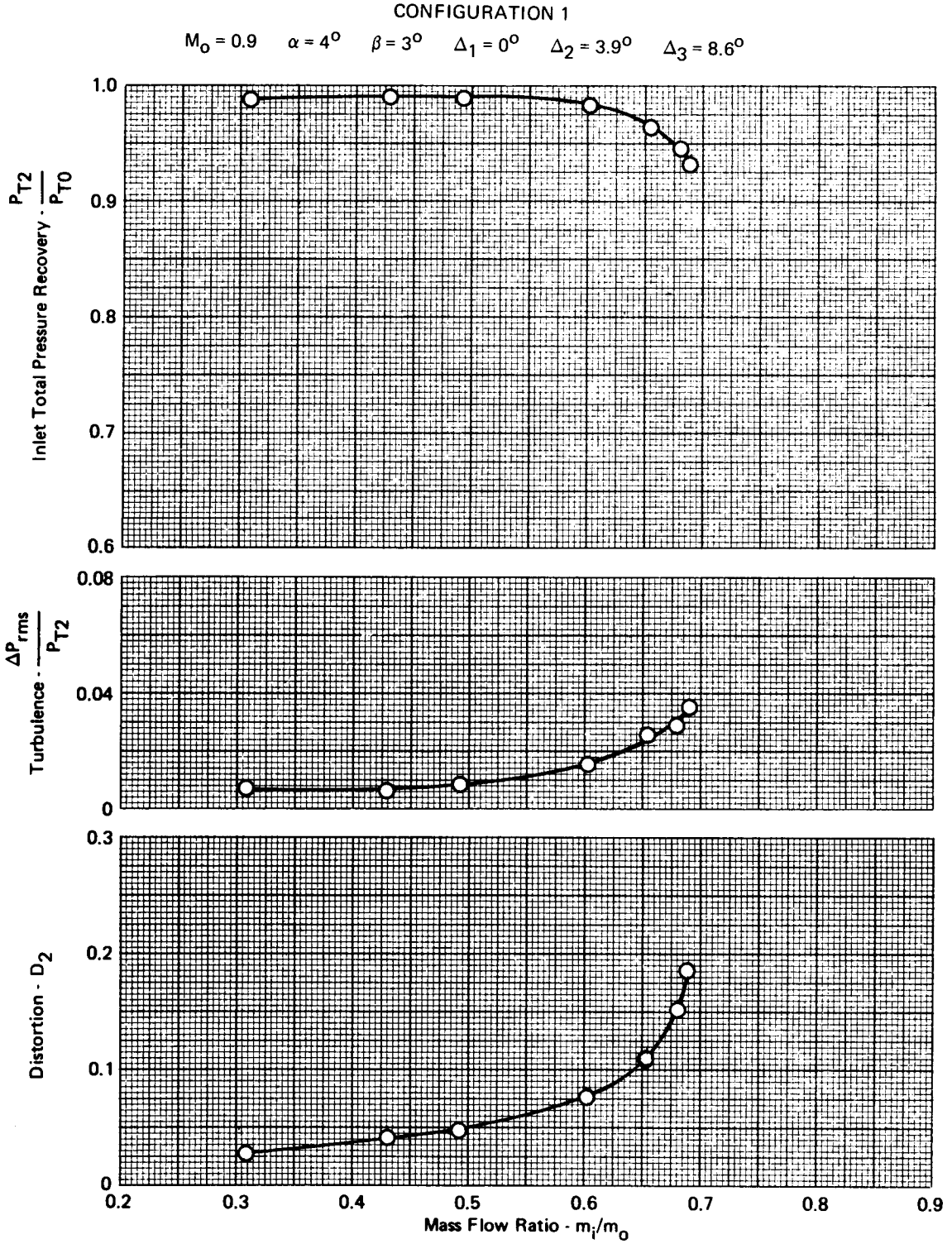

FIGURE A-89 - EFFECTS OF ANGLE OF SIDESLIP ON PRESSURE RECOVERY, TURBULENCE, AND DISTORTION

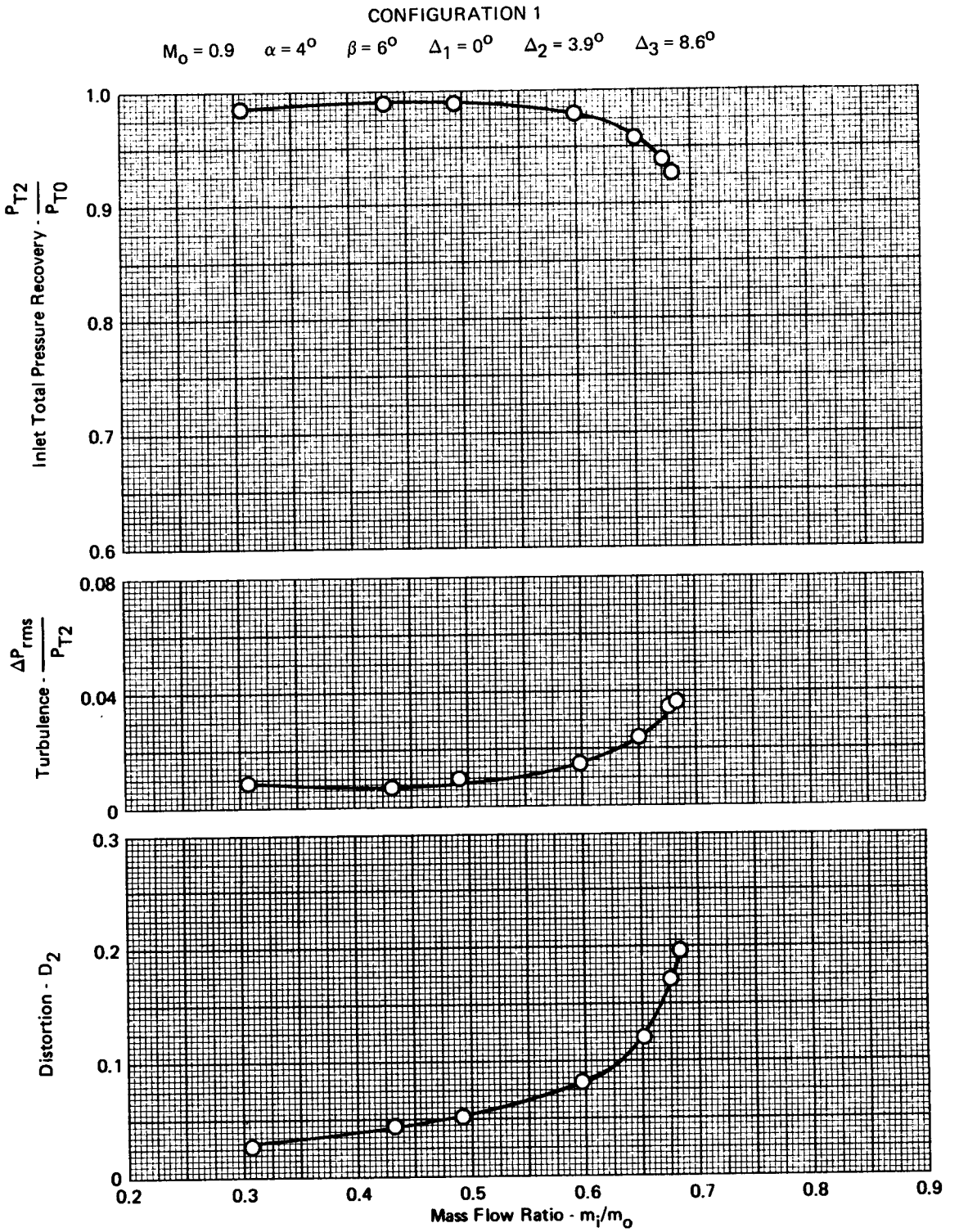

FIGURE A-90 - EFFECTS OF ANGLE OF SIDESLIP ON PRESSURE RECOVERY, TURBULENCE, AND DISTORTION

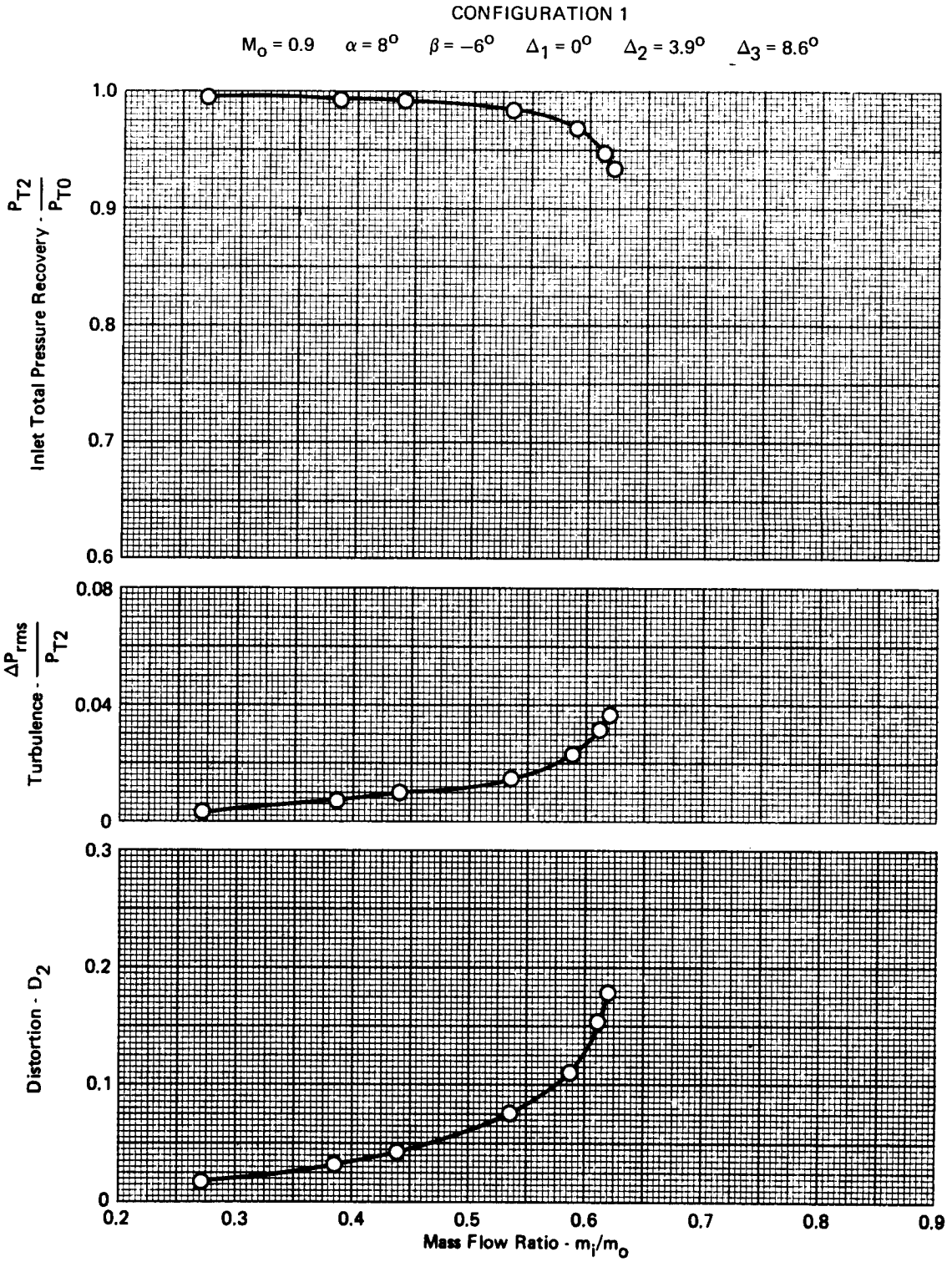

FIGURE A-91 - EFFECTS OF ANGLE OF SIDESLIP ON PRESSURE RECOVERY, TURBULENCE, AND DISTORTION

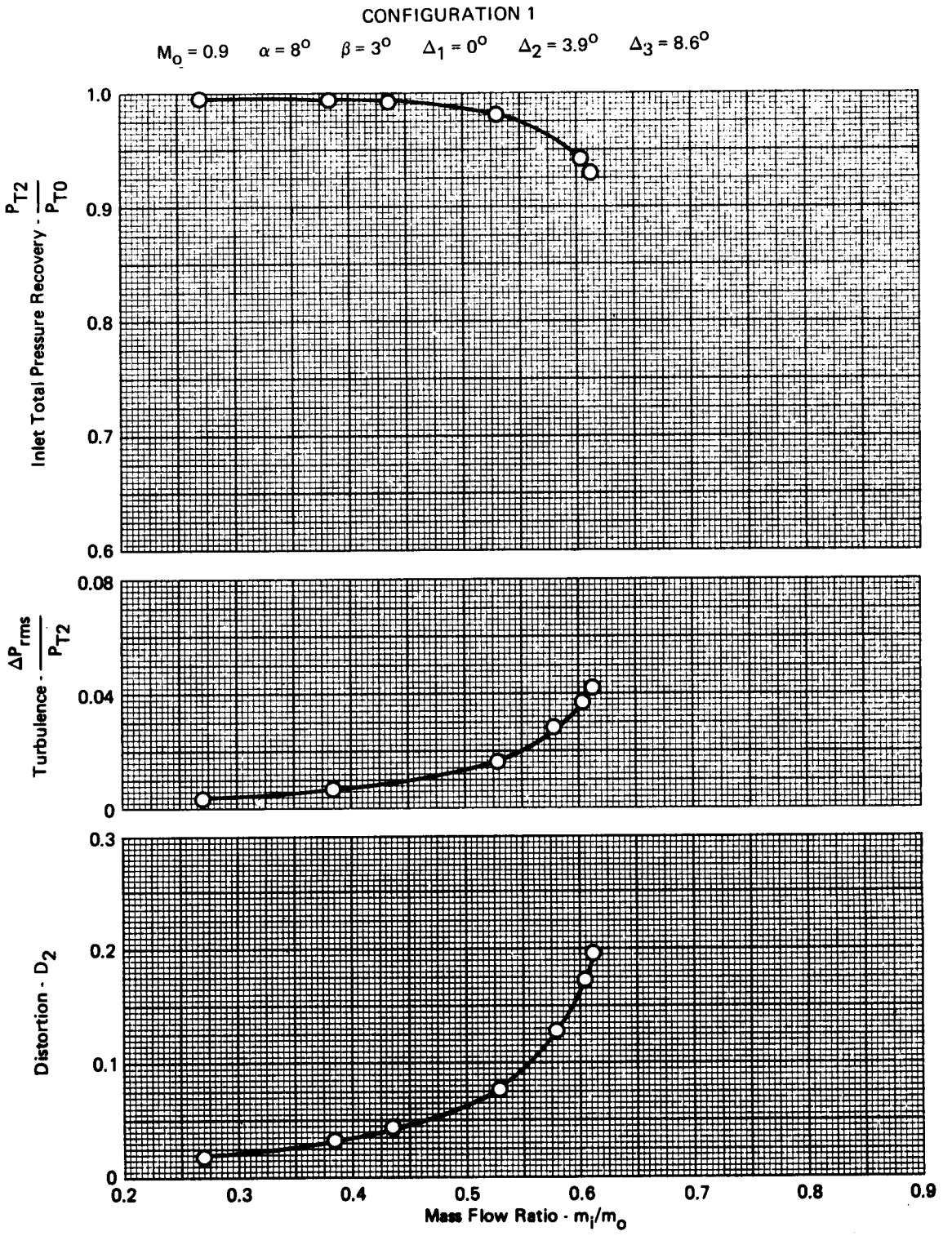

FIGURE A-92 - EFFECTS OF ANGLE OF SIDESLIP ON PRESSURE RECOVERY, TURBULENCE, AND DISTORTION

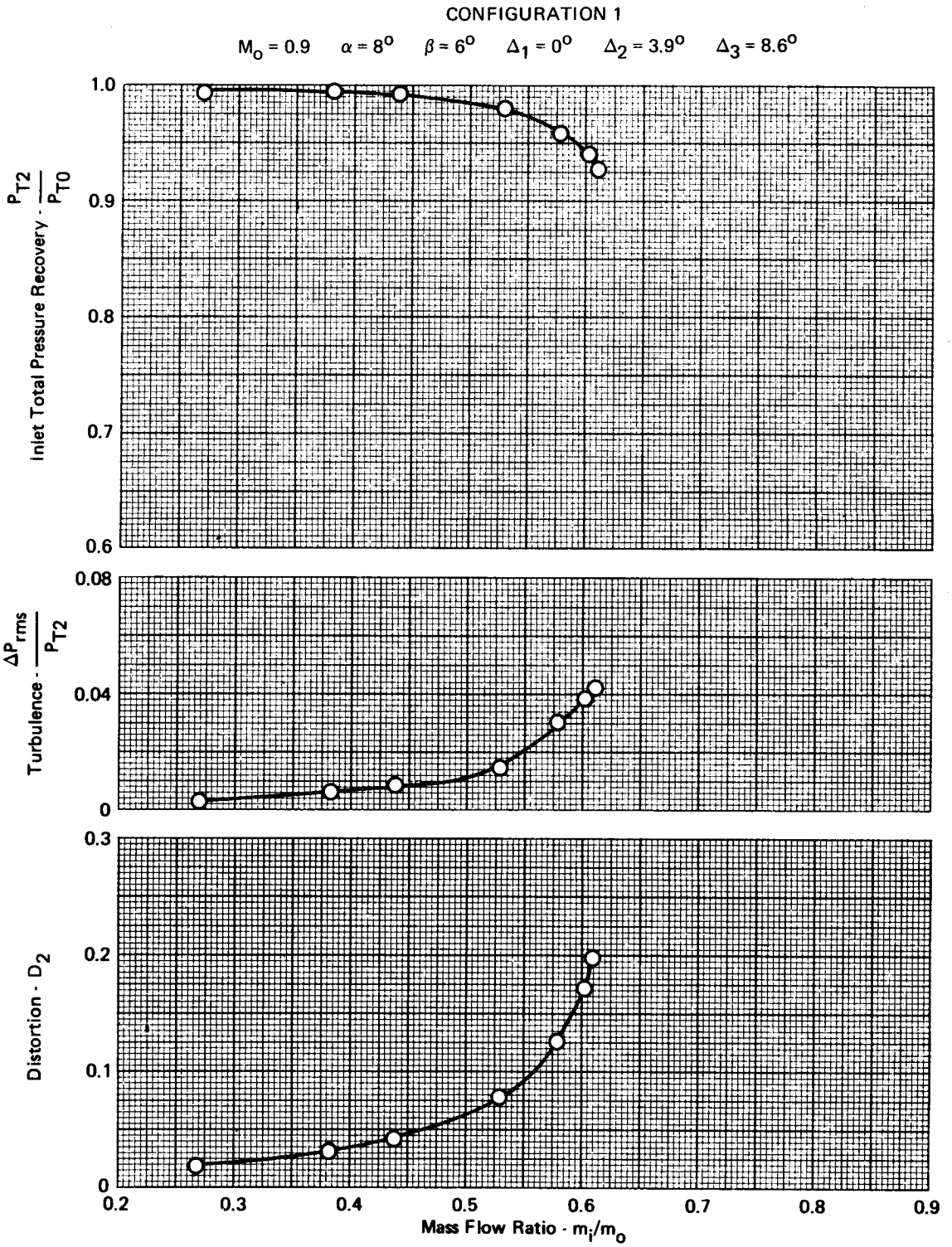

FIGURE A-93 - EFFECTS OF ANGLE OF SIDESLIP ON PRESSURE RECOVERY, TURBULENCE, AND DISTORTION

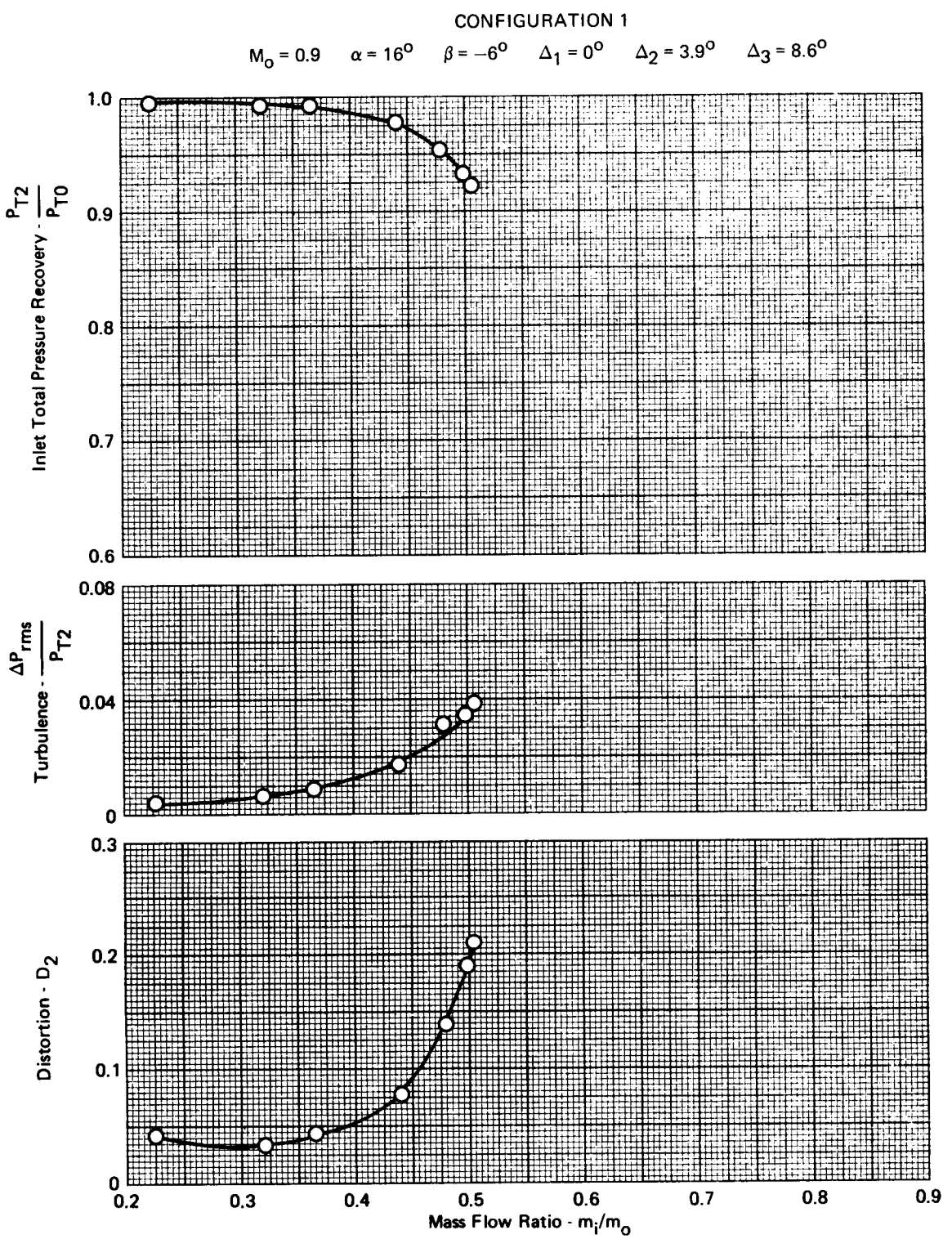

FIGURE A-94 - EFFECTS OF ANGLE OF SIDESLIP ON PRESSURE RECOVERY, TURBULENCE, AND DISTORTION

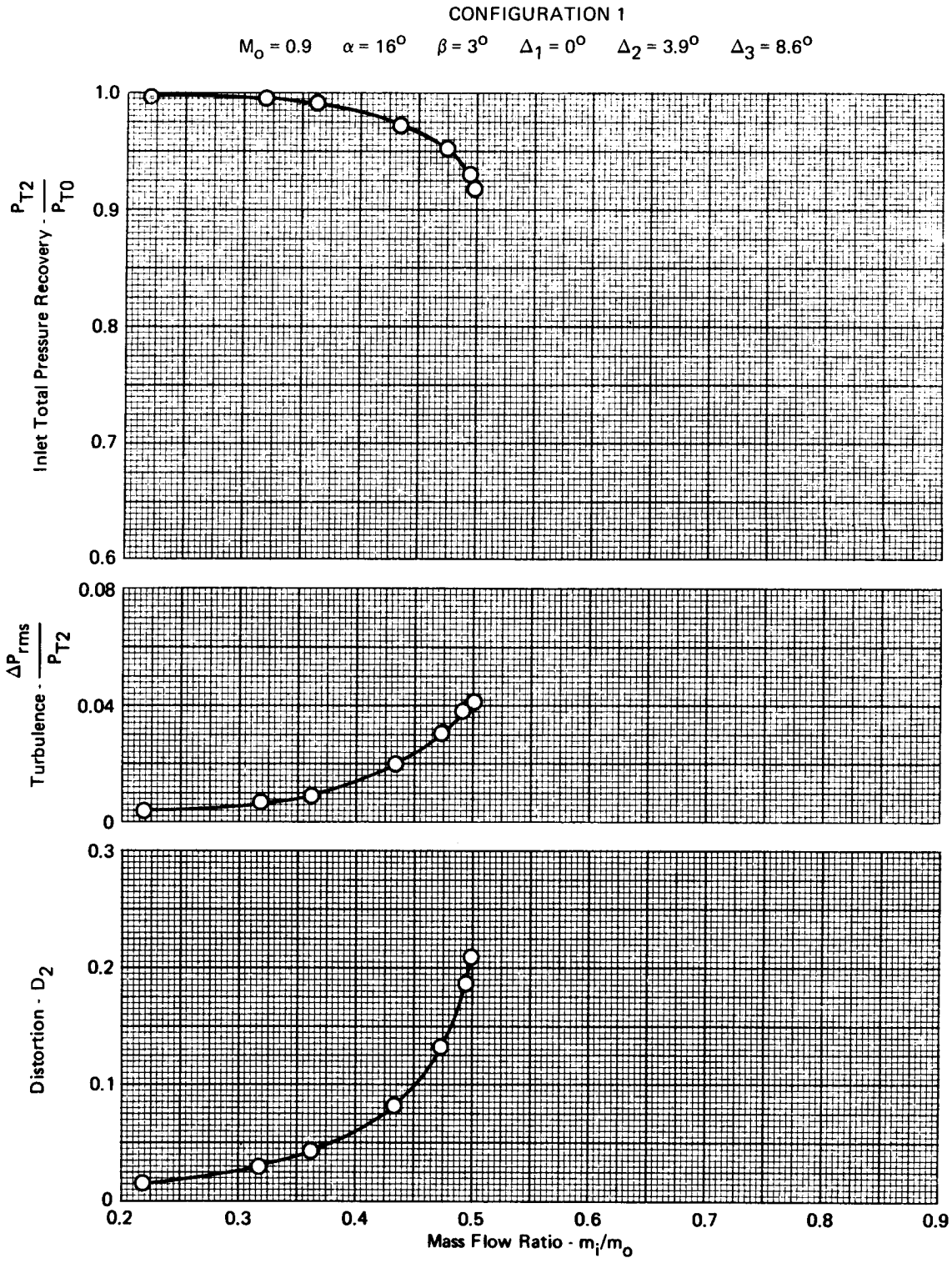

FIGURE A-95 - EFFECTS OF ANGLE OF SIDESLIP ON PRESSURE RECOVERY, TURBULENCE, AND DISTORTION

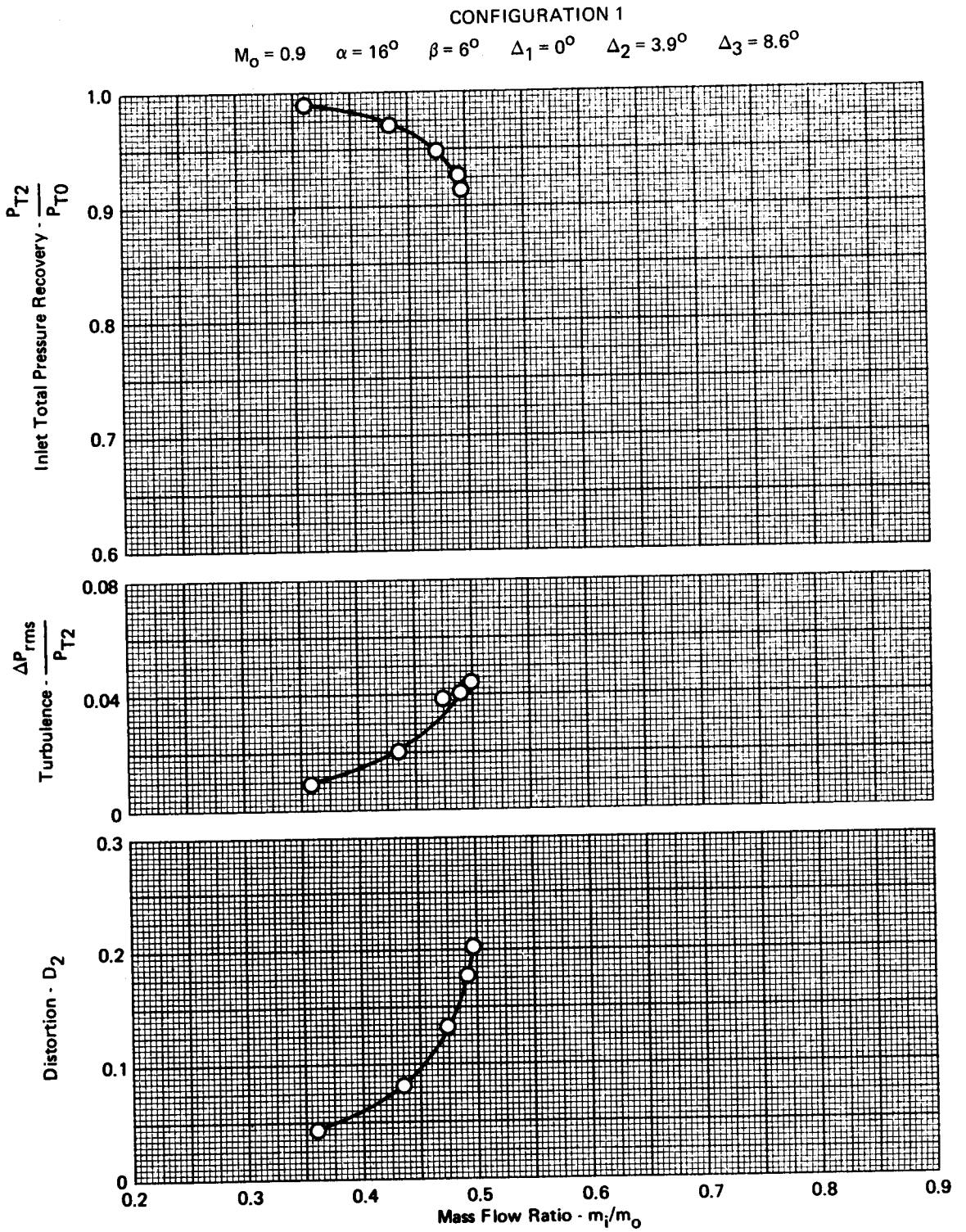

FIGURE A-96 - EFFECTS OF ANGLE OF SIDESLIP ON PRESSURE RECOVERY, TURBULENCE, AND DISTORTION

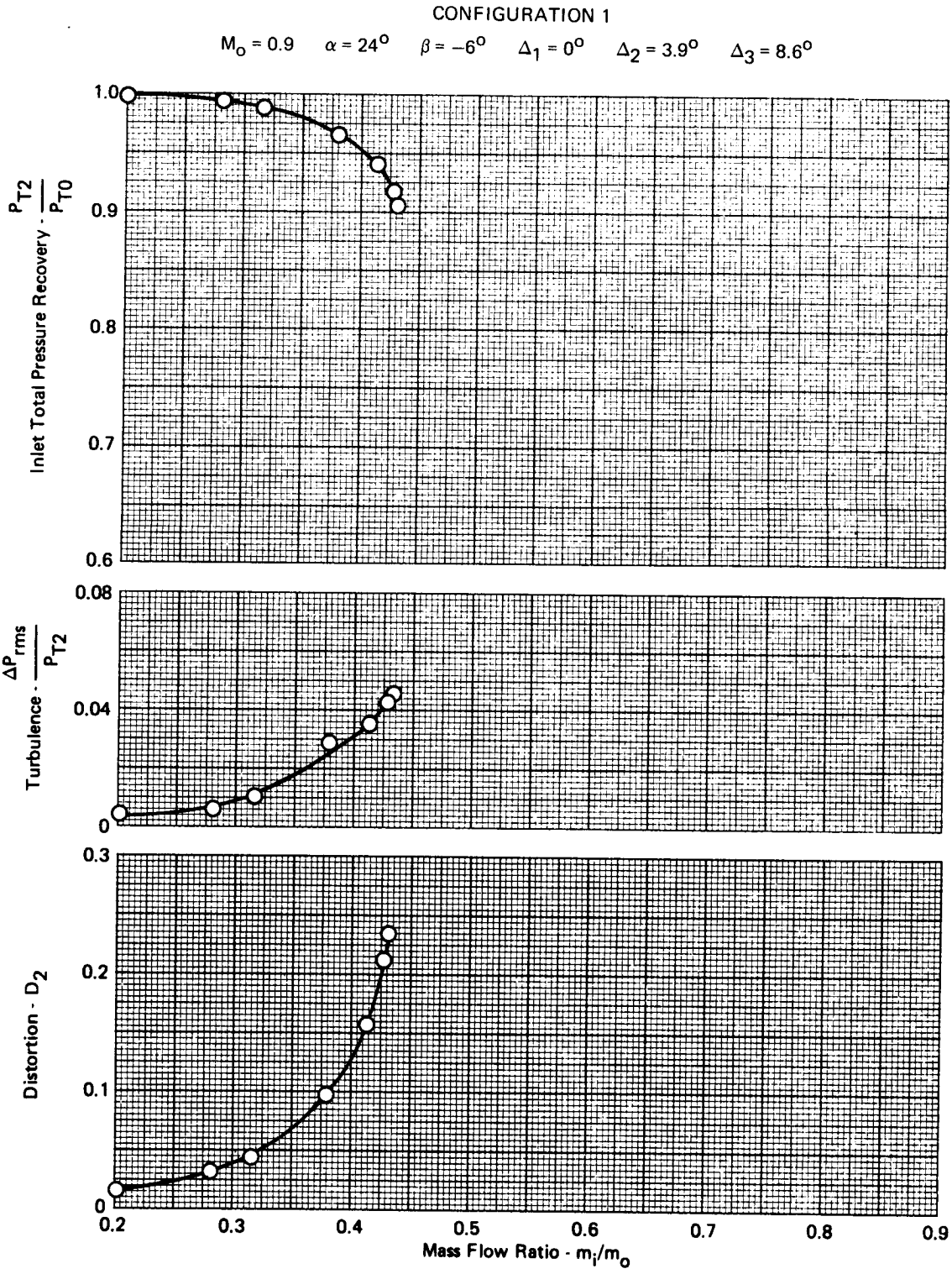

FIGURE A-97 - EFFECTS OF ANGLE OF SIDESLIP ON PRESSURE RECOVERY, TURBULENCE, AND DISTORTION

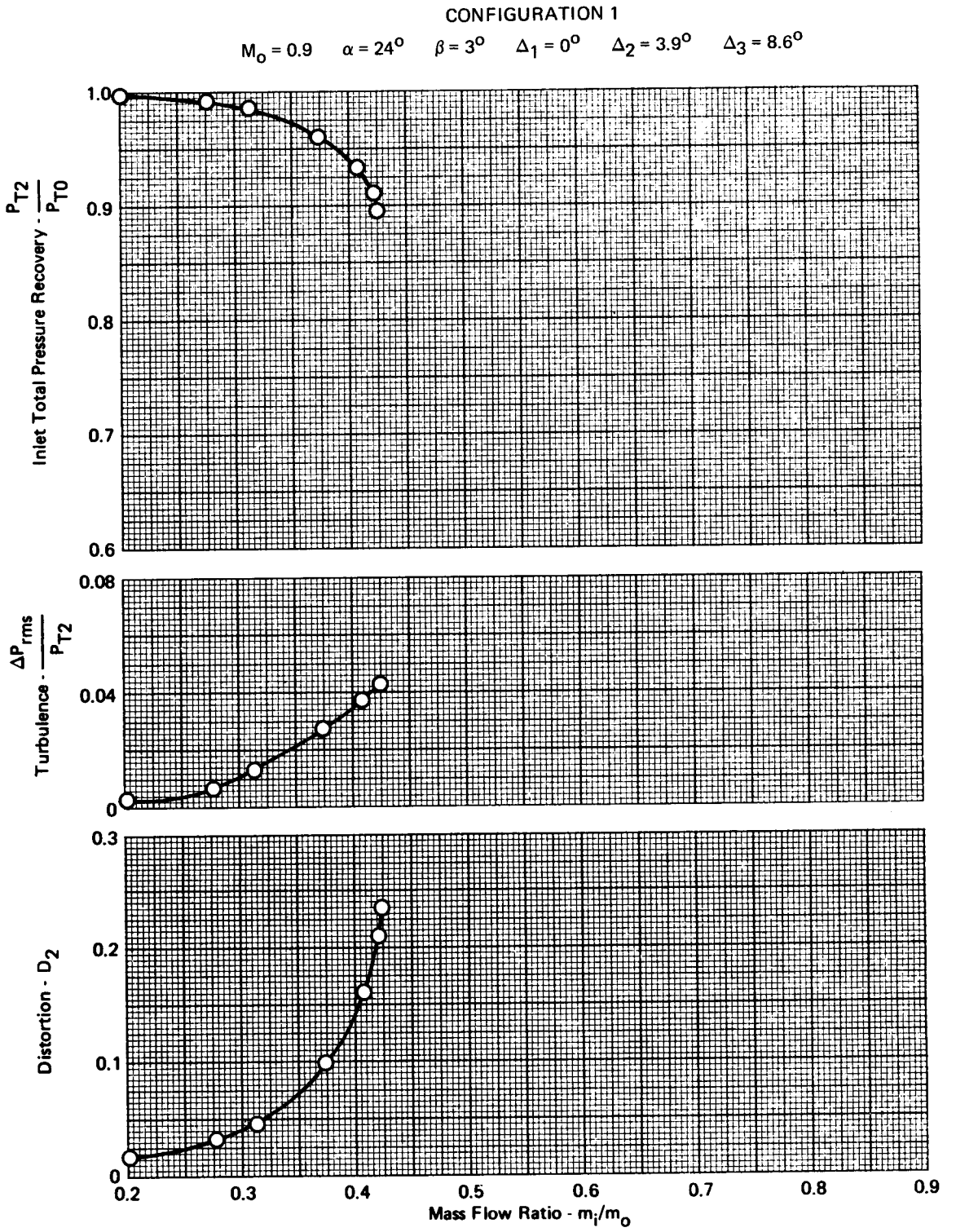

FIGURE A-98 - EFFECTS OF ANGLE OF SIDESLIP ON PRESSURE RECOVERY, TURBULENCE, AND DISTORTION

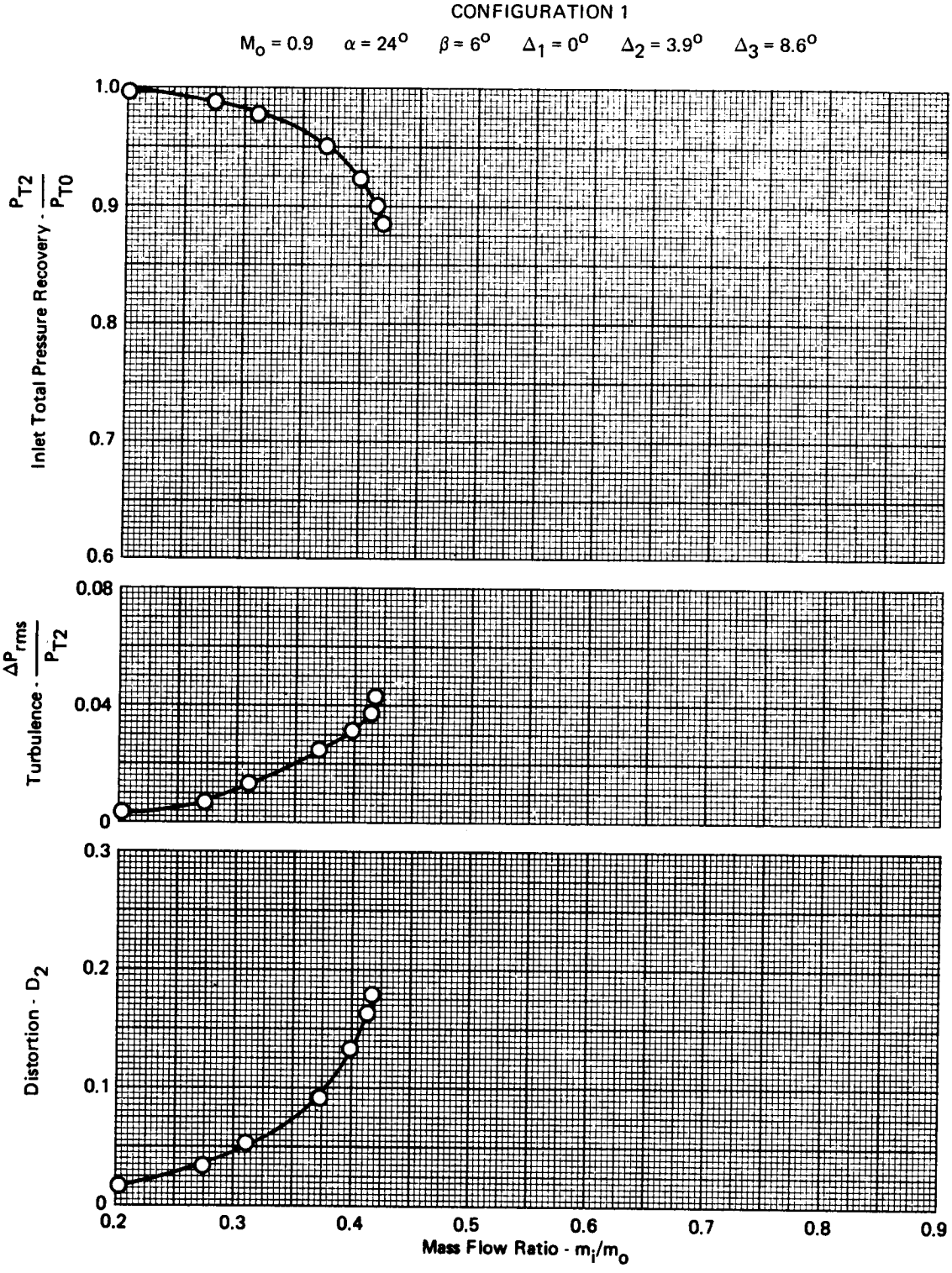

FIGURE A-99 - EFFECTS OF ANGLE OF SIDESLIP ON PRESSURE RECOVERY, TURBULENCE, AND DISTORTION

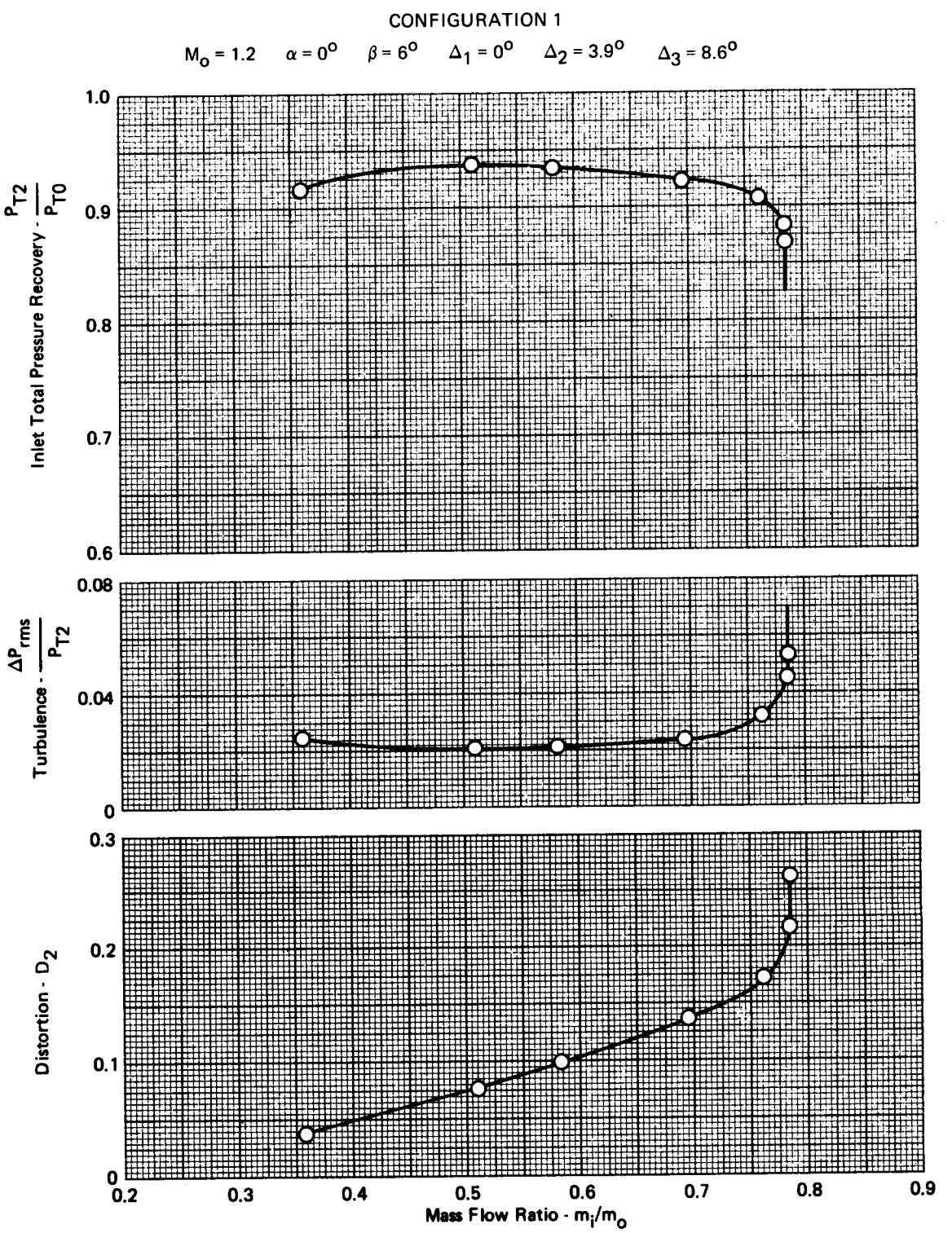

FIGURE A-100 - EFFECTS OF ANGLE OF SIDESLIP ON PRESSURE RECOVERY, TURBULENCE, AND DISTORTION

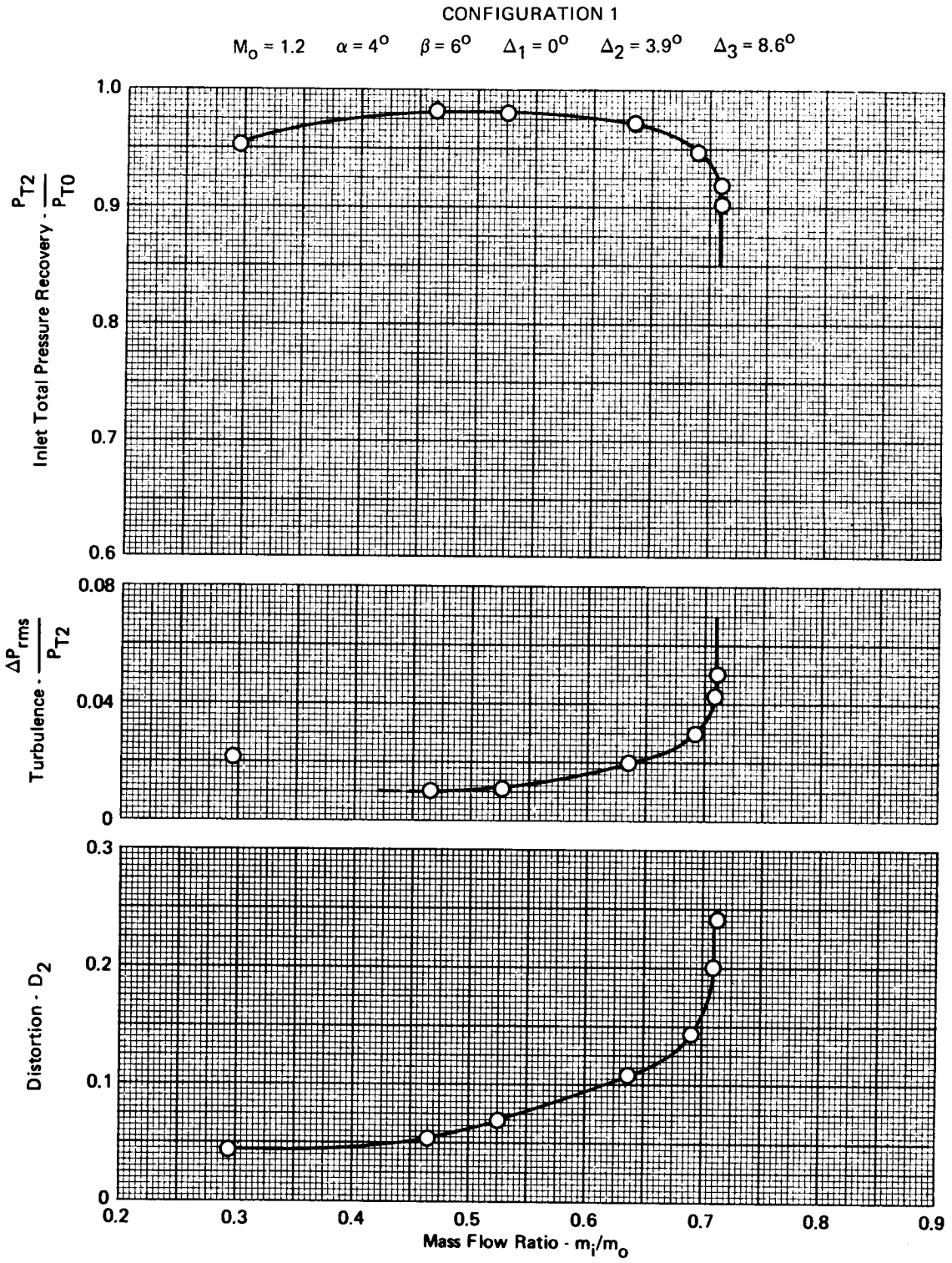

FIGURE A-101- EFFECTS OF ANGLE OF SIDESLIP ON PRESSURE RECOVERY, TURBULENCE, AND DISTORTION

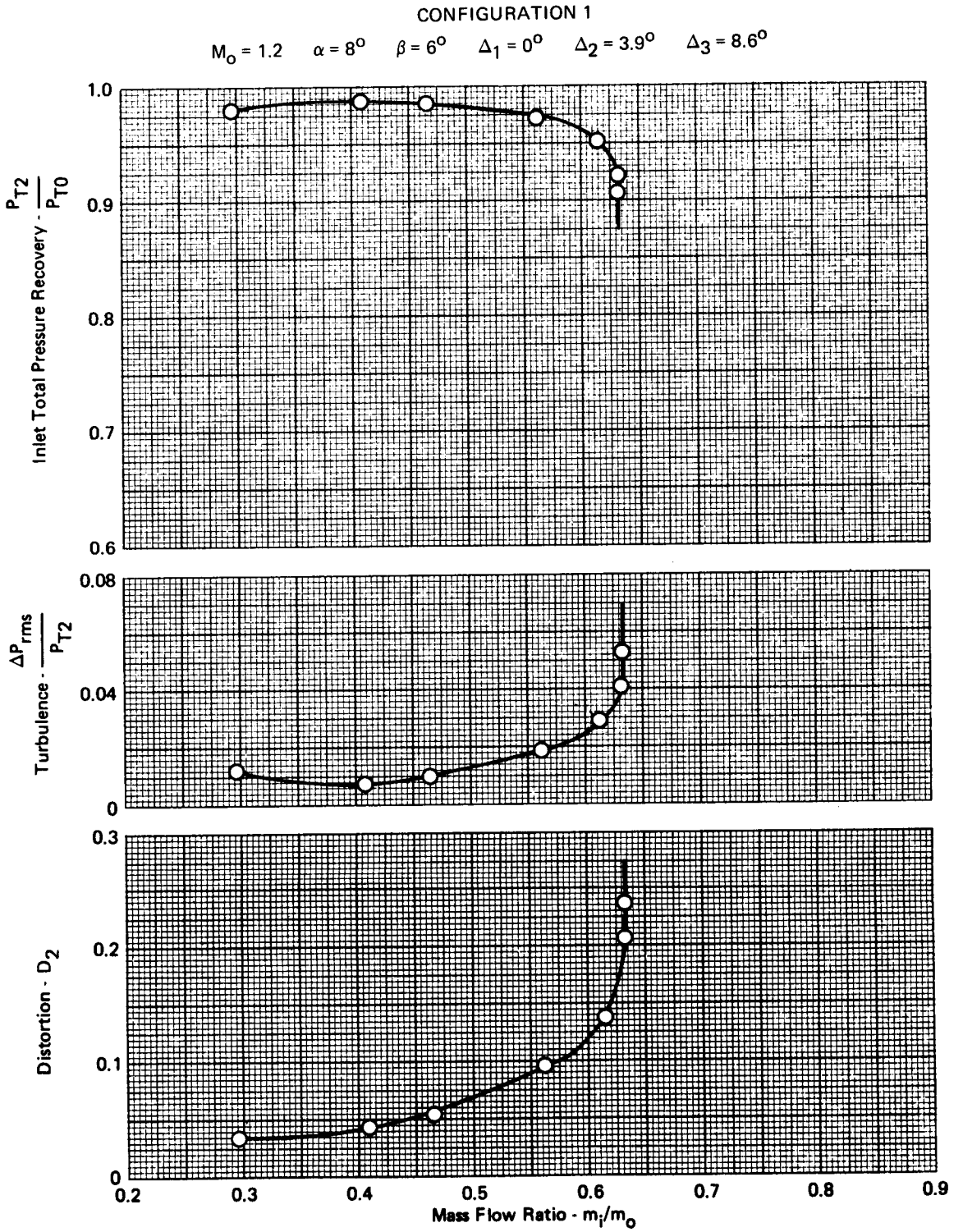

FIGURE A-102- EFFECTS OF ANGLE OF SIDESLIP ON PRESSURE RECOVERY, TURBULENCE, AND DISTORTION

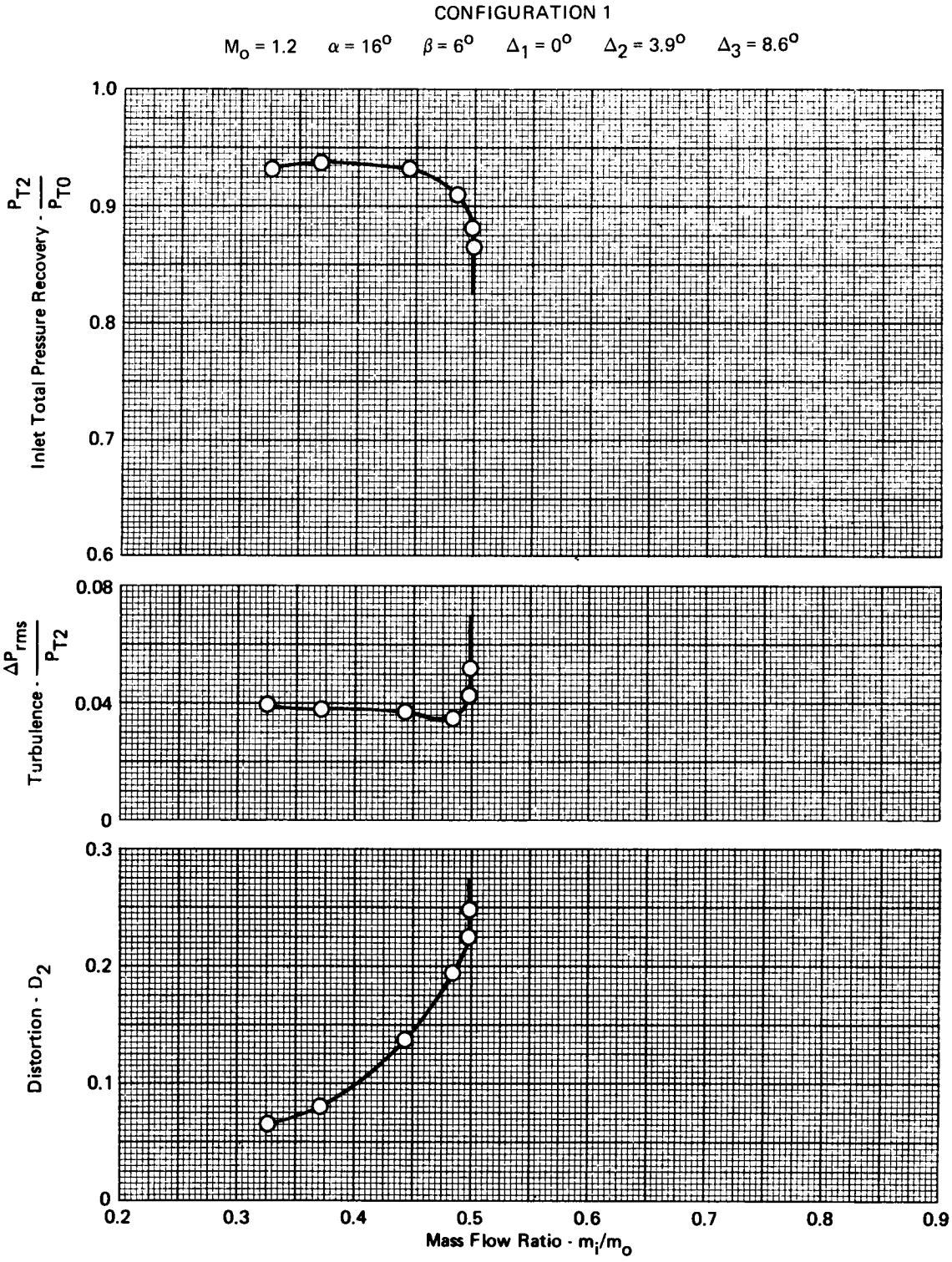

FIGURE A-103 - EFFECTS OF ANGLE OF SIDESLIP ON PRESSURE RECOVERY, TURBULENCE, AND DISTORTION

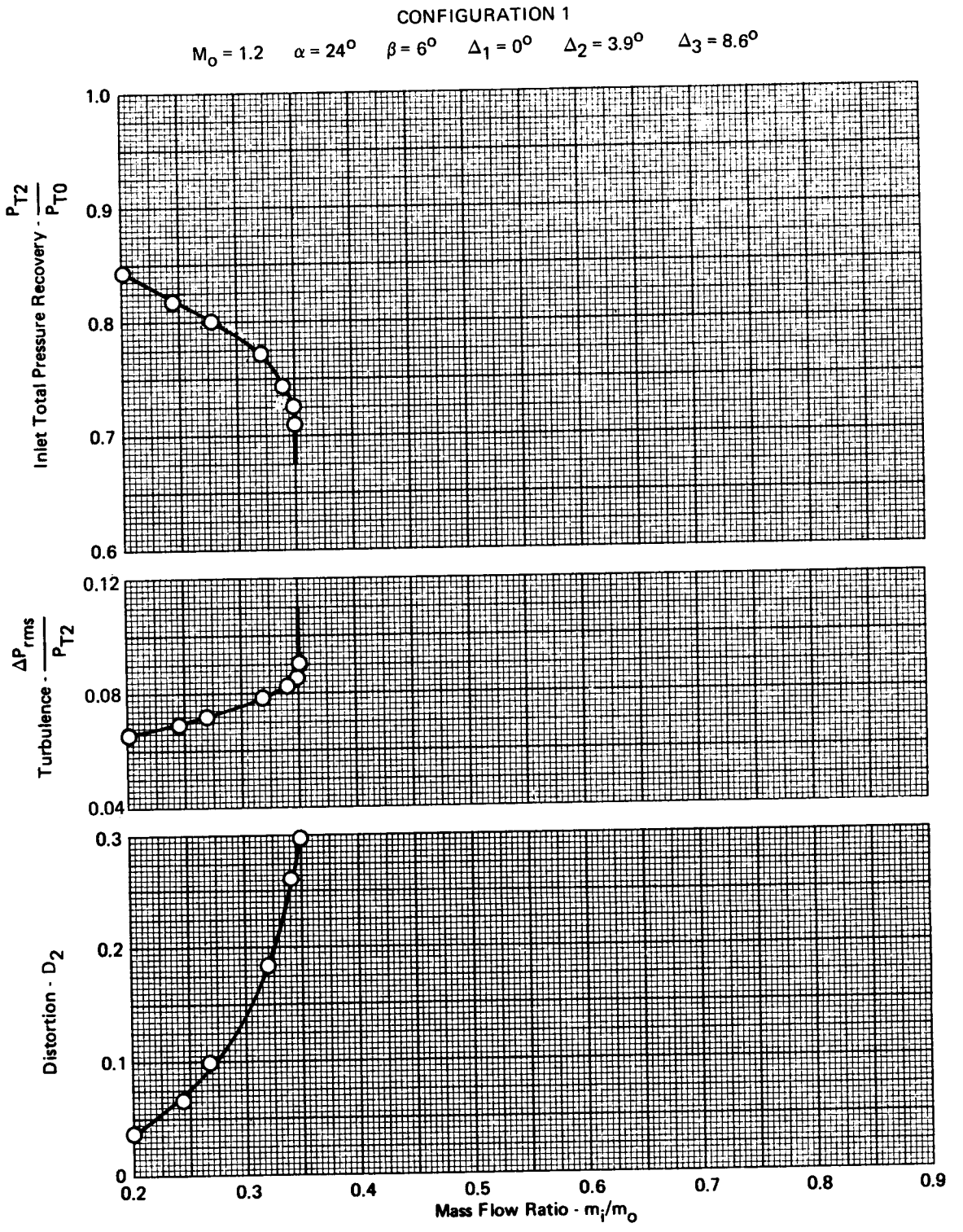

FIGURE A-104 - EFFECTS OF ANGLE OF SIDESLIP ON PRESSURE RECOVERY, TURBULENCE, AND DISTORTION

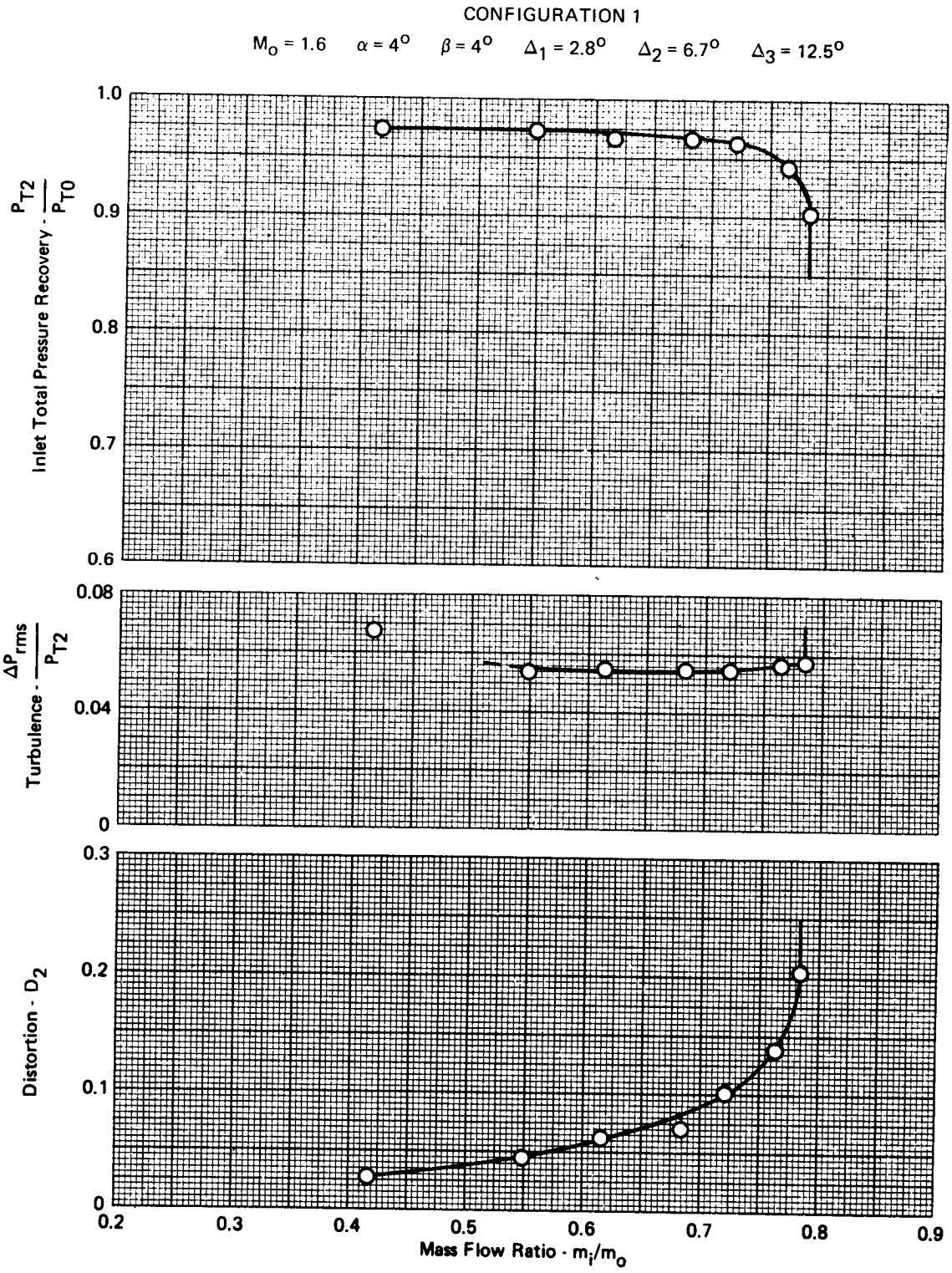

FIGURE A-105 - EFFECTS OF ANGLE OF SIDESLIP ON PRESSURE RECOVERY, TURBULENCE, AND DISTORTION

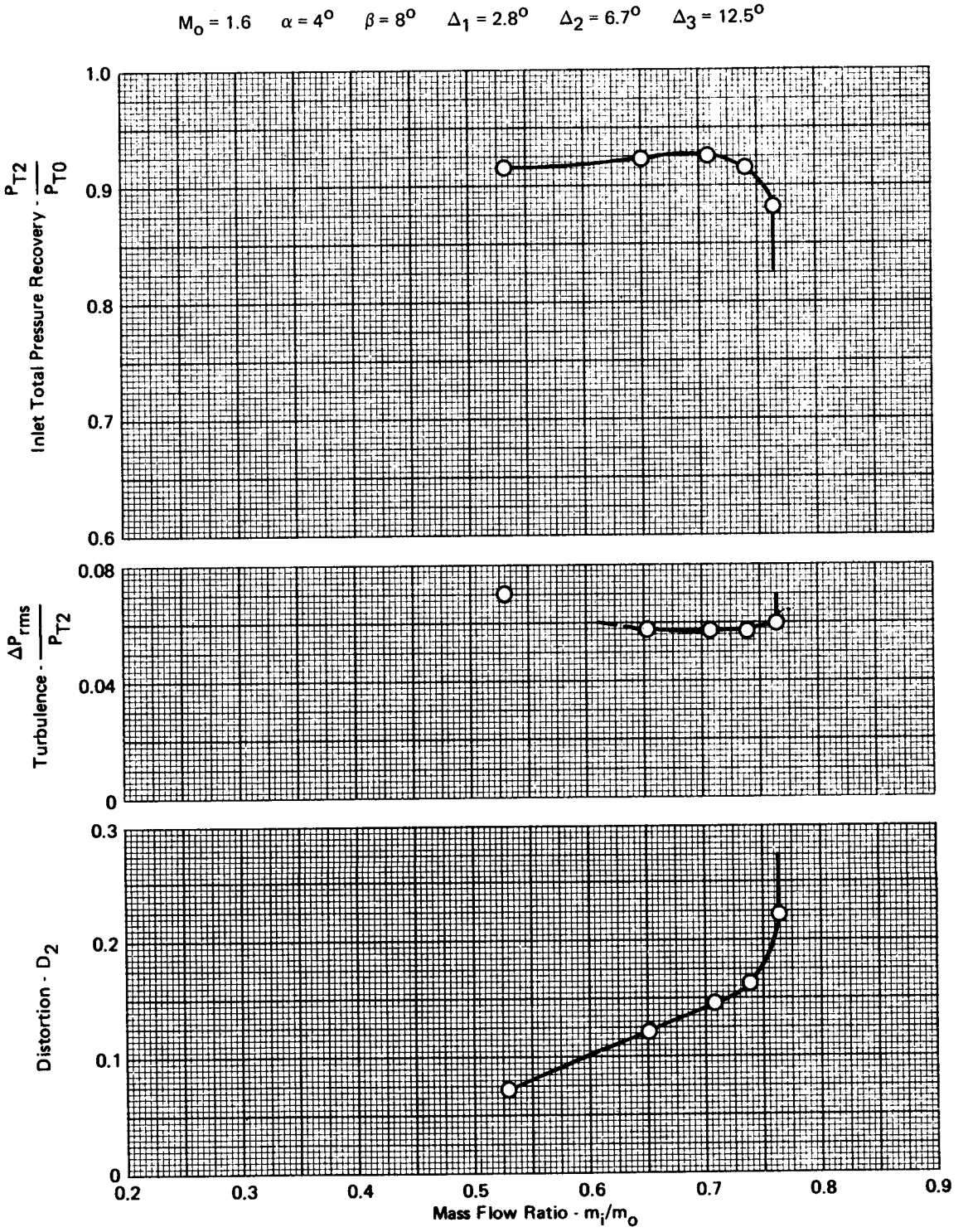

FIGURE A-106 - EFFECTS OF ANGLE OF SIDESLIP ON PRESSURE RECOVERY, TURBULENCE, AND DISTORTION

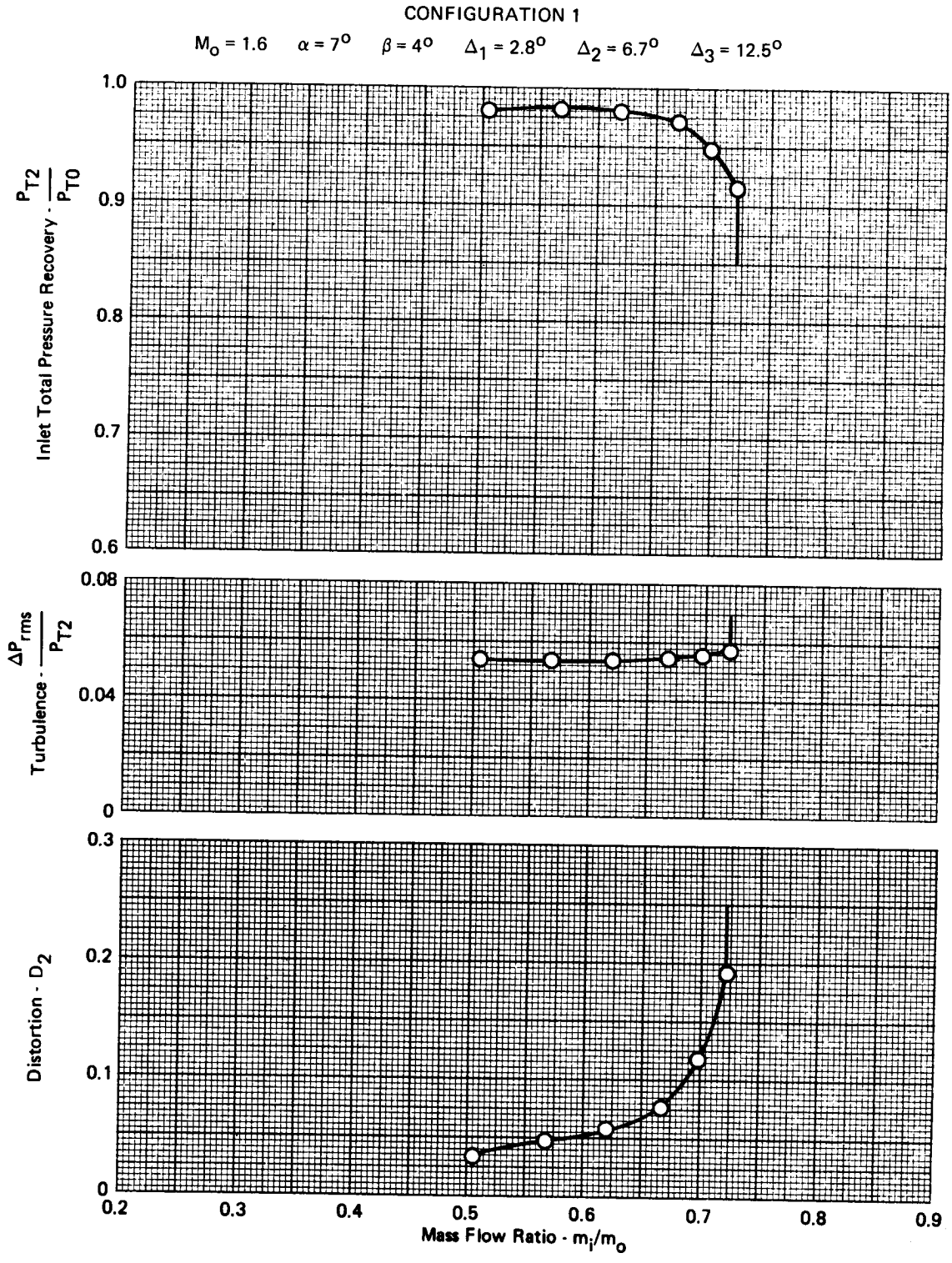

FIGURE A-107 - EFFECTS OF ANGLE OF SIDESLIP ON PRESSURE RECOVERY, TURBULENCE, AND DISTORTION

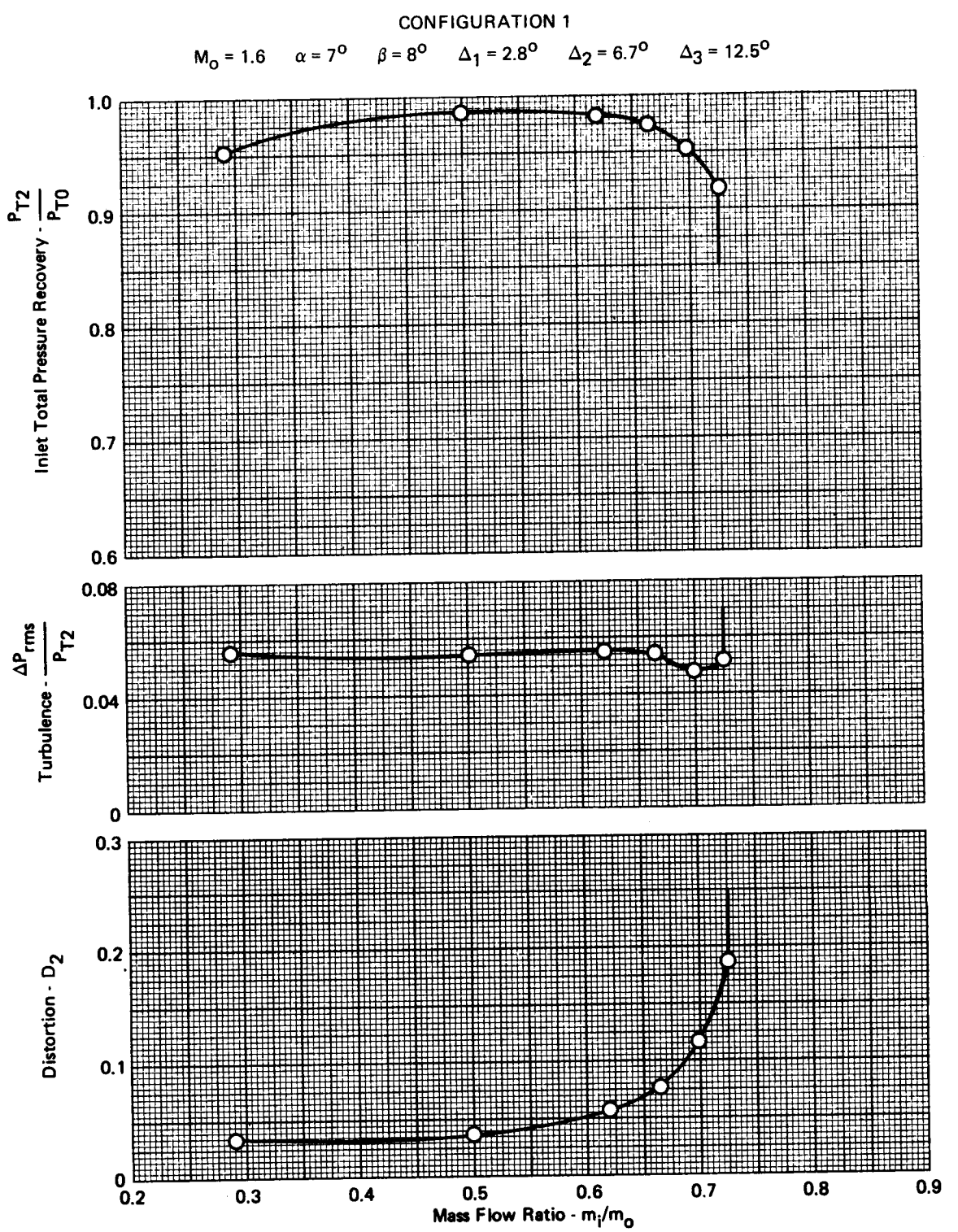

FIGURE A-108 - EFFECTS OF ANGLE OF SIDESLIP ON PRESSURE RECOVERY, TURBULENCE, AND DISTORTION

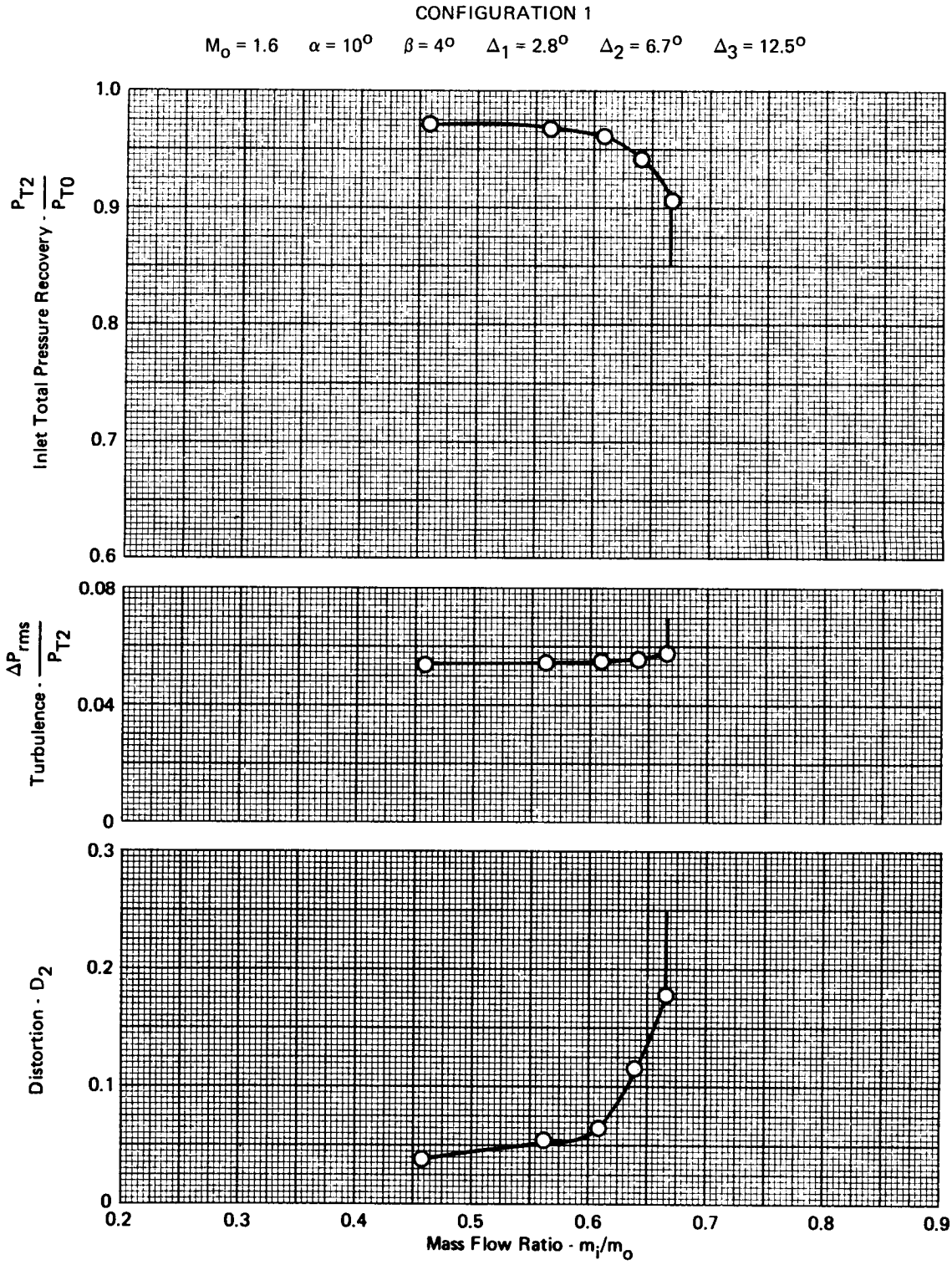

FIGURE A-109 - EFFECTS OF ANGLE OF SIDESLIP ON PRESSURE RECOVERY, TURBULENCE, AND DISTORTION

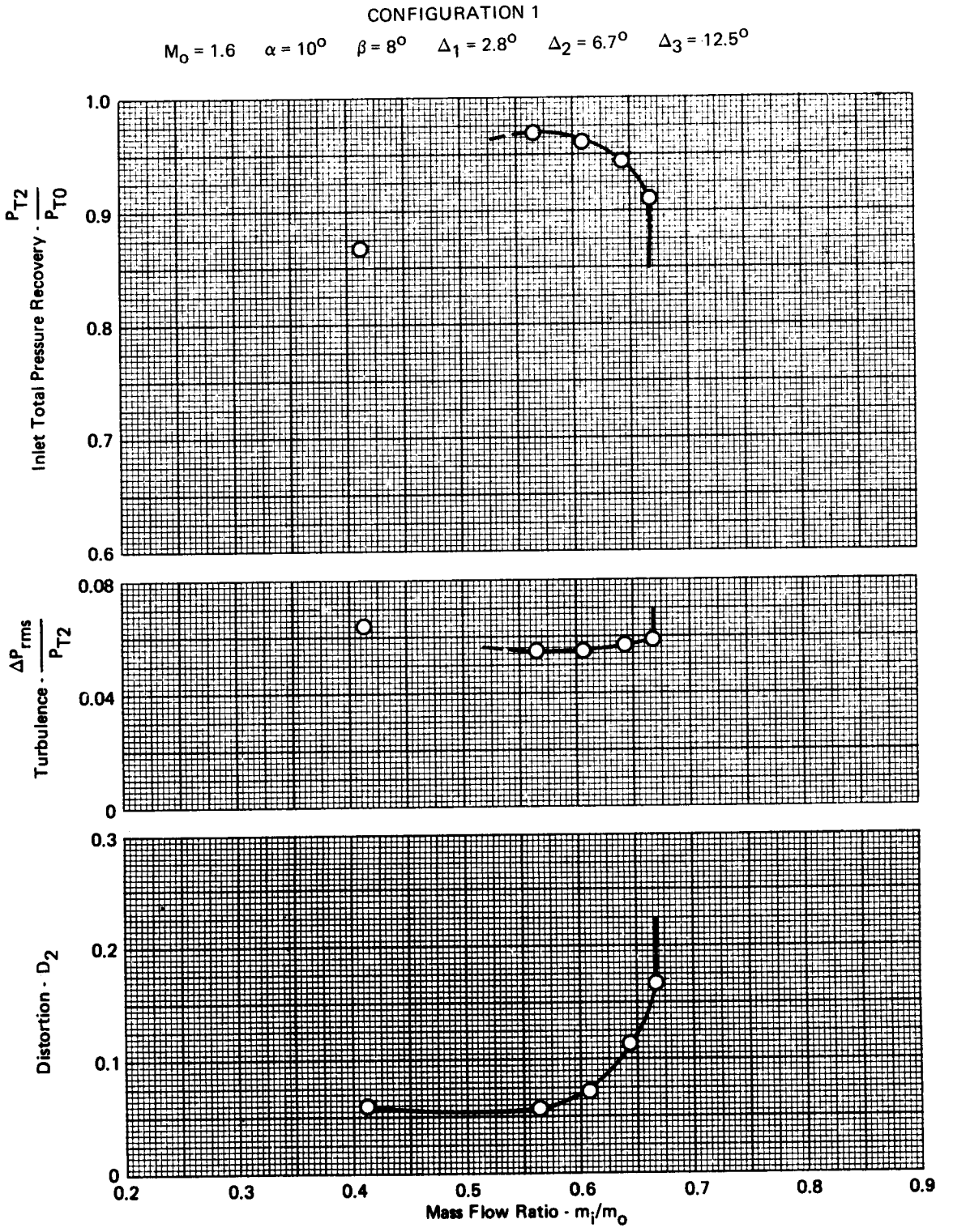

FIGURE A-110 - EFFECTS OF ANGLE OF SIDESLIP ON PRESSURE RECOVERY, TURBULENCE, AND DISTORTION

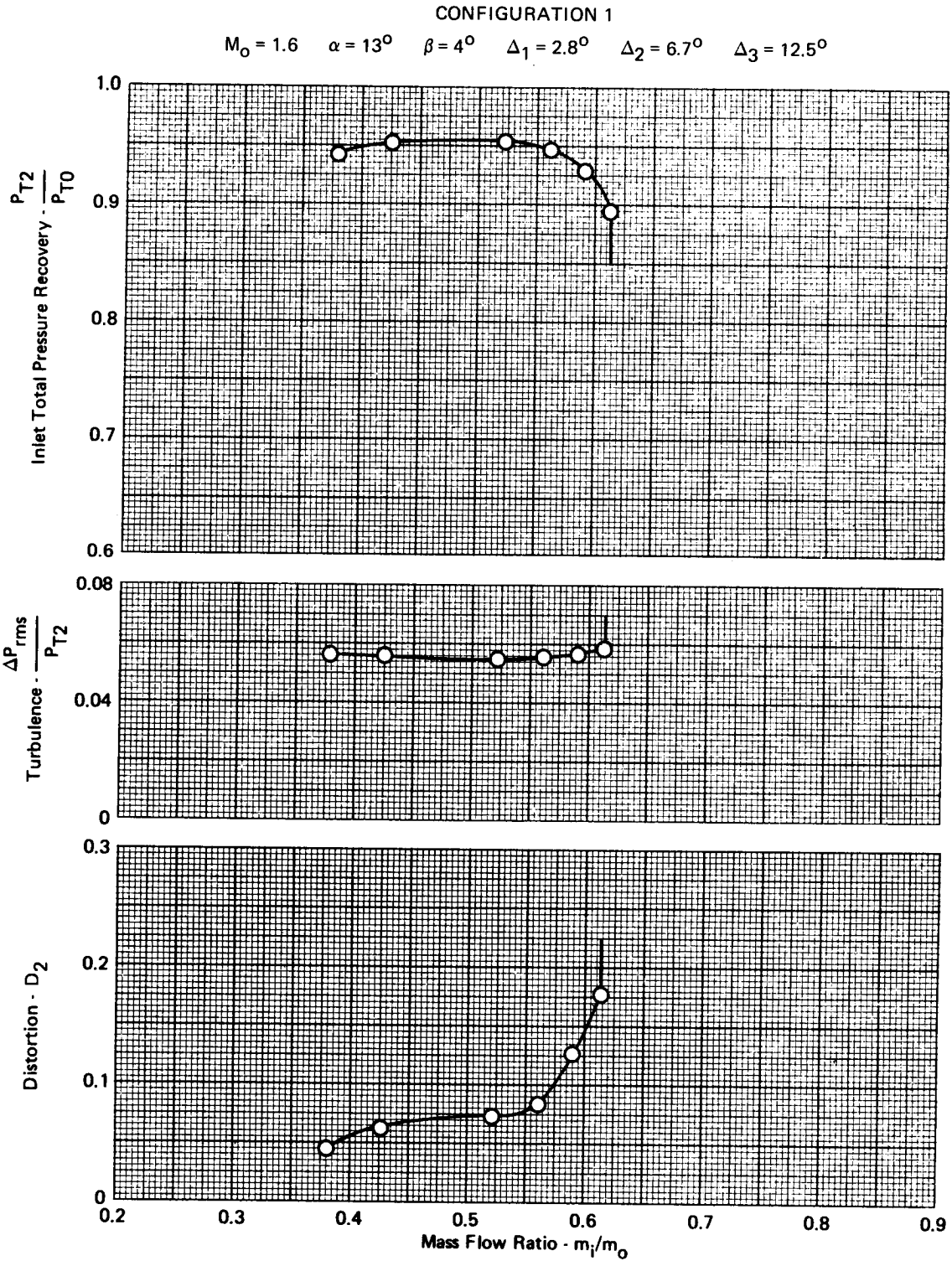

FIGURE A-111 - EFFECTS OF ANGLE OF SIDESLIP ON PRESSURE RECOVERY, TURBULENCE, AND DISTORTION

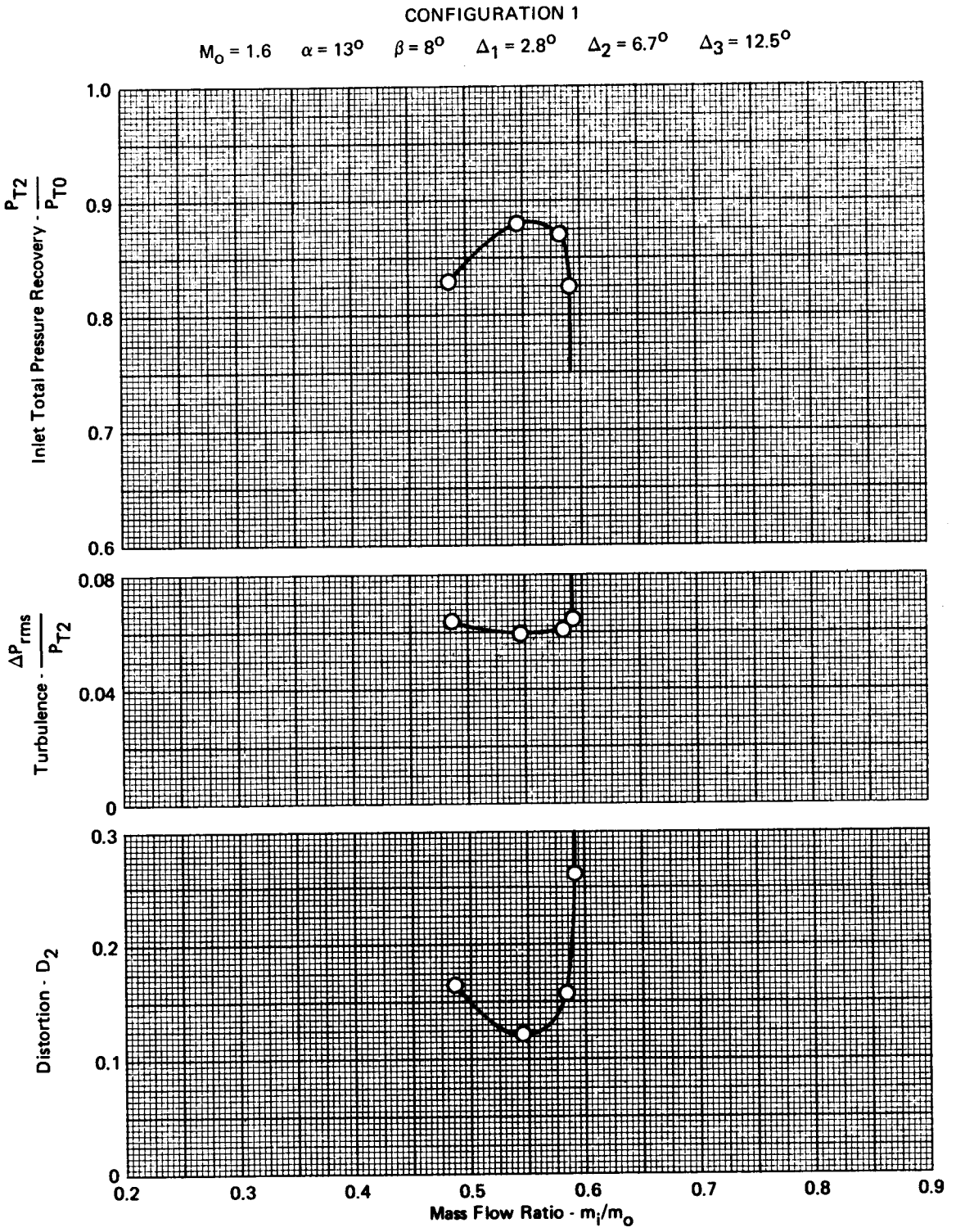

FIGURE A-112 - EFFECTS OF ANGLE OF SIDESLIP ON PRESSURE RECOVERY, TURBULENCE, AND DISTORTION

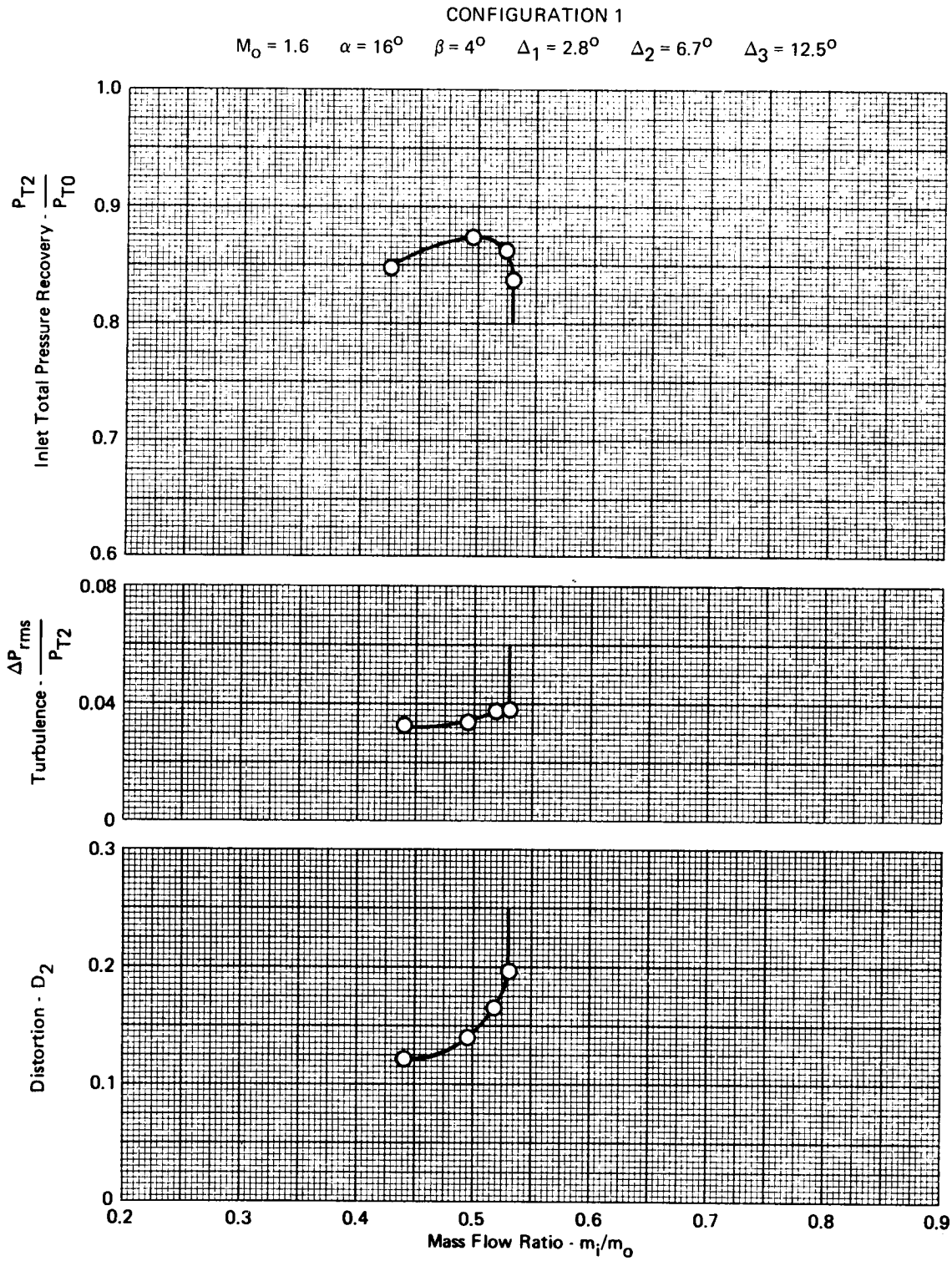

FIGURE A-113- EFFECTS OF ANGLE OF SIDESLIP ON PRESSURE RECOVERY, TURBULENCE, AND DISTORTION

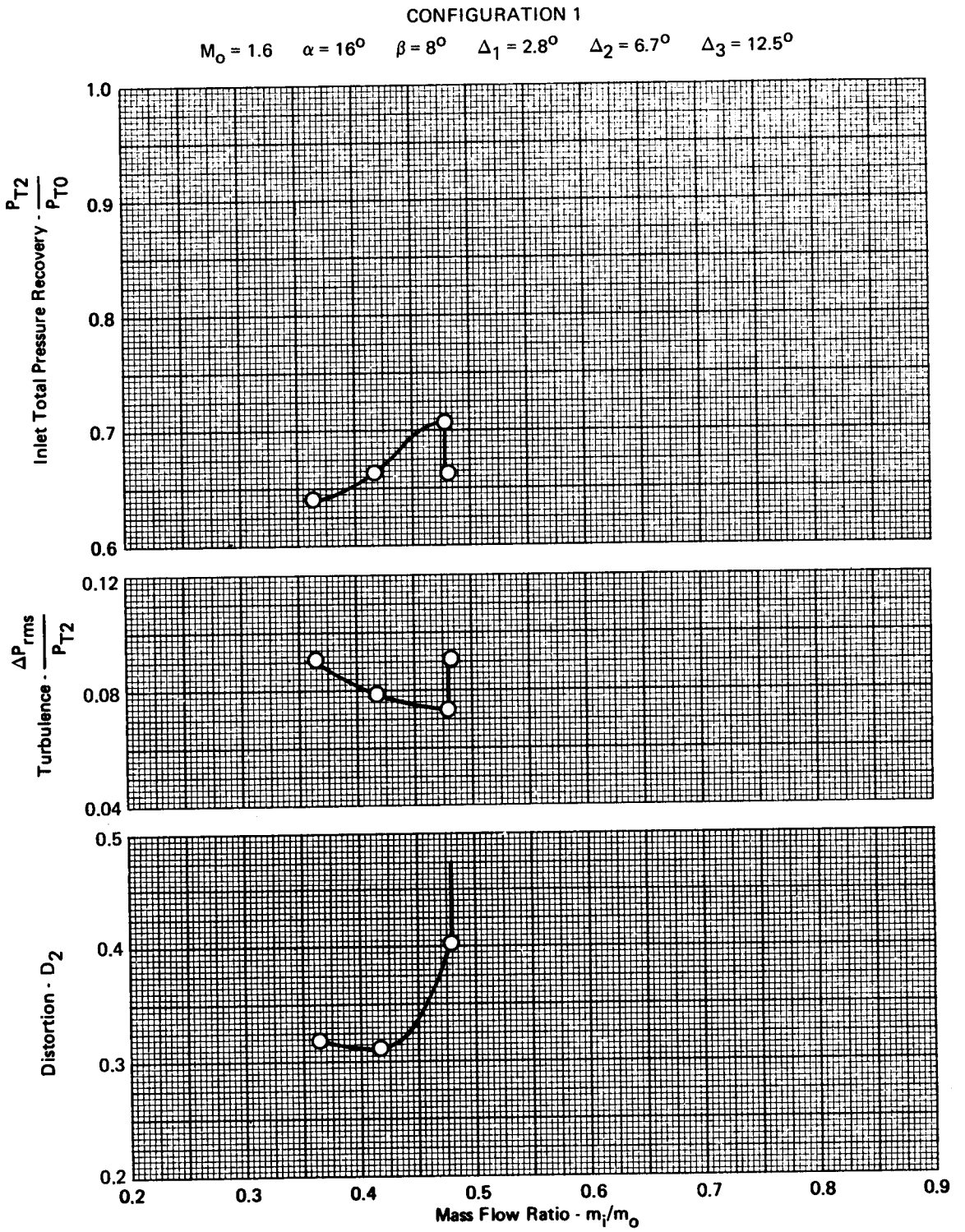

FIGURE A-114 - EFFECTS OF ANGLE OF SIDESLIP ON PRESSURE RECOVERY, TURBULENCE, AND DISTORTION

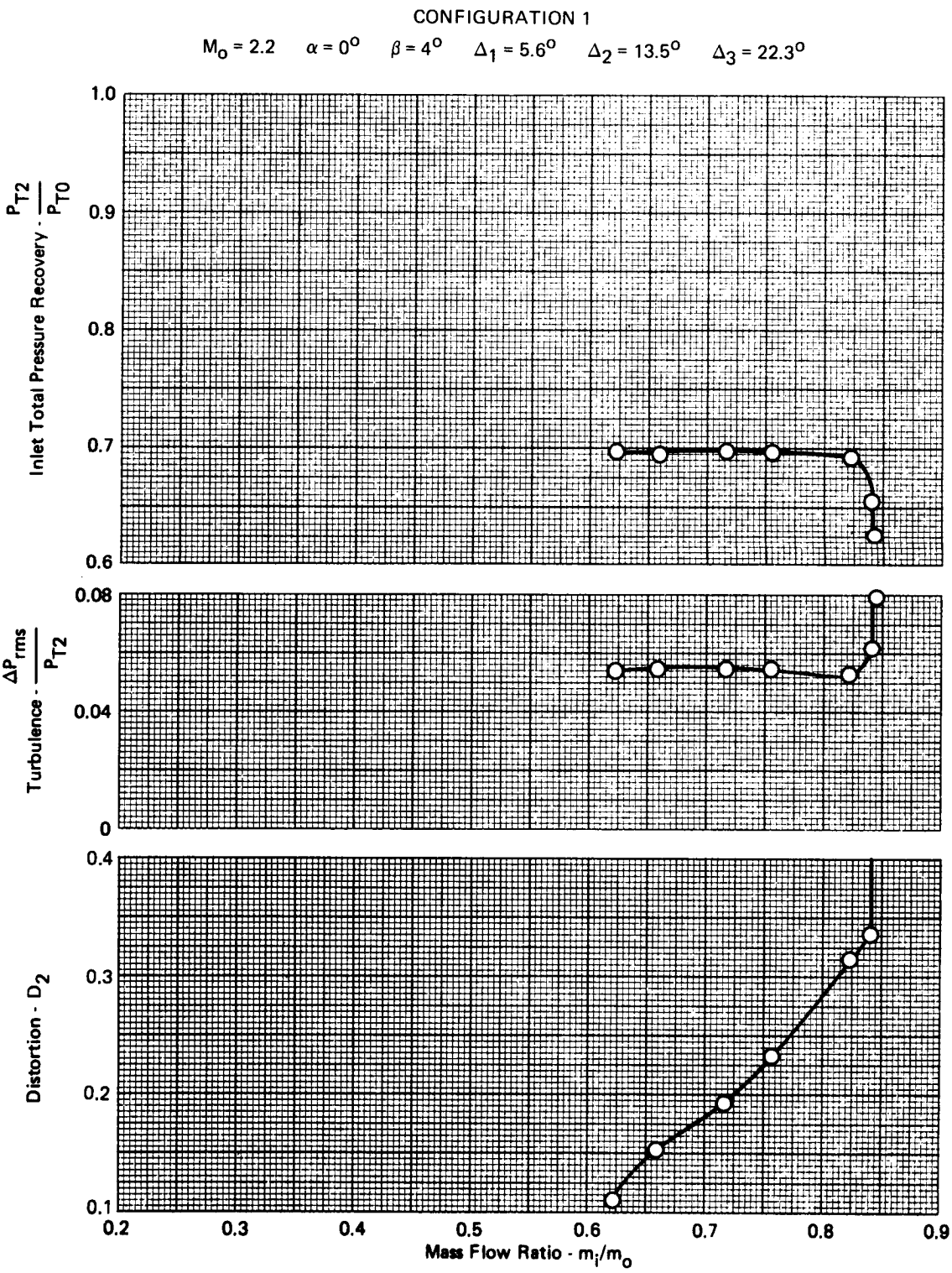

FIGURE A-115 - EFFECTS OF ANGLE OF SIDESLIP ON PRESSURE RECOVERY, TURBULENCE, AND DISTORTION

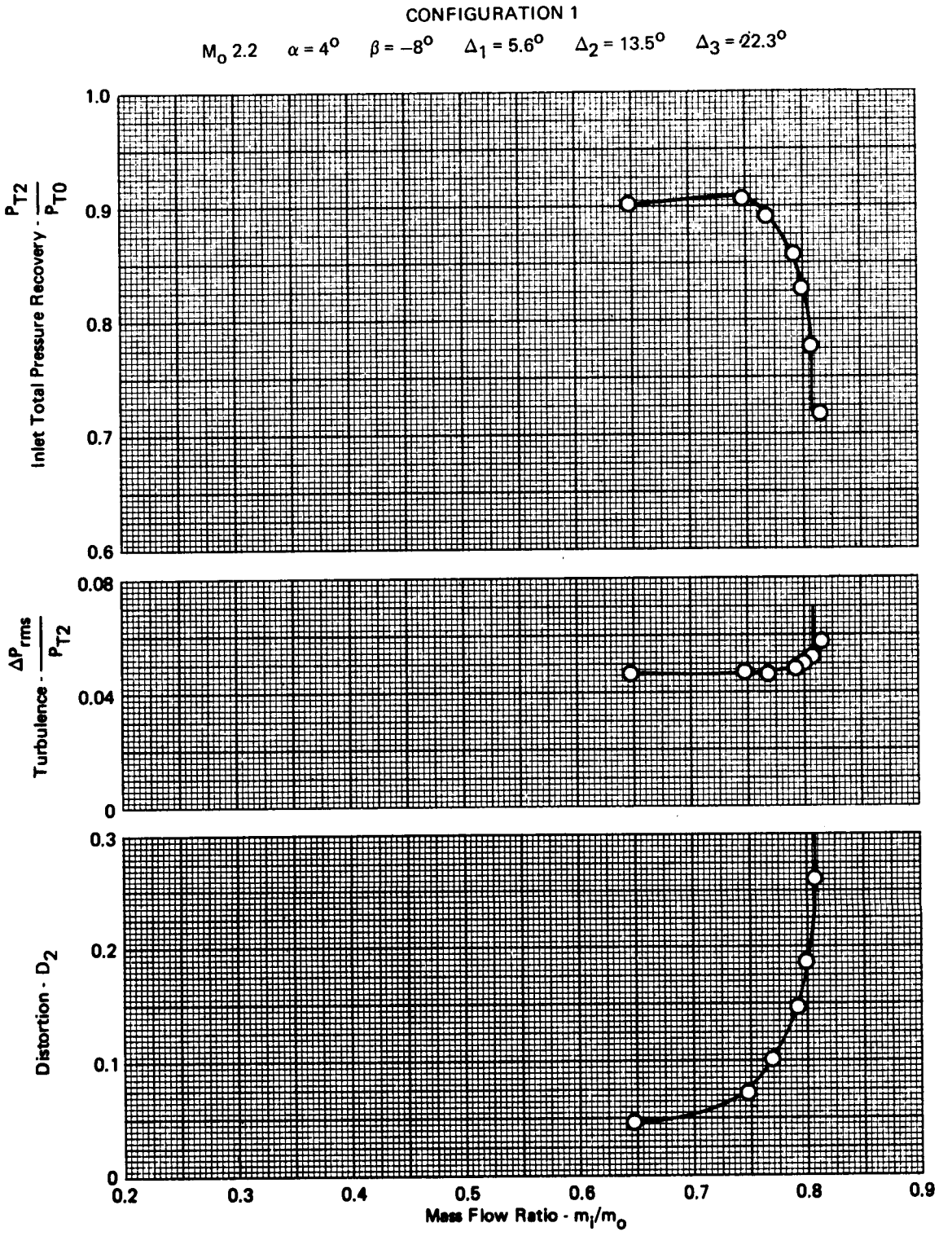

FIGURE A-116 - EFFECTS OF ANGLE OF SIDESLIP ON PRESSURE RECOVERY, TURBULENCE, AND DISTORTION

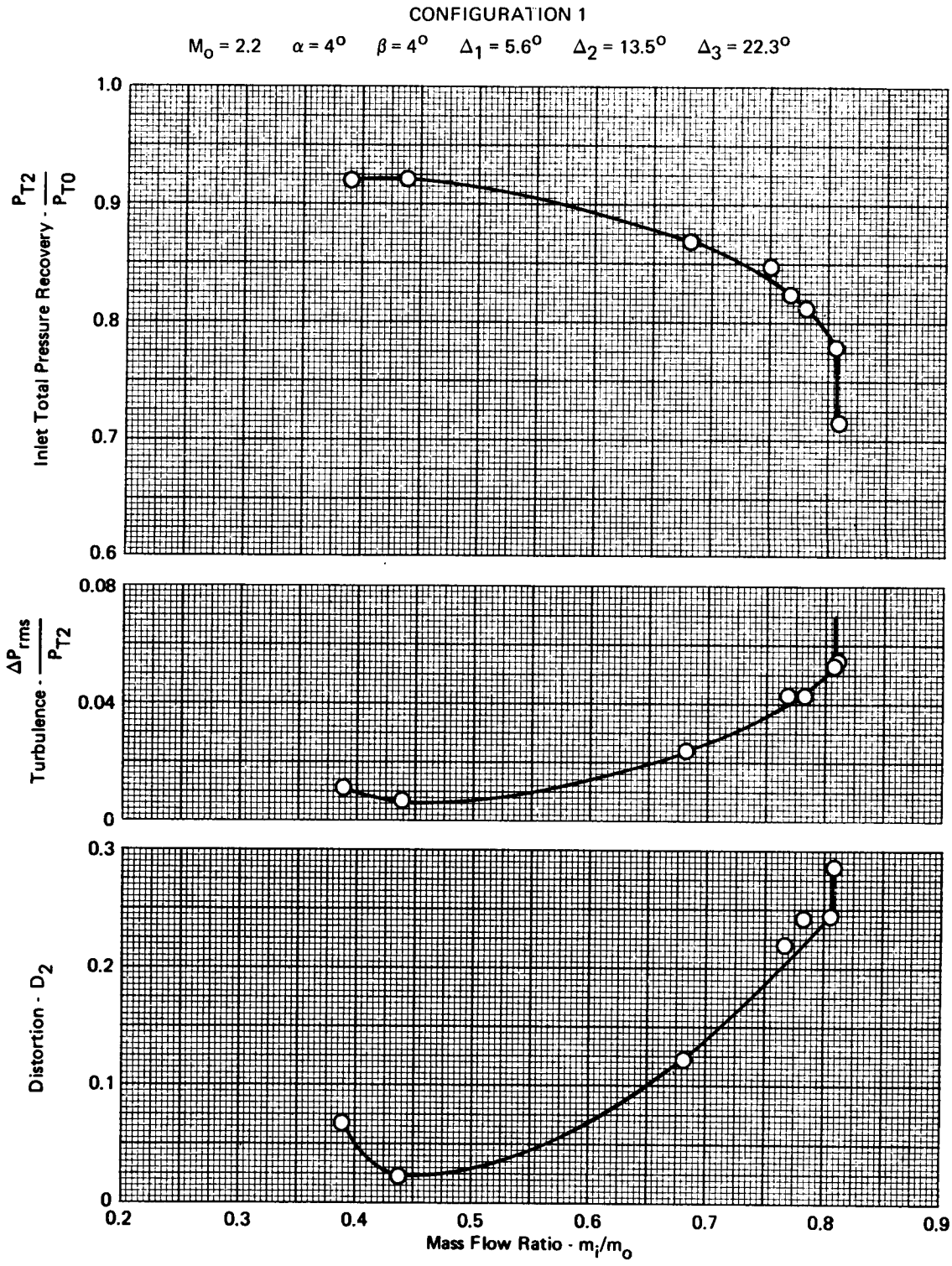

FIGURE A-117 - EFFECTS OF ANGLE OF SIDESLIP ON PRESSURE RECOVERY, TURBULENCE, AND DISTORTION

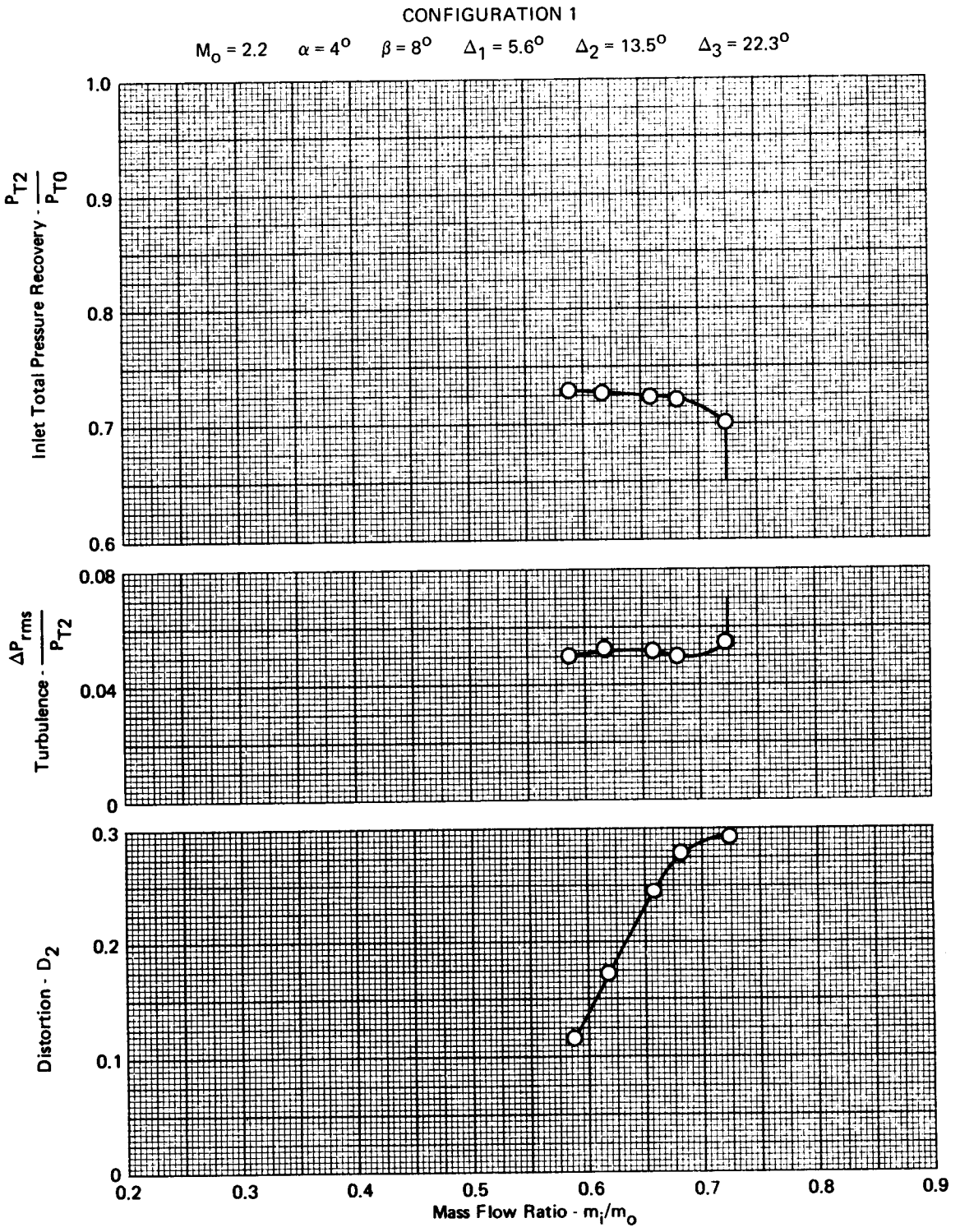

FIGURE A-118 - EFFECTS OF ANGLE OF SIDESLIP ON PRESSURE RECOVERY, TURBULENCE, AND DISTORTION

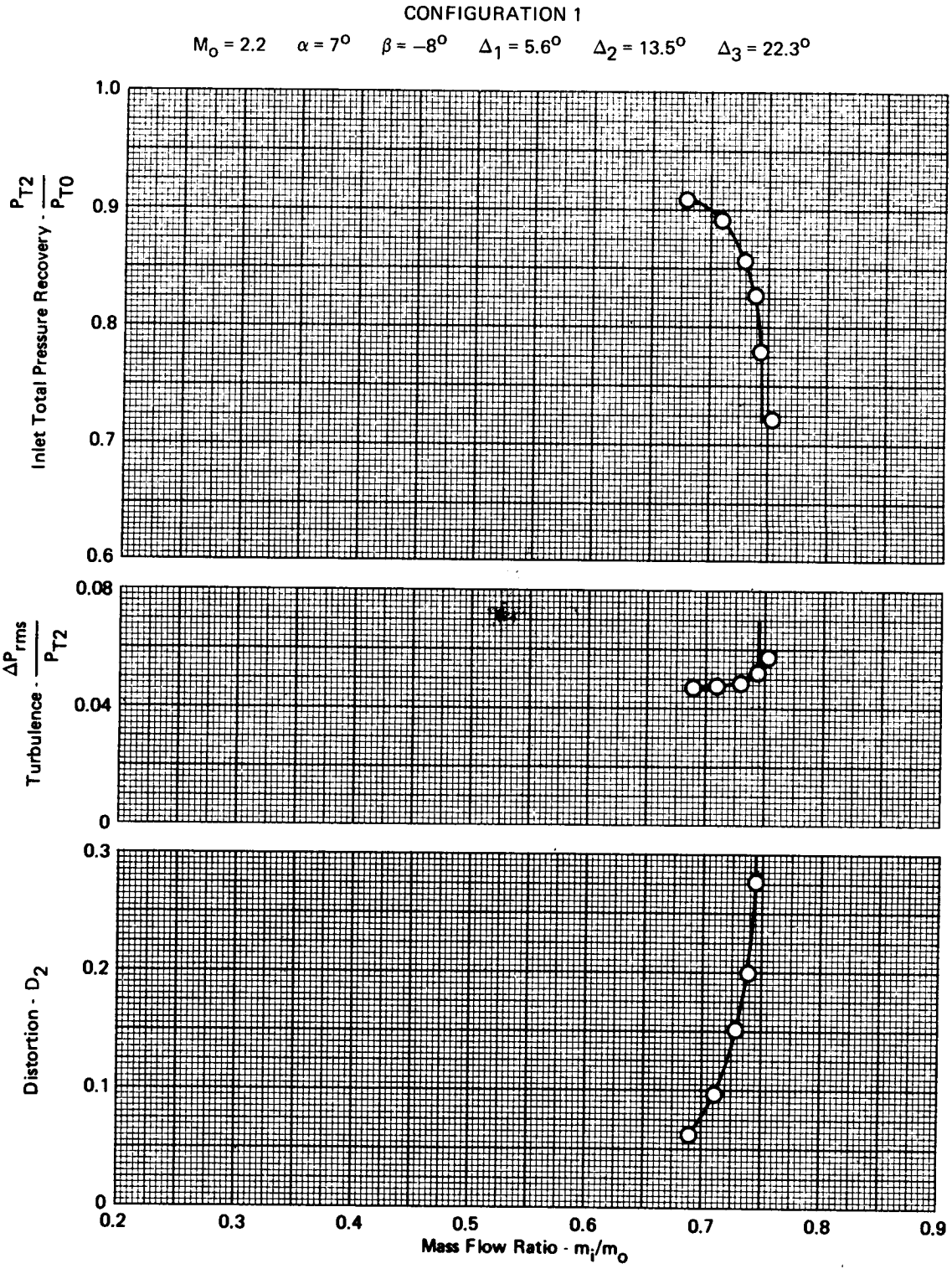

FIGURE A-119 - EFFECTS OF ANGLE OF SIDESLIP ON PRESSURE RECOVERY, TURBULENCE, AND DISTORTION

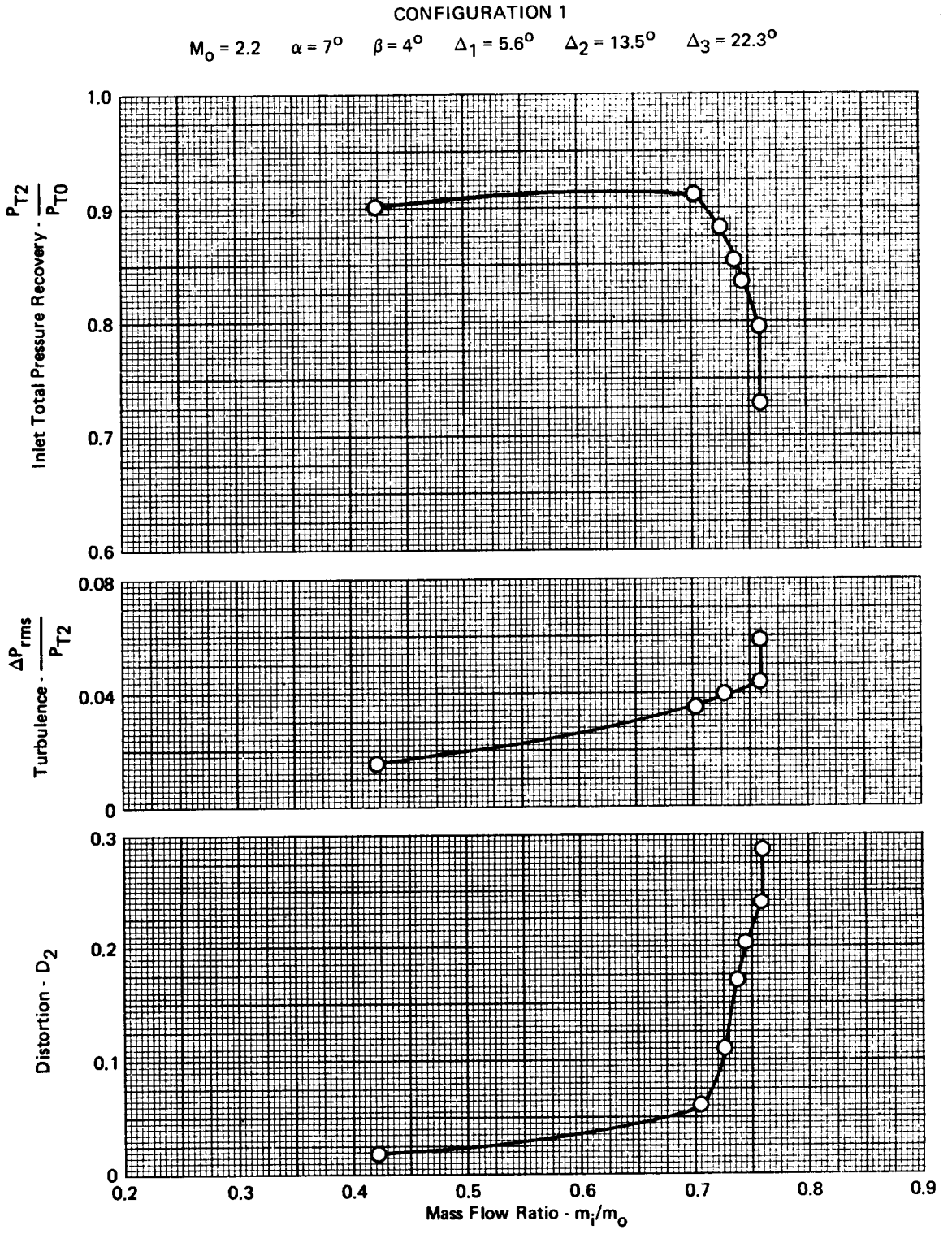

FIGURE A-120- EFFECTS OF ANGLE OF SIDESLIP ON PRESSURE RECOVERY, TURBULENCE, AND DISTORTION

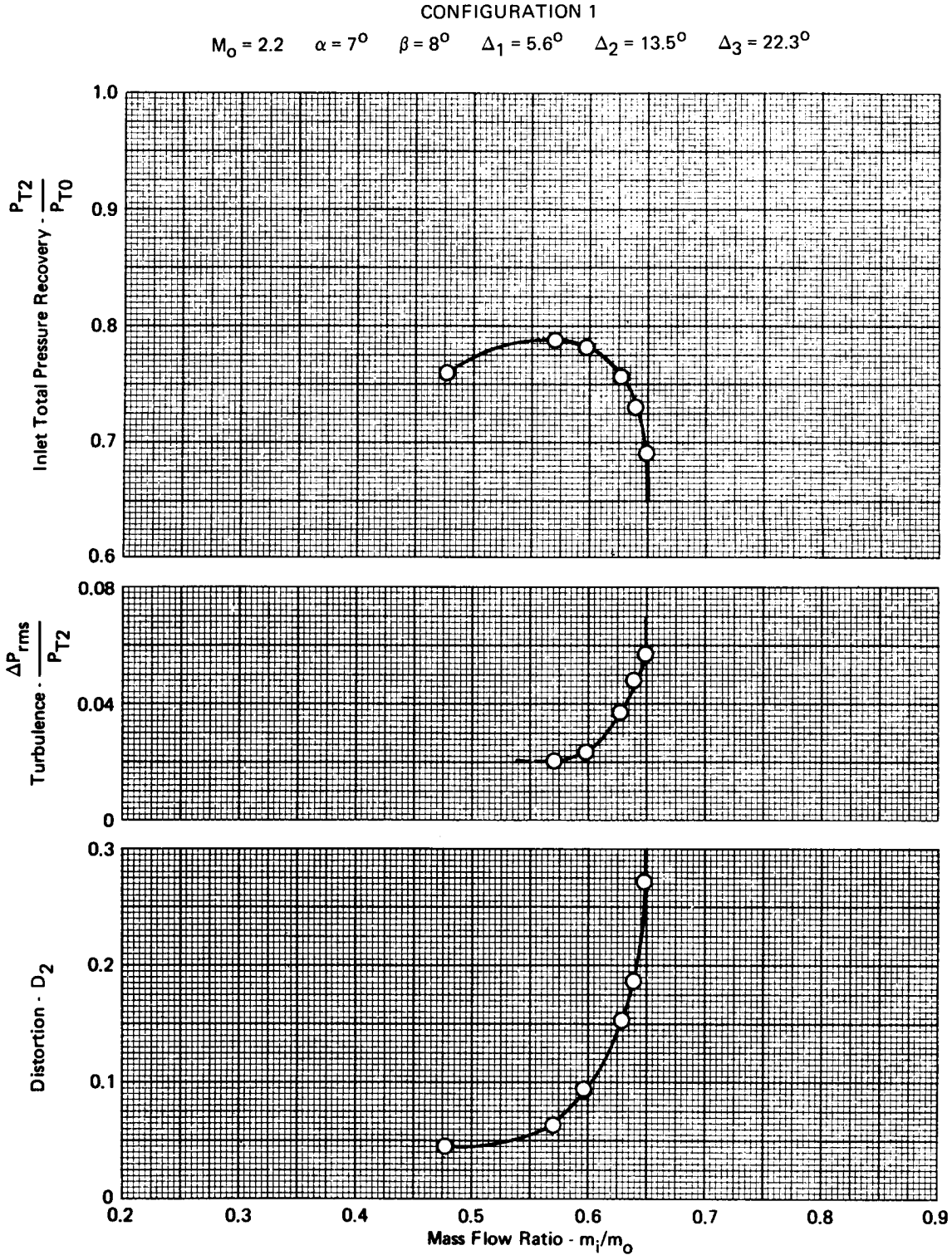

FIGURE A-121 - EFFECTS OF ANGLE OF SIDESLIP ON PRESSURE RECOVERY, TURBULENCE, AND DISTORTION

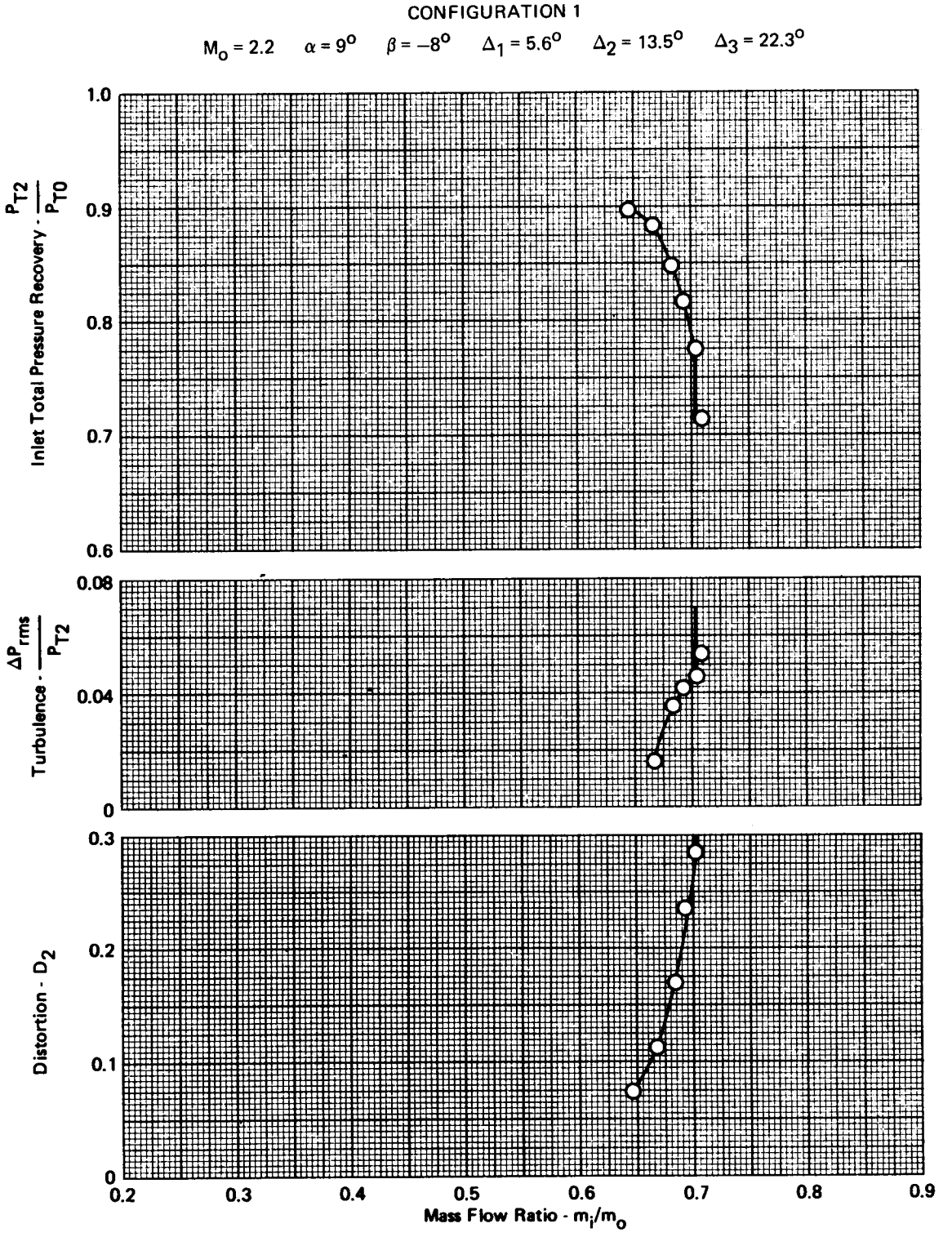

FIGURE A-122- EFFECTS OF ANGLE OF SIDESLIP ON PRESSURE RECOVERY, TURBULENCE, AND DISTORTION

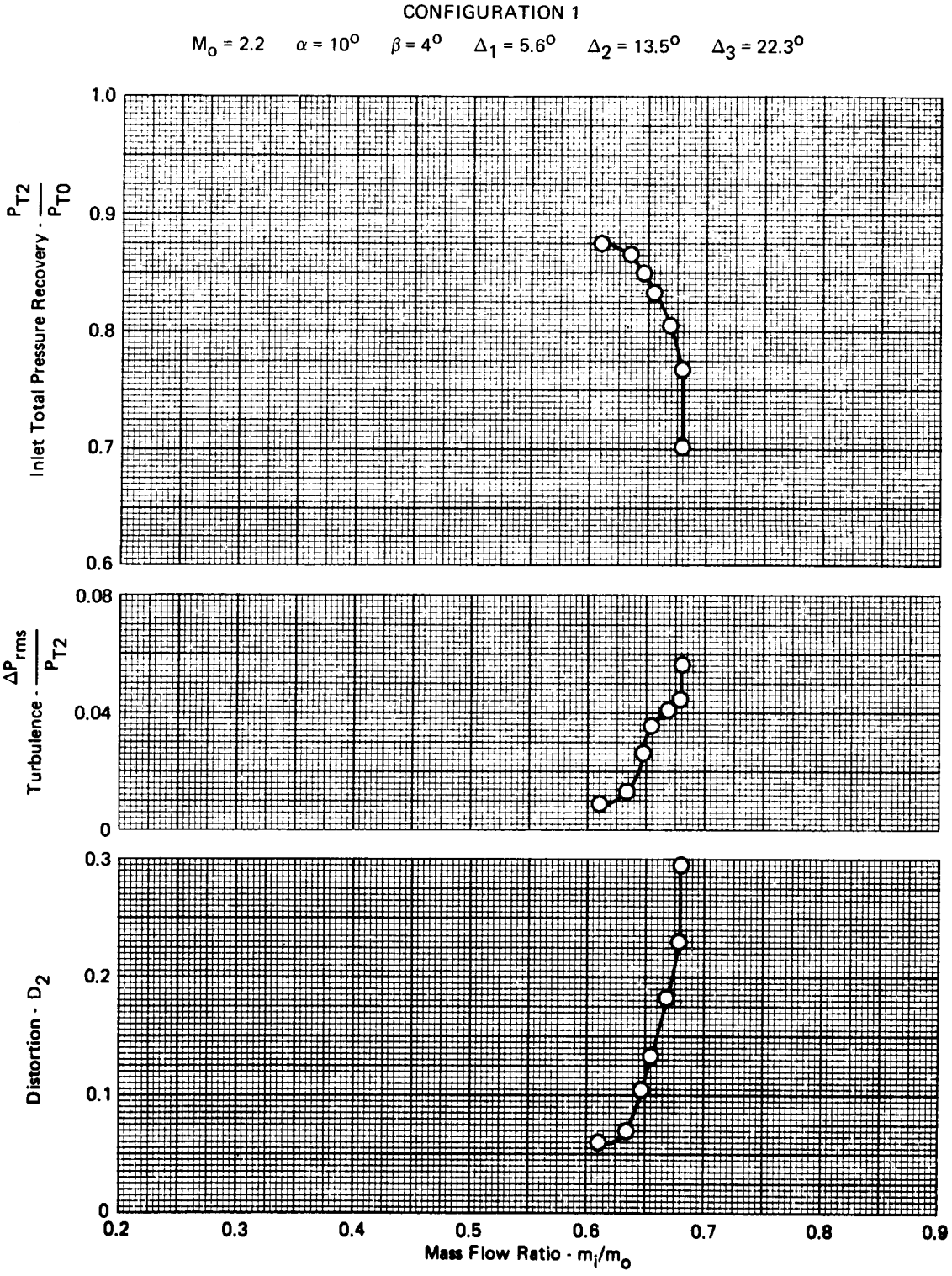

FIGURE A-123 - EFFECTS OF ANGLE OF SIDESLIP ON PRESSURE RECOVERY, TURBULENCE, AND DISTORTION

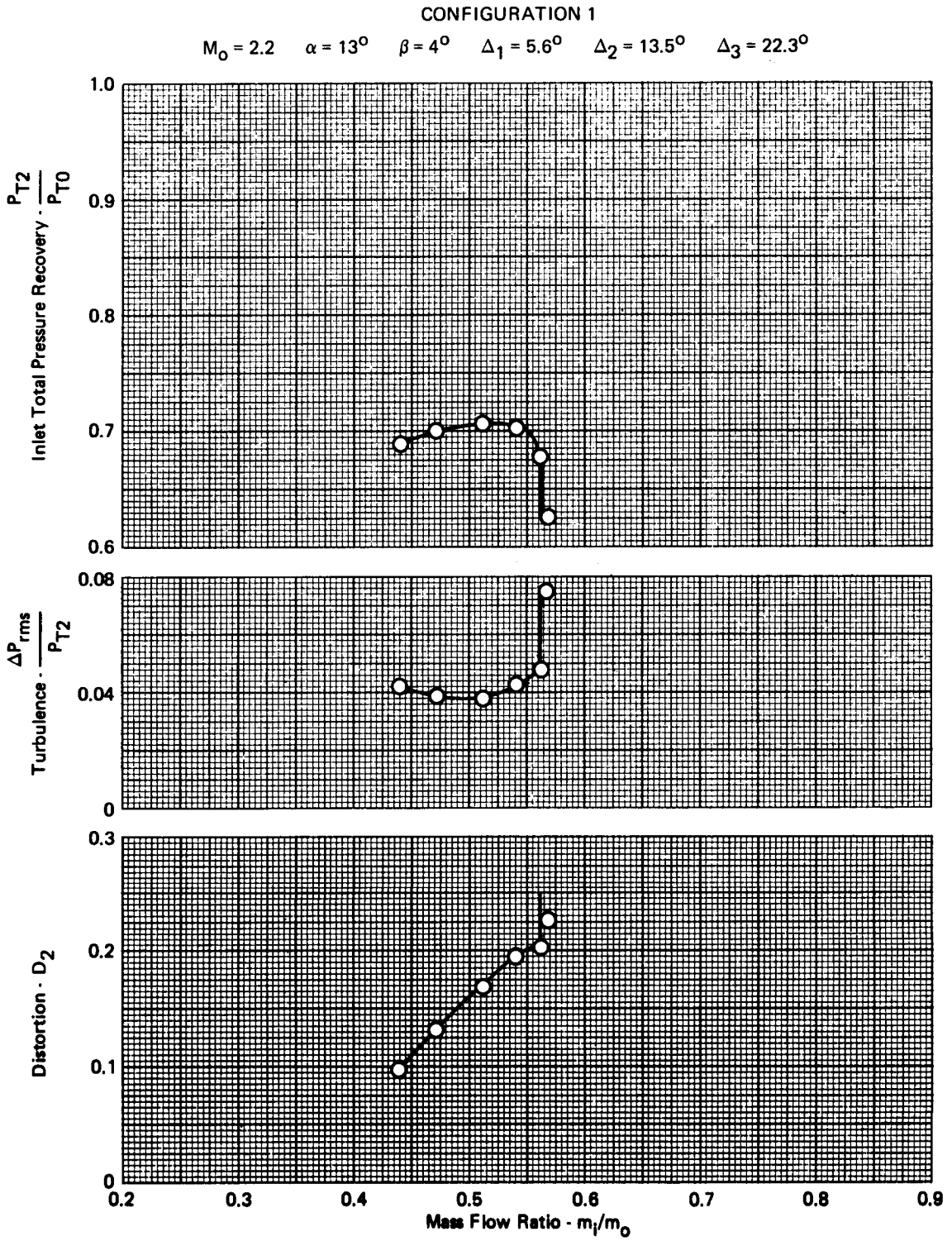

FIGURE A-124- EFFECTS OF ANGLE OF SIDESLIP ON PRESSURE RECOVERY, TURBULENCE, AND DISTORTION

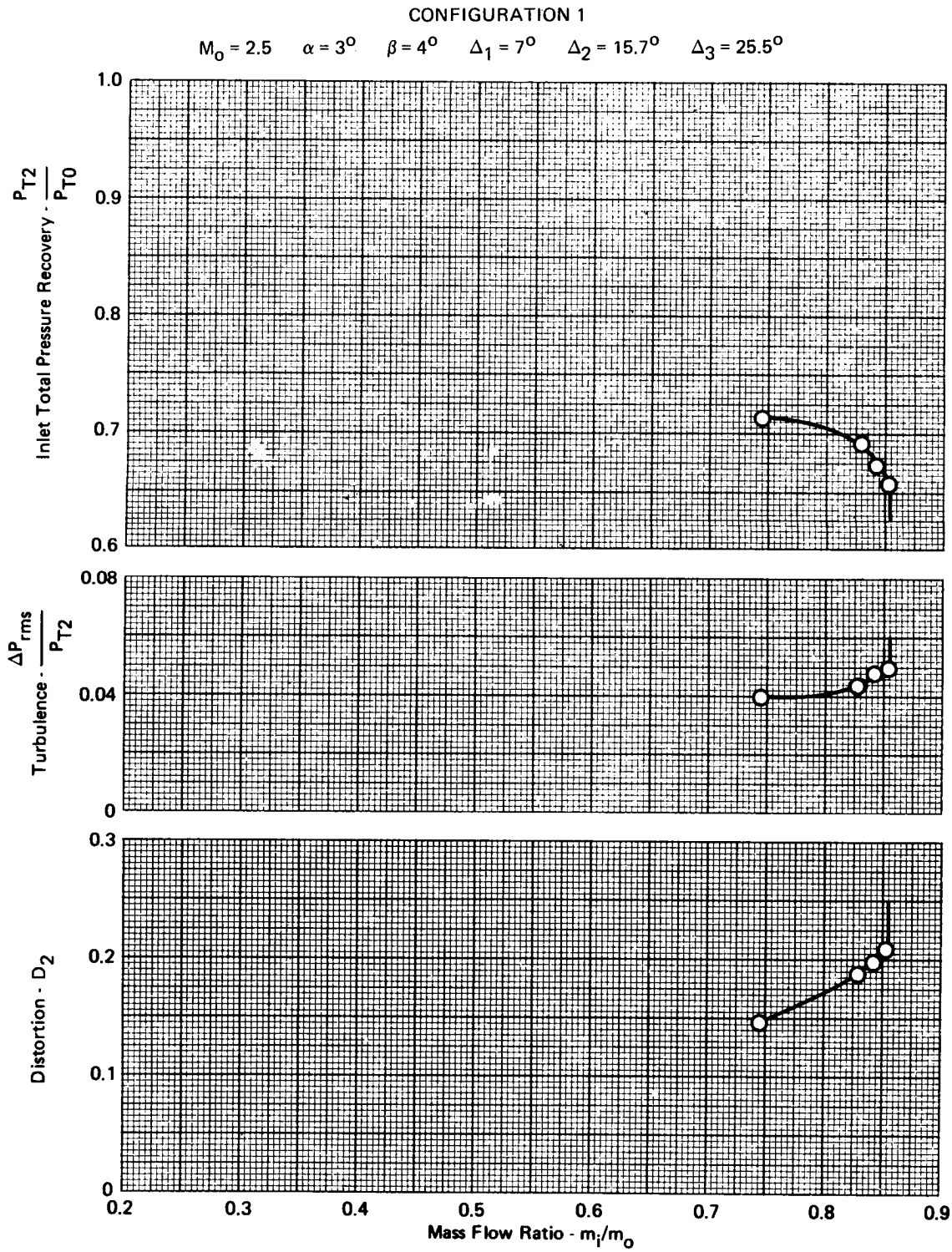

FIGURE A-125 - EFFECTS OF ANGLE OF SIDESLIP ON PRESSURE RECOVERY, TURBULENCE, AND DISTORTION

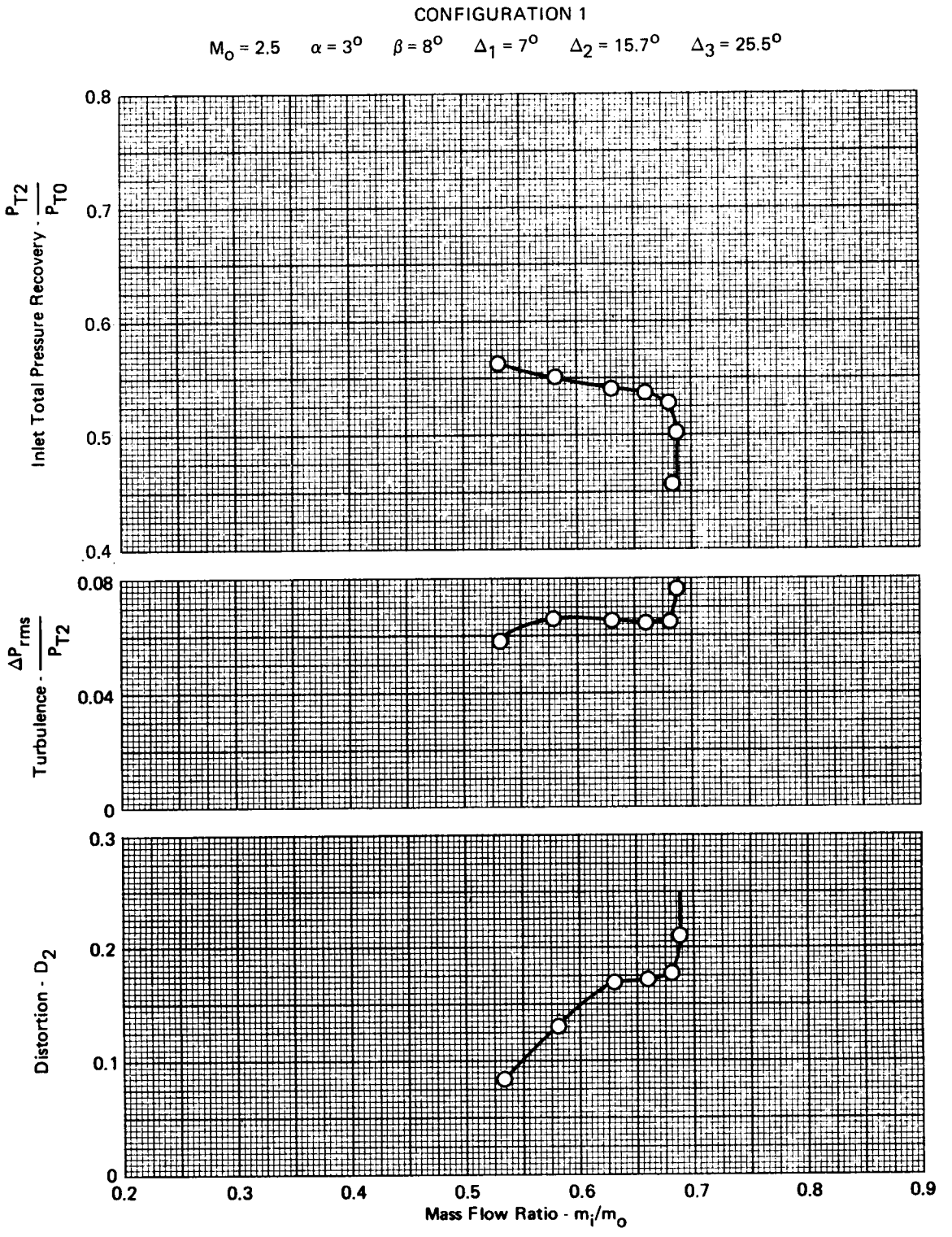

FIGURE A-126- EFFECTS OF ANGLE OF SIDESLIP ON PRESSURE RECOVERY, TURBULENCE, AND DISTORTION

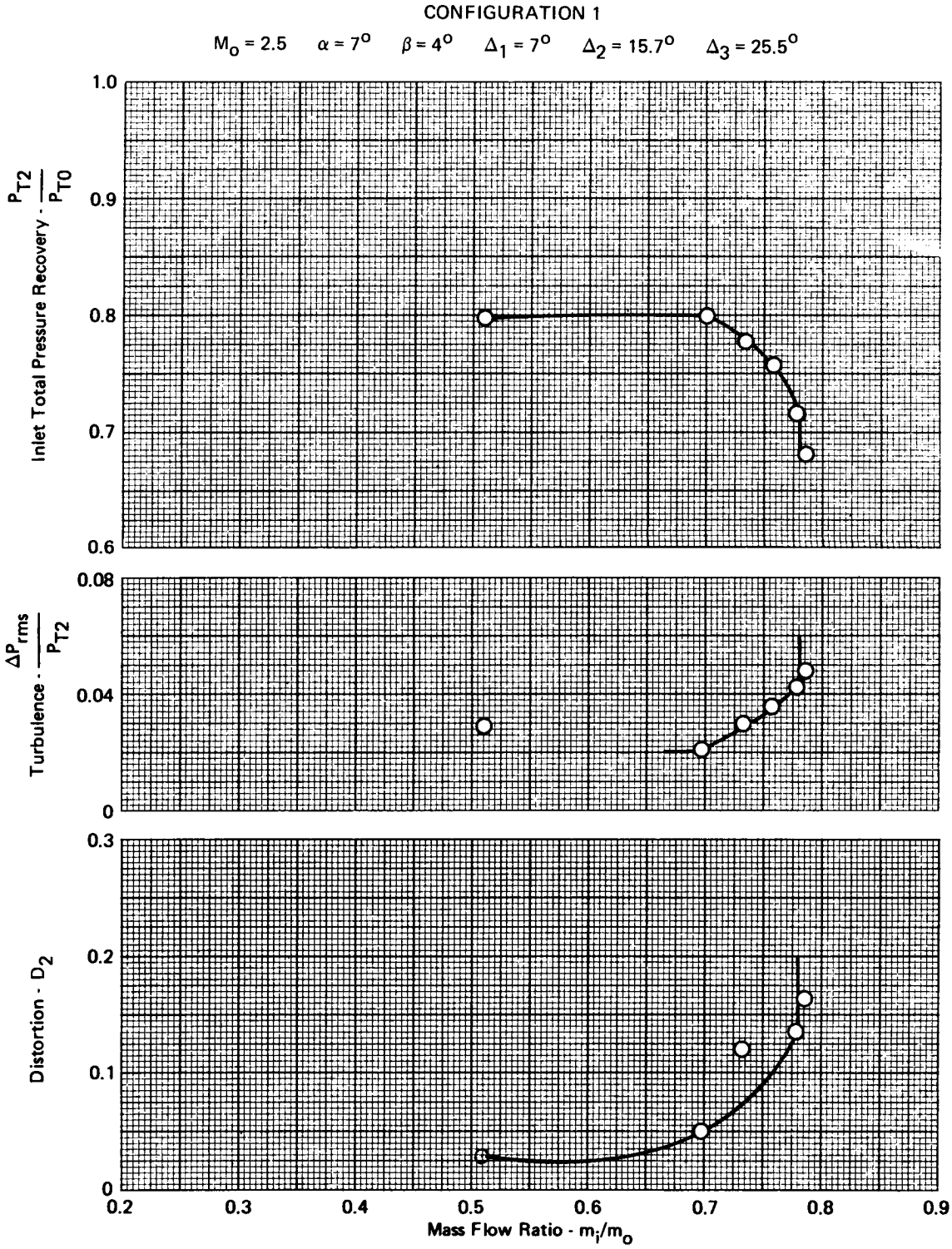

FIGURE A-127 - EFFECTS OF ANGLE OF SIDESLIP ON PRESSURE RECOVERY, TURBULENCE, AND DISTORTION

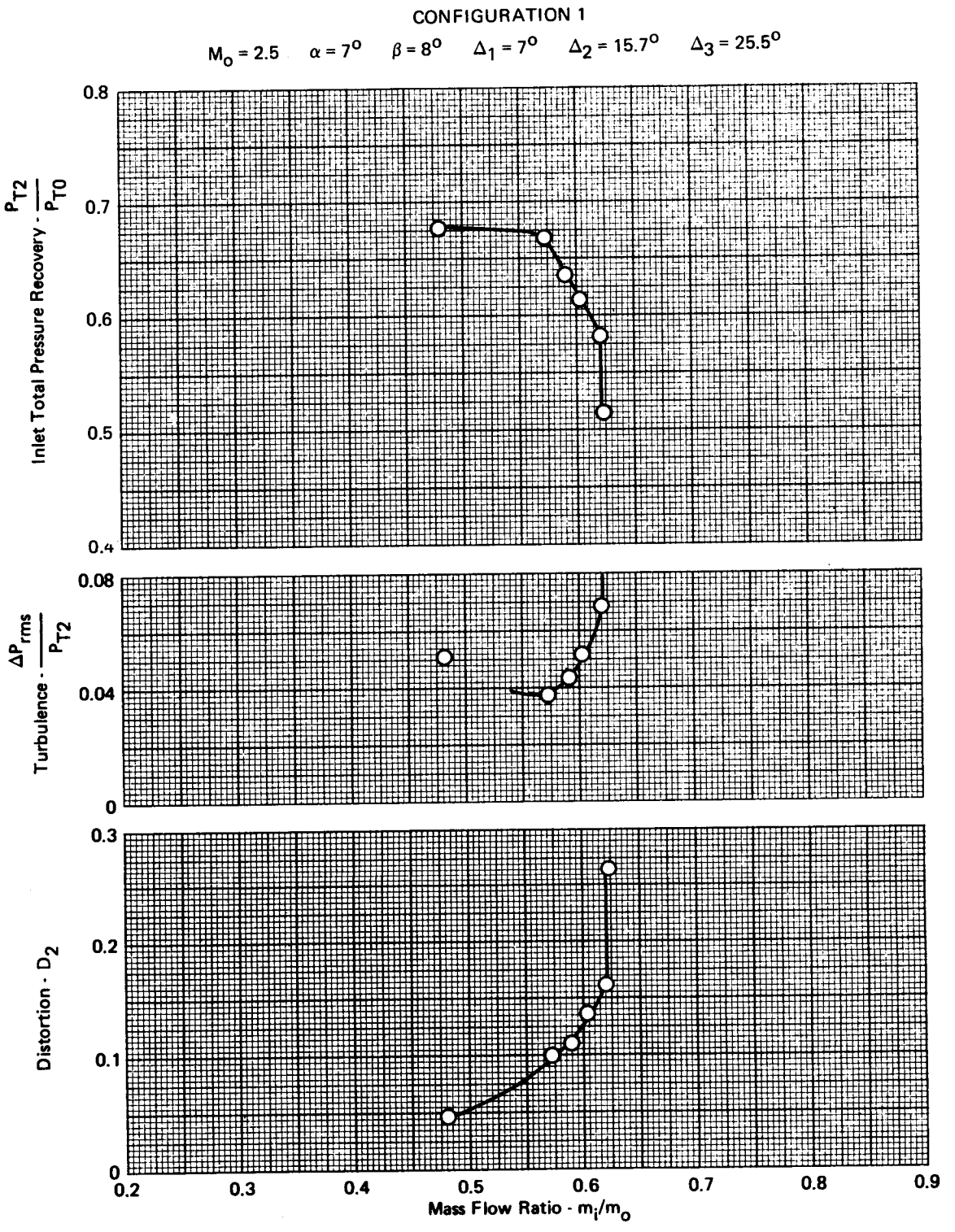

FIGURE A-128 - EFFECTS OF ANGLE OF SIDESLIP ONPRESSURE RECOVERY, TURBULENCE, AND DISTORTION

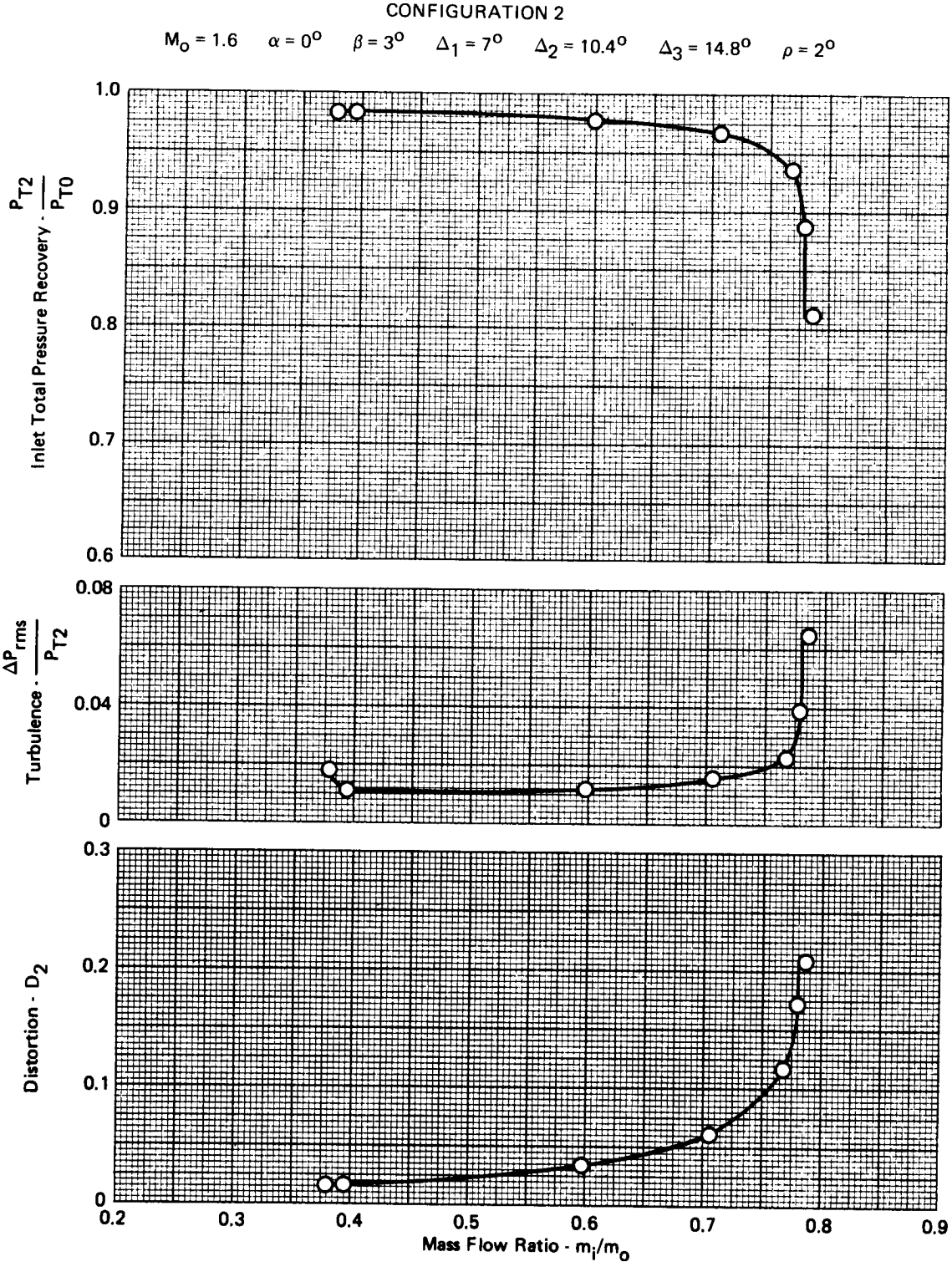

FIGURE A-129- EFFECTS OF ANGLE OF SIDESLIP ON PRESSURE RECOVERY, TURBULENCE, AND DISTORTION

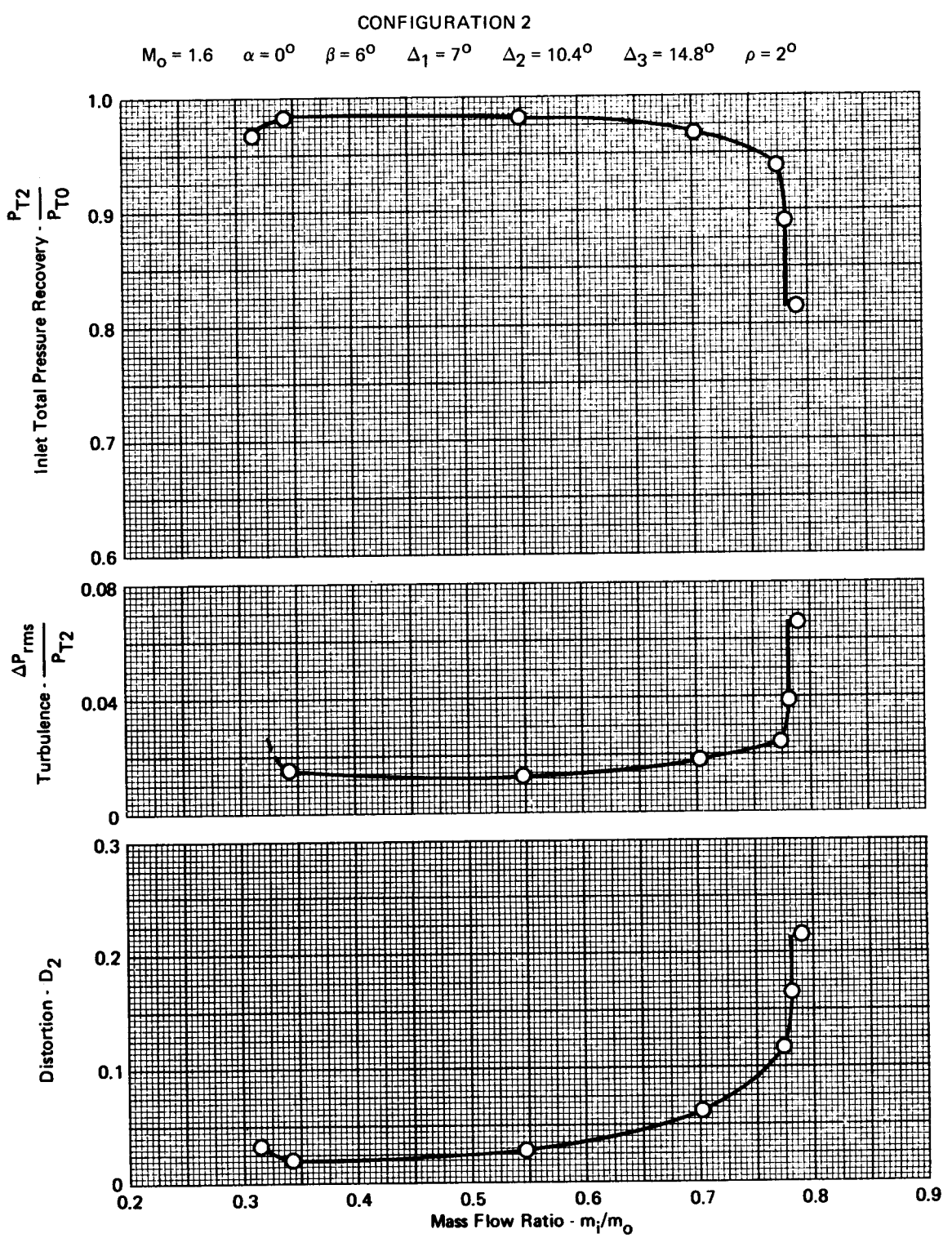

FIGURE A-130 - EFFECTS OF ANGLE OF SIDESLIP ON PRESSURE RECOVERY, TURBULENCE, AND DISTORTION

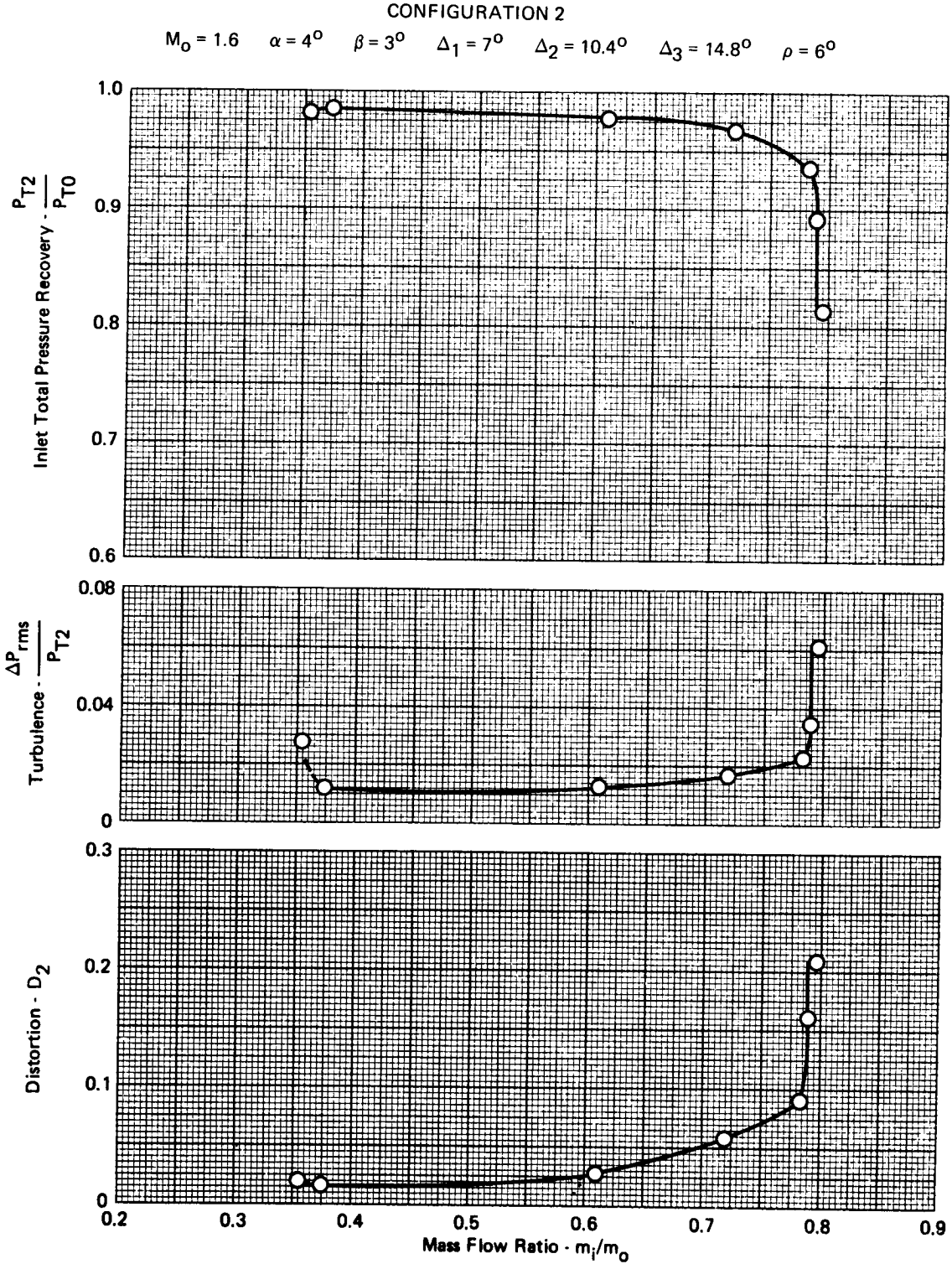

FIGURE A-131 - EFFECTS OF ANGLE OF SIDESLIP ON PRESSURE RECOVERY, TURBULENCE, AND DISTORTION

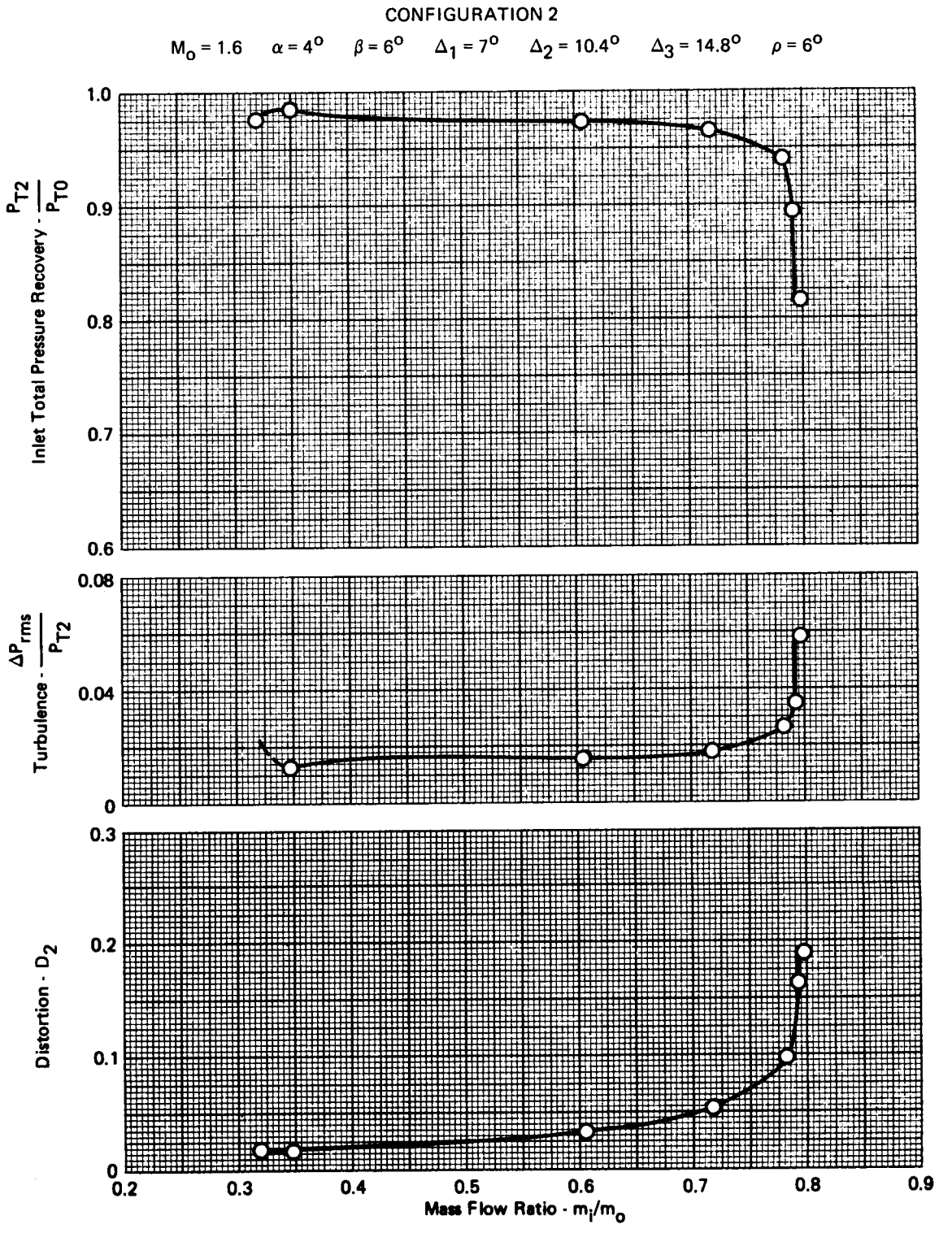

FIGURE A-132 - EFFECTS OF ANGLE OF SIDESLIP ON PRESSURE RECOVERY, TURBULENCE, AND DISTORTION

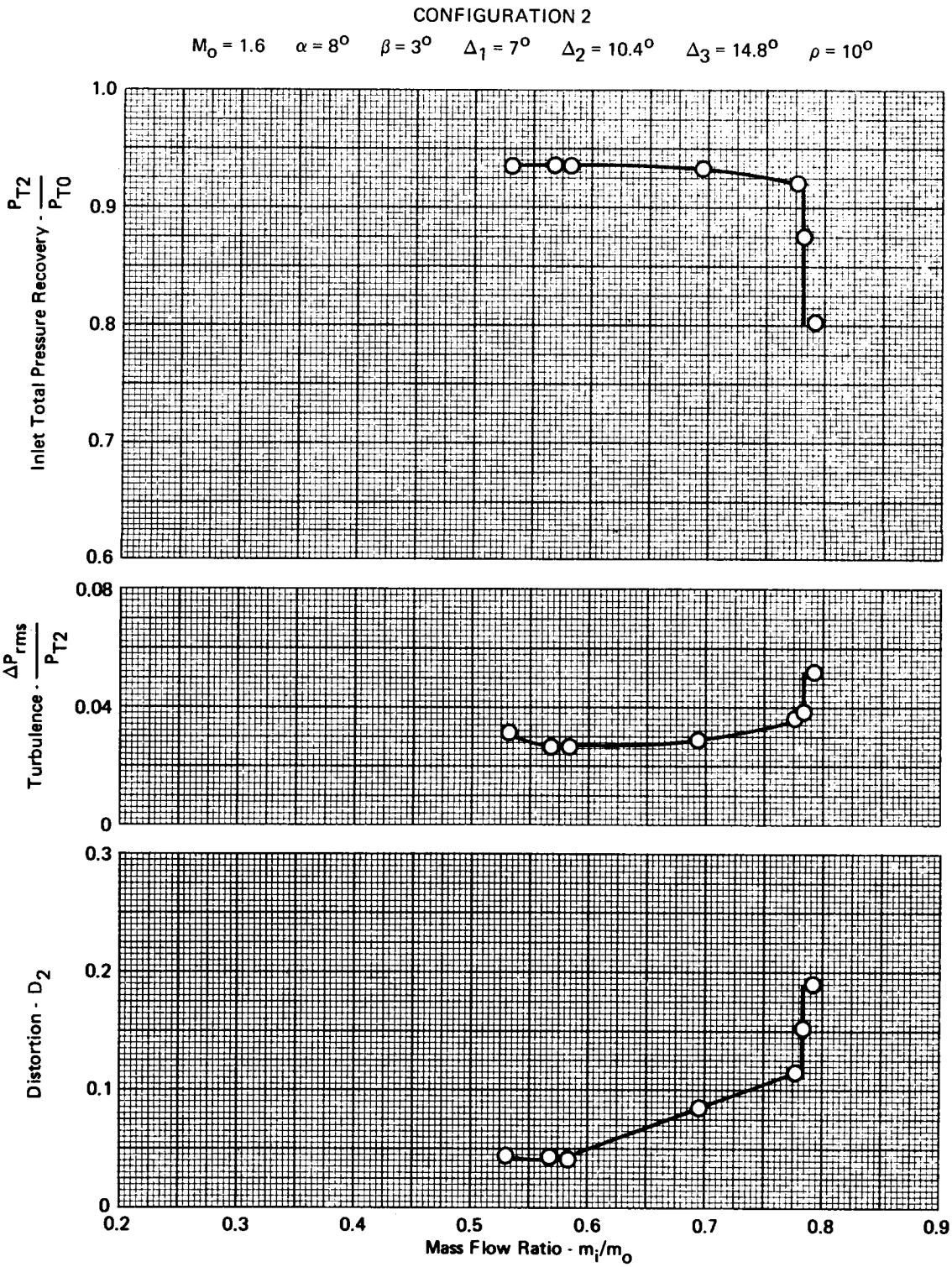

FIGURE A-133 - EFFECTS OF ANGLE OF SIDESLIP ON PRESSURE RECOVERY, TURBULENCE, AND DISTORTION

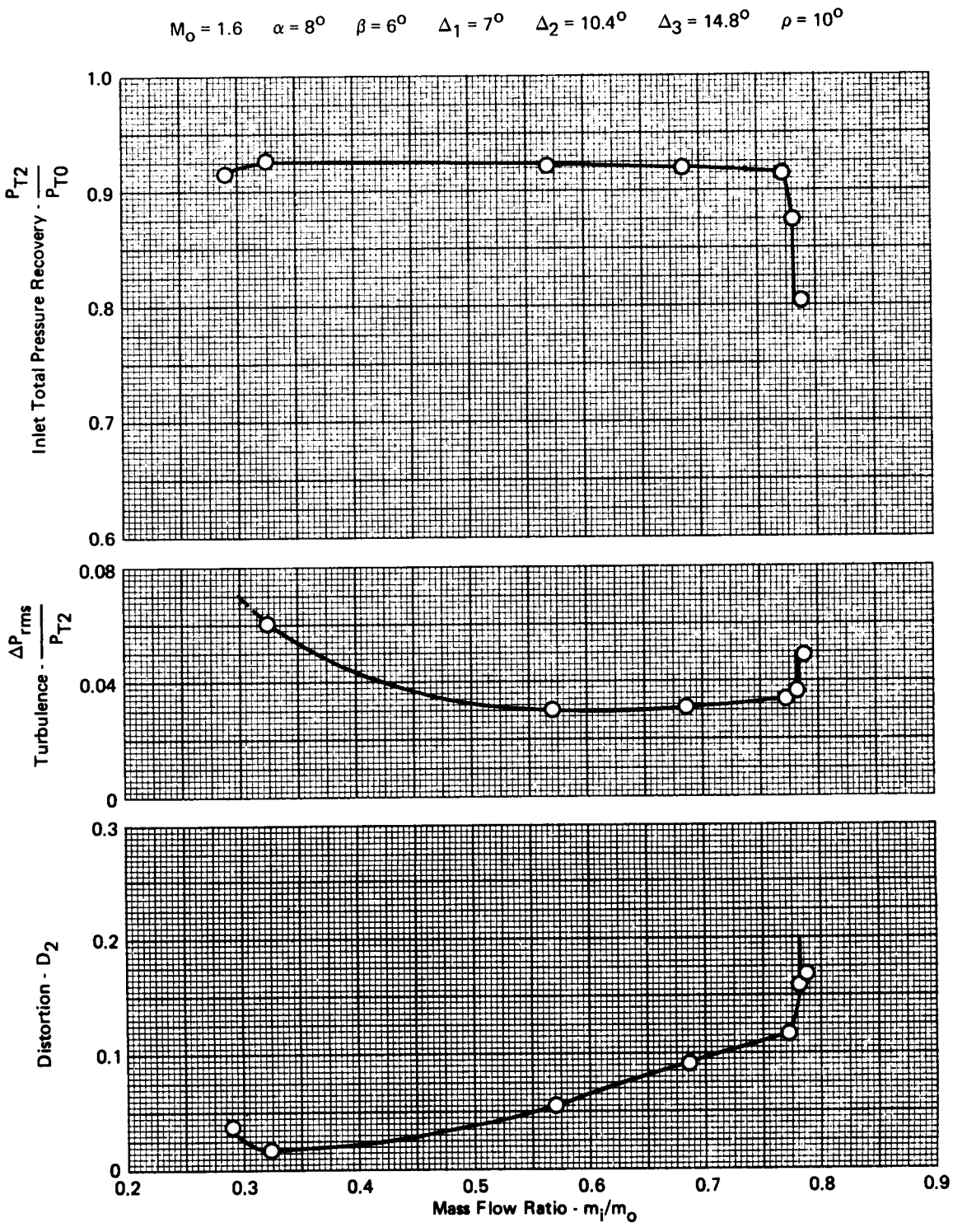

FIGURE A-134 - EFFECTS OF ANGLE OF SIDESLIP ON PRESSURE RECOVERY, TURBULENCE, AND DISTORTION

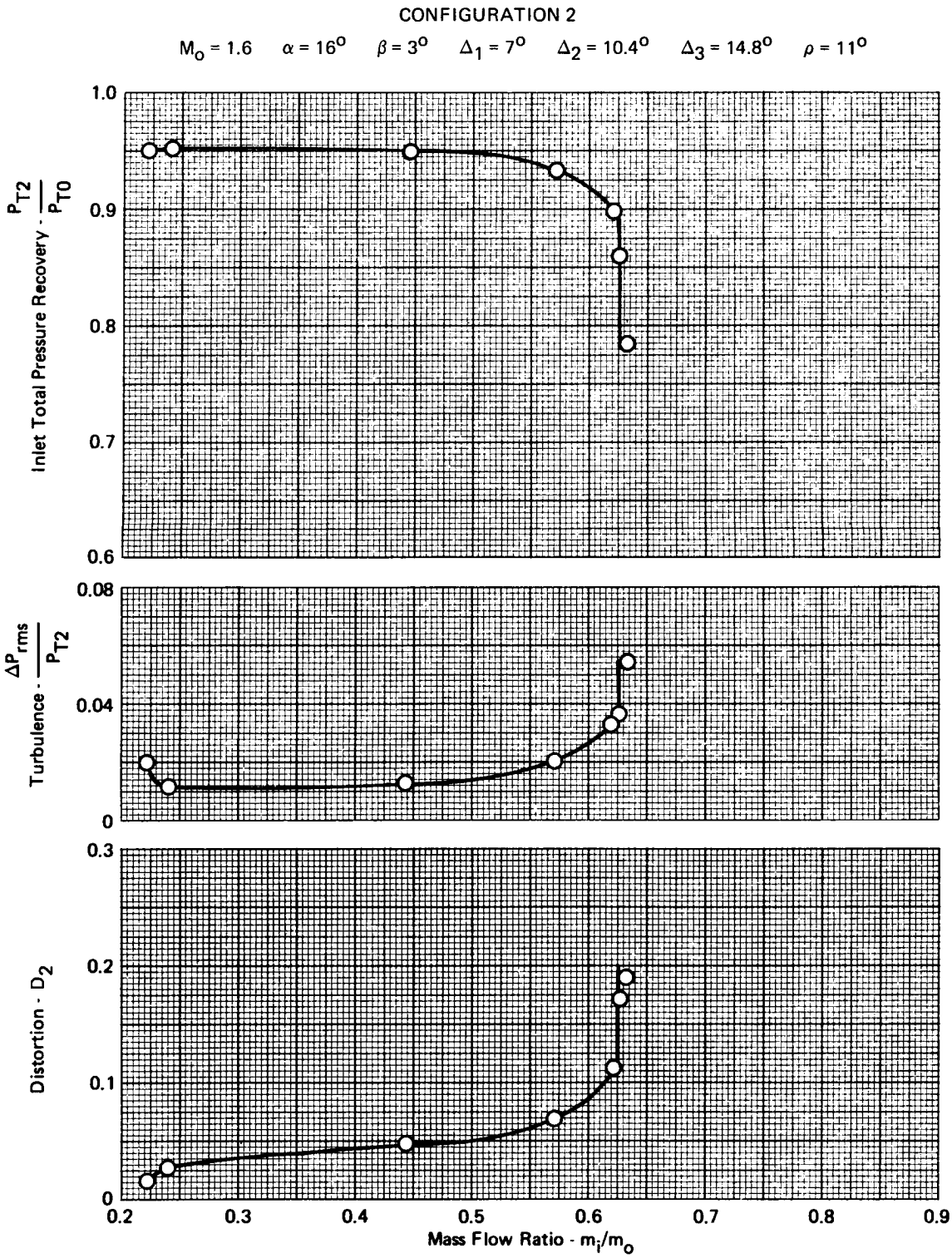

FIGURE A-135 - EFFECTS OF ANGLE OF SIDESLIP ON PRESSURE RECOVERY, TURBULENCE, AND DISTORTION

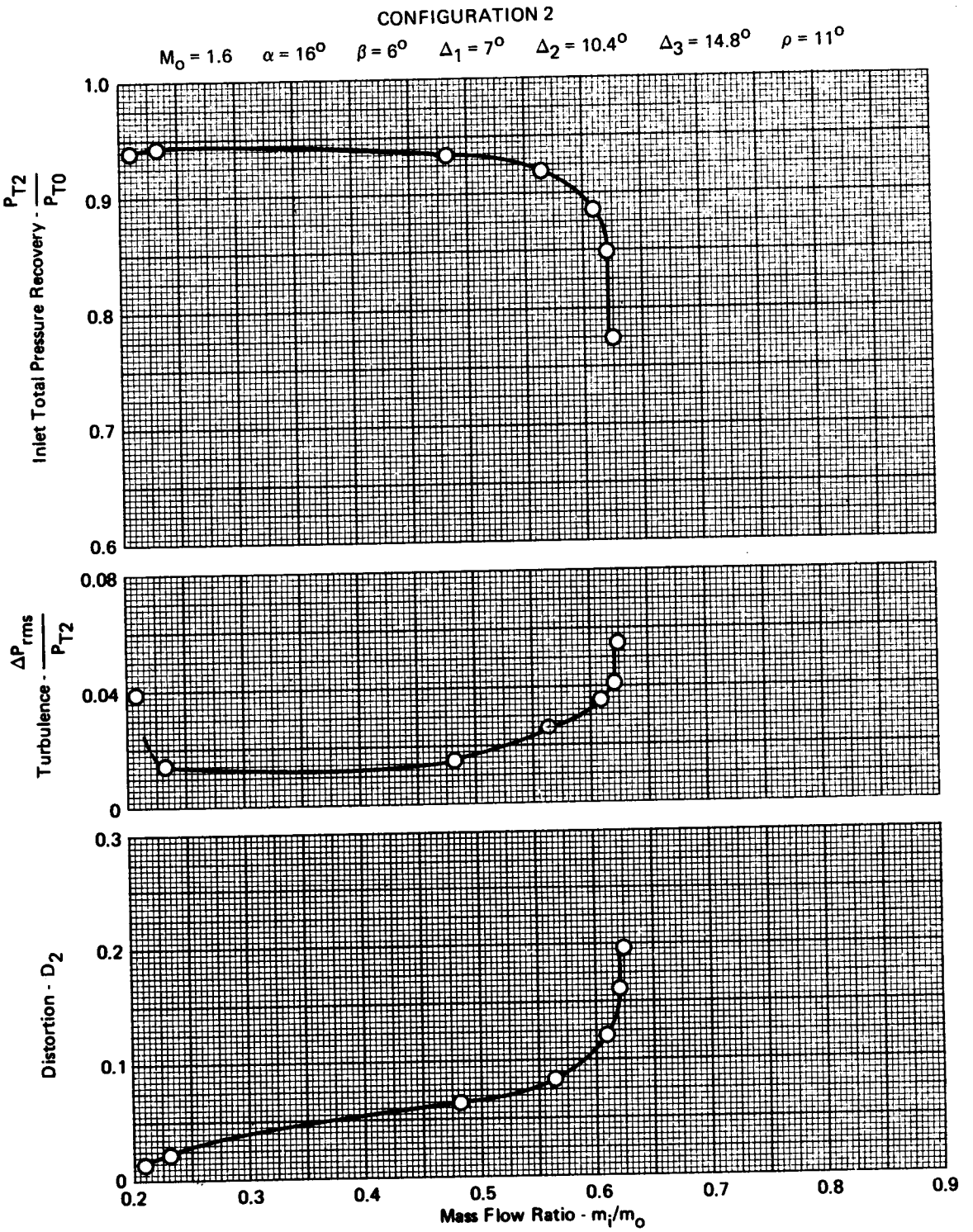

FIGURE A-136· EFFECTS OF ANGLE OF SIDESLIP ON PRESSURE RECOVERY, TURBULENCE, AND DISTORTION

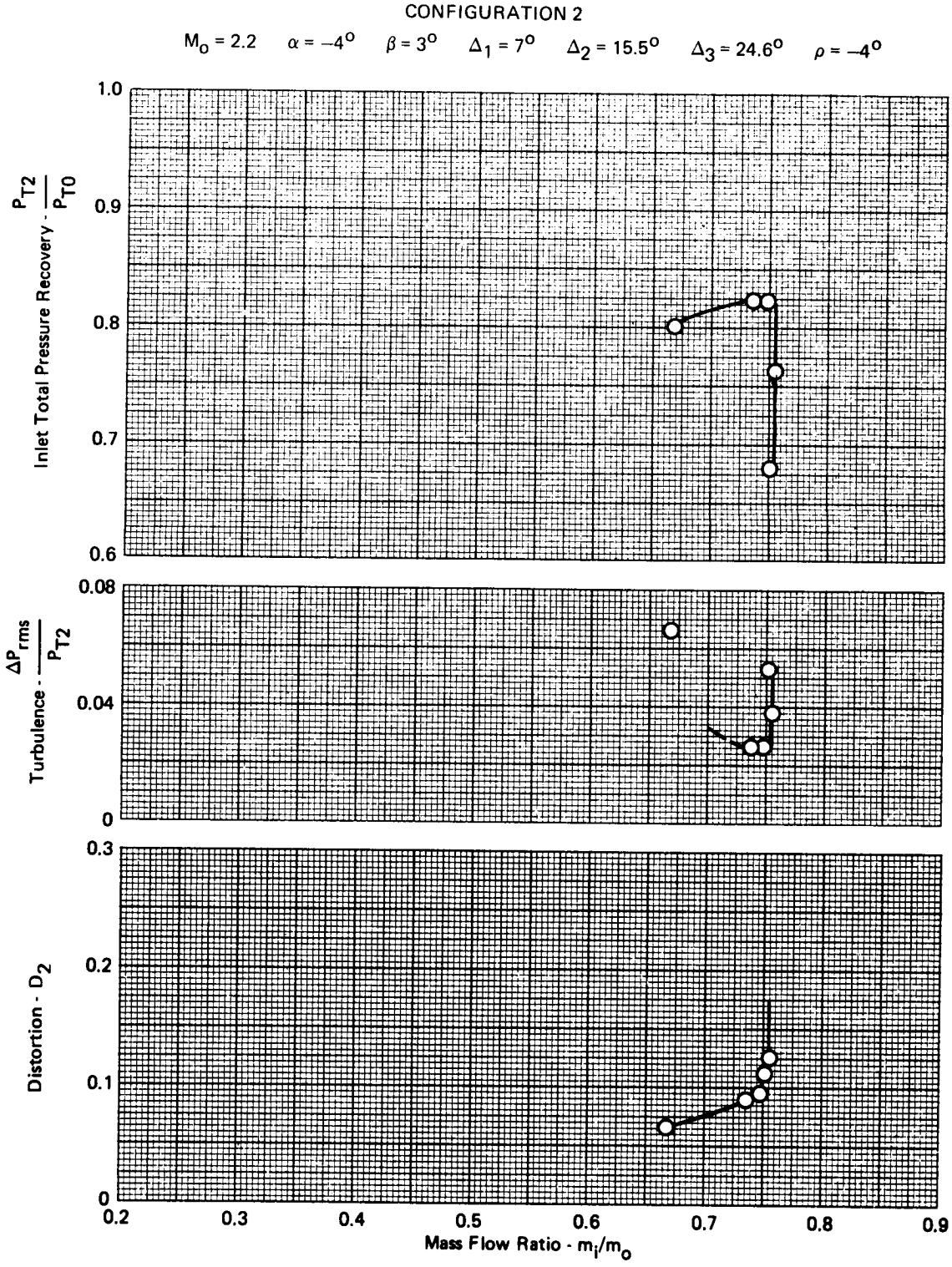

FIGURE A-137- EFFECTS OF ANGLE OF SIDESLIP ON PRESSURE RECOVERY, TURBULENCE, AND DISTORTION

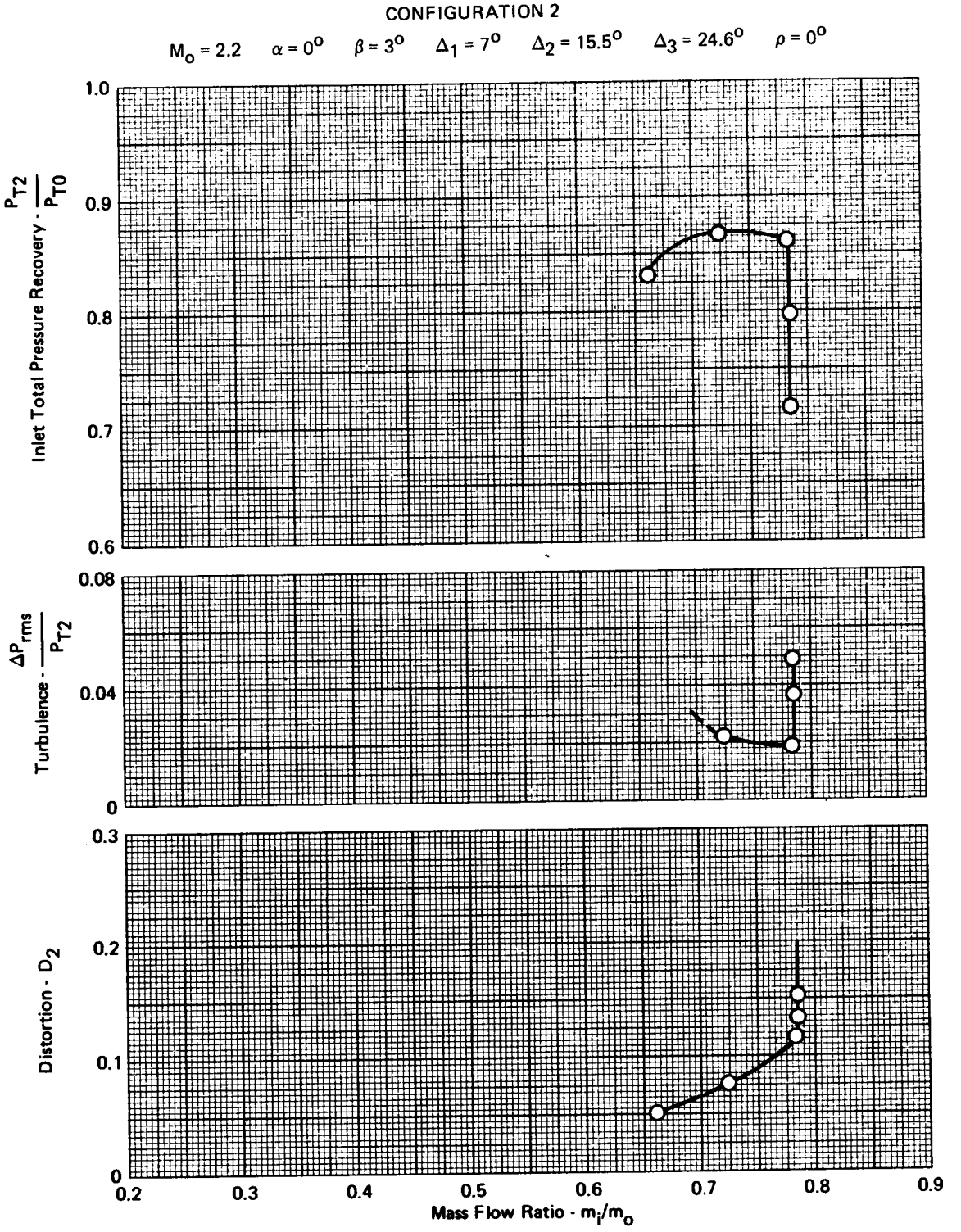

FIGURE A-138 - EFFECTS OF ANGLE OF SIDESLIP ON PRESSURE RECOVERY, TURBULENCE, AND DISTORTION

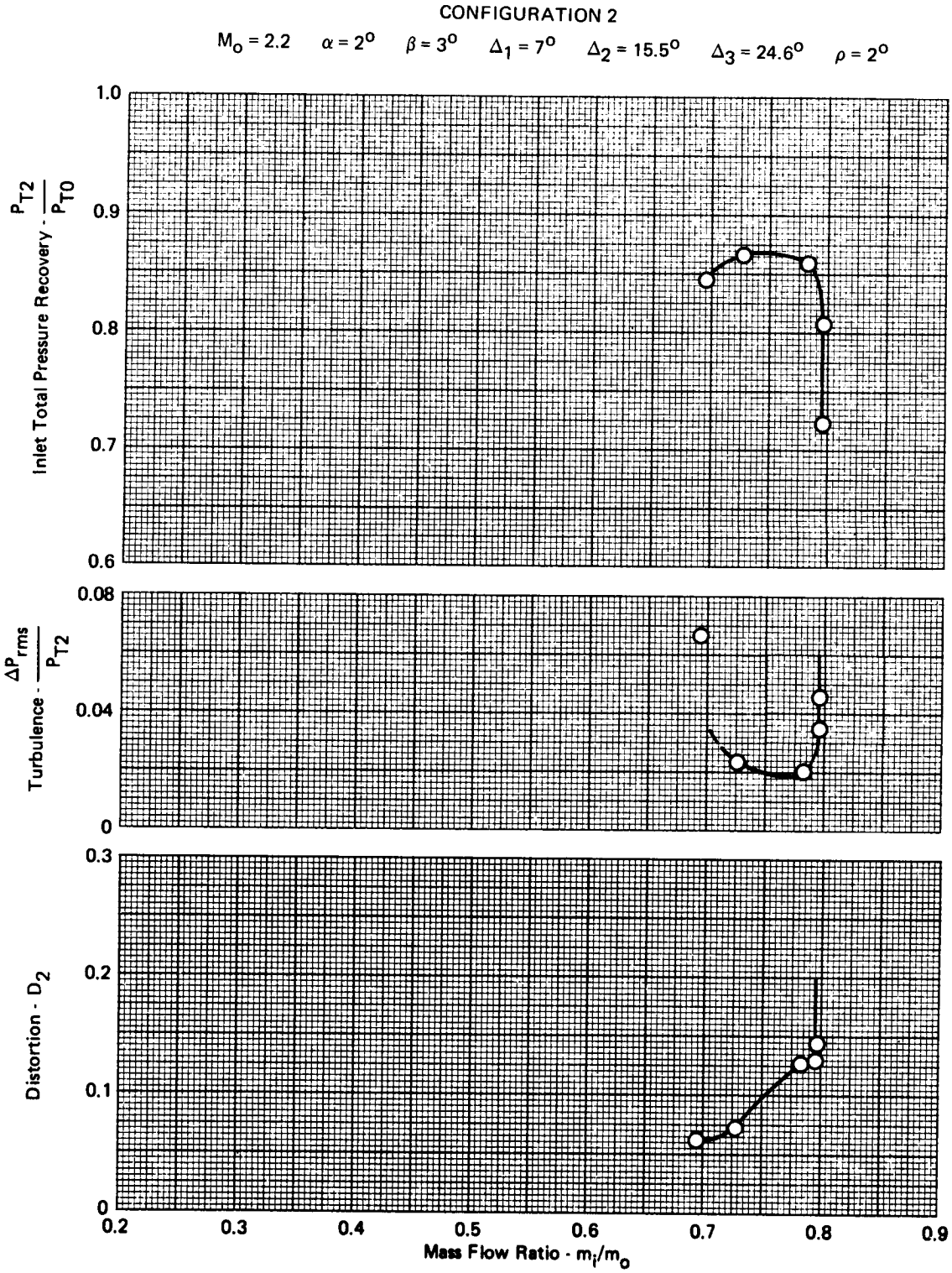

FIGURE A-139. EFFECTS OF ANGLE OF SIDESLIP ON PRESSURE RECOVERY, TURBULENCE, AND DISTORTION

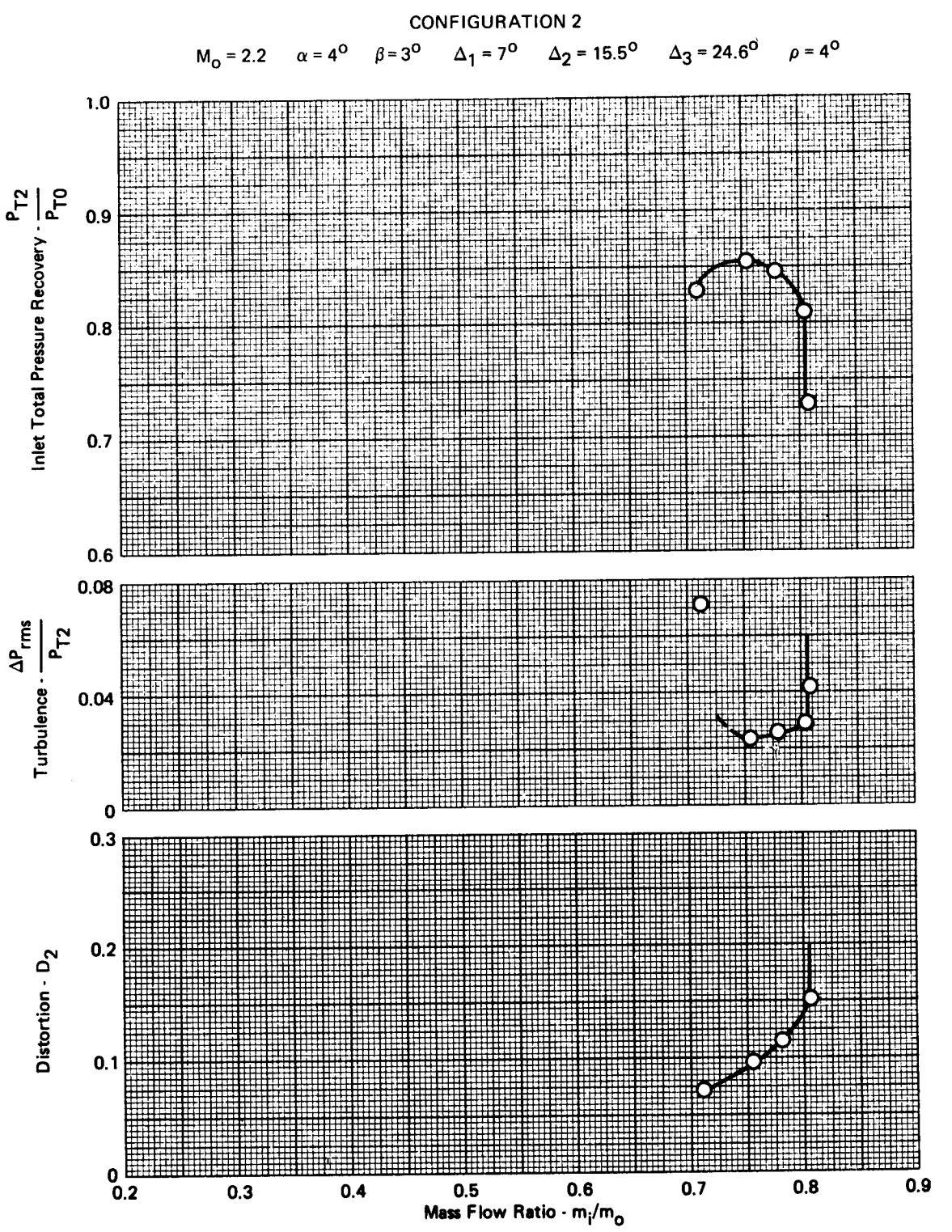

FIGURE A-140- EFFECTS OF ANGLE OF SIDESLIP ON PRESSURE RECOVERY, TURBULENCE, AND DISTORTION

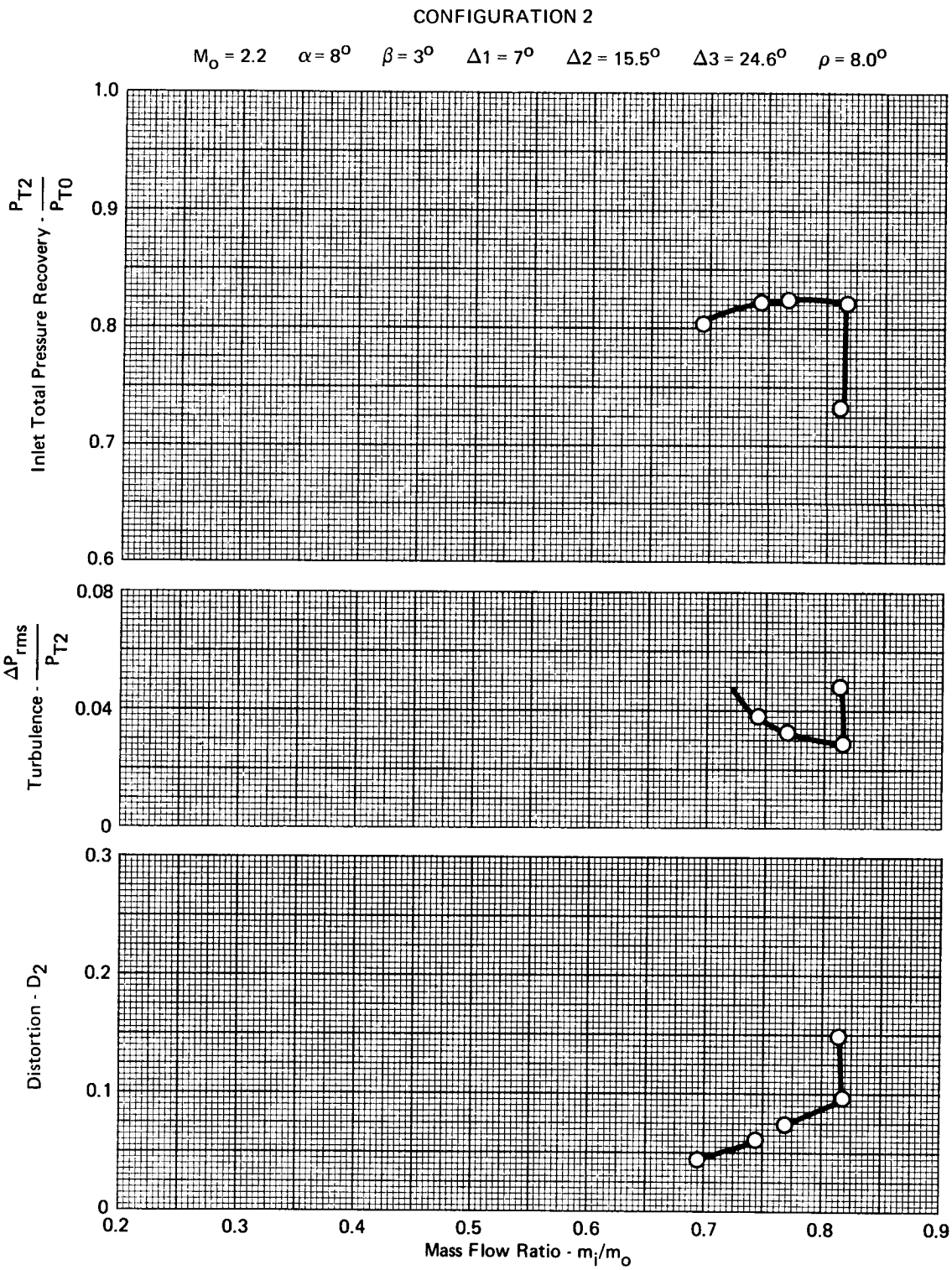

FIGURE A-141 - EFFECTS OF ANGLE OF SIDESLIP ON PRESSURE RECOVERY, TURBULENCE, AND DISTORTION

GP73-0449-76

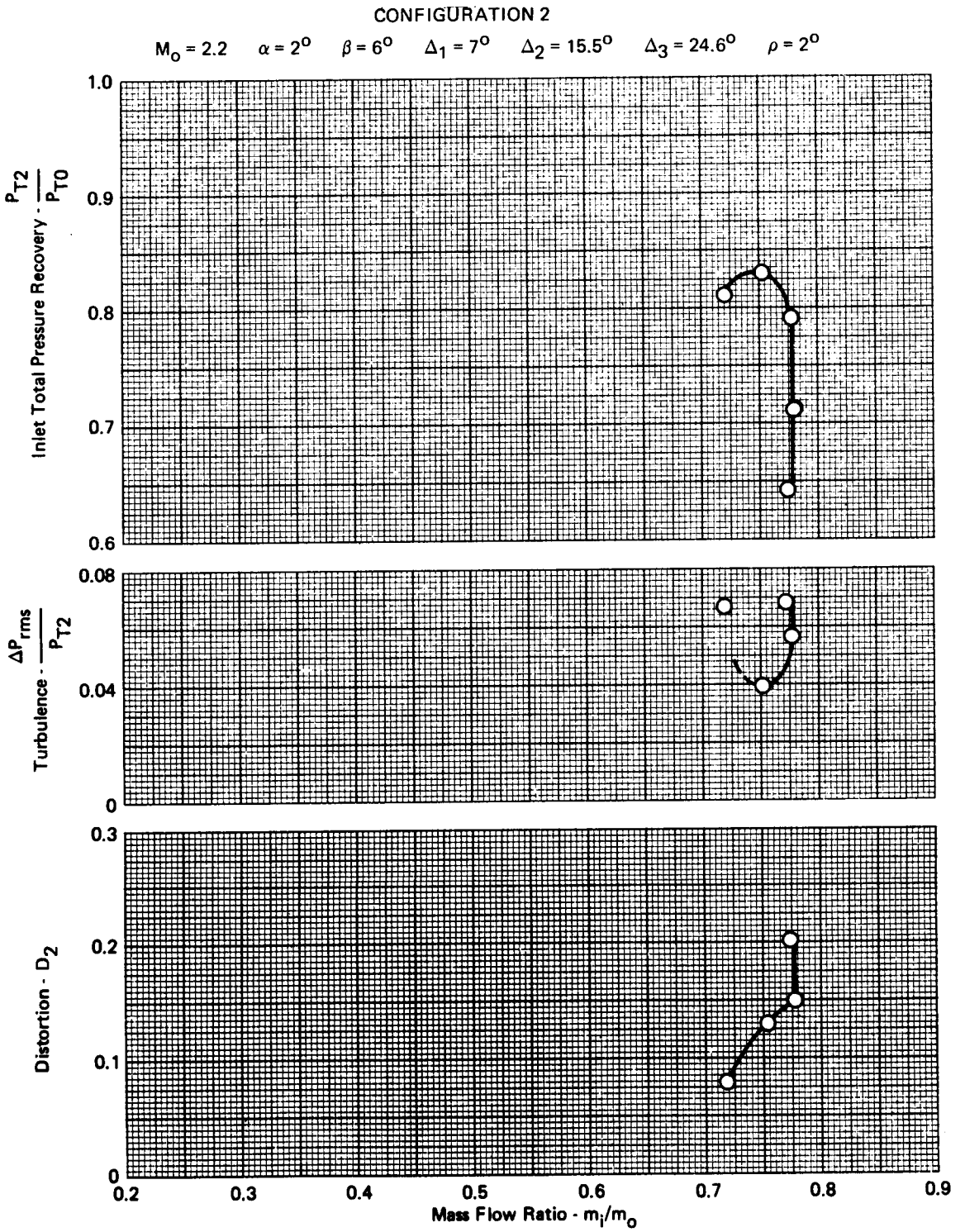

FIGURE A-142- EFFECTS OF ANGLE OF SIDESLIP ON PRESSURE RECOVERY, TURBULENCE, AND DISTORTION

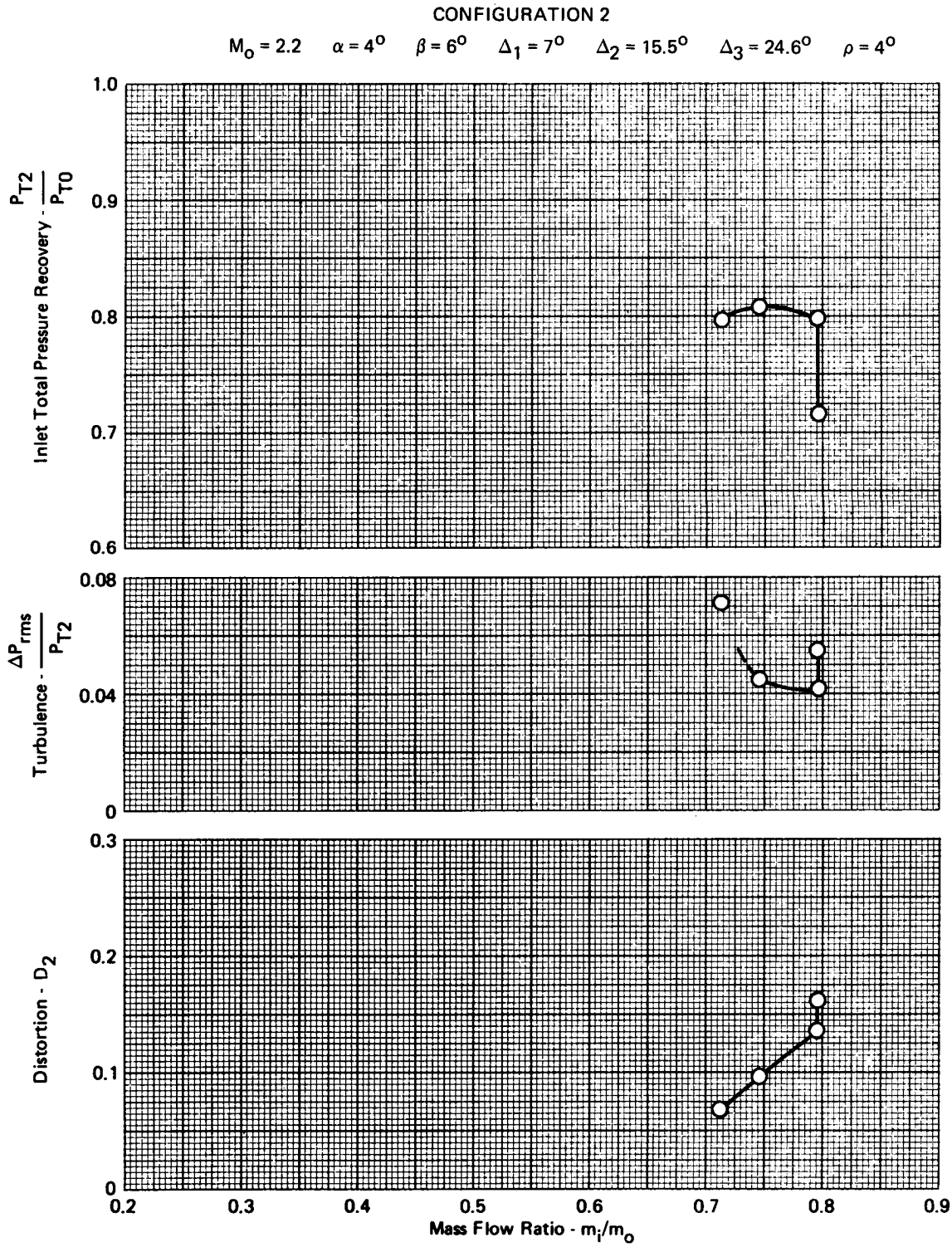

FIGURE A-143- EFFECTS OF ANGLE OF SIDESLIP ON PRESSURE RECOVERY, TURBULENCE, AND DISTORTION

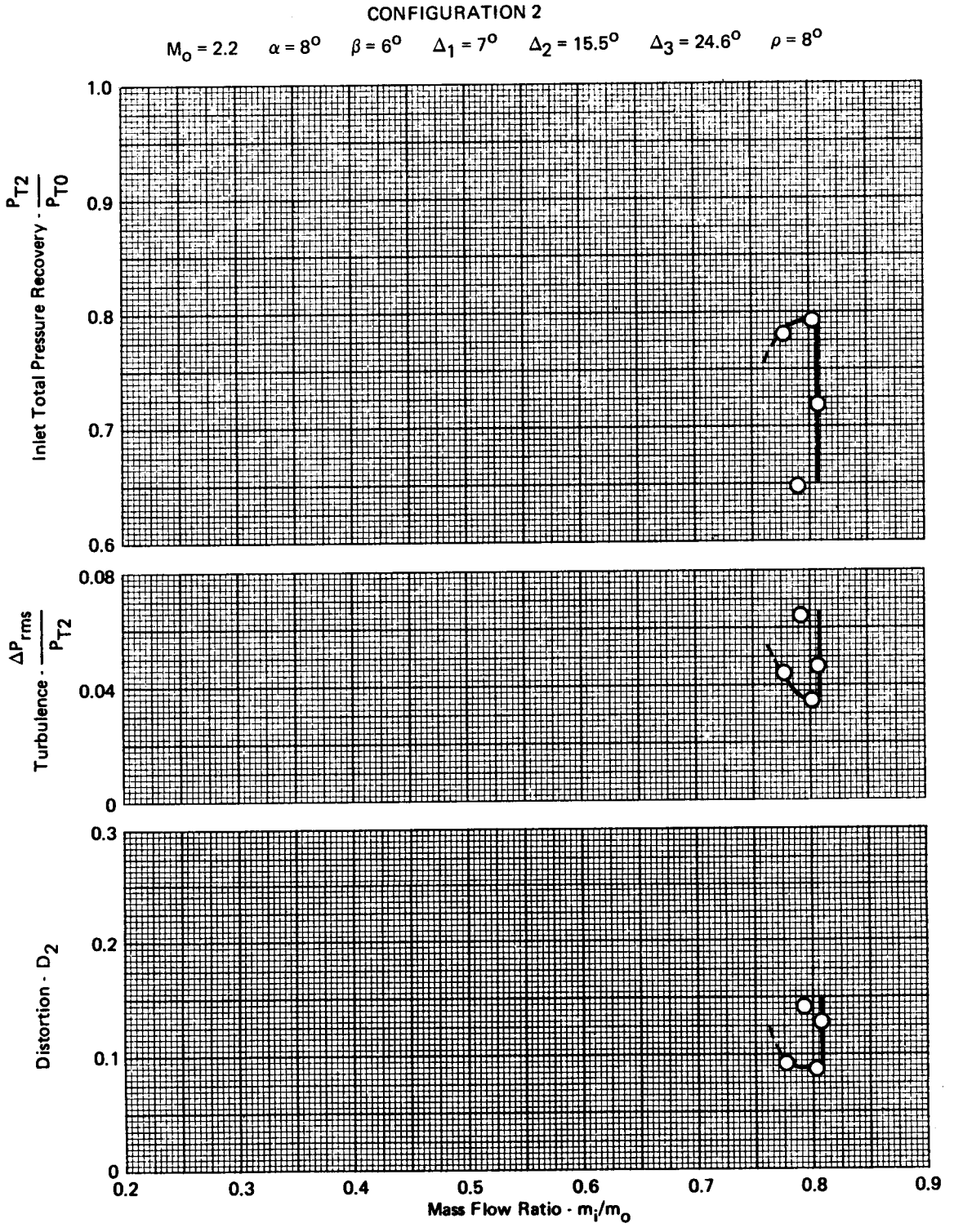

FIGURE A-144 - EFFECTS OF ANGLE OF SIDESLIP ON PRESSURE RECOVERY, TURBULENCE, AND DISTORTION

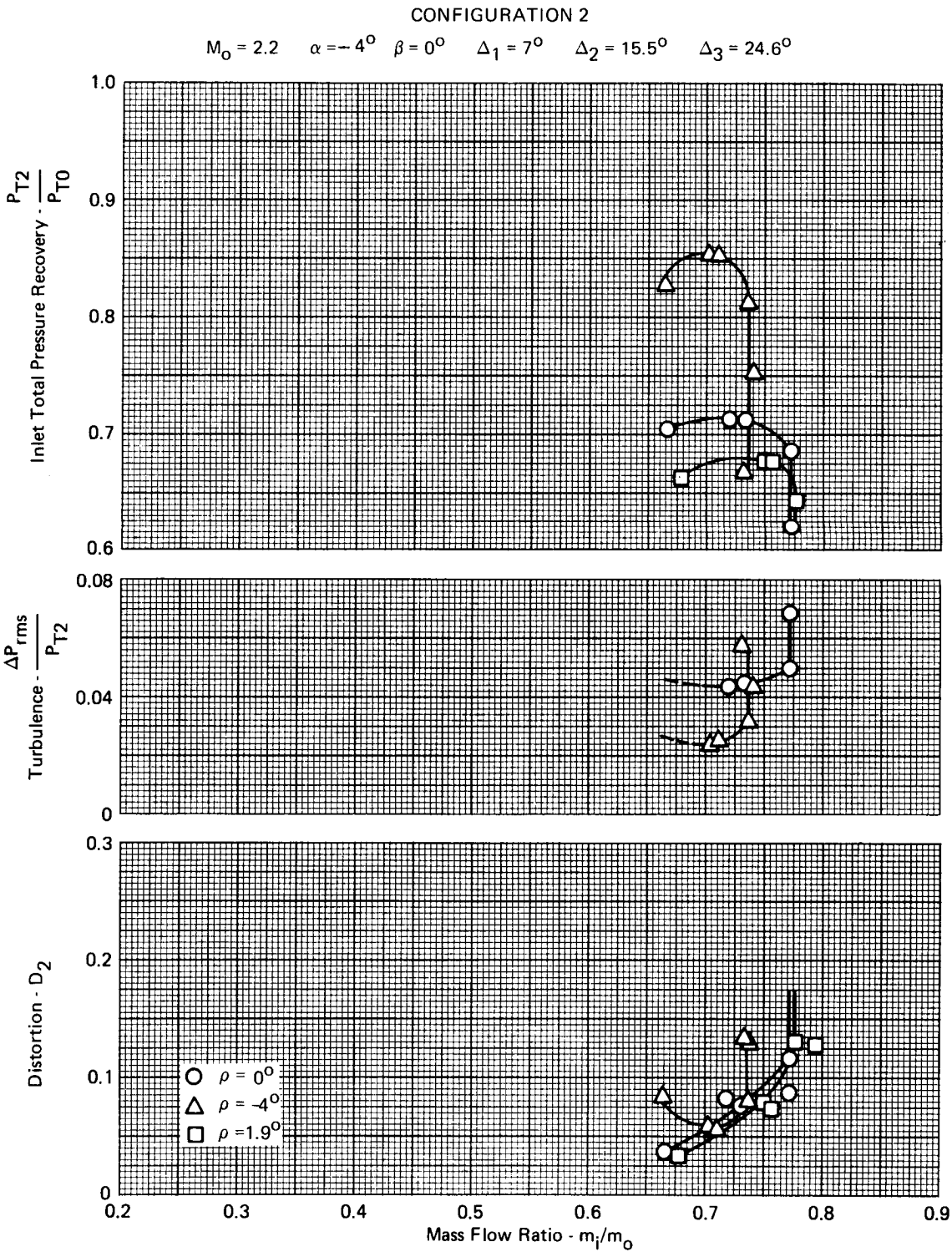

FIGURE A-145 - FFFECTS OF RAMP SYSTEM ROTATION ON PRESSURE RECOVERY, TURBULENCE, AND DISTORTION

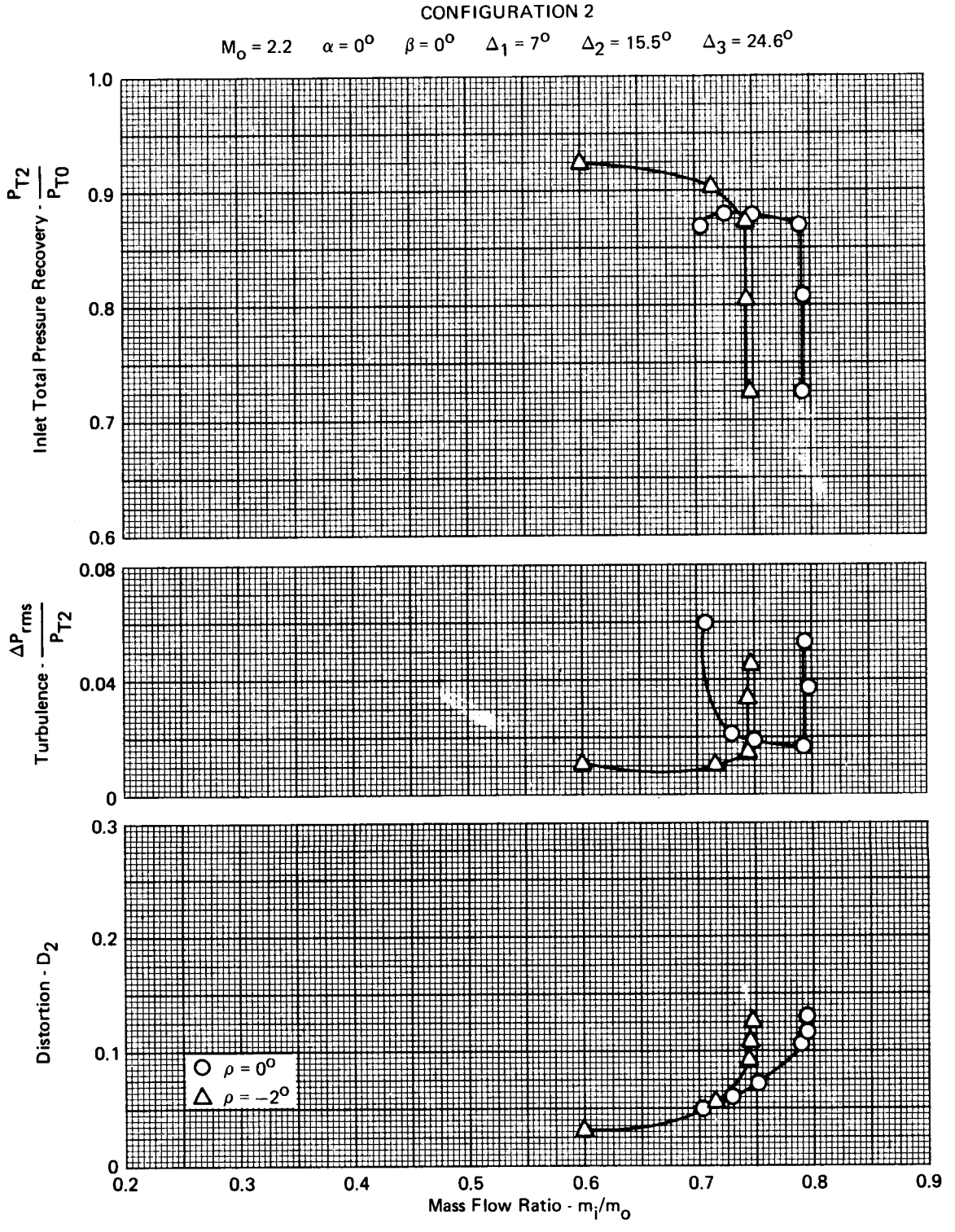

FIGURE A-146 - EFFECTS OF RAMP SYSTEM ROTATION ON PRESSURE RECOVERY, TURBULENCE, AND DISTORTION

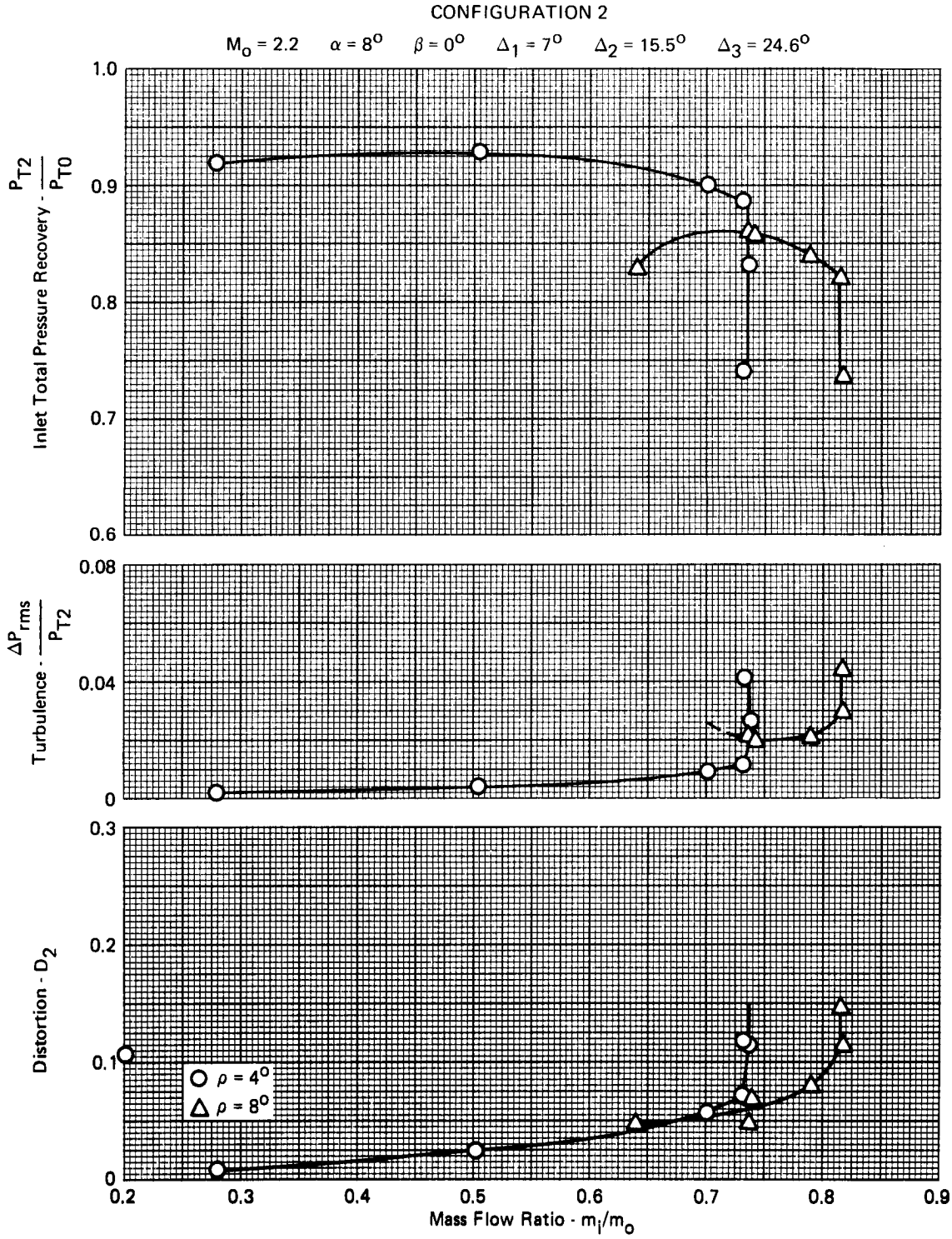

FIGURE A-147 - EFFECTS OF RAMP SYSTEM ROTATION ON PRESSURE RECOVERY, TURBULENCE, AND DISTORTION

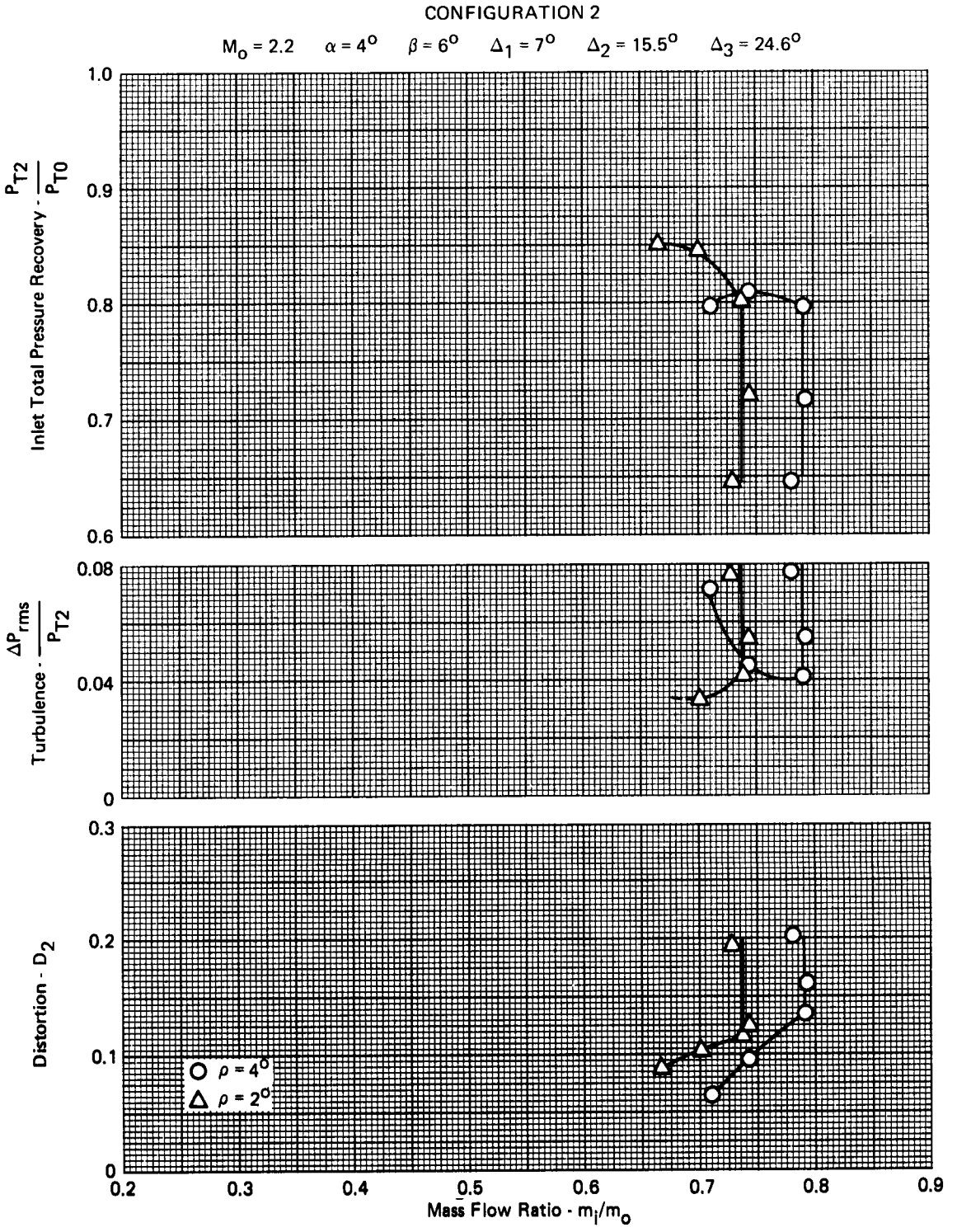

FIGURE A-148 - EFFECTS OF RAMP SYSTEM ROTATION ON PRESSURE RECOVERY, TURBULENCE, AND DISTORTION

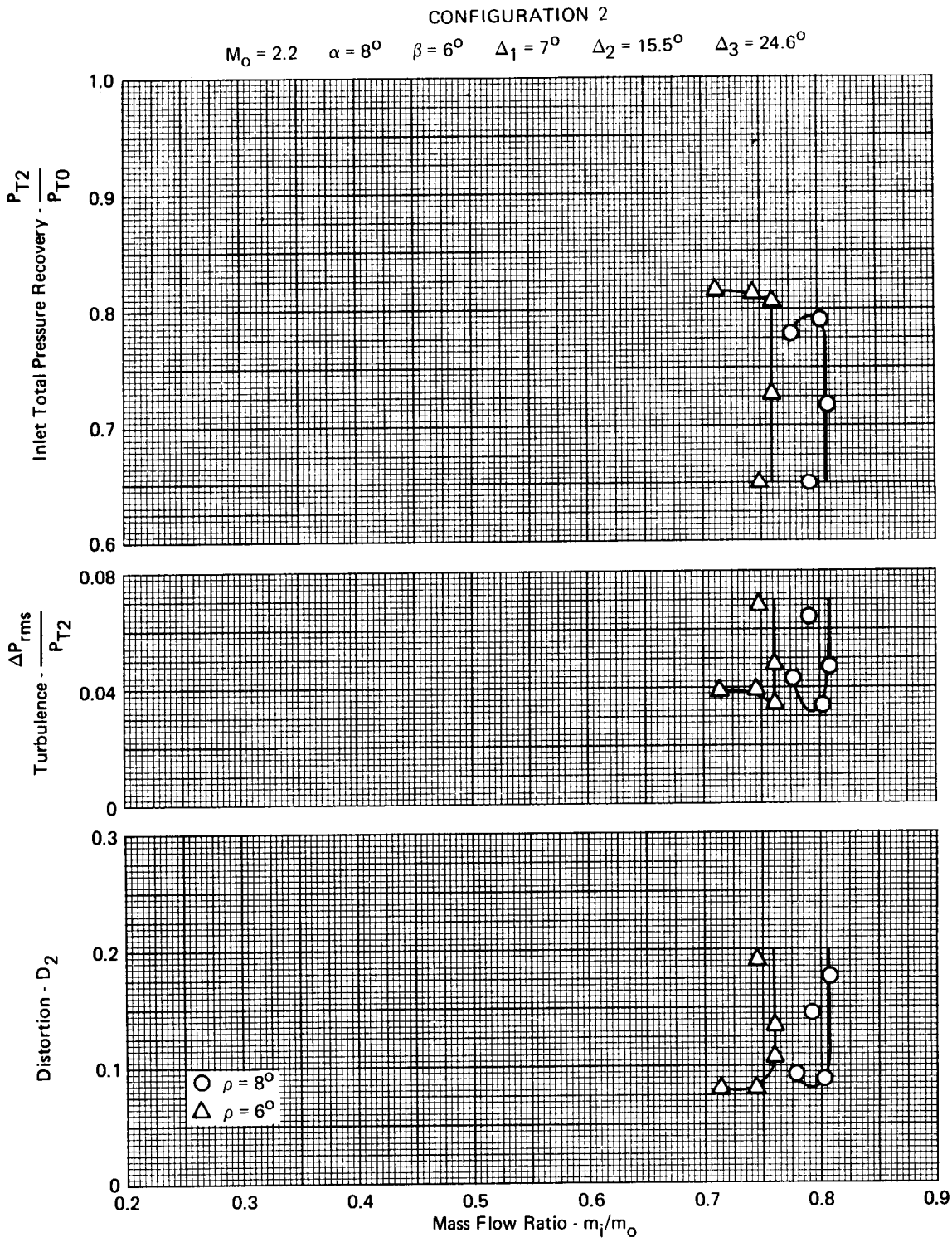

FIGURE A-149 - EFFECTS OF RAMP SYSTEM ROTATION ON PRESSURE RECOVERY, TURBULENCE, AND DISTORTION

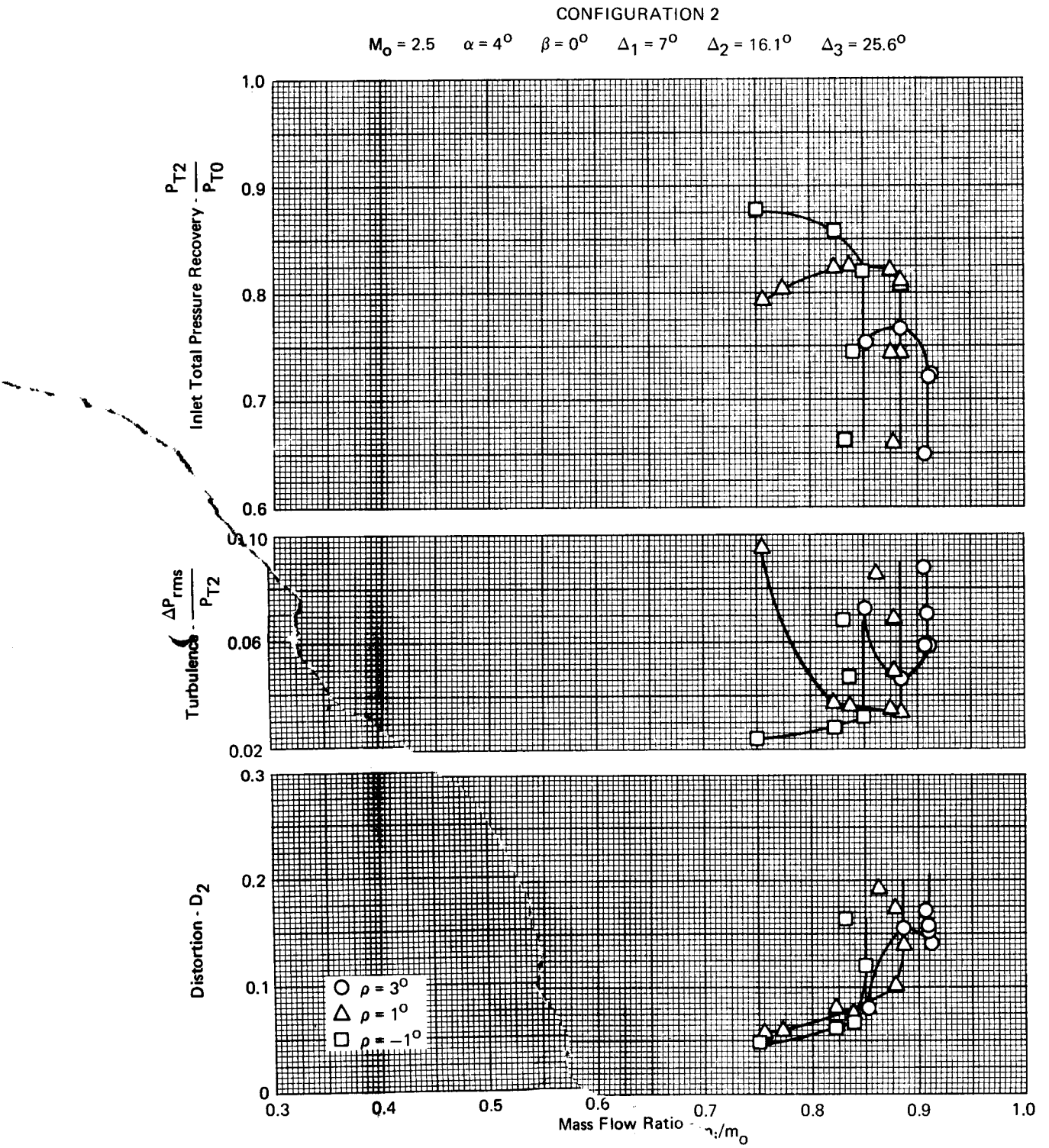

FIGURE A-150 - EFFECTS OF RAMP SYSTEM ROTATION ON PRESSURE RECOVERY, TURBULENCE, AND DISTORTION

APPENDIX B

BLEED/BYPASS DRAG CALCULATION PROCEDURE

The second and third ramp bleed drag, throat slot bleed drag, and bypass drag used to evaluate the effect of selected design variables on net propulsive force are analytically determined. The procedure used to calculate these bleed and bypass drags is outlined below.

SYMBOLS

C_V	Thrust coefficient
D	Drag force
F	Thrust
g	Standard gravitational acceleration
m	Mass flow rate
M	Mach number
P_T	Total pressure
p	Static pressure
q	Dynamic pressure - $1/2\ \gamma\ p_o M_o^2$
R	Gas constant
T	Static temperature
T_T	Total temperature
V	Velocity
$\frac{w\sqrt{\theta}}{\delta_2}$	Corrected mass flow rate
γ	Ratio of specific heats
δ_2	Ratio of average duct total pressure to sea level standard pressure
θ	Ratio of duct total temperature to sea level standard temperature
ϕ	Exit angle of mass flow

APPENDIX B

Subscripts

exit	Bleed/bypass exit conditions
ISEN	Conditions following isentropic expansion to ambient pressure
0	Freestream conditions
2	Engine face conditions

The bleed and bypass drags are evaluated by determining the loss in momentum between the inlet and exit of each system. Thus, in general,

$$D]_{\substack{\text{bleed or}\\ \text{bypass}}} = mV_o - F_{exit}$$

Rearranging the equation results in the following:

$$\frac{D/q_o}{\frac{w\sqrt{\theta}}{\delta_2}} = \left(\frac{p}{q}\right)_o \left(\frac{P_T}{P}\right)_o \left(\frac{\sqrt{\gamma R}\ (1.55)}{144\ g}\right)\left(\frac{P_{T_2}}{P_{T_o}}\right)\left[M_o \sqrt{(T/T_T)_o} - M_{ISEN} \sqrt{(T/T_T)_{ISEN}}\ C_V\right]$$

where C_V is the flush exit thrust coefficient from References B-1 and B-2 based on isentropic expansion to ambient pressure.

For ease of calculation, the equation can be reduced to the form:

$$\left.\frac{D/q}{\frac{w\sqrt{\theta}}{\delta_2}}\right]_{\text{at exit}} = F_1(M_o)\left[\frac{P_{T_2}}{P_{T_o}}\right]_{\substack{@\ \text{operating}\\ \text{point}}} \left[F_2(M_o) - F_3\left(\frac{P_{T_{exit}}}{P_o},\ M_o\right)\ \frac{\cos\phi}{\cos 15^\circ}\right]$$

where $F_1(M_o) = \left(\frac{p}{q}\right)_o \left(\frac{P_T}{P}\right)_o \left(\frac{\sqrt{\gamma R}\ (1.55)}{g\ 144}\right)$

$$F_2(M_o) = M_o \sqrt{(T/T_T)_o}$$

and

$$F_3\left(\frac{P_{T_{exit}}}{P},\ M_o\right) = M_{ISEN} \sqrt{(T/T_T)_{ISEN}} \cdot C_V$$

ϕ = exit angle of mass flow, degrees
(referenced to nominal 15° exit angle)

APPENDIX B

The values of F_1, F_2, and F_3 are obtained from the curves shown in Figures B-1 through B-6.

For the bleed/bypass drag calculations performed in the inlet performance analyses, the exit angle of the ramp bleeds is assumed to be 30° and the exit angle for the bypass flow, both forward and aft, is assumed to be 45°.

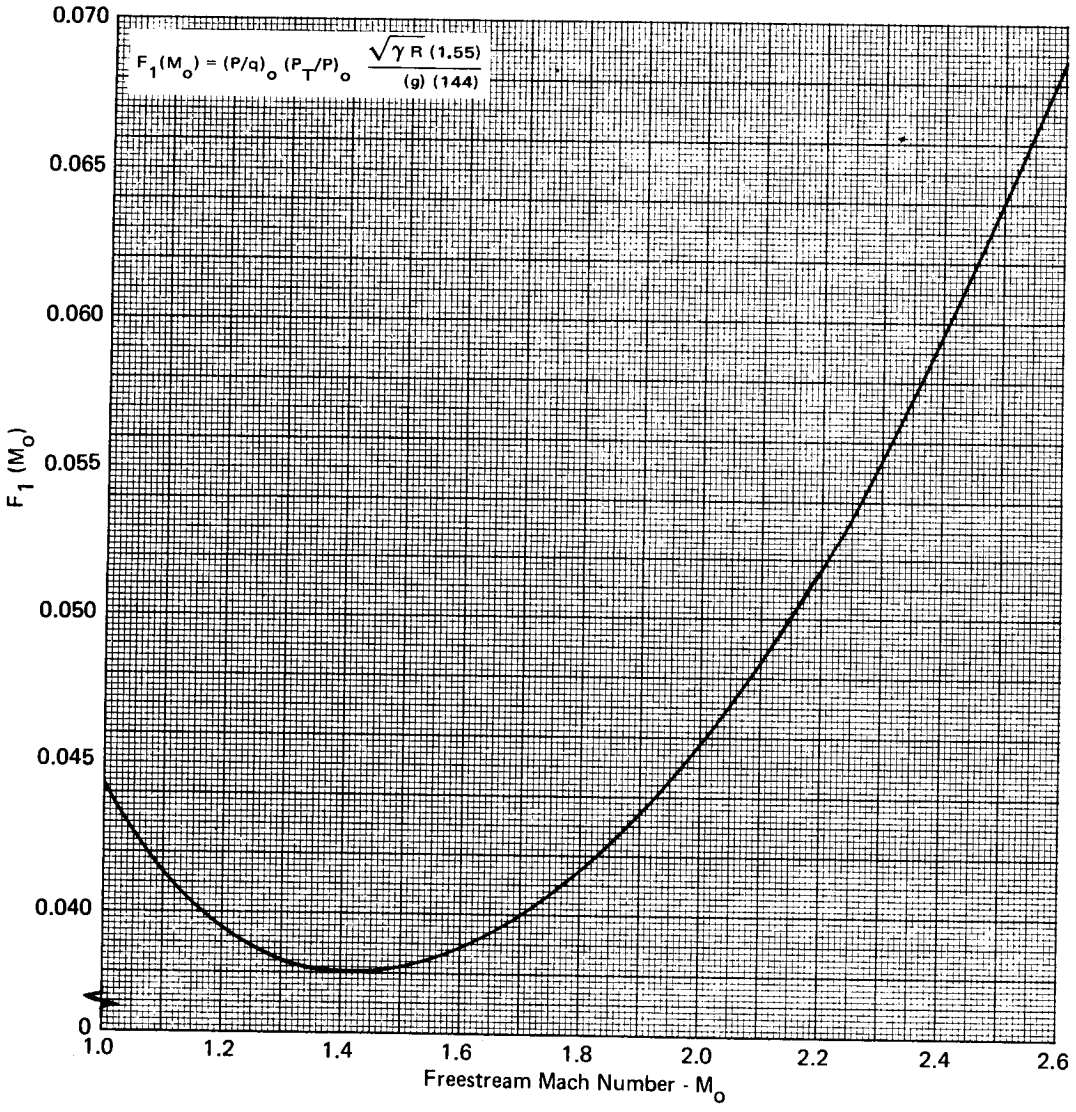

FIGURE B-2 - F_1 (M_o) vs M_o

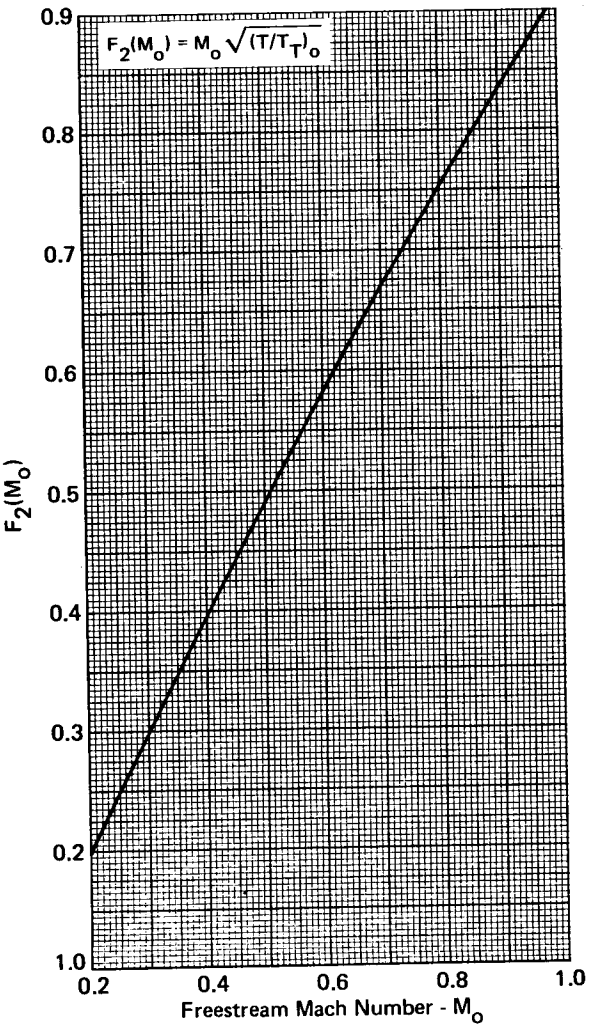

FIGURE B-3 - F_2 (M_o) vs M_o

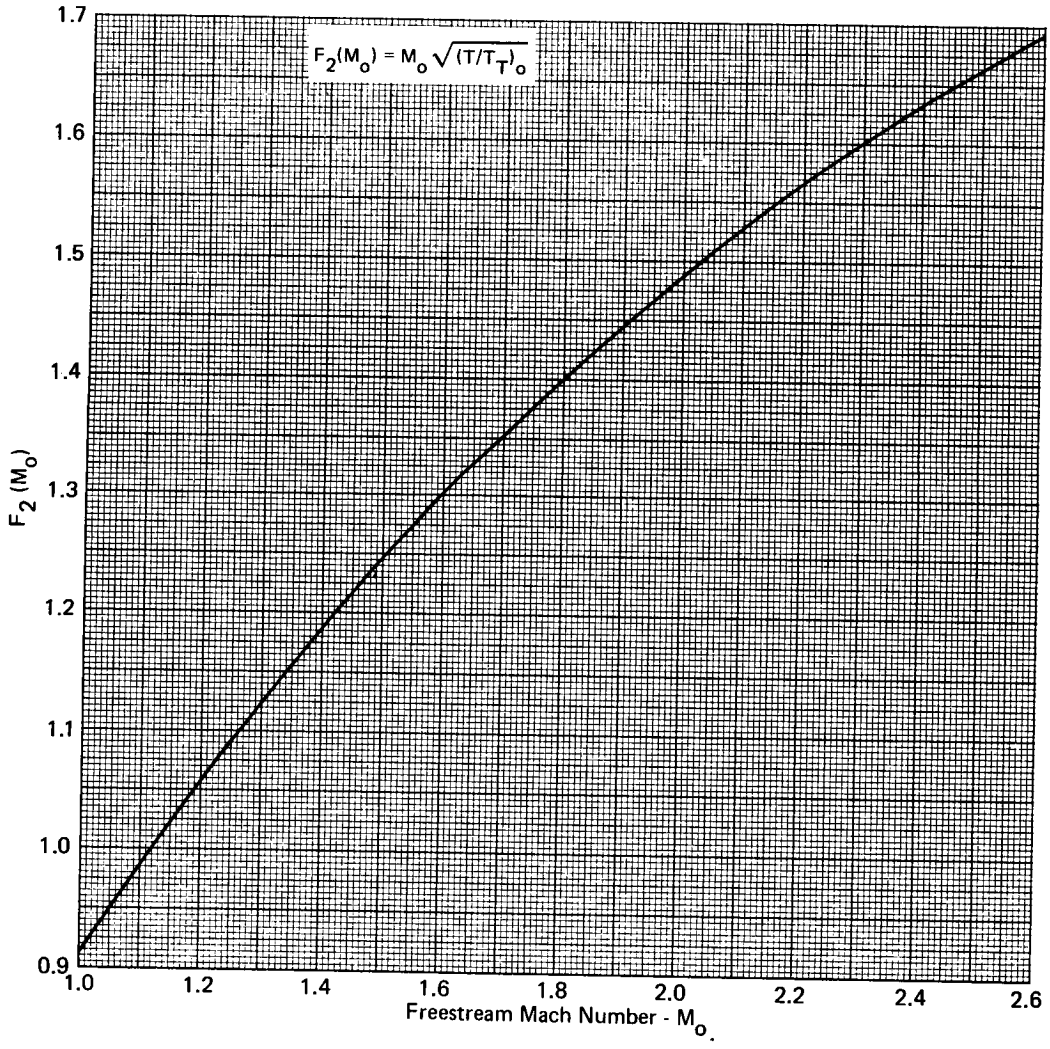

GP72-0979-112

FIGURE B-4 - $F_2(M_o)$ vs M_o

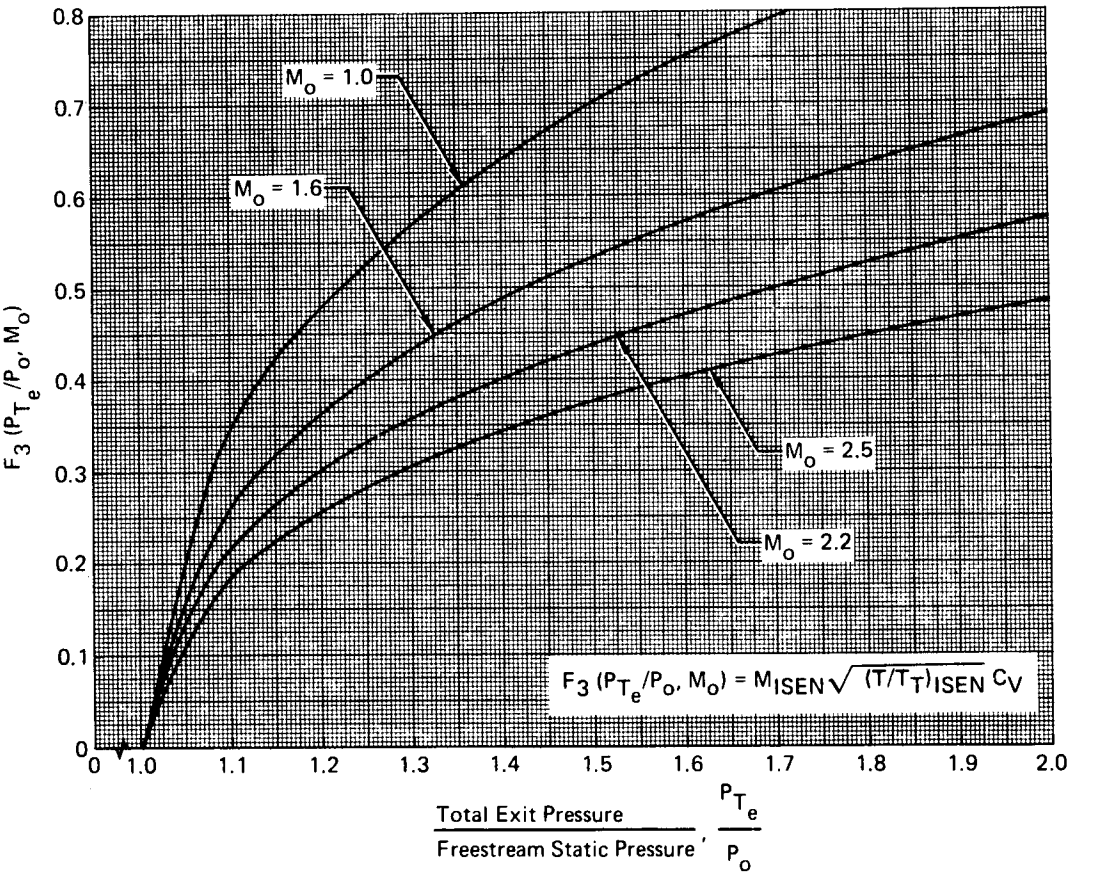

FIGURE B-5 - $F_3\left(\frac{P_{T_e}}{P_o}, M_o\right)$ vs $\frac{P_{T_e}}{P_o}$

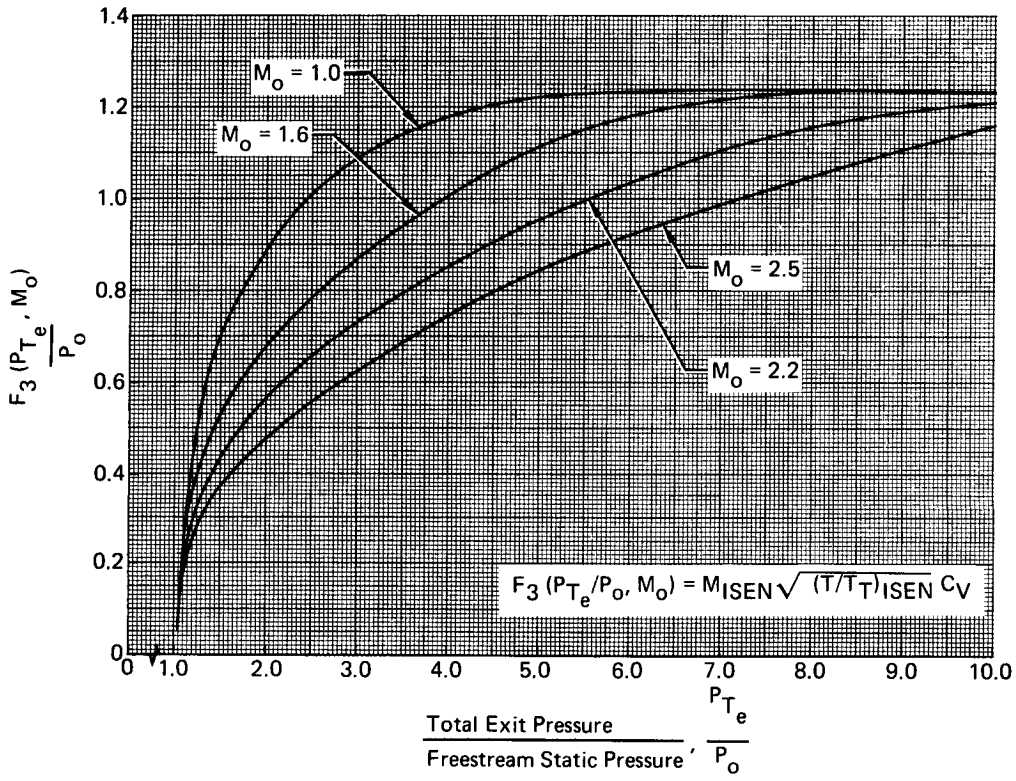

GP72-0979-113

FIGURE B-6 - $F_3 \left(\frac{P_{T_e}}{P_o}, M_o \right)$ vs $\frac{P_{T_e}}{P_o}$

REFERENCES - APPENDIX B

B-1 Anderson, D. C., "Efficiency of Flush and Protruding Oblique Exhaust Nozzles With and Without External Flow," UAC Research Dept. Rpt. R-0955-22, October 1957.

B-2 Crossen, J. W., "Efficiency of Flush Oblique Nozzles Exhausting into Supersonic Streams Having Mach Numbers Up to 4.0," UAC Research Department Rpt. R-1285-10, September 1959.

APPENDIX C

INLET DRAG ANALYSIS METHOD

Inlet spillage drag used to evaluate the effect of selected design variables on net propulsive force is analytically determined at supersonic conditions. The method of computing spillage drag by extending the technique developed in References C-1 through C-4 to two-dimensional inlets with pre-compression is described below.

SYMBOLS

A	Area
B	$(A^*/A)_o/(P_{t_s}/P_{t_o})$
C_D	Drag coefficient, D/qA
D	Drag force
h	Height
K	$\frac{Q + B \sin\eta}{1 - B \cos\eta}$
L	Normal shock wave distance upstream of cowl lip
M	Mach number
m	Mass flow rate
P	Pressure
Q	$\left[\frac{\text{Tan}\phi s}{ts} - \frac{\text{Tan}\phi o}{to}\right]\left(\frac{\cot^2\mu}{\frac{1}{ts} - \frac{1}{to}}\right)$
q	Dynamic pressure
t	$[\tan^2\phi - \tan^2\mu]^{1/2}$
V	Velocity
W	Inlet width
γ	Ratio of specific heats
δ	Compression surface angle
Δ	Increment

η	Maximum deflection angle for attached shock waves in plane flow
θ	Angle
μ	Mach angle (= $\mathrm{Sin}^{-1}[1/M]$)
ν	Locus angle
ρ	Density
ϕ	Local shock (wave) angle

Subscripts

add	Additive
c	Capture
i	Refers to conditions at the inlet cowl lip plane
in	Inlet
ℓ	Locus
m	Maximum capture
ns	Normal shock
S	Sonic
t	Total
VSI	Vortex sheet ingestion
W	Wave
o	Freestream conditions
1, 2, 3	Refers to regions behind the first, second, and third oblique shocks, respectively

In this discussion inlet drag is defined as inlet additive drag plus the change in cowl drag from maximum air capture conditions. In the procedure the additive drag is calculated at supersonic conditions and maximum capture, and then an inlet drag slope is calculated for reduced capture ratios. This slope is not constant with capture ratio but changes as the terminal normal shock moves upstream with reducing capture.

APPENDIX C

The additive drag at maximum capture conditions with all shock waves attached is illustrated in Figure C-1. The additive drag is calculated by pressure integration along the stagnation streamline.

$$D_{add} = [(p_1-p_o)\Delta h_1 + (p_2-p_o)\Delta h_2 + (p_3-p_o)\Delta h_3]W$$

where: p_1, p_2, and p_3 are the static pressures behind the respective shock waves.

The calculation procedure for the slope of the drag curve at reduced capture ratios with detached shock waves is given in References C-1, C-2, C-3, and C-4. This method can best be presented by first deriving the equations for a pitot inlet and then extending the analysis to inlets with pre-compression.

Pitot Intakes - Consider a pitot inlet in a supersonic flow field as illustrated in Figure C-2. Assuming the subsonic flow behind the shock wave is potential, incompressible flow:

$$D'add + D'cowl = 0$$

where: prime refers to the subsonic flow problem.

$$D'cowl = -D'add \tag{C-1}$$

Now: $$\Delta D'cowl = D'cowl - D'cowl_m \tag{C-2}$$

thus: $$\Delta D'cowl = -(pi-pw)\ A_c - (\rho AV^2)_i + (\rho AV^2)_w$$

Since D'cowl = 0 using the same reasoning as for Equation (C-1), the complete flow problem can be considered.

In equation form:

$$Din = Dcowl + Dadd$$

$$= \Delta Dcowl + Dcowl_m + Dadd$$

assuming that $\Delta Dcowl = \Delta D'cowl$

$$Din = Dcowl_m - (pi-pw)\ A_c - (\rho AV^2)_i + (\rho AV^2)_w$$

$$+ (pi-po)\ A_c + (\rho AV^2)_i - (\rho AV^2)_o$$

$$= Dcowl_m + (pw-pi)\ A_c + (\rho V^2|_w - \rho V^2|_o)A_o \tag{C-3}$$

From a momentum balance across the shock wave

$$AoPo + \rho AV^2|_o = AwPw + \rho AV^2|_w \tag{C-4}$$

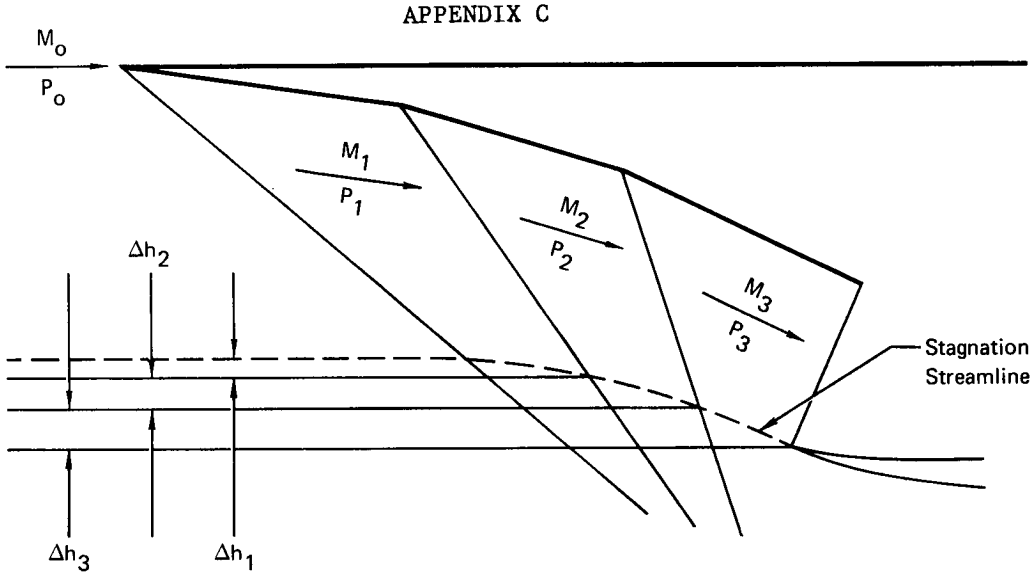

FIGURE C-1 - ADDITIVE DRAG AT MAXIMUM AIR CAPTURE CONDITIONS

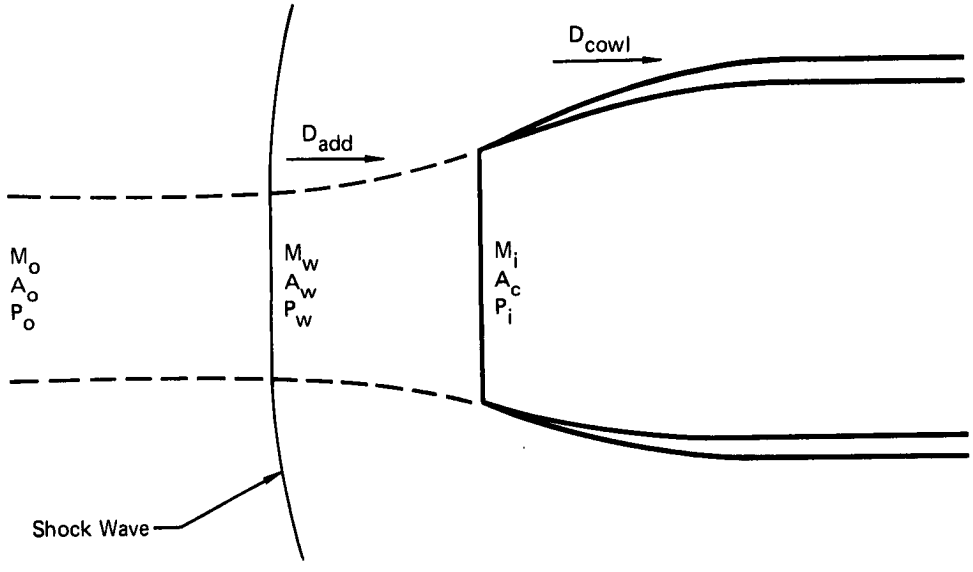

FIGURE C-2 - PITOT INLET IN SUPERSONIC FLOW FIELD GP72-0979-187

Noting that Aw = Ao and substituting Equation (C-4) into (C-3), we obtain

$$D_{in} = D_{cowl_m} + (A_c - A_o)\ (p_w - p_o)$$

$$C_{D_{in}} = \frac{D_{in}}{q_o A_c} = C_{D_{cowl_m}} + \left(\frac{p}{q}\right)_o \left(\frac{p_w}{p_o} - 1\right)\left(1 - \frac{A_o}{A_c}\right) \qquad \text{(C-5)}$$

$$\frac{\partial C_{D_{in}}}{\partial (A_o/A_c)} = -\left(\frac{p}{q}\right)_o \left(\frac{p_w}{p_o} - 1\right) \qquad \text{(C-6)}$$

Thus, the problem of drag estimation for a pitot intake is reduced to determining the cowl drag at maximum capture and then applying the normal shock pressure ratio to the deflected streamtube. Figure C-3 shows the excellent agreement of this data with experiment.

Inlets with Pre-Compression - Reference C-3 modified the above results for application to an axisymmetric centerbody inlet. It was noted that when the terminal normal shock is expelled sufficiently far that the spilled air is processed only by a normal (or strong) shock wave such as that shown in Figure C-4, the system can be considered to operate as a "pitot inlet."

Considering the capture ratio at the condition where the inlet streamtube passes through the intersection of the normal and oblique shock waves (termed the vortex sheet ingestion point), one can see from Figure C-5 that the drag for all lower capture ratio conditions is defined. As in Reference C-3, it is then assumed that the drag slope is linear between the maximum capture condition and the vortex sheet ingestion point. This assumption is unnecessary for a two-dimensional plane inlet, since the "pitot" inlet analogy can be used for flow along the ramp surface as shown in Figure C-6. However, when the normal shock intersects the oblique shock beneath the cowl lip, the approach of Reference C-3 is used, unless a solution of the three-shock intersection is impossible (to be discussed later).

Determining the "vortex sheet ingestion point" requires knowledge of the position of the terminal shock as a function of the capture ratio. Reference C-3 used Moeckel's theory (Reference C-2) for closed bodies and pitot inlets to determine the shock location for centerbody inlets. The following analysis was developed on a similar basis.

For a two-dimensional plane inlet the equation of the shock position is as follows:

$$\frac{L}{h_c} = \left(\frac{A_s}{A_c}\right)(Q + \tan\eta) - \left(\frac{A_o}{A_c}\right)(Q - \tan\eta) \qquad \text{(C-7)}$$

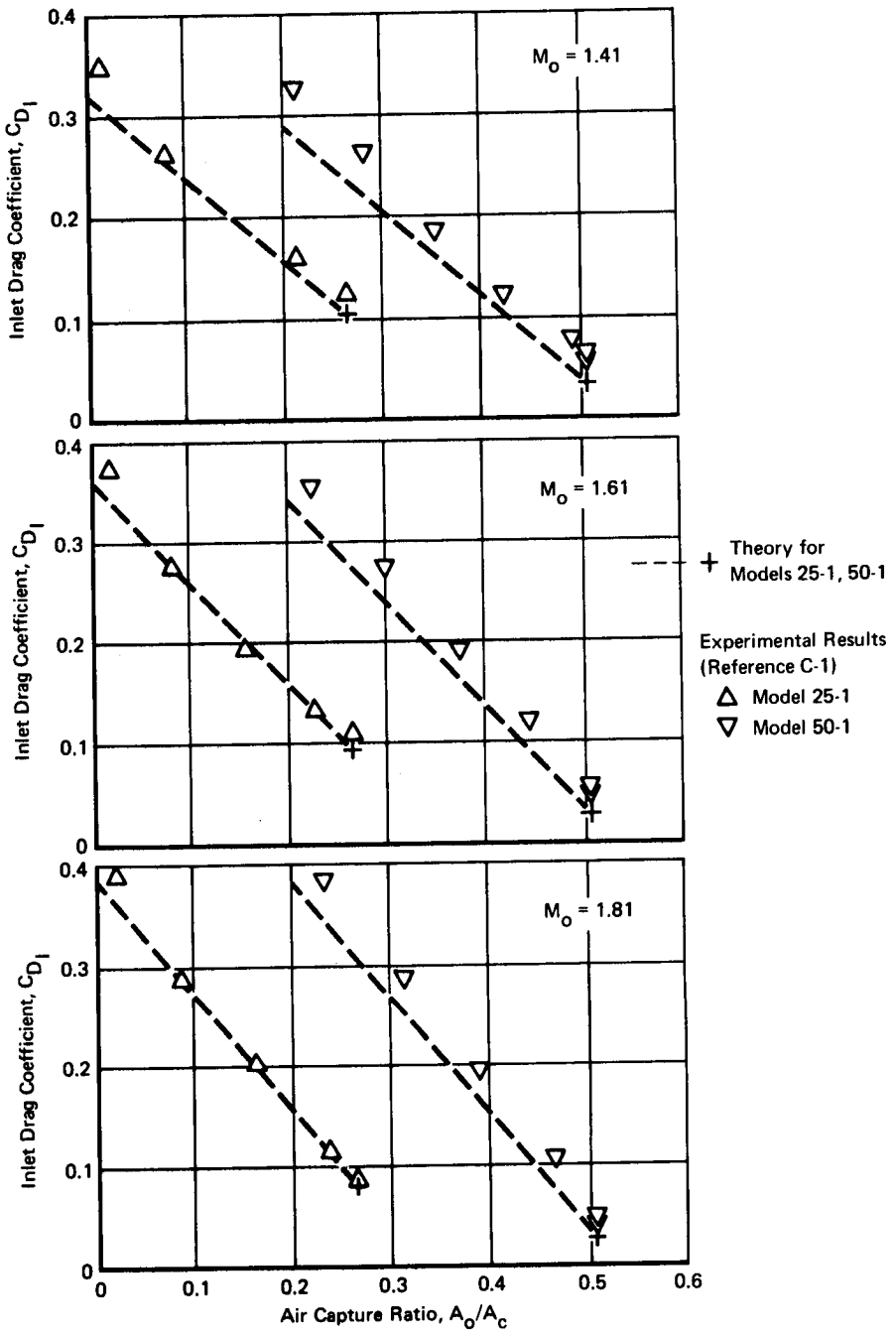

FIGURE C-3 - COMPARISON OF EXPERIMENTAL AND THEORETICAL INLET DRAG FOR AXISYMMETRIC INLETS

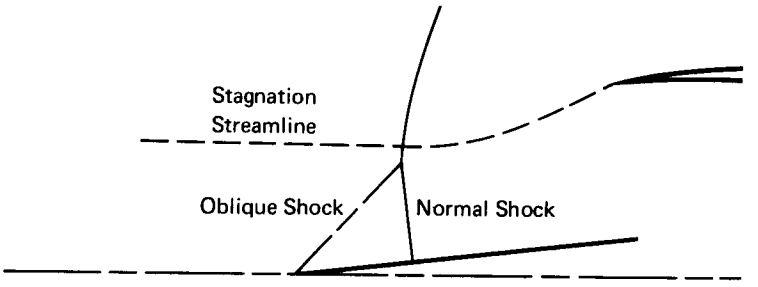

FIGURE C-4 - SUBCRITICAL OPERATION

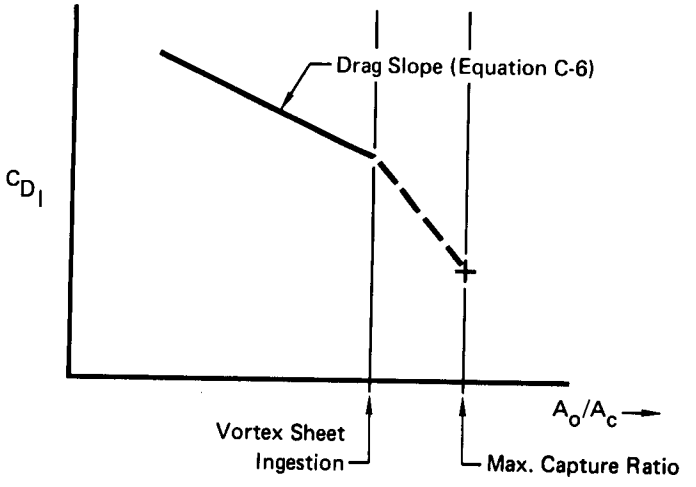

FIGURE C-5 - VARIATION OF INLET DRAG WITH AIR CAPTURE RATIO

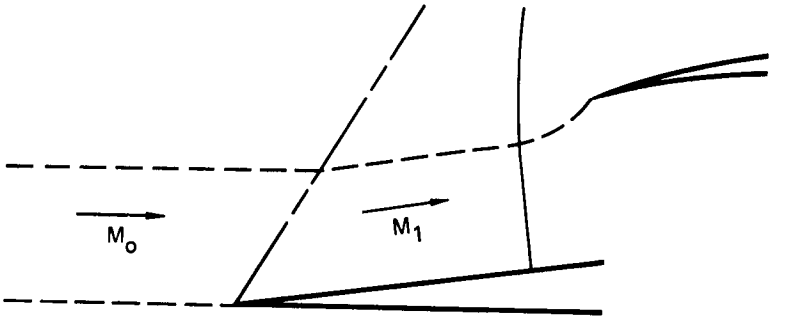

FIGURE C-6 - PITOT INLET ANALOGY FOR TWO-DIMENSIONAL PLANE INLET

GP72-0979-185

where:

$$Q = \frac{\cot^2 \mu}{(1/t_s - 1/t_o)} \left[\frac{\tan \phi_s}{t_s} - \frac{\tan \phi_o}{t_o} \right]$$

$$t = (\tan^2 \phi - \tan^2 \mu)^{1/2}$$

η = maximum wedge angle for attached flow at $M = M_o$.

By applying continuity to the flow across the sonic line:

$$\frac{A_s}{A_c} = \left(\frac{1 - B \cos\eta \, A_o/A_c}{1 - B \cos\eta} \right) \tag{C-8}$$

where:

$$B = \frac{(A^*/A_o)}{(P_{ts}/P_{to})}$$

substituting Equation (C-8) into (C-1):

$$\frac{L}{h_c} = K_o \left(1 - \frac{A_o}{A_c}\right) \tag{C-9}$$

where:

$$K_o = \left(\frac{Q + B \sin\eta}{1 - B \sin\eta} \right)_o$$

The shock geometry for a two dimensional plane inlet is shown in Figure C-7. It is seen that the shock position is a function of the freestream Mach number and the compression surface angle. The angle of the "third" shock wave, ϕ_o, must be calculated by solution of the intersection of the two shockwave polars for M_o and for M_1.

Equation (C-9) defines the slope of the captured streamtube when the shockwave-streamtube intersection at the shock defines an angle equal to $\cot^{-1}(K_o)$. The vortex sheet ingestion point is the intersection of this streamline locus and the oblique shock wave, hence:

$$\left(\frac{A_o}{A_c}\right)_{VSI} = \left(\frac{\cot \theta_\ell - K_o}{\cot \theta_\omega - K_o} \right) \tag{C-10}$$

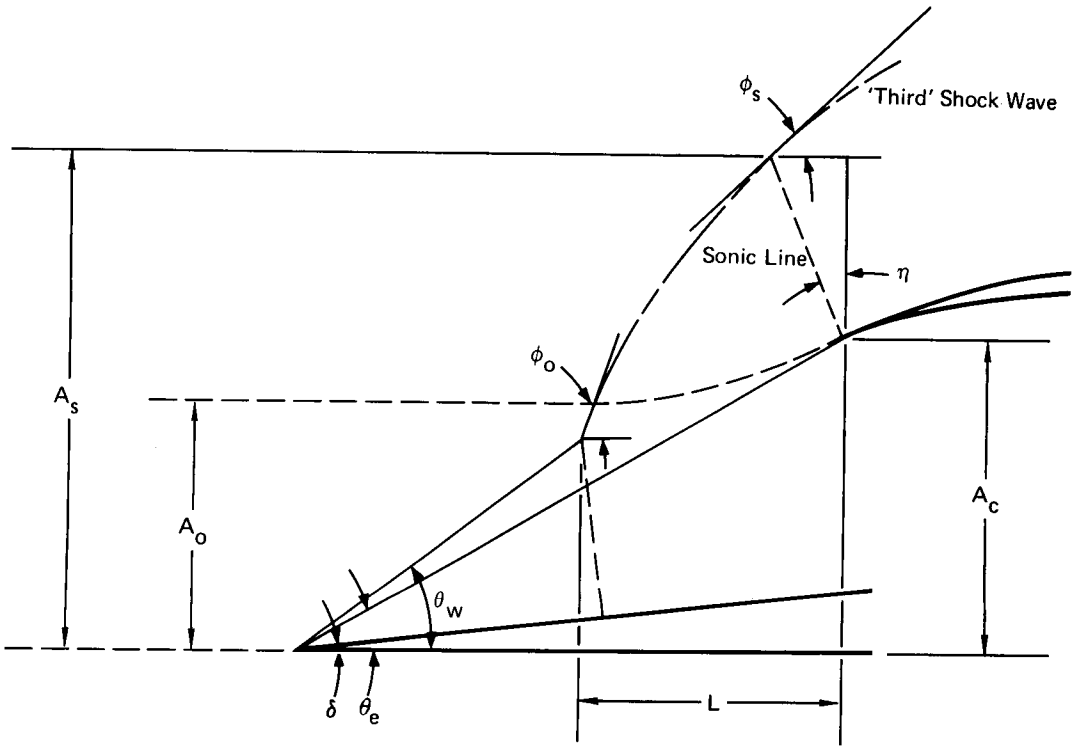

FIGURE C-7 - TWO-DIMENSIONAL PLANE INLET

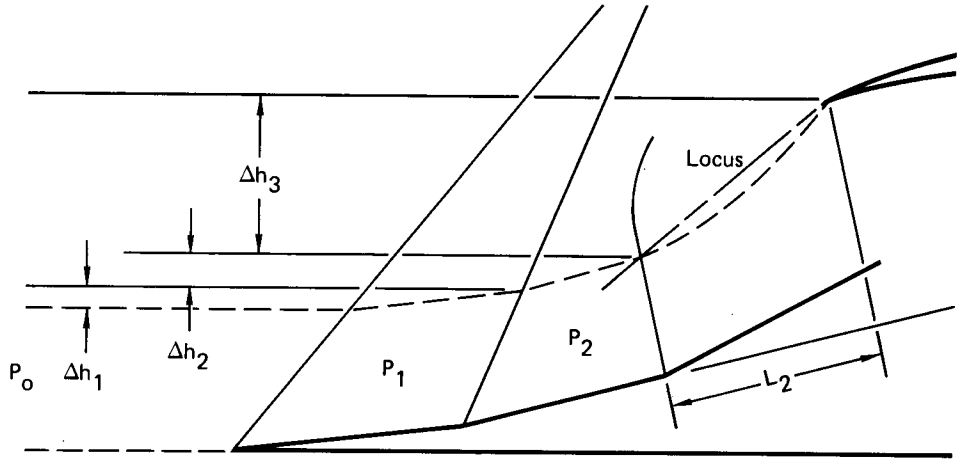

FIGURE C-8 - THREE RAMP INLET WITH THIRD SHOCK WAVE DETACHED

GP72-0979-183

Applying the theory to the flow on any surface of the wedge, the locus angle relative to the wedge is defined by $\cot^{-1}(K_1)$. Thus, an alternative value of $(A_o/A_c)_{VSI}$ is given by

$$\left(\frac{A_o}{A_c}\right)_{VSI} = \left(\frac{\cot \theta_\ell - \nu}{\cot \theta_\omega - \nu}\right) \tag{C-11}$$

where:

$$\nu = \delta + \cot^{-1}(K_1)$$

This value is not used unless a value of ϕ_o cannot be calculated. The drag coefficient at this capture ratio is given by substitution into Equation (C-5):

$$C_{D_{in}} = C_{D_{cowl_m}} + \left(\frac{p}{q}\right)_o \left(\frac{p_\omega}{p_o} - 1\right)\left[1 - \left(\frac{A_o}{A_c}\right)_{VSI}\right] \tag{C-12}$$

where the drag slope for lower captures is given by Equation (C-6). This analysis can be applied to a multiple compression surface inlet by referring all the surfaces to their respective approach conditions.

The drag at maximum capture conditions on a three-ramp inlet with the third shock wave detached is given by:

$$D_{in} = D_{cowl_m} + [\Delta h_1(p_1 - p_o) + \Delta h_2(p_2 - p_o) + \Delta h_3(p_3 - p_o)]W$$

where:

$$p_3 = p_2\left[\frac{p_{ns}}{p}\right]_{M=M_2}$$

and Δh_3 can be found from Equation (C-9) as follows:

The locus angle relative to the wind axes is

$$\nu_2 = \cot^{-1}(K_2) + \delta_2$$

thus

$$\Delta h_3 = \frac{L_2 \sin \nu_2}{\cos[\cot^{-1} K_2]}$$

APPENDIX C

A schematic of a three ramp inlet with the third oblique shock wave detached is presented in Figure C-8. This same technique can also be used for lower capture ratios by defining other values of L_2.

Comparison of Theory and Experiment - All the comparisons have been made with single wedge inlets. It is seen from Figures C-9 through C-12 that excellent agreement is obtained at all but the transonic flow region. The poor agreement which occurs at transonic conditions is due to the large sidespill for these conditions where the three-dimensional effects predominate.

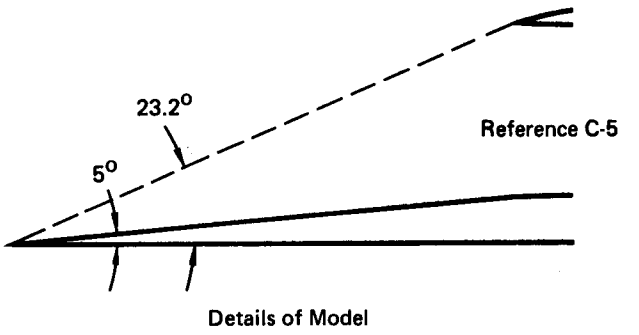

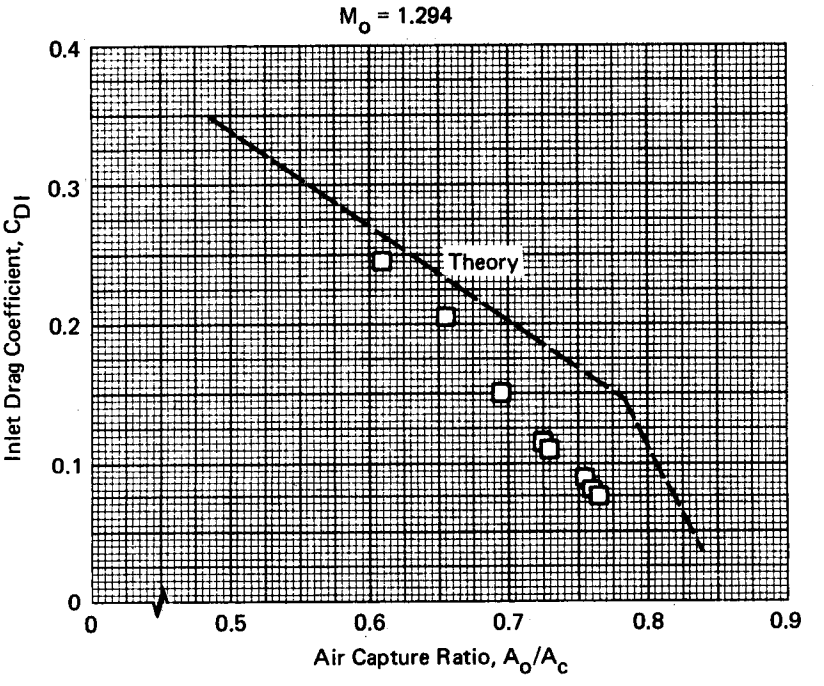

FIGURE C-9 - COMPARISON OF EXPERIMENTAL AND THEORETICAL INLET DRAG FOR 5° WEDGE CENTERBODY INLET

GP72-0979-184

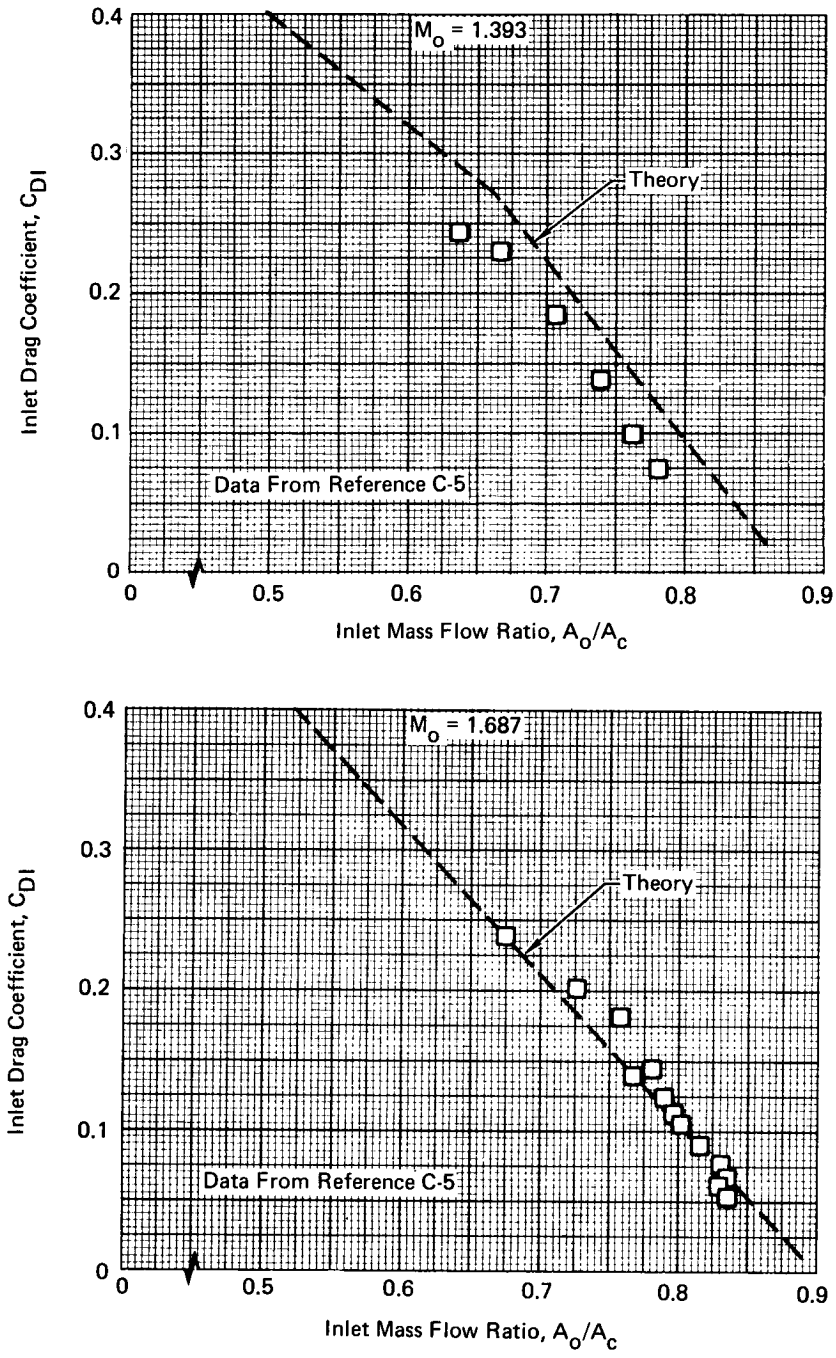

FIGURE C-10 - COMPARISON OF EXPERIMENTAL AND THEORETICAL INLET DRAG FOR 5° WEDGE CENTERBODY INLET

GP72-0979-180

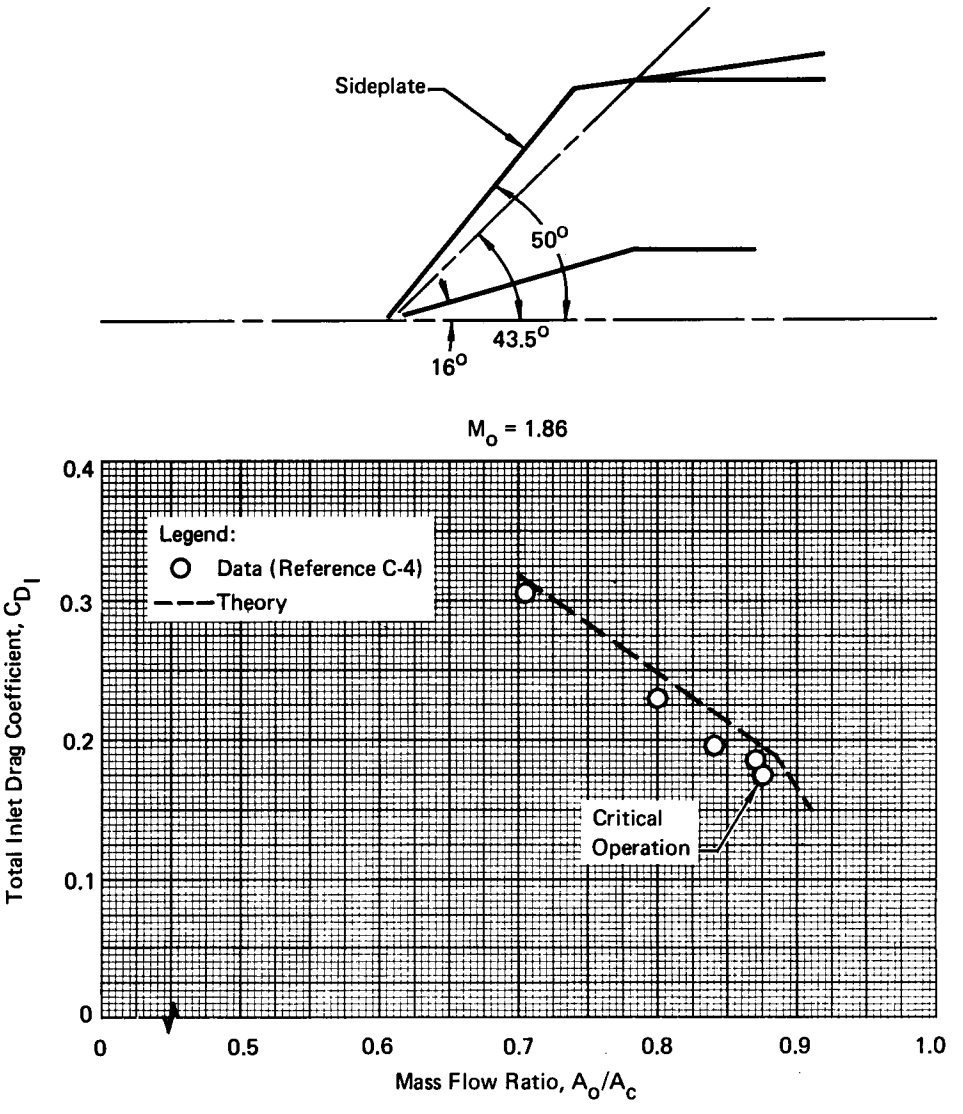

FIGURE C-11 - COMPARISON OF EXPERIMENTAL AND THEORETICAL INLET DRAG FOR 16° WEDGE CENTERBODY INLET

GP72-0979-181

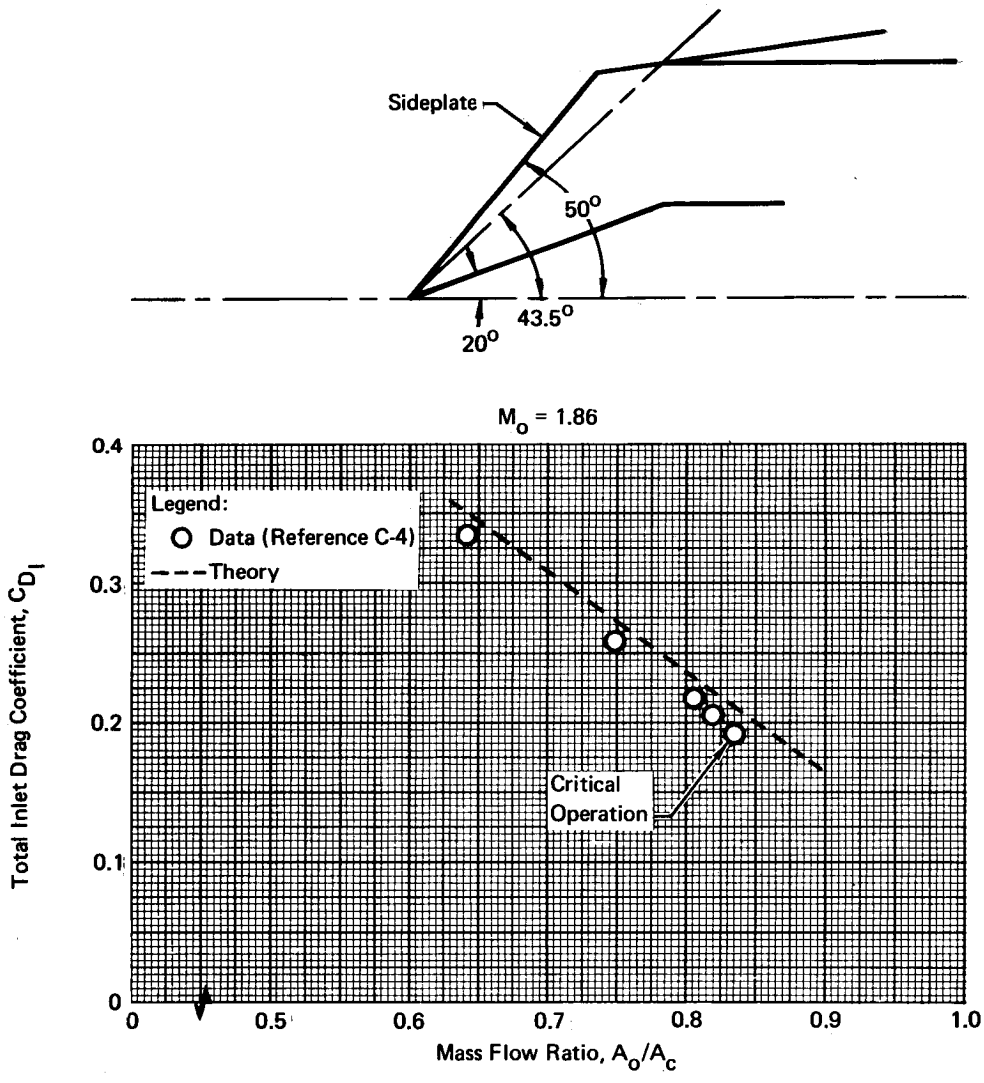

FIGURE C-12 - COMPARISON OF EXPERIMENTAL AND THEORETICAL INLET DRAG FOR 20° WEDGE CENTERBODY INLET

GP72-0979-182

REFERENCES - APPENDIX C

C-1 Frankel, L. E., "The External Drag of Some Pitot-Type Intakes at Supersonic Speeds," Brit. Report No. Aero 2380, 1950.

C-2 Moeckel, W. E., "Approximate Method for Predicting Form and Location of Detached Shock Waves Ahead of Plane or Axially Symmetric Bodies," NACA TN 1921, 1949.

C-3 Goldsmith, E. L. and Griggs, C. F., "The Estimation of Shock Pressure Recovery and External Drag of Conical Centre-Body Intakes at Supersonic Speeds," Brit. R&M No. 3035, 1959.

C-4 Dutton, R. A. and Goldsmith, E. L., "The Drag of Some Wedge Centre-Body Intakes at Mach Numbers of 1.56, 1.86, and 2.14," Brit. C.P. No. 968, 1966.

C-5 Petersen, M. W. and Tamplin, G. C., "Experimental Review of Transonic Spillage Drag of Rectangular Inlets," North American Aviation Inc. Report No. NA-66-10; Air Force Report No. APL-TR-66-30, May 1966.

REFERENCES

1. Fraenkel, L. E.: The External Drag of Some Pitot-Type Intakes at Supersonic Speeds, Part I. RAE Report Aero. 2380, June 1950.

2. Goldsmith, E. L.; and Griggs, C. E.: The Estimation of Shock Pressure Recovery and External Drag of Conical Centre-Body Intakes at Supersonic Speeds. ARC Technical Report R&M No. 3035, November 1953.

3. Anderson, D. C.: Efficiency of Flush and Protruding Oblique Exhaust Nozzles with and without External Flow. UAC Research Dept. Rpt. R-0955-22, October 1957.

4. Crossen, J. W.: Efficiency of Flush Oblique Nozzles Exhausting Into Supersonic Streams Having Mach Numbers up to 4.0. UAC Research Dept. Rpt. R-1285-10, September 1959.

5. Cebeci, T.; Smith, A. M. O.; and Wang, L. C.: A Finite-Difference Method for Calculating Compressible Laminar and Turbulent Boundary Layers. Douglas Aircraft Company Report No. DAC-67131, Part I, March 1969.

6. Cebeci, T.; Misinskis, G.; and Wang, L. C.: A Finite-Difference Method for Calculating Compressible Laminar and Turbulent Boundary Layers. Douglas Aircraft Company Report No. DAC-67131, Part II, May 1969.

7. Ferri, Antonio; and Nucci, Louis M.: The Origin of Aerodynamic Instability of Supersonic Inlets at Subcritical Conditions. NACA RM L50K30, January 1951.

☆ U. S. GOVERNMENT PRINTING OFFICE: 1975—635-047 / 50